Astrophysics and Space Science Library 456

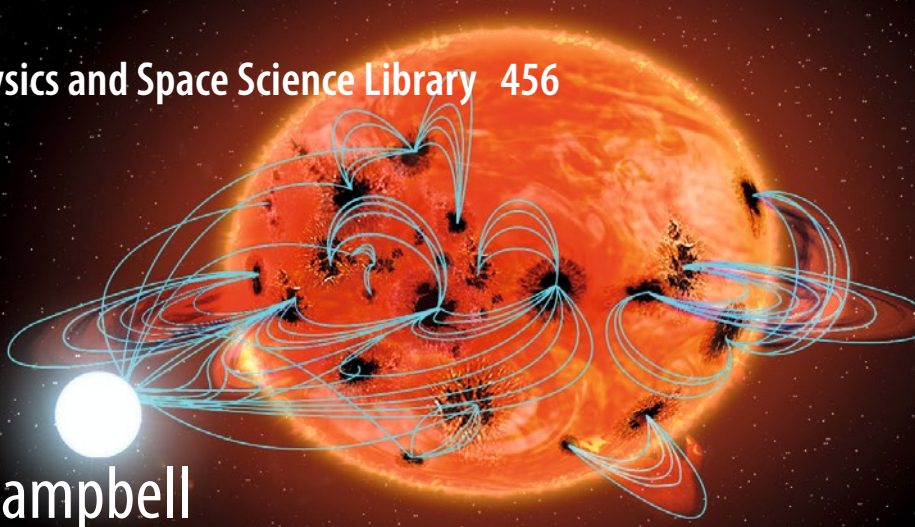

C. G. Campbell

Magneto-hydrodynamics in Binary Stars

Second Edition

ASSL

Springer

Magnetohydrodynamics in Binary Stars

Astrophysics and Space Science Library

C. G. Campbell

Magnetohydrodynamics in Binary Stars

Second Edition

Springer

C. G. Campbell
School of Mathematics
Statistics and Physics
Newcastle University
Newcastle upon Tyne, UK

ISSN 0067-0057 ISSN 2214-7985 (electronic)
Astrophysics and Space Science Library
ISBN 978-3-319-97645-7 ISBN 978-3-319-97646-4 (eBook)
https://doi.org/10.1007/978-3-319-97646-4

Library of Congress Control Number: 2018951221

Cover illustration: This artist's concept shows an interacting binary star system known as a polar (or a magnetic cataclysmic variable). The white star is a very dense, highly magnetic white dwarf in which the magnetic poles of the star are not aligned with its rotation axis. The cool, low-mass red star is distorted due to the strong gravity of the much more massive white dwarf. New research has provided the first direct observational evidence that significant stellar activity in the red star (such as large starspots, prominences, and flares) can be induced by interactions with the strong magnetic field of the white dwarf (blue lines), a phenomenon dubbed hyperactivity. Credit: P. Marenfeld and NOAO/AURA/NSF

This Springer imprint is published by the registered company Springer Nature Switzerland AG
The registered company address is: Gewerbestrasse 11, 6330 Cham, Switzerland

To my family, Aileen, Graham, Helena and Barney

Preface

Since the publication of the first edition, the area of magnetic fields in binary stars has continued to expand. The number of known AM Herculis binaries has more than doubled in the last 20 years, confirming the importance of these systems, and many new intermediate polars have also been discovered. The second edition is a major revision of the first, including new chapters covering the stellar magnetic fields and accretion disc magnetic winds. The development of numerical simulation techniques has enabled much progress to be made in understanding the nature of magnetically influenced accretion flows. These have been applied to study accretion streams in AM Her systems, disc disruption and curtain flows in systems containing strongly magnetic white dwarfs or neutron stars, and for disc magnetic winds. Dynamo simulations in rotating M dwarfs and in accretion discs have also been performed. Analytic and semi-analytic studies have made significant progress, and, when results are compared with those of the simulations, a clearer picture emerges for the structure and behaviour of these important systems.

The theme of the book remains the redistribution of angular momentum by magnetic stresses and the associated spin and orbital evolution. A comprehensive description of MHD in binary stars is given, from the pioneering work up to the latest results.

Chapter 1 contains a description of close binary stars and reviews the MHD problems arising in these systems. Chapter 2 describes the basic theory of MHD, considering the fundamental equations and their applications, including dynamo theory. The descriptions of force-free magnetic fields and those of wave motions have been extended. The theory of close binary stars is then presented, including the Roche model, a new section on tidal theory, mass transfer and the classic viscous accretion disc model. The essentials of spin dynamics are reviewed, in connection with the response of primary stars to applied torques.

Chapter 3 reviews AM Herculis binaries, including tables of all the confirmed systems and their main parameters. An extensive range of references is given, and the associated MHD problems are discussed. Chapter 4 addresses the approach to synchronism, involving inductive magnetic coupling. As well as the case with

vacuum surroundings, the effects of a magnetosphere are now also investigated. The resulting spin–orbit coupling can significantly affect the mass transfer rates and the modifications are calculated for gravitational wave driving and magnetic wind braking. The theoretically predicted synchronization time-scales are compared with those that can now be estimated from observations of asynchronous systems, which are in the process of evolving towards a synchronous state.

Chapter 5 considers the nature of the accretion stream, including the latest simulation results related to the extent of magnetic channelling for different magnetic orientations of the primary. The accretion torque is considered for total and partial magnetic channelling and for synchronous and asynchronous cases. Chapter 6 analyses how non-dissipative torques can balance the accretion torque, in two and three dimensions, to produce synchronous states. Magnetic and gravitational torques are considered. In Chap. 7, it is shown that even when a stable synchronous state exists, certain conditions must be satisfied for the primary to attain such a state. Formulae are given, in convenient forms, that can be used to compare theory with the observations.

Chapter 8 reviews binaries containing accretion discs which have been partially disrupted by the magnetic field of the accretor. These include the intermediate polars, the X-ray binary pulsars and the accreting millisecond pulsars. Detailed tables of these systems are given, together with an extensive range of references.

Chapters 9 and 10 have been completely rewritten. Chapter 9 addresses the mechanism of disc disruption due to the primary's magnetic field, together with an analysis of the accretion curtain flow that transfers matter from the inner edge of the disc to the stellar surface. This includes a review from the pioneering work up to the results of the latest numerical simulations, and these are compared with the results of analytic and semi-analytic studies. Chapter 10 considers the spin evolution of the accreting star due to its interaction with the disc and curtain flows, including an analysis of torque reversals.

Chapter 11 first reviews standard dynamo theory in accretion discs. The magnetorotational instability is then discussed together with its non-linear development, including MHD dynamos. The effects of a large-scale magnetic field on the radial and vertical structures of the disc are investigated, using more recent calculations.

Chapter 12 considers the sources of the stellar component magnetic fields, including dynamo operation in the secondary star. Simulations of dynamos in fully convective stars are outlined. The latest observations relating to the structure and strength of surface magnetic fields on rapidly rotating M dwarf stars are discussed. These are particularly relevant to theories of the maintenance of synchronism in AM Her binaries, and to theories of magnetic wind braking, together with tidal coupling, which are relevant to mass transfer rates above the period gap and in explanations of the gap. The possible effects of dynamo processes occurring during the common envelope evolutionary phase on white dwarf magnetic fields are described, and the effects of accretion on the surface magnetic fields of white dwarfs and neutron stars are discussed.

Chapter 13 describes the basic theory of stellar magnetic winds, with particular application to fast rotators. The theory is used to calculate braking torques on the

secondary stars in binaries and hence calculate mass transfer rates in systems above the period gap. The theory of the period gap, and why AM Her systems appear not to be affected by it, is discussed.

Chapter 14 considers accretion disc magnetic winds, beginning with the launching and field source problems. Wind structure models are described, from the early work up to the latest results. A detailed solution is presented for the structure of the disc and the well sub-Alfvénic region of the wind. It is shown that the spin rate of the accretor can affect the wind mass loss rate in the inner part of the disc, leading to significantly enhanced values near the star. Finally, wind flow stability is analysed, particularly in relation to potential field bending instabilities and the possible quenching effects of turbulent viscosity.

An appendix is included containing basic data, vector identities, vector operators in coordinate systems, special functions and derivations related to viscous force and gravitational torques.

SI units are employed, but magnetic field values are often quoted in Gauss since many astronomers and astrophysicists have a more immediate feel for magnitudes expressed in these units. It should be remembered that 1 Tesla $= 10^4$ Gauss.

The book should be of interest to observers as well as to theorists, with many useful formulae being included which can be compared to observations, and there is a wide range of references. Although the main focus is on binary stars, much of the material on accretion discs, stellar winds and disc winds has more general relevance. The text is mainly aimed at research workers, but some material (particularly in Chap. 2) could be useful for postgraduate courses in magnetic stellar astrophysics.

I am grateful to Michael Beaty for invaluable help with the LaTeX production of the manuscript. I should like to thank the Physics Department at Durham University for affording me the use of its facilities and for warm hospitality, with particular thanks to Chris Done, Carlos Frenk, Alan Lotts and Martin Ward. I am indebted to Ramon Khanna and Christina Fehling at Springer Nature for their kind support and advice during the publication process.

Newcastle, UK Chris Campbell

Contents

Chapter 1
Magnetism in Binary Stars

Abstract Magnetic fields are of fundamental importance in close binary stars due to the angular momentum transport that can occur via the action of magnetic stresses. The strongly magnetic AM Herculis stars and the intermediate polars are believed to account for approximately 25% of all cataclysmic variables. In the AM Her binaries an accretion disc cannot form and the accretion stream is magnetically channelled to form at least one localized column above the white dwarf surface. The strongly magnetic primary star usually spins in synchronism with the orbit, even though it will experience a strong magnetically influenced accretion torque. Partially disrupted discs form in the intermediate polars and an inner accretion curtain flow channels matter on to the primary. The X-ray binary pulsars and the accreting millisecond pulsars have magnetic neutron stars which partially disrupt their accretion discs.

Sub-thermal magnetic fields lead to a magnetorotational instability in accretion discs which is believed to be the source of the turbulent viscosity needed to account for the inflow. Disc dynamos can generate large-scale magnetic fields which can lead to radial transport of angular momentum, or its vertical removal via a channelled wind flow, depending on the magnetic field geometry. Dynamos can generate magnetic fields in secondary stars, and channelled wind flows lead to a braking torque. This, together with tidal coupling, can cause orbital angular momentum loss that is consistent with the mass transfer rates believed to occur in cataclysmic variables above the period gap. These topics are outlined here.

1.1 Close Binaries

A close binary system is one in which the separation of the component stars is sufficiently small for them to be strongly interacting. If the size of a stellar component is a significant fraction of the orbital separation, then its outer layers will be strongly distorted by the gravitational field of its companion. The rapid stellar rotation occurring in such systems gives additional distortion due to centrifugal force.

C. G. Campbell, *Magnetohydrodynamics in Binary Stars*, Astrophysics and Space Science Library 456, https://doi.org/10.1007/978-3-319-97646-4_1

The basic description of a binary system is based on a model proposed by Roche (1873), which was formulated in connection with planets and their satellites. In the application of this model to binary stars, the stellar components are treated as point gravitational sources so, relative to a frame with horizontal axes rotating with the line of stellar centres, a simple total potential results. This is the sum of the point gravitational potentials plus the centrifugal potential. For circular orbits, time-independent equipotentials can be found. Near the stellar centres these surfaces are almost spherical, but further away they become pear-shaped. Critical surfaces result when the apexes of the equipotentials due to each star touch. These surfaces contain the masses of their respective stars and are referred to as their Roche lobes. The point of contact, known as the inner Lagrangian point, L_1, is an unstable equilibrium position.

The Roche model gives a good approximation for the total potential surfaces in a binary system. A large fraction of the mass of a main sequence star is contained in its central regions and consequently its gravitational potential does not deviate greatly from that of a point source in its outer layers. This remains true for tidally and rotationally distorted stars, since the fractional density perturbations are greatest in their outer, most tenuous layers and these only make a small contribution to the potential. Work by Chandrasekhar (1933a,b) and Plavec (1958) showed that the equipotentials of distorted stars in close binaries approach those of the Roche model to a very good approximation. The gravitational potential of the compact star can be taken to be monopolar. The more detached a star is from its Roche lobe, the weaker its tidal distortion.

Wood (1950) suggested dividing close binary stars into two classes; one containing systems in which both stellar surfaces lie beneath their Roche lobes, known as detached systems, and the other containing binaries in which at least one component fills its Roche lobe. Kopal (1955) suggested dividing the latter class into two groups; the first containing systems in which only one component fills its Roche lobe, known as semi-detached systems, while in the second group both components fill their Roche lobes to form contact binaries.

Most work has been focused on semi-detached systems in which a main sequence star fills its Roche lobe and orbits with a more massive compact component, the latter usually being a white dwarf or a neutron star. The main sequence component is generally referred to as the secondary star, and the compact object as the primary star. Systems with orbital periods of < 10 h have lower main sequence secondary stars.

Strong interest in close binary stars began when photometric work by Linnell (1950) on a new eclipsing variable, later designated UX Ursae Majoris, established it as the first known representative of a new class of subdwarf binaries. Subsequently, Walker (1956) discovered that Nova Herculis 1934 is an eclipsing variable (DQ Herculis) consisting of a pair of subdwarfs with an orbital period of 4 h and 39 min. Further searches among stars of this type led to the discovery of the binary nature of several other post-novae (e.g. GK Per/Nova Persei 1901; WZ Sge/Nova Sagittae 1913 and 1946). This supported the contention that nova outbursts occur only among the components of close binary systems. The stars SS Cygni (Joy 1956)

and U Geminorum (Mumford 1962), which exhibit more frequent outbursts of light than classical or recurrent novae, were also found to be short period binaries. This, together with the foregoing discoveries, suggested that all eruptive variables, with the possible exception of supernovae, are binary objects.

Observations of close binaries led to theoretical models. Crawford and Kraft (1956) realized that the secondary star in AE Aqr fills its Roche lobe. They interpreted the observed emission lines as arising from gas passing from the secondary to orbit around the white dwarf primary. Krzeminski (1965) suggested that the cooler star in U Geminorum fills its Roche lobe, and that the hotter star is surrounded by a rotating disc. A similar model had been proposed for DQ Herculis by Kraft et al. (1962). This picture was later adopted as the standard model of short period semi-detached binaries containing white dwarf primary stars, designated the cataclysmic variables (Warner and Nather 1971; Smak 1971).

The lobe-filling secondary transfers material, through the unstable inner Lagrangian region, to an accretion disc surrounding the compact primary. At the point of intersection of the stream and the disc a shock is formed, producing a bright spot on the disc. This manifests itself as a prominent hump in the optical light curve of those systems in which emission from the rest of the disc is weak (e.g. many dwarf novae in their quiescent states). Matter spiralling in through the disc liberates its binding energy and is accreted on to the surface of the primary. If the mass transfer time-scale greatly exceeds the thermal adjustment time-scale of the secondary, then the star remains in thermal equilibrium and consequently shrinks as it loses mass. However, material is kept in contact with the L_1 point since the secondary's Roche lobe also shrinks as a result of orbital angular momentum loss. This is driven by gravitational radiation losses, or by a magnetically influenced wind flowing from the secondary together with tidal coupling to the orbit. Figure 1.1 illustrates the basic structure of a cataclysmic variable. A detailed description of the observational techniques used in the study of cataclysmic variables is given in Warner (1995).

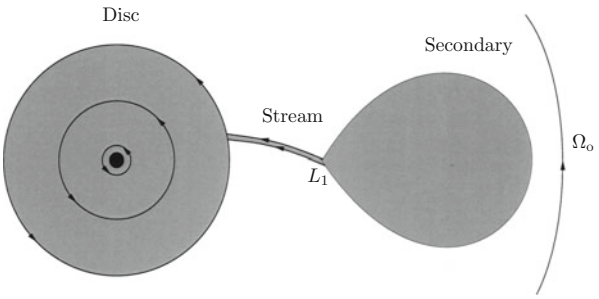

Fig. 1.1 The standard model of a cataclysmic variable, viewed down the rotational pole of the system. The tidally and rotationally distorted secondary loses matter from the unstable L_1 region. The resulting stream feeds an accretion disc, centred on the white dwarf primary, through which matter slowly spirals inwards

In a standard cataclysmic variable the primary star is a non-magnetic white dwarf, and the accretion disc extends down to its surface. Originally the designation cataclysmic variable included dwarf novae, nova-like variables and old novae. This was extended to include the AM Herculis binaries and the intermediate polars, which contain strongly magnetic white dwarf primary stars. In the AM Herculis systems the accretion disc is totally disrupted due to the influence of the primary's magnetic field, and a channelled stream results, while the intermediate polars accrete from a partially disrupted disc via curtain flows. These magnetic systems are now believed to account for approximately 25% of all cataclysmic variables. Some X-ray binary pulsars and the accreting millisecond pulsars have strongly magnetic neutron stars accreting material from a disrupted disc, and so these systems have a similar accretion geometry to that of the intermediate polars.

1.2 Magnetic Fields in Binaries

The presence of a strong magnetic field can significantly modify the standard structure of a close binary. A white dwarf or neutron star is capable of sustaining a far stronger magnetic field than a main sequence star. Such compact objects contain highly conducting degenerate matter and so are generally believed not to require dynamo action to sustain their magnetic fields, which have very long decay times (see Landstreet 1994 for a discussion of the fossil field theory for white dwarfs, and Chap. 12 for further discussion). Hence the strongest source of magnetism in binaries is usually the compact primary. Strong magnetic fields have been detected via linear and circular optical polarization, resulting from cyclotron radiation emitted by accreting gas. Photospheric Zeeman split spectral lines are sometimes observed. X-rays are emitted from hot shocked gas in accretion columns, and pulsation periods in the observed intensity result due to the rotation of the primary.

The magnetic field effect is strongest in the AM Herculis systems. AM Her was identified as an X-ray source by Hearn et al. (1976). Linear and circular polarization were observed in the V and I spectral bands by Tapia (1977), of a strength that indicated the presence of a high magnetic field. Many similar systems were subsequently found and these objects now form an important class of close binary stars. The primary stars are white dwarfs with strong magnetic moments. The secondary stars are M or K dwarfs and the orbital periods range from 1.3 to 4.8 h, with the exception of one system having a period of 8.0 h. The magnetic field completely prevents the formation of an accretion disc. Matter lost from the L_1 region of the secondary becomes channelled by the primary's magnetic field and converges to form an accretion column above its surface. Accreting supersonic material passes through a standing shock at the top of the column and undergoes compressional heating. The intensity of the radiations emitted from the hot post-shock flow is observed to be modulated due to the changing orientation of the column resulting from the primary's rotation.

One of the most striking features of the AM Her binaries is that the angular velocity of the primary appears to be the same as that of the orbit. This synchronization, unique amongst close binaries, is most likely related to the strong magnetic field. The magnetic field interacts with the accretion stream and the secondary star. It is probable that the secondary star has a dynamo-generated magnetic field, since it has at least a deep convective envelope and is rapidly rotating.

The X-ray binary pulsars were discovered by Giacconi et al. (1971). In these systems a lobe-filling secondary transfers material on to a magnetic neutron star. The magnetic moment is not as large as that of a white dwarf in an AM Her system, so a partially disrupted accretion disc forms. After passing through the disc, material is transferred via a magnetically channelled curtain flow to form accretion columns above the neutron star. A range of spin behaviour of the neutron star is observed. Magnetic interaction with the disc, as well as field channelling of material, will generate a torque on the neutron star. A similar disrupted disc model is adopted for the intermediate polars, in which the primary is a white dwarf with a surface magnetic field typically an order of magnitude less than in the AM Her binaries. The model is also used for the accreting millisecond pulsars.

Accretion discs require an anomalous form of viscosity to explain their mass inflow rates. Turbulence has been employed to generate the necessary stresses for the radial transport of angular momentum, but an instability to explain the generation of such turbulence has not been found in a non-magnetic disc. However, this apparent dilemma is believed to have been resolved by Balbus and Hawley (1991) who showed that Keplerian discs are dynamically unstable in the presence of a weak poloidal magnetic field. Subsequent work has shown that this magnetic shear instability leads to the generation of turbulence and can result in a self-sustaining dynamo. The resulting stresses due to the large-scale magnetic field can lead to radial transport of angular momentum at least comparable to the viscous transport. Hence magnetic fields are believed to play a fundamental role in accretion discs. Also, a magnetic field of suitable geometry, together with a disc wind, can lead to effective loss of angular momentum and make a major contribution to driving the inflow. Wind outflows can develop into channelled jets in the inner region of the disc.

It is likely that the secondary star in most close binary systems has a magnetic field. Fast rotation and the presence of convection can lead to dynamo action and the generation of large-scale magnetic fields. A magnetically channelled wind from a tidally synchronized secondary is invoked to generate the orbital angular momentum loss necessary to sustain mass transfer in systems with periods of $P \gtrsim 3\,\mathrm{h}$. A transition to gravitational radiation driving for $P \lesssim 3\,\mathrm{h}$ may be related to the period gap of width 2–3 h in which systems are not observed because the mass transfer process, which is the main luminosity source, has temporarily ceased in binaries evolving through this period range.

1.3 Magnetohydrodynamics

The theory of magnetohydrodynamics describes the fluid mechanics of plasmas and the behaviour of their magnetic fields. Maxwell's equations for the electromagnetic field are combined with the equations of hydrodynamics. For non-relativistic flow speeds, the magnetic force can be expressed as a function of the field **B** and its spatial derivatives, and this dominates the electric force. The electric field and charge density can be eliminated from the equations, and so do not have to be explicitly considered. Faraday's law of induction, combined with the Lorentz transformations and Ohm's law, shows how **B** is affected by the fluid motions and diffused with an associated dissipation of the electric currents. The momentum equation accounts for the effect of the magnetic force on the motions, and the heat equation has a source due to the dissipation of currents.

Simplified forms of the equations can be used in some problems. For example, the diffusion term in the induction equation can be ignored if the diffusion time-scale is much longer than the flow time-scale. In this case a useful picture emerges in which the magnetic field lines are frozen to the plasma. Material is therefore threaded on to field lines which are advected and distorted by the flow. In the other extreme, the effect of the velocity term is small and the induction equation becomes purely diffusive, so material can move freely across field lines. Kinematic theory is appropriate when the magnetic force only has a small effect on the motions. The velocity solution of the non-magnetic fluid equations can then be used in the induction equation to calculate **B**.

Dynamo theory describes how magnetic fields can be generated and sustained by fluid motions, in the presence of dissipation. Mean-field equations describe the generation of poloidal and toroidal fields due to differential rotation and turbulence, coupled with stratification. Certain conditions are necessary for dynamo action, and various types of dynamos can be defined. Dynamo theory beyond the kinematic approach has been developed to an increasing extent, to incorporate dynamical and thermal effects.

Large-scale magnetic fields can have associated stresses that lead to the transport of angular momentum. Such magnetic transport can occur in many different situations in binary stars, including coupling between the stars, spin-orbit coupling, accretion stream channelling, coupling between a disc and its accreting star, radial and vertical transport of angular momentum in discs and braking due to magnetic stellar wind flows.

1.4 Types of Problems

The synchronization problem in AM Her binaries involves a range of MHD problems. An asynchronous primary, having a magnetic axis tilted to its rotation axis, causes the tidally synchronized secondary star to experience a time varying

magnetic field and shears due to magnetospheric motions. Electric currents will be induced in the secondary and primary stars, as well as in the connecting magnetosphere. Toroidal magnetic field will be created and the resulting magnetic stresses will lead to torques on the stars and on the orbit. Magnetic spin-orbit coupling causes the primary to approach synchronism on a time-scale less than the lifetime of the binary. An over-synchronous primary leads to magnetic orbital torques which can reduce the mass transfer rate.

Magnetic channelling of the accretion stream results in a 3D flow and an accretion torque with components normal and parallel to the orbital angular momentum vector. These must be balanced, in a stable way, if synchronous states are to exist. A large-scale magnetic field generated in the secondary star can give a balancing torque on the primary. Such a field could be produced by dynamo action. Distortion of the primary by non-radial internal magnetic forces leads to a tidal torque which can play a part in creating a synchronous state. Even if such a state exists, conditions are necessary to attain corotation.

The problem of inner disc disruption in the intermediate polars, and in some X-ray binary pulsars and the millisecond accreting pulsars, involves the MHD interaction of the stellar magnetic field and its magnetosphere with the disc. Poloidal field which penetrates the disc is sheared due to the differential rotation between the disc and magnetosphere to create toroidal field and associated electric currents. Magnetic heating of the disc inside the corotation radius leads to pressure increases which cannot be balanced by the vertical gravity and disruption occurs over a narrow radial region. Vertical pressure gradients in this region accelerate material through a sonic point beyond which it flows through a channelled curtain to accrete on to the star. The star and the disc can exchange angular momentum via magnetic torques and this affects the stellar spin evolution.

Magnetorotational instability due to sub-thermal magnetic fields in Keplerian accretion discs leads to the generation of turbulence. This, and the strong radial shear, can result in dynamo action which creates large-scale magnetic fields. Fields having quadrupolar symmetry result in the outward radial transport of angular momentum which drives an inflow through the disc. If a dipole symmetry magnetic field is generated then channelled wind flows may be favoured and these can be very effective at removing angular momentum and causing disc inflows.

Dynamos are likely to generate a magnetic field in the secondary star, since it has at least a deep convective envelope and is rapidly rotating. A magnetically channelled stellar wind will cause magnetic braking and drive the secondary into an under-synchronous state. Tidal torques will then spin the star up at the expense of orbital angular momentum. This can drive mass transfer at rates consistent with those occurring in CVs above the period gap. A change in the structure of the stellar magnetic field due to the transition to fully convective stars, involving the vanishing of a tachocline region connecting the radiative core to the convective envelope, may explain the creation of the period gap.

References

Balbus, S.A., Hawley, J.F., 1991, ApJ, 376, 214.
Chandrasekhar, S., 1933a, MNRAS, 93, 390.
Chandrasekhar, S., 1933b, MNRAS, 93, 449.
Crawford, J.A., Kraft, R.P., 1956, ApJ, 123, 44.
Giacconi, R., Gursky, H., Kellogg, E., Schreier, E., Tananbaum, H., 1971, ApJ, 167, L67.
Hearn, D.R., Richardson, J.A., Clark, G.W., 1976, ApJ, 210, L23.
Joy, A.H., 1956, ApJ, 124, 317.
Kopal, Z., 1955, AnAp, 18, 379.
Kraft, R.P., Matthews, J., Greenstein, J.L., 1962, ApJ, 136, 312.
Krzeminski, W., 1965, ApJ, 142, 1051.
Landstreet, J.D., 1994, in Cosmical Magnetism, ed., Lynden-Bell, D., Kluwer Academic Publishers, Dordrecht.
Linnell, A.P., 1950, HarCi, 455, 1.
Mumford, G.S., 1962, S&T, 23, 135.
Plavec, M., 1958, LIACo, 8, 411.
Roche, E.N., 1873, Ann de l'Acad Sci Montpelier, 8, 235.
Smak, J., 1971, AcA, 21, 15.
Tapia, S., 1977, ApJ, 212, L125.
Walker, M.F., 1956, ApJ, 123, 68.
Warner, B., 1995, Cataclysmic Variable Stars, Cambridge University Press.
Warner, B., Nather, R.E., 1971, MNRAS, 152, 219.
Wood, F.B., 1950, ApJ, 112, 196.

Chapter 2
Theoretical Prerequisites

Abstract The essentials of plasma physics are outlined in relation to the derivation of the equations describing magnetohydrodynamics. The Maxwell equations are then combined with the equations of hydrodynamics to derive the equations of MHD, with viscosity and the associated energy transport equations included. The main types of magnetic wave solutions are derived, and their relevance to different types of flows is considered. Mathematical representations of the magnetic field are given, with application examples. Magnetic diffusion processes and their related transport coefficients are discussed, and then the basic theory of mean-field dynamos is presented, including a classification of the various types.

The theory of close binary stars is presented, including the Roche model and an outline of tidal theory. Mass transfer, due to Roche lobe overflow, is considered and the driving mechanisms of gravitational radiation and magnetic braking are described. The steady viscous accretion disc model is presented, and the fundamental time-scales in discs are derived. The essentials of spin dynamics are given, in relation to the response of compact stellar components to torques and in the analysis of stability.

2.1 Introduction

This chapter contains the basic essentials of magnetohydrodynamics, binary star theory and spin dynamics. In Sect. 2.2 the necessary conditions for classical fluid dynamics to apply to plasmas are discussed. The equations describing the electromagnetic field are then combined with the equations of fluid mechanics, to first order in v/c, to form the equations of MHD, and their general properties are discussed. Hydromagnetic wave motions, which redistribute energy and momentum, are derived, followed by convenient mathematical representations of the field **B**. The decay of **B** fields and various types of diffusion processes are then considered. In Sect. 2.3 the basic dynamo problem is formulated and the main types of mean-field dynamos are defined.

Section 2.4 presents the theory of close binary stars. Firstly, the Roche model is considered and the unstable nature of the inner Lagrangian point is analysed. A

C. G. Campbell, *Magnetohydrodynamics in Binary Stars*, Astrophysics and Space Science Library 456, https://doi.org/10.1007/978-3-319-97646-4_2

summary of tidal theory is given, related to the synchronization of the secondary star. Mass transfer and the subsequent formation of an accretion disc are then addressed. The classic steady viscous accretion disc model is presented, since this acts as a basis for understanding magnetic modifications in discs. The time-dependent disc equations are formulated and various important time-scales are defined, and the principles of viscous diffusion and instability are discussed.

Section 2.5 considers rigid body dynamics, which is relevant to the response of compact primary stars when they are subjected to torques. A highly magnetic primary is likely to have some distortion from spherical symmetry due to non-radial internal magnetic forces. Hence, in general, its angular velocity and angular momentum vectors will not be parallel and full spin dynamics theory is needed to analyse the motion. The relevant frame transformations are discussed. The spin evolution of such stars is of central importance and accurate observations relating to this are available in a variety of systems.

2.2 Behaviour of B Fields in Plasmas

2.2.1 Plasma Fluids

A plasma is a mixture of an electron gas and an ion gas. The electrons and ions interact with each other through their Coulomb attractions and repulsions. A plasma differs from an atomic or molecular gas in that its inter-particle forces can be longer range than the short-range forces between neutral particles. A charged particle can interact with many others at any instant. The presence of a large-scale magnetic field can further complicate matters by introducing anisotropic properties. However, if certain conditions are met, the bulk motions in a plasma can be described by classical fluid mechanics, with additional effects due to a large-scale magnetic field.

If the ions result from atoms each losing Z electrons of charge magnitude e, then the total charge density is

$$\rho_{\rm c} = n_{\rm i} Ze - n_{\rm e} e, \tag{2.1}$$

where $n_{\rm i}$ and $n_{\rm e}$ are the number densities of ions and electrons, respectively. Any local charge separation cannot be large, since this would result in a very strong electric field rapidly restoring neutrality. It follows that

$$n_{\rm e} \simeq Z n_{\rm i} \tag{2.2}$$

and $\rho_{\rm c}$ is small. This equation is referred to as the plasma approximation. Since $m_{\rm i} \gg m_{\rm e}$, where $m_{\rm i}$ and $m_{\rm e}$ are the ion and electron masses, electrons are relatively easily accelerated. A small local excess of electrons results in a restoring electric

field leading to plasma oscillations about the neutral state with a characteristic frequency

$$\omega_{\mathrm{p}} = \left(\frac{n_{\mathrm{e}} e^2}{\epsilon_0 m_{\mathrm{e}}}\right)^{\frac{1}{2}}, \tag{2.3}$$

where n_{e} is the unperturbed electron number density and ϵ_0 the permittivity of free space. This is referred to as the plasma frequency.

The length-scale associated with charge oscillations is $l_{\mathrm{c}} \sim v_{\mathrm{e}}/\omega_{\mathrm{p}}$, where v_{e} is a typical electron velocity. The electric field resulting from the charge imbalance is limited in range to $\sim l_{\mathrm{c}}$ by the shielding effect of the electrons. In the absence of perturbations charge neutrality would hold, with l_{c} vanishing and the electrons totally shielding the ions. However, the formation and maintenance of the plasma state requires sufficiently high temperatures and hence charge fluctuations due to the thermal motions of the electrons are always present. A fundamental shielding length $l_{\mathrm{c}} = \lambda_{\mathrm{D}}$, known as the Debye length, can be defined by taking v_{e} to be the mean thermal velocity of an electron. Hence

$$v_{\mathrm{e}} \sim \omega_{\mathrm{p}} \lambda_{\mathrm{D}} = \left(\frac{kT}{m_{\mathrm{e}}}\right)^{\frac{1}{2}}, \tag{2.4}$$

where k is Boltzmann's constant and the electron temperature $T_{\mathrm{e}} = T_{\mathrm{i}} = T$ for a gas in local thermodynamic equilibrium. The use of (2.3) for the plasma frequency ω_{p} then yields

$$\lambda_{\mathrm{D}} = \left(\frac{\epsilon_0 kT}{n_{\mathrm{e}} e^2}\right)^{\frac{1}{2}}. \tag{2.5}$$

This is the length-scale of local electric fields resulting from thermally induced charge separation, and hence it gives an effective range for Coulomb collisions in a plasma. On length-scales $< \lambda_{\mathrm{D}}$ thermal charge separation is significant and the plasma approximation (2.2) does not hold.

Provided the macroscopic length-scale L satisfies $L \gg \lambda_{\mathrm{D}}$, the electromagnetic field may be divided into a large-scale, collective field and a small-scale, random field. The large-scale field has the macroscopic charge density and current density as its sources. The small-scale random field is essentially the sum of the unshielded Coulomb fields of individual particles; it acts to keep the velocity distribution function close to a Maxwellian form, and to inhibit the drift of electrons relative to ions. The plasmas occurring in binary stars generally well satisfy $L \gg \lambda_{\mathrm{D}}$, so the macroscopic field equations can be employed.

In discussing plasma properties, a mean free path can be defined, using elementary kinetic theory, by

$$\lambda = \frac{1}{n\pi b^2}, \tag{2.6}$$

where n is the number density of scattering particles and b is an effective collision radius. The quantity πb^2 is a collision cross-section. For elastic scattering, such as electrons by ions, an estimate for b can be made by equating the Coulomb interaction energy to the mean thermal kinetic energy, giving

$$b \simeq \frac{Ze^2}{6\pi\epsilon_0 kT}. \tag{2.7}$$

An estimate for the average value of b including long-range scattering, employing the differential Rutherford cross-section, increases (2.7) by a factor of $\simeq 9/4$.

If the plasma behaves like a nearly perfect gas, the Coulomb interaction energy at the mean inter-particle distance of $\simeq n^{-1/3}$ must be small compared to the thermal energy. This requires

$$\frac{Ze^2 n^{\frac{1}{3}}}{4\pi\epsilon_0} \ll \frac{3}{2}kT \tag{2.8}$$

which, by the use of (2.7), is equivalent to

$$bn^{\frac{1}{3}} \ll 1. \tag{2.9}$$

The ratio of the mean free path to the Debye length can be found using (2.2) and (2.5)–(2.7), noting that $n = n_\mathrm{i}$. The result is

$$\frac{\lambda}{\lambda_\mathrm{D}} \simeq \left(\frac{6}{\pi}\right)^{\frac{1}{2}} \frac{1}{(bn^{\frac{1}{3}})^{\frac{3}{2}}}. \tag{2.10}$$

In the perfect gas regime (2.9) holds for $bn^{1/3}$ and hence $\lambda \gg \lambda_\mathrm{D}$. So, as expected in this case, the mean free path is much greater than the Coulomb screening radius. It is simple to show that the average collision radius $b \ll \lambda_\mathrm{D}$, consistent with short-scale interactions in a perfect gas, and that $\lambda_\mathrm{D} > n^{-1/3}$. Hence the necessary ordering of length-scales is

$$\lambda \gg \lambda_\mathrm{D} > n^{-\frac{1}{3}} \gg b. \tag{2.11}$$

A mean collision time can be defined for scattering of electrons by ions as

$$\tau_\mathrm{ei} = \frac{\lambda_\mathrm{ei}}{(v_\mathrm{th})_\mathrm{e}}, \tag{2.12}$$

where λ_ei is the mean free path. This is the time-scale in which a sub-thermal electron drift velocity relative to ions is randomized. Similar time-scales can be defined for ion-ion and electron-electron encounters.

In a fully ionized gas the presence of a magnetic field can introduce an anisotropy. An electron spirals about a uniform field **B** with the gyration frequency

$$\omega_{\mathrm{e}} = \frac{eB}{m_{\mathrm{e}}}, \tag{2.13}$$

with a similar expression for ions. The gyration time-scale of $\sim 1/\omega_{\mathrm{e}}$ can be compared with the collision time-scale τ_{ei}, given by (2.12). If $\omega_{\mathrm{e}}\tau_{\mathrm{ei}} \gg 1$ then an electron performs a number of spiral turns before having its motion randomized by collisions with the ion gas, and hence the field introduces a microscopic anisotropy. This can result in a reduced conductivity across field lines. However, inside most stars, with plausible values of B, $\omega_{\mathrm{e}}\tau_{\mathrm{ei}} \ll 1$ applies, but anisotropic conductivity can occur in stellar magnetospheres.

The classical fluid mechanics approach can be applied to plasmas when the macroscopic length-scale L is large compared to the particle mean free paths, and the macroscopic time-scale is long compared to the collision times. A fluid element of volume $\sim l^3$ can be defined with $\lambda \ll l \ll L$, so the gas within it contains many colliding particles representing a continuous distribution of momenta and is essentially uniform. The effect of collisions is then to randomize the particle velocities about a mean velocity **v**, which is the bulk velocity of the fluid element. Viewed in a frame moving with velocity **v**, the particles have a velocity distribution very close to Maxwellian, and a temperature T can be defined for the element. Small deviations, of order λ/L, from a Maxwellian distribution yield the transport quantities of resistivity and viscosity. The centre of mass of the fluid element has a local position **r**, at a time t, in a global frame. Such a plasma can be regarded as a continuous fluid with velocity $\mathbf{v}(\mathbf{r}, t)$ and mass density $\rho(\mathbf{r}, t)$. Since the ion mass $m_{\mathrm{i}} \gg m_{\mathrm{e}}$, it follows that $\rho \simeq n_{\mathrm{i}} m_{\mathrm{i}}$ and the bulk velocity $\mathbf{v} \simeq \mathbf{v}_{\mathrm{i}}$ to good approximations. Because $L \gg \lambda_{\mathrm{D}}$, large-scale electric and magnetic fields can be defined, with macroscopic charge and current density sources. Magnetohydrodynamics (MHD) considers the motions, and equilibria, of such an electrically conducting fluid and the behaviour of its **B** field.

The magneto-fluid equations can be derived by applying macroscopic principles. They can also be derived from appropriately weighted integrals involving the particle distribution function $f(\mathbf{r}, \mathbf{p}, t)$. This function is a phase space, statistical description, with $f d^3\mathbf{r} d^3\mathbf{p}$ being the number of particles with position and momentum in a given six-dimensional volume element $d^3\mathbf{r} d^3\mathbf{p}$ at a time t. A separate f can be defined for each species of particle. The phase space evolution of f is described by Boltzmann's equation

$$\frac{\partial f}{\partial t} + \frac{1}{m}\mathbf{p} \cdot \nabla f + \mathbf{F} \cdot \nabla_p f = \Gamma, \tag{2.14}$$

where m is the particle mass, ∇_p the gradient operator in momentum space, and **F** is the force on a particle, excluding the short-range interactive forces associated with collisions. The term Γ gives the effect of collisions.

The number density of particles is

$$n = \int_{\mathbf{p}} f d^3\mathbf{p}, \tag{2.15}$$

where the integral is over all momentum space, and f vanishes as $p \to \pm\infty$. Since $m_\mathrm{i} \gg m_\mathrm{e}$, the velocity of a fluid element is the mean ion velocity in the real space volume element $d^3\mathbf{r}$, given by

$$\mathbf{v}(\mathbf{r}, t) = \left\langle \frac{\mathbf{p}_\mathrm{i}}{m_\mathrm{i}} \right\rangle = \frac{1}{n} \int_{\mathbf{p}} \frac{1}{m_\mathrm{i}} \mathbf{p}_\mathrm{i} f d^3\mathbf{p}. \tag{2.16}$$

The macroscopic fluid dynamic equations can be derived by taking appropriately weighted integrals of the Boltzmann equation (2.14), for ions and electrons (e.g. Battaner 1996). Extensive descriptions of astrophysical plasmas are given by Kulsrud (2004) and by Chiuderi and Velli (2014).

In classical fluid mechanics two types of analysis of the flow properties are possible. In the Eulerian representation fixed spatial points are considered and a fluid quantity $Q(\mathbf{r}, t)$ has $\mathbf{r}$ and t as independent variables. Hence temporal rates of change involve partial time derivatives. In the Lagrangian representation fluid elements of conserved mass are followed and hence rates of change must account for the effect of displacement due to the flow. The vector $\mathbf{r}$ now defines the instantaneous position of a fluid element, so $\mathbf{r} = \mathbf{r}(t)$ and the velocity $\mathbf{v} = d\mathbf{r}/dt$. First order Taylor expansion gives a total differential change in $Q(\mathbf{r}(t), t)$ as

$$dQ = d\mathbf{r} \cdot \nabla Q + \frac{\partial Q}{\partial t} dt, \tag{2.17}$$

and hence

$$\frac{dQ}{dt} = \frac{\partial Q}{\partial t} + \mathbf{v} \cdot \nabla Q. \tag{2.18}$$

This is referred to as the material, or Lagrangian derivative of Q. The derivative also applies to vector quantities; for example, the acceleration of the fluid is

$$\mathbf{a} = \frac{d\mathbf{v}}{dt} = \frac{\partial \mathbf{v}}{\partial t} + (\mathbf{v} \cdot \nabla)\mathbf{v} \tag{2.19}$$

and this must be employed in deriving the momentum equation. The Lagrangian operator is therefore

$$\frac{d}{dt} = \frac{\partial}{\partial t} + \mathbf{v} \cdot \nabla. \tag{2.20}$$

Certain fluid properties become clearer when viewed using the Lagrangian picture.

In the remainder of this section the macroscopic electromagnetic field equations are combined with the fluid equations, in the non-relativistic regime, to obtain the equations of MHD.

2.2.2 Maxwell's Equations

Maxwell's equations describing the macroscopic electric and magnetic fields **E** and **B** are

$$\nabla \cdot \mathbf{E} = \frac{\rho_c}{\epsilon_0}, \tag{2.21}$$

$$\nabla \times \mathbf{E} = -\frac{\partial \mathbf{B}}{\partial t}, \tag{2.22}$$

$$\nabla \cdot \mathbf{B} = 0, \tag{2.23}$$

$$\nabla \times \mathbf{B} = \mu_0 \mathbf{J} + \frac{1}{c^2}\frac{\partial \mathbf{E}}{\partial t}, \tag{2.24}$$

where ρ_c is the charge density, **J** the current density, ϵ_0 the permittivity, μ_0 the permeability and $c = 1/(\epsilon_0\mu_0)^{1/2}$ the speed of light. These equations are local expressions of Gauss's electric flux law, Faraday's law of induction, the magnetic flux law, and Ampere's law with the addition of the displacement current term.

The fields **E** and **B** can be derived from scalar and vector potential functions. Equation (2.23) enables **B** to be expressed as

$$\mathbf{B} = \nabla \times \mathbf{A}, \tag{2.25}$$

where **A** is the magnetic vector potential. Substitution of this in (2.22) gives

$$\nabla \times \left(\mathbf{E} + \frac{\partial \mathbf{A}}{\partial t}\right) = \mathbf{0}, \tag{2.26}$$

which is satisfied by

$$\mathbf{E} = -\nabla\psi - \frac{\partial \mathbf{A}}{\partial t}, \tag{2.27}$$

where $\psi(\mathbf{r}, t)$ is the electric potential. It follows from (2.25) and (2.27) that **B** and **E** are unchanged by the transformations

$$\tilde{\mathbf{A}} = \mathbf{A} + \nabla\Phi, \tag{2.28}$$

$$\tilde{\psi} = \psi - \frac{\partial \Phi}{\partial t}, \tag{2.29}$$

where Φ is an arbitrary scalar function. The consequent freedom of choice in the divergence of $\mathbf{A}$ enables separate equations to be derived relating $\mathbf{A}$ to $\mathbf{J}$ and ψ to ρ_c.

Substituting (2.25) for $\mathbf{B}$ and (2.27) for $\mathbf{E}$ in the Maxwell equation (2.24), and using the vector identity (A7), gives

$$\nabla^2\mathbf{A} - \frac{1}{c^2}\frac{\partial^2\mathbf{A}}{\partial t^2} - \nabla\left(\nabla\cdot\mathbf{A} + \frac{1}{c^2}\frac{\partial\psi}{\partial t}\right) = -\mu_0\mathbf{J}. \tag{2.30}$$

Eliminating $\mathbf{E}$ between (2.21) and (2.27) yields

$$\nabla^2\psi + \frac{\partial}{\partial t}(\nabla\cdot\mathbf{A}) = -\frac{\rho_c}{\epsilon_0}. \tag{2.31}$$

These equations involving $\mathbf{A}$ and ψ can be decoupled by choosing

$$\nabla\cdot\mathbf{A} = -\frac{1}{c^2}\frac{\partial\psi}{\partial t}, \tag{2.32}$$

which is referred to as the Lorentz gauge. The separated equations are then

$$\nabla^2\mathbf{A} - \frac{1}{c^2}\frac{\partial^2\mathbf{A}}{\partial t^2} = -\mu_0\mathbf{J}, \tag{2.33}$$

$$\nabla^2\psi - \frac{1}{c^2}\frac{\partial^2\psi}{\partial t^2} = -\frac{\rho_c}{\epsilon_0}. \tag{2.34}$$

If the sources $\mathbf{J}$ and ρ_c are known then these inhomogeneous wave equations have formal integral solutions for $\mathbf{A}$ and ψ, incorporating retardation effects due to the finite speed of propagation of the fields (e.g. Jackson 2001). The fields $\mathbf{B}$ and $\mathbf{E}$ then follow from (2.25) and (2.27).

The electric and magnetic fields, $\mathbf{E}'$ and $\mathbf{B}'$, measured in a frame moving with velocity $\mathbf{v}$ relative to the frame in which $\mathbf{E}$ and $\mathbf{B}$ are measured, are given by the Lorentz transformations

$$\mathbf{E}' = (1-\gamma)\frac{(\mathbf{v}\cdot\mathbf{E})}{v^2}\mathbf{v} + \gamma(\mathbf{E} + \mathbf{v}\times\mathbf{B}), \tag{2.35}$$

$$\mathbf{B}' = (1-\gamma)\frac{(\mathbf{v}\cdot\mathbf{B})}{v^2}\mathbf{v} + \gamma\left(\mathbf{B} - \frac{1}{c^2}\mathbf{v}\times\mathbf{E}\right), \tag{2.36}$$

where

$$\gamma = \left(1 - \frac{v^2}{c^2}\right)^{-\frac{1}{2}}. \tag{2.37}$$

The Lorentz force on a charge q moving with velocity $\mathbf{v}_c$ in the presence of **E** and **B** fields is

$$\mathbf{F}_L = q(\mathbf{E} + \mathbf{v}_c \times \mathbf{B}). \tag{2.38}$$

2.2.3 The Induction Equation

The magnetic fields present in binary systems interact with conducting plasma. This plasma can consist of the secondary star, the atmosphere of a white dwarf primary, the accretion stream and disc, wind material, and sometimes a magnetosphere. The largest fluid velocities occur in the stream flow, the circular motions in the disc and in the outer regions of winds. These have characteristic values of $v \sim 10^6\,\mathrm{m\,s^{-1}}$ and hence fluid motions in binary stars usually satisfy $v/c \lesssim 3 \times 10^{-3} \ll 1$. The inner regions of accretion flows on to strongly magnetic neutron stars can have significantly larger speeds, but these become reduced as the star is approached. Provided that $v/c \ll 1$ is satisfied, the theory of non-relativistic magnetohydrodynamics is appropriate. The induction equation is fundamental in this theory.

The equations of non-relativistic MHD are derived using the condition $v \ll c$ and working to first order in v/c. Since **v**, **E** and **B** are causally inter-related, a typical velocity is $v \sim \ell/\tau$ where ℓ and τ are the length and time-scales for **E** and **B**. The induction equation (2.22) then gives

$$\frac{E}{B} \sim \frac{\ell}{\tau} \sim v. \tag{2.39}$$

It therefore follows in the Maxwell equation (2.24) for $\nabla \times \mathbf{B}$ that

$$\frac{|\partial \mathbf{E}/\partial t|}{c^2 |\nabla \times \mathbf{B}|} \sim \frac{\ell E}{c^2 \tau B} \sim \left(\frac{v}{c}\right)^2 \ll 1, \tag{2.40}$$

so the displacement current can be neglected and

$$\nabla \times \mathbf{B} = \mu_0 \mathbf{J}. \tag{2.41}$$

Taking the divergence of (2.24), noting that $\nabla \cdot (\nabla \times \mathbf{B}) = 0$ and using (2.21) to eliminate $\nabla \cdot \mathbf{E}$, gives

$$\nabla \cdot \mathbf{J} = -\frac{\partial \rho_c}{\partial t}. \tag{2.42}$$

This expresses the conservation of charge. Equation (2.41) yields $\nabla \cdot \mathbf{J} = 0$ which implies that in non-relativistic MHD the electric currents flow in closed

loops. Equation (2.42) then shows that the time derivative of the charge density is ignorable, to first order in v/c.

The current density can be expressed as the sum of the ion and electron contributions by

$$\mathbf{J} = n_{\mathrm{i}} Z e \mathbf{v}_{\mathrm{i}} - n_{\mathrm{e}} e \mathbf{v}_{\mathrm{e}}, \tag{2.43}$$

where n_{i} and n_{e} are the ion and electron number densities, $\mathbf{v}_{\mathrm{i}}$ and $\mathbf{v}_{\mathrm{e}}$ the mean drift velocities of ions and electrons, and $e > 0$. Using (2.1) for the total charge density ρ_{c}, it follows that (2.43) can be written

$$\mathbf{J} = \rho_{\mathrm{c}} \mathbf{v}_{\mathrm{i}} - n_{\mathrm{e}} e (\mathbf{v}_{\mathrm{e}} - \mathbf{v}_{\mathrm{i}}). \tag{2.44}$$

Noting that, since $m_{\mathrm{i}} \gg m_{\mathrm{e}}$, the bulk velocity $\mathbf{v} \simeq \mathbf{v}_{\mathrm{i}}$ to a good approximation, and hence the current density becomes

$$\mathbf{J} = \rho_{\mathrm{c}} \mathbf{v} + \rho_{\mathrm{e}} (\mathbf{v}_{\mathrm{e}} - \mathbf{v}), \tag{2.45}$$

with $\rho_{\mathrm{e}} = -n_{\mathrm{e}} e$. It is noted that $(\mathbf{v}_{\mathrm{e}} - \mathbf{v})$ is the mean drift velocity of electrons relative to the centre of mass of a fluid element, and hence

$$\mathbf{J} = \mathbf{J}' + \rho_{\mathrm{c}} \mathbf{v}, \tag{2.46}$$

where $\mathbf{J}' = \rho_{\mathrm{e}} (\mathbf{v}_{\mathrm{e}} - \mathbf{v})$ is the electron current density measured in the fluid element frame.

Expanding (2.37) for γ, and using (2.39) for E/B, it follows that the Lorentz transformations (2.35) and (2.36) become

$$\mathbf{E}' = \mathbf{E} + \mathbf{v} \times \mathbf{B}, \tag{2.47}$$

$$\mathbf{B}' = \mathbf{B}, \tag{2.48}$$

if terms of order $(v/c)^2$ are neglected. The current density $\mathbf{J}$ is given by

$$\mathbf{J} = \sigma \mathbf{E}' + \rho_{\mathrm{c}} \mathbf{v}, \tag{2.49}$$

where σ is the plasma conductivity and $\mathbf{E}'$ is measured in a frame moving with the local fluid velocity $\mathbf{v}$. This expression for $\mathbf{J}$ follows from (2.46) with $\mathbf{J}' = \sigma \mathbf{E}'$ being Ohm's law in a fluid element frame, while $\rho_{\mathrm{c}} \mathbf{v}$ is the contribution to $\mathbf{J}$ due to charge advection by the flow. It follows from (2.21) for ρ_{c} and (2.41) for $\mathbf{J}$ that

$$\frac{\rho_{\mathrm{c}} |\mathbf{v}|}{|\mathbf{J}|} \sim \mu_0 \epsilon_0 \frac{|\mathbf{v}||\mathbf{E}|}{|\mathbf{B}|} \sim \left(\frac{v}{c} \right)^2, \tag{2.50}$$

where the last relation derives from (2.39) for E/B. Hence, to first order in v/c, charge advection is ignorable in (2.49) so $\mathbf{J} = \mathbf{J}' = \sigma\mathbf{E}'$ and the use of (2.47) for $\mathbf{E}'$ then gives

$$\mathbf{J} = \sigma(\mathbf{E} + \mathbf{v} \times \mathbf{B}). \tag{2.51}$$

Combining Faraday's law (2.22) with the curls of (2.41) and (2.51) gives the MHD induction equation

$$\nabla \times (\mathbf{v} \times \mathbf{B}) - \nabla \times (\eta \nabla \times \mathbf{B}) = \frac{\partial \mathbf{B}}{\partial t}, \tag{2.52}$$

where $\eta = 1/\mu_0\sigma$ is the magnetic diffusivity.

Using the vector identity (A6), the induction equation (2.52) can be written as

$$\frac{d\mathbf{B}}{dt} = -\mathbf{B}\,\nabla \cdot \mathbf{v} + (\mathbf{B} \cdot \nabla)\mathbf{v} - \nabla \times (\eta \nabla \times \mathbf{B}), \tag{2.53}$$

where d/dt is the Lagrangian time derivative, measuring the rate of change moving with the fluid velocity. The first and second terms on the right side of this equation represent the rates of change of **B** in a fluid element due to compression and stretching of the field lines by the motion, respectively. The last term gives the diffusion of **B**, which has an associated dissipation of electric currents.

The relative importance of the convective and diffusive terms in the induction equation (2.52) can be gauged using the typical length and time-scales ℓ and τ. The magnetic Reynolds number is defined as

$$R_\mathrm{m} = \frac{\ell v}{\eta} \sim \frac{|\nabla \times (\mathbf{v} \times \mathbf{B})|}{|\nabla \times (\eta \nabla \times \mathbf{B})|}, \tag{2.54}$$

where $v \sim \ell/\tau$ is a typical fluid velocity. The cases of large and small values of R_m are of particular significance.

In the case $R_\mathrm{m} \gg 1$ the induction equation becomes

$$\nabla \times (\mathbf{v} \times \mathbf{B}) = \frac{\partial \mathbf{B}}{\partial t}. \tag{2.55}$$

There are several ways of showing that in this limit the magnetic field is 'frozen' to the plasma, so fluid elements are attached to field lines and flux freezing results. One method is to represent **B** as

$$\mathbf{B} = \nabla\alpha \times \nabla\beta = \nabla \times (\alpha \nabla \beta), \tag{2.56}$$

where α and β are referred to as Euler potentials. This satisfies $\nabla \cdot \mathbf{B} = 0$ and, since $\mathbf{B} \cdot \nabla\alpha = \mathbf{B} \cdot \nabla\beta = 0$, α and β are constant on field lines and so can be used to label these lines. The substitution of (2.56) in (2.55) gives

$$\begin{aligned}\nabla\alpha \times \nabla\frac{\partial\beta}{\partial t} - \nabla\beta \times \nabla\frac{\partial\alpha}{\partial t} &= \nabla \times [\mathbf{v} \times (\nabla\alpha \times \nabla\beta)] \\ &= \nabla \times [(\mathbf{v} \cdot \nabla\beta)\nabla\alpha - (\mathbf{v} \cdot \nabla\alpha)\nabla\beta] \\ &= \nabla(\mathbf{v} \cdot \nabla\beta) \times \nabla\alpha - \nabla(\mathbf{v} \cdot \nabla\alpha) \times \nabla\beta, \end{aligned} \tag{2.57}$$

making use of the vector identity (A5). Hence

$$\nabla\times\left(\alpha\nabla\frac{\partial\beta}{\partial t}\right)-\nabla\times\left(\beta\nabla\frac{\partial\alpha}{\partial t}\right) = -\nabla\times[\alpha\nabla(\mathbf{v}\cdot\nabla\beta)]+\nabla\times[\beta\nabla(\mathbf{v}\cdot\nabla\alpha)], \tag{2.58}$$

and so the induction equation becomes

$$\nabla \times \left(\alpha\nabla\frac{d\beta}{dt} - \beta\nabla\frac{d\alpha}{dt}\right) = \mathbf{0}, \tag{2.59}$$

where d/dt is the Lagrangian time derivative. Equation (2.59) has a family of solutions, but the simplest is

$$\frac{d\alpha}{dt} = \frac{d\beta}{dt} = 0, \tag{2.60}$$

corresponding to magnetic field lines moving with the fluid.

Another way of demonstrating the frozen field property of (2.55) is to consider the magnetic flux through a contour c. This is given by

$$\Phi = \int_S \mathbf{B} \cdot d\mathbf{S}, \tag{2.61}$$

where S is an open surface ending on c. If the contour and its surface are taken to be always composed of the same fluid elements, then conservation of Φ is consistent with the field being frozen to the plasma. Hence the material derivative $d\Phi/dt$ should vanish if (2.55) is satisfied.

Denote the material contour at time t by c, and at time $t + \delta t$ by c'. In the time interval δt an arc length $d\mathbf{l}$ of c sweeps out an area $d\mathbf{l} \times \mathbf{v}\delta t$. A closed surface can be considered consisting of a surface S ending on c, a surface S' ending on c', and the band joining c and c'. The total flux through this closed surface at time $t + \delta t$ is

$$-\int_S \mathbf{B}(\mathbf{r}, t+\delta t)\cdot d\mathbf{S}+\int_{S'} \mathbf{B}(\mathbf{r}, t+\delta t)\cdot d\mathbf{S}'+\oint_c \mathbf{B}(\mathbf{r}, t+\delta t)\cdot d\mathbf{l}\times\mathbf{v}\delta t = 0. \tag{2.62}$$

The negative sign arises since the outward normal is required on S, and the total flux of $\mathbf{B}$ through any closed surface is zero since $\nabla \cdot \mathbf{B} = 0$. The change in flux through the moving contour is therefore

$$\begin{aligned}\delta\Phi &= \int_{S'} \mathbf{B}(\mathbf{r}, t+\delta t) \cdot d\mathbf{S}' - \int_S \mathbf{B}(\mathbf{r}, t) \cdot d\mathbf{S} \\ &= \int_S [\mathbf{B}(\mathbf{r}, t+\delta t) - \mathbf{B}(\mathbf{r}, t)] \cdot d\mathbf{S} + \delta t \oint_c \mathbf{B}(\mathbf{r}, t) \cdot \mathbf{v} \times d\mathbf{l} \\ &= \delta t \left\{ \int_S \frac{\partial \mathbf{B}}{\partial t} \cdot d\mathbf{S} - \oint_c \mathbf{v} \times \mathbf{B} \cdot d\mathbf{l} \right\}. \end{aligned} \tag{2.63}$$

Dividing by δt, letting $\delta t \to 0$ and using Stokes's integral theorem, gives

$$\frac{d\Phi}{dt} = \int_S \left(\frac{\partial \mathbf{B}}{\partial t} - \nabla \times (\mathbf{v} \times \mathbf{B}) \right) \cdot d\mathbf{S}. \tag{2.64}$$

Equation (2.55) then shows $d\Phi/dt = 0$, which is consistent with frozen $\mathbf{B}$.

Finally, it can be noted that the ideal induction equation (2.55) is identical to the equation describing the evolution of the vorticity $\boldsymbol{\omega} = \nabla \times \mathbf{v}$ in an inviscid flow, with $\mathbf{B}$ replacing $\boldsymbol{\omega}$. Kelvin's circulation theorem is consistent with the vortex lines moving with the fluid (e.g. Batchelor 2005) and hence (2.55) is consistent with the lines of $\mathbf{B}$ moving with the fluid. Like $\mathbf{B}$, the vortex field satisfies $\nabla \cdot \boldsymbol{\omega} = 0$.

In the general case, with diffusion present, (2.52) and (2.64) yield

$$\frac{d\Phi}{dt} = -\int_S \nabla \times (\eta \nabla \times \mathbf{B}) \cdot d\mathbf{S}, \tag{2.65}$$

showing that the flux through a material contour changes due to diffusion of $\mathbf{B}$.

When $R_\mathrm{m} \ll 1$ the induction equation becomes

$$\nabla \times (\eta \nabla \times \mathbf{B}) = -\frac{\partial \mathbf{B}}{\partial t}. \tag{2.66}$$

For constant η this yields

$$\eta \nabla^2 \mathbf{B} = \frac{\partial \mathbf{B}}{\partial t}, \tag{2.67}$$

which is a standard diffusion equation for $\mathbf{B}$. The rate of dissipation of the electric current in a fluid element can be found by considering the rate at which the electric field does work on the electrons. This rate of work, per unit volume, is

$$Q_\mathrm{m} = (\mathbf{v}_\mathrm{e} - \mathbf{v}_\mathrm{i}) \cdot (\rho_\mathrm{e} \mathbf{E}'), \tag{2.68}$$

where $(\mathbf{v}_e - \mathbf{v}_i)$ and $\mathbf{E}'$ are the electron mean drift velocity and the electric field both measured in the centre of mass frame of the element, remembering $\mathbf{v}_i \simeq \mathbf{v}$. Since $\mathbf{E}' = \mu_0 \eta \mathbf{J}'$ and $\mathbf{J}' = \rho_e(\mathbf{v}_e - \mathbf{v}_i)$ while, to first order in v/c, $\mathbf{J}' = \mathbf{J}$, it follows that

$$Q_m = \mu_0 \eta \mathbf{J}^2. \tag{2.69}$$

The kinetic energy imparted to the electrons is dissipated due to collisions with the ions, resulting in heating of the plasma. Hence (2.69) represents the rate of dissipation of electric current per unit volume. In the absence of significant fluid motions and external sources, (2.67) shows that a magnetic field with length-scale ℓ decays on a characteristic diffusion time-scale

$$\tau_d = \frac{\ell^2}{\eta} \sim \frac{B^2/2\mu_0}{Q_m}, \tag{2.70}$$

where the last ratio derives from the Ampere law (2.41) for $\mathbf{J}$ and (2.69) for the magnetic dissipation function Q_m. This gives the time-scale on which the magnetic energy density decays at a point due to dissipation of the current density.

It follows from (2.54) and (2.70) that the magnetic Reynolds number is

$$R_m = \frac{\ell^2/\eta}{\ell/v} = \frac{\tau_d}{\tau_{kin}}, \tag{2.71}$$

where τ_{kin} is the flow time-scale (kinematic time). When $R_m \gg 1$, then $\tau_{kin} \ll \tau_d$ and the flow distorts the magnetic field faster than it can diffuse. Conversely, when $R_m \ll 1$, then $\tau_d \ll \tau_{kin}$ and rapid diffusion prevents the flow from significantly affecting the field. Separate magnetic Reynolds numbers can occur, involving various velocity components and length-scales. Turbulent magnetic Reynolds numbers can also be defined.

An expression for the rate of change of the magnetic energy density can be derived from the Faraday induction equation (2.22). Taking the scalar product of this with $\mathbf{B}$ and using the vector identity (A4), together with (2.41) for $\mathbf{J}$, gives

$$\frac{\partial}{\partial t}\left(\frac{B^2}{2\mu_0}\right) = -\nabla \cdot (\mathbf{E} \times \mathbf{H}) - \mathbf{E} \cdot \mathbf{J}, \tag{2.72}$$

where $\mathbf{H} = \mathbf{B}/\mu_0$. The use of (2.51) for $\mathbf{J}$ yields

$$\mathbf{E} \cdot \mathbf{J} = \mu_0 \eta \mathbf{J}^2 - (\mathbf{v} \times \mathbf{B}) \cdot \mathbf{J} = \mu_0 \eta \mathbf{J}^2 + \mathbf{v} \cdot (\mathbf{J} \times \mathbf{B}). \tag{2.73}$$

It is shown below that $\mathbf{J} \times \mathbf{B}$ is the magnetic force density $\mathbf{F}_m$, so

$$\frac{\partial}{\partial t}\left(\frac{B^2}{2\mu_0}\right) = -\nabla \cdot (\mathbf{E} \times \mathbf{H}) - \mu_0 \eta \mathbf{J}^2 - \mathbf{v} \cdot \mathbf{F}_m. \tag{2.74}$$

The first term on the right hand side of this equation is the divergence of the Poynting energy flux $\mathbf{E} \times \mathbf{H}$. A positive divergence corresponds to magnetic energy flowing away from a point, leading to a decrease in the energy density. The second term is the dissipation of currents, always causing a decrease in field energy. The term $\mathbf{v} \cdot \mathbf{F}_{\mathrm{m}}$ is the rate at which the magnetic force does work on the fluid motions, allowing an exchange between magnetic and kinetic energy. This term can correspond to an increase or a decrease in the magnetic energy density, depending on whether $\mathbf{v}$ is antiparallel or parallel to $\mathbf{F}_{\mathrm{m}}$.

The concept of magnetic flux tubes is important. A flux tube is the volume enclosed by the set of field lines which intercept a simple closed curve. Since no field lines cross the surface of the tube, it follows from $\nabla \cdot \mathbf{B} = 0$ that for any volume of it contained between two cross-sections as much flux enters one section as leaves the other. Hence the flux Φ through any section of the tube, given by (2.61) with $d\mathbf{S}$ having the same sense as $\mathbf{B}$, is constant. When $R_{\mathrm{m}} \gg 1$ matter can flow along flux tubes but not across them. The flux tubes can have infinitesimal or finite cross-sections.

It is sometimes convenient to express the induction equation, or part of it, in terms of the vector potential $\mathbf{A}$. In the general theory of electromagnetism, $\mathbf{A}$ is related to $\mathbf{J}$ by the inhomogeneous wave equation (2.33), subject to the Lorentz gauge (2.32). In the non-relativistic approximation of MHD terms of order $(v/c)^2$ are ignored. The potentials $\mathbf{A}$ and ψ, like $\mathbf{E}$ and $\mathbf{B}$, vary with length and time-scales ℓ and τ, and $v \sim \ell/\tau$. It then follows in (2.33) that

$$\frac{|\partial^2 \mathbf{A}/\partial t^2|}{c^2 |\nabla^2 \mathbf{A}|} \sim \frac{\ell^2/\tau^2}{c^2} \sim \frac{v^2}{c^2}, \tag{2.75}$$

and hence, to first order in v/c, the magnetic vector potential is related to the current density by

$$\nabla^2 \mathbf{A} = -\mu_0 \mathbf{J}. \tag{2.76}$$

In this approximation, the delay effects due to the finite speed of propagation of the fields is ignorable. The Lorentz gauge (2.32) has a ratio of terms given by

$$\frac{|\partial \psi/\partial t|}{c^2 |\nabla \cdot \mathbf{A}|} \sim \frac{(\ell/\tau)\psi}{c^2 A} \sim \frac{(\ell/\tau)\ell E}{c^2 \ell B} \sim \frac{(\ell/\tau)v}{c^2} \sim \frac{v^2}{c^2}, \tag{2.77}$$

using (2.25), (2.27) and (2.39) to estimate the fields B and E. The Lorentz gauge condition therefore becomes

$$\nabla \cdot \mathbf{A} = 0. \tag{2.78}$$

It will be seen that in axisymmetric problems it is particularly useful to express the poloidal magnetic field in terms of a vector potential.

2.2.4 Magnetic Force

The Lorentz force density on ions and electrons is

$$\mathbf{F} = n_{\mathrm{i}} Ze(\mathbf{E} + \mathbf{v}_{\mathrm{i}} \times \mathbf{B}) - n_{\mathrm{e}} e(\mathbf{E} + \mathbf{v}_{\mathrm{e}} \times \mathbf{B}). \tag{2.79}$$

The use of (2.1) for ρ_{c} and (2.43) for $\mathbf{J}$ then gives

$$\mathbf{F} = \rho_{\mathrm{c}} \mathbf{E} + \mathbf{J} \times \mathbf{B}. \tag{2.80}$$

The ratio of the electric to magnetic force is

$$\frac{\rho_{\mathrm{c}} |\mathbf{E}|}{|\mathbf{J} \times \mathbf{B}|} \sim \epsilon_0 \mu_0 \left(\frac{E}{B} \right)^2 \sim \left(\frac{v}{c} \right)^2, \tag{2.81}$$

where the first relation follows from (2.21) for ρ_{c} and (2.41) for $\mathbf{J}$, and the second from (2.39) for E/B. The electric force density is therefore negligible so

$$\mathbf{F} = \mathbf{F}_{\mathrm{m}} = \mathbf{J} \times \mathbf{B}, \tag{2.82}$$

and the use of (2.41) gives the magnetic force per unit volume as

$$\mathbf{F}_{\mathrm{m}} = \frac{1}{\mu_0} (\nabla \times \mathbf{B}) \times \mathbf{B}. \tag{2.83}$$

Employing the vector identity (A2), (2.83) can be written as

$$\mathbf{F}_{\mathrm{m}} = \frac{1}{\mu_0} (\mathbf{B} \cdot \nabla) \mathbf{B} - \nabla \left(\frac{B^2}{2\mu_0} \right). \tag{2.84}$$

Hence $\mathbf{F}_{\mathrm{m}}$ can be expressed in the Cartesian tensor form

$$F_{\mathrm{m}i} = \frac{\partial M_{ij}}{\partial x_j}, \tag{2.85}$$

where the summation convention is used and

$$M_{ij} = \frac{1}{\mu_0} B_i B_j - \frac{B^2}{2\mu_0} \delta_{ij} \tag{2.86}$$

is the Maxwell stress tensor. The $B_i B_j / \mu_0$ term represents a tension along the magnetic field, while $B^2/2\mu_0$ is a pressure.

Writing $\mathbf{B} = B\hat{\mathbf{s}}$ and $\hat{\mathbf{s}} \cdot \nabla = d/ds$, where s is the distance along a field line, then

$$(\mathbf{B} \cdot \nabla)\mathbf{B} = B^2 \frac{d}{ds}(\hat{\mathbf{s}}) + \hat{\mathbf{s}} \frac{d}{ds}\left(\frac{B^2}{2}\right) = \frac{B^2}{R_c}\hat{\mathbf{n}} + \nabla_{\parallel}\left(\frac{B^2}{2}\right), \tag{2.87}$$

where R_c is the local radius of curvature of a field line, $\hat{\mathbf{n}}$ is a unit vector directed at the centre of curvature and $\nabla_{\parallel}$ measures the spatial rate of change along **B**. Substitution in (2.84) gives

$$\mathbf{F}_{\mathrm{m}} = \frac{B^2}{\mu_0 R_c}\hat{\mathbf{n}} - \nabla_{\perp}\left(\frac{B^2}{2\mu_0}\right). \tag{2.88}$$

The magnetic force therefore results from curvature of the field lines, which are stressed along their length, and from the variation of magnetic pressure across field lines. A flux tube of infinitesimal cross-section acts like an elastic string, and also has a pressure exerted on it by neighbouring tubes. The first term in (2.88) acts like an elastic restoring force, while the second term makes a contribution if B varies across field lines.

There are two non-trivial cases in which the magnetic force density vanishes. A current-free region has $\mathbf{J} = \mathbf{0}$ and hence zero $\mathbf{F}_{\mathrm{m}}$. Equation (2.41) for **J** then shows that $\nabla \times \mathbf{B} = \mathbf{0}$ and hence a current-free field can be expressed as

$$\mathbf{B} = -\nabla \Psi_{\mathrm{m}}, \tag{2.89}$$

where, by virtue of $\nabla \cdot \mathbf{B} = 0$, the magnetic scalar Ψ_{m} satisfies Laplace's equation

$$\nabla^2 \Psi_{\mathrm{m}} = 0. \tag{2.90}$$

The second case of vanishing $\mathbf{F}_{\mathrm{m}}$ arises when **J** is finite but parallel to **B**. This case leads to the concept of a force-free field and (2.83) yields

$$(\nabla \times \mathbf{B}) \times \mathbf{B} = \mathbf{0}. \tag{2.91}$$

This condition is satisfied by

$$\nabla \times \mathbf{B} = f(\mathbf{r})\mathbf{B}. \tag{2.92}$$

Taking the divergence of this equation, and using the vector identity (A3), shows that

$$\mathbf{B} \cdot \nabla f = 0, \tag{2.93}$$

so $f(\mathbf{r})$ is constant along lines of $\mathbf{B}$. The curl of (2.92), together with the vector identities (A5) and (A7), yields

$$\nabla^2\mathbf{B} + f^2\mathbf{B} = -\nabla f \times \mathbf{B}. \tag{2.94}$$

In the degenerate case $f = 0$ and the force-free field becomes current-free.

In the case of an axisymmetric force-free field, the poloidal field can be expressed as

$$\mathbf{B}_\mathrm{p} = \nabla \times \left(\frac{\psi_\mathrm{m}}{\varpi}\hat{\boldsymbol{\phi}}\right) = \frac{1}{\varpi}\nabla\psi_\mathrm{m} \times \hat{\boldsymbol{\phi}}, \tag{2.95}$$

where $2\pi\psi_\mathrm{m}(\varpi, z)$ is the poloidal flux through a circular contour of cylindrical radius ϖ at height z. It follows that

$$\mathbf{B}_\mathrm{p} \cdot \nabla\psi_\mathrm{m} = 0, \tag{2.96}$$

so that ψ_m is conserved along poloidal field lines.

The toroidal component of the force-free equation (2.91) yields

$$\mathbf{B}_\mathrm{p} \cdot \nabla(\varpi B_\phi) = 0, \tag{2.97}$$

so ϖB_ϕ is also conserved along poloidal field lines. It then follows from (2.96) and (2.97) that ϖB_ϕ can be expressed as a function

$$W(\psi_\mathrm{m}) = \varpi B_\phi. \tag{2.98}$$

The cylindrical components of (2.95) are

$$B_\varpi = -\frac{1}{\varpi}\frac{\partial\psi_\mathrm{m}}{\partial z}, \tag{2.99a}$$

$$B_z = \frac{1}{\varpi}\frac{\partial\psi_\mathrm{m}}{\partial\varpi}. \tag{2.99b}$$

The toroidal current density can be expressed as

$$J_\phi = -\frac{1}{\mu_0}\left[\nabla^2\left(\frac{\psi_\mathrm{m}}{\varpi}\right) - \frac{1}{\varpi^2}\frac{\psi_\mathrm{m}}{\varpi}\right]. \tag{2.100}$$

Using this, together with (2.99a) and (2.99b), in the poloidal components of the force-free condition (2.91) leads to the Grad-Shafranov equation

$$\nabla^2\left(\frac{\psi_\mathrm{m}}{\varpi}\right) - \frac{1}{\varpi^2}\frac{\psi_\mathrm{m}}{\varpi} = -\frac{1}{2\varpi}\frac{d}{d\psi_\mathrm{m}}\left(W^2\right), \tag{2.101}$$

where $W(\psi_{\rm m})$ is given by (2.98). This shows how B_ϕ is related to $\psi_{\rm m}$ for an axisymmetric force-free field. Such a field must have a twist, and this is associated with a modification of the poloidal field from its current-free state.

The amount of poloidal field modification is related to the field winding ratio $|B_\phi/B_{\rm p}|$, and in the formal limit $B_\phi \to 0$ the force-free equation (2.101) reduces to

$$\nabla^2\left(\frac{\psi_{\rm m}}{\varpi}\right) - \frac{1}{\varpi^2}\frac{\psi_{\rm m}}{\varpi} = 0. \tag{2.102}$$

By (2.100), this corresponds to the current-free limit $J_\phi = 0$ and $B_\phi = 0$ for an axisymmetric field. It follows from the field component expressions (2.98), (2.99a) and (2.99b) that the ratio of the right hand side to either of the terms on the left hand side of (2.101) is $\sim B_\phi^2/B_{\rm p}^2$. Hence if $|B_\phi/B_{\rm p}| \ll 1$ occurs, then the right hand side is small compared to either of the terms on the left hand side so the left hand terms must nearly cancel and (2.101) reduces to (2.102) for the poloidal flux function. This corresponds to $|J_\phi| \ll |J_{\rm p}|$, so $\mathbf{B}_{\rm p}$ can be considered as essentially current-free while a relatively small but finite B_ϕ field satisfies the force-free condition (2.97).

Formally, a force-free magnetic field has $\mathbf{F}_{\rm m} = \mathbf{J}\times\mathbf{B} = \mathbf{0}$, with $\mathbf{J}$ exactly parallel to $\mathbf{B}$. In practice, the state of $\mathbf{J}$ parallel to $\mathbf{B}$ is approached when $B^2/2\mu_0 \gg P$ and, if a flow is present, when $v \ll (B^2/\mu_0\rho)^{1/2}$. These conditions correspond to $v_{\rm A}^2 \gg c_{\rm s}^2$ and $v_{\rm A}^2 \gg v^2$, respectively, where $v_{\rm A}$ is the Alfvén speed (see Sect. 2.2.6) The magnetic energy density then dominates the thermal and kinetic energy densities, and the terms in the momentum equation are balanced by having $\mathbf{J}$ nearly parallel to $\mathbf{B}$ to prevent the magnetic force term from dominating. A finite magnetic force results because the large magnetic energy density, which is intrinsic to $\mathbf{J}\times\mathbf{B}$ as a scaling factor, compensates for $\mathbf{J}$ being nearly parallel to $\mathbf{B}$. The solution of the force-free equation gives the structure of the magnetic field to a good approximation. Strictly speaking, such fields should be referred to as nearly force-free but they are usually just described as force-free. In force-free field situations the geometry of the poloidal magnetic field largely determines the poloidal geometry of the flow. In binary stars, force-free fields occur in the well sub-Alfvénic regions of magnetic stellar and disc wind flows, and in magnetically channelled accretion flows. They also occur in magnetically dominated, nearly corotating stellar magnetospheres.

2.2.5 The Magneto-Fluid Equations

The plasma motion is governed by the equations of continuity, momentum and thermal energy. The equation of mass conservation can be derived by considering a mass M contained in a stationary volume V enclosed by a surface S. The mass flux through a point is $\rho\mathbf{v}$, so $\rho\mathbf{v}\cdot d\mathbf{S}$ is the rate of flow of mass through dS. Equating the

rate of change of the volume integral of ρ to minus the rate of mass flow through S and then using Gauss's divergence theorem gives the local condition

$$\nabla \cdot (\rho \mathbf{v}) = -\frac{\partial \rho}{\partial t}. \tag{2.103}$$

This expresses the fact that the density at a point increases if mass flows into the surrounding volume element, while it decreases if there is a positive divergence of mass flux. Expanding the divergence gives

$$\rho \nabla \cdot \mathbf{v} = -\left(\frac{\partial \rho}{\partial t} + \mathbf{v} \cdot \nabla \rho \right), \tag{2.104}$$

so it follows that the continuity equation can be expressed as

$$\nabla \cdot \mathbf{v} = -\frac{1}{\rho} \frac{d\rho}{dt}, \tag{2.105}$$

where d/dt is the Lagrangian time derivative. In general, a fluid element contracts or expands as it moves with the flow, corresponding to negative and positive $\nabla \cdot \mathbf{v}$ respectively. In the special case when fluid elements conserve their volume, $d\rho/dt = 0$. Equation (2.105) shows that such incompressible flows have $\nabla \cdot \mathbf{v} = 0$.

The equation of motion equates the rate of change of the linear momentum of a fluid element to the sum of the forces acting on it. In an inertial frame, this gives

$$\frac{\partial \mathbf{v}}{\partial t} + (\mathbf{v} \cdot \nabla)\mathbf{v} = -\frac{1}{\rho} \nabla P - \nabla \psi + \frac{1}{\mu_0 \rho} (\nabla \times \mathbf{B}) \times \mathbf{B} + \frac{1}{\rho} \mathbf{F}_{\mathrm{v}}, \tag{2.106}$$

where P is the pressure, ψ the gravitational potential, and the acceleration of the element is the Lagrangian derivative of $\mathbf{v}$ given by (2.19). The first force term is derived from the isotropic nature of the stress due to the gas or radiation pressure, giving a stress tensor $S_{ij} = -P\delta_{ij}$. This yields a corresponding force per unit volume of $\partial S_{ij}/\partial x_j = -\partial P/\partial x_i = -\nabla P$, and hence a force per unit mass of $-\nabla P/\rho$. The second force follows from the conservative nature of the gravity field, giving $\nabla \times \mathbf{g} = \mathbf{0}$, and hence a force per unit mass of $\mathbf{g} = -\nabla \psi$. The gravitational potential obeys Poisson's equation

$$\nabla^2 \psi = 4\pi G \rho. \tag{2.107}$$

The last two terms in the momentum equation (2.106) are the specific magnetic and viscous forces.

In a frame rotating with instantaneous angular velocity $\mathbf{\Omega}$ the equation of motion has apparent force terms which are part of the inertial acceleration. A particle has a position in a Cartesian frame given by

$$\mathbf{r} = x_i \hat{\mathbf{x}}_i, \tag{2.108}$$

where the tensor summation convention is employed. If the rotating frame is used, then in inertial space the unit vector $\hat{\mathbf{x}}_i$ traces a circle about $\boldsymbol{\Omega}$ at a rate

$$\frac{d}{dt}(\hat{\mathbf{x}}_i) = \boldsymbol{\Omega} \times \hat{\mathbf{x}}_i. \tag{2.109}$$

The inertial space particle velocity is therefore

$$\frac{d\mathbf{r}}{dt} = \frac{d}{dt}(x_i \hat{\mathbf{x}}_i) = v_i \hat{\mathbf{x}}_i + x_i \boldsymbol{\Omega} \times \hat{\mathbf{x}}_i, \tag{2.110}$$

where $v_i = \dot{x}_i$ are the velocity components relative to the rotating axes. The inertial acceleration is then

$$\frac{d^2\mathbf{r}}{dt^2} = \dot{v}_i \hat{\mathbf{x}}_i + 2v_i \boldsymbol{\Omega} \times \hat{\mathbf{x}}_i + x_i \left[\frac{d\boldsymbol{\Omega}}{dt} \times \hat{\mathbf{x}}_i + \boldsymbol{\Omega} \times (\boldsymbol{\Omega} \times \hat{\mathbf{x}}_i) \right]. \tag{2.111}$$

Hence the accelerations in the inertial and rotating frames are related by

$$\frac{d^2\mathbf{r}}{dt^2} = \ddot{\mathbf{r}} + 2\boldsymbol{\Omega} \times \mathbf{v} + \boldsymbol{\Omega} \times (\boldsymbol{\Omega} \times \mathbf{r}) + \frac{d\boldsymbol{\Omega}}{dt} \times \mathbf{r}. \tag{2.112}$$

In a binary star orbital frame the time-scale for changes in $\boldsymbol{\Omega}$ far exceeds any flow time-scales and so the term $(d\boldsymbol{\Omega}/dt) \times \mathbf{r}$ is ignorable. This leaves two terms that are related to the Coriolis force and the centrifugal force . The latter can be expressed as a gradient by noting that

$$(\boldsymbol{\Omega} \times \mathbf{r}) \cdot (\boldsymbol{\Omega} \times \mathbf{r}) = [(\boldsymbol{\Omega} \times \mathbf{r}) \times \boldsymbol{\Omega}] \cdot \mathbf{r} = \left[\Omega^2 r^2 - (\boldsymbol{\Omega} \cdot \mathbf{r})^2 \right], \tag{2.113}$$

and hence

$$\begin{aligned} \nabla(|\boldsymbol{\Omega} \times \mathbf{r}|^2) &= 2\Omega^2 r \nabla r - 2(\boldsymbol{\Omega} \cdot \mathbf{r}) \nabla(\boldsymbol{\Omega} \cdot \mathbf{r}) \\ &= 2\Omega^2 \mathbf{r} - 2(\boldsymbol{\Omega} \cdot \mathbf{r}) \boldsymbol{\Omega} \\ &= -2\boldsymbol{\Omega} \times (\boldsymbol{\Omega} \times \mathbf{r}). \end{aligned} \tag{2.114}$$

The inertial acceleration of a fluid element can therefore be expressed as

$$\frac{d^2\mathbf{r}}{dt^2} = \ddot{\mathbf{r}} + 2\boldsymbol{\Omega} \times \mathbf{v} - \nabla \left(\frac{1}{2} |\boldsymbol{\Omega} \times \mathbf{r}|^2 \right). \tag{2.115}$$

Substitution of this in the inertial frame equation of motion (2.106) gives the equation of motion in the rotating frame as

$$\frac{\partial \mathbf{v}}{\partial t} + (\mathbf{v}\cdot\nabla)\mathbf{v} = -\frac{1}{\rho}\nabla P - \nabla\left(\psi - \frac{1}{2}|\boldsymbol{\Omega}\times\mathbf{r}|^2\right) - 2\boldsymbol{\Omega}\times\mathbf{v} + \frac{1}{\mu_0\rho}(\nabla\times\mathbf{B})\times\mathbf{B} + \frac{1}{\rho}\mathbf{F}_{\mathrm{v}}. \tag{2.116}$$

The second force term is the gradient of an effective potential, arising from the sum of the gravitational and centrifugal potentials, while the third term is the Coriolis force per unit mass.

The force due to ordinary molecular viscosity is usually too small to be significant. However, the presence of turbulence can lead to a much larger effective viscous force. Turbulence is a field of random macroscopic velocities superposed on a mean laminar flow. The standard picture of hydrodynamic turbulence has an inertial range in which the non-linear inertial terms cause a dissipation-free cascade of energy from the larger to the smaller eddies, until scales are reached at which the micro-viscosity operates. The micro-viscosity fixes the minimum scale at which turbulent motions persist. The time-scale of the dissipative process is that of the cascade, being typically the turn-over time of the larger eddies. The micro-viscosity is replaced by a macro eddy-viscosity acting on the mean flow, with a macro length-scale and a turbulent velocity replacing the mean free path and the thermal velocity, respectively. Hence the turbulent viscous force per unit volume is expressed in the Cartesian tensor form

$$F_{\mathrm{v}i} = \frac{\partial s_{ij}}{\partial x_j}, \tag{2.117}$$

where

$$s_{ij} = \rho\nu\left(2e_{ij} - \frac{2}{3}\nabla\cdot\mathbf{v}\,\delta_{ij}\right) \tag{2.118}$$

is the viscous stress tensor, with

$$e_{ij} = \frac{1}{2}\left(\frac{\partial v_i}{\partial x_j} + \frac{\partial v_j}{\partial x_i}\right) \tag{2.119}$$

the rate of strain tensor. The viscosity coefficient ν is usually expressed as

$$\nu = \frac{1}{3}v_{\mathrm{T}}\lambda_{\mathrm{T}}, \tag{2.120}$$

where v_{T} and λ_{T} are the rms turbulent speed and the mixing length, respectively. This turbulent form of ν has values which exceed those of the molecular form by

several orders of magnitude, since λ_T greatly exceeds a typical molecular mean free path. The use of (2.117)–(2.119) for $\mathbf{F}_v$ in (2.106) assumes subsonic turbulence, so the associated density fluctuations are modest.

The viscous force can be expressed in vector operator terms by expanding (2.117)–(2.119) and using the vector identity (A6). This gives, (see the Appendix),

$$\mathbf{F}_v = \rho\nu\nabla^2\mathbf{v} - [\nabla^2(\rho\nu)]\mathbf{v} + \nabla\left(\nabla\cdot(\rho\nu\mathbf{v}) - \frac{2}{3}\rho\nu\nabla\cdot\mathbf{v}\right) + \nabla\times[\mathbf{v}\times\nabla(\rho\nu)]. \tag{2.121}$$

It is often the case in stars and discs that the shears due to differential rotation dominate those due to poloidal flows, so $\mathbf{F}_v$ is principally azimuthal. For an axisymmetric flow, expressed in cylindrical coordinates (ϖ, ϕ, z), with angular velocity $\Omega(\varpi, z)$, (2.121) yields

$$F_{v\phi} = \frac{1}{\varpi^2}\frac{\partial}{\partial\varpi}\left(\rho\nu\varpi^3\frac{\partial\Omega}{\partial\varpi}\right) + \frac{\partial}{\partial z}\left(\rho\nu\varpi\frac{\partial\Omega}{\partial z}\right), \tag{2.122}$$

where $\Omega = v_\phi/\varpi$.

The rate of work done, per unit volume, by the viscous force on the fluid at a fixed point is

$$\mathbf{v}\cdot\mathbf{F}_v = v_i\frac{\partial s_{ij}}{\partial x_j} = \frac{\partial}{\partial x_j}(v_i s_{ij}) - s_{ij}\frac{\partial v_i}{\partial x_j}. \tag{2.123}$$

The first term on the right hand side is the divergence of the viscous stress flow vector $v_i s_{ij}$. This represents an advection of viscous stress. By Gauss's divergence theorem, the volume integral of this term will vanish if the normal component of $v_i s_{ij}$ vanishes on the surface of the region containing the fluid. This is usually the case for astrophysical bodies. The second term represents a dissipation of energy due to the work done by shears in deforming fluid elements, and hence is a source of heat. The magnitude of this dissipation can be written

$$Q_v = s_{ij}\frac{\partial v_i}{\partial x_j} = \frac{1}{2}s_{ij}\left(\frac{\partial v_i}{\partial x_j} + \frac{\partial v_j}{\partial x_i}\right) = s_{ij}e_{ij}, \tag{2.124}$$

where the second equality employs the symmetry of s_{ij}. It then follows from (2.118) for s_{ij} and (2.119) for e_{ij} that

$$Q_v = 2\rho\nu\left[e_{ij}e_{ij} - \frac{1}{3}(\nabla\cdot\mathbf{v})^2\right]. \tag{2.125}$$

This is the viscous dissipation rate per unit volume.

The heat equation is obtained by equating the rate of heat transfer in a fluid element, evaluated following the flow, to its net energy losses and gains. The first law of thermodynamics gives the rate of heat transfer per unit mass in a fluid element as

$$\frac{dQ}{dt} = \frac{dE}{dt} - \frac{P}{\rho^2}\frac{d\rho}{dt}, \tag{2.126}$$

where E is the internal energy per unit mass, and the last term is the rate at which work is done due to compression or expansion. In general, the state variable E will be a function of P and ρ, so (2.126) gives

$$\frac{dQ}{dt} = P\left(\frac{\partial E}{\partial P}\right)_\rho \frac{d}{dt}\ln P + \rho\left[\left(\frac{\partial E}{\partial \rho}\right)_P - \frac{P}{\rho^2}\right]\frac{d}{dt}\ln\rho. \tag{2.127}$$

The adiabatic exponents Γ_1 and Γ_3 are defined as

$$\Gamma_1 = \left(\frac{d\ln P}{d\ln\rho}\right)_{\text{ad}} \tag{2.128a}$$

$$= \frac{\gamma\rho}{P}\left(\frac{\partial P}{\partial\rho}\right)_T, \tag{2.128b}$$

$$\Gamma_3 - 1 = \left(\frac{d\ln T}{d\ln\rho}\right)_{\text{ad}} \tag{2.129a}$$

$$= \frac{1}{\rho c_V}\left(\frac{\partial P}{\partial T}\right)_\rho, \tag{2.129b}$$

where $\gamma = c_P/c_V$ with c_V and c_P the specific heat capacities at constant volume and pressure, given by

$$c_V = \left(\frac{\partial E}{\partial T}\right)_\rho, \tag{2.130a}$$

$$c_P = \left(\frac{\partial E}{\partial T}\right)_P - \frac{P}{\rho^2}\left(\frac{\partial\rho}{\partial T}\right)_P. \tag{2.130b}$$

Setting $dQ = 0$ in (2.127), and using (2.128a) for Γ_1, shows that dQ/dt can be expressed as

$$\frac{dQ}{dt} = P\left(\frac{\partial E}{\partial P}\right)_\rho\left(\frac{d}{dt}\ln P - \Gamma_1\frac{d}{dt}\ln\rho\right). \tag{2.131}$$

The derivative $(\partial E/\partial P)_\rho$ can be related to $(\Gamma_3 - 1)$. From an equation of state $P = P(\rho, T)$ it follows that E can be expressed as a function of ρ and T, then setting $dQ = 0$ in (2.127) and using (2.129a) for $(\Gamma_3 - 1)$ yields

$$\Gamma_3 - 1 = \frac{\rho\left[P/\rho^2 - (\partial E/\partial\rho)_T\right]}{T\,(\partial E/\partial T)_\rho}. \tag{2.132}$$

Since

$$\left(\frac{\partial E}{\partial T}\right)_\rho = \left(\frac{\partial E}{\partial P}\right)_\rho \left(\frac{\partial P}{\partial T}\right)_\rho, \tag{2.133}$$

(2.132) gives

$$\left(\frac{\partial E}{\partial P}\right)_\rho = \frac{\left[P - \rho^2(\partial E/\partial\rho)_T\right]}{(\Gamma_3 - 1)\rho T\,(\partial P/\partial T)_\rho}. \tag{2.134}$$

For reversible changes $dQ = TdS$, where S is the entropy per unit mass. Hence it follows from (2.126) that

$$\frac{dE}{dt} = T\frac{dS}{dt} + \frac{P}{\rho^2}\frac{d\rho}{dt}, \tag{2.135}$$

which yields

$$T = \left(\frac{\partial E}{\partial S}\right)_\rho, \quad P = \rho^2\left(\frac{\partial E}{\partial\rho}\right)_S. \tag{2.136}$$

Then using $E(\rho, T) = E(S(\rho, T), \rho)$ and the Maxwell relation

$$\left(\frac{\partial P}{\partial T}\right)_\rho = -\rho^2\left(\frac{\partial S}{\partial\rho}\right)_T, \tag{2.137}$$

gives

$$\left(\frac{\partial E}{\partial\rho}\right)_T = \frac{P}{\rho^2} - \frac{T}{\rho^2}\left(\frac{\partial P}{\partial T}\right)_\rho. \tag{2.138}$$

It therefore follows from (2.134) that

$$\left(\frac{\partial E}{\partial P}\right)_\rho = \frac{1}{\rho(\Gamma_3 - 1)}, \tag{2.139}$$

which proves (2.129b), since $c_V = (\partial E/\partial T)_\rho$. Hence using (2.139) in (2.131) gives

$$\frac{dQ}{dt} = \frac{P}{(\Gamma_3 - 1)\rho}\left(\frac{d}{dt}\ln P - \Gamma_1 \frac{d}{dt}\ln \rho\right). \tag{2.140}$$

The heat equation is

$$\rho \frac{dQ}{dt} = \mathfrak{L}, \tag{2.141}$$

where $\mathfrak{L}$ represents heat sources and sinks. Using (2.20) for d/dt in (2.140) allows (2.141) to be expressed as

$$\frac{\partial P}{\partial t} - \frac{\Gamma_1 P}{\rho}\frac{\partial \rho}{\partial t} + \mathbf{v}\cdot\left(\nabla P - \frac{\Gamma_1 P}{\rho}\nabla\rho\right) = (\Gamma_3 - 1)\mathfrak{L}, \tag{2.142}$$

where

$$\mathfrak{L} = \rho\epsilon + \mu_0 \eta \mathbf{J}^2 + Q_{\mathrm{v}} - \nabla\cdot\mathbf{F}. \tag{2.143}$$

The first three terms on the right hand side of (2.143) are due to nuclear sources, dissipation of electric currents and viscous dissipation, the latter being given by (2.125). The last term is the divergence of the heat flux.

The heat flux $\mathbf{F}$ will depend on the energy transport mechanism. In an optically thick region the radiative flux is given by

$$\mathbf{F}_{\mathrm{R}} = -\frac{16\sigma_{\mathrm{B}} T^3}{3\kappa\rho}\nabla T, \tag{2.144}$$

where σ_{B} is the Stefan-Boltzmann constant and κ is the Rosseland mean opacity. When the magnitude of the radiative temperature gradient is super adiabatic instability results and convection occurs, leading to a convective flux

$$\mathbf{F}_{\mathrm{c}} = \rho c_P v_{\mathrm{T}} \lambda_{\mathrm{T}} \Delta\nabla T\, \mathbf{e}, \tag{2.145}$$

where v_{T} is the rms turbulent velocity, λ_{T} the mixing length, and $\Delta\nabla T$ is the temperature gradient excess over the adiabatic value (see Cox and Giuli 1968 for an account of radiative transfer and mixing length theory). The unit vector $\mathbf{e}$ is antiparallel to the vertical gravity.

It is noted that for a perfect gas $\Gamma_3 = \gamma$, so (2.139) then integrates to give the thermal energy per unit mass as

$$E = \frac{P}{\rho(\gamma - 1)}. \tag{2.146}$$

Since the thermal energy per unit volume is $\rho E \sim P$, the net heat flow time-scale for a fluid element is $\tau_{\rm th} \sim P/|\mathfrak{L}|$. The flow time-scale associated with the fluid motion is $\tau_{\rm kin} \sim \ell/v$, where ℓ is its length-scale. The ratio of a term on the left of (2.142) to $|\mathfrak{L}|$ is therefore typically

$$\frac{|\mathbf{v}\cdot\nabla P|}{|\mathfrak{L}|} \sim \frac{vP}{\ell|\mathfrak{L}|} \sim \frac{\tau_{\rm th}}{\tau_{\rm kin}}. \tag{2.147}$$

If $\tau_{\rm th} \gg \tau_{\rm kin}$, then net heat flows can be ignored on the gas flow time-scale and the motion is essentially adiabatic. The ratio (2.147) then gives $|\mathbf{v}\cdot\nabla P| \gg |\mathfrak{L}|$ and (2.142) is approximately satisfied by the vanishing of both its sides. Hence $dQ/dt = 0$ and (2.140) yields

$$\frac{dP}{dt} - \frac{\Gamma_1 P}{\rho}\frac{d\rho}{dt} = 0 \tag{2.148}$$

for adiabatic motions . For constant Γ_1, this integrates to give the adiabatic relation

$$P = K\rho^{\Gamma_1}, \tag{2.149}$$

where K is a constant following the motion.

For a non-degenerate gas the equation of state is

$$P = \frac{\mathcal{R}}{\mu}\rho T + \frac{4\sigma_{\rm B}}{3c}T^4, \tag{2.150}$$

where $\mathcal{R}$ and μ are the gas constant and mean molecular weight. The second term represents radiation pressure, which can become important in upper main sequence stars and in the inner parts of some accretion discs. When radiation pressure is ignorable, (2.128b) and (2.150) give $\Gamma_1 = \gamma$. For a fully ionized plasma, μ is given by

$$\frac{1}{\mu} = \frac{3}{2}X + \frac{1}{4}Y + \frac{1}{2}, \tag{2.151}$$

where X and Y are the fractions by mass of hydrogen and helium, respectively (e.g. Cox and Giuli 1968).

2.2.6 Magnetohydrodynamic Waves

Disturbances introduced into a conducting fluid containing a magnetic field are propagated away by the stresses in the field and fluid. If a stable equilibrium state exists, perturbations propagate in the form of hydromagnetic waves. When

gravitational and viscous forces are ignorable, and adiabatic motions are considered, the momentum and heat equations become

$$\frac{\partial \mathbf{v}}{\partial t} + (\mathbf{v}\cdot\nabla)\mathbf{v} = -\frac{1}{\rho}\nabla P + \frac{1}{\mu_0\rho}(\nabla\times\mathbf{B})\times\mathbf{B}, \tag{2.152}$$

$$\frac{\partial P}{\partial t} - \frac{\gamma P}{\rho}\frac{\partial \rho}{\partial t} + \mathbf{v}\cdot\left(\nabla P - \frac{\gamma P}{\rho}\nabla\rho\right) = 0, \tag{2.153}$$

where $\Gamma_1 = \gamma$ for a perfect gas. The simplest wave solutions arise in the high magnetic Reynolds number case, in which the diffusionless form of the induction equation, given by (2.55), applies. If the properties of the undisturbed medium vary with a length-scale ℓ, then these can be considered essentially uniform over a length-scale $\lambda_0 \ll \ell$. Wave solutions with wavelengths $\lambda \lesssim \lambda_0$ will be considered here.

The equilibrium state has $\mathbf{v} = \mathbf{0}$ and is taken to have a uniform magnetic field $\mathbf{B}_0$ and a uniform density ρ_0. The sound speed is $c_s = (dP/d\rho)^{1/2}$. The magnetic field in the perturbed state can be written

$$\mathbf{B} = \mathbf{B}_0 + \mathbf{B}_1(\mathbf{r}, t), \tag{2.154}$$

so $\mathbf{B}_1$ is the field perturbation. Similar expressions hold for other quantities. The Alfvén velocity for the medium is defined as

$$\mathbf{v}_A = \frac{\mathbf{B}_0}{(\mu_0\rho)^{\frac{1}{2}}}. \tag{2.155}$$

Consider, first, a medium in which the sound speed c_s is much greater than v_A and v. The motions are then essentially incompressible, so that $\nabla\cdot\mathbf{v} = 0$. Defining a velocity

$$\mathbf{w} = \frac{\mathbf{B}_1}{(\mu_0\rho)^{\frac{1}{2}}}, \tag{2.156}$$

then using (2.84) for the magnetic force, together with (2.154) and (2.156), the momentum and induction equations can be written as

$$\frac{\partial \mathbf{v}}{\partial t} + (\mathbf{v}\cdot\nabla)\mathbf{v} - [(\mathbf{v}_A + \mathbf{w})\cdot\nabla]\mathbf{w} = -\nabla\left(\frac{P}{\rho} + \frac{B^2}{2\mu_0\rho}\right), \tag{2.157}$$

$$\frac{\partial \mathbf{w}}{\partial t} + (\mathbf{v}\cdot\nabla)\mathbf{w} - [(\mathbf{v}_A + \mathbf{w})\cdot\nabla]\mathbf{v} = \mathbf{0}, \tag{2.158}$$

where ρ is uniform. For a velocity

$$\mathbf{v} = \pm\mathbf{w}, \tag{2.159}$$

the use of (2.158) in (2.157) leads to

$$P + \frac{1}{2}\rho(\mathbf{v}_A + \mathbf{w})^2 = C, \tag{2.160}$$

with C a constant, so the thermal and magnetic pressure gradients cancel. Then $\mathbf{v}$ satisfies the equations

$$\frac{\partial \mathbf{v}}{\partial t} \mp (\mathbf{v}_A \cdot \nabla)\mathbf{v} = \mathbf{0}, \tag{2.161}$$

which have the general solutions

$$\mathbf{v} = \mathbf{v}(\mathbf{r} \pm \mathbf{v}_A t). \tag{2.162}$$

These represent arbitrary waveforms moving with the Alfvén velocity $\mathbf{v}_A$, defined by (2.155). Such Alfvén waves are non-linear solutions, since $|\mathbf{B}_1|$ does not necessarily have to be small relative to $|\mathbf{B}_0|$. It follows from (2.156) and (2.159), relating $\mathbf{v}$ to $\mathbf{B}_1$, that the Alfvén wave has a net energy flux given by

$$\left(\frac{1}{2}\rho v^2 + \frac{B_1^2}{2\mu_0}\right)\mathbf{v}_A = \rho v^2 \mathbf{v}_A, \tag{2.163}$$

showing that the kinetic and magnetic energies are transported along $\mathbf{B}_0$ at the Alfvén speed v_A with equal contributions.

Consider, now, the more general case in which c_s is not necessarily large compared to v_A and v, so compressible motions can occur. Take small perturbations about the equilibrium state, so the equations can be linearized. Equations (2.152), (2.55), (2.103) and (2.153) then respectively yield

$$\frac{\partial \mathbf{v}}{\partial t} = -\frac{1}{\rho_0}\nabla P_1 + \frac{1}{\mu_0 \rho_0}(\nabla \times \mathbf{B}_1) \times \mathbf{B}_0, \tag{2.164}$$

$$\frac{\partial \mathbf{B}_1}{\partial t} = \nabla \times (\mathbf{v} \times \mathbf{B}_0), \tag{2.165}$$

$$\frac{\partial \rho_1}{\partial t} = -\rho_0 \nabla \cdot \mathbf{v}, \tag{2.166}$$

$$\frac{\partial P_1}{\partial t} = c_s^2 \frac{\partial \rho_1}{\partial t}, \tag{2.167}$$

where

$$c_s^2 = \frac{\gamma P_0}{\rho_0}, \tag{2.168}$$

and the equilibrium state is uniform. Differentiating (2.164) with respect to time, and using (2.165)–(2.167) to eliminate the time derivatives of $\mathbf{B}_1$ and P_1, gives the linear wave equation

$$\frac{\partial^2 \mathbf{v}}{\partial t^2} = c_{\rm s}^2 \nabla(\nabla \cdot \mathbf{v}) + \frac{1}{\mu_0 \rho_0}(\nabla \times [\nabla \times (\mathbf{v} \times \mathbf{B}_0)]) \times \mathbf{B}_0. \tag{2.169}$$

For a region with $\mathbf{B}_0 = \mathbf{0}$ the magnetic force term vanishes in the momentum equation (2.164), and it then follows that $\nabla \times \mathbf{v} = \mathbf{0}$. The vector identity (A7) then gives $\nabla(\nabla \cdot \mathbf{v}) = \nabla^2 \mathbf{v}$ and hence (2.169) reduces to a standard equation for sound waves, having the adiabatic speed $c_{\rm s}$ given by (2.168). The restoring force is purely due to the gradient of the thermal pressure perturbation P_1, giving a compressional force and longitudinal modes with the displacement along the wave vector. The presence of a magnetic field $\mathbf{B}_0$ leads to the modified linear wave equation (2.169) and this allows three types of wave solutions, one of which does not involve pressure perturbations and is the linear form of the foregoing Alfvén wave.

For an unbounded medium, plane wave solutions of (2.169) can be sought with the form

$$\mathbf{v} = \mathbf{u} \exp[i(\mathbf{k} \cdot \mathbf{r} - \omega t)], \tag{2.170}$$

where $\mathbf{u}$ is a constant vector. The operator ∇ can then be replaced by $i\mathbf{k}$ and the time derivative $\partial/\partial t$ by $-i\omega$, so using (2.170) in (2.169) yields the time-independent equation

$$\omega^2 \mathbf{u} = c_{\rm s}^2 (\mathbf{k} \cdot \mathbf{u})\mathbf{k} + \frac{1}{\mu_0 \rho_0}(\mathbf{k} \times [\mathbf{k} \times (\mathbf{u} \times \mathbf{B}_0)]) \times \mathbf{B}_0, \tag{2.171}$$

which, employing the vector identity (A1), can be written as

$$\omega^2 \mathbf{u} = v_{\rm A}^2 \Big[(\mathbf{k} \cdot \hat{\mathbf{B}}_0)^2 \mathbf{u} - (\mathbf{k} \cdot \mathbf{u})(\mathbf{k} \cdot \hat{\mathbf{B}}_0)\hat{\mathbf{B}}_0 + \{(1 + c_{\rm s}^2/v_{\rm A}^2)(\mathbf{k} \cdot \mathbf{u}) - (\mathbf{k} \cdot \hat{\mathbf{B}}_0)(\hat{\mathbf{B}}_0 \cdot \mathbf{u})\}\mathbf{k} \Big], \tag{2.172}$$

where $\hat{\mathbf{B}}_0 = \mathbf{B}_0/|\mathbf{B}_0|$ and $v_{\rm A}$ is given by (2.155) with $\rho = \rho_0$. Taking the scalar product of (2.172) with $\mathbf{k}$ and then with $\hat{\mathbf{B}}_0$ gives

$$(-\omega^2 + k^2 c_{\rm s}^2 + k^2 v_{\rm A}^2)(\mathbf{k} \cdot \mathbf{u}) = k^3 v_{\rm A}^2 \cos\theta_B (\hat{\mathbf{B}}_0 \cdot \mathbf{u}), \tag{2.173}$$

$$k c_{\rm s}^2 \cos\theta_B (\mathbf{k} \cdot \mathbf{u}) = \omega^2 (\hat{\mathbf{B}}_0 \cdot \mathbf{u}), \tag{2.174}$$

where

$$\cos\theta_B = \hat{\mathbf{k}} \cdot \hat{\mathbf{B}}_0. \tag{2.175}$$

An incompressible solution exists with $\nabla \cdot \mathbf{v} = 0$ and hence $\mathbf{k} \cdot \mathbf{u} = 0$. Equations (2.173) and (2.174) show that for this mode

$$\hat{\mathbf{B}}_0 \cdot \mathbf{u} = 0, \tag{2.176}$$

so the fluid velocity is perpendicular to the equilibrium magnetic field. The equation of motion (2.172) then yields the dispersion relation

$$\omega = \pm v_{\mathrm{A}} \hat{\mathbf{B}}_0 \cdot \mathbf{k} = \pm k v_{\mathrm{A}} \cos\theta_B, \tag{2.177}$$

where the different signs of ω correspond to oppositely directed waves, when substituted in (2.170). This is the linear form of the foregoing Alfvén wave solution. The phase speed is

$$v_p = \frac{\omega}{k} = \pm v_{\mathrm{A}} \cos\theta_B, \tag{2.178}$$

so propagation is not possible in directions perpendicular to $\mathbf{B}_0$. Noting that $k \cos\theta_B = k_j \hat{B}_{0j}$, the group velocity follows from (2.177) as

$$\mathbf{v}_{\mathrm{g}} = \frac{\partial \omega}{\partial \mathbf{k}} = \pm v_{\mathrm{A}} \hat{\mathbf{B}}_0, \tag{2.179}$$

showing that the energy is carried along $\mathbf{B}_0$ at the Alfvén velocity $\mathbf{v}_{\mathrm{A}}$, consistent with the non-linear result (2.163).

Equations (2.165) and (2.170) give

$$-\omega \mathbf{B}_1 = \mathbf{k} \times (\mathbf{v} \times \mathbf{B}_0) = (\mathbf{k} \cdot \mathbf{B}_0)\mathbf{v}, \tag{2.180}$$

since $\mathbf{k} \cdot \mathbf{v} = 0$. The use of (2.177) for ω then shows that

$$\mathbf{v} = \mp \frac{\mathbf{B}_1}{(\mu_0 \rho_0)^{\frac{1}{2}}}, \tag{2.181}$$

in agreement with (2.156) and (2.159). It follows from (2.176) and (2.181) that

$$\mathbf{B}_0 \cdot \mathbf{B}_1 = 0. \tag{2.182}$$

The first order magnetic force for this mode is therefore

$$\mathbf{J}_1 \times \mathbf{B}_0 = \frac{1}{\mu_0}(\mathbf{B}_0 \cdot \nabla)\mathbf{B}_1 = \frac{i}{\mu_0}(\mathbf{B}_0 \cdot \mathbf{k})\mathbf{B}_1, \tag{2.183}$$

illustrating that the restoring force is purely due to magnetic tension in this incompressible transverse Alfvén mode. The infinitesimal flux tubes act like elastic strings, with the tethered plasma giving a mass per unit length. The magnetic tension

gives the restoring force resulting from a transverse displacement from the current-free unperturbed state.

Equations (2.173) and (2.174) yield two compressible magnetosonic modes, for which $\mathbf{k}\cdot\mathbf{u}\neq 0$. The elimination of $(\mathbf{k}\cdot\mathbf{u})/(\hat{\mathbf{B}}_0\cdot\mathbf{u})$ between these equations leads to the dispersion relation

$$\omega^4-(c_{\rm s}^2+v_{\rm A}^2)k^2\omega^2+c_{\rm s}^2v_{\rm A}^2k^4\cos^2\theta_B=0. \tag{2.184}$$

The two solutions for ω^2 have phase speeds

$$v_{\rm f}=\left[\frac{1}{2}(c_{\rm s}^2+v_{\rm A}^2)+\frac{1}{2}\left\{(c_{\rm s}^2+v_{\rm A}^2)^2-4c_{\rm s}^2v_{\rm A}^2\cos^2\theta_B\right\}^{\frac{1}{2}}\right]^{\frac{1}{2}}, \tag{2.185}$$

$$v_{\rm sl}=\left[\frac{1}{2}(c_{\rm s}^2+v_{\rm A}^2)-\frac{1}{2}\left\{(c_{\rm s}^2+v_{\rm A}^2)^2-4c_{\rm s}^2v_{\rm A}^2\cos^2\theta_B\right\}^{\frac{1}{2}}\right]^{\frac{1}{2}}, \tag{2.186}$$

and are referred to as the fast and slow magnetosonic modes, respectively. The Alfvén mode phase speed satisfies $v_{\rm sl}<v_{\rm A}\cos\theta_B<v_{\rm f}$, and hence this mode is sometimes referred to as the intermediate mode. It is noted that the expressions for $v_{\rm f}$ and $v_{\rm sl}$ are symmetric with respect to the interchange of $c_{\rm s}$ and $v_{\rm A}$, so it follows that $v_{\rm sl}<c_{\rm s}\cos\theta_B<v_{\rm f}$ holds. The cases $v_{\rm A}<c_{\rm s}$ or $v_{\rm A}>c_{\rm s}$ can occur, depending on the value of the ratio B_0^2/μ_0P_0.

The equation of motion for a plane wave disturbance can be written as

$$-\omega\mathbf{v}=-\frac{1}{\rho_0}\left(P_1+\frac{1}{\mu_0}\mathbf{B}_0\cdot\mathbf{B}_1\right)\mathbf{k}+\frac{1}{\mu_0\rho_0}(\mathbf{B}_0\cdot\mathbf{k})\mathbf{B}_1. \tag{2.187}$$

This shows that the force acting on the gas is the sum of a longitudinal component, acting along the wave vector $\mathbf{k}$, and a transverse component, acting normal to $\mathbf{k}$, noting that $\nabla\cdot\mathbf{B}_1=0$ gives $\mathbf{k}\cdot\mathbf{B}_1=0$. The transverse component is proportional to $\cos\theta_B$. The longitudinal component involves the sum of the perturbations to the gas pressure and the magnetic pressure. The first order perturbation to $B^2/2\mu_0$ is $\mathbf{B}_0\cdot\mathbf{B}_1/\mu_0$. Using the plane wave solution (2.170) in the first order MHD equations (2.164)–(2.167) shows that the perturbation in $B^2/2\mu_0$ is related to the pressure perturbation by

$$\frac{1}{\mu_0}\mathbf{B}_0\cdot\mathbf{B}_1=\frac{v_{\rm A}^2}{c_{\rm s}^2}\left(1-\frac{c_{\rm s}^2}{v_p^2}\cos^2\theta_B\right)P_1, \tag{2.188}$$

where $v_p=\omega/k$ is the phase speed of the wave. It then follows from the above result of $v_{\rm sl}<c_{\rm s}\cos\theta_B<v_{\rm f}$ that the bracket in the expression (2.188) is positive for the fast mode and negative for the slow mode. Hence the fast mode motions have perturbations $\mathbf{B}_0\cdot\mathbf{B}_1/\mu_0$ and P_1 of the same sign, while in the slow mode these

perturbations have opposite signs. So in the fast mode the magnetic and thermal pressure perturbations act together, while in the slow mode they are in opposition. The longitudinal force, shown in (2.187), is therefore larger in the fast mode than in the slow mode.

The magnetic field perturbation, which follows from the induction equation, can be expressed as

$$\mathbf{B}_1 = \frac{1}{\gamma}\frac{P_1}{P_0}\mathbf{B}_0 - \frac{1}{\omega}(\mathbf{k}\cdot\mathbf{B}_0)\mathbf{v}. \tag{2.189}$$

This is the sum of a compressive contribution, containing P_1 and derived from the term $(\nabla\cdot\mathbf{v})\mathbf{B}_0$, and a stretching contribution, derived from the term $(\mathbf{B}_0\cdot\nabla)\mathbf{v}$, which is proportional to $\cos\theta_B$. Hence, in the slow and fast modes, the $(\mathbf{B}_0\cdot\mathbf{k})\mathbf{B}_1$ tension force term in (2.187) has a component along $\mathbf{B}_0$ due to the compression and expansion of flux tubes, as well as a contribution along $\mathbf{v}$ due to stretching of the field. In the Alfvén mode there are no gas and magnetic pressure perturbations, leaving only the transverse force which becomes normal to $\mathbf{B}_0$ and parallel to $\mathbf{v}$. It can be shown that the fast mode propagates most energy in directions near to that of the wave vector $\mathbf{k}$, while the slow mode transports most energy in directions nearer to $\hat{\mathbf{B}}_0$.

A weak magnetic field limit can be defined by $v_\mathrm{A} \ll c_\mathrm{s}$, corresponding to $B_0^2/2\mu_0 \ll P_0$ so the magnetic energy density is small compared to the thermal energy density. The fast and slow mode phase speed expressions, given by (2.185) and (2.186), can then be expanded in powers of $v_\mathrm{A}/c_\mathrm{s}$ which leads to the first order results $v_\mathrm{f} = c_\mathrm{s}$ and $v_\mathrm{sl} = v_\mathrm{A}\cos\theta_B$. Hence, in this limit, the fast mode becomes a pure sound wave and the slow mode becomes degenerate with the Alfvén mode. So, to first order in $v_\mathrm{A}/c_\mathrm{s}$, there is a pure magnetic mode, the Alfvén wave, and a pure non-magnetic mode, the sound wave. This separation can result in a well sub-thermal magnetic field being dynamically significant. An example of this occurs in Keplerian accretion discs, in which a sub-thermal magnetic field destabilizes the flow and leads to turbulence. Such effects are particularly relevant to dynamo theory.

In the strong field limit of $v_\mathrm{A} \gg c_\mathrm{s}$ first order expansion in $c_\mathrm{s}/v_\mathrm{A}$ yields $v_\mathrm{f} = v_\mathrm{A}$ and $v_\mathrm{sl} = c_\mathrm{s}\cos\theta_B$. This result also follows from the interchange symmetry with respect to c_s and v_A of the expressions (2.185) and (2.186) for v_f and v_sl, so it can be obtained from the weak magnetic limit by exchanging c_s and v_A to give the strong field limit. Hence, in this limit, the fast mode transmits energy nearly isotropically at the Alfvén speed, while the slow mode has a group velocity of $c_\mathrm{s}\hat{\mathbf{B}}_0$ and so transmits energy along the unperturbed magnetic field at the sound speed.

In the non-linear regime, like sound waves, the slow and fast magnetosonic modes become their corresponding shock waves (e.g. Priest 2014). Standing slow shock fronts can occur just above the surface of a compact accretor where the incoming supersonic and sub-Alfvénic, magnetically channelled stream becomes dissipated.

2.2.7 Mach Numbers

The importance of the pressure gradient and magnetic force terms in the momentum equation (2.106) can be gauged by defining the dimensionless Mach numbers

$$\mathfrak{M}_{\rm s} = \frac{v_0}{c_{\rm s}}, \tag{2.190a}$$

$$\mathfrak{M}_{\rm A} = \frac{v_0}{v_{\rm A}}, \tag{2.190b}$$

where v_0 is a characteristic fluid speed. These are acoustic and Alfvén Mach numbers. If the characteristic length-scale for variations in the medium is ℓ, then the ratio of the inertial term to the thermal pressure term in the momentum equation is

$$\frac{|(\mathbf{v}\cdot\nabla)\mathbf{v}|}{|\nabla P|/\rho} \sim \frac{v_0^2}{P/\rho} \sim \left(\frac{v_0}{c_{\rm s}}\right)^2 = \mathfrak{M}_{\rm s}^2. \tag{2.191}$$

For highly supersonic flow $\mathfrak{M}_{\rm s} \gg 1$, and hence the pressure gradient term is ignorable along the flow direction. The physical reason for this is that the sound speed determines how fast pressure disturbances propagate through the gas. The magnitude of $c_{\rm s}$ therefore limits the rapidity with which the flowing gas can respond to pressure changes. For $\mathfrak{M}_{\rm s} \gg 1$, the flow time-scale, ℓ/v_0, is much shorter than the sound travel time, $\ell/c_{\rm s}$, so the gas does not have time to respond to pressure changes. In energy terms, the kinetic energy density, $\rho v^2/2$, far exceeds the thermal energy density of $\sim P$ when $\mathfrak{M}_{\rm s} \gg 1$, so the flow is not significantly affected by the pressure.

For a highly subsonic flow $\mathfrak{M}_{\rm s} \ll 1$ holds and, to a good approximation, the velocity terms are ignorable in the momentum equation. This corresponds to an equilibrium state in which the relevant forces approximately balance. Because of the vector nature of the momentum equation, it sometimes happens that $\mathbf{v}$ has subsonic and supersonic components. Thin accretion discs are an example of this, in which the poloidal velocity components are subsonic while the azimuthal velocity is supersonic.

A similar argument applies for the effect of the magnetic force term in the momentum equation. Then

$$\frac{|(\mathbf{v}\cdot\nabla)\mathbf{v}|}{|(\nabla\times\mathbf{B})\times\mathbf{B}|/\mu_0\rho} \sim \frac{v_0^2}{B^2/\mu_0\rho} = \left(\frac{v_0}{v_{\rm A}}\right)^2 = \mathfrak{M}_{\rm A}^2, \tag{2.192}$$

using (2.155) for the Alfvén speed $v_{\rm A}$. The cases with high and low values of this ratio have important relevance.

When $\mathfrak{M}_{\rm A} \gg 1$ the flow is highly super-Alfvénic and the gas does not have time to respond to spatial changes in the magnetic field (i.e. to the $\mathbf{J}\times\mathbf{B}$ force), since the Alfvén travel time, $\ell/v_{\rm A}$, is much longer than the flow time, ℓ/v_0. The

effect of the magnetic force is therefore ignorable in such flows. The velocity is then determined by the non-magnetic equations and this solution for **v** can be used in the induction equation to determine **B**. The hydrodynamic and hydromagnetic problems are essentially decoupled in such kinematic situations. An example of this occurs in the super-Alfvénic regions of magnetic stellar wind flows, in which the weakly magnetically affected flow nearly conserves its angular momentum and causes the poloidal magnetic field to have a more radial geometry.

When $\mathfrak{M}_{\rm A} \ll 1$ the flow is highly sub-Alfvénic and the magnetic force can constrain its geometry, causing effective channelling. This leads to nearly force-free field structures, as occur in magnetically channelled accretion streams and in magnetically controlled inner regions of wind flows.

2.2.8 The Free-Fall Alfvén Radius

An estimate of where the magnetic field becomes dynamically significant (i.e. $\mathfrak{M}_{\rm A} \sim 1$) for accretion on to a magnetized star can be made for the idealized case of spherically symmetric, radial inflow. The simplest case is that without significant thermal pressure support, so the resulting supersonic radial velocity has an approximately free-fall variation with distance r from the centre of the accretor.

Taking the star to have a dipole magnetic field, and ignoring angular variations, gives

$$B \simeq \frac{B_0 R_{\rm p}^3}{r^3}, \tag{2.193}$$

where $R_{\rm p}$ is the stellar radius and B_0 the surface field. The free-fall radial velocity has magnitude

$$|v_r| = \left(\frac{2GM_{\rm p}}{r}\right)^{\frac{1}{2}}, \tag{2.194}$$

where $M_{\rm p}$ is the stellar mass.

Ignoring field distortion, a free-fall Alfvén radius $r_{\rm A}$ can be defined by equating the kinetic and magnetic energy densities, so $\rho v_r^2 = B^2/\mu_0$, where $|v_r| = v_{\rm A}$. Using this and the above equations, together with the mass conservation equation $\dot{M}_{\rm p} = 4\pi r^2 \rho |v_r|$ to eliminate $\rho|v_r|$, where $\dot{M}_{\rm p}$ is the accretion rate, yields

$$r_{\rm A} = 3.5 \times 10^6 \frac{\left(\frac{B_0}{10^{12}\,{\rm G}}\right)^{\frac{4}{7}} \left(\frac{R_{\rm p}}{10^4\,{\rm m}}\right)^{\frac{12}{7}}}{\left(\frac{M_{\rm p}}{1.4\,M_\odot}\right)^{\frac{1}{7}} \left(\frac{\dot{M}_{\rm p}}{10^{-9}\,M_\odot\,{\rm year}^{-1}}\right)^{\frac{2}{7}}}\,{\rm m}, \tag{2.195}$$

where quantities are normalized with respect to parameters typical of accreting magnetic neutron stars.

For highly conducting material, this gives an estimate of the radius at which the stellar magnetic field starts to affect the accretion flow when this has velocities close to free-fall values. For $r \ll r_{\rm A}$ the flow is highly sub-Alfvénic and magnetic channelling constrains its geometry.

2.2.9 *Poloidal and Toroidal Representations of* **B**

The magnetic field, being divergenceless, can be separated into poloidal and toroidal parts as

$$\mathbf{B} = \mathbf{B}_{\rm p} + \mathbf{B}_{\rm T} = \nabla \times [\nabla \times (\Phi_{\rm p}\hat{\mathbf{r}})] + \nabla \times (\Phi_{\rm T}\hat{\mathbf{r}}), \tag{2.196}$$

where $\Phi_{\rm p}$ and $\Phi_{\rm T}$ are the poloidal and toroidal scalars (Chandrasekhar 1961). These magnetic field representations are often used.

In spherical polar coordinates (r, θ, ϕ) the components of the poloidal and toroidal fields are

$$B_{{\rm p}r} = \frac{1}{r^2} L^2 \Phi_{\rm p}, \tag{2.197}$$

$$B_{{\rm p}\theta} = \frac{1}{r} \frac{\partial^2 \Phi_{\rm p}}{\partial r \partial \theta}, \tag{2.198}$$

$$B_{{\rm p}\phi} = \frac{1}{r \sin\theta} \frac{\partial^2 \Phi_{\rm p}}{\partial r \partial \phi}, \tag{2.199}$$

and

$$B_{{\rm T}r} = 0, \tag{2.200}$$

$$B_{{\rm T}\theta} = \frac{1}{r \sin\theta} \frac{\partial \Phi_{\rm T}}{\partial \phi}, \tag{2.201}$$

$$B_{{\rm T}\phi} = -\frac{1}{r} \frac{\partial \Phi_{\rm T}}{\partial \theta}, \tag{2.202}$$

where

$$L^2 = -\frac{1}{\sin\theta} \frac{\partial}{\partial \theta} \left(\sin\theta \frac{\partial}{\partial \theta} \right) - \frac{1}{\sin^2\theta} \frac{\partial^2}{\partial \phi^2}. \tag{2.203}$$

It is noted that these fields are generalizations of the canonical axisymmetric poloidal and toroidal fields. Equations (2.197)–(2.199) and (2.200)–(2.202) show

that only in an axisymmetric case will $\mathbf{B}_\mathrm{p}$ lie in a meridional plane and $\mathbf{B}_\mathrm{T}$ be purely azimuthal. Nevertheless, the generalized fields have similar useful analytic properties to the axisymmetric fields.

It is seen from (2.196) that the curl of a toroidal vector is a poloidal vector, the converse also being true since vector identities yield

$$\nabla \times \mathbf{B}_\mathrm{p} = \nabla \times \left[\left\{ -r\nabla^2 \left(\frac{\Phi_\mathrm{p}}{r} \right) \right\} \hat{\mathbf{r}} \right]. \tag{2.204}$$

The current density can therefore be written as

$$\mathbf{J} = \mathbf{J}_\mathrm{p} + \mathbf{J}_\mathrm{T} = \frac{1}{\mu_0} \nabla \times [\nabla \times (\Phi_\mathrm{T} \hat{\mathbf{r}})] + \frac{1}{\mu_0} \nabla \times \left[\left\{ -r\nabla^2 \left(\frac{\Phi_\mathrm{p}}{r} \right) \right\} \hat{\mathbf{r}} \right]. \tag{2.205}$$

In an insulator this shows, in general, that

$$\nabla^2 \left(\frac{\Phi_\mathrm{p}}{r} \right) = 0, \tag{2.206a}$$

$$\Phi_\mathrm{T} = 0. \tag{2.206b}$$

Since

$$\nabla^2 = \frac{1}{r^2} \frac{\partial}{\partial r} \left(r^2 \frac{\partial}{\partial r} \right) - \frac{1}{r^2} L^2, \tag{2.207}$$

it follows from (2.89), (2.197)–(2.199) and (2.206a) that in an insulator **B** can be expressed as

$$\mathbf{B} = \nabla \left(\frac{\partial \Phi_\mathrm{p}}{\partial r} \right). \tag{2.208}$$

It is often convenient to express Φ_p and Φ_T as expansions in a basis of radial functions and spherical harmonics, so

$$\Phi_\mathrm{p} = \sum_{l=1}^{\infty} \sum_{m=-l}^{l} U_{lm}(r) Y_l^m(\theta, \phi) f_{lm}(t), \tag{2.209}$$

$$\Phi_\mathrm{T} = \sum_{l=1}^{\infty} \sum_{m=-l}^{l} V_{lm}(r) Y_l^m(\theta, \phi) g_{lm}(t), \tag{2.210}$$

where $f_{lm}(t)$ and $g_{lm}(t)$ are time dependences appropriate to the specific problem.

Spherical harmonics are eigenfunctions of L^2 since

$$L^2 Y_l^m(\theta,\phi) = l(l+1)Y_l^m(\theta,\phi), \tag{2.211}$$

(see Appendix). They are given by

$$Y_l^m(\theta,\phi) = P_l^{|m|}(\cos\theta)e^{im\phi}, \tag{2.212}$$

where

$$P_l^{|m|}(\mu) = \frac{(1-\mu^2)^{\frac{|m|}{2}}}{2^l l!}\left(\frac{d}{d\mu}\right)^{l+|m|}(\mu^2-1)^l, \tag{2.213}$$

with $\mu = \cos\theta$, are associated Legendre functions obeying the differential equation (A32) and having the orthogonality relation (A35). If the problem has an appropriate small dimensionless parameter, finite expansions involving the first few terms in (2.209) and (2.210) can be used.

2.2.10 *Decay Modes of* **B** *in a Conductor*

In a plasma with no significant motions and a constant magnetic diffusivity, **B** obeys the diffusion equation

$$\eta\nabla^2\mathbf{B} = \frac{\partial\mathbf{B}}{\partial t}. \tag{2.214}$$

In the absence of an externally applied field, **B** decays on the time-scale τ_d, given by (2.70). Exact solutions of (2.214) can be found for the magnetic decay modes in a spherical conductor. The magnetic field can be split into poloidal and toroidal parts, as in (2.196). If the external medium is taken as a vacuum, only the poloidal field extends beyond the sphere, so the decay of this component will be considered.

In spherical coordinates (r,θ,ϕ) the poloidal scalar can be expressed in harmonics of the form

$$\Phi_\mathrm{p} = U_l(r)Y_l^m(\theta,\phi)\exp(-\lambda^2 t), \tag{2.215}$$

where λ^2 is the decay rate to be determined. The poloidal magnetic field is

$$\mathbf{B}_\mathrm{p} = \nabla\times[\nabla\times(\Phi_\mathrm{p}\hat{\mathbf{r}})]. \tag{2.216}$$

Substituting (2.215) and (2.216) in (2.214) shows that $U_l(r)$ must satisfy

$$\frac{d^2U_l}{dr^2} + \left[\frac{\lambda^2}{\eta} - \frac{l(l+1)}{r^2}\right] U_l = 0. \tag{2.217}$$

The solution of this equation, free of singularity at $r = 0$, is

$$U_l(r) = r^{\frac{1}{2}} J_{l+\frac{1}{2}}\left(\frac{\lambda}{\eta^{\frac{1}{2}}} r\right), \tag{2.218}$$

where $J_{l+1/2}$ is a Bessel function of the first kind of order $l + 1/2$, given by (A31).

In the surrounding vacuum $\eta \to \infty$ and the solution of (2.217) which vanishes as $r \to \infty$ is

$$U_l(r) = \frac{A}{r^l}, \tag{2.219}$$

where A is a constant. It follows from (2.197)–(2.199) that the continuity of $\mathbf{B}_\mathrm{p}$ at the surface requires U_l and dU_l/dr to be continuous at $r = R_\mathrm{s}$. Applying these conditions, using the internal and external solutions (2.218) and (2.219) and eliminating A, gives

$$R_\mathrm{s} J'_{l+\frac{1}{2}}\left(\frac{\lambda}{\eta^{\frac{1}{2}}} R_\mathrm{s}\right) + \left(l + \frac{1}{2}\right) J_{l+\frac{1}{2}}\left(\frac{\lambda}{\eta^{\frac{1}{2}}} R_\mathrm{s}\right) = 0, \tag{2.220}$$

where the prime denotes differentiation with respect to r. Using the recurrence relation

$$x\frac{dJ_\nu}{dx} + \nu J_\nu(x) = x J_{\nu-1}(x), \tag{2.221}$$

with $x = (\lambda/\eta^{1/2})r$, (2.220) can be written as

$$J_{l-\frac{1}{2}}\left(\frac{\lambda}{\eta^{\frac{1}{2}}} R_\mathrm{s}\right) = 0. \tag{2.222}$$

Denoting the jth zero of $J_{l-1/2}$ as $\alpha_{lj} = \lambda_{lj} R_\mathrm{s}/\eta^{1/2}$, (2.218) becomes

$$U_{lj}(r) = r^{\frac{1}{2}} J_{l+\frac{1}{2}}\left(\alpha_{lj}\frac{r}{R_\mathrm{s}}\right). \tag{2.223}$$

The corresponding magnetic decay times of these modes are $\tau_{lj} = \lambda_{lj}^{-2}$ and so (2.218) and (2.223) give

$$\tau_{lj} = \frac{R_{\rm s}^2}{\alpha_{lj}^2 \eta}. \tag{2.224}$$

The length-scales of the corresponding magnetic fields are $R_{\rm s}/\alpha_{lj}$. The higher modes have shorter length-scales and hence their field components have higher spatial derivatives, resulting in larger values of $|\mathbf{J}|$. They therefore dissipate more rapidly, in accordance with (2.69) for the magnetic dissipation rate $Q_{\rm m}$, and consequently have shorter decay times.

2.2.11 Magnetic Diffusivity

The electrical conductivity of a fully-ionized, collision-dominated plasma is given by Spitzer (1962) as

$$\sigma = 1.5 \times 10^{-2} \frac{T^{\frac{3}{2}}}{\ln \Lambda} (\text{ohm-metre})^{-1}. \tag{2.225}$$

The Coulomb logarithm is typically $5 < \ln \Lambda < 20$, having a weak dependence on density and temperature. The magnetic diffusivity $\eta = 1/\mu_0 \sigma$ and using the Ohmic conductivity yields

$$\eta_{\rm ohm} = 5.2 \times 10^7 \ln \Lambda \, T^{-\frac{3}{2}} \, \text{m}^2 \text{s}^{-1}. \tag{2.226}$$

As discussed in Sect. 2.2.1, the conductivity becomes anisotropic if $\omega_{\rm e} \tau_{\rm ei} \gg 1$, where $\omega_{\rm e}$ is the electron gyro-frequency and $\tau_{\rm ei}$ the collision time for scattering of electrons by ions.

When the hydrogen plasma is partially ionized (2.226) for $\eta_{\rm ohm}$ should be multiplied by $(1 + \tau_{\rm ei}/\tau_{\rm en})$, where the ratio of effective electron collision times with ions and neutral particles is

$$\frac{\tau_{\rm ei}}{\tau_{\rm en}} = 5.2 \times 10^{-11} \frac{n_{\rm n}}{n_{\rm e}} \frac{T^2}{\ln \Lambda}, \tag{2.227}$$

with $n_{\rm n}$ and $n_{\rm e}$ being the number densities of neutral particles and electrons, respectively. The diffusivity $\eta_{\rm ohm}$ is used for non-turbulent plasmas.

In most cases the secondary stars in close binaries have masses $\lesssim 0.8 M_\odot$ and hence possess deep convective envelopes, becoming fully convective for $M_{\rm s} \leq 0.35\, M_\odot$. Equation (2.226) is then inappropriate for η, since the presence of turbulence is believed to greatly enhance the diffusion of magnetic fields in plasmas.

Due to the absence of a rigorous theory of stellar turbulence, the mixing length approach is usually adopted to estimate η. If the turbulent eddies have an rms speed $v_{\rm T}$ and a length-scale $\lambda_{\rm T}$, an eddy magnetic diffusivity can be defined as

$$\eta_{\rm T} = \frac{1}{3} v_{\rm T} \lambda_{\rm T}. \tag{2.228}$$

This is analogous to the eddy viscosity coefficient given by (2.120). The form (2.228) for $\eta_{\rm T}$ arises when the cascade picture of hydrodynamic turbulence is combined with field freezing, provided the field does not react back on the dynamics of the turbulence. The validity of such assumptions is discussed later, in the context of dynamo theory. For a perfect gas equation of state, the convective heat flux is given by

$$F_{\rm c} = 10 \rho v_{\rm T}^3 \frac{\lambda_P}{\lambda_{\rm T}}, \tag{2.229}$$

(e.g. Cox and Giuli 1968) where λ_P is the pressure scale height. It follows that

$$v_{\rm T} = \left(\frac{\lambda_{\rm T}}{\lambda_P} \frac{L}{40 \pi r^2 \rho} \right)^{\frac{1}{3}}, \tag{2.230}$$

where L is the luminosity and the star is taken as non-rotating. The mixing length is usually taken to be λ_P in the main body of the star. In a fully convective star a different form for $\lambda_{\rm T}$ must be used near the stellar centre, since λ_P diverges there.

The secondary stars in close binary systems are expected to be synchronized with the orbital motion, due to tidal effects (e.g. Campbell and Papaloizou 1983). Their rotation periods are therefore typically $P \lesssim 7\,\mathrm{h}$, while a typical convective time-scale in the stellar interior is $\tau_{\rm T} \sim \lambda_P / v_{\rm T} \sim 4$ months. Since $P \ll \tau_{\rm T}$ in the inner regions some modification should be made in the calculation of $\eta_{\rm T}$, to estimate the effect of rotation on convection. A Rossby number can be defined, as a measure of the effect of rotation on the turbulence, as

$$R_{\rm T} = \frac{v_{\rm T}}{\ell \Omega} \sim \frac{|(\mathbf{v}_{\rm T} \cdot \nabla) \mathbf{v}_{\rm T}|}{|2 \boldsymbol{\Omega} \times \mathbf{v}_{\rm T}|} \sim \frac{P}{\tau_{\rm T}}, \tag{2.231}$$

where $\mathbf{v}_{\rm T}$ is measured in the orbital frame. Goldreich and Keeley (1977) adopt the local formula

$$\eta_{\rm T} = \eta_0 G_{\rm R}, \tag{2.232}$$

where

$$G_{\rm R} = \begin{cases} 1, & R_{\rm T} > 1, \\ R_{\rm T}^2, & R_{\rm T} < 1. \end{cases} \tag{2.233}$$

Both $v_{\rm T}$ and $\lambda_{\rm T}$ are modified in (2.228) and using (2.230) for $v_{\rm T}$ gives

$$\eta_0 = \frac{1}{3}\lambda_P \left(\frac{\lambda_{\rm T}}{\lambda_P}\right)^{\frac{4}{3}} \left(\frac{L}{40\pi r^2 \rho}\right)^{\frac{1}{3}}. \tag{2.234}$$

In turbulent accretion discs a simple prescription similar to (2.228) is often used for $\eta_{\rm T}$, with $v_{\rm T}$ being a fraction of the sound speed and $\lambda_{\rm T}$ a fraction of the disc height h. Hence

$$\eta_{\rm T} = \epsilon_{\rm T} c_{\rm s} h, \tag{2.235}$$

with $\epsilon_{\rm T} < 1$. A modification similar to (2.232) can be made for the effect of rotation.

Magnetic buoyancy is believed to play a role in the diffusion of the field in stars and discs. The basic mechanism can be understood by considering a horizontal flux tube with uniform field **B** surrounded by a gas with a locally weak magnetic field. The vertical gravitational field **g** is taken to be uniform, and the medium is assumed to be isothermal with temperature T. If $P_{\rm in}$ and $P_{\rm ex}$ are the thermal pressures in the tube and in the exterior medium, respectively, horizontal force balance across **B** yields

$$P_{\rm ex} = P_{\rm in} + \frac{B^2}{2\mu_0}. \tag{2.236}$$

The gas equation and isothermality then give

$$\frac{\rho_{\rm ex} - \rho_{\rm in}}{\rho_{\rm ex}} = \frac{B^2}{2\mu_0 P_{\rm ex}}. \tag{2.237}$$

This implies $\rho_{\rm in} < \rho_{\rm ex}$ so the tube experiences a magnetic buoyancy force per unit volume of

$$F_{\rm B} = (\rho_{\rm ex} - \rho_{\rm in})g = \frac{g\rho_{\rm ex} B^2}{2\mu_0 P_{\rm ex}}. \tag{2.238}$$

As the tube rises it will become curved and feel a force due to magnetic tension of $\sim B^2/\mu_0 R_c$, where R_c is its characteristic radius of curvature. This will be small compared to $F_{\rm B}$ if

$$R_c > \frac{B^2}{\mu_0 g(\rho_{\rm ex} - \rho_{\rm in})} = \frac{2P_{\rm ex}}{g\rho_{\rm ex}} = \frac{2P_{\rm ex}}{|dP_{\rm ex}/dz|}, \tag{2.239}$$

where the last equality uses vertical equilibrium in the surroundings. Hence magnetic tension is small if $R_c > 2\lambda_P$, where λ_P is the pressure scale height. In the presence of turbulence the rising tube will experience a frictional force opposing $F_{\rm B}$. Writing the resultant force density as $\zeta F_{\rm B}$, where $\zeta < 1$, the tube velocity $v_{\rm B}$

attained in moving a distance ℓ can be found by equating the kinetic energy gained to the work done, so

$$\frac{1}{2}\rho_{\rm in} v_{\rm B}^2 \simeq \zeta F_{\rm B} \ell = \frac{\zeta g \ell \rho_{\rm ex} B^2}{2\mu_0 P_{\rm ex}} = \frac{\ell}{\lambda_P}\frac{\zeta B^2}{2\mu_0}, \tag{2.240}$$

giving

$$v_{\rm B} \simeq \left(\frac{\ell}{\lambda_P}\zeta\right)^{\frac{1}{2}} \left(\frac{B^2}{\mu_0 \rho_{\rm in}}\right)^{\frac{1}{2}} = \left(\frac{\ell}{\lambda_P}\zeta\right)^{\frac{1}{2}} v_{\rm A}, \tag{2.241}$$

where the Alfvén speed $v_{\rm A} = (B^2/\mu_0\rho_{\rm in})^{1/2}$. Taking the magnetic field to be dissipated over the length-scale $\ell \sim \lambda_P$, which has an associated tube velocity $v_{\rm B} \simeq \sqrt{\zeta} v_{\rm A}$, leads to a magnetic buoyancy transport coefficient

$$\eta_{\rm B} = v_{\rm B}\lambda_P = \frac{\xi |B_\perp|}{(\mu_0\rho)^{\frac{1}{2}}}\lambda_P, \tag{2.242}$$

where $\xi = \sqrt{\zeta}$, the subscript has been dropped from $\rho_{\rm in}$, and $B_\perp$ is the horizontal field. The field is dissipated via small-scale turbulent reconnection causing a friction between rising tubes. The detailed magnetic buoyancy instability was analysed by Parker (1979).

Usually $\eta_{\rm T}$ and $\eta_{\rm B}$ are several orders of magnitude larger than $\eta_{\rm ohm}$. In cases where poloidal field winding occurs, due to shears in the flow, an effective dynamical diffusivity $\eta_{\rm dyn}$ is sometimes used to represent the limiting effects of instabilities and reconnections likely to occur. The transport speed is of the order of a typical dynamical speed, and a suitable mixing length is adopted. Tensor forms can be adopted for the magnetic diffusivity in accretion discs, to account for the differing radial and vertical length-scales.

2.3 Basic Dynamo Theory

2.3.1 Field Generation

The induction equation, given by (2.52), describes the evolution of a magnetic field in a plasma with finite conductivity and fluid motions. In the absence of significant motions (i.e. $R_{\rm m} \ll 1$), the diffusive limit (2.66) holds. Without an externally imposed field, this equation has decaying solutions with $|\mathbf{B}|$ decreasing on the diffusion time-scale $\tau_{\rm d}$, given by (2.70). It is often the case with astrophysical bodies that $\tau_{\rm d}$ is shorter than their age, so internal motions are necessary to explain observed magnetic fields which would otherwise have decayed to negligible values. This is

especially true in turbulent bodies in which the diffusion of $\mathbf{B}$ is believed to be greatly enhanced compared to that in Ohmic conductors, as discussed above.

This situation results in the need for a dynamo mechanism to generate $\mathbf{B}$ and counter its dissipation. It was seen that the $\mathbf{v} \times \mathbf{B}$ term in (2.52) by itself (i.e. $R_\mathrm{m} \gg 1$) corresponds to the plasma being threaded on the field lines. With significant diffusion (i.e. $R_\mathrm{m} \sim 1$) a fluid element can move across field lines, but there is still some freezing effect with motions affecting the field structure. The induction equation shows how this process operates. In general, the magnetic force $\mathbf{J} \times \mathbf{B}$ affects the motions and a full non-linear MHD problem results. However, the basic dynamo mechanism can be understood by just considering the induction equation, which illustrates what types of motion are necessary for sustained field generation.

Consider, first, an axisymmetric situation so quantities are independent of ϕ in the cylindrical coordinate system (ϖ, ϕ, z). The magnetic field can then be split into poloidal and toroidal components, as

$$\mathbf{B} = \mathbf{B}_\mathrm{p} + B_\phi \hat{\boldsymbol{\phi}}. \tag{2.243}$$

The velocity $\mathbf{v}$ can be resolved in a similar way. The poloidal magnetic field may be expressed in terms of a toroidal vector potential by

$$\mathbf{B}_\mathrm{p} = \nabla \times (A\hat{\boldsymbol{\phi}}), \tag{2.244}$$

so $\nabla \cdot \mathbf{B} = 0$ is satisfied. The induction equation then splits into two components, one for the time derivative of B_ϕ and the other for that of A.

The toroidal equation follows from taking the scalar product of (2.52) with $\hat{\boldsymbol{\phi}}/\varpi$ and employing the result

$$\nabla \times \left(\frac{1}{\varpi} \hat{\boldsymbol{\phi}} \right) = \mathbf{0}, \tag{2.245}$$

together with standard vector identities. This gives

$$\frac{\partial B_\phi}{\partial t} + \varpi \mathbf{v}_\mathrm{p} \cdot \nabla \left(\frac{B_\phi}{\varpi} \right) = \varpi \mathbf{B}_\mathrm{p} \cdot \nabla \Omega - B_\phi \nabla \cdot \mathbf{v}_\mathrm{p} + \eta \left(\nabla^2 B_\phi - \frac{B_\phi}{\varpi^2} \right) \tag{2.246}$$

where $\Omega = v_\phi/\varpi$ and η is taken as constant. It is noted that, due to axisymmetry, $\mathbf{v}_\mathrm{p}$ can be replaced by $\mathbf{v}$ in this equation. After division by ϖ, the left hand side represents the rate of change of B_ϕ/ϖ following the motion of a fluid element (i.e. the Lagrangian derivative). The first term on the right hand side gives the rate of change of the angular velocity along the poloidal field. When Ω varies along $\mathbf{B}_\mathrm{p}$ the shearing motion draws out $\mathbf{B}_\mathrm{p}$ in the azimuthal direction. Hence this term represents the creation of B_ϕ from $\mathbf{B}_\mathrm{p}$, being referred to as the Ω-effect. The second term, involving $\nabla \cdot \mathbf{v}$, corresponds to a rate of change of B_ϕ due to compressibility in the flow. Compression of a fluid element causes an increase in $|B_\phi|$, due to azimuthal

field lines being squeezed together, while an expansion dilutes the field strength. The final term represents the diffusion of B_ϕ, this being a decay term with an associated dissipation of poloidal electric currents.

The equation describing the evolution of A, the vector potential corresponding to $\mathbf{B}_\mathrm{p}$, follows from substituting (2.244) in the induction equation, giving

$$\frac{\partial A}{\partial t} + \frac{1}{\varpi}\mathbf{v}_\mathrm{p} \cdot \nabla(\varpi A) = \eta\left(\nabla^2 A - \frac{A}{\varpi^2}\right). \tag{2.247}$$

After multiplying by ϖ, the left hand side of this equation is the Lagrangian time derivative of the poloidal flux function $\psi_\mathrm{m} = \varpi A$, while the right hand side represents the diffusion of A. The poloidal flux, and hence $\mathbf{B}_\mathrm{p}$, therefore decays in a fluid element due to diffusion, since (2.247) lacks a field creation term. Although (2.246) contains a term corresponding to the creation of B_ϕ from $\mathbf{B}_\mathrm{p}$, this term will decay with $\mathbf{B}_\mathrm{p}$ and hence B_ϕ will also decay. This situation is summarized in the theorem due to Cowling (1933) which states that 'a steady axisymmetric magnetic field cannot be maintained by dynamo action'.

Since many astrophysical bodies, such as stars and discs, are essentially axisymmetric and magnetic fields of this symmetry were observed, Cowling's theorem cast serious doubts on dynamo theory for over 20 years. A suggestion for resolving the problem was made by Parker (1955). He noted that if small-scale convective motions are present in a rotating body then rising plasma elements tend to rotate due to the Coriolis force. With significant advection of the magnetic field, such twisting motions convert toroidal field to a poloidal component. Falling elements rotate the field in the opposite direction and there must be some asymmetry between the up and down motions for a net effect. Stratification, with rising elements expanding and falling ones contracting, was used to provide the asymmetry. Parker modelled the net effect of many convective cells as a toroidal electric field

$$E_\phi = \alpha B_\phi. \tag{2.248}$$

This is the so-called α-effect. The quantity α is a measure of the mean helicity of the turbulence. Since the anticyclonic motions have odd symmetry about the equatorial plane, α is an odd function of the vertical coordinate.

In astrophysical bodies turbulence is usually assumed to generate the α-effect. The theory of mean-field electrodynamics can be used to formulate the effect, if certain assumptions are made. The velocity and magnetic fields are expressed as sums of mean and turbulent fluctuating parts, so

$$\mathbf{v} = \mathbf{v}_0 + \mathbf{v}_\mathrm{T}, \quad \mathbf{v}_0 = \langle \mathbf{v} \rangle, \tag{2.249}$$

$$\mathbf{B} = \mathbf{B}_0 + \mathbf{B}_\mathrm{T}, \quad \mathbf{B}_0 = \langle \mathbf{B} \rangle, \tag{2.250}$$

where the spatial average is over a volume large enough to contain many turbulent eddies, but with a length-scale small compared to that of the mean fields. A local

time average, or an ensemble average, can also be adopted. Substituting (2.249) and (2.250) in the induction equation and taking averages, noting that $\langle \mathbf{v}_0 \rangle = \mathbf{v}_0$ and $\langle \mathbf{B}_0 \rangle = \mathbf{B}_0$ while $\langle \mathbf{v}_\mathrm{T} \rangle = \langle \mathbf{B}_\mathrm{T} \rangle = \mathbf{0}$, leads to the mean-field equation

$$\frac{\partial \mathbf{B}_0}{\partial t} = \nabla \times (\mathbf{v}_0 \times \mathbf{B}_0) + \nabla \times \boldsymbol{\mathcal{E}} - \nabla \times (\eta \nabla \times \mathbf{B}_0), \tag{2.251}$$

where

$$\boldsymbol{\mathcal{E}} = \langle \mathbf{v}_\mathrm{T} \times \mathbf{B}_\mathrm{T} \rangle. \tag{2.252}$$

The fluctuating part of the induction equation is obtained by subtracting (2.251) from the total equation for $\mathbf{B}$, giving

$$\frac{\partial \mathbf{B}_\mathrm{T}}{\partial t} = \nabla \times (\mathbf{v}_0 \times \mathbf{B}_\mathrm{T} + \mathbf{v}_\mathrm{T} \times \mathbf{B}_0) + \nabla \times \mathbf{G} - \nabla \times (\eta \nabla \times \mathbf{B}_\mathrm{T}), \tag{2.253}$$

where

$$\mathbf{G} = \mathbf{v}_\mathrm{T} \times \mathbf{B}_\mathrm{T} - \langle \mathbf{v}_\mathrm{T} \times \mathbf{B}_\mathrm{T} \rangle. \tag{2.254}$$

The electric field $\boldsymbol{\mathcal{E}}$ is of crucial importance since it leads to the generation of toroidal electric currents which are the source of the poloidal magnetic field. If it is assumed that $\mathbf{v}$ can be specified independently of $\mathbf{B}$, then (2.253) is a linear relationship between $\mathbf{B}_\mathrm{T}$ and $\mathbf{B}_0$, while (2.252) shows that $\boldsymbol{\mathcal{E}}$ is linear in $\mathbf{B}_\mathrm{T}$ and hence in $\mathbf{B}_0$. Since the turbulent eddies are assumed to have length-scales much smaller than that of $\mathbf{B}_0$, $\boldsymbol{\mathcal{E}}$ should be expressible as a functional involving the local value of $\mathbf{B}_0$. This takes the form

$$\mathcal{E}_i = \alpha_{ij} B_{0j} + \beta_{ijk} \frac{\partial B_{0j}}{\partial x_k}, \tag{2.255}$$

where the summation convention is used. If the first order smoothing approximation is valid then the tensors α_{ij} and β_{ijk} can be calculated, if the statistical properties of the turbulence are prescribed. This approximation involves ignoring the $\nabla \times \mathbf{G}$ in (2.253), and can be justified only if the turbulence does not significantly distort the magnetic field, so that $|\mathbf{B}_\mathrm{T}| \ll |\mathbf{B}_0|$. This is the case if the diffusion time is small compared to the turnover time, τ_0, for a turbulent eddy, or if the correlation time, τ_cor, is much less than τ_0.

For locally isotropic turbulence

$$\alpha_{ij} = \alpha \delta_{ij}, \tag{2.256a}$$

$$\beta_{ijk} = \beta \epsilon_{ijk}. \tag{2.256b}$$

When $\tau_{\rm cor} \ll \tau_0$, mean-field theory yields

$$\alpha = -\frac{1}{3}\tau_{\rm cor}\langle \mathbf{v}_{\rm T} \cdot \nabla \times \mathbf{v}_{\rm T}\rangle, \tag{2.257a}$$

$$\beta = \frac{1}{3}\tau_{\rm cor}\langle \mathbf{v}_{\rm T} \cdot \mathbf{v}_{\rm T}\rangle. \tag{2.257b}$$

The quantity $\langle \mathbf{v}_{\rm T} \cdot \nabla \times \mathbf{v}_{\rm T}\rangle$ is referred to as the mean helicity of the turbulence. Mirror-asymmetric turbulence is required to produce finite α. Turbulence that is statistically isotropic, but non-mirror symmetric, is referred to as pseudo-isotropic. Gravity and rotation are believed to be important in the generation of such turbulence.

The β coefficient given by (2.257b) can be found, in principle, if the spectrum of the turbulence is known. This quantity is equivalent to a turbulent diffusivity $\eta_{\rm T}$. In the absence of a detailed knowledge of the turbulence, $\eta_{\rm T}$ is usually estimated from the simple form (2.228). It should be noted that if the Lorentz force $\mathbf{J} \times \mathbf{B}$ is significant in the momentum equation for $\mathbf{v}$, then α_{ij} and β_{ijk} will depend on the local value of $\mathbf{B}_0$.

The use of (2.256a) and (2.256b) for α_{ij} and β_{ijk} in (2.255) gives an electric field

$$\boldsymbol{\mathcal{E}} = \alpha \mathbf{B}_0 - \eta_{\rm T} \nabla \times \mathbf{B}_0. \tag{2.258}$$

Dropping the subscript zero from the mean fields and substituting $\boldsymbol{\mathcal{E}}$ in the mean field equation (2.251) yields

$$\frac{\partial \mathbf{B}}{\partial t} = \nabla \times (\mathbf{v} \times \mathbf{B}) - \nabla \times (\eta_{\rm T} \nabla \times \mathbf{B}) + \nabla \times (\alpha \mathbf{B}), \tag{2.259}$$

writing $\eta + \eta_{\rm T}$ as $\eta_{\rm T}$ for a dominant turbulent diffusivity. Steady, axisymmetric solutions are now possible for the mean magnetic field.

2.3.2 *Types of Mean-Field Dynamos*

Two extreme types of dynamo can be identified, by considering the field creation terms in (2.259). The equations for B_ϕ and A can now be written in the forms

$$\frac{\partial B_\phi}{\partial t} + \varpi \mathbf{v}_{\rm p} \cdot \nabla \left(\frac{B_\phi}{\varpi}\right) = \varpi \mathbf{B}_{\rm p} \cdot \nabla \Omega - \alpha \triangle A - \frac{1}{\varpi} \nabla \alpha \cdot \nabla (\varpi A) - B_\phi \nabla \cdot \mathbf{v}_{\rm p} + \eta_{\rm T} \triangle B_\phi, \tag{2.260}$$

$$\frac{\partial A}{\partial t} + \frac{1}{\varpi} \mathbf{v}_{\rm p} \cdot \nabla (\varpi A) = \alpha B_\phi + \eta_{\rm T} \triangle A, \tag{2.261}$$

where $\triangle = \nabla^2 - \varpi^{-2}$. The first term on the right hand side of (2.260) is the rate of creation of B_ϕ by the shearing of $\mathbf{B}_\mathrm{p}$, giving the Ω-effect. The α-effect terms in the above equations generate toroidal and poloidal field

The magnetic Reynolds number, defined by (2.54), measures the ratio of the magnitudes of the velocity and diffusion terms in the induction equation. Magnetic Reynolds numbers for the Ω and α-effects can be defined as

$$R_\Omega = \frac{\Omega_0 \ell^2}{\eta_\mathrm{T}}, \tag{2.262a}$$

$$R_\alpha = \frac{\alpha_0 \ell}{\eta_\mathrm{T}}, \tag{2.262b}$$

where subscripts zero denote characteristic values and ℓ is the length-scale of the field variation.

The axisymmetric dynamo equations (2.260) and (2.261) are usually solved in a finite region enclosed by a surface S. If the external region is a vacuum then the continuity of $\mathbf{B}$ requires B_ϕ to vanish on S, and A and its normal derivative must be continuous.

The relative importance of the Ω and α-effects depends on the ratio R_Ω / R_α. There are two extreme types of dynamo possible. If $R_\Omega \ll R_\alpha$ then the Ω-effect is negligible and (2.260) and (2.261) show that the α-effect acts not only to produce A from B_ϕ, but also B_ϕ from A. This is referred to as an α^2 dynamo. The dynamo becomes self-sustaining when R_α attains a critical value.

The other extreme is when $R_\Omega \gg R_\alpha$ so the α-effect can be ignored in the creation of B_ϕ from A, described by (2.260). However, the α-term in (2.261) remains crucial in creating A from B_ϕ. In this $\alpha\Omega$ dynamo the product

$$D = R_\alpha R_\Omega, \tag{2.263}$$

referred to as the dynamo number, must attain a critical value for field maintenance. If the poloidal flow is insignificant then (2.261) for A and (2.244) for $\mathbf{B}_\mathrm{p}$ show that $|B_\mathrm{p}| \sim R_\alpha |B_\phi|$, while (2.260) gives $|B_\phi| \sim R_\Omega |B_\mathrm{p}|$. It follows that the critical dynamo number is $D_c \sim 1$ and

$$\frac{|B_\phi|}{|B_\mathrm{p}|} \sim \left(\frac{R_\Omega}{R_\alpha} \right)^{\frac{1}{2}} > 1. \tag{2.264}$$

If v_ϖ and Ω are symmetric, with v_z and α antisymmetric under reflection in the equatorial plane (i.e. $z \to -z$), then the eigenfunctions of (2.260) and (2.261) fall into one of the following groups;

dipole modes:

$$A(\varpi, -z, t) = A(\varpi, z, t), \tag{2.265a}$$

$$B_\phi(\varpi, -z, t) = -B_\phi(\varpi, z, t). \tag{2.265b}$$

quadrupole modes:

$$A(\varpi, -z, t) = -A(\varpi, z, t), \tag{2.266a}$$

$$B_\phi(\varpi, -z, t) = B_\phi(\varpi, z, t). \tag{2.266b}$$

The foregoing kinematic dynamo theory ignores the effects of magnetic force on the motions, so the velocity field is specified independently of the magnetic field. A linear problem then results in which the magnetic diffusivity and the α function can be determined if the turbulent velocity is specified. The theory has had considerable success in giving dynamo solutions in a wide range of situations, generating large-scale magnetic fields which are able to transport angular momentum in suitable ways. However, a more rigorous and self-consistent theory is required which incorporates dynamical and thermal processes. As will be shown, significant progress has been made towards this aim, particularly in the case of accretion discs, although a mean-field theory which incorporates dynamical and thermal effects in a self-consistent way has yet to be formulated. A detailed review of stellar dynamo theory is given in Mestel (2012).

2.4 Close Binary Stars

2.4.1 The Roche Model

The basic model of a close binary system is based on the orbiting two body system due to Roche (1873), with the introduction of a much smaller third mass. Hence this corresponds to a restricted three-body problem, with the two main bodies orbiting about their centre of mass. The motion of the third particle is then determined by its initial position and velocity, together with the gravitational force exerted on it by the orbiting bodies. In the Roche model of a close binary the stellar components are the massive bodies, while transferred material can be considered as low mass particles. The stars are treated as gravitational point sources. This is essentially exact for a spherical white dwarf or a neutron star, and is a reasonable first approximation for main sequence stars since even a star of mass $0.2M_\odot$ has a central density $\rho_c \sim 6\bar{\rho}$, where $\bar{\rho}$ is the mean density. Circular orbits are considered in the standard model, this being consistent with observations which show that the eccentricities are usually small. Tidal interactions circularize orbits on time-scales shorter than the binary lifetime.

Since the mean free path of ions in the accretion stream is many orders of magnitude smaller than the orbital separation, a hydrodynamical analysis of the flow, including the pressure gradient, is appropriate. However, Lubow and Shu (1975) showed that, provided the pressure gradient along the stream is small, the locus of its centre can be described accurately by purely ballistic considerations. In

thin accretion discs, in which self-gravity is small, the radial pressure gradient is ignorable and consequently the azimuthal motion of material corresponds to that of individual particle orbits. However, pressure gradients normal to the orbital plane are important in streams and discs, opposing gravitational collapse due to the vertical component of stellar gravity. Although the ballistic approach allows the following basic model of a binary system to be formulated, ultimately hydrodynamics is required to fully describe the structure of accretion streams and discs.

The orbital frame $Oxyz$ is defined to have its origin O at the centre of mass, its y-axis along the line joining the stellar centres and its z-axis along the orbital angular velocity $\mathbf{\Omega}_{\rm o}$. The total potential, Ψ, in this rotating frame is

$$\Psi = -\frac{GM_{\rm s}}{|\mathbf{r}-\mathbf{r}_{\rm s}|} - \frac{GM_{\rm p}}{|\mathbf{r}-\mathbf{r}_{\rm p}|} - \frac{1}{2}|\mathbf{\Omega}_{\rm o}\times\mathbf{r}|^2, \tag{2.267}$$

where $M_{\rm s}$ is the mass of the main sequence secondary star and $M_{\rm p}$ the mass of the compact primary, while $\mathbf{r}_{\rm s}$ and $\mathbf{r}_{\rm p}$ are the positions of the centres of mass of the respective stars. The last term is the centrifugal potential. The equipotential surfaces of Ψ are therefore given by the equation

$$\frac{GM_{\rm s}}{[x^2+(y-y_{\rm s})^2+z^2]^{\frac{1}{2}}} + \frac{GM_{\rm p}}{[x^2+(y-y_{\rm p})^2+z^2]^{\frac{1}{2}}} + \frac{1}{2}\Omega_{\rm o}^2(x^2+y^2) = K, \tag{2.268}$$

where K is a constant. Close to the stellar centres these surfaces are nearly spherical, but at larger distances they become pear-shaped. A critical surface occurs when the stellar lobes meet on the line of centres. The point of contact is referred to as the inner Lagrangian point, denoted L_1, and the critical surfaces are known as the Roche lobes. A particle placed at L_1 experiences zero force since $(\nabla\Psi)_{L_1} = \mathbf{0}$. Figure 2.1 shows the critical equipotentials and coordinates used.

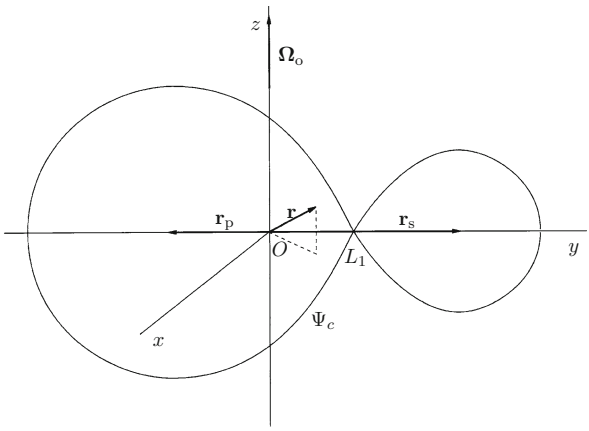

Fig. 2.1 The orbital frame $Oxyz$, showing the critical equipotential Ψ_c and the inner Lagrangian point L_1. The system centre of mass is at O, and the secondary and primary centres of mass are at $\mathbf{r}_{\rm s}$ and $\mathbf{r}_{\rm p}$ respectively

The stability of a particle at the L_1 point can be investigated by considering a small displacement $\Delta\mathbf{r}$. The equation of motion of a particle relative to the orbital frame is

$$\ddot{\mathbf{r}} = -\nabla\Psi - 2\boldsymbol{\Omega}_\mathrm{o} \times \dot{\mathbf{r}}. \tag{2.269}$$

A small displacement from L_1 then satisfies the equations

$$\Delta\ddot{x} + \omega_x^2 \Delta x = 2\Omega_\mathrm{o}\Delta\dot{y}, \tag{2.270}$$

$$\Delta\ddot{y} - \omega_y^2 \Delta y = -2\Omega_\mathrm{o}\Delta\dot{x}, \tag{2.271}$$

$$\Delta\ddot{z} + \omega_z^2 \Delta z = 0, \tag{2.272}$$

where

$$\omega_x^2 = \left(\frac{\partial^2\Psi}{\partial x^2}\right)_{L_1} = -\Omega_\mathrm{o}^2 + \frac{GM_\mathrm{s}}{r_{1\mathrm{s}}^3} + \frac{GM_\mathrm{p}}{r_{1\mathrm{p}}^3}, \tag{2.273}$$

$$\omega_y^2 = -\left(\frac{\partial^2\Psi}{\partial y^2}\right)_{L_1} = \Omega_\mathrm{o}^2 + \frac{2GM_\mathrm{s}}{r_{1\mathrm{s}}^3} + \frac{2GM_\mathrm{p}}{r_{1\mathrm{p}}^3}, \tag{2.274}$$

$$\omega_z^2 = \left(\frac{\partial^2\Psi}{\partial z^2}\right)_{L_1} = \frac{GM_\mathrm{s}}{r_{1\mathrm{s}}^3} + \frac{GM_\mathrm{p}}{r_{1\mathrm{p}}^3}, \tag{2.275}$$

and $r_{1\mathrm{s}}$ and $r_{1\mathrm{p}}$ are the distances of the L_1 point from the secondary and primary star centres.

Equations (2.270)–(2.272) show that small vertical motions are independent of those in a horizontal plane. Since $\omega_z^2 > 0$, it follows that the vertical motions are stable. The stability of the horizontal motions can be investigated by taking

$$\Delta x = ae^{i\omega t}, \tag{2.276a}$$

$$\Delta y = be^{i\omega t}, \tag{2.276b}$$

where a and b are constants, and finding the sign of ω^2. Substitution in the equations of motion (2.270) and (2.271) gives

$$\omega^4 - (\omega_x^2 - \omega_y^2 + 4\Omega_\mathrm{o}^2)\omega^2 - \omega_x^2\omega_y^2 = 0, \tag{2.277}$$

which has roots

$$\omega^2 = \frac{1}{2}(\omega_x^2 - \omega_y^2 + 4\Omega_\mathrm{o}^2) \pm \frac{1}{2}\left[(\omega_x^2 - \omega_y^2 + 4\Omega_\mathrm{o}^2)^2 + 4\omega_x^2\omega_y^2\right]^{\frac{1}{2}}. \tag{2.278}$$

Since

$$\Omega_{\rm o}^2 = \frac{G(M_{\rm s} + M_{\rm p})}{D^3}, \tag{2.279}$$

where $D = r_{1\rm s} + r_{1\rm p}$, it follows from (2.273) that

$$\omega_x^2 = GM_{\rm p}\left(\frac{1}{r_{1\rm p}^3} - \frac{1}{D^3}\right) + GM_{\rm s}\left(\frac{1}{r_{1\rm s}^3} - \frac{1}{D^3}\right) > 0, \tag{2.280}$$

and (2.274) shows $\omega_y^2 > 0$. Hence $\omega_x^2\omega_y^2 > 0$ and (2.278) yields positive and negative eigenvalues for ω^2, the unstable negative case being

$$\omega^2 = \frac{1}{2}(\omega_x^2 - \omega_y^2 + 4\Omega_{\rm o}^2) - \frac{1}{2}\left[(\omega_x^2 - \omega_y^2 + 4\Omega_{\rm o}^2)^2 + 4\omega_x^2\omega_y^2\right]^{\frac{1}{2}}. \tag{2.281}$$

This can be used to find the direction of the unstable eigenvector.

Substituting the displacement components (2.276a) and (2.276b) in the equations of motion (2.270) and (2.271) relates the amplitudes a and b, giving the horizontal displacement as

$$(\Delta\mathbf{r})_{\rm h} = b\left[-i\frac{(\omega^2 + \omega_y^2)}{2\omega\Omega_{\rm o}}\hat{\mathbf{x}} + \hat{\mathbf{y}}\right]e^{i\omega t}. \tag{2.282}$$

Using the eigenvalue given by (2.281) then yields

$$(\Delta\mathbf{r})_{\rm h} = b\left[\frac{(\omega^2 + \omega_y^2)}{2\Omega_{\rm o}\sqrt{Q}}\hat{\mathbf{x}} + \hat{\mathbf{y}}\right]e^{i\omega t}, \tag{2.283}$$

where

$$Q = \frac{1}{2}\left[(\omega_x^2 - \omega_y^2 + 4\Omega_{\rm o}^2)^2 + 4\omega_x^2\omega_y^2\right]^{\frac{1}{2}} - \frac{1}{2}(\omega_x^2 - \omega_y^2 + 4\Omega_{\rm o}^2). \tag{2.284}$$

The direction of motion therefore follows from the components of (2.283) as

$$\frac{\Delta x}{\Delta y} = \frac{\omega^2 + \omega_y^2}{2\Omega_{\rm o}\sqrt{Q}}. \tag{2.285}$$

It is noted that $\Delta x/\Delta y > 0$ results and, from Fig. 2.1, the relevant displacement has $\Delta x < 0$ and $\Delta y < 0$, with $(\Delta\mathbf{r})_{\rm h}$ leading the motion of the line of stellar centres.

It can now be shown that this direction lies well inside the critical lobe. The change in Ψ due to a small displacement from L_1 in the $z = 0$ plane is

$$\Delta\Psi = \frac{1}{2}\omega_x^2(\Delta x)^2 - \frac{1}{2}\omega_y^2(\Delta y)^2. \tag{2.286}$$

Along the critical lobe, $\Delta\Psi = 0$ and hence

$$\left(\frac{\Delta x}{\Delta y}\right)_c = \pm\left(\frac{\omega_y^2}{\omega_x^2}\right)^{\frac{1}{2}}, \tag{2.287}$$

where the different signs yield the two intersecting tangents to the critical equipotential in the $z = 0$ plane. The use of (2.273) for ω_x^2 and (2.274) for ω_y^2 allows the ratios (2.285) and (2.287) to be expressed as functions of the dimensionless quantity

$$\delta = \frac{\epsilon_\mathrm{s}\epsilon_\mathrm{p}}{\epsilon_\mathrm{s} + \epsilon_\mathrm{p}}, \tag{2.288}$$

where

$$\epsilon_\mathrm{s} = \frac{M}{M_\mathrm{s}}\left(\frac{r_{1\mathrm{s}}}{D}\right)^3, \tag{2.289a}$$

$$\epsilon_\mathrm{p} = \frac{M}{M_\mathrm{p}}\left(\frac{r_{1\mathrm{p}}}{D}\right)^3, \tag{2.289b}$$

with $M = M_\mathrm{s} + M_\mathrm{p}$. Typically $\epsilon_\mathrm{s} \sim \epsilon_\mathrm{p} \sim 0.2$ and hence $\delta \sim 0.1$. Expansion to first order in δ then yields

$$\frac{\Delta x}{\Delta y} = \frac{4}{3}\left(\frac{\delta}{2}\right)^{\frac{1}{2}}\left(1 + \frac{17}{36}\delta\right), \tag{2.290}$$

and

$$\left|\left(\frac{\Delta x}{\Delta y}\right)_c\right| = \sqrt{2}\left(1 + \frac{3}{4}\delta\right). \tag{2.291}$$

It follows that

$$\frac{\Delta x/\Delta y}{|(\Delta x/\Delta y)_c|} = \frac{2}{3}\delta^{\frac{1}{2}}\left(1 - \frac{5}{18}\delta\right). \tag{2.292}$$

This ratio is always less than unity, being typically 0.2, so the unstable mode lies well inside the critical lobe. For $\delta = 0.1$ the critical lobe makes an angle of $\theta_c = \tan^{-1}(\Delta x/\Delta y)_c = 56.7°$ with the line of stellar centres at L_1 in the orbital plane,

and the unstable eigenvector makes an angle of $\theta = 17.3°$ leading the orbital motion of this line.

It is noted that substituting the real solution for ω from the positive sign case of (2.278) into (2.282) for $(\Delta\mathbf{r})_{\rm h}$ gives components Δx and Δy of different amplitudes, oscillating with a phase difference of $\pi/2$. This is a stable mode, corresponding to elliptical particle orbits about L_1.

The distance of the L_1 point from the centre of the compact primary, denoted $r_{1\rm p}$, can be found from the condition $(\partial\Psi/\partial y)_{L_1} = 0$ together with the y-coordinates shown in Fig. 2.1, noting that $y_{\rm s} = (M_{\rm p}/M)D$. This yields

$$\frac{M_{\rm s}}{M} - \frac{r_{1\rm p}}{D} + \frac{M_{\rm p}}{M}\left(\frac{D}{r_{1\rm p}}\right)^2 - \frac{M_{\rm s}}{M}\left(1 - \frac{r_{1\rm p}}{D}\right)^{-2} = 0, \tag{2.293}$$

from which $r_{1\rm p}$ can be found numerically. It follows from this equation that $r_{1\rm p}/D$ is a pure function of the mass ratio $M_{\rm s}/M_{\rm p}$ and that, since $r_{1\rm s} = D - r_{1\rm p}$, $r_{1\rm s}/D$ is also a pure function of this ratio. The shapes of the Roche lobes depend only on $\epsilon_{\rm s}$ and $\epsilon_{\rm p}$ and hence, from (2.289a) and (2.289b), are pure functions of $M_{\rm s}/M_{\rm p}$ (e.g. the critical angle $\theta_c = \tan^{-1}(\Delta x/\Delta y)_c$, with $(\Delta x/\Delta y)_c$ given by (2.291) together with (2.288) for δ). A good accuracy fitted formula for $r_{1\rm p}$ is given by Plavec and Kratochvil (1964) as

$$\frac{r_{1\rm p}}{D} = 0.500 - 0.227\log\left(\frac{M_{\rm s}}{M_{\rm p}}\right). \tag{2.294}$$

A mean radius, $R_{\rm L}$, can be defined for the secondary star's critical lobe as the radius of a sphere of equal volume. Eggleton (1983) gives a formula for this radius as

$$\frac{R_{\rm L}}{D} = \frac{0.49q^{\frac{2}{3}}}{0.6q^{\frac{2}{3}} + \ln(1 + q^{\frac{1}{3}})}, \tag{2.295}$$

where $q = M_{\rm s}/M_{\rm p}$, accurate to $\simeq 99\%$ for all q values. A simpler formula for $R_{\rm L}$, valid for $0.1 \lesssim M_{\rm s}/M_{\rm p} \lesssim 0.8$ to $\simeq 98\%$ accuracy, is

$$\frac{M}{M_{\rm s}}\left(\frac{R_{\rm L}}{D}\right)^3 = 0.1, \tag{2.296}$$

due to Paczyński (1967). If the mean radius of the secondary star equals $R_{\rm L}$ then it fills its Roche lobe and material is in contact with L_1.

The existence of the unstable mode for horizontal displacements from L_1 indicates that a lobe-filling secondary star will lose mass through this region due to thermal motions of gas particles. The higher speed particles moving towards the L_1 region will have sufficient kinetic energy to surmount the effective potential barrier and escape from the star. However, Lubow and Shu (1975) argued that the mass loss process is not simply due to such evaporation. By considering the

hydrodynamic equations, they showed that a subsonic flow will develop inside the secondary in its surface layers. This flow will pass through a sonic point at a distance of $\simeq (c_{\rm s}/\Omega_{\rm o} D) R_{\rm s}$ from the L_1 point. This bulk flow gives the mass loss from a small region surrounding the L_1 point.

Lower main sequence stars obey the approximate mass-radius relation

$$\frac{R_{\rm s}}{R_\odot} \simeq q \frac{M_{\rm s}}{M_\odot}, \tag{2.297}$$

with $q \sim 1.1$ (Kippenhahn and Weigert 1990). Using this, together with the lobe size expression (2.296), $R_{\rm s} = R_L$ and $\Omega_{\rm o}^2 = GM/D^3$, gives a mass-period relation for a lobe-filling secondary as

$$\left(\frac{P}{\rm h}\right) \simeq 9 q^{\frac{3}{2}} \left(\frac{M_{\rm s}}{M_\odot}\right). \tag{2.298}$$

The equipotentials of Ψ correspond to the zero-velocity surfaces of the restricted three-body problem. These surfaces arise from the energy integral which is derived from the equation of motion of a particle relative to the orbital frame, given by (2.269). Taking the scalar product of this with $\dot{\mathbf{r}}$ removes the Coriolis force and gives

$$\frac{d}{dt}\left(\frac{1}{2}v^2 + \Psi\right) = 0, \tag{2.299}$$

in which the conserved quantity is the energy per unit mass, E, so

$$\frac{1}{2}v^2 + \Psi = E. \tag{2.300}$$

The particle speed is therefore

$$v = [2(E - \Psi)]^{\frac{1}{2}}, \tag{2.301}$$

requiring $|\Psi| \geq |E|$. The speed vanishes on the surface $\Psi = E$, with E being fixed by the particle's initial position and velocity.

2.4.2 *Tidal Theory*

The secondary star in a close binary is usually assumed to be tidally synchronized. It is natural to use the orbital frame to analyse the asynchronous motions. If a spherical polar coordinate system (r, θ, ϕ) is used, with an origin at the centre of

mass of the secondary and the $\phi = 0$ line taken as the line of stellar centres, then the gravitational potential of the primary can be expressed as

$$\psi_{\rm p} = -\frac{GM_{\rm p}}{D}\left[1 - 2\frac{r}{D}\sin\theta\cos\phi + \frac{r^2}{D^2}\right]^{-\frac{1}{2}}. \tag{2.302}$$

The mean radius of the secondary typically satisfies $R_{\rm s}/D \lesssim 1/3$, and the tidal torque can be expressed as a series in powers of $(R_{\rm s}/D)^2$. Hence, as a reasonable approximation, $\psi_{\rm p}$ is usually expanded to second order in r/D which yields

$$\psi_{\rm p} = -\frac{GM_{\rm p}}{D}\left[1 + \frac{r}{D}P_1^1\cos\phi - \frac{1}{2}\frac{r^2}{D^2}\left(P_2^0 - \frac{1}{2}P_2^2\cos 2\phi\right)\right], \tag{2.303}$$

where $P_l^{|m|}$ are associated Legendre functions. The first term gives zero force, while the second yields a constant force on the centre of mass of the secondary which is balanced by part of the centrifugal force to give a circular orbit. The remaining centrifugal force has a potential which can be expressed as

$$\psi_{\rm c} = -\frac{1}{3}\Omega_{\rm o}^2 r^2 + \frac{1}{3}\Omega_{\rm o}^2 r^2 P_2^0. \tag{2.304}$$

The remaining $l = 2$ part of the gravitational potential is the tidal potential

$$\psi_{\rm T} = \frac{GM_{\rm p}r^2}{2D^3}\left[P_2^0 - \frac{1}{2}P_2^2\cos 2\phi\right]. \tag{2.305}$$

The total perturbing force is

$$\mathbf{F} = -\nabla(\psi_{\rm T} + \psi_{\rm c}) \tag{2.306}$$

and this causes a distortion of the secondary star from its spherical shape with an associated perturbation to its structure.

The perturbation in the density acts as a source which contributes to the external gravity field. The corresponding potential must contain the same harmonics as the tidal field, obey Laplace's equation and vanish as $r \to \infty$. The required form is then

$$\psi_{\rm ex} = \frac{\alpha}{r^3}P_2^0 + \frac{\beta}{r^3}P_2^2\cos 2\phi, \tag{2.307}$$

where α and β are constants. Hydrostatic equilibrium in the secondary yields $P = P(\psi)$ and, for a baratropic equation of state, $P = P(\rho)$ and hence $\rho = \rho(\psi)$. A single coordinate can then be defined as

$$r_\psi = r + \sum_{l,m} c_{lm}a_l(r)P_l^{|m|}\cos m\phi, \tag{2.308}$$

which is constant on the equipotential surfaces of ψ. The Poisson equation for the total potential in the secondary becomes

$$\nabla^2\psi = 4\pi G\rho(r_\psi) - 2\Omega_o^2. \tag{2.309}$$

Transforming the derivatives, using $r_\psi = r_\psi(r, \theta, \phi)$, then leads to an equation for the distortion functions $a_l(r)$ given by

$$\frac{d^2a_l}{dr^2} + 2\left(\frac{4\pi r^2\rho}{M(r)} - \frac{1}{r}\right)\frac{da_l}{dr} + \left\{\frac{2 - l(l+1)}{r^2}\right\}a_l = 0, \tag{2.310}$$

where the function $M(r)$ is the mass contained in a sphere of radius r. Only the function $a_2(r)$ is required.

Equation (2.310) can be solved numerically, for a given stellar model, subject to the central condition $a_2(0) = 0$. The potential in the secondary can be expanded as

$$\psi(r_\psi) = \psi(r) + a_2(r)\psi'(r)\left[c_1 P_2^0 + c_2 P_2^2 \cos 2\phi\right]. \tag{2.311}$$

where c_1 and c_2 are constants. Matching ψ and $\partial\psi/\partial r$ to the total external potential at the stellar surface determines c_1 and c_2.

Secondary stars having $M_s < 0.35\, M_\odot$ will be fully convective and hence have their pressure and density related by the polytropic equation

$$P = K\rho^{\frac{5}{3}}, \tag{2.312}$$

where K is a constant. The unperturbed density can be expressed in terms of an Emden function $\theta(\xi)$ as

$$\rho(r) = \rho_c\theta^{\frac{3}{2}}, \tag{2.313}$$

where $\theta(\xi)$ satisfies

$$\frac{d}{d\xi}\left(\xi^2\frac{d\theta}{d\xi}\right) + \xi^2\theta^{\frac{3}{2}} = 0, \tag{2.314}$$

and $\xi = r/\ell$, with ℓ the Emden unit of length (e.g. Cox and Giuli 1968). The boundary conditions are

$$\theta(0) = 1, \tag{2.315a}$$

$$\left(\frac{d\theta}{d\xi}\right)_{\xi=0} = 0, \tag{2.315b}$$

$$\theta(\xi_s) = 0. \tag{2.315c}$$

The first condition follows from (2.313), while the second is a regularity condition. The third condition corresponds to ρ vanishing at the first zero of the Emden function at the stellar surface $\xi = \xi_s$.

The linearized momentum equation for asynchronous motions can be expressed as

$$\frac{\partial \mathbf{v}}{\partial t} + 2\boldsymbol{\Omega}_o \times \mathbf{v} = -\nabla W + \mathbf{F}_v, \tag{2.316}$$

where

$$W = \psi' + \frac{P'}{\rho}, \tag{2.317}$$

with the prime denoting perturbations. A turbulent viscous force, $\mathbf{F}_v$, can lead to significant dissipation of the asynchronous motions. Solutions of (2.316) for $\mathbf{v}$ have a time dependence of $\exp(-\lambda t)$, with the decay rate λ. The dissipation time-scale is long compared to the asynchronous flow time-scales, so $\mathbf{v}$ evolves through quasi-steady states. The quasi-steady form of (2.316) is obtained by ignoring $\partial \mathbf{v}/\partial t$ and $\mathbf{F}_v$, giving inviscid solutions for $\mathbf{v}$. In the absence of tides the only non-vanishing velocity component is of the form $u_\phi(\varpi)$, with $\varpi = r \sin\theta$, corresponding to an arbitrary differential rotation. With tidal distortion, additional velocity components arise with the forms $v_\varpi(\varpi, \phi)$, $v_\phi(\varpi, \phi)$ and $v_z(\varpi, \phi, z)$, so the horizontal motions are two-dimensional. It can be shown that $|\mathbf{v}| \to 0$ as the L_1 point is approached, so the mass loss rate will not be affected by the presence of asynchronism (see Campbell and Papaloizou 1983).

The imposition of a viscous force determines W in the steady form of (2.316) as an eigenfunction, and hence determines $u_\phi(\varpi)$, with the decay rate λ as the corresponding eigenvalue. A modification of the viscosity ν can be made, to allow for the effects of rotation, using a form similar to (2.232). A standard form of viscous stress tensor leads to a uniform rotation form for $u_\phi(\varpi)$. However, non-standard forms of stress tensor can be postulated which lead to differential rotation states (e.g. Wasiutynski 1946; Kippenhahn 1963; Tayler 1973). The dissipation causes the tidal bulge to lag the motion of the line of stellar centres, and the resulting tidal torque allows the star to exchange angular momentum with the orbit. The time-scales for attaining synchronism, or a final non-synchronous state, are significantly less than the lifetime of the binary system.

For $M_s > 0.35\, M_\odot$ a radiative core will exist and some asynchronous motions may remain in this, depending on the strength of coupling to the convective envelope. Tidal torques also tend to circularize initially elliptical orbits (e.g. Zahn 1977).

2.4.3 Mass Transfer

If the secondary star fills its Roche lobe material will be in contact with the L_1 point. As shown by Lubow and Shu (1975), a subsonic flow will develop inside the secondary and attain the sound speed close to the L_1 point. Hence the initial velocity of material is $\simeq c_s$ on leaving the L_1 region, but matter rapidly gains speeds of $\sim \Omega_o D$, characteristic of orbital speeds. Since $c_s \ll \Omega_o D$, the speed of material at L_1 can be taken as effectively zero in (2.301) which therefore yields

$$v = [2(\Psi_c - \Psi)]^{\frac{1}{2}}, \tag{2.318}$$

for the subsequent speed, where Ψ_c is the critical potential value on the Roche lobes. Matter is then trapped within the Roche lobe of the primary, since this is its zero-velocity surface with $\Psi_c = E$.

The mass loss rate from the secondary can be expressed as

$$\dot{M}_s = -\rho_{L_1} c_s \Delta S, \tag{2.319}$$

where ΔS is an effective cross-sectional area perpendicular to the line of stellar centres, at a small distance Δy into the secondary from the L_1 point. This effective area is determined by considering the density scale height normal to the line of centres at $y = y_{L_1} + \Delta y$.

For a synchronous star, hydrostatic equilibrium is

$$-\frac{1}{\rho}\nabla P = \nabla \Psi, \tag{2.320}$$

where Ψ is the sum of the stellar gravitational potentials and the rotational potential. In the tenuous outer layers of the secondary it is a good approximation to take Ψ as the Roche potential, since the main gravitational sources are the compact primary and the central regions of the secondary. The scale height in the orbital plane, H_x, slightly exceeds the vertical scale height, H_z, due to the effect of centrifugal force. However, since the difference is only a few per cent, the area ΔS will be essentially circular with radius $H \simeq H_x \simeq H_z$.

To calculate H, consider the z-direction at $x = 0$, $y = y_{L_1} + \Delta y$. It is reasonable to take the gas as isothermal in this direction. The gas equation of state and (2.320) then give

$$\frac{c_s^2}{\rho}\frac{\partial \rho}{\partial z} = -\frac{\partial \Psi}{\partial z}, \tag{2.321}$$

where

$$c_s^2 = \frac{\mathcal{R}}{\mu}T. \tag{2.322}$$

Using the fact that $|z|$ is small for points in the star near L_1 and that $\Delta y \ll y$, (2.267) for the Roche potential gives

$$\frac{\partial \Psi}{\partial z} = \left(\frac{GM_\mathrm{s}}{r_{1\mathrm{s}}^3} + \frac{GM_\mathrm{p}}{r_{1\mathrm{p}}^3} \right) z, \tag{2.323}$$

along the required line, with $r_{1\mathrm{s}} = y_\mathrm{s} - y_{L_1}$ and $r_{1\mathrm{p}} = y_{L_1} - y_\mathrm{p}$ (see Fig. 2.1 for coordinates). Equation (2.321) then has the solution

$$\rho = \rho_\mathrm{c} e^{-z^2/H^2}, \tag{2.324}$$

where ρ_c is the density in the central plane and the scale height is

$$H = \sqrt{2} c_\mathrm{s} \left(\frac{GM_\mathrm{s}}{r_{1\mathrm{s}}^3} + \frac{GM_\mathrm{p}}{r_{1\mathrm{p}}^3} \right)^{-\frac{1}{2}}. \tag{2.325}$$

This can be expressed as

$$H = f \frac{c_\mathrm{s}}{\Omega_0 D} R_\mathrm{s}, \tag{2.326}$$

where

$$f = \left[\left(\frac{2\epsilon_\mathrm{s}\epsilon_\mathrm{p}}{\epsilon_\mathrm{s} + \epsilon_\mathrm{p}} \right) \left(\frac{D}{R_\mathrm{s}} \right)^2 \right]^{\frac{1}{2}}, \tag{2.327}$$

with ϵ_s and ϵ_p given by (2.289a) and (2.289b). The dimensionless factor f is a slowly varying function of the orbital parameters, with $f \simeq 1$. The mass loss rate is

$$\dot{M}_\mathrm{s} = -\pi \rho_{L_1} c_\mathrm{s} H^2. \tag{2.328}$$

The mass transfer process can only continue if the secondary remains in contact with its Roche lobe. If the mass transfer time-scale of $\tau_M = M_\mathrm{s}/|\dot{M}_\mathrm{s}|$ is significantly larger than the stellar thermal time-scale of τ_th, then the secondary will adjust quasi-steadily through thermal equilibrium states as its loses mass. However, the radius of a main-sequence star in thermal equilibrium decreases as its mass decreases so, unless the Roche lobe shrinks, stellar material will lose contact with the L_1 region and mass loss will cease.

To investigate the change in the Roche lobe size it is necessary to consider the angular momentum of the system. The orbital angular momentum can be written as

$$\mathbf{L}_\mathrm{o} = \left(\frac{GD}{M} \right)^{\frac{1}{2}} M_\mathrm{s} M_\mathrm{p} \hat{\mathbf{z}}. \tag{2.329}$$

The angular momentum of the secondary is $L_s = k_s^2 M_s R_s^2 \Omega_o$, where $k_s^2 \sim 0.1$. Using (2.279) for Ω_o, it follows that

$$\frac{L_s}{L_o} = k_s^2 \frac{M}{M_p} \left(\frac{R_s}{D} \right)^2, \tag{2.330}$$

which is typically $\sim 10^{-2}$. The primary's spin angular momentum is typically $\lesssim 10^{-2} L_s$, so the stellar rotations only make a small contribution to the total angular momentum.

Consider continuous mass transfer from the secondary to the primary with L_o and M conserved. Differentiating (2.329) with respect to time then gives

$$\frac{\dot{D}}{D} = -2 \left(1 - \frac{M_s}{M_p} \right) \frac{\dot{M}_s}{M_s}. \tag{2.331}$$

Since $\dot{M}_s$ is negative it follows that, for $M_p \geq M_s$, the orbital separation increases. The mean radius of the secondary's Roche lobe is given by (2.296) which, together with (2.331), yields

$$\frac{\dot{R}_L}{R_L} = -\frac{5}{3} \left(1 - \frac{6}{5} \frac{M_s}{M_p} \right) \frac{\dot{M}_s}{M_s}. \tag{2.332}$$

Hence, for $M_p > (6/5) M_s$, the secondary's lobe expands as the star loses mass. However, a main-sequence secondary in thermal equilibrium contracts as its mass decreases, obeying the approximate lower main-sequence mass-radius relation (2.297). The secondary therefore becomes detached from its Roche lobe and mass transfer ceases, if angular momentum is conserved. Continuous mass transfer requires the orbital angular momentum to decrease with time, and there are two main mechanisms for achieving this.

Gravitational Radiation This mechanism was proposed by Kraft et al. (1962) and Paczyński (1967). Gravitational waves, a general relativistic effect, remove orbital angular momentum at a rate

$$\frac{dL_o}{dt} = -\frac{32G}{5c^5} \left(\frac{M_s M_p}{M} \right)^2 D^4 \Omega_o^5, \tag{2.333}$$

(Landau and Lifshitz 1951). Faulkner (1971) calculated the resulting mass transfer rate from a secondary in thermal equilibrium. Using (2.296), (2.297) and (2.329) for the lobe-filling condition, the mass-radius relation and the orbital angular momentum, together with (2.333), and $R_s = R_L$, gives

$$\dot{M}_s = -1.9 \times 10^{-10} \frac{(1-\mu)^2}{(4-7\mu)\mu^{\frac{2}{3}}} M_\odot \, \text{year}^{-1}, \tag{2.334}$$

where $\mu = M_s/M$.

Magnetic Braking If the secondary has a magnetic field and a stellar wind then rotational angular momentum is removed. Material flows along the open magnetic field lines and the associated stresses lead to a braking torque on the star (see Chap. 13). Since the secondary is kept close to orbital corotation by tidal torques, the magnetic wind drains angular momentum from the orbit.

A simple expression can be obtained for the braking of the secondary by using angular velocity observations of single stars and assuming them to be magnetically braked. This law, due to Skumanich (1972), is

$$R_{\rm s}\Omega_{\rm s}(t) = 10^{12}\,\bar{f}\,t^{-\frac{1}{2}}\,{\rm m\,s^{-1}}, \tag{2.335}$$

where $0.73 < \bar{f} < 1.78$. Verbunt and Zwaan (1981) applied this to find $\dot{M}_{\rm s}$. Taking the star's spin angular momentum as

$$L_{\rm s} = k_{\rm s}^2 M_{\rm s} R_{\rm s}^2 \Omega_{\rm s}, \tag{2.336}$$

and using $\dot{L}_{\rm s} = \dot{L}_{\rm o}$, yields

$$\dot{M}_{\rm s} = -1.9\times 10^{-7}\frac{k_{\rm s}^2}{\bar{f}^2}\frac{M}{M_\odot}\frac{\mu^{\frac{5}{3}}}{(4-7\mu)}\,M_\odot\,{\rm year}^{-1}. \tag{2.337}$$

Alternative expressions for $\dot{M}_{\rm s}$ are derived in Chap. 13, using fast rotator magnetic wind braking theory.

The absence of an accretion disc in the AM Herculis binaries, and the magnetic orbital coupling resulting from an asynchronous primary, lead to modifications of the mass transfer rates (2.334) and (2.337). The modified expressions are derived in Chap. 4.

2.4.4 Accretion Discs

Disc Formation and Luminosity

In the process of Roche lobe overflow material is lost from the secondary through the L_1 region, at a distance $r_{1\rm p}$ from the primary. Matter passing through L_1 has a small velocity component ($\simeq c_{\rm s}$) along the line of stellar centres. Relative to the orbital frame, the stream will experience a Coriolis force causing some initial deflection from the line of centres. As material approaches the compact primary its central force becomes dominant and the stream orbits around it, subsequently intersecting itself. An estimate of the size of this orbit, occurring at the initial stage of disc formation, can be made by considering the specific angular momentum of material.

In an inertial frame centred on the primary, the specific angular momentum of material at L_1 is $r_{1\rm p}^2\Omega_{\rm o}$. Matter in the stream experiences the gravitational fields

of the primary and secondary stars. The angular momentum of material about the primary is not exactly conserved, since the stream deviates from the line of stellar centres so generating a gravitational torque on the secondary, and angular momentum can be exchanged with the orbit. However, for a free stream, the angular momentum exchange is small ($\simeq$ 6%) because the stream does not make large angles to the line of centres in the region of L_1, in which its gravitational interaction with the secondary is greatest. The angular momentum of material can therefore be taken to be approximately conserved. The radius, R_c, of a circular orbit about the primary then follows from

$$R_c \left(\frac{GM_p}{R_c} \right)^{\frac{1}{2}} = r_{1p}^2 \Omega_o. \tag{2.338}$$

Since $\Omega_o^2 = GM/D^3$, this yields

$$\frac{R_c}{D} = \left(1 + \frac{M_s}{M_p} \right) \left(\frac{r_{1p}}{D} \right)^4. \tag{2.339}$$

This gives an estimate of the characteristic size of the initial orbit of material about the primary. Taking the mean radius of the primary's Roche lobe, R_1, to be given by an expression similar to (2.296), yields

$$\frac{R_1}{D} = 0.46 \left(\frac{M_p}{M} \right)^{\frac{1}{3}}, \tag{2.340}$$

and hence

$$\frac{R_c}{R_1} = 2.16 \left(\frac{M}{M_p} \right)^{\frac{4}{3}} \left(\frac{r_{1p}}{D} \right)^4. \tag{2.341}$$

The radius R_c is always smaller than R_1, being typically $R_c = 0.4R_1$, so material orbits the primary well inside its Roche lobe.

As matter is fed into the initial ring it spreads in the orbital plane, due to dissipation and angular momentum transfer processes, to form a differentially rotating disc. Internal friction causes material to spiral in through the disc, losing energy and angular momentum. Dissipation heats the disc and energy is radiated from its surfaces. The luminosity of the disc can be found from a simple consideration of the rate of energy release as matter spirals inwards to accrete on the star. It is shown below that the azimuthal velocity of disc material is close to a Keplerian distribution with v_K, given by (2.359), being highly supersonic. It will be found that the inflow speed v_ϖ is well subsonic. Since the self-gravity is ignorable, and $|v_\varpi| \ll v_K$, the energy per unit mass in a thin disc is

$$E = \frac{1}{2} v_K^2 - \frac{GM_p}{\varpi} = -\frac{GM_p}{2\varpi}, \tag{2.342}$$

where ϖ is the distance from the centre of the accreting primary star. A ring of mass dM therefore has energy

$$dE = -\frac{GM_{\rm p}}{2\varpi} dM. \tag{2.343}$$

In a time interval dt this mass moves inwards through a distance $d\varpi$ releasing energy at a rate

$$d\dot{E} = \frac{GM_{\rm p}}{2\varpi^2}\frac{d\varpi}{dt} dM = \frac{GM_{\rm p}\dot{M}}{2\varpi^2} d\varpi, \tag{2.344}$$

where the constant mass transfer rate $\dot{M}$ is positive and $d\varpi < 0$. Since $\dot{M} = \dot{M}_{\rm p}$, the total rate of energy release is

$$\dot{E} = \frac{1}{2} GM_{\rm p}\dot{M}_{\rm p} \int_{R_{\rm D}}^{R_{\rm p}} \frac{d\varpi}{\varpi^2} = -\frac{GM_{\rm p}\dot{M}_{\rm p}}{2R_{\rm p}}, \tag{2.345}$$

using $R_{\rm D} \gg R_{\rm p}$, where $R_{\rm D}$ is the disc radius. The disc luminosity is therefore

$$L_{\rm D} = \frac{GM_{\rm p}\dot{M}_{\rm p}}{2R_{\rm p}}. \tag{2.346}$$

This shows that matter releases one half of its gravitational accretion energy per unit mass, $GM_{\rm p}/R_{\rm p}$, in spiralling in through the disc. The other half is retained as azimuthal kinetic energy, available for release through an inner boundary layer.

The Steady Viscous Disc

The classic model of a steady viscous disc was formulated by Shakura and Sunyaev (1973). The internal friction is generated by viscosity, allowing angular momentum transport radially outwards through the disc. Values of the viscosity, ν, characteristic of a turbulent origin are needed to lead to the transport of matter through the disc at the externally imposed rate.

In a cylindrical coordinate system (ϖ, ϕ, z) centred on the accreting primary, the components of the steady, axisymmetric momentum equation are

$$\frac{\partial}{\partial\varpi}\left(\frac{v_\varpi^2}{2}\right) + v_z\frac{\partial v_\varpi}{\partial z} - \frac{v_\phi^2}{\varpi} = -\frac{1}{\rho}\frac{\partial P}{\partial\varpi} - \frac{\partial\psi}{\partial\varpi}, \tag{2.347}$$

$$\frac{v_\varpi}{\varpi}\frac{\partial}{\partial\varpi}(\varpi^2\Omega) + \frac{v_z}{\varpi}\frac{\partial}{\partial z}(\varpi^2\Omega) = \frac{1}{\varpi^2\rho}\frac{\partial}{\partial\varpi}\left(\rho\nu\varpi^3\frac{\partial\Omega}{\partial\varpi}\right), \tag{2.348}$$

$$\frac{\partial}{\partial z}\left(\frac{v_z^2}{2}\right) + v_\varpi\frac{\partial v_z}{\partial\varpi} = -\frac{1}{\rho}\frac{\partial P}{\partial z} - \frac{\partial\psi}{\partial z}, \tag{2.349}$$

where $\Omega = v_\phi/\varpi$, ν is the viscosity coefficient, ψ is the gravitational potential, and other symbols have their usual meanings. It is assumed that the viscous force due to turbulence has the standard form given by (2.121). Since the dominant disc shear is that due to differential rotation, the poloidal components of $\mathbf{F}_\mathrm{v}$ are ignorable compared to $F_{\mathrm{v}\phi}$, where the latter is given by (2.122). The vertical derivative term in this expression is dropped here since, for vanishing ρ at the disc surfaces, it gives zero net torque on rings of material. For thin discs the mass of the disc is very small relative to the stellar mass and so self-gravity is negligible and ψ is the potential of the compact primary star given by

$$\psi = -\frac{GM_\mathrm{p}}{(\varpi^2 + z^2)^{\frac{1}{2}}}. \tag{2.350}$$

The main body of the disc lies well inside the primary's Roche lobe, so tidal distortion due to the secondary is small, allowing an axisymmetric structure to be considered.

The continuity equation (2.103) becomes

$$\frac{1}{\varpi}\frac{\partial}{\partial\varpi}(\varpi\rho v_\varpi) + \frac{\partial}{\partial z}(\rho v_z) = 0. \tag{2.351}$$

The equations of the disc surfaces can be written as

$$z = \pm h(\varpi). \tag{2.352}$$

A thin disc will satisfy the condition

$$\frac{dh}{d\varpi} \sim \frac{h}{\varpi} \ll 1. \tag{2.353}$$

The disc pressure and density are expected to have maximum values in the central plane $z = 0$, and fall vertically with the length-scale h. The medium surrounding the disc is taken to be essentially a vacuum, so surface conditions can be defined as

$$P(\varpi, \pm h) = 0, \tag{2.354a}$$

$$\rho(\varpi, \pm h) = 0. \tag{2.354b}$$

The continuity equation (2.351) and the thin disc condition (2.353) give

$$\left|\frac{v_z}{v_\varpi}\right| \lesssim \frac{h}{\varpi} \ll 1. \tag{2.355}$$

The thin nature of the disc enables the equations to be simplified. The azimuthal component of the momentum equation, given by (2.348), yields an order of magnitude estimate for the inflow speed as

$$|v_\varpi| \sim \frac{\nu}{\varpi}. \tag{2.356}$$

Firstly, the importance of the velocity terms in the vertical momentum equation (2.349) can be examined. Equation (2.355) gives

$$\left|\frac{\partial}{\partial z}\left(\frac{v_z^2}{2}\right)\right| \sim \left|v_\varpi \frac{\partial v_z}{\partial \varpi}\right| \sim \frac{v_\varpi^2}{\varpi}\frac{h}{\varpi}. \tag{2.357}$$

Differentiation of the gravitational potential (2.350) gives, to first order in z/ϖ,

$$\frac{\partial \psi}{\partial z} = \frac{v_\mathrm{K}^2}{\varpi}\frac{z}{\varpi}, \tag{2.358}$$

where the square of the Keplerian speed is

$$v_\mathrm{K}^2 = \frac{GM_\mathrm{p}}{\varpi}. \tag{2.359}$$

It follows that

$$\frac{|v_\varpi\, \partial v_z/\partial \varpi|}{|\partial \psi/\partial z|} \sim \left(\frac{v_\varpi}{v_\mathrm{K}}\right)^2, \tag{2.360}$$

and similarly for the v_z^2 inertial term.

The inflow speed can be estimated from (2.356) if the viscosity coefficient ν is known. Ordinary molecular values of ν are far too small to give the required inflow speeds, so a turbulent viscosity is used. In the absence of a rigorous theory of turbulent transport coefficients, a parametrized form is adopted given by

$$\nu = \epsilon_\mathrm{T} c_\mathrm{s} h, \tag{2.361}$$

where c_s is the isothermal sound speed

$$c_\mathrm{s} = \left(\frac{P}{\rho}\right)^{\frac{1}{2}} = \left(\frac{\mathcal{R}}{\mu}T_\mathrm{c}\right)^{\frac{1}{2}}. \tag{2.362}$$

The form (2.361) is the product of a mean subsonic transport speed and a mixing length $< h$. The dimensionless parameter incorporates the speed and length factors, so $\epsilon_\mathrm{T} < 1$. Using (2.361) for ν in (2.356) gives

$$\frac{|v_\varpi|}{v_\mathrm{K}} \sim \epsilon_\mathrm{T}\frac{c_\mathrm{s}}{v_\mathrm{K}}\frac{h}{\varpi}, \tag{2.363}$$

with

$$\frac{c_s}{v_K} = \left(\frac{\mathcal{R}\varpi T}{\mu G M_p}\right)^{\frac{1}{2}}. \tag{2.364}$$

Since $\epsilon_T(h/\varpi) \ll 1$ holds, (2.363) shows that the inflow speed v_ϖ is well subsonic. Taking $\mu = 0.6$, $M_p = 0.6\,M_\odot$, $\varpi = 10^8$ m and $T = 10^4$ K gives $c_s/v_K = 1.3 \times 10^{-2}$, so it follows from (2.363) that

$$\frac{|v_\varpi|}{v_K} \ll 1. \tag{2.365}$$

Equations (2.360) and (2.365) then show that the inertial terms, which involve the subsonic poloidal velocity components, are ignorable in the vertical momentum equation (2.349), which therefore becomes

$$\frac{1}{\rho}\frac{\partial P}{\partial z} + \frac{\partial \psi}{\partial z} = 0, \tag{2.366}$$

corresponding to hydrostatic equilibrium.

Consider, next, the radial momentum equation (2.347). Using (2.350) for ψ, the gravity term can be written

$$\frac{\partial \psi}{\partial \varpi} = \frac{v_K^2}{\varpi}. \tag{2.367}$$

Then

$$\frac{|\partial(v_\varpi^2/2)/\partial\varpi|}{\partial\psi/\partial\varpi} \sim \frac{|v_z \partial v_\varpi/\partial z|}{\partial\psi/\partial\varpi} \sim \left(\frac{v_\varpi}{v_K}\right)^2 \ll 1, \tag{2.368}$$

so these inertial terms, involving the subsonic poloidal velocity components, are small and (2.347) becomes

$$\frac{v_\phi^2}{\varpi} = \frac{v_K^2}{\varpi} + \frac{1}{\rho}\frac{\partial P}{\partial \varpi}. \tag{2.369}$$

It follows from (2.362) for c_s that

$$\frac{|\partial P/\partial\varpi|}{\rho v_K^2/\varpi} \sim \left(\frac{c_s}{v_K}\right)^2. \tag{2.370}$$

However, the vertical equilibrium equation (2.366), together with (2.358) for $\partial\psi/\partial z$ and (2.362) for c_s, gives

$$\frac{c_s}{v_K} \sim \frac{h}{\varpi} \ll 1, \tag{2.371}$$

so, to first order in h/ϖ, the radial momentum for a thin disc yields

$$v_\phi = v_K = \left(\frac{GM_p}{\varpi}\right)^{\frac{1}{2}}, \tag{2.372}$$

with a corresponding angular velocity

$$\Omega = \Omega_K = \left(\frac{GM_p}{\varpi^3}\right)^{\frac{1}{2}}. \tag{2.373}$$

The continuity equation (2.351) can be integrated vertically through the disc, using the surface condition (2.354b) for ρ, to give

$$\frac{d}{d\varpi}\int_{-h}^{h} \varpi \rho v_\varpi \, dz = 0. \tag{2.374}$$

The thin disc condition (2.353) allows the radial differential operator to be taken out of the integral, even though its limits depend on ϖ. The integral is then a constant, being related to the steady mass transfer rate through the disc by

$$\dot{M} = -2\pi \int_{-h}^{h} \varpi \rho v_\varpi \, dz, \tag{2.375}$$

where the factor of 2π arises from azimuthal integration.

The azimuthal momentum equation (2.348) describes how the inward advection of specific angular momentum $\varpi^2\Omega$ through the disc is balanced by its outward radial transport due to the viscous torque. Combining this with the continuity equation (2.351) gives

$$\frac{\partial}{\partial\varpi}(\varpi\rho v_\varpi \varpi^2\Omega) + \frac{\partial}{\partial z}(\varpi\rho v_z \varpi^2\Omega) = \frac{\partial}{\partial\varpi}\left(\rho\nu\varpi^3\frac{d\Omega}{d\varpi}\right). \tag{2.376}$$

Integrating vertically, taking ν as z-independent, yields

$$-\frac{d}{d\varpi}(\dot{M}\varpi^2\Omega) = \frac{d}{d\varpi}\left(2\pi\varpi^3\nu\Sigma\frac{d\Omega}{d\varpi}\right), \tag{2.377}$$

where

$$\Sigma = \int_{-h}^{h} \rho dz \tag{2.378}$$

is twice the mass per unit surface area. Radial integration of (2.377) gives

$$\dot{M}\varpi^2\Omega + 2\pi\varpi^3\nu\Sigma\frac{d\Omega}{d\varpi} = C, \tag{2.379}$$

where C is a constant equal to the rate of angular momentum transport, being the sum of material and viscous contributions. For a non-magnetic primary, the disc extends to the stellar surface $\varpi = R_\mathrm{p}$. For material to accrete the star must be rotating below break-up speed at its equator, requiring $\Omega_\mathrm{p} < \Omega_\kappa(R_\mathrm{p})$. It follows that Ω must turn over and decrease to Ω_p through a boundary layer . If this layer has width δ, then $d\Omega/d\varpi = 0$ at $\varpi = R_\mathrm{p} + \delta$ where $\delta \ll R_\mathrm{p}$. For a sharp turn over at the outer edge of the layer, Ω will be close to its Keplerian value so (2.379) yields

$$C = \dot{M}(R_\mathrm{p} + \delta)^2\Omega_\kappa(R_\mathrm{p} + \delta). \tag{2.380}$$

Since $\delta \ll R_\mathrm{p}$, this can be written as

$$C = \dot{M}R_\mathrm{p}^2\Omega_\kappa(R_\mathrm{p}), \tag{2.381}$$

provided it is remembered that $\varpi > R_\mathrm{p} + \delta$ applies in the subsequent disc solution. Using (2.373) for Ω in (2.379) then gives

$$\nu\Sigma = \frac{\dot{M}}{3\pi}\left[1 - \left(\frac{R_\mathrm{p}}{\varpi}\right)^{\frac{1}{2}}\right]. \tag{2.382}$$

For a thin disc, it follows from (A25) that the dominant elements in the rate of strain tensor are

$$e_{\varpi\phi} = e_{\phi\varpi} = \frac{1}{2}\varpi\frac{\partial\Omega}{\partial\varpi}. \tag{2.383}$$

Hence (2.125) gives the viscous dissipation rate per unit volume as

$$Q_\mathrm{v} = 4\rho\nu e_{\varpi\phi}e_{\varpi\phi} = \rho\nu\left(\varpi\frac{\partial\Omega}{\partial\varpi}\right)^2. \tag{2.384}$$

The viscous dissipation per unit area of disc surface is then

$$U(\varpi) = \int_0^h Q_\mathrm{v}dz = \frac{1}{2}\nu\Sigma(\varpi\Omega')^2, \tag{2.385}$$

so the use of (2.373) for Ω and (2.382) for $\nu\Sigma$ gives

$$U(\varpi) = \frac{3GM_{\rm p}\dot{M}_{\rm p}}{8\pi\varpi^3}\left[1-\left(\frac{R_{\rm p}}{\varpi}\right)^{\frac{1}{2}}\right]. \tag{2.386}$$

Integration of this radially across the disc yields the luminosity $L_{\rm D}$, in agreement with (2.346).

The inflow speed v_ϖ can now be found. Since $\Omega_{\rm K}$ is independent of z, the azimuthal momentum equation (2.348) gives

$$v_\varpi \frac{d}{d\varpi}(\varpi^2\Omega_{\rm K}) = \frac{1}{\varpi\rho}\frac{\partial}{\partial\varpi}\left(\rho\nu\varpi^3\frac{d\Omega_{\rm K}}{d\varpi}\right). \tag{2.387}$$

This shows that if ν varies slowly with z, then so does v_ϖ. The mass transfer rate integral (2.375) then yields

$$\dot{M} = -2\pi\varpi\Sigma v_\varpi. \tag{2.388}$$

The inflow speed follows by eliminating $\Sigma/\dot{M}$ between this and (2.382), so

$$v_\varpi = -\frac{3\nu}{2\varpi}\left[1-\left(\frac{R_{\rm p}}{\varpi}\right)^{\frac{1}{2}}\right]^{-1}, \tag{2.389}$$

which justifies the estimate of $|v_\varpi| \sim \nu/\varpi$ used previously.

The thermal problem remains to be solved. In an optically thick disc with heat transport via radiation, (2.144) gives the radiative flux through a z =constant surface as

$$F_{\rm R} = -\frac{16\sigma_{\rm B}T^3}{3\kappa\rho}\frac{\partial T}{\partial z}, \tag{2.390}$$

where $\sigma_{\rm B}$ is the Stefan-Boltzmann constant and κ the Rosseland mean opacity. The ratio of the advection term to the viscous dissipation term in the heat equation (2.142) is $\sim |\mathbf{v}\cdot\nabla P|/Q_{\rm v} \sim c_{\rm s}^2/v_{\rm K}^2 \sim h^2/\varpi^2$. Hence the advection term is ignorable, to first order, and the steady heat equation gives a balance between the divergence of the heat flux and the rate of viscous dissipation per unit volume. Since the vertical derivative term dominates in $\nabla\cdot\mathbf{F}$, the heat equation becomes

$$\frac{\partial F_{\rm R}}{\partial z} = Q_{\rm v}. \tag{2.391}$$

Then, noting that $F_{\rm R}(\varpi, 0) = 0$,

$$F_{\rm R}(\varpi, h) = \int_0^h Q_{\rm v}dz = U(\varpi), \tag{2.392}$$

where $U(\varpi)$ is the dissipation per unit surface area, given by (2.386). Equation (2.390) yields

$$\int_0^h \kappa\rho F_{\rm R} dz = \frac{4\sigma_{\rm B}}{3} T_{\rm c}^4. \tag{2.393}$$

Approximating the integral as $\kappa_{\rm c}\rho_c h F_{\rm R}(\varpi, h)$, and taking the optical depth as

$$\tau = \kappa_{\rm c}\rho_{\rm c} h, \tag{2.394}$$

gives

$$F_{\rm R}(\varpi, h) = \frac{4\sigma_{\rm B}}{3\tau} T_{\rm c}^4. \tag{2.395}$$

The foregoing equations describing a thin steady viscous disc are;

$$v_\varpi = -\frac{3\nu}{2\varpi}\left[1 - \left(\frac{R_{\rm p}}{\varpi}\right)^{\frac{1}{2}}\right]^{-1}, \tag{2.396}$$

$$v_\phi = \left(\frac{GM_{\rm p}}{\varpi}\right)^{\frac{1}{2}}, \tag{2.397}$$

$$h = \sqrt{2}\frac{c_{\rm s}}{v_\phi}\varpi, \tag{2.398}$$

$$c_{\rm s} = \left(\frac{P_{\rm c}}{\rho_{\rm c}}\right)^{\frac{1}{2}}, \tag{2.399}$$

$$\rho_{\rm c} = \frac{\Sigma}{h}, \tag{2.400}$$

$$P_{\rm c} = \frac{\mathcal{R}}{\mu}\rho_{\rm c} T_{\rm c}, \tag{2.401}$$

$$\frac{4\sigma_{\rm B}}{3\tau} T_{\rm c}^4 = \frac{3GM_{\rm p}\dot{M}_{\rm p}}{8\pi\varpi^3}\left[1 - \left(\frac{R_{\rm p}}{\varpi}\right)^{\frac{1}{2}}\right], \tag{2.402}$$

where (2.398) employs the mean value theorem using the average $\langle z\rho\rangle = \rho_{\rm c} h/2$ in the vertical equilibrium (2.366), and (2.400) uses $\langle\rho\rangle = \rho_{\rm c}/2$ in the column density (2.378). These equations are valid for $\varpi > R_{\rm p} + \delta$, where δ is the width of the boundary layer through which Ω changes from $\Omega_{\rm K}$ to $\Omega_{\rm p}$. Azimuthal kinetic energy is dissipated in this highly sheared layer.

The standard disc model uses a simple mixing length prescription for the viscosity due to turbulence. The mean transport speed is taken to be a fraction of the isothermal sound speed and this is multiplied by a turbulent mixing length which is

a fraction of the disc height. The mixing length is several orders of magnitude larger than the mean free path occurring in the microscopic form of viscous coefficient. Hence the turbulent viscosity coefficient can be expressed as

$$\nu = \epsilon_{\mathrm{T}} c_{\mathrm{s}} h, \tag{2.403}$$

where $\epsilon_{\mathrm{T}} < 1$ for subsonic turbulence. This enhanced viscosity allows a thin disc solution to be found consistent with the expected mass transfer rates.

Assuming that electron scattering opacity is small compared to the contributions from free-free and bound-free transitions, the Rosseland mean opacity can be approximated by Kramers' law as

$$\kappa = 6.6 \times 10^{18} \rho T^{-\frac{7}{2}}\,\mathrm{m^2\,kg^{-1}}. \tag{2.404}$$

The set of disc equations is then algebraic and their solution for the radial structure yields,

$$h = 1.59 \times 10^6 \frac{\dot{M}_{10}^{\frac{3}{20}}}{\epsilon_{\mathrm{T}}^{\frac{1}{10}} M_1^{\frac{3}{8}}} x^{\frac{9}{8}} f^{\frac{3}{20}}\,\mathrm{m}, \tag{2.405}$$

$$\rho_{\mathrm{c}} = 2.41 \times 10^{-5} \frac{\dot{M}_{10}^{\frac{11}{20}} M_1^{\frac{5}{8}}}{\epsilon_{\mathrm{T}}^{\frac{7}{10}}} \frac{f^{\frac{11}{20}}}{x^{\frac{15}{8}}}\,\mathrm{kg\,m^{-3}}, \tag{2.406}$$

$$T_{\mathrm{c}} = 1.22 \times 10^4 \frac{\dot{M}_{10}^{\frac{3}{10}} M_1^{\frac{1}{4}}}{\epsilon_{\mathrm{T}}^{\frac{1}{5}}} \frac{f^{\frac{3}{10}}}{x^{\frac{3}{4}}}\,\mathrm{K}, \tag{2.407}$$

$$\tau = 30 \frac{\dot{M}_{10}^{\frac{1}{5}}}{\epsilon_{\mathrm{T}}^{\frac{4}{5}}} f^{\frac{1}{5}}, \tag{2.408}$$

$$\nu = 1.57 \times 10^{10} \epsilon_{\mathrm{T}}^{\frac{4}{5}} \frac{\dot{M}_{10}^{\frac{3}{10}}}{M_1^{\frac{1}{4}}} x^{\frac{3}{4}} f^{\frac{3}{10}}\,\mathrm{m^2\,s^{-1}}, \tag{2.409}$$

$$v_{\varpi} = -2.35 \times 10^2 \epsilon_{\mathrm{T}}^{\frac{4}{5}} \frac{\dot{M}_{10}^{\frac{3}{10}}}{M_1^{\frac{1}{4}}} \frac{1}{x^{\frac{1}{4}} f^{\frac{7}{10}}}\,\mathrm{m\,s^{-1}}, \tag{2.410}$$

where $\dot{M}_{10} = \dot{M}_{\mathrm{p}}/10^{-10}\,M_{\odot}\mathrm{year}^{-1}$, $M_1 = M_{\mathrm{p}}/M_{\odot}$, $x = \varpi/10^8\,\mathrm{m}$, and

$$f = 1 - \left(\frac{R_{\mathrm{p}}}{\varpi}\right)^{\frac{1}{2}}. \tag{2.411}$$

Equation (2.405) gives $h/\varpi \ll 1$, consistent with a thin disc. The optical depth vertically through the disc is given by (2.408) which yields $\tau \gg 1$, justifying the use of the diffusion approximation for the radiative transfer equation. Equation (2.410) gives $|v_\varpi| \ll c_s$, so the inflow speed is highly subsonic.

The foregoing steady viscous disc solution involves vertical integrations from the central plane to the disc surface, so the details of the vertical structure are not considered. This separation of the radial and vertical structures is facilitated by the large difference in the radial and vertical length-scales of disc quantities. The accretor is assumed to be essentially non-magnetic, so the disc extends down to the stellar surface with accretion occurring through a boundary layer. The disc is assumed not to contain any significant magnetic field and to be surrounded by a vacuum. However, it will be shown that internal magnetic fields provide the mechanism for generating turbulence in the disc, and that large-scale magnetic fields are likely to be generated by dynamo action. Discs may have magnetically influenced wind flows emanating from their surfaces, and these can be effective at removing angular momentum and contributing to driving the inflow. Enhanced mass loss may occur in the inner region of the disc.

If the accreting star has a significant magnetic moment then its field will interact with the disc. A high stellar magnetic moment with an associated magnetosphere can result in complete disruption of the disc, which occurs in the AM Herculis systems, or in partial disruption as occurs in the intermediate polars, the X-ray binary pulsars and the accreting millisecond pulsars. Disrupted discs are considered in Chap. 9. A magnetic modification to the viscous disc due to a dynamo generated large-scale field is presented in Chap. 11, while the effects of magnetic wind driving are investigated in Chap. 14, with the vertical structure included in both cases.

Time-Dependent Viscous Discs

For a time-dependent, axisymmetric viscous disc, the azimuthal momentum and continuity equations can be written

$$\frac{\partial}{\partial t}(\varpi^2\Omega) + v_\varpi \frac{\partial}{\partial \varpi}(\varpi^2\Omega) + v_z \frac{\partial}{\partial z}(\varpi^2\Omega) = \frac{1}{\varpi\rho}\frac{\partial}{\partial \varpi}\left(\rho\nu\varpi^3\frac{\partial\Omega}{\partial\varpi}\right), \tag{2.412}$$

$$-\frac{\partial\rho}{\partial t} = \frac{1}{\varpi}\frac{\partial}{\partial\varpi}(\varpi\rho v_\varpi) + \frac{\partial}{\partial z}(\rho v_z). \tag{2.413}$$

If Ω remains Keplerian at all heights in the disc, then $\partial\Omega/\partial t = 0$ and $\partial\Omega/\partial z = 0$ so (2.412) gives

$$\varpi\rho v_\varpi \frac{d}{d\varpi}(\varpi^2\Omega_K) = \frac{\partial}{\partial\varpi}\left(\rho\nu\varpi^3\frac{d\Omega_K}{d\varpi}\right). \tag{2.414}$$

Vertical integration of (2.413) and (2.414) through the disc yields

$$-\frac{\partial \Sigma}{\partial t} = \frac{1}{\varpi}\frac{\partial}{\partial \varpi}(\varpi \Sigma v_{\varpi}), \tag{2.415}$$

$$\varpi \Sigma v_{\varpi}\frac{d}{d\varpi}(\varpi^2 \Omega_{\mathrm{K}}) = \frac{\partial}{\partial \varpi}\left(\nu \Sigma \varpi^3 \frac{d\Omega_{\mathrm{K}}}{d\varpi}\right), \tag{2.416}$$

where Σ is the surface density function given by (2.378), and $\rho(\varpi, \pm h) = 0$ is used. Elimination of $\varpi \Sigma v_{\varpi}$ between (2.415) and (2.416), together with the use of (2.373) for Ω_{K}, leads to

$$\frac{\partial \Sigma}{\partial t} = \frac{3}{\varpi}\frac{\partial}{\partial \varpi}\left(\varpi^{\frac{1}{2}}\frac{\partial}{\partial \varpi}\left(\varpi^{\frac{1}{2}}\nu \Sigma\right)\right). \tag{2.417}$$

This is a viscous diffusion equation for Σ. For realistic disc models ν will depend on Σ and hence the diffusion equation will be non-linear.

The viscosity has the effect of spreading material in the disc, at a rate which increases with spatial gradients. If ν and Σ have radial length-scales of $\sim \varpi$, then (2.417) yields a characteristic viscous time-scale of

$$\tau_{\mathrm{v}} \sim \frac{\varpi^2}{\nu}. \tag{2.418}$$

Using (2.373) for Ω_{K} in (2.416) gives the instantaneous radial velocity as

$$v_{\varpi}(\varpi, t) = -\frac{3}{\varpi^{\frac{1}{2}}\Sigma}\frac{\partial}{\partial \varpi}\left(\varpi^{\frac{1}{2}}\nu \Sigma\right), \tag{2.419}$$

and hence

$$|v_{\varpi}| \sim \frac{\nu}{\varpi}. \tag{2.420}$$

Employing this to eliminate ν in (2.418) shows that τ_{v} may be expressed as

$$\tau_{\mathrm{v}} \sim \frac{\varpi}{|v_{\varpi}|}, \tag{2.421}$$

which is also the radial drift time-scale. The viscosity redistributes angular momentum and mass radially through the disc on the time-scale τ_{v}. Density distributions of length-scale $\ell < \varpi$ diffuse more rapidly with larger associated radial drift velocities.

Other time-scales relevant to discs are the dynamical time and the thermal time. The dynamical time-scale associated with the Keplerian rotation is

$$\tau_\phi \sim \frac{\varpi}{v_\phi} \sim \frac{1}{\Omega_{\rm K}}. \tag{2.422}$$

Deviations from vertical hydrostatic equilibrium are smoothed out on the dynamical time-scale

$$\tau_z \sim \frac{h}{c_{\rm s}}. \tag{2.423}$$

Since $c_{\rm s} \sim (h/\varpi)v_{\rm K}$ for a thin viscous disc, it follows that $\tau_z \sim \tau_\phi$.

The thermal time-scale $\tau_{\rm th}$ gives the evolution time of perturbations from thermal equilibrium. This can be estimated by noting that the thermal energy density in a perfect gas is $\sim P = \rho c_{\rm s}^2$, while the viscous dissipation rate per unit volume is $\sim \nu\Sigma(\varpi\Omega_{\rm K}')^2/h$. Hence, since $|\varpi\Omega_{\rm K}'| \sim \Omega_{\rm K}$,

$$\tau_{\rm th} \sim \frac{\rho h c_{\rm s}^2}{\nu\Sigma\Omega_{\rm K}^2} \sim \left(\frac{c_{\rm s}}{v_{\rm K}}\right)^2 \frac{\varpi^2}{\nu}, \tag{2.424}$$

so that

$$\tau_{\rm th} \sim \left(\frac{h}{\varpi}\right)^2 \tau_{\rm v}. \tag{2.425}$$

Hence the thermal time-scale is much shorter than the viscous/inflow time-scale.

The dynamical time-scale can be related to the viscous time-scale by using the viscosity prescription (2.361), together with $c_{\rm s} \sim (h/\varpi)v_{\rm K}$. Then

$$\tau_{\rm v} \sim \frac{\varpi^2}{\nu} \sim \frac{\varpi^2}{\epsilon_{\rm T} c_{\rm s} h} \sim \frac{1}{\epsilon_{\rm T}}\left(\frac{\varpi}{h}\right)^2 \frac{\varpi}{v_{\rm K}} \sim \frac{1}{\epsilon_{\rm T}}\left(\frac{\varpi}{h}\right)^2 \tau_\phi, \tag{2.426}$$

giving

$$\tau_\phi \sim \epsilon_{\rm T}\left(\frac{h}{\varpi}\right)^2 \tau_{\rm v} \sim \epsilon_{\rm T}\tau_{\rm th}. \tag{2.427}$$

It follows that, since $\epsilon_{\rm T} < 1$, the ordering of the time-scales is

$$\tau_\phi \sim \tau_z < \tau_{\rm th} \ll \tau_{\rm v}. \tag{2.428}$$

One of the main uses of time-dependent disc theory is in the analysis of waves and instabilities. The significant differences between the various time-scales, shown

by (2.428), means that different types of perturbations can be identified. Consider an axisymmetric perturbation in the surface density function, so

$$\Sigma = \Sigma_0(\varpi) + \delta\Sigma(\varpi, t). \tag{2.429}$$

Substitution in the viscous diffusion equation (2.417) gives

$$\frac{\partial}{\partial t}(\delta\Sigma) = \frac{3}{\varpi}\frac{\partial}{\partial\varpi}\left(\varpi^{\frac{1}{2}}\frac{\partial}{\partial\varpi}\left(\varpi^{\frac{1}{2}}\delta\mu\right)\right), \tag{2.430}$$

where $\mu = \nu\Sigma$. Since (2.428) shows that the dynamical and thermal time-scales are short compared to the viscous time-scale, the disc can adjust quasi-steadily on the viscous time-scale. Then the viscosity can be expressed in the form $\nu = \nu(\varpi, \Sigma)$, with $\nu \propto \varpi^{15/14}\Sigma^{3/7}$ resulting from the foregoing model. Hence $\mu = \mu(\varpi, \Sigma)$, so

$$\delta\mu = \left(\frac{\partial\mu}{\partial\Sigma}\right)_{\rm sd}\delta\Sigma, \tag{2.431}$$

with the subscript sd denoting the steady state. Then $\delta\Sigma$ can be eliminated from the diffusion equation to give

$$\frac{\partial}{\partial t}(\delta\mu) = \left(\frac{\partial\mu}{\partial\Sigma}\right)_{\rm sd}\frac{3}{\varpi}\frac{\partial}{\partial\varpi}\left(\varpi^{\frac{1}{2}}\frac{\partial}{\partial\varpi}\left(\varpi^{\frac{1}{2}}\delta\mu\right)\right). \tag{2.432}$$

The diffusion coefficient is therefore proportional to $(\partial\mu/\partial\Sigma)_{\rm sd}$. For positive $(\partial\mu/\partial\Sigma)_{\rm sd}$ a perturbation decays on the viscous time-scale $\tau_{\rm v}$. However, if $(\partial\mu/\partial\Sigma)_{\rm sd}$ is negative a perturbation in Σ will grow due to viscous instability. More material will be fed into regions that are denser than their surroundings, and the disc will tend to break up into rings on the time-scale $\tau_{\rm v}$. A steady flow therefore requires $(\partial\mu/\partial\Sigma)_{\rm sd} > 0$.

2.5 Spin Dynamics

In spin evolution calculations the compact white dwarf, or neutron star, is assumed to act approximately like a rigid body, due to the action the strong internal forces acting in these compact objects. A strongly magnetic primary star will experience some distortion from spherical symmetry due to non-radial internal magnetic forces. The essentials of the spin dynamics of rigid bodies are presented here.

The angular momentum of a rigid body of volume V rotating with instantaneous angular velocity $\boldsymbol{\omega}$ is

$$\mathbf{L} = \int_V \mathbf{r} \times (\boldsymbol{\omega} \times \mathbf{r})\rho dV, \tag{2.433}$$

where ρ is the density and $\mathbf{r}$ is measured from the centre of mass, O. Expanding the cross product gives

$$\mathbf{L} = \int_V [r^2\boldsymbol{\omega} - (\mathbf{r}\cdot\boldsymbol{\omega})\mathbf{r}]\rho dV. \tag{2.434}$$

In an inertial coordinate frame $Oxyz$ the components of $\mathbf{L}$ can be written

$$L_x = I_{xx}\omega_x + I_{xy}\omega_y + I_{xz}\omega_z, \tag{2.435}$$

$$L_y = I_{yx}\omega_x + I_{yy}\omega_y + I_{yz}\omega_z, \tag{2.436}$$

$$L_z = I_{zx}\omega_x + I_{zy}\omega_y + I_{zz}\omega_z, \tag{2.437}$$

where

$$I_{xx} = \int_V (y^2 + z^2)\rho dV, \qquad I_{yy} = \int_V (x^2 + z^2)\rho dV,$$
$$I_{zz} = \int_V (x^2 + y^2)\rho dV \tag{2.438}$$

are moments of inertia, while

$$I_{xy} = I_{yx} = -\int_V xy\rho dV, \qquad I_{xz} = I_{zx} = -\int_V xz\rho dV, \tag{2.439}$$

$$I_{yz} = I_{zy} = -\int_V yz\rho dV \tag{2.440}$$

are products of inertia. Equation (2.435)–(2.437) can be expressed in Cartesian tensor form as

$$L_i = I_{ij}\omega_j, \tag{2.441}$$

where the repeated index is summed over. The inertia tensor I_{ij} is symmetric and (2.441) shows that, in general, $\mathbf{L}$ and $\boldsymbol{\omega}$ are not parallel.

Since the inertia tensor is symmetric it corresponds to a real Hermitian matrix. Such a matrix has a complete set of eigenvectors which therefore form a basis in which an arbitrary vector can be represented. The matrix elements I_{ij} will depend on the basis used to represent the column vector on which I acts. The simplest form of I results when its eigenvectors are chosen as the basis. This diagonalization process involves the similarity transformation

$$I(\text{diag}) = X^{-1} I X, \tag{2.442}$$

where the modal matrix $X = (X_1 X_2 X_3)$ with X_i the eigenvectors of I. This rotates the frame $Oxyz$ to be coincident with the orthogonal eigenvectors. The inertia tensor then has the form

$$I = \begin{pmatrix} I_1 & 0 & 0 \\ 0 & I_2 & 0 \\ 0 & 0 & I_3 \end{pmatrix}. \tag{2.443}$$

The diagonal elements are the principal moments of inertia about the eigenvectors of I which have directions denoted by the unit vectors $\mathbf{e}_1$, $\mathbf{e}_2$ and $\mathbf{e}_3$. These orthogonal principal axes are fixed in the body. Relative to these axes, the angular velocity and angular momentum are

$$\boldsymbol{\omega} = \omega_1 \mathbf{e}_1 + \omega_2 \mathbf{e}_2 + \omega_3 \mathbf{e}_3, \tag{2.444}$$

$$\mathbf{L} = I_1 \omega_1 \mathbf{e}_1 + I_2 \omega_2 \mathbf{e}_2 + I_3 \omega_3 \mathbf{e}_3. \tag{2.445}$$

It is noted that $\boldsymbol{\omega}$ and $\mathbf{L}$ are only parallel if the body is spherical or its spin axis is coincident with a principal axis.

The motion of a rigid body is described by the angular momentum evolution equation

$$\frac{d\mathbf{L}}{dt} = \mathbf{T}, \tag{2.446}$$

where the time derivative is measured in inertial space, and $\mathbf{T}$ is the torque. The principal unit vectors of the body frame have inertial time derivatives given by

$$\frac{d\mathbf{e}_i}{dt} = \boldsymbol{\omega} \times \mathbf{e}_i. \tag{2.447}$$

Denoting the time derivative relative to the body frame by a dot, it follows that

$$\frac{d\mathbf{L}}{dt} = \frac{d}{dt}(L_i \mathbf{e}_i) = \dot{L}_i \mathbf{e}_i + L_i \boldsymbol{\omega} \times \mathbf{e}_i, \tag{2.448}$$

and hence (2.446) can be written as

$$\dot{\mathbf{L}} + \boldsymbol{\omega} \times \mathbf{L} = \mathbf{T}. \tag{2.449}$$

The orientation of a rigid body about its centre of mass is specified by three angles. The Euler angles (α, ϕ, ψ) are usually chosen. The angles α and ϕ define the orientation of one axis, say $\mathbf{e}_3$, relative to inertial axes, while ψ defines a rotation of the body about the $\mathbf{e}_3$ axis from a standard position. Figure 2.2 shows how the

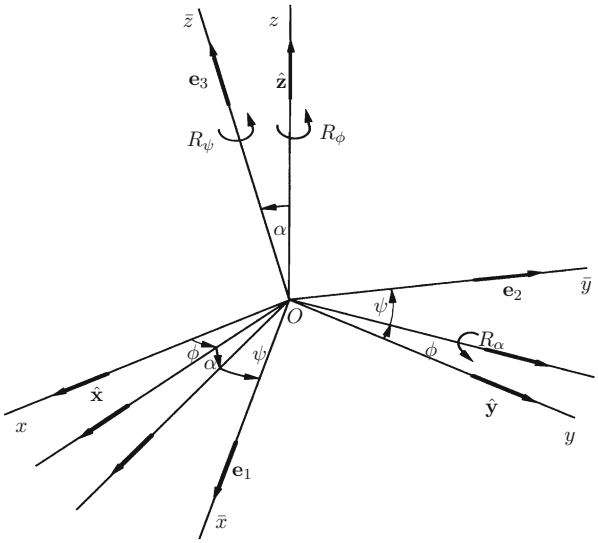

Fig. 2.2 The rotation sequence generating an orientation with Euler angles (α, ϕ, ψ)

orientation (α, ϕ, ψ) can be attained by three rotations. Firstly, a rotation of ϕ about the z-axis is generated by the matrix

$$R_\phi = \begin{pmatrix} \cos\phi & \sin\phi & 0 \\ -\sin\phi & \cos\phi & 0 \\ 0 & 0 & 1 \end{pmatrix}. \tag{2.450}$$

Secondly, a rotation of α about the new y-axis is generated by

$$R_\alpha = \begin{pmatrix} \cos\alpha & 0 & -\sin\alpha \\ 0 & 1 & 0 \\ \sin\alpha & 0 & \cos\alpha \end{pmatrix}. \tag{2.451}$$

Finally, a rotation of ψ about the new z-axis is given by

$$R_\psi = \begin{pmatrix} \cos\psi & \sin\psi & 0 \\ -\sin\psi & \cos\psi & 0 \\ 0 & 0 & 1 \end{pmatrix}. \tag{2.452}$$

The total rotation is then the matrix product.

$$R = R_\psi R_\alpha R_\phi. \tag{2.453}$$

Equations (2.450)–(2.453) give the elements of the rotation matrix as;

$$\begin{aligned}
R_{11} &= \cos\alpha\cos\phi\cos\psi - \sin\phi\sin\psi,\\
R_{12} &= \cos\alpha\sin\phi\cos\psi + \cos\phi\sin\psi,\\
R_{13} &= -\sin\alpha\cos\psi,\\
R_{21} &= -\cos\alpha\cos\phi\sin\psi - \sin\phi\cos\psi,\\
R_{22} &= -\cos\alpha\sin\phi\sin\psi + \cos\phi\cos\psi,\\
R_{23} &= \sin\alpha\sin\psi,\\
R_{31} &= \sin\alpha\cos\phi,\\
R_{32} &= \sin\alpha\sin\phi,\\
R_{33} &= \cos\alpha.
\end{aligned} \tag{2.454}$$

The components of a vector $\mathbf{V}$ relative to the inertial frame $Oxyz$ are related to those relative to the body frame $O\bar{x}\bar{y}\bar{z}$ by

$$\bar{V}_i = R_{ij}V_j, \tag{2.455}$$

where the summation convention is used.

The instantaneous angular velocity can be expressed as the sum of the angular velocities $\dot{\alpha}$, $\dot{\phi}$ and $\dot{\psi}$ measured about the directions $\hat{\boldsymbol{\alpha}}$, $\hat{\boldsymbol{\phi}}$ and $\hat{\boldsymbol{\psi}}$, so

$$\boldsymbol{\omega} = \dot{\alpha}\,\hat{\boldsymbol{\alpha}} + \dot{\phi}\,\hat{\boldsymbol{\phi}} + \dot{\psi}\,\hat{\boldsymbol{\psi}}. \tag{2.456}$$

It follows from Fig. 2.2 that the Euler angular velocities relative to the body frame are

$$\dot{\boldsymbol{\alpha}} = \dot{\alpha}\sin\psi\,\mathbf{e}_1 + \dot{\alpha}\cos\psi\,\mathbf{e}_2, \tag{2.457}$$

$$\dot{\boldsymbol{\phi}} = -\dot{\phi}\sin\alpha\cos\psi\,\mathbf{e}_1 + \dot{\phi}\sin\alpha\sin\psi\,\mathbf{e}_2 + \dot{\phi}\cos\alpha\,\mathbf{e}_3, \tag{2.458}$$

$$\dot{\boldsymbol{\psi}} = \dot{\psi}\,\mathbf{e}_3. \tag{2.459}$$

Equations (2.456)–(2.459) give the components of $\boldsymbol{\omega}$ in the body frame in terms of the Euler angles α, ϕ and ψ as

$$\omega_1 = \dot{\alpha}\sin\psi - \dot{\phi}\sin\alpha\cos\psi, \tag{2.460}$$

$$\omega_2 = \dot{\alpha}\cos\psi + \dot{\phi}\sin\alpha\sin\psi, \tag{2.461}$$

$$\omega_3 = \dot{\phi}\cos\alpha + \dot{\psi}. \tag{2.462}$$

The torque **T** in the angular momentum equation (2.449) will, in general, be a function of α, ϕ, and ψ, so the components of this equation yield a set of coupled differential equations. The solution of these gives the Euler angles as functions of time, and hence the rotational motion of the body.

In spin stability problems the equation of motion is linearized about a given state. Normal mode solutions can then be sought involving the Euler angle perturbations. In the binary star problems to be considered the basic state is dynamical, so independent normal modes may not always exist. However, the high rotation rates occurring in close binaries can lead to essentially separate modes.

References

Batchelor, G.K., 2005, An Introduction to Fluid Dynamics, Cambridge Mathematical Library, Cambridge University Press.
Battaner, E., 1996, Astrophysical Fluid Dynamics, Cambridge University Press.
Campbell, C.G., Papaloizou, J.C.B., 1983, MNRAS, 204, 433.
Chandrasekhar, S., 1961, Hydrodynamic and Hydromagnetic Stability, Clarendon Press, Oxford.
Chiuderi, C., Velli, M., 2014, Basics of Plasma Astrophysics, Springer.
Cowling, T.G., 1933, MNRAS, 94, 39.
Cox, J.P., Giuli, R.T., 1968, Principles of Stellar Structure, Vol I, Gordon and Breach.
Eggleton, P.P., 1983, ApJ, 268, 368.
Faulkner, J., 1971, ApJ, 170, L99.
Goldreich, P., Keeley, D.A., 1977, ApJ, 211, 934.
Jackson, D.J., 2001, Classical Electrodynamics, Wiley.
Kippenhahn, R., 1963, ApJ, 137, 664.
Kippenhahn, R., Weigert, A., 1990, Stellar Structure and Evolution, Springer-Verlag.
Kraft, R.P., Mathews, J., Greenstein, J.L., 1962, ApJ, 136, 312.
Kulsrud, R.M., 2004, Plasma Physics for Astrophysics, Princeton University Press.
Landau, L., Lifshitz, E., 1951, The Classical Theory of Fields, Addison Wesley.
Lubow, S.H., Shu, F.H., 1975, ApJ, 198, 383.
Mestel, L., 2012, Stellar Magnetism, Second Edition, Oxford University Press.
Paczyński, B., 1967, AcA, 17, 287.
Parker, E.N., 1955, ApJ, 122, 293.
Parker, E.N., 1979, Cosmical Magnetic Fields, Oxford University Press.
Plavec, M., Kratochvil, P., 1964, BAICz, 15, 165.
Priest, E., 2014, Magnetohydrodynamics of the Sun, Cambridge University Press.
Roche, E.N., 1873, Ann. de l'Acad. Sci. Montpelier, 8, 235.
Shakura, N.I., Sunyaev, R.A., 1973, A&A, 24, 337.
Skumanich, A., 1972, ApJ, 171, 565.
Spitzer, L., 1962, Physics of Fully Ionized Gases, Interscience, London.
Tayler, R.J., 1973, MNRAS, 165, 39.
Verbunt, F., Zwaan, C., 1981, A&A, 100, L7.
Wasiutynski, J., 1946, Hydrodynamics and Structure of Stars and Planets, AstNor, 4.
Zahn, J.P., 1977, A&A, 57, 383.

Chapter 3
AM Herculis Stars

Abstract The AM Herculis binaries have white dwarf primary stars with the strongest magnetic fields observed in the cataclysmic variables. They are unique in having no accretion discs and primary stars rotating in synchronism with the orbit. The accretion stream becomes magnetically channelled and reaches the primary by one or more localized columns. Unlike other cataclysmic variables, a significant fraction of AM Her binaries occupy the orbital period gap while undergoing mass transfer. These properties pose a range of MHD problems.

Inductive coupling to a tidally synchronized secondary leads to a synchronization torque, but the maintenance of a synchronous state requires non-dissipative torques to act. The 3D nature of the channelled accretion stream results in an accretion torque which has components parallel and normal to the orbital angular momentum vector, leading to restrictions on the nature of the required balancing torque. Certain conditions are necessary for the attainment of synchronism. Asynchronous rotation of the primary can significantly affect the mass transfer rate, due to magnetic spin-orbit coupling. The essential properties of the AM Her binaries are described here, together with a list of the confirmed systems.

3.1 The Nature of AM Herculis Systems

3.1.1 AM Herculis

AM Herculis was identified by Wolf at Heidelberg in 1923 during a routine search for variable stars. It was subsequently listed in the General Catalogue of Variable Stars as an irregular variable with a range of magnitude 12 to magnitude 14. Over five decades later the development of X-ray and polarization observations allowed the nature of this extraordinary system to begin to be revealed. Berg and Duthie (1977) suggested that AM Her could be the optical counterpart of the high galactic latitude X-ray source 3U 1809+50. Further evidence was available from Hearn et al. (1976), which indicated AM Her to be a soft X-ray source. These suggestions were confirmed by Hearn and Richardson (1977). Szkody and Brownlee (1977) found the visual light curve of AM Her to have a broad, deep minimum which repeated

C. G. Campbell, *Magnetohydrodynamics in Binary Stars*, Astrophysics and Space Science Library 456, https://doi.org/10.1007/978-3-319-97646-4_3

on a time-scale of 3.1 h. Linear and circular polarization were observed in the V and I spectral bands by Tapia (1977a), of a strength an order of magnitude larger than previously observed in any object. This suggested the presence of a strong magnetic field, with $B \sim 10^8$ G, assuming the fundamental cyclotron frequency to be observed. Large variations of the polarization were found with a period of 3.1 h.

Models of AM Her involving an accreting magnetic white dwarf in a binary system were discussed by various authors (e.g. Chanmugam and Wagner 1977; Michalsky et al. 1977; Stockman 1977). The rotation of the white dwarf was taken to be synchronous with the orbital period, based on the fact that all the observed radiations had the same period of intensity variations. The short orbital period of AM Her put it in the category of close binary stars. However, unlike the standard cataclysmic variables, there was no evidence for an accretion disc around the white dwarf. The large linear and circular optical polarization were consistent with cyclotron radiation being emitted by accreting gas in a strong magnetic field. Highly conducting matter would be channelled by the field, and the 3.1 h variations could result from a localized radiating accretion column changing its orientation to the line of sight due to the white dwarf's rotation.

Matter is lost from the secondary star through the inner Lagrangian region and falls towards the white dwarf primary. The gas in the accretion stream is ionized and motion of the conducting stream across the primary's magnetic field generates electric currents and a magnetic force is exerted on the material. The infalling matter experiences an increasingly strong magnetic field and ultimately becomes channelled by it on to the surface of the white dwarf. The incoming supersonic stream passes through a standing shock and settles on to the stellar surface through an accretion column. X-rays are emitted in the hot post-shock flow; most of these are reprocessed by the white dwarf's surface and re-emitted as a softer X-ray component. The basic theory of the accretion column on magnetized white dwarfs was considered by King and Lasota (1979). The shock temperature is given by

$$T_\mathrm{s} = 3.7 \times 10^8 \left(\frac{M_\mathrm{p}}{M_\odot}\right)\left(\frac{R_\mathrm{p}}{10^7 \mathrm{m}}\right) \mathrm{K}, \tag{3.1}$$

where M_p and R_p are the mass and radius of the primary. Electrons in the ionized stream close to the shock spiral around the magnetic field lines and emit strongly polarized cyclotron radiation. The field strength results in this radiation being emitted at optical and near infra-red wavelengths. Figure 3.1 is a simple illustration of an AM Her system, for the case of single pole accretion.

Chanmugam and Wagner (1979) showed that the shocked gas in the accretion column will be optically thick to the lowest cyclotron harmonics, suggesting that the previously measured field strengths were too high since they assumed low harmonics. Evidence for a lower field value was given by Schmidt et al. (1981) who presented spectropolarimetry, obtained during a faint state of AM Her, which showed strong circular polarization and absorption features characteristic of hydrogen in a range of magnetic fields $\sim$ 10–20 MG.

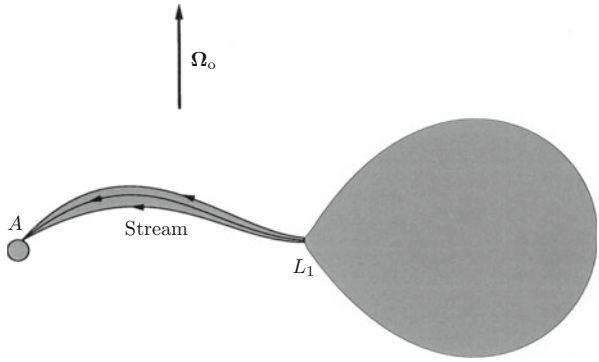

Fig. 3.1 An AM Herculis binary, showing the simplest case of single pole accretion. Material lost from the L_1 region of the secondary becomes channelled by the primary's magnetic field and accretes on to its surface through a localized column, A

A field structure more complicated than that of a centred dipole was also indicated.

Young et al. (1981) observed AM Her in a low state and measured a 3.1 h period in emission line velocities. Their observations indicated the secondary star to be an M5 red dwarf, which is consistent with a lobe-filling star of a mass theoretically expected for the observed orbital period.

3.1.2 Other Polars

Three new members of the class were discovered soon after AM Her; AN UMa (Krzeminski and Serkowski 1977), VV Pup (Tapia 1977b) and EF Eri (Tapia 1979). Many new systems were discovered in the ROSAT all-sky survey and there are, at present, 121 confirmed systems, also referred to as the polars. Tables 3.1, 3.2, and 3.3, shown in the Appendix below, list these systems with their orbital periods, secondary masses estimated using the period-mass relation (2.298) for lobe-filling lower main sequence stars with $q = 1.1$ and, where known, white dwarf surface fields. Estimated values are given for cyclotron harmonic determined magnetic fields, with some systems having two poles. Field values obtained from photospheric Zeeman splitting are shown, where available. References are given for each system related to orbital period and magnetic field measurements. It is noted that 28 AM Her binaries, representing $\simeq 23\%$ of the known systems, lie in the 2–3 h period gap, usually unoccupied by accreting cataclysmic variables. A possible explanation for this is discussed in Chap. 13. The main features of the AM Her systems are discussed below. Extensive reviews of the observational aspects of these systems are given by Cropper (1990) and Warner (1995).

3.2 Essential Features

3.2.1 Magnetic Fields

Two methods are used to estimate the surface magnetic field value on the white dwarf. The first, and most frequently employed method, involves measurements of the field at the cyclotron emission regions for those systems showing cyclotron humps in their optical/IR spectra. The magnetic field at the emission region can be determined from the spacings between the cyclotron harmonics (see Harrison and Campbell 2015 for a detailed description of such measurements). The cyclotron-determined fields are denoted by $B_{\rm cyc}$ in Tables 3.1, 3.2, and 3.3, with the second values referring to field strengths at second poles, where available. The second method involves the observation, during episodes of low accretion, of photospheric Zeeman split absorption lines from the white dwarf. This method has been used to measure the magnetic fields in several systems, as shown in the tables. The mean field over the observable photosphere is calculated, denoted $\bar{B}_{\rm ph}$.

Observations suggest that the white dwarfs in some AM Her systems have magnetic fields more complicated than centred dipoles. Meggitt and Wickramasinghe (1989) analysed the linear pulse and polarization data of EF Eri and found three cyclotron emission regions on the white dwarf surface. A quadrupolar component could be consistent with this data. A complex field structure is also indicated in CE Gru (Wickramasinghe et al. 1991) and in DP Leo (Cropper and Wickramasinghe 1993). Beuermann et al. (2007) employed Zeeman tomography to observations taken in the low states of EF Eri, BL Hyi and CP Tuc and found that truncated multipole expansions give the best fit to the magnetic field data, rather than pure dipole fields.

It is likely that the secondary star has a significant magnetic field. The star will be largely or fully convective, and rapidly rotating due to the action of tides, so a dynamo mechanism could generate a magnetic field. Surface magnetic fields with values of $\sim 10^2 - 10^3$ G are needed to give magnetic torques that may maintain synchronism. Models of rotating M dwarfs give such field values via $\alpha\Omega$ and α^2 dynamos, and surface poloidal field values of several kG have been observed on rapidly rotating M dwarfs (see Chap. 12). Secondary magnetic fields are believed to channel winds from the star which lead to magnetic braking in systems above the orbital period gap.

3.2.2 The Stellar Components

The masses of the white dwarf primaries are not well known, since their determinations require accurate measurements of the radial velocities of both stars and the

orbital inclination. A helium white dwarf obeys the mass-radius relation

$$R_{\rm p} = 7.8 \times 10^6 \left[\left(\frac{M_{\rm p}}{M_{\rm c}} \right)^{-\frac{2}{3}} - \left(\frac{M_{\rm p}}{M_{\rm c}} \right)^{\frac{2}{3}} \right]^{\frac{1}{2}} \text{m}, \tag{3.2}$$

where the Chandrasekhar mass $M_{\rm c} = 1.44\, M_\odot$ (Nauenberg 1972). Hence, for similar surface field strengths, the primary magnetic moments can vary significantly for a range of $M_{\rm p}$ since they are proportional to $R_{\rm p}^3$.

The secondary stars in AM Her systems are M or K dwarfs. Using the condition that the star fills its Roche lobe and obeys a main sequence mass-radius relation, its mass can be estimated from the orbital period. Equation (2.298), with $q = 1.1$, gives a mass range of $0.13 < M_{\rm s}/M_\odot < 0.46$, with the one higher mass system V1309 Ori having $M_{\rm s} = 0.77\, M_\odot$. Spectroscopic observations of the secondary are difficult because most of the energy is emitted from the primary. When phase resolved, high resolution red spectroscopy is available, the radial velocities can be used for locating the position of the secondary in non-eclipsing systems. For eclipsing systems, high resolution observations made during eclipses confirm the expected nature of the secondary.

3.2.3 The Accretion Stream

The spectra of AM Her systems, in the UV, optical and infra-red, are rich in emission lines. Phase resolved and high resolution studies of the optical spectra reveal lines with multiple components, each with distinctive radial velocity variations. These lines are thought to arise in the accretion stream. Cowley and Crampton (1977) identified a broad base component, a narrower peak component and a very narrow component in VV Pup. Most of the polars have such components. Schneider and Young (1980) modelled these by assuming the broad component came from near the accretion regions, and the narrower components from further away. A phase shift between broad and narrow components was identified with curvature of the stream. Mukai (1988) suggested that some of the narrow components from QQ Vul, ST LMi and VV Pup arise in an initial part of the stream before it is channelled by the primary's magnetic field. Ferrario et al. (1989) obtained a reasonable fit to the emission line data of V834 Cen, ST LMi, and UZ For with a model in which field channelling becomes effective at a distance from the L_1 point which is about a third of its distance, A, from the primary. The stream was broadened before converging on the primary. Observations of the eclipsing system HU Aqr by Schwope et al. (1997), using Doppler tomography, also indicated a partially channelled stream. Analysis of the data suggested that the initial, weakly channelled stream forms a tenuous curtain of material above the orbital plane. The bulk of the stream subsequently lifts out of the orbital plane.

Heerlein et al. (1999) developed a simple model for the accretion stream, taking Gaussian profiles for the density variations perpendicular to the flow direction.

Magnetic channelling was taken to become effective where the magnetic energy density starts to exceed the kinetic energy of the flow, so occurring inside the Alfvén radius. The model gave good results when applied to HU Aqr. Numerical simulations have been performed to investigate the effect of the magnetic field on the accretion stream. These are described in Chap. 5.

3.2.4 Synchronous Rotation of the Primary

Synchronous rotation of the primary with the orbit has always been assumed in AM Her systems, based on the modulation of their emissions at single periods. However, the periodic variations seen in the optical light curves, the X-rays and optical polarization are due to the rotation of the accretion column with the white dwarf. Observations of the relatively faint secondary star are necessary in order to measure the orbital period. The first direct support for synchronism of the primary came when Young and Schneider (1979) observed absorption lines from the secondary in AM Her. Orbital periods were subsequently measured in other polars, either from eclipses or ellipsoidal variations in the infra-red (e.g. Bailey et al. 1985). The primary and orbital angular velocities were found to be the same, to the accuracy limits of the methods employed. For the eclipsing system DP Leo, over a baseline of 4 years, Biermann et al. (1985) obtained $|\omega|/\Omega_o < 2 \times 10^{-6}$, where ω is the synodic angular velocity of the primary and Ω_o is the orbital angular velocity. Cropper (1988) compiled data for twelve polars and found a tendency for the main accreting pole to lead the motion of the line of stellar centres. However, Bailey et al. (1993) showed that the longitudes of the magnetic poles in DP Leo and WW Hor can vary by up to 20° over several years. Beuermann et al. (2014) used phase resolved orbital light curves of DP Leo over a 4 year period and found that the data was best explained by an oscillation of the accreting poles about a synchronous state with a period of $\simeq 60$ year.

In addition to the asynchronous oscillations of DP Leo and WW Hor, five other systems are known to have asynchronism of the white dwarf; V1432 Aql (Littlefield et al. 2015b), BY Cam (Pavlenko 2006), V1500 Cyg (Katz 1991; Schmidt et al. 1995), V4633 Sgr (Lipkin and Leibowitz 2008) and CD Ind (Ramsay et al. 2000). These systems appear to be synchronizing on time-scales of typically 10^2 year $\lesssim \tau_{syc} \lesssim 10^3$ year. These observational estimates are compared to theoretical synchronization times in Chap. 4.

3.3 MHD Problems

The synchronous rotation of the primary and channelling of the accretion stream present problems of magnetohydrodynamics. The removal of asynchronous motions from the primary requires a synchronizing torque to act, and magnetic interaction

with an orbitally synchronized secondary will be shown to generate such a torque. Asynchronous motions of the primary induce electric currents in the conducting secondary, in the magnetosphere and in the atmosphere of the white dwarf primary. An inductive torque results on the primary, causing its spin to approach synchronism. Magnetic forces result on the secondary and primary which lead to an orbital torque, allowing angular momentum to be exchanged between the stellar spins and the orbital motion. For an over-synchronous primary, this can lead to a lowering of the mass transfer rate.

The accretion stream interacts with the white dwarf's magnetic field, ultimately being channelled by it. Magnetic torques resulting from the field stresses in the stream cause angular momentum to be transferred continuously to the primary, giving an accretion torque. This torque depends on the geometry of the stream, and hence on the magnetic orientation of the primary relative to the secondary. The torque will be time-dependent for an asynchronous primary.

The inductive magnetic torque, which removes asynchronous motions, cannot balance the accretion torque to produce a synchronous state, since the former vanishes at corotation. A non-dissipative torque is necessary and interaction of the primary with a magnetized secondary generates such a torque. The secondary's field could be produced by dynamo action. Also, a gravitational torque will result if the primary is distorted from spherical symmetry due to internal non-radial magnetic forces. This may balance or exceed the accretion torque. The torque balance must be stable to all perturbations.

Even if a stable synchronous state exists it is not clear that the white dwarf can reach it while accreting material. Over-shooting could occur if the dissipation is insufficient to remove the primary's synodic rotational energy over one synodic period, close to synchronism. The magnetic diffusivity of the secondary plays a key role here. These problems are addressed in the next four chapters.

Appendix: Tables of Confirmed Systems

The following tables list the confirmed AM Herculis systems. The orbital periods are known to high accuracy. There are a significant number of accreting systems with periods lying in the 2–3 h period gap, usually unoccupied by accreting cataclysmic variables. A possible explanation for this is given in Chap. 13. The secondary masses have been estimated using the approximate mass-radius relation for lower main sequence stars, given by (2.298) with $q = 1.1$. Most secondaries lie in the M dwarf mass range, with a large fraction being fully convective. A few longer period systems have K dwarf secondaries.

The magnetic field values are mainly obtained from cyclotron harmonic observations. A few systems have fields determined by photospheric Zeeman splitting observations, giving a mean surface field. Every system has at least one reference related to detailed observations of its properties.

Table 3.1 The AM Herculis binaries

Name	P (h)	$M_s/M_\odot$	B_{cyc} (MG)	$\bar{B}_{ph}$ (MG)	References
V1309 Ori	7.983	0.769	27		41, 104
V859 Cen	4.765	0.459			44
AI Tri	4.602	0.443	32, 73		41, 83
J0649	4.392	0.423	26		41, 54
MQ Dra	4.391	0.423	60		105, 107
J2048	4.200	0.404			46
V1043 Cen	4.190	0.405	56		111, 120
HS0922	4.039	0.389	60, 81		69, 115
VY For	3.806	0.367			22, 41
J0227	3.787	0.365			100
J1424	3.732	0.359			52
QQ Vul	3.708	0.357	36		20, 38
J0749	3.600	0.347			54
V358 Aqr	3.491	0.336			73
J1007	3.477	0.335	94		41, 112
MN Hya	3.390	0.326	28		41, 47
V388 Peg	3.375	0.325	20		41, 117
J1422	3.369	0.324			52
V1432 Aql	3.366	0.324			41, 51
BY Cam	3.354	0.323	41		41, 58
V1500 Cyg	3.351	0.323			41, 76
J0733	3.338	0.321			33
J0837	3.180	0.306			42, 80
V519 Ser	3.175	0.306			114
V1033 Cen	3.156	0.304			15, 72
J1453	3.156	0.304			53, 62
AM Her	3.094	0.298	14	13	19, 75
CW Hyi	3.030	0.292			93
V4633 Sgr	3.014	0.290			48
J2319	3.011	0.290			98
J2250	2.904	0.280			68
HY Eri	2.855	0.275			18
WX LMi	2.782	0.268	61, 70		41, 122
EU Lyn	2.736	0.264			43
V349 Pav	2.662	0.256	29, 7		41, 67
PZ Vir	2.645	0.255			103
J0524	2.620	0.252			85
AP CrB	2.531	0.244	110		94, 113
V654 Aur	2.496	0.240			43
J1543	2.400	0.231			97

Table 3.2 The AM Herculis binaries (Continued)

Name	P (h)	$M_s/M_\odot$	B_{cyc} (MG)	$\bar{B}_{ph}$ (MG)	References
J0859	2.400	0.231	30		34, 41
QS Tel	2.332	0.225	47, 75		91
V516 Pup	2.285	0.220	39		41, 82
V381 Vel	2.234	0.215	52		35, 41
V1189 Her	2.232	0.215			34
UW Pic	2.232	0.214	19		41, 70, 74
J1503	2.223	0.214			130
J1333	2.208	0.213			103
HU Leo	2.187	0.211			102
J2218	2.160	0.208			4
MT Dra	2.145	0.207			84
UZ For	2.109	0.203	55, 28		6, 23, 30, 41
J0325	2.093	0.202			39
EU Cnc	2.090	0.201	42		127
HU Aqr	2.084	0.201	32	20	41, 90, 95
J1743	2.078	0.200			25
V1901 Aql	2.035	0.196			1
J0328	2.033	0.196			106
V2951 Oph	2.003	0.193	42		10
V1007 Her	1.999	0.193	50		36
V808 Aur	1.953	0.188	36, 69		96, 129
J1344	1.944	0.187			109
V1237 Her	1.939	0.187			43
J0810	1.936	0.186			130
AR UMa	1.932	0.186	155		41, 77
WW Hor	1.925	0.185	25		2, 41, 57
AN UMa	1.914	0.184	32		12, 41
EK UMa	1.909	0.184	48		9
J0357	1.900	0.183			88
ST LMi	1.898	0.183	19		41, 99
BL Hyi	1.894	0.182	18		8, 124, 128
MR Ser	1.891	0.182	27		27, 41, 126
FR Lyn	1.888	0.182			28
V884 Her	1.884	0.181	30		37, 41, 78
V2301 Oph	1.883	0.181	7		32, 41
CD Ind	1.848	0.178	12		41, 66
CE Gru	1.810	0.174			63
J1002	1.783	0.172	32		41, 64
EP Dra	1.744	0.168	15		41, 71, 87
J0953	1.729	0.167			5

Table 3.3 The AM Herculis binaries (Continued)

Name	P (h)	$M_s/M_\odot$	B_{cyc} (MG)	$\bar{B}_{ph}$ (MG)	References
RS Cae	1.702	0.164			119
J0706	1.702	0.164			39
V834 Cen	1.692	0.163	23	22, 39	7, 31, 41, 89
V379 Tel	1.684	0.162	20		60
VV Pup	1.674	0.161	31, 56		41, 45
EG Lyn	1.656	0.159			93
J1344	1.656	0.159			109
V393 Pav	1.647	0.159		16	110
HS Cam	1.637	0.158	8		41, 116
LW Cam	1.621	0.156	20		41, 118
BS Tri	1.605	0.155			13, 26
PW Aqr	1.570	0.151			61
EQ Cet	1.547	0.149		45	41, 92
J1944	1.532	0.148			21
J1321	1.531	0.147			50
J1312	1.531	0.147			123
J1745	1.503	0.145			55
EU UMa	1.502	0.145	43		67
V347 Pav	1.501	0.145	29, 7		41, 67
J0257	1.500	0.144			121
J0502	1.500	0.144	35		41, 49
DP Leo	1.497	0.144	31, 59		3, 11
CP Tuc	1.484	0.143	15		8, 41, 65
J1514	1.479	0.142			14
V379 Vir	1.474	0.142	7		24, 29
FL Cet	1.452	0.140	29		41, 79
IW Eri	1.452	0.140	30		41, 93
J1250	1.439	0.139			14
J0425	1.430	0.138			40
J0921	1.404	0.135			103
BM CrB	1.404	0.135			34
IL Leo	1.392	0.134	42		81
EF Eri	1.350	0.130	100		86, 108, 125
FH UMa	1.334	0.128			101
J0154	1.334	0.128			16
J0528	1.334	0.128			33
GG Leo	1.331	0.128	24		41, 67
EV UMa	1.328	0.128	35		56, 64
J1845	1.318	0.127			59
V4738 Sgr	1.300	0.125	67		17
CV Hyi	1.297	0.125			17

Tables 3.1–3.3 Reference Number Key: 1. Afanasiev et al. 2015; 2. Bailey et al. 1988; 3. Bailey et al. 1993; 4. Bernardini et al. 2014; 5. Beuermann and Burwitz 1995; 6. Beuermann et al. 1988; 7. Beuermann et al. 1989; 8. Beuermann et al. 2007; 9. Beuermann et al. 2009; 10. Bhalerao et al. 2010; 11. Biermann et al. 1985; 12. Bonnet-Bidaud et al. 1996; 13. Borisov et al. 2015; 14. Breedt et al. 2012; 15. Buckley et al. 2000; 16. Burwitz et al. 1993; 17. Burwitz et al. 1997; 18. Burwitz et al. 1999; 19. Campbell et al. 2008; 20. Catalan et al. 1999; 21. Coppejans et al. 2014; 22. Cropper 1997; 23. Dai et al. 2010; 24. Debes et al. 2006; 25. Denisenko and Martinelli 2012; 26. Denisenko et al. 2006; 27. Diaz and Cieslinski 2009; 28. Dillon et al. 2008; 29. Farihi et al. 2008; 30. Ferrario et al. 1989; 31. Ferrario et al. 1992; 32. Ferrario et al. 1995; 33. Gabdeev 2015; 34. Gansicke et al. 2009; 35. Greiner and Schwarz 1998; 36. Greiner et al. 1998a; 37. Greiner et al. 1998b; 38. Halevin et al. 2002, 39. Halpern and Thorstensen 2015; 40. Halpern et al. 1998; 41. Harrison and Campbell 2015; 42. Hilton et al. 2009; 43. Homer et al. 2005; 44. Howell et al. 1997; 45. Howell et al. 2006; 46. Kafka et al. 2010; 47. Kato 2015; 48. Lipkin and Leibowitz 2008; 49. Littlefair et al. 2005; 50. Littlefield et al. 2015a; 51. Littlefield et al. 2015b; 52. Marsh et al. 2002; 53. Masetti et al. 2006; 54. Motch et al. 1998; 55. Muno et al. 2003; 56. Osborne et al. 1994; 57. Pandel et al. 2002; 58. Pavlenko 2006; 59. Pavlenko et al. 2011; 60. Potter et al. 2005; 61. Potter et al. 2006; 62. Potter et al. 2010; 63. Ramsay and Cropper 2002; 64. Ramsay and Cropper 2003; 65. Ramsay et al. 1999; 66. Ramsay et al. 2000; 67. Ramsay et al. 2004; 68. Ramsay et al. 2009; 69. Reimers and Hagen 2000; 70. Reinsch et al. 1994; 71. Remillard et al. 1991; 72. Rodrigues et al. 1998; 73. Rodrigues et al. 2006; 74. Romero-Colmenero et al. 2003; 75. Schmidt et al. 1981; 76. Schmidt et al. 1995; 77. Schmidt et al. 1999; 78. Schmidt et al. 2001; 79. Schmidt et al. 2005a; 80. Schmidt et al. 2005b; 81. Schmidt et al. 2007; 82. Schwarz and Greiner 1999; 83. Schwarz et al. 1998; 84. Schwarz et al. 2002; 85. Schwarz et al. 2007; 86. Schwope and Christensen 2010; 87. Schwope and Mengel 1997; 88. Schwope and Thinius 2012; 89. Schwope et al. 1993a; 90. Schwope et al. 1993b; 91. Schwope et al. 1995; 92. Schwope et al. 1999; 93. Schwope et al. 2002; 94. Schwope et al. 2006; 95. Schwope et al. 2011; 96. Schwope et al. 2015; 97. Servillat et al. 2012; 98. Shafter et al. 2008; 99. Shahbaz and Wood 1996; 100. Silva et al. 2015; 101. Singh et al. 1995; 102. Southworth et al. 2010; 103. Southworth et al. 2015; 104. Staude et al. 2001; 105. Szkody et al. 2003; 106. Szkody et al. 2007; 107. Szkody et al. 2008; 108. Szkody et al. 2010; 109. Szkody et al. 2014; 110. Thomas et al. 1996; 111. Thomas et al. 2000; 112. Thomas et al. 2012; 113. Thorstensen and Fenton 2002; 114. Thorstensen et al. 2015; 115. Tovmassian and Zharikov 2007; 116. Tovmassian et al. 1997; 117. Tovmassian et al. 2000; 118. Tovmassian et al. 2001; 119. Traulsen et al. 2014; 120. van der Heyden et al. 2002; 121. Vladimirov et al. 2014; 122. Vogel et al. 2007; 123. Vogel et al. 2008; 124. Wickramasinghe et al. 1984; 125. Wickramasinghe et al. 1990; 126. Wickramasinghe et al. 1991; 127. Williams et al. 2013; 128. Wolff et al. 1999; 129. Worpel and Schwope 2015; 130. Woudt et al. 2012.

References

Afanasiev, V.L., Borisov, N.V., Gabdeev, M.M., 2015, AstBu, 70, 328.
Bailey, J.A., et al., 1985, MNRAS, 215, 179.
Bailey, J.A., Wickramasinghe, D.T., Hough, J.H., Cropper, M.S., 1988, MNRAS, 234, 19P.
Bailey, J.A., Wickramasinghe, D.T., Ferrario, L., Hough, J.H., Cropper, M.S., 1993, MNRAS, 261, L31.
Berg, R.A., Duthie, J.G., 1977, ApJ, 211, 859.
Bernardini, F., de Martino, D., Mukai, K., Falanga, M., 2014, MNRAS, 445, 1403.
Beuermann, K., Burwitz, V., 1995, ASPC, 85, 99.
Beuermann, K., Thomas, H.C., Schwope, A.D., 1988, A&A, 195, L15.
Beuermann, K., Thomas, H.C., Schwope, A.D., 1989, IAUC., 4775.
Beuermann, K., Euchner, F., Reinsch, K., Jordan, S., Gansicke, B.T., 2007, A&A, 463, 647.
Beuermann, K., Diese, J., Paik, S., Ploch, A., Zachmann, J., Schwope, A.D., Hessman, F.V., 2009, A&A, 507, 385.
Beuermann, K., Dreizler, S., Hessman, F.V., Schwope, A.D., 2014, A&A, 562, A63.
Bhalerao, V.B., van Kerkwijk, M.H., Harrison, F.A., Kasliwal, M.M., Kulkarni, S.R., Rana, V.R., 2010, ApJ, 721, 412.
Biermann, P., Schmidt, G.D., Liebert, J., Stockman, H.S., Tapia, S., Kuhr, H., Strittmatter, P.A., West, S., Lamb, D.Q., 1985, ApJ, 293, 303.
Bonnet-Bidaud, J.M., Mouchet, M., Somova, T.A., Somov, N.N., 1996, A&A, 306, 199.
Borisov, N.V., Gabdeev, M.M., Shimansky, V.V., Katysheva, N.A., Shugarov, S.Y., 2015, AstL, 41, 646.
Breedt, E., Gansicke, B.T., Girven, J., Drake, A.J., Copperwheat, C.M., Parsons, S.G., Marsh, T.R., 2012, MNRAS, 423, 1437.
Buckley, D.A.H., Cropper, M., van der Heyden, K., Potter, S.B., Wickramasinghe, D.T., 2000, MNRAS, 318, 187.
Burwitz, V., Reinsch, K., Beuermann, K., Thomas, H.C., Schwope, A.D., 1993, AGAb, 9, 137.
Burwitz, V., Reinsch, K., Beuermann, K., Thomas, H.C., 1997, A&A, 327, 183.
Burwitz, V., Reinsch, K., Beuermann, K., Thomas, H.C., 1999, ASPC, 157, 127.
Campbell, R.K., Harrison, T.E., Kafka, S., 2008, ApJ, 683, 409.
Catalan, M.S., Schwope, A.D., Smith, R.C., 1999, MNRAS, 310, 123.
Chanmugam, G., Wagner, R.L., 1977, ApJ, 213, L13.
Chanmugam, G., Wagner, R.L., 1979, ApJ, 232, 895.
Coppejans, D.L., Woudt, P.A., Warner, B., Kording, E., Macfarlane, S.A., Schurch, M.P.E., Kotze, M.M., Breytenbach, H.B., Gulbis, A., Coppejans, R., 2014, MNRAS, 437, 510.
Cowley, A.P., Crampton, D., 1977, ApJ, 212, L121.
Cropper, M.S., 1988, MNRAS, 231, 597.
Cropper, M.S., 1990, SSRv, 54, 195.
Cropper, M.S., 1997, MNRAS, 289, 21.
Cropper, M.S., Wickramasinghe, D.T., 1993, MNRAS, 260, 696.
Dai, Z.B., Qian, S.B., Fernandez Lajus, E., Baume, G.L., 2010, MNRAS, 409, 1195.
Debes, J.H., Lopez-Morales, M., Bonanos, A.Z., Weinberger, A.J., 2006, ApJ, 647, 147.
Denisenko, D.V., Martinelli, F., 2012, Var Stars, 32, 3.
Denisenko, D.V., Pavlinsky, M.N., Sunyaev, R.A., Aslan, K., Khamitov, I., Parmaksizoglu, M., 2006, AstL, 32, 252.
Diaz, M.P., Cieslinski, D., 2009, ApJ, 137, 296.
Dillon, M., Gansicke, B.T., Aungwerojwit, A., Rodriguez-Gil, P., Marsh, T.R., Barros, S.C.C., Szkody, P., Brady, S., Krajci, T., Oksanen, A., 2008, MNRAS, 386, 1568.
Farihi, J., Burleigh, M.R., Hoard, D.W., 2008, ApJ, 674, 421.
Ferrario, L., Wickramasinghe, D.T., Bailey, J.A., Tuohy, I.R., Hough, J.H., 1989, ApJ, 337, 832.
Ferrario, L., Wickramasinghe, D.T., Bailey, J.A., Hough, J.H., Tuohy, I.R., 1992, MNRAS, 256, 252.

Ferrario, L., Wickramasinghe, D.T., Bailey, J.A., Buckley, D., 1995, MNRAS, 273, 17.
Gabdeev, M.M., 2015, AstBu, 70, 460.
Gansicke, B.T., et al., 2009, MNRAS, 397, 2170.
Greiner, J., Schwarz, R., 1998, A&A, 340, 129.
Greiner, J., Schwarz, R., Wenzel, W., 1998a, MNRAS, 296, 437.
Greiner, J., Remillard, R.A., Motch, C., 1998b, A&A, 336, 191.
Halevin, A.V., Shakhovskoy, N.M., Andronov, I.L., Kolesnikov, S.V., 2002, A&A, 394, 171.
Halpern, J.P., Thorstensen, J.R., 2015, AJ, 150, 170.
Halpern, J.P., Leighly, K.M., Marshall, H.L., Eracleous, M., Storhi-Bergmann, T., 1998, PASP, 110, 1394.
Harrison, T.E., Campbell, R.K., 2015, ApJS, 219, 32.
Hearn, D.R., Richardson, J.A., 1977, ApJ, 213, L115.
Hearn, D.R., Richardson, J.A., Clark, G.W., 1976, ApJ, 210, L23.
Heerlein, C., Horne, K., Schwope, A.D., 1999, MNRAS, 304, 145.
Hilton, E.J., Szkody, P., Mukadam, A., Henden, A., Dillon, W., Schmidt, G.D., 2009, AJ, 137, 3606.
Homer, L., Szkody, P., Chen, B., Henden, A., Schmidt, G.D., Fraser, O.J., Saloma, K., Silvestri, N.M., Taylor, H., Brinkmann, J., 2005, ApJ, 620, 929.
Howell, S.B., Craig, N., Roberts, B., McGee, P., Sirk, M., 1997, AJ, 113, 2231.
Howell, S.B., Harrison, H.E., Campbell, R.K., Cordova, F.A., Szkody, P., 2006, AJ, 131, 2216.
Kafka, S., Tappert, C., Honeycutt, R.K., 2010, MNRAS, 403, 755.
Kato, T., 2015, PASJ, 67, 105.
Katz, J.H., 1991, ComAp, 15, No. 4, 177.
King, A.R., Lasota, J.P., 1979, MNRAS, 188, 653.
Krzeminski, W., Serkowski, K., 1977, ApJ, 216, L45.
Lipkin, Y.M., Leibowitz, E. M., 2008, MNRAS, 387, 289.
Littlefair, S.P., Dhillon, V.S., Martin, E.L., 2005, A&A, 437, 637.
Littlefield, C., Garnavich, P., Magno, K., Murison, M., deal, S., McClelland, C., Rose, B., 2015a, IBVS, 6129, 1.
Littlefield, C., et al., 2015b, MNRAS, 449, 3107.
Marsh, T.R., et al., 2002, ASPC, 261, 200.
Masetti, N., et al., 2006, A&A, 459, 21.
Meggitt, S.M.A., Wickramasinghe, D.T., 1989, MNRAS, 236, 31.
Michalsky, J.J., Stokes, G.M., Stokes, R.A., 1977, ApJ, 216, L35.
Motch, C., Guillout, P., Haberl, F., Krautter, J., Pakull, M.W., Pietsch, W., Reinsch, K., Voges, W., Zickgraf, F., 1998, A&AS, 132, 341.
Mukai, K., 1988, MNRAS, 232, 175.
Muno, M.P., Baganoff, F.K., Bautz, M.W., Brandt, W.N., Garmire, G.P., Ricker, G.R., 2003, ApJ, 599, 465.
Nauenberg, P., 1972, ApJ, 175, 417.
Osborne, J.P., Beardmore, A.P., Wheatley, P.J., Hakala, P., Watson, M.G., Mason, K.O., Hassall, B.J.M., King, A.R., 1994, MNRAS, 270, 650.
Pandel, D., Cordova, F.A., Shirey, R.E., Ramsay, G., Cropper, M., Mason, K.O., Moch, R., Kilkenny, D., 2002, MNRAS, 332, 116.
Pavlenko, E.P., 2006, Ap, 49, 105.
Pavlenko, E.P., Sokolovsky, K., Baklanov, A., Antonyuk, K., Antonyuk, O., Denisenko, D., 2011, ATel, 3436, 1.
Potter, S.B., Augusteijn, T., Tappert, C., 2005, MNRAS, 364, 565.
Potter, S.B., O'Donoghue, D., Romero-Colomenero, E., Buckley, D.A.H., Woudt, P.A., Warner, B., 2006, MNRAS, 371, 727.
Potter, S.B., et al., 2010, MNRAS, 402, 1161.
Ramsay, G., Cropper, M., 2002, MNRAS, 335, 918.
Ramsay, G., Cropper, M., 2003, MNRAS, 338, 219.
Ramsay, G., Potter, S.B., Buckley, D.A.H., Wheatley, P.J., 1999, MNRAS, 306, 809.

Ramsay, G., Potter, S.B., Cropper, M., Buckley, D.A.H., Harrop-Allin, M.K., 2000, MNRAS, 316, 225.
Ramsay, G., Cropper, M., Mason, K.O., Cordova, S.A., Priedhorsky, W., 2004, MNRAS, 347, 95.
Ramsay, G., Rosen, S., Hakala, P., Barclay, T., 2009, MNRAS, 395, 416.
Reimers, D., Hagen, H.J., 2000, A&A, 358, L45.
Reinsch, K., Burwitz, V., Beuermann, K., Schwope, A.D., Thomas, H.C., 1994, A&A, 291, L27.
Remillard, R.A., Stroozas, B.A., Tapia, S., Sibler, A., 1991, ApJ, 379, 715.
Rodrigues, C.V., Cieslinski, D., Steiner, J.E., 1998, A&A, 335, 979.
Rodrigues, C.V., Jablonski, F.J., D'Amico, F., Cieslinski, D., Steiner, J.E., Diaz, M.P., Hickel, G.R., 2006, MNRAS, 369, 1972.
Romero-Colmenero, E., Potter, S.B., Buckley, D.A.H., Barrett, P.E., Vrielmann, S., 2003, MNRAS, 339, 685.
Schmidt, G.D., Stockman, H.S., Margon, B., 1981, ApJ, 243, L157.
Schmidt, G.D., Liebert, J., Stockman, H.S., 1995, ApJ, 441, 414.
Schmidt, G.D., Hoard, D.W., Szkody, P., Melia, F., Honeycutt, R.K., Wagner, R.M., 1999, ApJ, 525, 407.
Schmidt, G.D., Ferrario, L., Wickramasinghe, D.T., Smith, P.S., 2001, ApJ, 553, 823.
Schmidt, G.D., Szkody, P., Homer, L., Smith, P.S., Chen, B., Henden, A., Solheim, J., Wolfe, M.A., Greimer, R., 2005a, ApJ, 620, 422.
Schmidt, G.D., et al., 2005b, ApJ, 630, 1037.
Schmidt, G.D., Szkody, P., Henden, A., Anderson, S.E., Lamb, D.Q., Margon, B., Schneider, D.P., 2007, ApJ, 654, 521.
Schneider, D.P., Young, P., 1980, ApJ, 238, 946.
Schwarz, R., Greiner, J., 1999, PASC, 157, 139.
Schwarz, R., et al., 1998, A&A, 338, 465.
Schwarz, R., Greiner, J., Tovmassian, G.H., Zharikov, S.V., Wenzel, W., 2002, A&A, 392, 505.
Schwarz, R., Schwope, A.D., Staude, A., Rau, A., Hasinger, G., Urratia, T., Motch, C., 2007, A&A, 473, 511.
Schwope, A.D., Christensen, L., 2010, A&A, 514, A89.
Schwope, A.D., Mengel, S., 1997, AN, 318, 25.
Schwope, A.D., Thinius, B., 2012, AN, 333, 717.
Schwope, A.D., Thomas, H.C., Beuermann, K., Reinsch, K., 1993a, A&A, 267, 103.
Schwope, A.D., Thomas, H.C., Beuermann, K., 1993b, A&A, 271, L25.
Schwope, A.D., Thomas, H.C., Beuermann, K., Burwitz, V., Jordan, S., Haefner, R., 1995, A&A, 293, 764.
Schwope, A.D., Mantel, K., Horne, K., 1997, A&A, 319, 894.
Schwope, A.D., Schwarz, R., Greiner, J., 1999, A&A, 348, 861.
Schwope, A.D., Brunner, H., Buckley, D., Greiner, J., Heyden, K., Neizvesty, S., Potter, S., Schwarz, R., 2002, A&A, 396, 895.
Schwope, A.D., Schreiber, M.R., Szkody, P., 2006, A&A, 452, 955.
Schwope, A.D., Horne, K., Steeghs, D., Still, M., 2011, A&A, 531, A34.
Schwope, A.D., Mackebrandt, Thinius, B.D., Littlefield, C., Garnavich, P., Oksanen, A., Granzer, T., 2015, AN, 336, 115.
Servillat, M., Grindlay, J., van der Berg, M., Hong, J., Zhao, P., Allen, B., 2012, ApJ, 748, 32.
Shafter, A.W., Davenport, J.R.A., Guth, T., Kattner, E., Sreenivasamurthy, N., 2008, PASP, 120, 374.
Shahbaz, T., Wood, J.H., 1996, MNRAS, 282, 362.
Silva, K.M.G., Rodrigues, C.V., Oliveira, A.S., Almeida, L.A., Cieslinski, D., Costa, J.E.R., Jablonski, F., 2015, MNRAS, 451, 4183.
Singh, K.P., Szkody, P., Barrett, P., White, N.E., Fierce, E., Silber, A., Hoard, D.W., Hakala, P.J., Piirola, V., Sohl, K., 1995, ApJ, 453, L95.
Southworth, J., Copperwheat, C.M., Gansicke, B.T., Pyrzas, S., 2010, A&A, 510, A100.
Southworth, J., Tappert, C., Gansicke, B.T., Copperwheat, C.M., 2015, A&A, 573, A61.
Staude, A., Schwope, A.D., Schwarz, R., 2001, A&A, 374, 588.

Stockman, H.S., 1977, ApJ, 218, L57.
Szkody, P., Brownlee, D.E., 1977, ApJ, 212, L113.
Szkody, P., et al., 2003, ApJ, 583, 902.
Szkody, P., et al., 2007, ApJ, 134, 185.
Szkody, P., Linnell, A.P., Campbell, R.K., Plotkin, R.N., Harrison, T.E., Holtzman, J., Seibert, M., Howell, S.B., 2008, ApJ, 683, 967.
Szkody, P., et al., 2010, ApJ, 716, 1531.
Szkody, P., Everett, M.E., Howell, S.B., Landolt, A.U., Bond, H.E., Silva, D.R., Vasquez-Soltero, S., 2014, AJ, 148, 63.
Tapia, S., 1977a, ApJ, 212, L125.
Tapia, S., 1977b, IAUC, 3054, 1.
Tapia, S., 1979, IAUC., 3327, 2.
Thomas, H.C., Beuermann, K., Schwope, A.D., Burwitz, V., 1996, A&A, 313, 833.
Thomas, H.C., Beuermann, K., Burwitz, V., Reinsch, K., Schwope, A.D., 2000, A&A, 353, 646.
Thomas, H.C., Beuermann, K., Reinsch, K., Schwope, A.D., Burwitz, V., 2012, A&A, 546, A104.
Thorstensen, J.R., Fenton, W.H., 2002, PASP, 114, 74.
Thorstensen, J.R., Taylor, C.J., Peters, C.S., Skinner, J.N., Southworth, J., Gansicke, B.T., 2015, ApJ, 149, 128.
Tovmassian, G.H., Zharikov, S.V., 2007, A&A, 468, 643.
Tovmassian, G.H., Greiner, J., Zickgraf, F.J., Kroll, P., Krautter, J., Thiering, I., Zharykov, S.V., Serrano, A., 1997, A&A, 328, 571.
Tovmassian, G.H., Greiner, K., Schwope, A.D., Szkody, P., Schmidt, G.D., Zickgraf, F.J., Serrano, A., Krautter, J., Thiering, I., Zharikov, S.V., 2000, ApJ, 537, 927.
Tovmassian, G.A., Szkody, P., Greiner, j., Zharikov, S.V., Zickgraf, F.J., Serrano, A., Krautter, J., Thiering, I., Neustroev, V., 2001, A&A, 379, 199.
Traulsen, I., Reinsch, K., Schwope, A.D., Schwarz, R., Walter, F.M., Burwitz, V., 2014, A&A, 562, 42.
van der Heyden, K.J., Potter, S.B., Buckley, D.A.H., 2002, MNRAS, 333, 241.
Vladimirov, V., et al, 2014, ATel, 5726, 1.
Vogel, J., Schwope, A.D., Gansicke, B.T., 2007, A&A, 464, 647.
Vogel, J., Byckling, K., Schwope, A.D., Osborne, J.P., Schwarz, R., Watson, M.G., 2008, A&A, 485, 787.
Warner, B., 1995, Cataclysmic Variable Stars, Cambridge Univ Press.
Wickramasinghe, D.T., Visvanathan, N., Tuohy, I.R., 1984, ApJ, 286, 328.
Wickramasinghe, D.T., Archilleos, N., Wu, K., Boyle, B.J., 1990, IAUC, 4962, 2.
Wickramasinghe, D.T., Cropper, M.S., Mason, K.O., Garlick, M., 1991, MNRAS, 250, 692.
Williams, K.A., Howell, S.B., Liebert, J., Smith, P.S., Bellini, A., Rubin, K.H.R., Bolte, M., 2013, AJ, 145, 129.
Wolff, M.T., Wood, K.S., Imamura, J.N., Middleditch, J., Steiman-Cameron, T.Y., 1999, ApJ, 526, 435.
Worpel, H., Schwope, A.D., 2015, A&A, 583, A130.
Woudt, P.A., Warner, B., de Bude, D., Macfarlane, S., Schurch, M.P.E., Zietsman, E., 2012, MNRAS, 421, 2414.
Young, P., Schneider, D.P., 1979, ApJ, 230, 502.
Young, P., Schneider, D.P., Shectman, S.A., 1981, ApJ, 245, 1043.

Chapter 4
AM Her Stars: Inductive Magnetic Coupling

Abstract Mechanisms that could cause the magnetic white dwarf primary to spin towards orbital synchronism are considered, and their effects on the mass transfer rate are investigated. An asynchronous primary results in two inductive processes due to its interaction with a tidally synchronized secondary star. With the primary magnetic axis inclined to its rotation axis, the secondary experiences a time varying magnetic field. A corotating white dwarf magnetosphere will impose tangential and normal motions near the surface of the secondary leading to motions in its interior. Both these effects lead to induced electric currents and associated perturbations to the stellar magnetic field. Magnetic torques result on both stars and on the orbit, allowing exchange of angular momentum.

The synchronization time of the primary is less than the lifetime of the binary, for a wide range of degrees of asynchronism. The magnetic transfer of angular momentum to the orbit can significantly affect the mass transfer rate occurring via Roche lobe overflow, and modified forms of $\dot{M}_s$ are derived. The inductive torques vanish at synchronism, and so cannot maintain a corotating state in the presence of an accretion torque.

4.1 Introduction

The first problem to consider in the AM Her binaries is how the white dwarf primary can approach synchronous rotation with the orbit. Spin angular momentum must be removed from or added to the primary, depending on whether it is initially over or under-synchronous, for corotation to be approached. A coupling mechanism, with associated torques, is therefore necessary and magnetic interaction with the secondary star can provide this. The white dwarf is likely to be surrounded by a low density extended magnetosphere, which will be highly conducting and is expected to be nearly corotating with the star.

The lower main sequence secondary is believed to be corotating with the orbit, this being achieved by tidal interaction and viscous dissipation. In general, for a tilted magnetic axis, if the primary is asynchronous the secondary will experience a time-dependent magnetic field, and the effects of motions of the magnetosphere

C. G. Campbell, *Magnetohydrodynamics in Binary Stars*, Astrophysics and Space Science Library 456, https://doi.org/10.1007/978-3-319-97646-4_4

near its surface. Magnetic field will penetrate the secondary and the induced $\mathbf{J} \times \mathbf{B}$ force will lead to motions in its surface regions where this force is comparable to the gravitational and pressure gradient forces. The induced electric field will drive currents in the star which are dissipated due to its electrical resistance. Currents will also flow in the highly conducting magnetosphere surrounding the stars and in the atmosphere of the white dwarf primary. Tables 3.1, 3.2, and 3.3 show that the secondary masses lie in the range $0.13\,M_\odot \lesssim M_\mathrm{s} \lesssim 0.77\,M_\odot$, and so these stars will have deep convective envelopes or be fully convective. Although there is no rigorous theory of turbulence, it is generally believed, and observationally suggested in the case of the sun, that it enhances the diffusion rate of magnetic fields compared to Ohmic processes. The chaotic motions break up the magnetic field, reducing its length-scale and allowing Ohmic dissipation to diffuse it at a greatly increased rate (e.g. Cowling 1945; Parker 1979; Moffatt 1998; Mestel 2012). The mean-field theory related to turbulence was discussed in Sect. 2.3.

The large-scale induced magnetic field in the secondary obeys the induction equation

$$\nabla \times (\mathbf{v} \times \mathbf{B}) - \nabla \times (\eta \nabla \times \mathbf{B}) = \frac{\partial \mathbf{B}}{\partial t}, \tag{4.1}$$

where η is the turbulent diffusivity, which has greatly enhanced values compared to those of the Ohmic form. It is natural to use the orbital frame, in which $\mathbf{v} = \mathbf{0}$ for a synchronized secondary. It is noted that the α-effect term $\nabla \times (\alpha \mathbf{B})$, discussed in Sect. 2.3 for a turbulent medium, is not considered here since the poloidal field in the secondary has the primary as its source. It is likely that the rapidly rotating turbulent secondary will have a dynamo-generated magnetic field. This possibility is considered later in relation to the maintenance of the synchronous state. Surface fields $\gtrsim 10^2$ G are significant in this context. A secondary magnetic field is required in order to have magnetic wind braking as the driving mechanism for mass transfer in systems with orbital periods greater than 3 h.

Equation (4.1) illustrates that there are two causes of induction in a plasma. The $\mathbf{v} \times \mathbf{B}$ term involves the generation of electric fields due to motions across lines of $\mathbf{B}$, while the $\partial \mathbf{B}/\partial t$ term induces electric fields if there is an explicit time dependence. There is conducting material in both stars and in the region surrounding them and, in general, both inductive processes will operate. However, to clarify the effects of these mechanisms, the case of vacuum surrounding with time dependent $\mathbf{B}$ will be considered first. This will illustrate the effects of the $\partial \mathbf{B}/\partial t$ term. Then the case with a magnetosphere, but with steady motions, will be analysed to investigate the role of the $\mathbf{v} \times \mathbf{B}$ term. The combined effects of these inductive processes can then be assessed.

4.2 Coupling with Vacuum Surroundings

4.2.1 Induction of Currents in the Secondary

The degree of asynchronism can be measured by the ratio ω/Ω_o, where

$$\omega = \omega_{in} - \Omega_o \tag{4.2}$$

is the synodic angular velocity of the primary with ω_{in} its inertial angular velocity and Ω_o the orbital angular velocity. Since the inductive torques are antisymmetric about $\omega = 0$, only the case with $\omega > 0$ needs to be calculated. The case of high asynchronism, ($\omega/\Omega_o \sim 1$), with vacuum surroundings, was considered by Papaloizou and Pringle (1978), and by Joss et al. (1979). They estimated the torque due to magnetic dissipation in the surface layers of the secondary. The rate of magnetic energy dissipation in a layer of depth δ is

$$W \simeq \frac{B^2}{2\mu_0}(4\pi R_s^2 \delta)\omega, \tag{4.3}$$

with the skin depth $\delta = (2\eta/\omega)^{1/2}$. The inductive torque has a magnitude W/ω, so taking a dipolar field gives a dissipative torque

$$\mathbf{T}_D = -\frac{4\pi}{\sqrt{2}}\frac{(B_p)_0^2 R_s^2 R_p^6}{\mu_0 D^6}\left(\frac{\eta}{\omega}\right)^{\frac{1}{2}}\mathbf{k}, \tag{4.4}$$

where R_s is the mean radius of the secondary, $(B_p)_0$ and R_p the surface polar field and radius of the white dwarf, and D is the orbital separation. A synchronization time can be defined as

$$\tau_{syc} = \frac{I\omega}{|T_D|}, \tag{4.5}$$

where I is the moment of inertia of the primary. Papaloizou and Pringle (1978) employed a turbulent form for η, while Joss et al. (1979) used an Ohmic form. Typically $\eta_T \sim 10^6 \eta_{ohm}$ and η_{ohm} yields $\tau_{syc} \sim 10^{10}$ year for $\omega/\Omega_o \sim 1$, so synchronism could not occur in the lifetime of the system which is measured by the mass transfer time-scale $\tau_M = M_s/|\dot{M}_s| \sim 2 \times 10^9$ year. Also, Ohmic values of η cannot explain synchronism for higher orbital separations and lower primary magnetic moments, so turbulent values are needed. Then, for $\omega/\Omega_o \sim 1$, $\eta_T = 5 \times 10^8 \mathrm{m^2 s^{-1}}$ and typical system parameters, (4.4) and (4.5) yield $\tau_{syc} \sim 10^7$ year $< \tau_M$. However, torque expressions such as (4.4) cannot be used for low values of ω/Ω_o since the field penetration then becomes large and $|T_D|$ must vanish as $\omega \to 0$.

A detailed analysis of the vacuum surroundings case was performed by Campbell (1983, 1999), enabling the full asynchronous range $0 < \omega/\Omega_o \lesssim 1$ to be investigated. The vector diffusion equation can be solved to find the induced **B** field in the secondary and this can be matched to the resulting total exterior vacuum field at the stellar surface. The stellar and orbital torques can then be calculated and the synchronization process considered.

4.2.2 Solution of the Diffusion Equation

Consider a secondary of mass M_s and a primary of mass M_p in circular orbits with separation D and period $2\pi/\Omega_o$. Figure 4.1 shows the orbital frame with the coordinates used in the analysis. The white dwarf is taken to have a centred dipole field with magnetic moment **m** having orientation angles (α, β), and a synodic angular velocity $\boldsymbol{\omega}$ parallel to $\boldsymbol{\Omega}_o$. The region between the stars is treated as a vacuum.

The primary's magnetic field $\mathbf{B}_p$ can be expressed in terms of a scalar potential Ψ_m where, relative to the origin O',

$$\Psi_m = \frac{\mu_0 m}{4\pi r'^3}\mathbf{r}' \cdot \hat{\mathbf{m}}(t), \tag{4.6}$$

with the unit dipole moment being

$$\hat{\mathbf{m}}(t) = \sin\alpha\cos\omega t\,\mathbf{i}' + \sin\alpha\sin\omega t\,\mathbf{j}' + \cos\alpha\,\mathbf{k}. \tag{4.7}$$

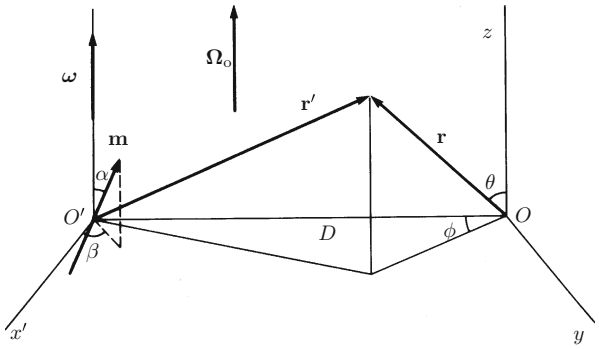

Fig. 4.1 The orbital frame, showing the coordinates used in the analysis. The centres of mass of the primary and secondary stars are at O' and O, respectively (from Campbell 1983)

It then follows, using the vector identity (A2), that

$$\mathbf{B}_{\mathrm{p}} = -\nabla \Psi_{\mathrm{m}} \tag{4.8a}$$

$$= -\frac{\mu_0 m}{4\pi r'^3}\left[\hat{\mathbf{m}} - 3(\hat{\mathbf{m}} \cdot \hat{\mathbf{r}}')\hat{\mathbf{r}}'\right]. \tag{4.8b}$$

The unit vector $\hat{\mathbf{m}}$ can be resolved into components parallel and perpendicular to $\boldsymbol{\omega}$. This enables $\mathbf{B}_{\mathrm{p}}$ to be expressed as the sum of a time-independent part $\mathbf{B}_0$ and a time-dependent part $\mathbf{B}_t$, so

$$\mathbf{B}_{\mathrm{p}} = \mathbf{B}_0 + \mathbf{B}_t, \tag{4.9}$$

where

$$\mathbf{B}_0 = -\frac{\mu_0 m}{4\pi r'^3}\cos\alpha\left(\mathbf{k} - \frac{3z}{r'}\hat{\mathbf{r}}'\right), \tag{4.10}$$

$$\mathbf{B}_t = -\frac{\mu_0 m}{4\pi r'^3}\left[\hat{\mathbf{m}}_\perp - \frac{3}{r'}(\hat{\mathbf{m}}_\perp \cdot \mathbf{r}')\hat{\mathbf{r}}'\right], \tag{4.11}$$

with

$$\hat{\mathbf{m}}_\perp = \sin\alpha\cos\omega t\,\mathbf{i}' + \sin\alpha\sin\omega t\,\mathbf{j}'. \tag{4.12}$$

The time-dependent component $\mathbf{B}_t$ induces currents in the secondary star which are dissipated at the expense of the synodic rotational energy of the primary. Hence, in the absence of other torques, ω tends to zero. The synchronization time-scale is

$$\tau_{\mathrm{syc}}(\omega) = \frac{\omega}{|\dot{\omega}|} = \frac{I\omega}{|T_{\mathrm{D}}|}, \tag{4.13}$$

where T_{D} is the dissipative torque and I is the moment of inertia of the primary, with the star taken to be spherical. Except very close to synchronism, the time-scale τ_{syc} greatly exceeds the synodic period so

$$\tau_{\mathrm{syc}} \gg \frac{2\pi}{\omega}. \tag{4.14}$$

It follows that $\boldsymbol{\omega}$ is essentially constant over a synodic period because the response time of the primary to the periodic variations of the torque far exceeds $2\pi/\omega$. It will be shown that $\boldsymbol{\omega}$ remains aligned with $\boldsymbol{\Omega}_{\mathrm{o}}$ during the synchronization process. The orbital motion acts as a large sink or source of angular momentum, so the compact primary can exchange angular momentum with the orbit without significantly affecting $\boldsymbol{\Omega}_{\mathrm{o}}$.

The magnetic potential $\Psi_{\rm m}$, given by (4.6), can be expressed relative to coordinates centred on the secondary's origin O. The required coordinate transformations are, from Fig. 4.1,

$$\begin{aligned} r' &= (r^2 + D^2 - 2rD\sin\theta\cos\phi)^{\frac{1}{2}}, \\ x' &= r\sin\theta\sin\phi, \\ y' &= D - r\sin\theta\cos\phi, \\ z &= r\cos\theta. \end{aligned} \tag{4.15}$$

Equations (4.6), (4.7), and (4.15) give the time-dependent part of $\Psi_{\rm m}$, to second order in r/D, as

$$\begin{aligned} \Psi_{\rm m} =& \frac{\mu_0 m\sin\alpha}{4\pi D^3} r P_1^1 (2\cos\phi\sin\omega t + \sin\phi\cos\omega t) \\ & - \frac{3\mu_0 m\sin\alpha}{8\pi D^4} r^2 \left[P_2^0 \sin\omega t - P_2^2 \left(\frac{1}{2}\cos 2\phi\sin\omega t + \frac{1}{3}\sin 2\phi\cos\omega t \right) \right], \end{aligned} \tag{4.16}$$

where $P_l^{|m|}$ are associated Legendre functions, given by (A34) as

$$\begin{aligned} P_1^1 &= \sin\theta, \\ P_2^0 &= \frac{1}{2}(3\cos^2\theta - 1), \\ P_2^2 &= 3\sin^2\theta. \end{aligned} \tag{4.17}$$

On and within the surface of the secondary, where $\Psi_{\rm m}$ will be required, the radial coordinate satisfies $r/D \lesssim 1/3$. The above second order expansion is therefore a reasonable approximation, particularly since the magnetic torques have expansions in powers of $(R_{\rm s}/D)^2$, where $R_{\rm s}$ is the mean radius of the secondary.

The time-varying magnetic field of the primary induces a current density $\mathbf{J}$ in the secondary. The resulting $\mathbf{J} \times \mathbf{B}$ magnetic force density will lead to motions, especially in the outer layers of the star where it can be comparable to the gravitational and pressure gradient forces. Such motions will have an inductive effect via the $\mathbf{v} \times \mathbf{B}$ term in (4.1). However, for clarity, only the effects of the $\partial\mathbf{B}/\partial t$ term are considered here. The effects of induced motions are considered later.

The induced electric currents are dissipated and the magnetic field obeys the diffusive induction equation

$$\nabla \times (\eta \nabla \times \mathbf{B}) = -\frac{\partial \mathbf{B}}{\partial t}, \tag{4.18}$$

where the turbulent subscript on η has been dropped. The magnetic field, being solenoidal, can be expressed as the sum of generalized poloidal and toroidal fields as in (2.196). Since the external field is of a poloidal nature, only that type of field will be generated in the secondary. Hence $\mathbf{B}$ can be expressed in terms of a poloidal scalar Φ as

$$\mathbf{B} = \nabla \times [\nabla \times (\Phi \hat{\mathbf{r}})]. \tag{4.19}$$

The function Φ can be expanded in a set of radial functions and spherical harmonics as in (2.209), where, due to the periodic nature of the external primary field, each harmonic has a time-dependence $\exp(i\omega t)$. By virtue of the synchronization time-scale condition (4.14), ω can be taken as time-independent in the process of solving (4.18). It is noted that in the following field expressions, involving general harmonics, summations over the appropriate values of the indices l and m with suitable coefficients, phases and complex conjugates needed to match the external field will be taken. The poloidal scalar is

$$\Phi = G_l(r) Y_l^m(\theta, \phi) e^{i\omega t}. \tag{4.20}$$

Equations (4.19) and (4.20) give the magnetic field components as

$$B_r = \frac{l(l+1)}{r^2} G_l Y_l^m e^{i\omega t}, \tag{4.21}$$

$$B_\theta = \frac{1}{r} \frac{dG_l}{dr} \frac{\partial Y_l^m}{\partial \theta} e^{i\omega t}, \tag{4.22}$$

$$B_\phi = \frac{1}{r \sin\theta} \frac{dG_l}{dr} \frac{\partial Y_l^m}{\partial \phi} e^{i\omega t}, \tag{4.23}$$

using the eigenvalue equation (2.211) for spherical harmonics. The components of the curl are

$$(\nabla \times \mathbf{B})_r = 0, \tag{4.24}$$

$$(\nabla \times \mathbf{B})_\theta = -\frac{1}{r \sin\theta} \left[\frac{d^2 G_l}{dr^2} - \frac{l(l+1)}{r^2} G_l \right] \frac{\partial Y_l^m}{\partial \phi} e^{i\omega t}, \tag{4.25}$$

$$(\nabla \times \mathbf{B})_\phi = \frac{1}{r} \left[\frac{d^2 G_l}{dr^2} - \frac{l(l+1)}{r^2} G_l \right] \frac{\partial Y_l^m}{\partial \theta} e^{i\omega t}, \tag{4.26}$$

and the current density is

$$\mathbf{J} = \frac{1}{\mu_0} \nabla \times \mathbf{B}. \tag{4.27}$$

Taking $\eta = \eta(r)$ in the diffusion equation (4.18), then using the field component equations (4.21)–(4.26) and equating harmonics, gives the differential equation for the radial functions as

$$\frac{d^2 G_l}{dr^2} - \left[\frac{i\omega}{\eta} + \frac{l(l+1)}{r^2}\right] G_l = 0. \tag{4.28}$$

Specifying η and solving this equation gives the radial dependence of the poloidal scalar Φ in the secondary star. The solutions in the outer region are found by solving (4.28) with $\eta \to \infty$. The inner and outer forms of Φ must then be matched at the surface of the secondary to satisfy the boundary conditions.

The secondary star will be tidally and rotationally distorted. However, to make the problem tractable, a spherical surface of radius R_s can be considered which encloses the same volume as the secondary's Roche lobe. The essential symmetries of the problem are preserved and no additional properties are introduced by using this simplification. The conditions at the secondary's surface are that $\hat{\mathbf{n}}\cdot\mathbf{J} = 0$, where $\hat{\mathbf{n}}$ is the unit normal, and that $\mathbf{B}$ is continuous. The radial current condition is met by (4.24) giving $(\nabla \times \mathbf{B})_r = 0$, while the field component equations (4.21)–(4.23) show that the continuity of $\mathbf{B}$ requires

$$G_l \quad \text{and} \quad \frac{dG_l}{dr} \quad \text{continuous at} \quad r = R_s. \tag{4.29}$$

Consider, first, the free-space solutions of (4.28), for which $\eta \to \infty$, so

$$\frac{d^2 G_l}{dr^2} - \frac{l(l+1)}{r^2} G_l = 0. \tag{4.30}$$

The general solution of this equation is

$$G_l = a r^{l+1} + \frac{b}{r^l}, \tag{4.31}$$

where a and b are constants. The solution r^{l+1} corresponds to the poloidal scalar of the primary's field, while the solution r^{-l} corresponds to the poloidal scalar of the outer field $\mathbf{B}_s$ resulting from the induced current source $\mathbf{J}$ in the secondary. Equations (4.8a) and (4.19) show that the magnetic potential and free-space poloidal scalar are related by

$$\Psi_m = -\frac{\partial \Phi}{\partial r}. \tag{4.32}$$

Using (4.16) for $\Psi_{\rm m}$ in (4.32), and integrating, gives the poloidal scalar of the primary's field as

$$\Phi_{\rm p} = -\frac{\mu_0 m \sin\alpha}{8\pi D^3} r^2 P_1^1 (2\cos\phi \sin\omega t + \sin\phi \cos\omega t) + \frac{\mu_0 m \sin\alpha}{8\pi D^4} r^3 \left[P_2^0 \sin\omega t - P_2^2 \left(\frac{1}{2}\cos 2\phi \sin\omega t + \frac{1}{3}\sin 2\phi \cos\omega t \right) \right]. \tag{4.33}$$

The poloidal scalar defining the field $\mathbf{B}_{\rm s}$ must then take the form

$$\Phi_{\rm s} = \frac{1}{r} P_1^1 \cos\phi (\alpha_1 \sin\omega t + \alpha_2 \cos\omega t) + \frac{1}{r} P_1^1 \sin\phi (\alpha_3 \sin\omega t + \alpha_4 \cos\omega t) + \frac{1}{r^2} P_2^0 (\beta_1 \sin\omega t + \beta_2 \cos\omega t) + \frac{1}{r^2} P_2^2 \cos 2\phi (\gamma_1 \sin\omega t + \gamma_2 \cos\omega t) + \frac{1}{r^2} P_2^2 \sin 2\phi (\gamma_3 \sin\omega t + \gamma_4 \cos\omega t), \tag{4.34}$$

where α_i, β_i and γ_i are constants.

Consider, now, the inner solution of the differential equation (4.28) for G_l, for which η is finite. Systems with orbital periods $P > 3.5$ h will have secondary stars containing a radiative core. However, all but one of these systems have $P < 5$ h so the radiative cores will be small. This has a negligible effect on the synchronization torque, so a turbulent form for η is justified. The simple mixing length theory of Sect. 2.2.11 suggests that the variation of η through the star is not large so, in the absence of a more rigorous theory of turbulence, η is taken as constant. None of the physical essentials of the problem are lost in making this mathematical simplification.

Making the substitution in (4.28) of

$$G_l = \left(\frac{\eta}{i\omega}\right)^{\frac{1}{4}} u^{\frac{1}{2}} F_l(u), \tag{4.35}$$

where $u = i^{3/2}(\omega/\eta)^{1/2} r$, gives

$$\frac{d^2 F_l}{du^2} + \frac{1}{u}\frac{dF_l}{du} + \left[1 - \frac{(l+\frac{1}{2})^2}{u^2}\right] F_l = 0. \tag{4.36}$$

This is Bessel's equation of order $\pm(l + 1/2)$. The solution of negative order is singular at $r = 0$, so the required non-singular solution of (4.28) is

$$G_l = i^{\frac{1}{2}} r^{\frac{1}{2}} J_{l+\frac{1}{2}} \left(i^{\frac{3}{2}} \left(\frac{\omega}{\eta}\right)^{\frac{1}{2}} r \right), \tag{4.37}$$

where $J_{l+\frac{1}{2}}$ is a Bessel function of the first kind of order $l + 1/2$, given by

$$J_{l+\frac{1}{2}}(u) = (-1)^l \left(\frac{2}{\pi}\right)^{\frac{1}{2}} u^{l+\frac{1}{2}} \frac{d^l}{(udu)^l} \left(\frac{\sin u}{u}\right). \tag{4.38}$$

The required radial functions are then

$$G_1 = -\left(\frac{2ir}{\pi}\right)^{\frac{1}{2}} \frac{1}{u^{\frac{1}{2}}} \left[\cos u - \frac{\sin u}{u}\right], \tag{4.39}$$

$$G_2 = \left(\frac{2ir}{\pi}\right)^{\frac{1}{2}} \frac{1}{u^{\frac{1}{2}}} \left[\left(\frac{3}{u^2} - 1\right) \sin u - \frac{3\cos u}{u}\right]. \tag{4.40}$$

The functions G_l can be expressed in the form

$$G_l(r) = C_l(r) \exp[i\delta_l(r)], \tag{4.41}$$

so the poloidal scalar, given by (4.20), is then

$$\Phi = C_l Y_l^m \exp[i(\omega t + \delta_l)]. \tag{4.42}$$

The boundary conditions, specified by (4.29), require Φ and $\partial\Phi/\partial r$ to be continuous across the stellar surface. Matching a suitable linear combination of the harmonics of Φ, and their radial derivatives, to those of $\Phi_\mathrm{p} + \Phi_\mathrm{s}$ with Φ_p and Φ_s given by (4.33) and (4.34), yields the inner poloidal scalar as

$$\begin{aligned}
\Phi =& C_1 P_1^1 \cos\phi[A_1 \sin(\omega t + \delta_1 - \delta_{1\mathrm{s}}) + A_2 \cos(\omega t + \delta_1 - \delta_{1\mathrm{s}})] \\
&- \frac{1}{2} C_1 P_1^1 \sin\phi[A_2 \sin(\omega t + \delta_1 - \delta_{1\mathrm{s}}) - A_1 \cos(\omega t + \delta_1 - \delta_{1\mathrm{s}})] \\
&+ C_2 P_2^0[B_1 \sin(\omega t + \delta_2 - \delta_{2\mathrm{s}}) + B_2 \cos(\omega t + \delta_2 - \delta_{2\mathrm{s}})] \\
&- \frac{1}{2} C_2 P_2^2 \cos 2\phi[B_1 \sin(\omega t + \delta_2 - \delta_{2\mathrm{s}}) + B_2 \cos(\omega t + \delta_2 - \delta_{2\mathrm{s}})] \\
&+ \frac{1}{3} C_2 P_2^2 \sin 2\phi[B_2 \sin(\omega t + \delta_2 - \delta_{2\mathrm{s}}) - B_1 \cos(\omega t + \delta_2 - \delta_{2\mathrm{s}})],
\end{aligned} \tag{4.43}$$

where the ω-dependent coefficients A_i and B_i are

$$A_1 = -\frac{3\mu_0 m R_\mathrm{s}^2 \sin\alpha}{4\pi D^3} (C_1 + R_\mathrm{s} C_1')_\mathrm{s} \left[(C_1 + R_\mathrm{s} C_1')_\mathrm{s}^2 + (R_\mathrm{s} C_1 \delta_1')_\mathrm{s}^2\right]^{-1}, \tag{4.44}$$

$$A_2 = -\frac{R_\mathrm{s} C_{1\mathrm{s}} \delta_{1\mathrm{s}}'}{(C_1 + R_\mathrm{s} C_1')_\mathrm{s}} A_1, \tag{4.45}$$

$$B_1 = \frac{5\mu_0 m R_s^3 \sin\alpha}{16\pi D^4}\left(C_2 + \frac{R_s}{2}C_2'\right)_s \left[\left(C_2 + \frac{R_s}{2}C_2'\right)_s^2 + \left(\frac{R_s}{2}C_2\delta_2'\right)_s^2\right]^{-1}, \tag{4.46}$$

$$B_2 = -\frac{R_s C_{2s}\delta_{2s}'}{(C_2 + \frac{1}{2}R_s C_2')_s} B_1, \tag{4.47}$$

with primes denoting differentiation with respect to r, and subscripts s surface values. The functions C_l and δ_l can be found from (4.39)–(4.41).

4.2.3 The Dissipation Torque

The dissipation of energy in the secondary and the torque acting on the primary can be simply related since, as will be shown, the angle α remains constant during the synchronization process. The electric currents induced in the secondary are dissipated, due to its finite diffusivity, with the total dissipation rate being

$$W = \frac{1}{\mu_0}\int_V \eta(\nabla \times \mathbf{B})^2 dV, \tag{4.48}$$

where the integral is over the stellar volume. It follows from (4.18)–(4.20) that

$$\nabla \times \mathbf{B} = \frac{i\omega}{\eta}\hat{\mathbf{r}} \times \nabla\Phi. \tag{4.49}$$

The dissipation is at the expense of the synodic rotational energy of the primary. The synchronization time-scale condition (4.14) means that the periodic time dependence of the torque will not affect ω over a synodic period. Only the secular variation of ω is then relevant and hence it is appropriate to consider the dissipation averaged over a synodic period, given by

$$\frac{dE}{dt} = -\frac{|\omega|}{2\pi}\int_0^{\frac{2\pi}{\omega}} W dt. \tag{4.50}$$

Using (4.43) for Φ in (4.49) to calculate $\nabla \times \mathbf{B}$, performing the angular integrations in (4.48) employing the orthogonality relation (A39) for spherical harmonics, and taking the time-average given by (4.50), yields

$$\frac{dE}{dt} = -\pi\mu_0\omega^2\left[\frac{5}{3}(A_1^2 + A_2^2)\int_0^{R_s}\frac{C_1^2}{\eta}dr + \frac{64}{5}(B_1^2 + B_2^2)\int_0^{R_s}\frac{C_2^2}{\eta}dr\right], \tag{4.51}$$

where A_i and B_i are given by (4.44)–(4.47).

The radial integrals can be expressed in terms of functions evaluated on the stellar surface. Substituting (4.41) for G_l into the differential equation (4.28), and equating the real and imaginary parts to zero, gives

$$\frac{d^2C_l}{dr^2} - \left[\delta_l'^2 + \frac{l(l+1)}{r^2}\right] C_l = 0, \tag{4.52}$$

$$\frac{d}{dr}(C_l^2\delta_l') - \frac{\omega}{\eta}C_l^2 = 0. \tag{4.53}$$

Equation (4.52) requires C_l to vanish at $r = 0$, so integrating (4.53) through the star gives

$$\int_0^{R_s} \frac{C_l^2}{\eta} dr = \frac{1}{\omega}(C_l^2\delta_l')_s. \tag{4.54}$$

Using (4.44)–(4.47) for the coefficients A_i and B_i together with (4.54) in (4.51), and simplifying, gives the dissipation rate as

$$\frac{dE}{dt} = -\frac{5\mu_0 m^2 R_s^3 \sin^2\alpha}{4\pi D^6}\omega f(\omega, \eta), \tag{4.55}$$

where the dimensionless function f is

$$f(\omega, \eta) = \frac{3}{4}(C_1^2\delta_1')_s F_1 + \left(\frac{R_s}{D}\right)^2 (C_2^2\delta_2')_s F_2, \tag{4.56}$$

with

$$F_1 = R_s C_{1s}^2 \left[(C_1^2 + R_s C_1 C_1')_s^2 + R_s^2 (C_1^2\delta_1')_s^2\right]^{-1}, \tag{4.57}$$

$$F_2 = R_s C_{2s}^2 \left[\left(C_2^2 + \frac{1}{2}R_s C_2 C_2'\right)_s^2 + \frac{1}{4}R_s^2 (C_2^2\delta_2')_s^2\right]^{-1}. \tag{4.58}$$

The real and imaginary parts of (4.39) for G_1 and (4.40) for G_2 give the functions C_l in (4.41), leading to

$$C_{1s}^2 = \frac{\sqrt{2}R_s}{\pi a_s}\left[\cosh a_s + \cos a_s - \frac{2}{a_s}(\sinh a_s + \sin a_s) + \frac{2}{a_s^2}(\cosh a_s - \cos a_s)\right], \tag{4.59}$$

$$C_{2s}^2 = \frac{\sqrt{2}R_s}{\pi a_s}\left[\cosh a_s - \cos a_s - \frac{6}{a_s}(\sinh a_s - \sin a_s)\right.$$
$$+\frac{18}{a_s^2}(\cosh a_s + \cos a_s) - \frac{36}{a_s^3}(\sinh a_s + \sin a_s)$$
$$\left.+\frac{36}{a_s^4}(\cosh a_s - \cos a_s)\right], \tag{4.60}$$

where a_s is a dimensionless similarity variable, given by

$$a_s = \left(\frac{2\omega}{\eta}\right)^{\frac{1}{2}} R_s. \tag{4.61}$$

It is noted that $a_s \sim (\tau_d/P_{syn})^{1/2}$, where τ_d is the characteristic diffusion time of a magnetic field through the secondary, and $P_{syn} = 2\pi/\omega$ is the synodic rotation period of the primary. The quantities $(C_l C_l')_s$ and $(C_l^2\delta_l')_s$ occurring in f are found from the real and imaginary parts of (4.39) and (4.40), and their relations to C_l and δ_l in (4.41). Some differentiation and lengthy algebra yields

$$(C_1C_1')_s = \frac{\sqrt{2}}{\pi}\left[\frac{1}{2}(\sinh a_s - \sin a_s) - \frac{1}{a_s}(\cosh a_s + \cos a_s)\right.$$
$$\left.+\frac{2}{a_s^2}(\sinh a_s + \sin a_s) - \frac{2}{a_s^3}(\cosh a_s - \cos a_s)\right], \tag{4.62}$$

$$(C_2C_2')_s = \frac{\sqrt{2}}{\pi}\left[\frac{1}{2}(\sinh a_s + \sin a_s) - \frac{3}{a_s}(\cosh a_s - \cos a_s)\right.$$
$$+\frac{12}{a_s^2}(\sinh a_s - \sin a_s) - \frac{36}{a_s^3}(\cosh a_s + \cos a_s)$$
$$\left.+\frac{72}{a_s^4}(\sinh a_s + \sin a_s) - \frac{72}{a_s^5}(\cosh a_s - \cos a_s)\right], \tag{4.63}$$

$$(C_1^2\delta_1')_s = \frac{1}{\pi\sqrt{2}}\left[\sinh a_s + \sin a_s - \frac{2}{a_s}(\cosh a_s - \cos a_s)\right], \tag{4.64}$$

$$(C_2^2\delta_2')_s = \frac{1}{\pi\sqrt{2}}\left[\sinh a_s - \sin a_s - \frac{6}{a_s}(\cosh a_s + \cos a_s)\right.$$
$$\left.+\frac{12}{a_s^2}(\sinh a_s + \sin a_s) - \frac{12}{a^3}(\cosh a_s - \cos a_s)\right]. \tag{4.65}$$

The dissipation rate, given by (4.55), can be related to the torque exerted on the primary by its interaction with $\mathbf{B}_s$, the outer field whose source is the current density induced in the secondary. This torque is

$$\mathbf{T} = \mathbf{m} \times \mathbf{B}_s(\mathbf{r}_p), \tag{4.66}$$

where, from (4.8a) and (4.32),

$$\mathbf{B}_s(\mathbf{r}_p) = \left[\nabla\left(\frac{\partial \Phi_s}{\partial r}\right)\right]_{\mathbf{r}=\mathbf{r}_p}, \tag{4.67}$$

and the position of the primary is $\mathbf{r}_p = D\mathbf{i}$. From Fig. 4.1, the polar components of $\mathbf{B}_s(\mathbf{r}_p)$ relative to $Oxyz$ can be related to its Cartesian components in $O'x'y'z$ by

$$B_{sr} = -B_{sy'}, \quad B_{s\theta} = -B_{sz}, \quad B_{s\phi} = B_{sx'}. \tag{4.68}$$

The components of the torque are then

$$T_{x'} = m(\hat{m}_z B_{sr} - \hat{m}_{y'} B_{s\theta}), \tag{4.69}$$

$$T_{y'} = m(\hat{m}_{x'} B_{s\theta} + \hat{m}_z B_{s\phi}), \tag{4.70}$$

$$T_z = -m(\hat{m}_{x'} B_{sr} + \hat{m}_{y'} B_{s\phi}), \tag{4.71}$$

at $(r, \theta, \phi) = (D, \pi/2, 0)$. Using (4.34) for Φ_s in (4.67) gives the required field components as

$$B_{sr} = \frac{1}{D^3}\left[2\alpha_1 - \frac{3}{D}(\beta_1 - 6\gamma_1)\right]\sin\omega t + \frac{1}{D^3}\left[2\alpha_2 - \frac{3}{D}(\beta_2 - 6\gamma_2)\right]\cos\omega t, \tag{4.72}$$

$$B_{s\theta} = 0, \tag{4.73}$$

$$B_{s\phi} = -\frac{1}{D^3}\left(\alpha_3 + \frac{12}{D}\gamma_3\right)\sin\omega t - \frac{1}{D^3}\left(\alpha_4 + \frac{12}{D}\gamma_4\right)\cos\omega t. \tag{4.74}$$

Using the components of $\hat{\mathbf{m}}$ from (4.7) together with (4.72)–(4.74) in (4.69)–(4.71), and averaging over a period $2\pi/\omega$, gives

$$\langle T_{x'}\rangle = \langle T_{y'}\rangle = 0, \tag{4.75}$$

$$\langle T_z\rangle = -\frac{m\sin\alpha}{D^3}\left[\alpha_2 - \frac{1}{2}\alpha_3 - \frac{3}{2D}(\beta_2 - 6\gamma_2 + 4\gamma_3)\right]. \tag{4.76}$$

Equation (4.75) shows that there is no tendency for secular changes in the tilt angle α of the dipole moment $\mathbf{m}$.

The quantities α_i, β_i and γ_i in (4.76) can be expressed in terms of A_2 and B_2, given by (4.45) and (4.47), by means of the boundary conditions at $r = R_s$. This gives

$$\alpha_2 = R_s C_{1s} A_2, \quad \alpha_3 = -\frac{1}{2}\alpha_2, \quad \beta_2 = R_s^2 C_{2s} B_2,$$
$$\gamma_2 = -\frac{1}{2}\beta_2, \quad \gamma_3 = \frac{1}{3}\beta_2. \tag{4.77}$$

Substitution of these in (4.76) yields

$$\langle T_z \rangle = -\frac{5\mu_0 m^2 R_s^3 \sin^2\alpha}{4\pi D^6}\left[\frac{3}{4}(C_1^2\delta_1')_s F_1 + \left(\frac{R_s}{D}\right)^2 (C_2^2\delta_2')_s F_2\right], \tag{4.78}$$

where the functions F_1 and F_2 are identical to those given by (4.57) and (4.58). The quantity in square brackets is therefore the function $f(\omega, \eta)$, appearing in (4.55) for the dissipation rate, and hence the synodic average of the total dissipative inductive torque is

$$\langle \mathbf{T} \rangle = \mathbf{T}_D = -\frac{5\mu_0 m^2 R_s^3 \sin^2\alpha}{4\pi D^6} f(\omega, \eta)\,\mathbf{k}. \tag{4.79}$$

The dissipation rate of the synodic rotational energy of the primary is therefore related to this torque by

$$\frac{dE}{dt} = \omega T_D. \tag{4.80}$$

The vanishing synodic averages of the horizontal torque components are a consequence of the intrinsic symmetry of the dipole field, and the initial condition of $\boldsymbol{\omega}$ parallel to $\boldsymbol{\Omega}_o$. Equations (4.11) and (4.12) show that the time-dependent part of the primary's magnetic field has a vanishing z-component in the orbital plane. The outer field $\mathbf{B}_s$, resulting from the current distribution induced in the secondary, also has this property. At the primary $B_{s\theta} = -B_{sz} = 0$, so (4.69) and (4.70) give

$$T_{x'} = m\cos\alpha B_{sr}, \tag{4.81}$$
$$T_{y'} = m\cos\alpha B_{s\phi}. \tag{4.82}$$

It then follows from (4.72) for B_{sr} and (4.74) for $B_{s\phi}$ that $\langle T_{x'} \rangle = \langle T_{y'} \rangle = 0$.

If $\boldsymbol{\omega}$ were initially misaligned from $\boldsymbol{\Omega}_o$ part of the dissipation in the secondary would be due to the component of $\boldsymbol{\omega}$ in the orbital plane. This component would be dissipated at a similar rate to that of the synchronization of ω_z so, in the absence of other torques, the horizontal components of $\boldsymbol{\omega}$ would approach zero on the time-scale τ_{syc} given by (4.13).

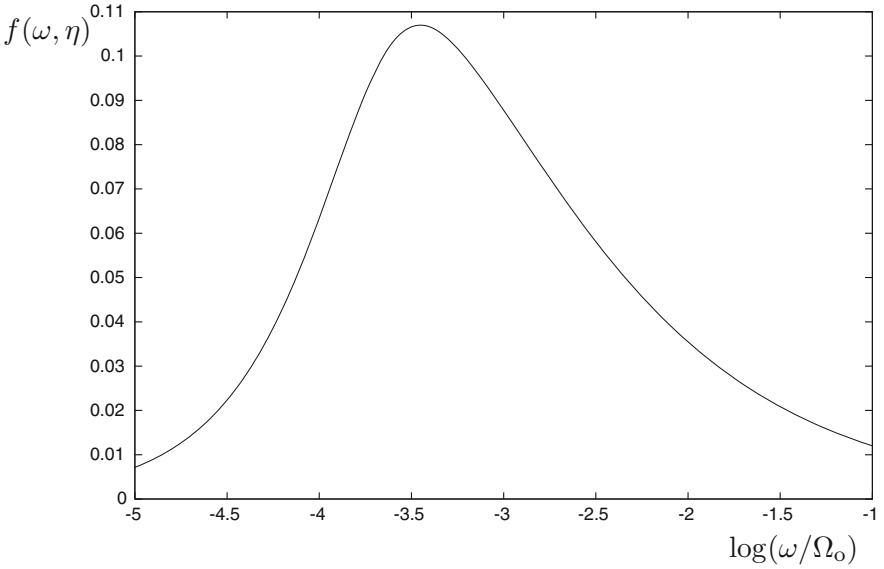

Fig. 4.2 The dimensionless primary magnetic torque function, for vacuum surroundings

Figure 4.2 is a plot of $f(\omega,\eta)$ against $\log(\omega/\Omega_o)$, The torque decreases with decreasing ω for $\omega/\Omega_o \lesssim 10^{-3.5}$ since, although the field penetration becomes large, its time variation, and hence the induced current density, becomes small. The torque decreases with increasing ω for $\omega/\Omega_o \gtrsim 10^{-3.5}$ because at higher frequencies the field becomes localized to a skin-depth $\delta \ll R_s$ beneath the stellar surface, and $\delta \to 0$ as ω increases.

For an under-synchronous state $\omega < 0$ applies and making the transformation $\omega \to -\omega$ in (4.61) gives $a_s \to i a_s$. Using this in (4.59), (4.60) and (4.62)–(4.65) for C_{ls}^2, $(C_l C_l')_s$ and $(C_l^2 \delta_l')_s$, then employing the results in (4.56)–(4.58) yields $f(-\omega,\eta) = -f(\omega,\eta)$. Hence, as expected, the induction torque is antisymmetric in ω.

4.2.4 Asymptotic Synchronization Times

The dimensionless quantity a_s, given by (4.61), can be expressed as

$$a_s = \frac{\sqrt{2} R_s \Omega_o^{\frac{1}{2}}}{\eta^{\frac{1}{2}}} \left(\frac{\omega}{\Omega_o}\right)^{\frac{1}{2}}. \tag{4.83}$$

Using the orbital, lobe-filling and mass-radius relations

$$\Omega_{\rm o}^2 = \frac{GM}{D^3}, \tag{4.84a}$$

$$\frac{M}{M_{\rm s}}\left(\frac{R_{\rm s}}{D}\right)^3 = 0.1 \tag{4.84b}$$

and

$$\frac{R_{\rm s}}{R_\odot} = q\frac{M_{\rm s}}{M_\odot}, \tag{4.84c}$$

where $M = M_{\rm s} + M_{\rm p}$, yields

$$a_{\rm s} = \frac{6.20\times 10^2 q^{\frac{1}{4}}(M_{\rm s}/M_\odot)^{\frac{1}{2}}}{(\eta/5\times 10^8\,{\rm m^2\,s^{-1}})^{\frac{1}{2}}}\left(\frac{\omega}{\Omega_{\rm o}}\right)^{\frac{1}{2}}. \tag{4.85}$$

It follows from (4.61) that

$$a_{\rm s} = 2\frac{R_{\rm s}}{\delta} = 2\sqrt{\pi}\left(\frac{\tau_{\rm d}}{P_{\rm syn}}\right)^{\frac{1}{2}} \tag{4.86}$$

where $\tau_{\rm d}$ is the magnetic diffusion time through the secondary, $P_{\rm syn} = 2\pi/\omega$, and $\delta = (2\eta/\omega)^{1/2}$ is the characteristic penetration depth of the magnetic field.

Asymptotic forms can be found for the dissipation torque $T_{\rm D} = \langle T\rangle$ for $\delta \ll R_s$ and $\delta > R_{\rm s}$. These regimes represent low and high magnetic field penetration into the secondary, respectively, and corresponding expressions can be found for the synchronization times.

Equations (4.84a), (4.84b), and (4.84c) enable P and D to be written as

$$P = 2\pi q^{\frac{3}{2}}\left(\frac{10}{G}\right)^{\frac{1}{2}}\left(\frac{R_\odot}{M_\odot}\right)^{\frac{3}{2}} M_{\rm s} \tag{4.87}$$

and

$$D = 10^{\frac{1}{3}} q\left(\frac{R_\odot}{M_\odot}\right) M^{\frac{1}{3}} M_{\rm s}^{\frac{2}{3}}. \tag{4.88}$$

These expressions will allow some formulas to be simplified by the elimination of P and D.

Low Field Penetration

For $a_s \gg 1$ the primary's magnetic field penetrates the secondary to a skin-depth $\delta \ll R_s$. Equations (4.56)–(4.65) and (4.79) yield

$$T_D = \mp \frac{15\sqrt{2}\pi}{8\mu_0} \left[1 + \frac{16}{3}\left(\frac{R_s}{D}\right)^2\right] \frac{(B_p)_0^2 R_p^6 R_s^2 \sin^2\alpha}{D^6} \left(\frac{\eta}{|\omega|}\right)^{\frac{1}{2}}, \tag{4.89}$$

where the negative and positive signs apply for $\omega > 0$ and $\omega < 0$, respectively. Using (4.84c), (4.87) and (4.88) to eliminate R_s, P and D leads to the synchronization time

$$\tau_{syc} = \frac{4.24 \times 10^7 q^{\frac{7}{4}} \left(\frac{k_p^2}{0.2}\right) \left(\frac{M_p}{0.6 M_\odot}\right) \left(\frac{M_s}{0.2\, M_\odot}\right)^{\frac{1}{2}} \left(\frac{M}{0.8\, M_\odot}\right)^2 \left(\frac{|\omega|}{\Omega_o}\right)^{\frac{3}{2}}}{N_1 \left(\frac{R_p}{8.67 \times 10^6\ \mathrm{m}}\right)^4 \left(\frac{(B_p)_0}{20\,\mathrm{MG}}\right)^2 \left(\frac{\eta}{5 \times 10^8\ \mathrm{m^2\,s^{-1}}}\right)^{\frac{1}{2}}} \text{ year}, \tag{4.90}$$

where $k_p R_p$ is the radius of gyration of the primary, and

$$N_1 = \left[1 + \frac{16}{3}\left(\frac{R_s}{D}\right)^2\right] \sin^2\alpha. \tag{4.91}$$

For $\eta = 5 \times 10^8\ \mathrm{m^2\,s^{-1}}$, these expressions hold to good accuracy for $a_s \geq 10$ corresponding to $|\omega|/\Omega_o \geq 10^{-3}$. It is seen that for $|\omega|/\Omega_o \sim 1$, τ_{syc} is less than the lifetime of the system, which is given by the mass transfer time-scale $\tau_M = M_s/|\dot{M}_s| \sim 2 \times 10^9$year. The torque expression (4.89) agrees with the estimate (4.4), except for a numerical factor which results from taking the field structure into account here.

High Field Penetration

For $a_s < 1$ the field penetration is essentially complete, with $\delta > R_s$, and Taylor expansion of f about $a_s = 0$ yields

$$T_D = \frac{\pi}{12\mu_0} \left[1 + \frac{48}{35}\left(\frac{R_s}{D}\right)^2\right] \frac{(B_p)_0^2 R_p^6 R_s^5 \sin^2\alpha}{D^6} \frac{\omega}{\eta}. \tag{4.92}$$

It follows that $|\omega|$ decreases exponentially on a time-scale

$$\tau_{\rm syc} = \frac{179q\left(\frac{k_{\rm p}^2}{0.2}\right)\left(\frac{M_{\rm p}}{0.6\,M_\odot}\right)\left(\frac{M}{0.8\,M_\odot}\right)^2\left(\frac{\eta}{5\times10^8\,{\rm m^2\,s^{-1}}}\right)}{N_2\left(\frac{(B_{\rm p})_0}{20\,{\rm MG}}\right)^2\left(\frac{R_{\rm p}}{8.67\times10^6\,{\rm m}}\right)^4\left(\frac{M_{\rm s}}{0.2\,M_\odot}\right)}\ {\rm year}, \tag{4.93}$$

where

$$N_2 = \left[1+\frac{48}{35}\left(\frac{R_{\rm s}}{D}\right)^2\right]\sin^2\alpha. \tag{4.94}$$

For $\eta = 5\times10^8\,{\rm m^2\,s^{-1}}$, these expressions hold to good accuracy for $a_{\rm s} \le 0.8$ corresponding to $\omega/\Omega_{\rm o} \le 10^{-5}$.

The period-mass relation (4.87) can be written in the form

$$\left(\frac{P}{\rm h}\right) = 8.8q^{\frac{3}{2}}\left(\frac{M_{\rm s}}{M_\odot}\right). \tag{4.95}$$

The radius of the primary can be found from

$$R_{\rm p} = 7.8\times10^6\left[\left(\frac{M_{\rm p}}{M_c}\right)^{-\frac{2}{3}} - \left(\frac{M_{\rm p}}{M_c}\right)^{\frac{2}{3}}\right]^{\frac{1}{2}}\ {\rm m}, \tag{4.96}$$

where $M_c = 1.44\,M_\odot$ (Nauenberg 1972).

4.2.5 *Comparison with Observations of Asynchronous Systems*

Five AM Her systems are believed to have asynchronous primary stars, and analyses of the observational data have been made to estimate synchronization times.

Staubert et al. (2003) used optical and X-ray data to estimate the asynchronism of V1432 Aql as $\omega/\Omega_{\rm o} \simeq -2.8\times10^{-3}$, suggesting an under-synchronous primary. A synchronization time-scale was estimated as $\tau_{\rm syc} \simeq 200$ year. This can be compared with the theoretical time-scale given by (4.90), which is appropriate for the estimated degree of asynchronism. The orbital period is $P = 3.366$ h and the period-mass relation (4.95) yields $M_{\rm s} \simeq 0.32\,M_\odot$. The formula (4.90) can give the estimated observational value of $\tau_{\rm syc}$ for $M_{\rm p} = 0.4\,M_\odot$, $N_1 = 1.4$, $(B_{\rm p})_0 = 50$ MG and $\eta = 5\times10^8\,{\rm m^2\,s^{-1}}$. Other reasonable values of these parameters can give the observationally estimated synchronization time-scale.

Pavlenko et al. (2013) analysed data collected from photometric observations over an 8 year period of BY Cam. This gave $\omega/\Omega_{\rm o} \simeq 9.6\times10^{-3}$ and $\tau_{\rm syc} \simeq$

270 year. The orbital period and estimated secondary mass are $P = 3.354\,\mathrm{h}$ and $M_\mathrm{s} \simeq 0.32\,M_\odot$. Estimates of the primary magnetic field give $(B_\mathrm{p})_0 \simeq 41\,\mathrm{MG}$. Using remaining parameters similar to those adopted above for V1432 Aql in (4.90) yields a synchronization time in agreement with the observational estimate.

Myers et al. (2017) combined observations taken in 1996 with those taken over the period 2007–2016 for CD Ind to estimate τ_syc. The degree of asynchronism was $\omega/\Omega_\mathrm{o} \simeq 1.1 \times 10^{-2}$ and $\tau_\mathrm{syc} \simeq (6.4 \pm 0.8) \times 10^3$ year was obtained. The orbital period and estimated secondary mass are $P = 1.848\,\mathrm{h}$ and $M_\mathrm{s} \simeq 0.18\,M_\odot$. The surface primary magnetic field is estimated as 12 MG. Taking this field, $M_\mathrm{p} = 0.3\,M_\odot$ and $N_1 = 1$ in (4.90) gives $\tau_\mathrm{syc} = 5.7 \times 10^3$ year, consistent with the observational estimate.

Harrison and Campbell (2018) suggested that V1500 Cyg, which was observed to be asynchronous, may have synchronized, but further investigations are needed to confirm this. A similar situation exists for V4633 Sgr (Lipkin & Leibowitz 2008).

4.2.6 The Magnetic Orbital Torque

There is a net force on the primary star, due to the spatial variation of the secondary's induced external magnetic field, given by

$$\mathbf{F} = [\nabla(\mathbf{m} \cdot \mathbf{B}_\mathrm{s})]_{\mathbf{r}=\mathbf{r}_\mathrm{p}}\,, \tag{4.97}$$

with

$$\mathbf{B}_\mathrm{s} = \nabla\left(\frac{\partial \Phi_\mathrm{s}}{\partial r}\right), \tag{4.98}$$

where Φ_s is given by (4.34) and

$$\hat{\mathbf{m}} \cdot \mathbf{B}_\mathrm{s} = \sin\alpha\cos\omega t\,(\mathbf{i}' \cdot \mathbf{B}_\mathrm{s}) + \sin\alpha\sin\omega t\,(\mathbf{j}' \cdot \mathbf{B}_\mathrm{s}) + \cos\alpha\,(\mathbf{k} \cdot \mathbf{B}_\mathrm{s}). \tag{4.99}$$

Substitution and time averaging over a synodic period gives the force components at $(D, \pi/2, 0)$ as

$$F_r = \frac{3m}{D^4}\left[\alpha_1 + \frac{1}{2}\alpha_4 - \frac{2}{D}\,(\beta_1 - 6\gamma_1 - 4\gamma_4)\right]\sin\alpha, \tag{4.100}$$

$$F_\phi = \frac{3m}{2D^4}\left[\alpha_2 - \alpha_3 - \frac{1}{D}\,(\beta_2 - 14\gamma_2 + 16\gamma_3)\right]\sin\alpha, \tag{4.101}$$

with $F_\theta = 0$. An equal and opposite force is exerted on the centre of mass of the secondary. Adding the primary and secondary torques that result about the binary

centre of mass gives the total magnetic orbital torque as

$$\mathbf{T}_{\rm mo} = -D\mathbf{j}' \times \mathbf{F} = DF_\phi \mathbf{k}. \tag{4.102}$$

Using (4.101) for F_ϕ in (4.102), with (4.77) for α_2, α_3, β_2, γ_2 and γ_3, then employing (4.45) and (4.47) for A_2 and B_2 leads to

$$\mathbf{T}_{\rm mo} = \frac{\mu_0 m^2 R_{\rm s}^3 \sin^2\alpha}{\pi D^6}\left[\frac{27}{16}\left(C_1^2\delta_1'\right)_{\rm s} F_1 + \frac{25}{8}\left(\frac{R_{\rm s}}{D}\right)^2\left(C_2^2\delta_2'\right)_{\rm s} F_2\right]\mathbf{k}. \tag{4.103}$$

4.2.7 The Total Magnetic Torque

This leaves the secondary magnetic torque to be found. Using (4.49) for $\nabla \times \mathbf{B}$, gives the torque as

$$\mathbf{T}_{\rm ms} = \frac{\omega}{\mu_0}\int_V \frac{ir}{\eta} B_r \hat{\mathbf{r}} \times \nabla\Phi \, dV, \tag{4.104}$$

with

$$B_r = \frac{1}{r^2}L^2\Phi = -\frac{1}{r^2}\left[\frac{1}{\sin\theta}\frac{\partial}{\partial\theta}\left(\sin\theta\frac{\partial\Phi}{\partial\theta}\right) + \frac{1}{\sin^2\theta}\frac{\partial^2\Phi}{\partial\phi^2}\right]. \tag{4.105}$$

Using

$$\hat{\boldsymbol{\theta}} = \cos\theta\sin\phi\,\mathbf{i}' - \cos\theta\cos\phi\,\mathbf{j}' - \sin\theta\,\mathbf{k}, \tag{4.106}$$

$$\hat{\boldsymbol{\phi}} = \cos\phi\,\mathbf{i}' + \sin\phi\,\mathbf{j}' \tag{4.107}$$

in $\hat{\mathbf{r}} \times \nabla\Phi$, (4.104) leads to

$$\mathbf{T}_{\rm ms} = \frac{\omega}{\mu_0}\int_V \frac{i}{\eta}\left(L^2\Phi\right)\frac{\partial\Phi}{\partial\phi} dV\,\mathbf{k} \tag{4.108}$$

Employing (4.43) for Φ, evaluating the angular integrals and time averages, yields

$$\mathbf{T}_{\rm ms} = -\frac{3\mu_0 m^2 R_{\rm s}^3 \sin^2\alpha}{4\pi D^6}\left[\left(C_1^2\delta_1'\right)_{\rm s} F_1 + \frac{5}{2}\left(\frac{R_{\rm s}}{D}\right)^2\left(C_2^2\delta_2'\right)_{\rm s} F_2\right]\mathbf{k}. \tag{4.109}$$

Adding (4.78), (4.103) and (4.109) gives

$$\mathbf{T}_{\rm mp} + \mathbf{T}_{\rm mo} + \mathbf{T}_{\rm ms} = \mathbf{0}. \tag{4.110}$$

Hence the total magnetic torque is zero, corresponding to no angular momentum being lost from the binary due to the action of these torques. Equation (4.110) gives the spin-orbit coupling allowing angular momentum exchange between the stars and the orbit.

4.3 Coupling with a Magnetosphere

4.3.1 Induction Effects

The previously considered vacuum surroundings case has magnetic coupling due to the explicit time dependence of the primary's magnetic field when the tilt angle α is finite. However, when $\alpha = 0$ the magnetic field is time-independent and the coupling vanishes. With a magnetosphere there will be coupling even when $\alpha = 0$.

It was pointed out by Chanmugan and Dulk (1983) and Lamb et al. (1983) that the spinning motion of the magnetic primary creates a $\mathbf{v} \times \mathbf{B}$ electric field within it. In a frame corotating with white dwarf, and its highly conducting magnetosphere, the electric field will essentially vanish, so in the orbital frame the Lorentz transformation to first order in v/c gives an electric field

$$\mathbf{E} = -\mathbf{v} \times \mathbf{B}, \tag{4.111}$$

where $\mathbf{v}$ is the asynchronous velocity. The high magnetic field and low density of the magnetosphere lead to an anisotropy in its conductivity, with high values along $\mathbf{B}$ but low values across field lines. Since $\mathbf{E} \cdot \mathbf{B} = 0$, the magnetic field lines are electric equipotentials and there is a potential difference between points at different latitudes on the surface of the primary. It follows that field lines that originate from such points and that thread the secondary will project this potential difference on to its surface, which will drive currents through the star. A circuit is set up connecting the stars through the magnetosphere. The resulting $\mathbf{J} \times \mathbf{B}$ force density will generate torques which allow stellar and orbital angular momentum to be exchanged and will cause spin evolution towards the synchronous state.

Chanmugan and Dulk (1983) estimated the synchronizing inductive torque by considering dissipation of electric currents via the resistance in the circuit. Their torque is linear in ω, and its derivation assumed that inductive effects due to interaction with the secondary only cause small perturbations in the magnetic field. This assumption will be shown to be valid for sufficiently small values of $\omega/\Omega_{\rm o}$.

Lamb et al. (1983) pointed out that the field aligned currents will act as a source of toroidal magnetic field, and the resulting $B_{\rm p} B_\phi$ stellar surface stresses will lead to magnetic torques. They estimated the primary torque, using dimensional

considerations, to be

$$\mathbf{T}_{\rm p} \simeq -f\frac{(B_{\rm p})_0^2}{\mu_0}\left(\frac{R_{\rm p}}{D}\right)^6 R_{\rm s}^2 D\,\mathbf{k}, \tag{4.112}$$

where f is a dimensionless factor which would incorporate the interaction of the magnetic field with the convective secondary, involving the field winding ratio $|B_{\phi{\rm s}}/B_{\rm ps}|$. They anticipated that this twist would become limited for $|B_{\phi{\rm s}}/B_{\rm ps}| \gtrsim 1$ by reconnection processes and large-scale MHD instabilities, as it is in other situations where field winding occurs. They assumed the torque to be approximately independent of ω and estimated a synchronization time. This was significantly less than a typical AM Her binary lifetime. A similar torque was estimated by Katz (1991). However, a frequency independent torque, such as (4.112), could only occur in a saturated higher ω regime. There is generally a dependence on ω, with $|T_{\rm p}| \propto \omega$ as $\omega \to 0$.

Another estimate of the torque involving a magnetospheric interaction was made by Kaburaki (1986). A spherical polar coordinate system (r, θ, ϕ) was used, centred on the primary. The potential difference across the secondary was found, assuming small perturbation of the primary magnetic field, and the resulting current was calculated by estimating the resistance of the secondary. The torque on the primary, due to the $\mathbf{J} \times \mathbf{B}$ force, can then be obtained and a synchronization time-scale calculated. The θ-dependence of the magnetic field was not included, but this can be incorporated in the Kaburaki model and the results can be expanded to first order in $R_{\rm s}/D$.

The tangential electric field in the surface layers of the primary is

$$E_{\theta{\rm s}} = -\frac{1}{R_{\rm p}}\frac{\partial V}{\partial \theta} = -v_{\phi{\rm s}}B_{r{\rm s}} = -\omega R_{\rm p}(B_{\rm p})_0 \sin\theta\cos\theta, \tag{4.113}$$

where the $\cos\theta$ dependence of $B_{r{\rm s}}$ is now accounted for. This expression can be integrated between θ values corresponding to the field lines which span the secondary. For a dipole field, this gives the limits θ_i, with $i = 1, 2$, where

$$\sin\theta_i = \left(\frac{R_{\rm p}}{A_i}\right)^{\frac{1}{2}}, \tag{4.114}$$

and A_i is the distance from the primary of the point of intersection of the field line with the orbital plane. This leads to a potential difference

$$\Delta V = V(\theta_2) - V(\theta_1) = \omega R_{\rm p}^2 (B_{\rm p})_0 \frac{R_{\rm p}}{D}\frac{R_{\rm s}}{D}, \tag{4.115}$$

to first order in $R_{\rm s}/D$. There is another such source of ΔV, having $\theta_j = \pi - \theta_i$, this being a mirror image region below the equatorial plane.

Applying Ohm's law, taking the simplification of a uniform current density through the secondary, gives a resistance of

$$R = 2\frac{\mu_0}{\pi}\frac{\eta}{R_\mathrm{s}}. \tag{4.116}$$

Since the turbulent secondary is the main resistance in the circuit, the current is

$$I = \frac{\Delta V}{R} = \frac{\pi}{2}\frac{(B_\mathrm{p})_0}{\mu_0}\left(\frac{R_\mathrm{p}}{D}\right)^3 R_\mathrm{s}^2 D\frac{\omega}{\eta}. \tag{4.117}$$

The source below the orbital plane also gives a potential difference of ΔV across the secondary, giving a total current of $2I$ through the star. The current density in a surface layer of depth h in the primary is

$$J_\theta = \frac{I}{hR_\mathrm{p}\Delta\phi}, \tag{4.118}$$

where the azimuthal interval $\Delta\phi$ incorporates the field lines connecting to the secondary star. The torque on the primary is then

$$T_\mathrm{p} = -2\int_0^h\int_{\theta_1}^{\theta_2}\int_0^{\Delta\phi} R_\mathrm{p}\sin\theta J_\theta (B_\mathrm{p})_0\cos\theta R_\mathrm{p}^2\sin\theta dr d\theta d\phi, \tag{4.119}$$

noting that the regions above and below the equatorial plane make equal contributions and that the $\cos\theta$ dependence of B_{rs} is included. Evaluating this to first order in R_s/D yields the inductive torque

$$\mathbf{T}_\mathrm{p} = -\pi\frac{(B_\mathrm{p})_0^2}{\mu_0}\left(\frac{R_\mathrm{p}}{D}\right)^{\frac{1}{2}}\left(\frac{R_\mathrm{p}}{D}\right)^6 R_\mathrm{s}^3 D^2\frac{\omega}{\eta}\mathbf{k}. \tag{4.120}$$

This result, derived using Kaburaki's model, will be shown to agree well with the low ω/Ω_o limit derived from the more detailed analysis of Campbell (2005, 2010), which allowed for inductive effects in the secondary and hence for modifications of the stellar magnetic field. The derivation of the synchronization torque presented below is based on this work.

4.3.2 Magnetospheric and Secondary Star Motions

With a magnetosphere there will be magnetic coupling for all values of α but, to clarify the mechanisms involved, the case of $\alpha = 0$ is considered. The orbital frame is shown in Fig. 4.3, with the polar coordinates (r, θ, ϕ) used with an origin at the centre of the secondary. The primary has a magnetic moment **m** parallel to

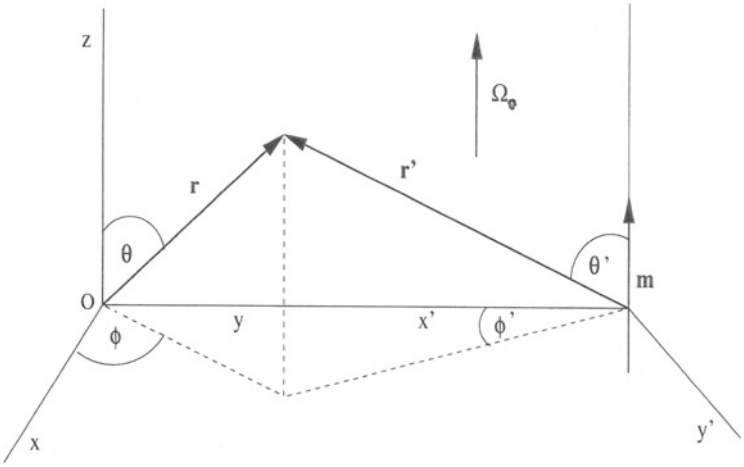

Fig. 4.3 The orbital frame coordinates (from Campbell 2010)

its synodic angular velocity $\boldsymbol{\omega}$. A magnetosphere corotating with the primary has velocity components, relative to the coordinates based on the secondary, given by

$$v_{\mathrm{m}r} = \omega D \sin\theta \cos\phi, \tag{4.121}$$

$$v_{\mathrm{m}\theta} = \omega D \cos\theta \cos\phi, \tag{4.122}$$

$$v_{\mathrm{m}\phi} = \omega (r \sin\theta - D \sin\phi). \tag{4.123}$$

The turbulent secondary will interact with the surrounding rotating magnetosphere and motions will be induced in the star.

The unperturbed primary magnetic field can be written as

$$\mathbf{B}_{\mathrm{p}} = -\nabla \Psi_{\mathrm{m}}, \tag{4.124}$$

where

$$\Psi_{\mathrm{m}} = \frac{\mu_0 m}{4\pi D^3} r \cos\theta \left[1 - 2\frac{r}{D}\sin\theta\cos\phi + \left(\frac{r}{D}\right)^2\right]^{-\frac{3}{2}}. \tag{4.125}$$

In and on the secondary $r/D \lesssim 1/3$ and so (4.125) can be expanded as a series in r/D. Since the torques involve series in powers of $(R_{\mathrm{s}}/D)^2$, it is a reasonable approximation to take the leading order term which gives

$$\Psi_{\mathrm{m}} = \frac{\mu_0 m}{4\pi D^3} r P_1, \tag{4.126}$$

where $P_1 = \cos\theta$. This field corresponds to the leading order part of $\mathbf{B}_0$ in (4.10) with $\alpha = 0$.

For the reasons previously discussed, the secondary can be taken to be a sphere of radius R_s with the same volume as its distorted form. Interaction with the secondary will perturb the primary's magnetic field and its magnetosphere. It will be argued that quenching mechanisms will keep the perturbations moderate, so the magnetosphere will remain close to corotation with the primary. Equations (4.121)–(4.123) show that there will be tangential and radial motions near the surface of the secondary, which depend on angular position. The azimuthal motions of the magnetosphere, given by (4.123), will result in a difference between the synodic angular velocity of the magnetosphere and that of the secondary star. A tidally synchronized secondary will have $\mathbf{v} = \mathbf{0}$, but magnetic forces associated with interaction with the magnetosphere will cause some synodic angular velocity in the outer layers of the star where the perturbation is largest. There will be a radial gradient in Ω which decays with depth as the magnetic forces decrease. The sign of Ω will be ϕ-dependent, as shown in (4.123).

The radial motions of the magnetosphere, given by (4.121), will result in material flowing into the secondary or away from it, depending on the azimuthal position. In an inflow region material will be carried inwards at the surface and become detached from the field lines as it experiences turbulent η values in the star. This influx will compress the surface layers and lead to a perturbation in the radial pressure gradient causing a radial velocity, $v_r < 0$, which decreases with depth. In an outflow region magnetospheric material will flow away from the star, carried by the field lines to which it is attached, causing an expansion. A perturbation will occur in the radial pressure gradient and an outflow will result, so $v_r > 0$ applies in the surface layers of the star in such a region. The v_θ component of the magnetospheric velocity, given by (4.122), will induce v_θ motions in the secondary. However, the essential effects related to the magnetic torques are contained in the v_r and v_ϕ velocity components and, to make the analysis tractable, the v_θ component will not be included in the solution. The extent of magnetic field penetration into the secondary, and hence the force distribution, will depend on the degree of asynchronism of the primary.

Ideally, the dynamical equations should be solved to obtain the induced velocity field. However, the essentials of the motions can be encapsulated by constructing a simple representation which matches the surface magnetospheric velocity field. The motions will decay with depth, as required, and depend on the asynchronism via the surface matching. The radial velocity component affects the depth of penetration of the magnetic field due to the advection terms it introduces in the induction equation. This component is represented by the form

$$v_r = \begin{cases} v_r(r), & 0 < \phi < \pi/2 \quad \text{and} \quad 3\pi/2 < \phi < 2\pi, \\ 0, & \phi = \pi/2 \quad \text{and} \quad \phi = 3\pi/2, \\ -v_r(r), & \pi/2 < \phi < 3\pi/2, \end{cases} \tag{4.127}$$

where

$$v_r(r) = \omega R_s \left(\frac{r}{R_s}\right)^k, \tag{4.128}$$

with $k > 0$. The surface value $v_r(R_s) = \omega R_s$ represents an average of the factor $\omega D \sin\theta$ occurring in (4.121) for v_{mr} over the interval $0 < \theta < \pi$. The azimuthal zeros of (4.127) represent the ϕ-dependence induced by v_{mr}, given by (4.121), by representing $\cos\phi$ as a square wave of unit height and corresponding zeros.

The angular velocity, $\Omega = v_\phi / r \sin\theta$, is represented by the form

$$\Omega = \begin{cases} -\Omega(r), & \phi_1 < \phi < \pi - \phi_1, \\ 0, & \phi = \phi_1 \quad \text{and} \quad \phi = \pi - \phi_1, \\ \Omega(r), & \pi - \phi_1 < \phi < 2\pi + \phi_1, \end{cases} \tag{4.129}$$

where

$$\Omega(r) = \omega \left(\frac{r}{R_s}\right)^n, \tag{4.130}$$

with $n > 0$. This represents the azimuthal motions induced by $v_{m\phi}$, given by (4.123), with the ϕ-dependence represented by a square wave of unit height with zeros at

$$\phi_1 = \sin^{-1}\left(\frac{R_s}{D}\sin\theta\right). \tag{4.131}$$

Suitable values will be taken for k and n to represent the fact that the motions will decay with depth in the secondary as the induced magnetic force weakens relative to the gravitational and pressure gradient forces.

These forms for v_r and Ω define four regions which arise for motions in the secondary, due to the ϕ-dependence of the magnetospheric velocity. These are

$$\text{Region I}: \quad \phi_1 < \phi < \pi/2, \quad \text{with} \quad v_r > 0,\ \Omega < 0, \tag{4.132}$$

$$\text{Region II}: \quad \pi/2 < \phi < \pi - \phi_1, \quad \text{with} \quad v_r < 0,\ \Omega < 0, \tag{4.133}$$

$$\text{Region III}: \quad \pi - \phi_1 < \phi < 3\pi/2, \quad \text{with} \quad v_r < 0,\ \Omega > 0, \tag{4.134}$$

$$\text{Region IV}: \quad 3\pi/2 < \phi < 2\pi + \phi_1, \quad \text{with} \quad v_r > 0,\ \Omega > 0. \tag{4.135}$$

Field solutions must be found for these regions, subject to centre and surface boundary conditions.

4.3.3 Magnetic Field Equations and Boundary Conditions

For $\alpha = 0$ there is no explicit time dependence and hence the induction equation (4.1) becomes

$$\nabla \times (\mathbf{v} \times \mathbf{B}) - \nabla \times (\eta \nabla \times \mathbf{B}) = \mathbf{0}. \tag{4.136}$$

The magnetic diffusivity is taken as

$$\eta = \eta_{\rm s} \left(\frac{r}{R_{\rm s}} \right)^m, \tag{4.137}$$

with m constant and $\eta_{\rm s}$ the surface value. The magnetic field can be expressed as

$$\mathbf{B} = \nabla \times \left[\nabla \times (\Phi_{\rm p} \hat{\mathbf{r}}) \right] + \nabla \times (\Phi_{\rm T} \hat{\mathbf{r}}), \tag{4.138}$$

where $\Phi_{\rm p}$ and $\Phi_{\rm T}$ are poloidal and toroidal scalars. This gives the field components as

$$B_r = \frac{1}{r^2} L^2 \Phi_{\rm p}, \tag{4.139a}$$

$$B_\theta = \frac{1}{r} \frac{\partial^2 \Phi_{\rm p}}{\partial r \partial \theta}, \tag{4.139b}$$

$$B_\phi = -\frac{1}{r} \frac{\partial \Phi_{\rm T}}{\partial \theta}, \tag{4.139c}$$

with

$$L^2 = -\frac{1}{\sin\theta} \frac{\partial}{\partial \theta} \left(\sin\theta \frac{\partial}{\partial \theta} \right). \tag{4.140}$$

The r-component, or the θ-component, of (4.136) together with the field components (4.139a), (4.139b), and (4.139c) leads to the poloidal scalar equation

$$\nabla^2 \left(\frac{\Phi_{\rm p}}{r} \right) - \frac{v_r}{r\eta} \frac{\partial \Phi_{\rm p}}{\partial r} = 0. \tag{4.141}$$

The first term represents the diffusion of poloidal field, while the second term corresponds to the advection, stretching and compression of poloidal flux tubes by the induced poloidal flow. The induced $v_r B_\theta$ electric field leads to a toroidal current density J_ϕ which acts as the source of the poloidal field perturbation.

The ϕ-component of (4.136) and the field components (4.139a), (4.139b), and (4.139c) give the toroidal scalar equation

$$\nabla^2\left(\frac{\Phi_{\mathrm{T}}}{r}\right)+\frac{1}{r\eta}\frac{d\eta}{dr}\frac{\partial\Phi_{\mathrm{T}}}{\partial r}-\frac{1}{r\eta}\frac{\partial}{\partial r}\left(v_r\Phi_{\mathrm{T}}\right)=-\frac{1}{r\eta}\frac{d\Omega}{dr}\sin\theta\frac{\partial\Phi_{\mathrm{p}}}{\partial\theta}. \tag{4.142}$$

The first two terms describe the diffusion of toroidal field, while the third term corresponds to advection, compression and stretching of toroidal flux tubes by the poloidal flow. The last term is a source of B_ϕ due to the radial shearing of $\mathbf{B}_{\mathrm{p}}$. The induced poloidal current density $\mathbf{J}_{\mathrm{p}}$ acts as a source of B_ϕ. The balance between toroidal field creation, advection, compression, stretching and diffusion determines the values of the ratio $|B_\phi/B_{\mathrm{p}}|$. The values of this ratio at the surface of the secondary influence the amount of poloidal field winding in the magnetosphere.

It will be argued that $(B_{\phi\mathrm{s}}/B_{\mathrm{ps}})^2$ remains significantly less than unity due to natural quenching processes. The magnetosphere will then adjust to a nearly force-free state having

$$\mathbf{J}\times\mathbf{B}=\mathbf{0}. \tag{4.143}$$

For moderate field winding the magnetosphere will remain near corotation with the primary, and J_ϕ will be ignorable relative to J_{p}. The poloidal magnetic field will then be approximately current-free, with Φ_{p} satisfying

$$\nabla^2\left(\frac{\Phi_{\mathrm{p}}}{r}\right)=0. \tag{4.144}$$

Equation (4.143) yields

$$\mathbf{B}_{\mathrm{p}}\cdot\nabla(r\sin\theta B_\phi)=0, \tag{4.145}$$

so $r\sin\theta B_\phi$ is conserved along poloidal field lines, corresponding to $\mathbf{J}_{\mathrm{p}}$ being nearly parallel to $\mathbf{B}_{\mathrm{p}}$. Using (4.139a), (4.139b), and (4.139c) for the field components in (4.145) gives the surface condition

$$\left[(L^2\Phi_{\mathrm{p}})\frac{\partial^2\Phi_{\mathrm{T}}}{\partial r\partial\theta}-\frac{\partial^2\Phi_{\mathrm{p}}}{\partial r\partial\theta}(L^2\Phi_{\mathrm{T}})\right]_{\mathrm{s}}=0. \tag{4.146}$$

4.3.4 The Poloidal Scalar

Equations (4.124), (4.126) and (4.139a) and (4.139b), relating $\mathbf{B}_\mathrm{p}$, Ψ_m and Φ_p, give the poloidal scalar for the unperturbed primary magnetic field as

$$\Phi_\mathrm{p} = -\frac{\mu_0 m}{8\pi D^3} r^2 P_1. \tag{4.147}$$

The poloidal magnetic field corresponding to this scalar penetrates the secondary due to diffusion and is modified by the induced motions. The associated toroidal current density is the source of the induced poloidal field. The external form of Φ_p/r for the induced field must satisfy the Laplace equation (4.144) and vanish as $r \to \infty$. This gives a dependence of $P_1(\cos\theta)/r$ for the induced external Φ_p field, and the total external poloidal scalar is the sum of the unperturbed and induced parts giving

$$\Phi_\mathrm{p}^\mathrm{ex} = -\frac{\mu_0 m R_\mathrm{s}^2}{8\pi D^3} \xi^2 P_1 + \frac{C}{\xi} P_1, \tag{4.148}$$

where C is a constant and ξ is a dimensionless radial length given by

$$\xi = \frac{r}{R_\mathrm{s}}. \tag{4.149}$$

The induced poloidal scalar inside the secondary must satisfy the poloidal induction equation (4.141) and have the form

$$\Phi_\mathrm{p} = A f(\xi) P_1, \tag{4.150}$$

where A is a constant. Substitution of this in (4.141), using (4.127) and (4.128) for v_r and (4.137) for η, yields the poloidal radial equation

$$\xi^2 f'' - p\epsilon \xi^\alpha f' - 2f = 0, \tag{4.151}$$

where

$$\alpha = k - m + 2, \tag{4.152}$$

and

$$\epsilon = \frac{R_\mathrm{s}^2}{\delta_\mathrm{s}^2}, \tag{4.153a}$$

with

$$\delta_{\rm s} = \left(\frac{\eta_{\rm s}}{\omega}\right)^{\frac{1}{2}} \tag{4.153b}$$

with $p = \pm 1$ corresponding to $v_r > 0$ and $v_r < 0$. The condition of continuity of $\mathbf{B}_{\rm p}$ at $r = R_{\rm s}$ leads to the surface conditions of the continuity of $\Phi_{\rm p}$ and $\partial\Phi_{\rm p}/\partial r$. Applying these, using (4.148) and (4.150), gives the external and internal solutions

$$\Phi_{\rm p}^{\rm ex} = -\frac{\mu_0 m R_{\rm s}^2}{8\pi D^3}\left[\xi^2 + \left(\frac{2f(1) - f'(1)}{f(1) + f'(1)}\right)\frac{1}{\xi}\right] P_1, \tag{4.154}$$

$$\Phi_{\rm p} = -\frac{3\mu_0 m R_{\rm s}^2}{8\pi D^3}\frac{f(\xi)}{[f(1) + f'(1)]} P_1. \tag{4.155}$$

As synchronism is approached $\epsilon \to 0$ and the differential equation (4.151) yields the asymptotic form $f(\xi) \sim \xi^2$, corresponding to $\Phi_{\rm p}$ having its unperturbed form (4.147) everywhere.

Equation (4.151) must be solved for $f(\xi)$ in the outflow and inflow regions, corresponding to $p = \pm 1$ respectively. Since η in a convective star has a radial length-scale much longer than that of the induced v_r function, it follows that $k - m > 0$ is satisfied and consequently (4.151) has a regular singularity at $\xi = 0$. Application of the Frobenius series method leads to two linearly independent solutions having the asymptotic forms of ξ^2 and ξ^{-1} near $\xi = 0$, with the first solution giving the required non-singular behaviour at $\xi = 0$. This solution is given by

$$f(\xi) = \sum_{i=0}^{\infty} a_{(\alpha-1)i}\xi^{2+(\alpha-1)i} \tag{4.156}$$

with

$$a_{(\alpha-1)i} = \left(\frac{p\epsilon}{\alpha - 1}\right)^i \frac{\Gamma[3(\alpha-1)^{-1} + 1]\Gamma[i + 2(\alpha-1)^{-1}]}{\Gamma[2(\alpha-1)^{-1}]\Gamma[i + 3(\alpha-1)^{-1} + 1]\Gamma(i+1)}, \tag{4.157}$$

where Γ is the gamma function and $a_0 = 1$ has been chosen. Taking the first 40 terms gives an accurate solution. Equation (4.151) can also be solved using a fourth order Runge-Kutta numerical scheme, but the series solution is more convenient to use.

4.3.5 The Toroidal Scalar

Using (4.155) for $\Phi_{\rm p}$ in the source term of (4.142) yields the toroidal scalar equation

$$\nabla^2\left(\frac{\Phi_{\rm T}}{r}\right)+\frac{1}{r\eta}\frac{\partial\Phi_{\rm T}}{\partial r}-\frac{1}{r\eta}\frac{\partial}{\partial r}(v_r\Phi_{\rm T})=\frac{E}{r\eta}\frac{d\Omega}{dr}f(\xi)\sin\theta\frac{dP_1}{d\theta}, \tag{4.158}$$

where

$$E=\frac{3\mu_0 m R_{\rm s}^2}{8\pi D^3}\frac{1}{[f(1)+f'(1)]}. \tag{4.159}$$

Noting that

$$\sin\theta\frac{dP_1}{d\theta}=\frac{2}{3}(P_2-P_0), \tag{4.160}$$

it follows that the source term contains the harmonics $l=0$ and $l=2$. Because the harmonic $l=0$ is independent of θ, it follows from (4.139a) and (4.139b) for B_r and B_θ that this will make no source contribution to B_ϕ since it would give a $\Phi_{\rm p}$ term with no θ dependence which would make no contribution to $\mathbf{B}_{\rm p}$ in the source term $\mathbf{B}_{\rm p}\cdot\nabla\Omega$. Hence only the P_2 term is relevant in (4.160) and $\Phi_{\rm T}$ has the form

$$\Phi_{\rm T}=g(\xi)P_2(\cos\theta), \tag{4.161}$$

where

$$P_2(\cos\theta)=\frac{1}{2}(3\cos^2\theta-1). \tag{4.162}$$

Substituting (4.160), with the P_0 term dropped, together with (4.161) for $\Phi_{\rm T}$ into (4.158), using (4.127)–(4.130) and (4.137) for v_r, Ω and η, leads to the toroidal scalar radial equation

$$g''+\left(\frac{m}{\xi}-p\epsilon\xi^{\alpha-2}\right)g'-\left(\frac{6}{\xi^2}+p\epsilon k\xi^{\alpha-3}\right)g=F(\xi), \tag{4.163}$$

where

$$F(\xi)=\gamma n\epsilon\frac{\mu_0 m R_{\rm s}}{4\pi D^3}\frac{\xi^{n-m-1}}{[f(1)+f'(1)]}f(\xi). \tag{4.164}$$

This equation has $p=\pm1$ corresponding to $v_r>0$ and $v_r<0$, while $\gamma=\pm1$ corresponds to $\Omega>0$ and $\Omega<0$ respectively. Equation (4.163) must be solved subject to boundary conditions at $\xi=0$ and $\xi=1$. To avoid a singularity at $\xi=0$,

(4.139c) for B_ϕ together with (4.161) for $\Phi_{\rm T}$ requires

$$g(0) = 0. \tag{4.165}$$

The surface condition follows by substituting $\Phi_{\rm p}$ and $\Phi_{\rm T}$ from (4.150) and (4.161) in the force-free surface condition (4.146), yielding

$$g'(1) - \frac{f'(1)}{f(1)} q(\theta) g(1) = 0, \tag{4.166}$$

where

$$q(\theta) = \frac{1}{2}\left(1 - \frac{1}{3\cos^2\theta}\right). \tag{4.167}$$

The function $q(\theta)$ is slowly varying, apart from an interval of $\simeq 30°$ centred on the equator. However, the surface stress $B_{rs} B_{\phi s}$ becomes small in this interval, vanishing as $\cos^2\theta$ at $\theta = 90°$, and it only makes a small contribution to the torque integral. Hence only the intervals $0° < \theta \lesssim 75°$ and $105° \lesssim \theta < 180°$ are significant. The function $q(\theta)$ has a variation of $-2 < \theta < 1/3$ over these intervals, with an average value of close to $\langle q(\theta)\rangle = -1$. This average value is used in the surface condition (4.166), and this is consistent with the θ average which was adopted for the surface values of the magnetospheric velocity components.

The inhomogeneous differential equation (4.163) can be solved by the method of variation of parameters. This is equivalent to a solution given by the integral

$$g(\xi) = \int_0^1 G(\xi, s) F(s) ds, \tag{4.168}$$

where the Green's function is

$$G(\xi, s) = \begin{cases} u_1(s) u_2(\xi)/W(s), & 0 \le s \le \xi, \\ u_2(s) u_1(\xi)/W(s), & \xi \le s \le 1, \end{cases} \tag{4.169}$$

having

$$u_1(\xi) = a v_1(\xi), \tag{4.170}$$

$$u_2(\xi) = b v_1(\xi) + c v_2(\xi), \tag{4.171}$$

with a, b and c constants, while $v_1(\xi)$ and $v_2(\xi)$ are linearly independent solutions of the associated homogeneous equation

$$v'' + \left(\frac{m}{\xi} - p\epsilon\xi^{\alpha-2}\right) v' - \left(\frac{6}{\xi^2} + p\epsilon k \xi^{\alpha-3}\right) v = 0, \tag{4.172}$$

and the Wronskian is

$$W = u_1 u_2' - u_1' u_2. \tag{4.173}$$

The Green's function $G(\xi, s)$ must satisfy the centre and surface conditions.

Because $\alpha - 2 = k - m > 0$, (4.172) has a regular singularity at $\xi = 0$ so the Frobenius method can be used to find the fundamental solutions v_1 and v_2. The roots of the indicial equation are

$$\beta_1 = \frac{1}{2}\left(\left[(m-1)^2 + 24\right]^{\frac{1}{2}} - (m-1)\right), \tag{4.174}$$

$$\beta_2 = -\frac{1}{2}\left(\left[(m-1)^2 + 24\right]^{\frac{1}{2}} + (m-1)\right), \tag{4.175}$$

giving $\beta_1 > 0$ and $\beta_2 < 0$. The solutions are

$$v_1(\xi) = \sum_{i=0}^{\infty} b_{(\alpha-1)i}(\beta_1)\xi^{\beta_1+(\alpha-1)i}, \tag{4.176}$$

$$v_2(\xi) = \sum_{i=0}^{\infty} b_{(\alpha-1)i}(\beta_2)\xi^{\beta_2+(\alpha-1)i}, \tag{4.177}$$

with

$$b_{(\alpha-1)i}(\beta) = \left(\frac{p\epsilon}{\alpha-1}\right)^i \frac{\Gamma[(2\beta+m-1)(\alpha-1)^{-1}+1]\Gamma[i+(\beta+k)(\alpha-1)^{-1}]}{\Gamma[(\beta+k)(\alpha-1)^{-1}]\Gamma[i+(2\beta+m-1)(\alpha-1)^{-1}+1]\Gamma(i+1)}, \tag{4.178}$$

where $b_0 = 1$ has been chosen and β is β_1 or β_2. The solution (4.177) for $v_2(\xi)$ is valid for $k > 2|\beta_2|$. Lower values of k would lead to a solution containing a logarithmic term, but this does not occur here because the short radial length-scale of v_r requires larger values of k. Accurate expressions result for v_1 and v_2 by taking the first 40 terms in the series.

Equations (4.170) and (4.171) for u_1 and u_2 give the Wronskian as

$$W = ac(v_1 v_2' - v_1' v_2). \tag{4.179}$$

A closed expression can be found for W. Writing $U = v_1 v_2' - v_1' v_2$, using $v = v_1$ and then $v = v_2$ in (4.172), multiplying the first equation by v_2 and the second by

v_1 and subtracting yields

$$U' - \left(p\epsilon\xi^{\alpha-2} - \frac{m}{\xi} \right) U = 0. \tag{4.180}$$

The solution of this contains an arbitrary constant which can be determined by equating the solution to another expression for U obtained by using the series solutions for v_1 and v_2. Then cancelling a common factor of ξ^{-m}, noting $m = 1 - \beta_1 - \beta_2$, $b_0(\beta_1) = b_0(\beta_2) = 1$ and putting $\xi = 0$ yields the constant. This gives

$$W = ac(\beta_2 - \beta_1)\xi^{-m} \exp\left[p\epsilon\xi^{\alpha-1}/(\alpha - 1) \right]. \tag{4.181}$$

The Green's function, given by (4.169), must satisfy the boundary conditions. Equations (4.170) and (4.176) show that u_1 satisfies the central condition (4.165). The product ac cancels in the ratio $u_1 u_2 / W$, leaving b/c. This ratio is determined by ensuring that u_2, given by (4.171), satisfies the surface condition (4.166) and this gives

$$\frac{b}{c} = -\frac{\left[f(1)v_2'(1) - qf'(1)v_2(1) \right]}{\left[f(1)v_1'(1) - qf'(1)v_1(1) \right]}. \tag{4.182}$$

The solution (4.168) then becomes

$$g(\xi) = -\frac{\gamma n\epsilon}{2(\beta_1 + |\beta_2|)} \left(\frac{R_\mathrm{p}}{D} \right)^3 R_\mathrm{s} B_0 \left[v_1(\xi) I_1(\xi) + \left\{ \frac{b}{c} v_1(\xi) + v_2(\xi) \right\} I_2(\xi) \right], \tag{4.183}$$

$$I_1(\xi) = \int_\xi^1 \left\{ \frac{b}{c} v_1(s) + v_2(s) \right\} s^{n-1} f_\mathrm{N}(s) \exp\left[-p\epsilon s^{\alpha-1}/(\alpha - 1) \right] ds, \tag{4.184}$$

$$I_2(\xi) = \int_0^\xi v_1(s) s^{n-1} f_\mathrm{N}(s) \exp\left[-p\epsilon s^{\alpha-1}/(\alpha - 1) \right] ds, \tag{4.185}$$

with

$$f_\mathrm{N}(\xi) = \frac{f(\xi)}{f(1) + f'(1)}. \tag{4.186}$$

The integrals are evaluated numerically.

4.3.6 The Magnetic Field Components

The magnetic field components are found from (4.139a), (4.139b), and (4.139c) using (4.155) for $\Phi_{\rm p}$ and (4.161) for $\Phi_{\rm T}$. This gives

$$B_r = -\frac{3}{2}B_0\left(\frac{R_{\rm p}}{D}\right)^3 f_r(\xi)\cos\theta, \tag{4.187}$$

$$B_\theta = \frac{3}{4}B_0\left(\frac{R_{\rm p}}{D}\right)^3 f_\theta(\xi)\sin\theta, \tag{4.188}$$

$$B_\phi = -\frac{3}{2}\left(\frac{R_{\rm p}}{D}\right)^3 f_\phi(\xi)\sin\theta\cos\theta, \tag{4.189}$$

where

$$f_r(\xi) = \frac{f_{\rm N}(\xi)}{\xi^2}, \tag{4.190}$$

$$f_\theta(\xi) = \frac{f'_{\rm N}(\xi)}{\xi}, \tag{4.191}$$

$$f_\phi(\xi) = \frac{\gamma n\epsilon}{(\beta_1+|\beta_2|)}\frac{1}{\xi}\left[v_1(\xi)I_1(\xi) + \left\{\frac{b}{c}v_1(\xi)+v_2(\xi)\right\}I_2(\xi)\right]. \tag{4.192}$$

The radial dependences are calculated for the inflow and outflow regions, for a range of degrees of asynchronism. The dimensionless quantity ϵ, given by (4.153a), can be expressed as

$$\epsilon = \frac{R_{\rm s}^2}{\eta_{\rm s}}\Omega_{\rm o}\left(\frac{\omega}{\Omega_{\rm o}}\right). \tag{4.193}$$

Using (4.84c) and (4.87) to eliminate $R_{\rm s}$ and $\Omega_{\rm o}$ then gives

$$\epsilon = \frac{2\times10^5(M_{\rm s}/M_\odot)}{(\eta_{\rm s}/5\times10^8\,{\rm m^2\,s^{-1}})}\frac{\omega}{\Omega_{\rm o}}. \tag{4.194}$$

The condition for moderate perturbation of the magnetosphere is that the field winding ratio satisfies $(B_{\phi{\rm s}}/B_{\rm ps})^2 \ll 1$, corresponding to $|J_\phi/J_{\rm p}| \ll 1$ and $\mathbf{B}_{\rm p}$ approximately current-free, with the magnetosphere close to corotation with the primary star. Values must be chosen for k, n and m, corresponding to the power law dependences of v_r, Ω and η respectively. For a realistic range of values of these quantities, and other parameters, it is found that the condition $|B_{\phi{\rm s}}/B_{\rm ps}| < 1$ is violated for $\omega/\Omega_{\rm o} \gtrsim 10^{-2}$. However, situations with $|B_{\phi{\rm s}}/B_{\rm ps}|$ significantly greater than unity are likely to be unstable and are inconsistent with near corotation. For

$\omega/\Omega_o > 10^{-2}$ the assumption of corotation leads to supersonic values of $|v_r|$ in the surface layers of the secondary. This would lead to the formation of shocks and high dissipation and it is expected that corotation of the magnetosphere would then break down in the region of the secondary's surface. Such processes would lower the values of the shear and the induced poloidal flow speeds due to interaction with the perturbed magnetosphere. To account for these processes, a quenching term can be introduced into (4.194) to give

$$\epsilon = \frac{2 \times 10^5 (M_s/M_\odot)}{(\eta_s/5 \times 10^8 \,\mathrm{m^2\,s^{-1}})} \frac{(\omega/\Omega_o)}{[1 + N(|\omega|/\Omega_o)^s]}, \tag{4.195}$$

where N and s are positive constants. The value of N is taken so the effects of asynchronism begin to saturate as $|B_{\phi s}/B_{ps}|$ approaches unity. This quenching term is equivalent to enhancing η_s by a factor of $1 + N(|\omega|/\Omega_o)^s$, corresponding to a dynamically enhanced diffusivity.

A typical example is considered with $M_s = 0.3\,M_\odot$, $\eta_s = 5 \times 10^8\,\mathrm{m^2\,s^{-1}}$, $q = -1$, $k = 6$, $n = 8$, $m = 0$, $N = 2 \times 10^4$ and $s = 1$. Figures 4.4 and 4.5 show the radial variations of B_r for the inflow and outflow regions, for two degrees of asynchronism. The inflow causes field to be accumulated in the inner parts of the secondary, so $f_r(\xi)$ increases with decreasing ξ, as illustrated in Fig. 4.4. The field strength is increased from its unperturbed values by the inflow for all ξ, corresponding to an anti-skin depth effect at higher asynchronism. The

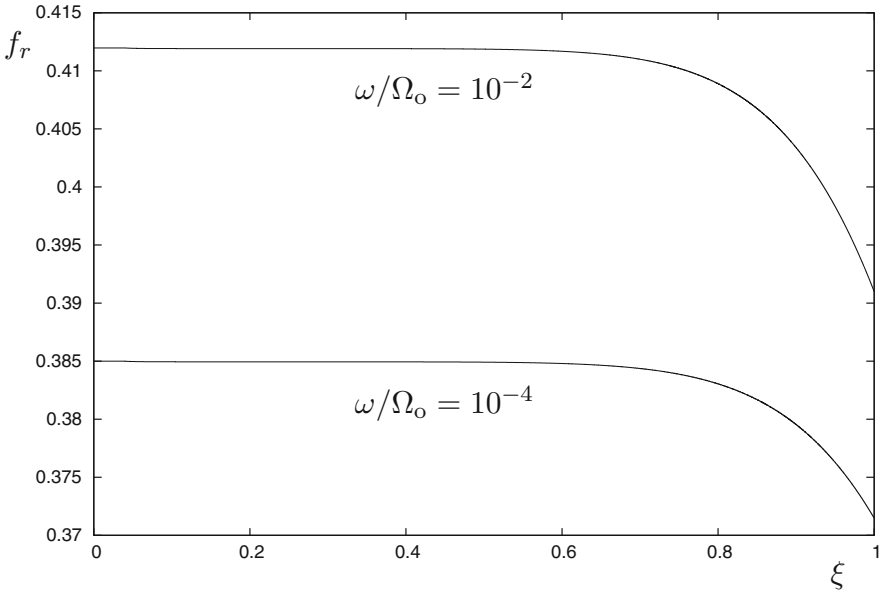

Fig. 4.4 The function $f_r(\xi)$ for the inflow regions

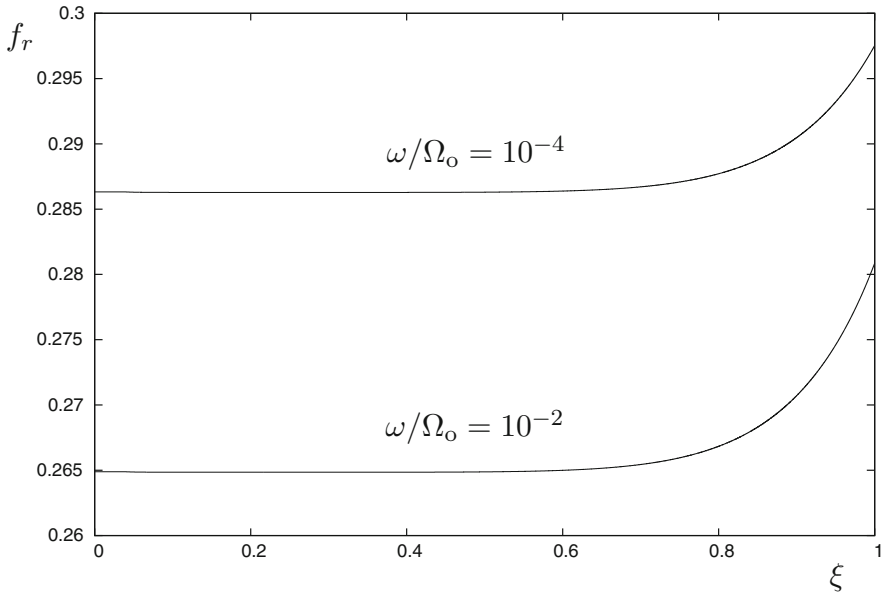

Fig. 4.5 The function $f_r(\xi)$ for the outflow regions

outflow accumulates field in the outer parts of the secondary, so $f_r(\xi)$ increases with increasing ξ, as shown in Fig. 4.5. The field strength is reduced from its unperturbed values by the outflow for all ξ, giving a skin depth effect at higher asynchronism. In both cases $f_r(\xi)$ is nearly independent of ξ in the inner regions, corresponding to a nearly uniform B_r. The unperturbed field $\mathbf{B}_0$ is independent of r across the secondary, to lowest order in R_s/D. The inflow leads to an enhanced uniform field in the central region, and a non-uniform field in the outer regions. The outflow causes a reduced uniform field in the inner region, and a non-uniform field in the outer regions. As $\omega/\Omega_o \to 0$, so the inflows and outflows become small, the poloidal field reverts to its uniform, unperturbed current-free state.

Similar behaviour occurs for B_θ in the inflow and outflow regions, as illustrated in Figs. 4.6 and 4.7. The effects are larger for this field component since advection, compression and stretching are more effective.

The variations of $|f_\phi(\xi)|$ are shown in Figs. 4.8 and 4.9. The inflow enhances the values of $|B_\phi|$ since its source B_r is enhanced in these regions. Conversely, in the outflow regions $|B_\phi|$ is reduced due to the lowered values of B_r. The toroidal field vanishes as $\omega \to 0$ since the shear creation term vanishes as synchronism is approached.

The values taken for k and n, which are measures of the radial length-scales of v_r and Ω, ensure that the magnetically induced motions are localised to the outer regions of the secondary where the perturbation to its structure is significant. However, it is noted from the above results that the effects of the induced surface region motions on the magnetic field are distributed throughout the star.

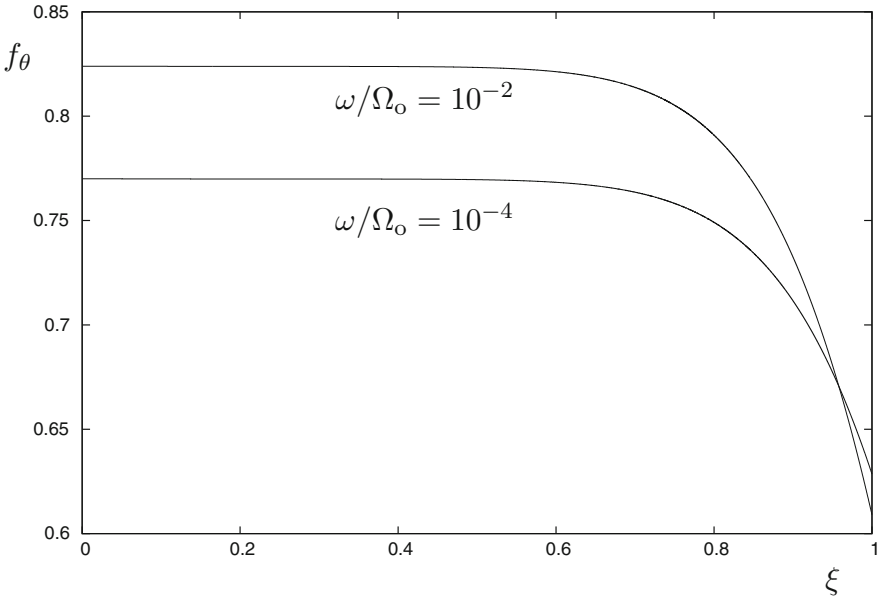

Fig. 4.6 The function $f_\theta(\xi)$ for the inflow regions

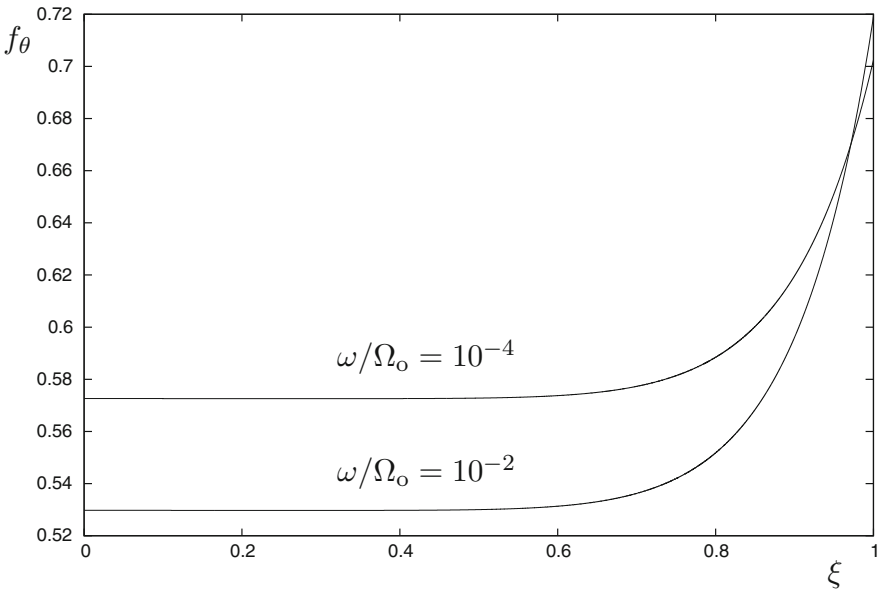

Fig. 4.7 The function $f_\theta(\xi)$ for the outflow regions

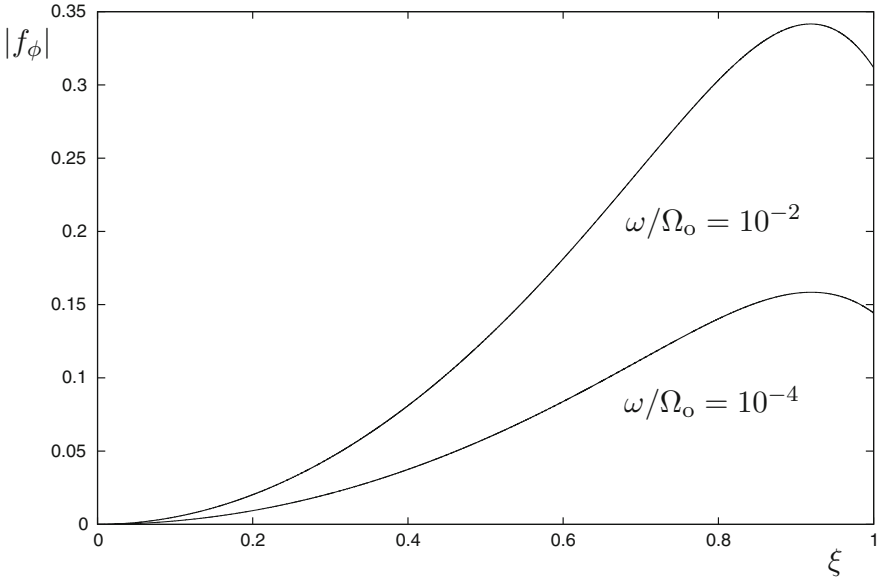

Fig. 4.8 The function $|f_\phi(\xi)|$ for the inflow regions

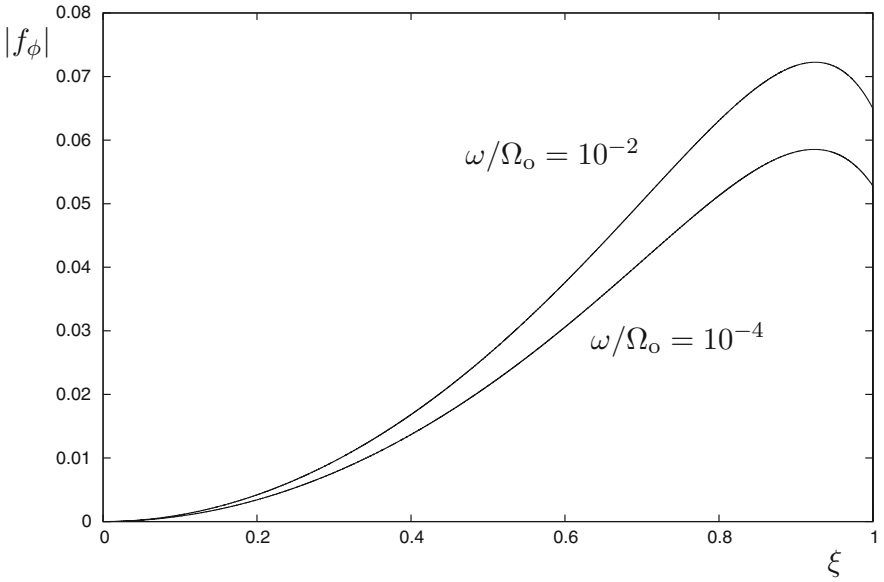

Fig. 4.9 The function $|f_\phi(\xi)|$ for the outflow regions

The field winding ratio must satisfy the condition $(B_{\phi s}/B_{ps})^2 \ll 1$ to justify ignoring $|J_\phi|$ relative to J_p in the magnetosphere. This corresponds to the perturbed $\mathbf{B}_p$ being approximately current-free in the magnetosphere. The field component equations (4.187)–(4.189) give

$$\frac{|B_{\phi s}|}{B_{ps}} = \frac{|f_{\phi s} \sin\theta \cos\theta|}{\left(f_{rs}^2 \cos^2\theta + \frac{1}{4} f_{\theta s}^2 \sin^2\theta\right)^{\frac{1}{2}}}. \tag{4.196}$$

A consideration of the values of f_{rs} and $f_{\theta s}$ for $0 \le \omega/\Omega_o \le 0.1$ shows that f_{rs} and $f_{\theta s}/2$ only differ by small amounts, so a small ratio can be defined as

$$\tilde{\epsilon} = \frac{\frac{1}{2} f_{\theta s} - f_{rs}}{f_{rs}}. \tag{4.197}$$

Using this in (4.196), and expanding to first order in $\tilde{\epsilon}$, leads to a maximum value for the winding ratio at

$$\sin\theta = \frac{1}{\sqrt{2}}\left(1 - \frac{1}{4}\tilde{\epsilon}\right). \tag{4.198}$$

The inflow regions have $\tilde{\epsilon} < 0$, while the outflow regions have $\tilde{\epsilon} > 0$. Using (4.198) in (4.196) leads to the first order result

$$\left|\frac{B_{\phi s}}{B_{ps}}\right|_{max} = \frac{1}{2}\frac{|f_{\phi s}|}{f_{rs}}\left(1 - \frac{1}{2}\tilde{\epsilon}\right). \tag{4.199}$$

Figure 4.10 shows $|B_{\phi s}/B_{ps}|_{max}$ as a function of ω/Ω_o, for the inflow and outflow regions. It is seen that $(B_{\phi s}/B_{ps})^2$ is sufficiently small everywhere on the surface of the secondary to justify the approximation of nearly current-free $\mathbf{B}_p$ in the magnetosphere.

4.3.7 *Magnetic Torques*

The electric current density induced in the secondary leads to a force distribution over its volume. This results in a torque on the star and a non-central force on its centre of mass. The magnetic torque is

$$\begin{aligned}\mathbf{T}_s &= \frac{1}{\mu_0}\int_V \mathbf{r} \times [(\nabla \times \mathbf{B}) \times \mathbf{B}]\, dV \\ &= \frac{1}{\mu_0}\int_S (\mathbf{r} \times \mathbf{B})\mathbf{B} \cdot d\mathbf{S} - \frac{1}{\mu_0}\int_S B^2 \mathbf{r} \times d\mathbf{S}.\end{aligned} \tag{4.200}$$

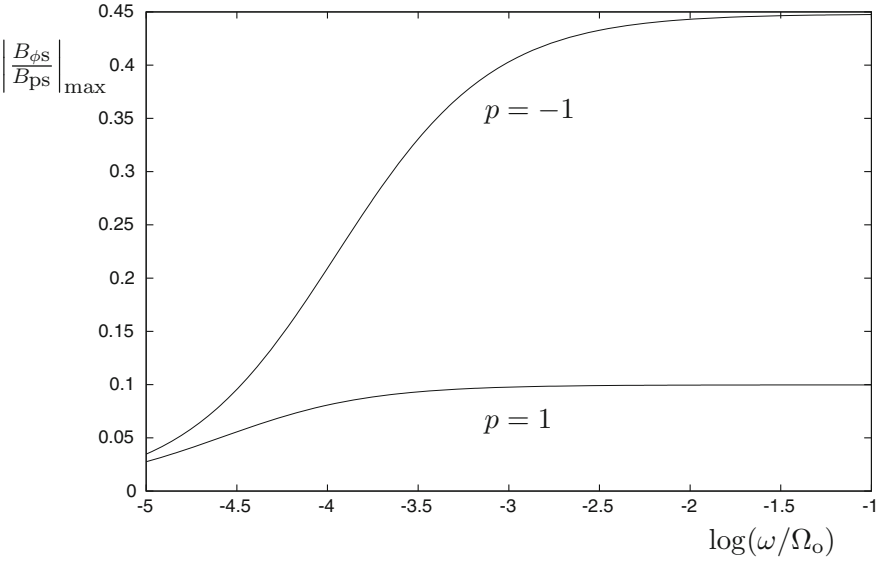

Fig. 4.10 The ratio $\left|B_{\phi s}/B_{ps}\right|_{max}$ for the inflow ($p = -1$) and outflow ($p = 1$) regions

The second surface integral vanishes for a sphere, while the first gives

$$\mathbf{T}_s = \frac{1}{\mu_0}\int_S r \sin\theta B_r B_\phi \, dS \, \hat{\mathbf{z}}, \tag{4.201}$$

where $dS = r^2 \sin\theta d\theta d\phi$.

It follows from (4.187)–(4.189), and the associated functions of ξ, that the field components have the symmetry properties given by

$$B_r^{\rm I}(r,\theta) = B_r^{\rm IV}(r,\theta), \qquad B_r^{\rm II}(r,\theta) = B_r^{\rm III}(r,\theta), \tag{4.202}$$

$$B_\theta^{\rm I}(r,\theta) = B_r^{\rm IV}(r,\theta), \qquad B_\theta^{\rm II}(r,\theta) = B_\theta^{\rm III}(r,\theta), \tag{4.203}$$

$$B_\phi^{\rm I}(r,\theta) = -B_\phi^{\rm IV}(r,\theta), \qquad B_\phi^{\rm II}(r,\theta) = -B_\phi^{\rm III}(r,\theta), \tag{4.204}$$

where the superscripts refer to the azimuthal regions given by (4.132)–(4.135). Evaluating the torque integral (4.201), using (4.202) and (4.204), leads to

$$\mathbf{T}_s = -\frac{6}{5}\phi_1 \frac{(B_p)_0^2}{\mu_0}\left(\frac{R_p}{D}\right)^6 R_s^3 \left[f_r^{\rm I} f_\phi^{\rm I} + f_r^{\rm II} f_\phi^{\rm II}\right]_{\xi=1} \hat{\mathbf{z}}. \tag{4.205}$$

This takes into account the change in the sign of Ω around the secondary, and the contributions from the inflow and outflow regions.

The magnetic force exerted on the centre of mass of the secondary is

$$\mathbf{F}_{\rm s} = \frac{1}{\mu_0}\int_V (\nabla \times \mathbf{B}) \times \mathbf{B}\, dV = \frac{1}{\mu_0}\int_S \mathbf{B} B_r\, dS - \frac{1}{\mu_0}\int_S B^2 dS\, \hat{\mathbf{r}}. \tag{4.206}$$

There is an equal and opposite force on the centre of mass of the primary. These forces only have components in the orbital plane, with the components normal to the line of stellar centres leading to torques about the centre of mass of the binary and a magnetic orbital torque

$$\mathbf{T}_{\rm mo} = D F_{{\rm s}x}\hat{\mathbf{z}}. \tag{4.207}$$

Equation (4.206) yields

$$F_{{\rm s}x} = \frac{1}{\mu_0}\int_S B_x B_r\, dS - \frac{1}{2\mu_0}\int_S B^2 \sin\theta\cos\phi\, dS, \tag{4.208}$$

with

$$B_x = \sin\theta\cos\phi B_r + \cos\theta\cos\phi B_\theta - \sin\phi B_\phi. \tag{4.209}$$

Evaluating the surface integrals, employing the azimuthal symmetry properties of the components, leads to

$$\begin{aligned}\mathbf{T}_{\rm mo} = &\frac{9\pi}{32}\frac{(B_{\rm p})_0^2}{\mu_0}\left(\frac{R_{\rm p}}{D}\right)^6 R_{\rm s}^2 D\left[\left(f_r^{\rm I\,2} - f_r^{\rm II\,2}\right) - \left(f_r^{\rm I} f_\theta^{\rm I} - f_r^{\rm II} f_\theta^{\rm II}\right)\right.\\ &\left. -\frac{3}{4}\left(f_\theta^{\rm I\,2} - f_\theta^{\rm II\,2}\right) - 2\left(f_r^{\rm I} f_\phi^{\rm I} + f_r^{\rm II} f_\phi^{\rm II}\right)\cos\phi_1 - \frac{1}{2}\left(f_\phi^{\rm I\,2} - f_\phi^{\rm II\,2}\right)\right]_{\xi=1}\hat{\mathbf{z}}.\end{aligned} \tag{4.210}$$

The stellar and orbital magnetic torques must balance since there is no magnetic coupling associated with these torques outside the binary system, because the poloidal field lines will be closed for moderate twisting. Hence the primary torque can be expressed as

$$\mathbf{T}_{\rm p} = -(\mathbf{T}_{\rm s} + \mathbf{T}_{\rm mo}). \tag{4.211}$$

Then the use of (4.205) for $\mathbf{T}_{\rm s}$ and (4.210) for $\mathbf{T}_{\rm mo}$ yields the inductive torque

$$\mathbf{T}_{\rm p} = -\frac{9\pi}{32}\frac{(B_{\rm p})_0^2}{\mu_0}\left(\frac{R_{\rm p}}{D}\right)^6 R_{\rm s}^2 D F(\omega, \eta_{\rm s})\hat{\mathbf{z}}, \tag{4.212}$$

where

$$F(\omega,\eta_{\rm s})=\Bigg[\left(f_r^{\rm I\,2}-f_r^{\rm II\,2}\right)-\left(f_r^{\rm I}f_\theta^{\rm I}-f_r^{\rm II}f_\theta^{\rm II}\right)-\frac{3}{4}\left(f_\theta^{\rm I\,2}-f_\theta^{\rm II\,2}\right)$$
$$-\frac{1}{2}\left(f_\phi^{\rm I\,2}-f_\phi^{\rm II\,2}\right)-2\left(\cos\phi_1+\frac{32}{15}\frac{\phi_1}{\pi}\frac{R_{\rm s}}{D}\right)\left(f_r^{\rm I}f_\phi^{\rm I}+f_r^{\rm II}f_\phi^{\rm II}\right)\Bigg]_{\xi=1}. \tag{4.213}$$

It can be shown that $F(-\omega,\eta_{\rm s})=-F(\omega,\eta_{\rm s})$, so the inductive torque is antisymmetric in ω, as expected.

Figure 4.11 shows the torque function $F(\omega,\eta_{\rm s})$ for a range of $\omega/\Omega_{\rm o}$. The torque saturates at a maximum value due to quenching effects for $s=1$. It was seen that in the inflow regions the poloidal magnetic field is enhanced relative to its unperturbed state, so an anti-skin depth effect occurs for higher degrees of asynchronism. The opposite effect occurs in the outflow regions where the field is everywhere lower than in its unperturbed state, corresponding to a skin depth effect. The lowered field penetration due to outflows in the secondary results in a lowered value of $|B_{\phi{\rm s}}|$, with the converse being true in the inflow regions. Without quenching, $F(\omega,\eta_{\rm s})$ increases monotonically with ω since the anti-skin depth inflow regions make a larger contribution to the torque integral than the skin depth effect outflow regions. The quenching mechanism leads to a decrease in the rate of increase of $F(\omega,\eta_{\rm s})$ with ω. A turn down results if $s>1$ is taken, due to ϵ decreasing with increasing $\omega/\Omega_{\rm o}$ after reaching a maximum value. However, it is more likely that

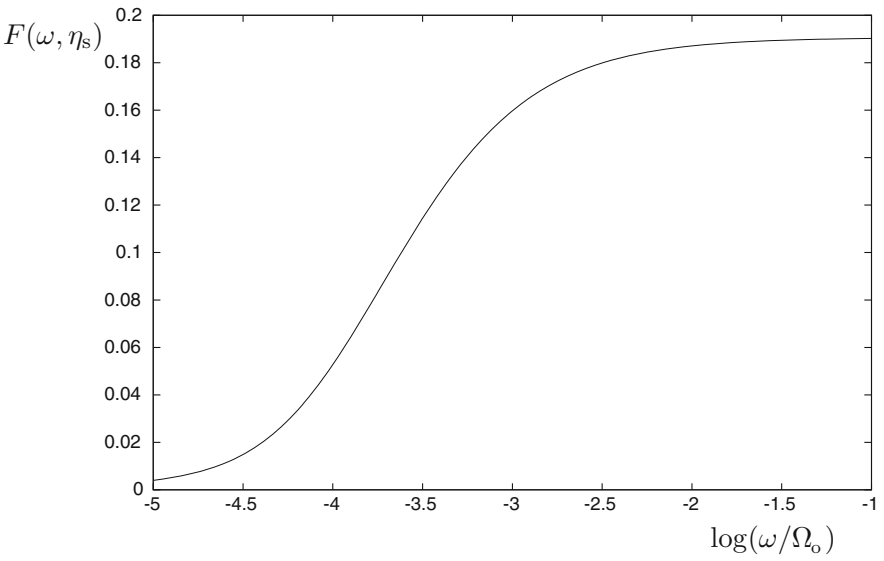

Fig. 4.11 The dimensionless primary magnetic torque function, with a magnetosphere

the quenching process will saturate ϵ at a maximum value, as described by the $s = 1$ case.

4.3.8 The Small Asynchronism Torque

A simplified expression can be obtained for $F(\omega, \eta_s)$ when ω/Ω_o is sufficiently small to give $\epsilon \ll 1$. The unquenched form (4.194) is then applicable for ϵ. To first order in ϵ, the solution (4.156) gives

$$f(\xi) = \xi^2 + a_{\alpha-1}\xi^{\alpha+1}, \tag{4.214}$$

where

$$a_{\alpha-1} = \frac{2p\epsilon}{(\alpha-1)(\alpha+2)}. \tag{4.215}$$

Using this in (4.190) and (4.191) yields

$$f_r(1) = \frac{1}{3}\left[1 - \frac{1}{3}(\alpha-1)a_{\alpha-1}\right], \tag{4.216}$$

$$f_\theta(1) = \frac{2}{3}\left[1 + \frac{1}{6}(\alpha-1)a_{\alpha-1}\right]. \tag{4.217}$$

The inflow and outflow cases correspond to $p = -1$ and $p = 1$ in (4.215) for $a_{\alpha-1}$.

It is noted that to calculate $f_\phi(\xi)$ to first order in ϵ, the square bracket term in (4.192) is only required to zeroth order since it is multiplied by a first order term arising from the $d\Omega/dr$ shear term. To zeroth order, the solutions (4.176) and (4.177) give

$$v_1(\xi) = \xi^{\beta_1} \tag{4.218a}$$

and

$$v_2(\xi) = \xi^{\beta_2}. \tag{4.218b}$$

A first order evaluation of f_ϕ then gives

$$f_\phi(1) = \frac{\gamma n\epsilon}{3(\beta_1 + 2|q|)(\beta_1 + n + 2)}, \tag{4.219}$$

with $\gamma = -1$ giving $f_\phi^{\rm I}(1) = f_\phi^{\rm II}(1)$. To this order only the unperturbed form of $\mathbf{B}_{\rm p}$ is required to calculate f_ϕ, so the inflow and outflow effects vanish. The unperturbed form of $\mathbf{B}_{\rm p}$ creates B_ϕ via a small shear.

Evaluating $F(\omega, \eta_{\rm s})$ to first order in ϵ and using the result in (4.212) leads to the torque expression

$$\mathbf{T}_{\rm p} = -\frac{\pi}{8} N \frac{(B_{\rm p})_0^2}{\mu_0} \left(\frac{R_{\rm p}}{D}\right)^6 R_{\rm s}^4 D \frac{\omega}{\eta_{\rm s}} \mathbf{k}, \tag{4.220}$$

where

$$N = \left(\cos\phi_1 + \frac{32}{15}\frac{\phi_1}{\pi}\frac{R_{\rm s}}{D}\right) \frac{n}{(\beta_1 + 2|q|)(\beta_1 + n + 2)} - \frac{4}{3(\alpha + 2)}. \tag{4.221}$$

This is in reasonable agreement with the expression (4.120) derived from the model of Kaburaki (1986). The Kaburaki model assumed small perturbations of the primary magnetic field, and the foregoing analysis shows this to be valid in the regime of sufficiently small asynchronism. The torque expression (4.220) is comparable to the small asynchronism vacuum case torque given by (4.92).

4.4 Orbital Evolution and Mass Transfer

4.4.1 Orbital Angular Momentum Evolution

The magnetic orbital torque affects the evolution rate of the orbital angular momentum and hence the mass loss rate from the secondary via Roche lobe overflow. The angular momentum evolution equations for the secondary, primary and orbit are

$$\dot{\mathbf{L}}_{\rm s} = \mathbf{T}_{\rm ms} + \mathbf{T}_{\rm tid}, \tag{4.222}$$

$$\dot{\mathbf{L}}_{\rm p} = \mathbf{T}_{\rm mp} + \mathbf{T}_{\rm a}, \tag{4.223}$$

$$\dot{\mathbf{L}}_{\rm o} = \mathbf{T}_{\rm mo} + \mathbf{T}_{\rm gr} - \mathbf{T}_{\rm tid} - \mathbf{T}_{\rm a}, \tag{4.224}$$

$$\dot{\mathbf{L}}_{\rm o} = \mathbf{T}_{\rm mo} + \mathbf{T}_{\rm br} - \mathbf{T}_{\rm tid} - \mathbf{T}_{\rm a}. \tag{4.225}$$

The torque $\mathbf{T}_{\rm tid}$ is due to tides, while $\mathbf{T}_{\rm gr}$ and $\mathbf{T}_{\rm br}$ are due to gravitational waves and magnetic wind braking. Equation (4.224) applies to systems with $P \lesssim 3\,{\rm h}$ and (4.225) to systems with $P \gtrsim 3\,{\rm h}$.

The magnetic secondary torque $\mathbf{T}_{\rm ms}$ will cause some spin evolution away from synchronism. However, a tidal torque will then operate and essentially cancel $\mathbf{T}_{\rm ms}$ so

the secondary is kept rotating close to synchronism with the orbital angular velocity $\boldsymbol{\Omega}_{\rm o}$ and consequently $\dot{\mathbf{L}}_{\rm s} \simeq \mathbf{0}$ holds. Hence (4.222) gives

$$T_{\rm ms} + T_{\rm tid} = 0, \tag{4.226}$$

where the vector notation is dropped since all the torques are in the z-direction. Using $T_{\rm ms} = -(T_{\rm mp}+T_{\rm o})$ and (4.226) to eliminate $T_{\rm ms}$ and $T_{\rm tid}$ in (4.224) and (4.225) yields

$$\dot{L}_{\rm o} = T_{\rm gr} - T_{\rm a} - T_{\rm mp}, \tag{4.227}$$

and

$$\dot{L}_{\rm o} = T_{\rm br} - T_{\rm a} - T_{\rm mp}. \tag{4.228}$$

The orbital angular momentum can be written as

$$L_{\rm o} = M_{\rm s} M_{\rm p} \left(\frac{GD}{M}\right)^{\frac{1}{2}}. \tag{4.229}$$

Using this and the Roche lobe formula (4.84b) leads to the evolution equation

$$\frac{\dot{R}_{\rm L}}{R_{\rm L}} = 2\frac{\dot{L}_{\rm o}}{L_{\rm o}} - 2\frac{\dot{M}_{\rm s}}{M_{\rm s}}\left(\frac{5}{6} - \frac{M_{\rm s}}{M_{\rm p}}\right). \tag{4.230}$$

Employing (4.84b) and the mass-radius relation (4.84c) gives

$$L_{\rm o} = 10^{\frac{1}{6}} q^{\frac{1}{2}} \left(\frac{GR_{\odot}}{M_{\odot}}\right)^{\frac{1}{2}} \frac{M_{\rm p} M_{\rm s}^{\frac{4}{3}}}{M^{\frac{1}{3}}}. \tag{4.231}$$

This then yields

$$\frac{\dot{L}_{\rm o}}{L_{\rm o}} = \left(\frac{4}{3} - \frac{M_{\rm s}}{M_{\rm p}}\right)\frac{\dot{M}_{\rm s}}{M_{\rm s}}. \tag{4.232}$$

Equations (4.231) and (4.232) give

$$\dot{L}_{\rm o} = 0.49 q^{\frac{1}{2}} \left(\frac{GR_{\odot}}{M_{\odot}}\right)^{\frac{1}{2}} \left(4 - 7\frac{M_{\rm s}}{M}\right)\left(\frac{M_{\rm s}}{M}\right)^{\frac{1}{3}} M\dot{M}_{\rm s}. \tag{4.233}$$

4.4.2 The Accretion and Magnetic Torques

The accretion torque and the magnetic orbital torque, for $\omega > 0$, cause increases and reductions in the mass transfer rates in AM Her systems compared to those in cataclysmic binaries with accretion discs. The angular momentum carried by material flowing from the L_1 region of the secondary is transferred to the primary via magnetic stresses acting through the accretion stream, leading to a large accretion torque. This transfer of orbital angular momentum causes an increase in the rate of shrinkage of the secondary's Roche lobe and hence an increase in its mass loss rate. This contrasts to systems with accretion discs in which the angular momentum is fed back into the orbit via tidal torques at the outer edge of the disc, so the material reaching the primary only exerts a small accretion torque.

For an over-synchronous primary, the magnetic orbital torque transfers angular momentum to the orbit and slows the shrinkage rate of the secondary's Roche lobe, hence decreasing its rate of mass loss via the L_1 region.

The time averaged accretion torque is

$$\mathbf{T}_{\rm a} = A^2 \Omega \dot{M}_{\rm p} \, \mathbf{k}, \tag{4.234}$$

where A is the distance from the L_1 point to the centre of mass of the primary. A fitted formula for this is given by Plavec and Kratochvil (1964) as

$$A = \left[0.50 - 0.23 \log \left(\frac{M_{\rm s}}{M_{\rm p}} \right) \right] D. \tag{4.235}$$

Using the expressions (4.87) and (4.88) enables $\Omega_{\rm o}$ and D to be eliminated in terms of $M_{\rm s}$. Then (4.234) and (4.235) lead to

$$T_{\rm a} = -1.47 q^{\frac{1}{2}} \left(\frac{G R_\odot}{M_\odot} \right)^{\frac{1}{2}} \left[0.50 - 0.23 \log \left(\frac{M_{\rm s}}{M_{\rm p}} \right) \right]^2 \left(\frac{M_{\rm s}}{M} \right)^{\frac{1}{3}} M \dot{M}_{\rm s}, \tag{4.236}$$

The magnetic primary torque for the vacuum case becomes

$$T_{\rm mp} = -\frac{\pi}{20 \mu_0} \frac{1}{q^3} \left(\frac{M_\odot}{R_\odot} \right)^3 \frac{(B_{\rm p})_0^2 R_{\rm p}^6}{M^3} \frac{M}{M_{\rm s}} f(a_{\rm s}) \sin^2 \alpha, \tag{4.237}$$

while the torque in the magnetospheric case is

$$T_{\rm mp} = -\frac{9\pi}{32 \mu_0} \frac{1}{10^{\frac{5}{3}}} \left(\frac{M_\odot}{R_\odot} \right)^3 \frac{(B_{\rm p})_0^2 R_{\rm p}^6}{q^3 M^3} \left(\frac{M}{M_{\rm s}} \right)^{\frac{4}{3}} F(\omega, \eta_{\rm s}). \tag{4.238}$$

4.4.3 Modified Gravitational Wave Driving

The gravitational radiation torque is

$$\mathbf{T}_{\rm gr} = -\frac{32}{5}\frac{G}{c^5}\left(\frac{M_{\rm s}M_{\rm p}}{M}\right)^2 D^4\Omega^5\,\mathbf{k}, \tag{4.239}$$

(Landau and Lifshitz 1951). This can be expressed as

$$T_{\rm gr} = -\frac{0.436G^{\frac{7}{2}}}{q^{\frac{7}{2}}c^5}\left(\frac{M_\odot}{R_\odot}\right)^{\frac{7}{2}}\left(\frac{M}{M_{\rm s}}\right)^{\frac{1}{3}}\left(1-\frac{M_{\rm s}}{M}\right)^2 M. \tag{4.240}$$

Substituting (4.236), (4.237) and (4.240) for $T_{\rm a}$, $T_{\rm mp}$ and $T_{\rm gr}$ in the orbital angular momentum equation (4.227) yields the mass transfer rate

$$\dot{M}_{\rm s} = -\frac{4.68\times10^{-10}\left[\mu^{\frac{2}{3}}(1-\mu)^2 - 5.73q^{\frac{1}{2}}Q_{\rm vac}f(a_{\rm s})\right]}{q^4\mu^{\frac{4}{3}}\left[4(4-7\mu)-3\left\{1-0.46\log[\mu/(1-\mu)]\right\}^2\right]}\,M_\odot\,{\rm year}^{-1}, \tag{4.241}$$

where $\mu = M_{\rm s}/M$ and

$$Q_{\rm vac} = \left(\frac{B_0}{40\,{\rm MG}}\right)^2\left(\frac{R_{\rm p}}{9.7\times10^6\,{\rm m}}\right)^6\left(\frac{M}{0.7M_\odot}\right)^{-4}. \tag{4.242}$$

Figure 4.12 shows the dependence of $|\dot{M}_{\rm s}|$, normalised with respect to the unmodified form of $|\dot{M}_{\rm gr}|$, on asynchronism. The unmodified form follows from putting $Q_{\rm vac} = 0$, and dropping the second term in the denominator in (4.241). The mass transfer rate is significantly reduced for a range of values of $\omega/\Omega_{\rm o}$ around the value at which $f(\omega,\eta)$ has its maximum. Outside this range $|\dot{M}_{\rm s}|/|\dot{M}_{\rm gr}|$ exceeds unity, this being due to the accretion torque term which extracts angular momentum from the orbit, due to the absence of a disc, and hence enhances $|\dot{M}_{\rm s}|$. The stellar surface near L_1 can adjust on a dynamical time-scale so $|\dot{M}_{\rm s}|$ can adjust quasi-steadily on the much longer angular momentum evolution time-scale.

For an under-synchronous primary the magnetic spin-orbit coupling increases the inertial space angular momentum of the star. The orbit then loses angular momentum and this enhances the accretion rate so aiding the approach to synchronism.

The mass transfer rate for the case of a magnetospheric primary torque is

$$\dot{M}_{\rm s} = -\frac{4.61\times10^{-10}\left[\mu(1-\mu^2) - Q_{\rm mag}F(\omega,\eta_{\rm s})\right]}{q^4\mu^{\frac{5}{3}}\left[4(4-7\mu)-3\left\{1-0.46\log[\mu/(1-\mu)]\right\}^2\right]}\,M_\odot{\rm year}^{-1}, \tag{4.243}$$

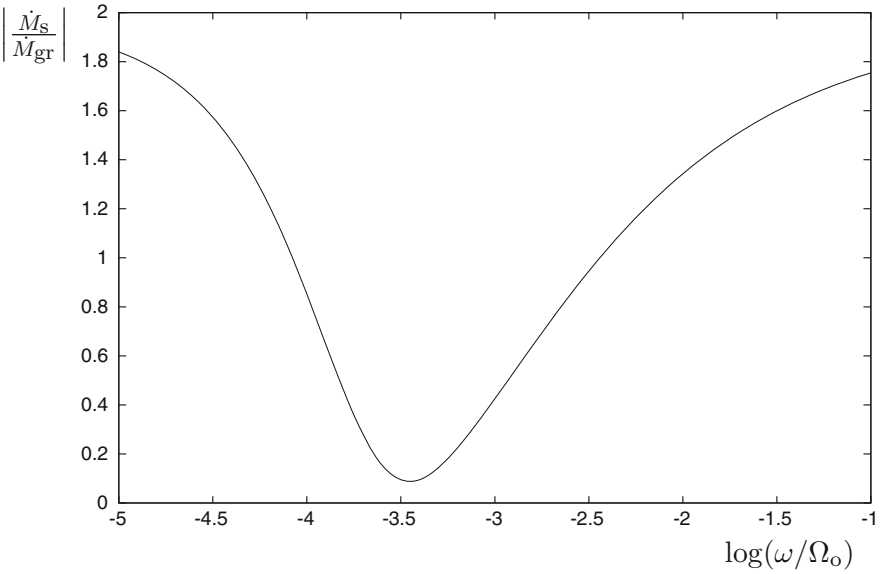

Fig. 4.12 The magnetically modified mass transfer rate due to vacuum torques, for gravitational wave braking, with $P = 2\,\mathrm{h}$, $M_\mathrm{p} = 0.6\,M_\odot$, and $B_{0\mathrm{p}} = 32\,\mathrm{MG}$, relative to the unmodified form

where

$$Q_\mathrm{mag} = 1.79 q^{\frac{1}{2}} \left(\frac{(B_\mathrm{p})_0}{40\mathrm{MG}}\right)^2 \left(\frac{R_\mathrm{p}}{9.65\times10^6\,\mathrm{m}}\right)^6 \left(\frac{M}{0.74 M_\odot}\right)^{-4}. \tag{4.244}$$

Figure 4.13 shows the ratio of this to the unmodified form. In this case the reduced rate is maintained at higher degrees of asynchronism because the magnetospheric torque does not turn down as the torque in the vacuum case does.

4.4.4 Modified Magnetic Wind Driving

Systems with orbital periods of $P > 3\,\mathrm{h}$ are believed to be magnetically braked via a channelled wind emanating from the secondary. The magnetic wind removes spin angular momentum from the star and drives it towards an under-synchronous state. Tidal coupling then operates and spins the star back towards synchronism at the expense of orbital angular momentum. The full details of this are presented in Chap. 13 and in Campbell (2001). The fast rotator magnetic wind theory of Mestel and Spruit (1987) is applied to find expressions for the mass transfer rate.

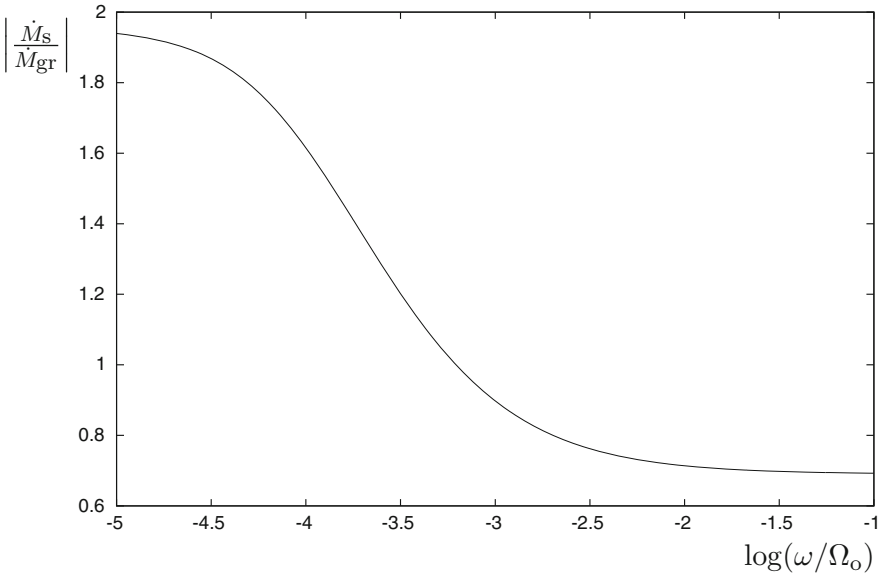

Fig. 4.13 The magnetically modified mass transfer rate due to magnetospheric torques, for gravitational wave braking, with $P = 2\,\mathrm{h}$, $M_\mathrm{p} = 0.6\,M_\odot$, and $B_{0\mathrm{p}} = 32\,\mathrm{MG}$, relative to the unmodified form

The secondary star is taken to have a magnetic field generated by a dynamo with a dependence of the surface polar field on the rotation rate given by

$$\frac{B_{0\mathrm{s}}}{B_\odot} = \left(\frac{\Omega_\mathrm{s}}{\Omega_\odot}\right)^{\frac{7}{4}}, \tag{4.245}$$

which leads to a braking torque of

$$T_\mathrm{br} = -\frac{2}{3}\left(\frac{2\pi}{\mu_0}\right)^{\frac{2}{3}} B_\odot^{\frac{4}{3}} \dot{M}_\odot^{\frac{1}{3}} \left(\frac{R_\mathrm{s}}{\bar{r}}\right)^{\frac{4}{3}} \left(\frac{B_{0\mathrm{s}}}{B_\odot}\right)^{\frac{4}{3}} \left(\frac{\dot{M}_\mathrm{w}}{\dot{M}_\odot}\right)^{\frac{1}{3}} R_\mathrm{s}^{\frac{8}{3}} \Omega_\mathrm{s}^{\frac{1}{3}}, \tag{4.246}$$

where $\dot{M}_\mathrm{w}$ is the wind mass loss rate, taken as being related to the rotation rate by

$$\frac{\dot{M}_\mathrm{w}}{\dot{M}_\odot} = \frac{\Omega_\mathrm{s}}{\Omega_\odot}, \tag{4.247}$$

and $\bar{r}$ is the equatorial extent of the dead zone (see Chap. 13).

Using (4.245) and (4.247) in (4.246), with saturation at a critical rotation rate of $\Omega_s = \Omega_c$, yields

$$T_{br} = -\frac{2}{3}\left(\frac{2\pi}{\mu_0}\right)^{\frac{2}{3}} B_\odot^{\frac{4}{3}} \dot{M}_\odot^{\frac{1}{3}} \left(\frac{R_s}{\bar{r}}\right)^{\frac{4}{3}} \left(\frac{\Omega_c}{\Omega_\odot}\right)^{\frac{8}{3}} R_s^{\frac{8}{3}} \Omega_s^{\frac{1}{3}}. \tag{4.248}$$

This can be expressed as

$$T_{br} = -3.31 \times 10^{24} \frac{q^{\frac{13}{6}}}{(\zeta_w)_\odot^{\frac{1}{3}}} \left(\frac{B_\odot}{1\,\mathrm{G}}\right)^2 \left(\frac{R_s}{\bar{r}}\right)^{\frac{5}{3}} \left(\frac{\Omega_c}{\Omega_\odot}\right)^{\frac{8}{3}} \left(\frac{M}{0.84\,M_\odot}\right)^{\frac{7}{3}} \mu^{\frac{7}{3}}. \tag{4.249}$$

Using this in the orbital angular momentum evolution equation (4.228) leads to the magnetic vacuum case expression

$$\dot{M}_s = -\frac{1.1 \times 10^{-8}\left[Q_{br}\mu^{\frac{10}{3}} - Q_{mp} f(a_s)\right]}{\mu^{\frac{4}{3}}\left[4(4-7\mu) - 3\{1 - 0.46\log[\mu/(1-\mu)]\}^2\right]} M_\odot\,\mathrm{year}^{-1}, \tag{4.250}$$

where

$$Q_{br} = 5.6 \times 10^{-5} q^{\frac{5}{3}} \left(\frac{B_\odot}{1\,\mathrm{G}}\right)^2 \left(\frac{R_s}{\bar{r}}\right)^{\frac{5}{3}} \left(\frac{\Omega_c}{\Omega_\odot}\right)^{\frac{8}{3}} \left(\frac{M}{0.8\,M_\odot}\right)^{\frac{4}{3}}, \tag{4.251}$$

$$Q_{mp} = \frac{1}{q^{\frac{7}{2}}} \left(\frac{B_{0s}}{60\,\mathrm{MG}}\right)^2 \left(\frac{R_p}{9.7 \times 10^6\,\mathrm{m}}\right)^6 \left(\frac{M}{M_\odot}\right)^{-4} \sin^2\alpha. \tag{4.252}$$

Figure 4.14 shows the ratio $|\dot{M}_s|/|\dot{M}_{br}|$, where $\dot{M}_{br}$ is the unmodified form of $\dot{M}_s$. There is a significant reduction in $|\dot{M}_s|$ with consequences that are similar to the foregoing gravitational radiation case.

The magnetospheric torque case yields

$$\dot{M}_s = -\frac{1.12 \times 10^{-9}\left[\tilde{Q}_{br}\mu^{\frac{11}{3}} - \tilde{Q}_{mp} F(\omega, \eta_s)\right]}{\mu^{\frac{5}{3}}\left[4(4-7\mu) - 3\{1 - 0.46\log[\mu/(1-\mu)]\}^2\right]} M_\odot\,\mathrm{year}^{-1}, \tag{4.253}$$

where

$$\tilde{Q}_{br} = 1.26 \times 10^{-3} \frac{q^{\frac{5}{3}}}{(\zeta_w)_\odot^{\frac{1}{3}}} \left(\frac{B_\odot}{1\,\mathrm{G}}\right)^2 \left(\frac{R_s}{\bar{r}}\right)^{\frac{5}{3}} \left(\frac{\Omega_c}{\Omega_\odot}\right)^{\frac{8}{3}} \left(\frac{M}{0.84\,M_\odot}\right)^{\frac{4}{3}}, \tag{4.254}$$

$$\tilde{Q}_{mp} = \frac{1}{q^{\frac{7}{2}}} \left(\frac{(B_p)_0}{60\,\mathrm{MG}}\right)^2 \left(\frac{R_p}{9.65 \times 10^6\,\mathrm{m}}\right)^6 \left(\frac{M}{0.84\,M_\odot}\right)^{-4}. \tag{4.255}$$

Figure 4.15 shows that there is a significant lowering of the magnetically braked mass transfer rate in this case.

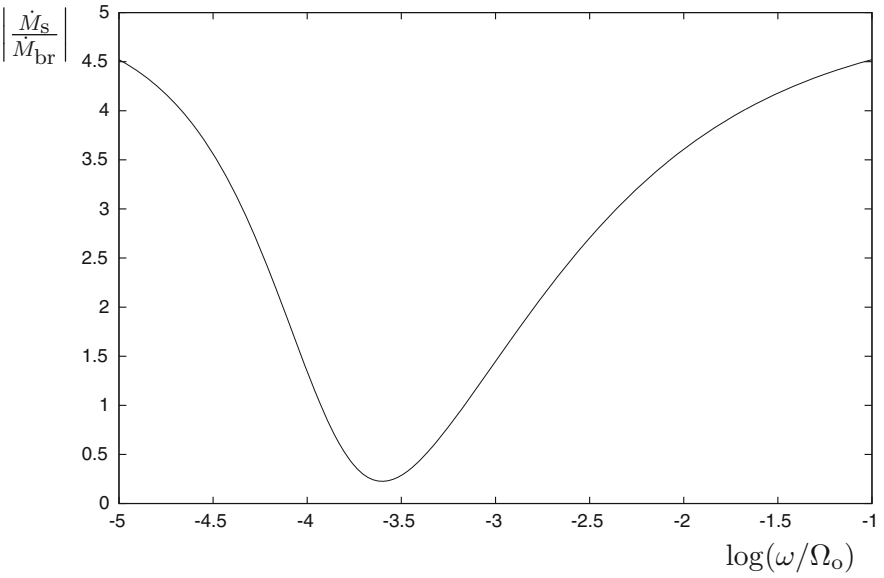

Fig. 4.14 The magnetically modified mass transfer rate due to vacuum torques, for magnetic wind braking with $P = 3\,\mathrm{h}$, $M_{\rm p} = 0.4\,M_{\odot}$, and $B_{0\rm p} = 80\,\mathrm{MG}$, relative to the unmodified form

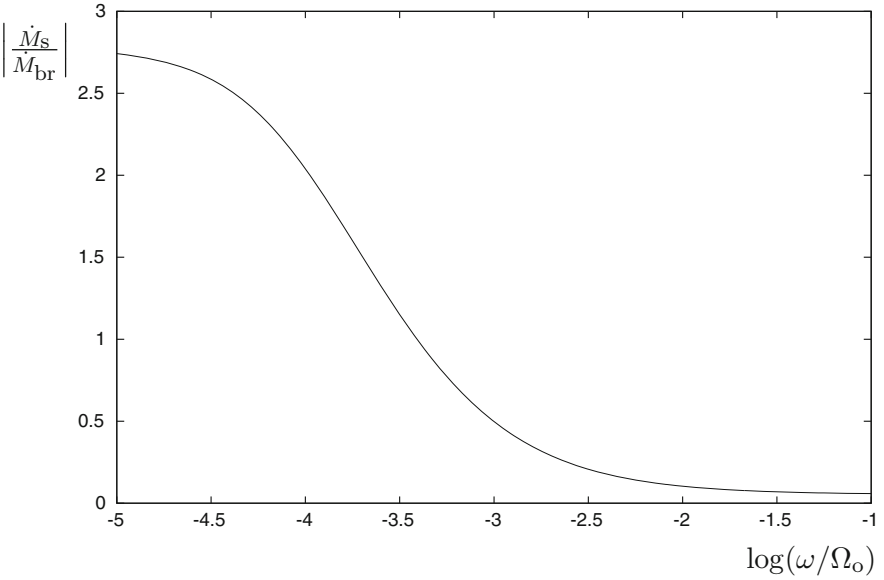

Fig. 4.15 The magnetically modified mass transfer rate due to magnetospheric torques, for magnetic wind braking with $P = 3\,\mathrm{h}$, $M_{\rm p} = 0.5\,M_{\odot}$, and $B_{0\rm p} = 60\,\mathrm{MG}$, relative to the unmodified form

4.5 Summary and Discussion

The interaction of the magnetic field of an asynchronous primary with the tidally synchronized secondary star can lead to a synchronizing torque. If the region between the stars is treated as a vacuum, then the magnetic moment of the primary must be inclined to its spin axis for an inductive torque to occur. A magnetic tilt leads to a time-dependent field in the orbital frame which penetrates the diffusive secondary and induces electric currents in the star which act as a source of magnetic field. The induced field extends beyond the secondary and interacts with the primary on which it generates a torque and a non-central force. The torque acts to spin the primary towards synchronism, and has the form of a resonance curve. For larger values of ω/Ω_o the field only penetrates the secondary to a skin depth leading to lower torque values. For smaller asynchronism the field penetrates deep into the star but the lower frequency leads to a lower torque. The torque is maximised at an intermediate value of ω/Ω_o at which the induction and field penetration act together to produce larger induced torques. All the observed AM Her systems have a magnetic tilt, but the primary is likely to have a magnetosphere surrounding the stars.

With a magnetosphere the time dependent induction effect will still occur, but electric currents can flow between the stars as well as through them. The motion of the magnetosphere relative to the secondary now introduces new inductive effects, described by the $\mathbf{v} \times \mathbf{B}$ term in the induction equation. This term has effects even when there is no explicit time dependence and hence magnetic torques are expected to be induced in an asynchronous state even for $\alpha = 0$. To illustrate these new effects the time-independent case of $\alpha = 0$ was considered, so the time dependent inductive effects, generated by the $\partial\mathbf{B}/\partial t$ term in the induction equation, are not operable. Although for $\alpha = 0$ there is no explicit time dependence, there is still an asynchronous frequency ω. This is the synodic angular velocity of material about a vertical axis through the primary, and this frequency occurs in the velocity components of its corotating magnetosphere measured from orbital axes centred on the secondary.

The magnetospheric magnetic field penetrates the diffusive secondary and the angular velocity difference between the magnetosphere and secondary will induce shearing motions in the surface regions of the star, caused by the induced magnetic forces. The shearing of poloidal magnetic field, described by the $\mathbf{B}_p \cdot \nabla\Omega$ term in the induction equation, causes the creation of B_ϕ field from $\mathbf{B}_p$. The magnetosphere also imposes radial motions on the star, and the compression and expansion effects will induce poloidal motions in its surface layers. These motions cause advection, compression and stretching of the induced magnetic field and this balances the effects of diffusion. For higher degrees of asynchronism the induced motions approach supersonic speeds and the field twisting, measured by $|B_{\phi s}/B_{ps}|$, becomes larger. This will lead to shocks, associated dissipation, likely field instability and a break down of corotation. Hence an effective quenching, limiting the growth of $|B_\phi|$, will occur. These processes can be modelled and they lead to a torque, via the

$B_r B_\phi$ surface stresses. This torque has a maximum value at least as large as that of the vacuum case torque.

Both inductive processes generate a magnetic orbital torque, allowing the stars to exchange angular momentum and energy with the orbit. For an over-synchronous primary, angular momentum is fed into the orbit and this can lead to a significant lowering of the mass transfer rate due to a decrease in the shrinkage rate of the secondary's Roche lobe. The lack of an accretion disc means that the angular momentum of material lost via Roche lobe overflow from the secondary is not returned to the orbit via tidal interaction with the outer parts of a disc. Instead, this angular momentum is transferred to the primary via magnetic channelling of the accretion stream. This has the opposite effect to over-synchronous inductive magnetic coupling, causing an increase in the mass transfer rate. However, an overall lowering of the mass transfer rate occurs for a range of frequencies.

The primary's magnetic field was taken as dipolar here, while there is some evidence of multipole components in the field. However, such higher multipole fields fall more rapidly with distance and, since the torque depends on B^2, these would only make significant contributions if they dominated the dipole component at the stellar surface. There is no compelling observational evidence, or theoretical reasons, to suggest dominant higher multipoles at the surface. However, even if higher multipoles were dominant, this would not affect the nature of the inductive processes considered.

Ideally the full MHD equations should be solved to determine the induced motions in the secondary, and the modification of the magnetosphere due to asynchronism of the primary. In particular, it was assumed in the analysis presented here that the surface field winding ratio $|B_{\phi \mathrm{s}}/B_{\mathrm{ps}}|$ becomes limited at higher degrees of asynchronism by the effects of instabilities and reconnection. However, if such processes did not enhance the magnetic diffusivity of the secondary sufficiently to limit field winding, then larger values of $|B_{\phi \mathrm{s}}/B_{\mathrm{ps}}|$ would result. This situation would be similar to the cases of the stellar-disc interaction discussed in Sect. 9.6.2. for systems containing discs around a magnetic star with a magnetosphere. The growth of B_ϕ^2 would lead to inflation of $\mathbf{B}_{\mathrm{p}}$ and ultimately to field line opening, particularly for field lines originating nearer to the stellar magnetic poles than to the equator. A channelled stellar wind is likely to result and, although the inductive magnetic coupling would be reduced due to the reduction of flux linkage to the secondary, the wind would result in a spin-down torque on the primary. The investigation of such processes is likely to require numerical simulations.

Despite the uncertainties, the analytic and semi-analytic calculations presented here suggest that magnetic coupling to the secondary can explain how the white dwarf can attain synchronism in the absence of other significant torques. The presence of the accretion torque requires the problems of the maintenance and attainment of synchronism to be carefully considered. These problems are addressed in the next three chapters.

References

Campbell, C.G., 1983, MNRAS, 205, 1031.
Campbell, C.G., 1999, MNRAS, 306, 307.
Campbell, C.G., 2001, MNRAS, 321, 96.
Campbell, C.G., 2005, MNRAS, 359, 835.
Campbell, C.G., 2010, MNRAS, 409, 433.
Chanmugan, G., Dulk, G.A., 1983, Cataclysmic Variables and Related Objects, Reidel, Holland, 101, 223.
Cowling, T.G., 1945, MNRAS, 105, 166.
Harrison, T.E., Campbell, R.K., 2018, MNRAS, 474, 1572.
Joss, P.C., Katz, J.I., Rappaport, S.A., 1979, Ap.J., 230, 176.
Kaburaki, O., 1986, Ap&SS, 119, 85.
Katz, J.I., 1991, ComAp, 15, 177.
Lamb, F.K., Aly, J.J., Cook, M.C., Lamb, D.Q., 1983, Ap.J., 274, L71.
Landau, L., Lifshitz, E., 1951, The Classical Theory of Fields, Addison Wesley.
Lipkin, Y.M., Leibowitz, E.M., 2008, MNRAS, 387, 289.
Mestel, L., 2012, Stellar Magnetism, Second Edition, Oxford University Press, Oxford.
Mestel, L., Spruit, H.C., 1987, MNRAS, 226, 57.
Moffatt, H.K., 1998, Magnetic Field Generation in Electrically Conducting Fluids, Cambridge University Press, Cambridge.
Myers, G., Patterson, J., de Miguel, E., Spain, H., Hambsh, F.J., Monard, B., Bolt, G., McCormick, J., Rea, R., Allen, W., 2017, PASP, 129, 4204.
Nauenberg, P., 1972, ApJ, 175, 417.
Papaloizou, J., Pringle, J.E., 1978, A&A, 70, L65.
Parker, E.N., 1979, Cosmical Magnetic Fields, Oxford University Press.
Pavlenko, E., Andreev, M., Babina, Y., Malanushenko, V., 2013, ASPC, 469, 343.
Plavec, M., Kratochvil, P., 1964, BAICz, 15, 165.
Staubert, R., Friedrich, S., Pottschmidt, K., Benlloch, S., Schuh, S.L., Kroll, P., Splittgerber, E., Rothschild, R., 2003, A&A, 407, 987.

Chapter 5
AM Her Stars: Stream Channelling and the Accretion Torque

Abstract The strong magnetic moment of the primary star results in a surrounding magnetic field which completely prevents the formation of an accretion disc. Matter lost from the L_1 region of the secondary becomes channelled by the primary's magnetic field and hence, in general, forms a 3D accretion flow. The flow causes distortions of the stellar magnetic field and the resulting stresses act through the stream to transfer angular momentum to the star. The consequent accretion torque depends on the orientation of the primary's magnetic axis and has components parallel and normal to the orbital angular momentum vector. These components can have comparable magnitudes for a significant range of magnetic orientations. The synchronous and asynchronous accretion torques are considered here, as well as the effects of partial field channelling. For a dipolar magnetic field and moderate degrees of asynchronism, the normal components of the accretion torque average to zero over a synodic rotation period, while the parallel component has a conservative averaged form for total field channelling.

5.1 Magnetic Field Channelling

Accretion discs do not form in the AM Herculis binaries. The effect of a strongly magnetic accretor on a disc is considered in Chap. 9. Inner disruption occurs due to magnetic heating causing an increase in the vertical gradient of the thermal and radiation pressures which cannot be balanced by the increase in the vertical component of the stellar gravity or the vertical magnetic force with decreasing distance from the primary. The ratio of the disruption radius to the distance of the L_1 point from the centre of the primary is given by

$$\frac{\varpi_{\rm m}}{A} = \frac{3.2\left(\frac{\gamma}{\epsilon_{\rm m}}\right)^{\frac{2}{7}}\left(\frac{(B_{\rm p})_0}{20{\rm MG}}\right)^{\frac{4}{7}}\left(\frac{R_{\rm p}}{8.67\times10^6\,{\rm m}}\right)^{\frac{12}{7}}\left(1-\xi^{\frac{3}{2}}_5\right)^{\frac{2}{7}}}{qN\left(\frac{\dot{M}_{\rm p}}{10^{-10}\,M_\odot\,{\rm year}^{-1}}\right)^{\frac{2}{7}}\left(\frac{M_{\rm p}}{0.6\,M_\odot}\right)^{\frac{1}{7}}\left(\frac{M}{0.8\,M_\odot}\right)^{\frac{1}{3}}\left(\frac{M_{\rm s}}{0.2\,M_\odot}\right)^{\frac{2}{3}}}, \tag{5.1}$$

C. G. Campbell, *Magnetohydrodynamics in Binary Stars*, Astrophysics and Space Science Library 456, https://doi.org/10.1007/978-3-319-97646-4_5

with

$$N = 1 - 0.46 \log\left(\frac{M_\mathrm{s}}{M_\mathrm{p}}\right), \tag{5.2}$$

where $\gamma/\epsilon_\mathrm{m} \sim 1$, $q \simeq 1.1$, while $(B_\mathrm{p})_0$, M_p and R_p are the surface polar field, mass and radius of the primary and

$$\xi^{\frac{3}{2}} = \frac{\Omega_\mathrm{p}}{\Omega_\kappa(\varpi_\mathrm{m})} \tag{5.3}$$

is the ratio of the stellar rotation rate to that of the inner edge of the disc. Equation (5.1) typically gives $\varpi_\mathrm{m} \gtrsim A$, so discs would not be expected to form in AM Her stars. This is confirmed by the numerical simulations of Zhilkin and Bisikalo (2010) which showed that for a primary surface polar magnetic field of $\gtrsim 5 \times 10^6$ G an accretion disc does not form.

Matter lost from the L_1 region of the secondary forms an accretion stream which interacts with the magnetic field of the primary. The ratio of the magnetic pressure to the gas pressure can be estimated in this region. Assuming the white dwarf to have a dipolar magnetic field, and taking its distance from L_1 as $A \simeq D/2$, gives

$$B_{L_1} \simeq \left(\frac{2R_\mathrm{p}}{D}\right)^3 (B_\mathrm{p})_0. \tag{5.4}$$

The density of material leaving the L_1 region can be estimated from the mass loss rate

$$\dot{M}_\mathrm{s} = -\pi \rho_{L_1} c_\mathrm{s} H^2, \tag{5.5}$$

where c_s is the isothermal sound speed and H is the density scale height perpendicular to the line of stellar centres, just beneath L_1. This height is given by (2.326) so, with $f = 1$,

$$H = \left(\frac{c_\mathrm{s}}{\Omega D}\right) R_\mathrm{s}, \tag{5.6}$$

where Ω is the orbital angular velocity, with the previously adopted subscript dropped here. Using (5.6) to eliminate H in (5.5) yields the density of material in the vicinity of L_1 as

$$\rho_{L_1} \simeq \frac{|\dot{M}_\mathrm{s}|\Omega^2}{\pi c_\mathrm{s}^3}\left(\frac{D}{R_\mathrm{s}}\right)^2. \tag{5.7}$$

The ratio of the magnetic pressure to the gas pressure is then given by (5.4) and (5.7), together with the relations (2.296)–(2.298) connecting the orbital parameters, as

$$\left(\frac{B^2}{2\mu_0 P}\right)_{L_1} = \frac{1.6\left(\frac{(B_\mathrm{p})_0}{20\,\mathrm{MG}}\right)^2\left(\frac{R_\mathrm{p}}{8.67\times10^6\,\mathrm{m}}\right)^6\left(\frac{T_{L_1}}{2\times10^3\,\mathrm{K}}\right)^{\frac{1}{2}}}{q^3\left(\frac{M_\mathrm{s}}{0.2\,M_\odot}\right)^{\frac{4}{3}}\left(\frac{M}{0.8\,M_\odot}\right)^{\frac{8}{3}}\left(\frac{\dot{M}_\mathrm{p}}{10^{-10}\,M_\odot\,\mathrm{year}^{-1}}\right)}. \tag{5.8}$$

This ratio has its strongest dependence on the magnetic moment of the primary, being $\propto m^2$. For typical parameters, $B^2/2\mu_0 \gtrsim P$ near the L_1 point and hence magnetic forces may affect the flow in this region.

Observations indicate that effective field channelling of material may occur at a distance from the L_1 region in some systems (e.g. Wu and Wickramasinghe 1993; Schwope et al. 1997). Although the magnetic field may affect the motion of material just inside L_1, the emerging stream becomes supersonic and then the relevant ratio becomes that of the poloidal kinetic energy density to the poloidal magnetic energy density. This ratio becomes unity at the Alfvén point in the flow and inside this point magnetic effects become strong and field channelling occurs.

A steady flow of highly conducting material obeys the induction equation

$$\nabla \times (\mathbf{v} \times \mathbf{B}) = \mathbf{0}, \tag{5.9}$$

which is satisfied by

$$\mathbf{v} = \kappa(\mathbf{r})\mathbf{B}. \tag{5.10}$$

In the strongly channelled region the local distortion of the magnetic field, $\mathbf{B}'$, caused by the flow is small. Matter then flows very nearly parallel to the unperturbed field, $\mathbf{B}_0$, and experiences a force per unit mass

$$\mathbf{F} = \frac{1}{\mu_0\rho}(\nabla \times \mathbf{B}') \times \mathbf{B}_0. \tag{5.11}$$

In general, the channelled part of the accretion stream will lie out of the orbital plane. There is a magnetic torque $\mathbf{r} \times \mathbf{F}$ per unit mass exerted on material and this is transmitted to the white dwarf via the associated magnetic stresses. A torque also results from the angular momentum flux of matter flowing on to the accretion pole, but this is small since most of the angular momentum has been transferred to the star via the magnetic field torques. Some angular momentum exchange between the stream and the orbit can occur due to gravitational interaction with the secondary star.

Numerical simulations of the accretion flow were performed by Zhilkin and Bisikalo (2010). The primary was taken to have a dipole magnetic field having orientation angles $\alpha = 30°$, $\beta = 270°$, and a range of polar field strengths given by

$10^7\,\mathrm{G} \leq (B_\mathrm{p})_0 \leq 10^8\,\mathrm{G}$. This orientation has the horizontal component of the dipole moment pointing away from the L_1 point, so accretion onto the south pole would be expected. Numerical solutions of the MHD equations were found, employing a 3D code, using coordinates relative to the orbital frame . Terms were included in the heat equation to simulate radiative heating and cooling, and a term describing magnetic dissipation. The flow speed at the L_1 point was taken to be the sound speed, with a temperature $T_{L_1} = 4 \times 10^3\,\mathrm{K}$, and a mass transfer rate $|\dot{M}_\mathrm{s}| = 10^{-9}\,M_\odot\,\mathrm{year}^{-1}$ was used. The region between the stars was taken to have initial values of $\rho_0 = 10^{-6}\rho_{L_1}$, $T_0 = 1.12 \times 10^4\,\mathrm{K}$ and $(v_\mathrm{p})_0 = 0$, with $\mathbf{B}_0$ the unperturbed stellar field. It typically took a time of $\simeq 5P$ for a steady state to be reached. The stream has a main core and a surrounding lower density envelope. For $(B_\mathrm{p})_0 = 10^7\,\mathrm{G}$ the centre of the stream initially lies in the orbital plane, but soon becomes field channelled and is directed to the south magnetic pole, as expected. For a field strength of $(B_\mathrm{p})_0 = 10^8\,\mathrm{G}$ the stream is strongly channelled, and hence vertically diverted, at the L_1 point.

Zhilkin et al. (2012) considered the case in which the primary has dipole and quadrupole components in its magnetic field. The magnetic axes of these components were taken to be parallel, but tilted to the spin axis at an angle $\alpha = 30°$. A range of azimuthal magnetic orientation angles was used, with $\beta = (0.75 - m) \times 360°$ where $0 \leq m \leq 0.9$ in increments of $\Delta m = 0.1$. The surface polar value of the dipole component was $(B_\mathrm{p})_0 = 28\,\mathrm{MG}$, while a surface quadrupolar value of 10 times this was employed. The conditions at the L_1 point, and the initial conditions in the region surrounding the star, were the same as those adopted in Zhilkin and Bisikalo (2010). Again, there is a main stream and a lower density envelope. For all values of β, the stream initially flows in the orbital plane but soon becomes magnetically diverted. The orientations $m = 0$ ($\beta = 270°$) and $m = 0.5$ ($\beta = 90°$) correspond to the horizontal component of the magnetic axis pointing away from and towards the L_1 point, respectively. For $m < 0.4$ ($\beta < 126°$) an accretion ring forms just beneath the magnetic equatorial plane, with most remaining material accreting on to the north magnetic pole. At $m = 0.4$ the main flow accretes into the magnetic ring, with a smaller amount of material reaching the north pole. The split flows become approximately equal at $m = 0.5$ ($\beta = 90°$). For $0.6 \leq m \leq 0.7$ ($18° \leq \beta \leq 54°$) nearly all the flow passes to the magnetic north pole. There is no compelling theoretical or observational reason for a surface quadrupole field to dominate the dipole field, but this case illustrates the effects on the accretion stream of a strong quadrupole field.

The simulations did not calculate the accretion torque on the primary. When the magnetic force is sufficiently strong the stream will be diverted out of the orbital plane into the strongly channelled region. This region will give the dominant contribution to the magnetic torque exerted on the white dwarf. Most angular momentum exchange with the orbit occurs in the flow region near L_1, where the gravitational coupling is largest. The flow at L_1 will be super-Alfvénic or sub-Alfvénic, depending on the combination of binary parameters.

The accretion torque is required for the synchronous and asynchronous cases. In the synchronous case the magnetic field lines are stationary in the orbital frame

and so, for steady mass loss from L_1, the accretion torque is time-independent. In the asynchronous case the geometry of the channelled stream changes, and the accretion torque will be time-dependent. In general, the torque will have components perpendicular and parallel to the orbital angular momentum vector. The ratio of these components, as a function of magnetic orientation, is of particular interest in relation to the maintenance of synchronism.

In Sect. 5.2 the angular momentum transfer is calculated due to a field-channelled flow from the L_1 region on to a synchronized white dwarf, for an arbitrary orientation. Section 5.3 considers the resulting accretion torque and also applies this to the case of small asynchronism. Section 5.4 considers partial field channelling of the accretion stream in relation to the position of the Alfvén point.

5.2 Angular Momentum Transfer

The precise nature of the white dwarf's magnetic field is unknown. It has been suggested that in some cases the field may have higher multipole components (e.g. Meggitt and Wickramasinghe 1989; Beuermann et al. 2007). Numerical simulations show that, with a sufficiently strong quadrupole component, the stream can split and lead to more than one accretion region, as appears to be observed in some systems. However, to investigate the effect of field channelling out of the orbital plane, a dipole geometry was considered by Campbell (1986). By assuming that matter links to the primary's magnetic field at L_1, an upper bound can be found for the angular momentum exchanged with the orbit. By considering the distribution of magnetic torque along the stream, cases of partial field channelling, and the associated angular momentum transfer, can then be investigated.

Figure 5.1 shows the orbital frame, with the primary's dipole moment having orientation angles (α, β). Material is lost from the lobe-filling secondary through the L_1 region, with speed $\simeq c_s \ll \Omega D$, at a steady rate $\dot{M}_s$ and is assumed to be immediately channelled by the primary's field. The case of a synchronized white dwarf is considered in this section, so the lines of $\mathbf{B}$ are stationary in the orbital frame. The accretion stream is centred on the field line passing through L_1. For a thin, steady stream the accretion torque is found by calculating the specific angular momentum imparted to the primary along this line and multiplying it by $\dot{M}_p = -\dot{M}_s$.

For a general orientation of the dipole moment $\mathbf{m}$ the unperturbed magnetic field $\mathbf{B}$ will be a function of all three coordinates if described in the spherical polar coordinate system (r, θ, ϕ). Since $\mathbf{B}$ is rotationally symmetric about $\mathbf{m}$, the natural coordinates to use are those of a spherical polar system (r, ψ, χ) with angles measured with respect to a Cartesian frame having its vertical axis along $\mathbf{m}$ and so having an orientation (α, β) in the orbital frame. Hence ψ is measured from $\hat{\mathbf{m}}$ and χ from a vector $\hat{\mathbf{m}}_\perp$ where, relative to the orbital frame,

$$\hat{\mathbf{m}} = \sin\alpha\cos\beta\,\mathbf{i} + \sin\alpha\sin\beta\,\mathbf{j} + \cos\alpha\,\mathbf{k}, \tag{5.12}$$

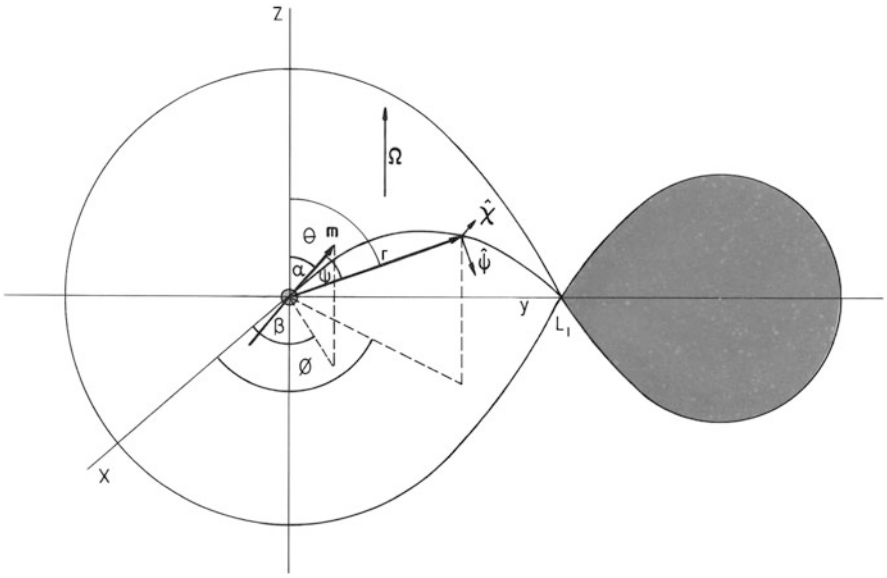

Fig. 5.1 The orbital frame, showing the rotated spherical polar coordinate system (r, ψ, χ) (from Campbell 1986)

and

$$\hat{\mathbf{m}}_{\perp} = \cos\alpha\cos\beta\,\mathbf{i} + \cos\alpha\sin\beta\,\mathbf{j} - \sin\alpha\,\mathbf{k}. \tag{5.13}$$

In this system the unperturbed field **B** will only depend on r and ψ and the equation of a field line will take its simplest form. The field **B** can be derived from a magnetic scalar potential $\Psi_{\mathrm{m}}(r, \psi)$ through

$$\mathbf{B} = -\nabla\Psi_{\mathrm{m}}. \tag{5.14}$$

By expressing the gradient operator in the two polar coordinate systems, it follows from (5.14) that the unit vectors $\hat{\boldsymbol{\psi}}$ and $\hat{\boldsymbol{\chi}}$ are related to $\hat{\boldsymbol{\theta}}$ and $\hat{\boldsymbol{\phi}}$ by

$$\hat{\boldsymbol{\psi}} = \frac{\partial\psi}{\partial\theta}\hat{\boldsymbol{\theta}} + \frac{1}{\sin\theta}\frac{\partial\psi}{\partial\phi}\hat{\boldsymbol{\phi}}, \tag{5.15}$$

$$\hat{\boldsymbol{\chi}} = -\frac{1}{\sin\theta}\frac{\partial\psi}{\partial\phi}\hat{\boldsymbol{\theta}} + \frac{\partial\psi}{\partial\theta}\hat{\boldsymbol{\phi}}, \tag{5.16}$$

and hence

$$\left(\frac{\partial\psi}{\partial\theta}\right)^2 + \frac{1}{\sin^2\theta}\left(\frac{\partial\psi}{\partial\phi}\right)^2 = 1. \tag{5.17}$$

Using the fact that $\cos\psi = \hat{\mathbf{m}} \cdot \hat{\mathbf{r}}$ and $\sin\chi = -\hat{\mathbf{m}}_\perp \cdot \hat{\boldsymbol{\chi}}$, together with (5.12), (5.13) and (5.16), it can be shown that ψ and χ are related to θ and ϕ through

$$\cos\psi = \sin\alpha \sin\theta \cos(\phi - \beta) + \cos\alpha \cos\theta, \tag{5.18}$$

$$\sin\psi \sin\chi = \sin\theta \sin(\phi - \beta). \tag{5.19}$$

The field line passing through L_1 lies in the plane containing $\hat{\mathbf{m}}$ and $\mathbf{j}$. By its definition, the unit vector $\hat{\boldsymbol{\chi}}$ is constant over the plane of a field line and for the required plane is, from (5.12),

$$\hat{\boldsymbol{\chi}} = \frac{1}{(1 - \sin^2\alpha \sin^2\beta)^{\frac{1}{2}}} \hat{\mathbf{m}} \times \mathbf{j}. \tag{5.20}$$

Since $\sin\chi = -\hat{\mathbf{m}}_\perp \cdot \hat{\boldsymbol{\chi}}$, (5.12), (5.13) and (5.20) give the constant value of χ over the required plane from

$$\sin\chi = \frac{\cos\beta}{(1 - \sin^2\alpha \sin^2\beta)^{\frac{1}{2}}}. \tag{5.21}$$

The magnetic potential for a dipole field is

$$\Psi_{\mathrm{m}} = \frac{\mu_0 m}{4\pi r^2} \cos\psi, \tag{5.22}$$

so (5.14) gives the magnetic field components as

$$B_r = \frac{\mu_0 m}{2\pi r^3} \cos\psi, \tag{5.23}$$

$$B_\psi = \frac{\mu_0 m}{4\pi r^3} \sin\psi. \tag{5.24}$$

The equation of the relevant field line is found by integrating the relation

$$\frac{1}{r}\frac{dr}{d\psi} = \frac{B_r}{B_\psi} \tag{5.25}$$

and applying the condition that the line passes through L_1. This gives

$$r(\psi, \alpha, \beta) = \frac{A \sin^2\psi}{1 - \sin^2\alpha \sin^2\beta}, \tag{5.26}$$

where A is the distance of the L_1 point from the centre of the primary.

For gas temperatures of $\sim 10^4$ K, the thermal pressure gradient along the stream has negligible effect on the speed of material since $v/c_{\mathrm{s}} \gg 1$. The equation of

motion for the accretion stream can be written

$$\ddot{\mathbf{r}} = -\nabla\Psi - 2\boldsymbol{\Omega} \times \dot{\mathbf{r}} + \mathbf{F}, \tag{5.27}$$

where $\Psi(r, \psi, \chi)$ is taken to be the Roche potential. The specific magnetic force $\mathbf{F}$, given by (5.11), is perpendicular to $\dot{\mathbf{r}}$ and so, in this strong magnetic limit, does no work on the material. The Roche potential $\Psi(r, \psi, \chi)$ is found by using (2.267) in the coordinates (r, θ, ϕ) and expressing the angular terms as functions of ψ and χ. The required transformations are obtained by using the z-component of $\hat{\mathbf{m}}_\perp$ expressed in (α, β) and in $(\theta, \phi, \psi, \chi)$, together with the angle relations (5.18) and (5.19). The result is

$$\Psi = -\frac{GM_\mathrm{p}}{r} - \frac{GM_\mathrm{s}}{D}\left[1 - 2\frac{r}{D}Q_1 + \left(\frac{r}{D}\right)^2\right]^{-\frac{1}{2}} + \frac{GM_\mathrm{s}}{D^2} r Q_1 - \frac{1}{2}\Omega^2 r^2 Q_2, \tag{5.28}$$

where

$$Q_1 = \sin\theta \sin\phi = \sin\alpha \sin\beta \cos\psi + \sin\psi(\cos\beta \sin\chi + \cos\alpha \sin\beta \cos\chi),$$
$$Q_2 = \sin^2\theta = 1 - (\cos\alpha \cos\psi - \sin\alpha \sin\psi \cos\chi)^2. \tag{5.29}$$

The angular momentum equation follows by taking the cross product of (5.27) with $\mathbf{r}$, and noting that $\dot{\mathbf{r}}$ lies in the plane of the relevant field line, so

$$\frac{d}{dt}(r^2\dot{\psi})\hat{\boldsymbol{\chi}} = -\mathbf{r} \times \nabla\Psi - 2\mathbf{r} \times (\boldsymbol{\Omega} \times \dot{\mathbf{r}}) + \mathbf{r} \times \mathbf{F}. \tag{5.30}$$

The left-hand side of this equation represents the rate of change of specific angular momentum of material, and it follows that the ψ-components on the right-hand side must sum to zero. Equation (5.30) therefore splits into two parts; one representing the rate of change of material angular momentum due to torques acting about the $\hat{\boldsymbol{\chi}}$ direction, and the other representing the balance of torques about the $\hat{\boldsymbol{\psi}}$ direction. The Coriolis force term can be split into its ψ and χ-components by expressing $\boldsymbol{\Omega}$ as $\Omega_\chi \hat{\boldsymbol{\chi}} + \boldsymbol{\Omega}_\parallel$, where $\boldsymbol{\Omega}_\parallel$ is the component of $\boldsymbol{\Omega}$ parallel to the plane of the stream. Equation (5.30) then gives

$$\frac{1}{\sin\psi}\frac{\partial\Psi}{\partial\chi}\hat{\boldsymbol{\psi}} - 2\mathbf{r} \times (\boldsymbol{\Omega}_\parallel \times \dot{\mathbf{r}}) - r F_\chi \hat{\boldsymbol{\psi}} = \mathbf{0}, \tag{5.31}$$

$$\frac{d}{dt}(r^2\dot{\psi}) = -\frac{\partial\Psi}{\partial\psi} - \frac{d}{dt}(r^2\Omega_\chi) + r F_\psi. \tag{5.32}$$

The above equations must be integrated along the stream to calculate the total specific angular momentum delivered to the white dwarf. This total consists of the integral of the magnetic torque, per unit mass, plus the specific angular momentum of material at the accretion pole. The magnetic torque can be expressed as a rate of transfer of specific angular momentum by

$$r F_\psi \hat{\boldsymbol{\chi}} - r F_\chi \hat{\boldsymbol{\psi}} = -\frac{d\mathbf{L}}{dt}, \tag{5.33}$$

where, for a steady flow along the path specified by (5.26), $d/dt = \dot{\psi} d/d\psi$. Equations (5.31) and (5.32) therefore become

$$\left(\frac{d\mathbf{L}}{d\psi}\right)_\psi \hat{\boldsymbol{\psi}} = \left[2r\left(r\Omega_r - \frac{dr}{d\psi}\Omega_\psi\right) + \frac{1}{\dot{\psi}\sin\psi}\frac{\partial\Psi}{\partial\chi}\right]\hat{\boldsymbol{\psi}}, \tag{5.34}$$

$$\frac{d}{d\psi}(r^2\dot{\psi}) + \frac{dL_\chi}{d\psi} = -\frac{d}{d\psi}(r^2\Omega_\chi) - \frac{1}{\dot{\psi}}\frac{\partial\Psi}{\partial\psi}. \tag{5.35}$$

Integrating these equations along the stream gives

$$\Delta\mathbf{L}_\parallel = \int_{\psi_1}^{\psi_a}\left[2r\left(r\Omega_r - \frac{dr}{d\psi}\Omega_\psi\right) + \frac{1}{\dot{\psi}\sin\psi}\frac{\partial\Psi}{\partial\chi}\right]\hat{\boldsymbol{\psi}}\,d\psi, \tag{5.36}$$

$$R_p^2\dot{\psi}_a + \Delta L_\chi = (A^2 - R_p^2)\Omega_\chi - \int_{\psi_1}^{\psi_a}\frac{1}{\dot{\psi}}\frac{\partial\Psi}{\partial\psi}d\psi, \tag{5.37}$$

where ψ_1 is the value of ψ at L_1 and ψ_a is its value at the accreting pole. The field line equation (5.26) gives these limits as

$$\psi_1 = \cos^{-1}(\sin\alpha\sin\beta), \tag{5.38}$$

$$\psi_a = \sin^{-1}\left[\frac{R_p(1-\sin^2\alpha\sin^2\beta)}{A}\right]^{\frac{1}{2}}. \tag{5.39}$$

The angular velocity of material, $\dot{\psi}$, can be found from the equation of motion (5.27). Taking the scalar product of this with $\dot{\mathbf{r}}$, integrating with respect to time using the condition of essentially vanishing speed (i.e. $c_s \ll \Omega D$) at L_1, and noting that r is a function of ψ along the stream, gives

$$\dot{\psi} = \pm\frac{[2(\Psi_1 - \Psi)]^{\frac{1}{2}}}{\left[r^2 + (dr/d\psi)^2\right]^{\frac{1}{2}}}, \tag{5.40}$$

where the negative sign applies for $0 < \beta < \pi$ and the positive sign for $\pi < \beta < 2\pi$. It is noted that in the strong field limit the magnetic force makes no explicit contribution to $\dot{\psi}$, since (5.11) shows $\mathbf{F}$ is perpendicular to $\mathbf{B}_0$ and hence to $\dot{\mathbf{r}}$. The term $\mathbf{F}$ acts as a perpendicular constraint force to the stream as it is channelled by the magnetic field. Equations (5.21), (5.28) and (5.38) for χ, Ψ and ψ_1 give the Roche potential in the plane of the stream as

$$\Psi(r,\psi) = -\frac{GM_\mathrm{p}}{r} - \frac{GM_\mathrm{s}}{D}\left[1 - 2\frac{r}{D}\cos(\psi_1 - \psi) + \left(\frac{r}{D}\right)^2\right]^{-\frac{1}{2}} + \frac{GM_\mathrm{s}}{D^2} r\cos(\psi_1 - \psi) - \frac{1}{2}\Omega^2 r^2\left[\frac{\sin^2\alpha\cos^2\beta + \cos^2\alpha\cos^2(\psi_1 - \psi)}{1 - \sin^2\alpha\sin^2\beta}\right]. \tag{5.41}$$

The unit vectors $\hat{\boldsymbol{\psi}}$ and $\hat{\boldsymbol{\chi}}$ must be expressed in terms of their components in the orbital frame $Oxyz$, in order to obtain the components of the specific angular momentum transfer along these axes. Equations (5.12) for $\hat{\mathbf{m}}$ and (5.20) for $\hat{\boldsymbol{\chi}}$ give the Cartesian components of $\hat{\boldsymbol{\chi}}$. The components of $\hat{\boldsymbol{\psi}}$ are then found using $\hat{\boldsymbol{\psi}} = \hat{\boldsymbol{\chi}} \times \hat{\mathbf{r}}$ and the angle relations (5.18), (5.21) and (5.38), together with the definition of Q_1 in (5.29). The results are

$$\hat{\boldsymbol{\psi}} = -\frac{\sin\alpha\cos\beta\cos(\psi_1 - \psi)}{(1 - \sin^2\alpha\sin^2\beta)^{\frac{1}{2}}}\mathbf{i} + \sin(\psi_1 - \psi)\mathbf{j} - \frac{\cos\alpha\cos(\psi_1 - \psi)}{(1 - \sin^2\alpha\sin^2\beta)^{\frac{1}{2}}}\mathbf{k}, \tag{5.42}$$

$$\hat{\boldsymbol{\chi}} = -\frac{\cos\alpha}{(1 - \sin^2\alpha\sin^2\beta)^{\frac{1}{2}}}\mathbf{i} + \frac{\sin\alpha\cos\beta}{(1 - \sin^2\alpha\sin^2\beta)^{\frac{1}{2}}}\mathbf{k}. \tag{5.43}$$

Using these relations together with the angular momentum equations (5.36) and (5.37) gives the components of the specific angular momentum transfer as

$$\Delta J_x = -\frac{(A^2 - R_\mathrm{p}^2)\Omega_\chi\cos\alpha}{(1 - \sin^2\alpha\sin^2\beta)^{\frac{1}{2}}} - \frac{2\sin\alpha\cos\beta}{(1 - \sin^2\alpha\sin^2\beta)^{\frac{1}{2}}}\int_{\psi_1}^{\psi_\mathrm{a}} r\left(r\Omega_r - \frac{dr}{d\psi}\Omega_\psi\right)\cos(\psi_1 - \psi)d\psi + \frac{1}{(1 - \sin^2\alpha\sin^2\beta)^{\frac{1}{2}}}\int_{\psi_1}^{\psi_\mathrm{a}}\frac{1}{\dot{\psi}}\left(\cos\alpha\frac{\partial\Psi}{\partial\psi} - \frac{\sin\alpha\cos\beta\cos(\psi_1 - \psi)}{\sin\psi}\frac{\partial\Psi}{\partial\chi}\right)d\psi, \tag{5.44}$$

$$\Delta J_y = 2\int_{\psi_1}^{\psi_\mathrm{a}} r\left(r\Omega_r - \frac{dr}{d\psi}\Omega_\psi\right)\sin(\psi_1 - \psi)d\psi + \int_{\psi_1}^{\psi_\mathrm{a}}\frac{\sin(\psi_1 - \psi)}{\dot{\psi}\sin\psi}\frac{\partial\Psi}{\partial\chi}d\psi, \tag{5.45}$$

$$\Delta J_z = \frac{(A^2 - R_\mathrm{p}^2)\Omega_\chi \sin\alpha\cos\beta}{(1-\sin^2\alpha\sin^2\beta)^{\frac{1}{2}}}$$
$$- \frac{2\cos\alpha}{(1-\sin^2\alpha\sin^2\beta)^{\frac{1}{2}}}\int_{\psi_1}^{\psi_\mathrm{a}} r\left(r\Omega_r - \frac{dr}{d\psi}\Omega_\psi\right)\cos(\psi_1-\psi)d\psi$$
$$- \frac{1}{(1-\sin^2\alpha\sin^2\beta)^{\frac{1}{2}}}\int_{\psi_1}^{\psi_\mathrm{a}} \frac{1}{\dot\psi}\left(\sin\alpha\cos\beta\frac{\partial\Psi}{\partial\psi} + \frac{\cos\alpha\cos(\psi_1-\psi)}{\sin\psi}\frac{\partial\Psi}{\partial\chi}\right)d\psi. \tag{5.46}$$

Equations (5.26), (5.42) and (5.43) for $r(\psi)$, $\hat{\boldsymbol{\psi}}$ and $\hat{\boldsymbol{\chi}}$ give

$$r\Omega_r - \frac{dr}{d\psi}\Omega_\psi = \frac{A\Omega\cos\alpha\sin\psi\,[\sin\psi\sin(\psi_1-\psi) + 2\cos\psi\cos(\psi_1-\psi)]}{(1-\sin^2\alpha\sin^2\beta)^{\frac{3}{2}}}. \tag{5.47}$$

The required derivatives of the Roche potential are obtained from (5.21), (5.28) and (5.38) for χ, Ψ and ψ_1 as

$$\frac{\partial\Psi}{\partial\psi} = -\frac{GM_\mathrm{s}}{D^2}r\left[\frac{M}{M_\mathrm{s}}\frac{r}{D}\frac{\cos^2\alpha\cos(\psi_1-\psi)}{(1-\sin^2\alpha\sin^2\beta)} + W^{-\frac{3}{2}} - 1\right]\sin(\psi_1-\psi), \tag{5.48}$$

where

$$W = 1 - 2\frac{r}{D}\cos(\psi_1-\psi) + \left(\frac{r}{D}\right)^2, \tag{5.49}$$

and

$$\frac{1}{\sin\psi}\frac{\partial\Psi}{\partial\chi} = \Omega^2 r^2\frac{\sin\alpha\cos\alpha\cos\beta}{1-\sin^2\alpha\sin^2\beta}\sin(\psi_1-\psi), \tag{5.50}$$

with $M = M_\mathrm{s} + M_\mathrm{p}$. It is noted that (5.50) is purely centrifugal. Substituting (5.26), (5.40), (5.41) for $r(\psi)$, $\dot\psi$ and Ψ and (5.47)–(5.50) in (5.44)–(5.46), and evaluating the Coriolis integrals, gives the components of the specific angular momentum transfer as

$$\Delta J_x = A^2\Omega f_x(\alpha,\beta), \tag{5.51}$$

$$\Delta J_y = A^2\Omega f_y(\alpha,\beta), \tag{5.52}$$

$$\Delta J_z + R_\mathrm{p}^2\Omega\sin^2\theta_\mathrm{a} = A^2\Omega f_z(\alpha,\beta). \tag{5.53}$$

The second term on the left-hand side of (5.53) represents the additional specific angular momentum of material about the z-axis at the accreting pole when measured in the inertial frame. The dimensionless functions $f_i(\alpha, \beta)$ are

$$f_x(\alpha,\beta) = \left(\frac{R_\mathrm{p}}{A}\right)^2 \frac{\sin 2\alpha \cos\beta \sin^2(\psi_1 - \psi_a)}{2(1 - \sin^2\alpha \sin^2\beta)} - \int_{\psi_\mathrm{a}}^{\psi_1} K_x(\alpha,\beta,\psi)d\psi, \tag{5.54}$$

$$f_y(\alpha,\beta) = \frac{\cos\alpha}{(1 - \sin^2\alpha \sin^2\beta)^{\frac{5}{2}}} J(\alpha,\beta) + \int_{\psi_\mathrm{a}}^{\psi_1} K_y(\alpha,\beta,\psi)d\psi, \tag{5.55}$$

$$f_z(\alpha,\beta) = 1 + \int_{\psi_\mathrm{a}}^{\psi_1} K_z(\alpha,\beta,\psi)d\psi, \tag{5.56}$$

where

$$K_x = \pm\frac{\cos\alpha \sin^3\psi \sin(\psi_1 - \psi)(\sin^2\psi + 4\cos^2\psi)^{\frac{1}{2}}}{(1 - \sin^2\alpha \sin^2\beta)^{\frac{5}{2}}\sqrt{2Q}}\bar{W}, \tag{5.57}$$

$$\begin{aligned} J =& \frac{3}{4}(\psi_\mathrm{a} - \psi_1) + \frac{3}{8}\sin(\psi_1 - \psi_\mathrm{a})\cos(\psi_1 + \psi_\mathrm{a}) \\ &+ \frac{1}{4}(\sin^3\psi_1 \cos\psi_1 - \sin^3\psi_\mathrm{a}\cos\psi_\mathrm{a}) \\ &+ \sin^4\psi_\mathrm{a}\sin(\psi_1 - \psi_\mathrm{a})\cos(\psi_1 - \psi_\mathrm{a}), \end{aligned} \tag{5.58}$$

$$K_y = \pm\frac{A}{D}\frac{\sin\alpha\cos\alpha\cos\beta\sin^2(\psi_1 - \psi)\sin^5\psi(\sin^2\psi + 4\cos^2\psi)^{\frac{1}{2}}}{(1 - \sin^2\alpha\sin^2\beta)^4\sqrt{2Q}}, \tag{5.59}$$

$$K_z = \pm\frac{M_\mathrm{s}}{M}\frac{\sin\alpha\cos\beta\sin(\psi_1 - \psi)\sin^3\psi(\sin^2\psi + 4\cos^2\psi)^{\frac{1}{2}}(W^{-\frac{3}{2}} - 1)}{(1 - \sin^2\alpha\sin^2\beta)^{\frac{5}{2}}\sqrt{2Q}}, \tag{5.60}$$

with W given by (5.49) and

$$\bar{W} = \frac{A}{D}\frac{\sin^2\psi\cos(\psi_1 - \psi)}{(1 - \sin^2\alpha\sin^2\beta)} + \frac{M_\mathrm{s}}{M}\left(W^{-\frac{3}{2}} - 1\right), \tag{5.61}$$

$$Q = \frac{M_\mathrm{p}}{M}\left(\frac{D}{r} - \frac{D}{A}\right) + \frac{M_\mathrm{s}}{M}\left[\frac{A}{D} - \frac{r}{D}\cos(\psi_1 - \psi)\right]$$

$$- \frac{M_\mathrm{s}}{M}\left[\left(1-\frac{A}{D}\right)^{-1} - W^{-\frac{1}{2}}\right]$$
$$- \frac{1}{2}\left[\left(\frac{A}{D}\right)^2 - \left(\frac{r}{D}\right)^2\left(\frac{\sin^2\alpha\cos^2\beta + \cos^2\alpha\cos^2(\psi_1-\psi)}{1-\sin^2\alpha\sin^2\beta}\right)\right]. \tag{5.62}$$

In Eqs. (5.57), (5.59) and (5.60) the positive signs apply for $0 < \beta < \pi$ and the negative signs for $\pi < \beta < 2\pi$. The integrals in the angular momentum functions (5.54)–(5.56) are evaluated numerically and the ratio A/D is found from (2.294) with $r_{1\mathrm{p}} = A$.

Having calculated the specific angular momentum transfer, the accretion torque can be considered.

5.3 The Accretion Torque

5.3.1 The Synchronous Case

Since the primary accretes matter at a steady rate $\dot{M}_\mathrm{p}$, the components of the accretion torque are

$$T_x = A^2\Omega\dot{M}_\mathrm{p} f_x(\alpha,\beta), \tag{5.63}$$
$$T_y = A^2\Omega\dot{M}_\mathrm{p} f_y(\alpha,\beta), \tag{5.64}$$
$$T_z = A^2\Omega\dot{M}_\mathrm{p} f_z(\alpha,\beta). \tag{5.65}$$

Because matter is lost from L_1 with a speed $\simeq c_\mathrm{s} \ll \Omega D$, it follows from energy conservation that the functions $f_i(\alpha,\beta)$ can only be evaluated at orientations for which the channelled stream lies entirely within the primary's Roche lobe. For a given value of α, a critical angle β_c will exist at which the primary's field line through L_1 is tangent to its Roche lobe at that point. Hence, for total field channelling, the calculation of the accretion torque can only be performed for $\beta_c \le \beta \le \pi - \beta_c$ and $\beta_c + \pi \le \beta \le 2\pi - \beta_c$. An expression can be derived for $\beta_c(\alpha)$ by performing a Taylor expansion of Ψ, given by (5.41), along the field line defined by (5.26). When $\beta = \beta_c$ it follows that $(d^2\Psi/d\psi^2)_{L_1} = 0$, giving

$$\beta_c(\alpha) = \sin^{-1}\left[\frac{\frac{M_\mathrm{s}}{M}\left(\frac{A}{D}\right)^2\left[\left(1-\frac{A}{D}\right)^{-3} - 1\right] + \left(\frac{A}{D}\right)^3\cos^2\alpha}{\left(\frac{M_\mathrm{s}}{M}\left(\frac{A}{D}\right)^2\bar{Q} + 4\left(\frac{A}{D}\right)^3 + 8\frac{M_\mathrm{p}}{M}\right)\sin^2\alpha}\right]^{\frac{1}{2}}, \tag{5.66}$$

where

$$\bar{Q} = \left(1 + 8\frac{A}{D}\right)\left(1 - \frac{A}{D}\right)^{-3} - 1. \tag{5.67}$$

As the inclination of the magnetic moment to the orbital plane increases (i.e. as α decreases) β_c increases and hence the range of β for which the fully-channelled calculation can be performed is reduced. A minimum value of α is reached when $\beta_c = \pi/2$ and so it follows from (5.66) that

$$\alpha_{\min} = \sin^{-1}\left[\frac{\frac{M_s}{M}\left(\frac{A}{D}\right)^2\left[\left(1-\frac{A}{D}\right)^{-3} - 1\right] + \left(\frac{A}{D}\right)^3}{\frac{M_s}{M}\left(\frac{A}{D}\right)^2 \bar{Q} + 5\left(\frac{A}{D}\right)^3 + 8\frac{M_p}{M}}\right]^{\frac{1}{2}}. \tag{5.68}$$

Taking $P = 2.0\,\mathrm{h}$, (2.298) gives a lobe-filling secondary with $M_s = 0.2\,M_\odot$. Using $M_p = 0.6\,M_\odot$, (2.294) yields $A/D = 0.61$ and (5.68) gives $\alpha_{\min} = 19°$. The functions $f_i(\alpha, \beta)$ were calculated for three values of α. The results are shown in Figs. 5.2, 5.3, and 5.4 and Tables 5.1, 5.2, and 5.3.

Figure 5.1 illustrates that if $\alpha_{\min} \le \alpha \le \pi/2$ then the accreting magnetic pole lies above the orbital plane for $\beta_c \le \beta \le \pi - \beta_c$ and beneath it for $\beta_c + \pi \le \beta \le 2\pi - \beta_c$. The situation is reversed for $\pi/2 < \alpha \le \pi - \alpha_{\min}$. Figures 5.2 and 5.3 show that $f_x(\alpha, \beta)$ and $f_y(\alpha, \beta)$ are negative when the accreting pole is above the orbital plane. For given values of α and β, it is seen that the magnitude of f_x is generally larger than that of f_y. Equations (5.44), (5.51) and (5.54) show

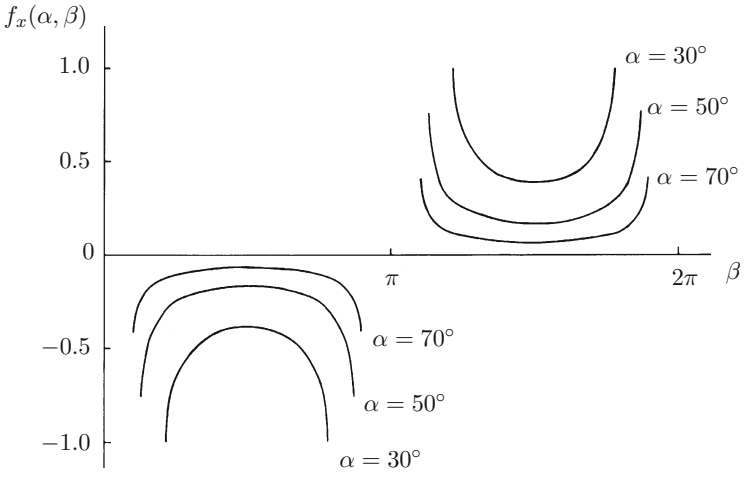

Fig. 5.2 The function $f_x(\alpha, \beta)$ (from Campbell 1986)

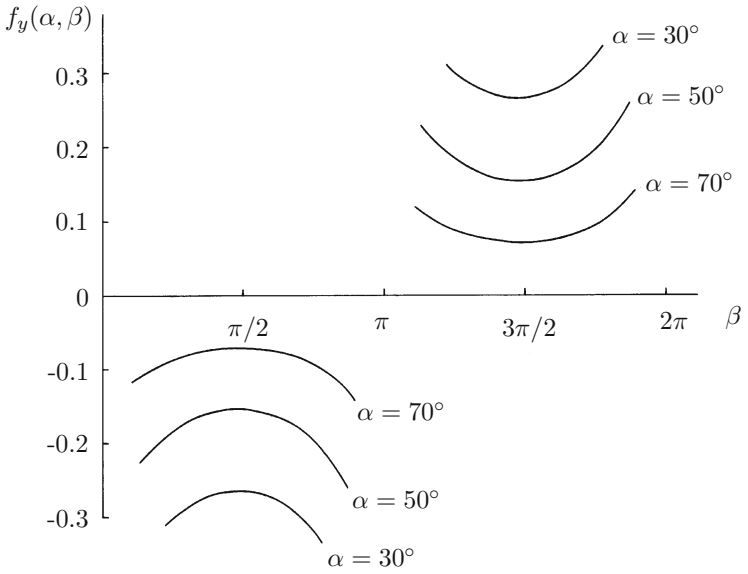

Fig. 5.3 The function $f_y(\alpha, \beta)$ (from Campbell 1986)

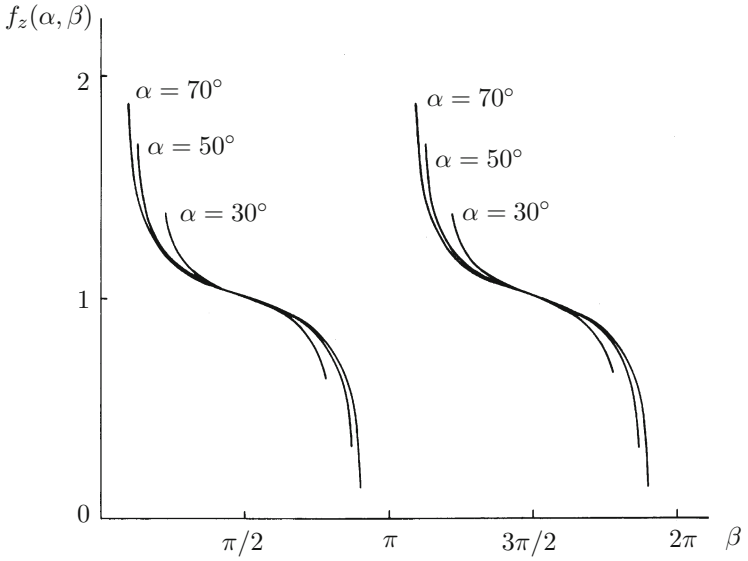

Fig. 5.4 The dimensionless function $f_z(\alpha, \beta)$ (from Campbell 1986)

Table 5.1 The torque component functions for $\alpha = 30°$, $\beta_c = 39.3°$ (from Campbell 1986)

β (deg)	f_x	f_y	f_z	$f_z/f_\perp$
β_c	−1.022	−0.312	1.370	1.282
50	−0.568	−0.293	1.168	1.827
60	−0.465	−0.279	1.106	2.038
70	−0.414	−0.270	1.064	2.154
90	−0.380	−0.265	1.000	2.157
100	−0.388	−0.268	0.969	2.054
110	−0.414	−0.276	0.936	1.881
120	−0.465	−0.289	0.894	1.632
130	−0.568	−0.308	0.832	1.288
180-β_c	−1.022	−0.334	0.630	0.586

Table 5.2 The torque component functions for $\alpha = 50°$, $\beta_c = 24°$ (from Campbell 1986)

β (deg)	f_x	f_y	f_z	$f_z/f_\perp$
β_c	−0.765	−0.226	1.680	2.107
30	−0.412	−0.212	1.338	2.888
40	−0.285	−0.191	1.204	3.509
50	−0.229	−0.176	1.137	3.942
60	−0.197	−0.165	1.092	4.242
70	−0.180	−0.158	1.057	4.417
90	−0.167	−0.154	1.000	4.398
110	−0.180	−0.162	0.943	3.903
120	−0.198	−0.171	0.908	3.478
130	−0.229	−0.185	0.863	2.935
140	−0.285	−0.205	0.796	2.265
150	−0.412	−0.234	0.662	1.397
180-β_c	−0.765	−0.258	0.320	0.396

Table 5.3 The torque component functions for $\alpha = 70°$, $\beta_c = 19°$ (from Campbell 1986)

β (deg)	f_x	f_y	f_z	$f_z/f_\perp$
β_c	−0.411	−0.119	1.872	4.381
30	−0.160	−0.102	1.299	6.844
40	−0.117	−0.091	1.192	8.050
50	−0.095	−0.083	1.131	8.960
60	−0.083	−0.077	1.088	9.608
70	−0.076	−0.074	1.055	9.992
90	−0.071	−0.071	1.000	9.952
110	−0.076	−0.075	0.945	8.849
120	−0.083	−0.080	0.912	7.913
130	−0.095	−0.087	0.869	6.732
140	−0.117	−0.098	0.808	5.304
150	−0.160	−0.113	0.701	3.575
180-β_c	−0.411	−0.141	0.128	0.294

that Coriolis, centrifugal and gravitational terms contribute to $f_x(\alpha, \beta)$, although the Coriolis term is small since $R_p/A \ll 1$. The torque component T_x therefore involves gravitational coupling of the stream to the orbit. Equations (5.45) and (5.50) show that T_y does not involve any gravitational coupling, since $\partial\Psi/\partial\chi$ is purely centrifugal in the required χ-plane. It can be shown that the Coriolis term gives the major contribution to T_y. It is noted that for $\alpha = \pi/2$, corresponding to the accreting pole lying in the orbital plane, (5.54) and (5.55) show that f_x and f_y vanish, as expected.

Figure 5.4 shows the variations of $f_z(\alpha, \beta)$. Equation (5.56) illustrates that all the orientation dependence of f_z is contained in the integral of K_z. This integral arose from the last term in (5.46) and is purely gravitational since the centrifugal part of the term in $\partial\Psi/\partial\psi$ cancels the term in $\partial\Psi/\partial\chi$. In an inertial frame centred on the white dwarf material at L_1 has specific angular momentum $A^2\Omega$. For $\beta \neq \pi/2$ or $3\pi/2$, the orbit adds to or subtracts from this and the integrated resultant is delivered to the white dwarf through the total magnetic torque. For $\beta = \pi/2$ or $3\pi/2$ the gravitational coupling term K_z is zero and specific angular momentum $A^2\Omega$ is delivered to the primary about the z-axis, so that $f_z = 1$. For $\beta_c \leq \beta < \pi/2$ and $\beta_c + \pi \leq \beta < 3\pi/2$ the accreting magnetic pole lags the motion of the line of stellar centres and the stream gains angular momentum about the z-axis from the orbit, resulting in $f_z > 1$. For $\pi/2 < \beta \leq \pi - \beta_c$ and $3\pi/2 < \beta \leq 2\pi - \beta_c$ the accreting pole leads the line of stellar centres and the stream loses angular momentum to the orbit, so $f_z < 1$. It is seen from Fig. 5.4 that for significant ranges of β centred on $\beta = \pi/2$ or $3\pi/2$, f_z is not sensitive to changes in α at fixed β. This is because for these ranges of β the gravitational coupling to the orbit, through the integral of K_z, is weak.

Figure 5.5 shows the ratio of the vertical to the horizontal component of the accretion torque, where $f_\perp = (f_x^2 + f_y^2)^{1/2}$. It is seen that for $\alpha = 30°$, corresponding to a high inclination of the accreting pole to the orbital plane, f_z and $f_\perp$ are comparable over the range of β.

It is noted that the critical angle β_c results from the condition of strong field channelling at L_1. This restriction can be removed by allowing material to become field-channelled at some distance from L_1. Provided this distance is a small fraction of A, the curves in Figs. 5.2, 5.3, 5.4, and 5.5 can be extended to all β values but will be less steep at their ends.

5.3.2 *The Asynchronous Case*

If the white dwarf primary is asynchronous with the orbit then its magnetic field geometry will vary with time in the orbital frame and matter will be channelled along moving field lines. Whatever the path taken by material, the transfer time from L_1 to the accretion pole is given by $\Delta t \sim P$, where P is the orbital period. It follows that two relevant regimes of asynchronism can be distinguished, defined by $P_{syn} \lesssim P$ and $P_{syn} \gg P$, where P_{syn} is the synodic period of the asynchronism.

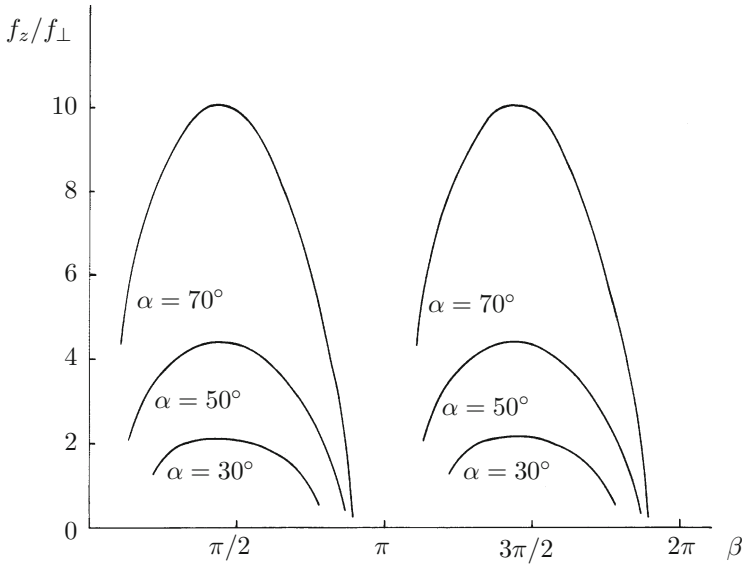

Fig. 5.5 The ratio $f_z(\alpha, \beta)/f_\perp(\alpha, \beta)$ (from Campbell 1986)

If $P_{\rm syn} \lesssim P$, equivalent to $\omega/\Omega \gtrsim 1$, then in the time during which a given flux tube is in contact with the L_1 region it can only be partly filled with material. As a result matter will be accreted on to the primary in discontinuous streams, reaching it at different times and along different paths. The analysis of the previous section can therefore not be used to calculate the time-dependent accretion torque in this case.

If $P_{\rm syn} \gg P$, or equivalently $\omega/\Omega \ll 1$ where $\omega = 2\pi/P_{\rm syn}$, then a given magnetic flux tube of the primary will completely fill with material during its time of contact with the L_1 region. A flux tube will correspondingly rapidly empty as soon as it becomes disconnected from the L_1 source. Hence, at a given time, the primary will experience a torque due to the single continuous stream along the flux tube connecting it to L_1. It then follows that the expressions for the components of $\mathbf{T}$ given by (5.63)–(5.65) for time-independent orientations (α, β) can be used to obtain the variation of $\mathbf{T}$ for time-dependent (α, β), provided that $\omega/\Omega \ll 1$. For the present, the case is considered in which $\boldsymbol{\omega}$ is parallel to $\boldsymbol{\Omega}$ so α is constant and $\beta = \omega t$. The time-dependent accretion torque is then simply obtained by making this substitution for β in (5.63)–(5.65). This case is applicable for $\omega/\Omega \lesssim 10^{-2}$, which covers the asynchronism regime of interest.

When considering the long term effect of the accretion torque on the primary, and comparing it with the dissipation torque given by (4.79), a synodic average is appropriate. This can be found by exploiting certain symmetry properties possessed by the functions $f_i(\alpha, \beta)$ defined by (5.54)–(5.56). First, consider magnetic orientations of the primary whose corresponding accretion streams are mirror images about the orbital plane $z = 0$. Figure 5.1 shows that, for fixed α, such paths are

characterized by orientations β and $\beta+\pi$, while mirror points on them about $z=0$ have angular positions ψ and $\pi-\psi$. It follows from (5.49), (5.57), (5.61), and (5.62) that

$$K_x(\alpha,\beta+\pi,\pi-\psi)=K_x(\alpha,\beta,\psi). \tag{5.69}$$

Defining the integral appearing in (5.54) for $f_x(\alpha,\beta)$ as

$$I_x(\alpha,\beta)=\int_{\psi_a}^{\psi_1}K_x(\alpha,\beta,\psi)d\psi, \tag{5.70}$$

it is then simple to show that

$$I_x(\alpha,\beta+\pi)=-I_x(\alpha,\beta). \tag{5.71}$$

In a similar way it can be shown that the integral in (5.55) for $f_y(\alpha,\beta)$ satisfies

$$I_y(\alpha,\beta+\pi)=-I_y(\alpha,\beta) \tag{5.72}$$

for mirror paths about the orbital plane. Since the Coriolis terms in (5.54) and (5.55) also possess the above antisymmetric property, it follows that

$$f_x(\alpha,\beta+\pi)=-f_x(\alpha,\beta), \tag{5.73}$$

$$f_y(\alpha,\beta+\pi)=-f_y(\alpha,\beta). \tag{5.74}$$

Consider, now, the $x=0$ plane. Figure 5.1 shows that for $\beta_c\le\beta\le\pi-\beta_c$ mirror paths about this plane are characterized by β and $\pi-\beta$, while mirror points have the same values of ψ. Equations (5.60) and (5.62) give

$$K_z(\alpha,\pi-\beta,\psi)=-K_z(\alpha,\beta,\psi). \tag{5.75}$$

Writing the integral in (5.56) for $f_z(\alpha,\beta)$ as $I_z(\alpha,\beta)$, it can be shown that

$$I_z(\alpha,\pi-\beta)=-I_z(\alpha,\beta). \tag{5.76}$$

The corresponding result for $\beta_c+\pi\le\beta\le2\pi-\beta_c$ is

$$I_z(\alpha,3\pi-\beta)=-I_z(\alpha,\beta). \tag{5.77}$$

Since the asynchronous motion considered here has constant α and $\beta=\omega t$, the average value of an accretion torque component over one synodic period is given by

$$\langle T_i\rangle=\frac{1}{2\pi}\int_0^{2\pi}T_i(\alpha,\beta)d\beta. \tag{5.78}$$

Equations (5.56), (5.63)–(5.65) and (5.73)–(5.78) then show that

$$\langle T_x \rangle = \langle T_y \rangle = 0, \tag{5.79}$$

$$\langle T_z \rangle = A^2 \Omega \dot{M}_{\rm p}. \tag{5.80}$$

Hence the average value of the accretion torque for this type of asynchronism is

$$\langle \mathbf{T} \rangle = A^2 \Omega \dot{M}_{\rm p} \, \mathbf{k}. \tag{5.81}$$

This corresponds to the specific angular momentum of material leaving the L_1 region being conserved over a synodic period in its transfer to the primary via 3D magnetic channelling.

5.4 Partial Field Channelling

Observations suggest that effective field channelling of the accretion stream may occur at a distance from the L_1 region in some systems (e.g. Liebert and Stockman 1985; Wu and Wickramasinghe 1993; Schwope et al. 1997). An estimate of the position of the Alfvén point, at which the flow speed equals the Alfvén speed, can be made. This corresponds to the magnetic energy density becoming equal to the flow kinetic energy density, so

$$\frac{B^2}{2\mu_0} = \frac{1}{2} \rho v^2. \tag{5.82}$$

The mass transfer rate in the accretion stream is

$$\dot{M}_{\rm p} = \pi H^2 \rho v, \tag{5.83}$$

taking the cross section of the stream to be approximately circular, with H the density length-scale normal to the flow. If the initial part of the stream is not magnetically channelled then after leaving L_1 its centre will lie in the orbital plane, leading the motion of the line of stellar centres, and cause large local distortions of the primary's magnetic field. Calculations in non-magnetic systems suggest that the initial part of the stream is essentially straight and at a small angle to the line of stellar centres (e.g. Lubow and Shu 1975). Hence the cross sectional area of the initial stream can be taken to be approximately that of the L_1 source, having an area of $A = \pi H^2$ with H given by (5.6). The mass flux in the initial stream then follows from (5.83) as

$$\rho v = \frac{\dot{M}_{\rm p} \Omega^2 D^2}{\pi (c_{\rm s}^2)_{L_1} R_{\rm s}^2}. \tag{5.84}$$

Apart from close to the primary, the stream speed will be significantly less than free-fall values since the gravity field of the secondary and centrifugal force partly cancel the gravity field of the primary. Taking the speed to be a fraction $\tilde{f}$ of the free-fall value gives

$$v = \tilde{f}\left(\frac{GM_{\rm p}}{r}\right)^{\frac{1}{2}}. \tag{5.85}$$

The unperturbed magnetic field can be used to find an approximate expression for the Alfvén radius, so

$$B \simeq (B_{\rm p})_0\left(\frac{R_{\rm p}}{r}\right)^3. \tag{5.86}$$

Using (5.84)–(5.86), together with (2.296)–(2.298) to relate $M_{\rm s}$, $R_{\rm s}$, D and P, gives the Alfvén radius as a fraction of the distance from the primary as

$$\frac{R_{\rm A}}{A} = \frac{0.82\left(\frac{0.25}{\tilde{f}}\right)^{\frac{2}{11}}\left(\frac{(B_{\rm p})_0}{60\,{\rm MG}}\right)^{\frac{4}{11}}\left(\frac{R_{\rm p}}{8.67\times10^6\,{\rm m}}\right)^{\frac{12}{11}}\left(\frac{T_{L_1}}{2\times10^3}\right)^{\frac{2}{11}}}{q^{\frac{5}{11}}N\left(\frac{M_{\rm s}}{0.2\,M_\odot}\right)^{\frac{6}{33}}\left(\frac{M_{\rm p}}{0.6\,M_\odot}\right)^{\frac{1}{11}}\left(\frac{M}{0.8\,M_\odot}\right)^{\frac{15}{33}}\left(\frac{\dot{M}_{\rm p}}{10^{-10}\,M_\odot\,{\rm year}^{-1}}\right)^{\frac{2}{11}}}, \tag{5.87}$$

where N is given by (5.2). For the observed range of primary magnetic fields, orbital periods, which are related to the secondary mass, and likely primary masses, the range $0.2 \lesssim R_{\rm A}/A \lesssim 1.5$ results. This corresponds to late magnetic channelling of the accretion stream up to total channelling from the L_1 region.

For partial channelling, as the field strength increases its distortion will decrease and effective channelling, in general out of the orbital plane, will ultimately occur. The dominant contribution to the accretion torque should arise from the channelled region, since this is where the generated magnetic stresses are greatest. An estimate of the accretion torque in the case of a partially channelled flow can therefore be made by considering the angular momentum transfer due to a section of the totally channelled stream lying inside a radius $R_{\rm m}(\alpha,\beta) < R_{\rm A}$. This will give an estimate of the relative magnitudes of the accretion torque components for varying degrees of field channelling.

The dominant contribution to $f_x(\alpha,\beta)$ arises from the second term on the right hand side of (5.54), involving the integral of K_x along the stream. The major contribution to $f_y(\alpha,\beta)$ comes from the first term on the right hand side of (5.55). This term arose from the Coriolis integral in (5.45) and hence the variation of its integrand, denoted by $K(\alpha,\beta,\psi)$, is required along the stream together with the variations of K_x and K_z. Although these integrands were expressed as functions of ψ, in the present context the coordinate r/A must be used in their integration. It

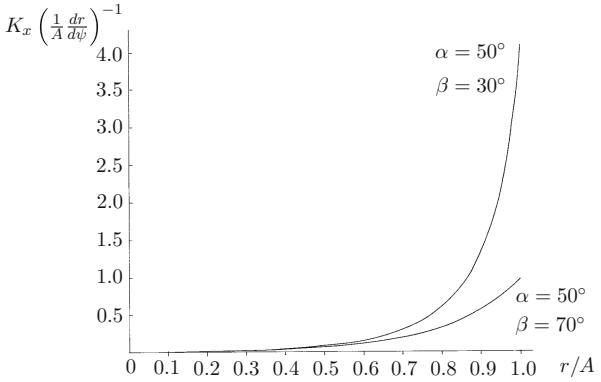

Fig. 5.6 The variation of $K_x A(dr/d\psi)^{-1}$ with r/A along primary field lines passing through L_1 (from Campbell 1986)

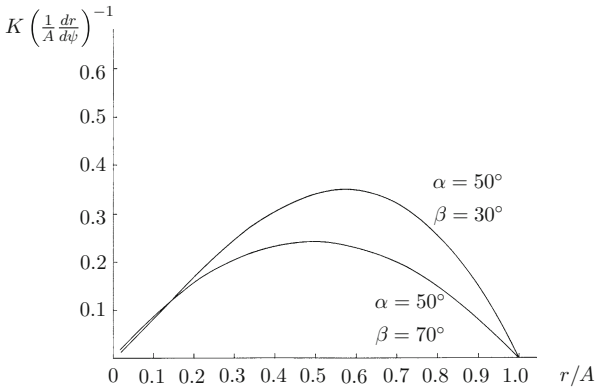

Fig. 5.7 The variation of $KA(dr/d\psi)^{-1}$ with r/A along primary field lines passing through L_1 (from Campbell 1986)

follows that the variation of $K_x(\alpha, \beta, \psi(r))A(dr/d\psi)^{-1}$ with r/A is required to estimate the contribution made between $r = R_\mathrm{p}$ and $r = R_\mathrm{m}$, and likewise for the other two integrands.

Figures 5.6, 5.7, and 5.8 show the variations of the relevant functions with r/A. Consider $R_\mathrm{m} = 0.5A$; Fig. 5.6 illustrates that the section of the stream having $r < R_\mathrm{m}$, and hence $r/A < 0.5$, contributes only a few per cent to the total line integral of $K_x A(dr/d\psi)^{-1}$. It therefore follows that, for such a partially channelled stream, the values of f_x will typically be reduced by an order of magnitude from those shown in Tables 5.1, 5.2, and 5.3.

Figure 5.7 shows that the section of the stream having $r < R_\mathrm{m}$ typically contributes $\sim 50\%$ to the total line integral of $KA(dr/d\psi)^{-1}$. Hence, for $R_\mathrm{m} = 0.5A$, the values of f_y shown in Tables 5.1, 5.2, and 5.3 will only be approximately

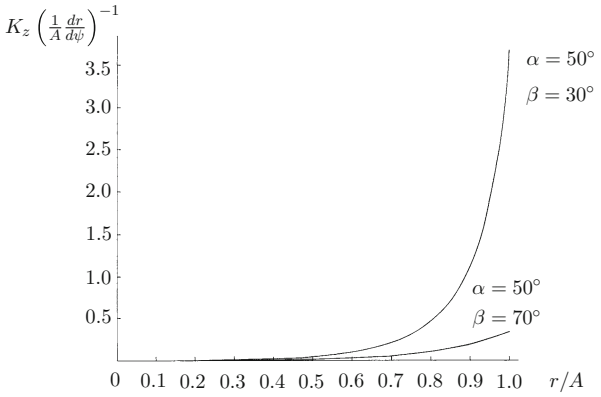

Fig. 5.8 The variation of $K_z A(dr/d\psi)^{-1}$ with r/A along primary field lines passing through L_1 (from Campbell 1986)

halved. The magnitude of f_y will then generally exceed that of f_x, this being the reverse of the case of a totally channelled stream.

For $R_m = 0.5A$, Fig. 5.8 illustrates that the integral on the right hand side of (5.56), for $f_z(\alpha, \beta)$, will typically be reduced by at least an order of magnitude from its value for total field channelling of the accretion stream. The deviations of $f_z(\alpha, \beta)$ from unity will therefore be significantly reduced from those shown in Tables 5.1, 5.2, and 5.3. This is a result of the fact that most of the exchange of the z-component of angular momentum with the orbit occurs near L_1, due to gravitational coupling to the secondary.

5.5 Summary and Discussion

The conclusions of the foregoing calculation can be summarized. For a stream channelled from the L_1 region, and high inclinations of the white dwarf dipole moment, the horizontal components of the accretion torque can be comparable to the vertical component. For slow asynchronous motions, with the primary's angular velocity parallel to $\boldsymbol{\Omega}$, the horizontal torque components average to zero over a synodic period, while the vertical component averages to the conserved form $A^2\Omega\dot{M}_p$.

For a partially channelled stream the magnitudes of the horizontal torque components are reduced. For a channelling radius of $0.5A$ the horizontal torque component perpendicular to the line of stellar centres becomes a small fraction of the vertical component. However, the torque component along the line of stellar centres can remain significant for some magnetic orientations, since it does not involve gravitational coupling to the orbit, being principally due to Coriolis torque.

The distribution of this torque is fairly uniform along the stream so, even for a channelling radius as small as $\sim 0.2A$, T_y can be a significant fraction of T_z for channelling well out of the orbital plane.

Observations of HU Aqr by Schwope et al. (1997), using Doppler tomography, indicate the existence of an accretion curtain of tenuous material above the initial stream. Closer to the white dwarf the whole stream lifts out of the orbital plane. This suggests that the field linkage process is continuous, beginning near L_1 but only becoming strongly effective closer to the primary. The observations indicate a channelling radius of at least $0.4A$ for this system, so the T_y component of the accretion torque would be significant.

The channelling radius will vary significantly, depending on the primary's magnetic moment and the orbital separation, as the simulations confirm. The results of this chapter have important consequences for the maintenance of synchronism, which are discussed in the next chapter.

References

Beuermann, K., Euchner, F., Reinsch, K., Jordan, S., Gansicke, B.T., 2007, A&A, 463, 647.
Campbell, C.G., 1986, MNRAS, 221, 599.
Liebert, J., Stockman, H.S., 1985, Cataclysmic Variables and Low Mass X-Ray Binaries, Reidel, Dordrecht, Holland, 113, 151.
Lubow, S.H., Shu, F.H., 1975, ApJ, 198, 383.
Meggitt, S.M.A., Wickramasinghe, D.T., 1989, MNRAS, 236, 31.
Schwope, A.D., Mantel, K., Horne, K., 1997, A&A, 319, 894.
Wu, K., Wickramasinghe, D.T., 1993, MNRAS, 260, 141.
Zhilkin, A.G., Bisikalo, D.V., 2010, ARep, 54, 1063.
Zhilkin, A.G., Bisikalo, D.V., Mason, P.A., 2012, ARep, 56, 257.

Chapter 6
AM Her Stars: The Maintenance of Synchronism

Abstract The problem of the maintenance of synchronism is addressed. Since the inductive synchronizing torque vanishes at corotation, there must be another torque present to balance the accretion torque. In general, a 3D torque is required and the balance must be stable. Because the secondary star has at least a convective envelope, and is rapidly rotating due to tidal synchronization, it is likely to have a large-scale magnetic field generated by dynamo action. The interaction of such a field with the magnetic primary can produce a torque which can balance the accretion torque, with stable orientations. Certain restrictions can result related to the surface polar strength and the orientation of the secondary's magnetic field.

Another possible balancing torque results if the primary is distorted from spherical symmetry due to non-radial internal magnetic forces, caused by the electric current sources of its magnetic field. A tidal torque acts on the distorted star and this can balance the magnetic torque to produce a synchronous state, if these torques significantly exceed the accretion torque. This can occur if the secondary has a surface magnetic field of a few kG. The effects of these torques in relation to the orbital evolution are also considered.

6.1 Non-Dissipative Torques

Before the attainment of synchronism can be considered, the nature of the corotating state must be investigated. The analysis of Chap. 4 shows that as the white dwarf approaches corotation the dissipative inductive torque tends to zero. However, the accretion torque, which is non-dissipative, remains finite and so for a spherical primary a non-dissipative torque must act to cancel it. In this case the total torque on the synchronous white dwarf vanishes and its angular velocity and angular momentum are conserved, both being parallel to the orbital angular velocity $\boldsymbol{\Omega}$. If the primary is non-spherical, in general, its inertial angular velocity $\boldsymbol{\omega}_{\rm in}$ and its angular momentum $\mathbf{L}$ will not be parallel. Since synchronism requires $\boldsymbol{\omega}_{\rm in} = \boldsymbol{\Omega}$ then $\mathbf{L}$ will precess about $\boldsymbol{\omega}_{\rm in}$ and a finite torque will act. This torque must have the required

C. G. Campbell, *Magnetohydrodynamics in Binary Stars*, Astrophysics and Space Science Library 456, https://doi.org/10.1007/978-3-319-97646-4_6

form to generate the precession in **L**. It will be seen that the accretion torque alone cannot satisfy this condition and hence a non-dissipative torque is again needed.

Early considerations of the maintenance of synchronism pointed out that a non-dissipative magnetostatic torque would result if the primary's field was excluded from the secondary. However, this can only happen if the decay time of a magnetic field in the secondary far exceeds the lifetime of the binary system. The magnetic decay times given by (2.224) correspond to the dissipation of poloidal modes. The longest-lived principal mode has $l = j = 1$ and has a decay time of

$$\tau_{\rm d} = \frac{R_{\rm s}^2}{\pi^2 \eta}, \tag{6.1}$$

where $\eta = 1/\mu_0 \sigma$ with σ the conductivity. The decay time is maximized by taking an Ohmic diffusivity, given by (2.226) as

$$\eta_{\rm ohm} = 5.2 \times 10^7 \ln \Lambda \, T^{-\frac{3}{2}} \, {\rm m}^2 \, {\rm s}^{-1}, \tag{6.2}$$

where T is the temperature and $\ln \Lambda$ a shielding factor of typical magnitude $5 \lesssim \ln \Lambda \lesssim 20$. Taking a mean temperature of 10^6 K, together with $\ln \Lambda = 6$ and $R_{\rm s} = 2.3 \times 10^8$ m gives $\tau_{\rm d} = 5.4 \times 10^8$ years. The binary lifetime is measured by the mass transfer time-scale $\tau_M = M_{\rm s}/|\dot{M}_{\rm s}|$, which is typically $\sim 4 \times 10^9$ years for an AM Her system. Hence $\tau_{\rm d} < \tau_M$ which invalidates a magnetostatic approach, since the primary's field would not be excluded from the secondary. In fact, as previously noted, the low mass secondaries in AM Her systems will be largely convective and η is then believed to be greatly enhanced, so shortening $\tau_{\rm d}$ by several orders of magnitude and making a magnetostatic torque even less valid.

Two mechanisms have been considered to generate suitable balancing torques. Firstly, it was pointed out by Joss et al. (1979) that the secondary could contain an intrinsic poloidal magnetic field and that this would extend to the primary and generate a torque on it. The existence of such a field is very likely since turbulence and rapid rotation are present and these can lead to dynamo action, as seen in Sect. 2.3. Secondly, Joss et al. (1979) and Katz (1989) proposed that the white dwarf could be distorted by a $\mathbf{J} \times \mathbf{B}$ force, where $\mathbf{J}$ is the current density source of its field. Tidal interaction with the secondary's gravitational field then leads to a torque on the primary. These mechanisms are investigated in detail in this chapter.

Sections 6.2 and 6.3 consider balances between a non-dissipative magnetic torque and the accretion torque, in two and three dimensions. The effects of quadrupolar fields are discussed in Sect. 6.4. In Sect. 6.5 the three-dimensional balance between a tidal torque, exerted on a magnetically distorted primary, and a magnetic torque is analysed. Orbital torques and their evolutionary effects are considered in Sect. 6.6.

6.2 Accretion and Magnetism in Two Dimensions

The simplest case, in which both stars have dipolar fields with moments $\mathbf{m}_\mathrm{p}$ and $\mathbf{m}_\mathrm{s}$ lying in the orbital plane, was considered in Campbell (1985). Figure 6.1 shows the orientation angles used to define this situation. The vector $\mathbf{m}_\mathrm{s}$ is fixed in the synchronous secondary star by dynamo processes, while $\mathbf{m}_\mathrm{p}$ can rotate with the white dwarf. The primary is taken to be spherical. Since the accretion stream is centred in the orbital plane, the torque components in the x and y directions, given by (5.63) and (5.64), vanish. If matter becomes field-channelled at some distance from the L_1 point then $f_z(\pi/2, \beta)$, given by (5.56), is close to unity and the accretion torque (5.65) can be written as

$$\mathbf{T}_\mathrm{a} = A^2 \Omega \dot{M}_\mathrm{p} \mathbf{k}, \tag{6.3}$$

where $\mathbf{k}$ is a unit vector in the z-direction.

The magnetic torque exerted on the primary by the field of the secondary is given by

$$\mathbf{T}_\mathrm{m} = -m_\mathrm{p} B_\mathrm{sp} \sin(\beta - \bar{\delta}) \mathbf{k}, \tag{6.4}$$

where $\mathbf{B}_\mathrm{sp}$ is the secondary's magnetic field at the position of the primary, and $\bar{\delta}$ is the tangent angle shown in Fig. 6.1. The components of $\mathbf{B}_\mathrm{sp}$ are

$$(B_\mathrm{sp})_x = \frac{\mu_0 m_\mathrm{s}}{4\pi D^3} \sin\delta, \tag{6.5}$$

$$(B_\mathrm{sp})_y = -\frac{\mu_0 m_\mathrm{s}}{2\pi D^3} \cos\delta. \tag{6.6}$$

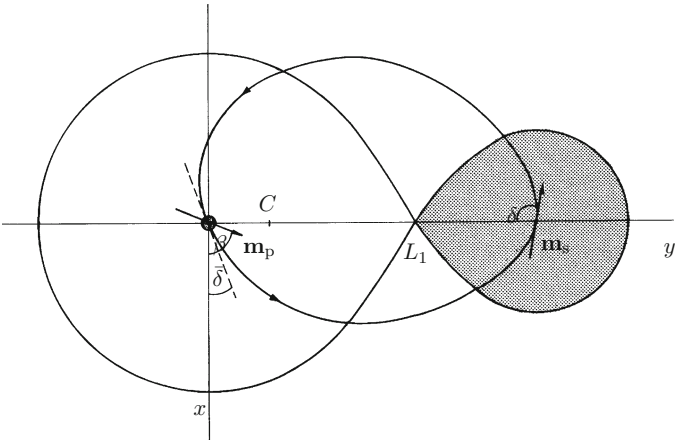

Fig. 6.1 The dipole orientations in the orbital plane (from Campbell 1985)

From the definition of $\bar{\delta}$, together with (6.5) and (6.6), it follows that

$$\sin\delta = \frac{2\cos\bar{\delta}}{(3\cos^2\bar{\delta}+1)^{\frac{1}{2}}}, \tag{6.7}$$

$$\cos\delta = -\frac{\sin\bar{\delta}}{(3\cos^2\bar{\delta}+1)^{\frac{1}{2}}}. \tag{6.8}$$

Equations (6.5)–(6.8) give the magnitude of $\mathbf{B}_{\rm sp}$ as

$$B_{\rm sp} = \frac{\mu_0 m_{\rm s}}{2\pi D^3}\frac{1}{(3\cos^2\bar{\delta}+1)^{\frac{1}{2}}}. \tag{6.9}$$

The sum of the accretion and magnetic torques acting on the primary is

$$\mathbf{T} = [A^2\Omega\dot{M}_{\rm p} - m_{\rm p}B_{\rm sp}\sin(\beta-\bar{\delta})]\mathbf{k}, \tag{6.10}$$

where its dipole moment is related to its radius and polar field by

$$m_{\rm p} = \frac{2\pi}{\mu_0}R_{\rm p}^3(B_{\rm p})_0, \tag{6.11}$$

with an equivalent expression for $m_{\rm s}$. For a synchronous primary at orientation $\beta = \beta_s$ the torque $\mathbf{T}$ must vanish. Equations (6.9)–(6.11) give this condition as

$$\frac{\sin(\beta_s-\bar{\delta})}{(3\cos^2\bar{\delta}+1)^{\frac{1}{2}}} = \frac{10\mu_0 A^2\dot{M}_{\rm p}M}{(B_{\rm s})_0(B_{\rm p})_0R_{\rm p}^3M_{\rm s}P}, \tag{6.12}$$

where $M = M_{\rm s} + M_{\rm p}$, $(B_{\rm s})_0$ is the secondary's polar magnetic field and P is the orbital period. The lobe-filling condition

$$\frac{M}{M_{\rm s}}\left(\frac{R_{\rm s}}{D}\right)^3 = 0.1, \tag{6.13}$$

due Paczyński (1967), has been employed, where $R_{\rm s}$ is the mean radius of the secondary. The torque balance condition (6.12) requires $\sin(\beta_s-\bar{\delta}) > 0$ and hence

$$\bar{\delta} < \beta_s < \bar{\delta}+\pi. \tag{6.14}$$

The linear stability of the synchronous state requires the sign of a torque perturbation due to a perturbation of β about β_s to be opposite to that of $\beta' = \beta-\beta_s$.

Hence

$$\left(\frac{dT}{d\beta}\right)_{\beta_s} < 0 \tag{6.15}$$

is necessary for stability. Applying this condition to (6.10) for the total torque T gives $\cos(\beta_s - \bar{\delta}) > 0$ and hence

$$\bar{\delta} < \beta_s < \bar{\delta} + \frac{\pi}{2} \quad \text{or} \quad \bar{\delta} + \frac{3\pi}{2} < \beta_s < \bar{\delta} + 2\pi. \tag{6.16}$$

A stable synchronous state must satisfy (6.14) and (6.16) and so requires

$$\bar{\delta} < \beta_s < \bar{\delta} + \frac{\pi}{2}. \tag{6.17}$$

It is clear from (6.12) that for a given value of β_s the condition of vanishing torque can be satisfied by choosing $(B_s)_0$ and δ independently, subject to the stability condition (6.17). For a given set of parameters there is only one stable synchronous orientation β_s, as illustrated in Fig. 6.2. Consider, as an example, an orbital period $P = 1.5\,\mathrm{h}$, giving a lobe-filling secondary with $M_\mathrm{s} = 0.14\,M_\odot$. For $M_\mathrm{p} = 0.6\,M_\odot$, it follows that $D = 4.2 \times 10^8\,\mathrm{m}$ and $A = 2.7 \times 10^8\,\mathrm{m}$, while $R_\mathrm{p} = 8.7 \times 10^6\,\mathrm{m}$. The accretion rate is taken as $\dot{M}_\mathrm{p} = 10^{-10}\,M_\odot \mathrm{year}^{-1}$. For $(B_\mathrm{p})_0 = 3.1 \times 10^3\,\mathrm{T}$, $(B_\mathrm{s})_0 = 6.4 \times 10^{-3}\,\mathrm{T}$ and $\bar{\delta} = 20°$, corresponding to $\delta = -100°$, (6.12) gives $\beta_s = 76°$, which satisfies the stability condition (6.17).

It is of interest to calculate the period of small oscillations of the primary about the synchronous state. An expression for this period can be found by equating the rate of change of angular momentum of the primary to the restoring torque resulting

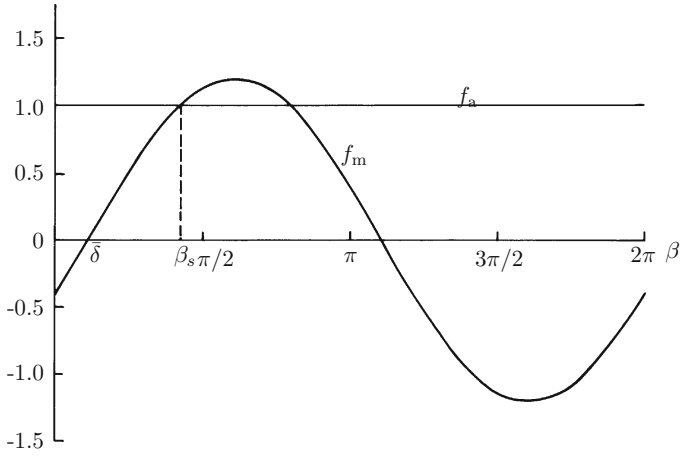

Fig. 6.2 The synchronous torque balance in two dimensions, normalized by $A^2\Omega\dot{M}_\mathrm{p}$

from a small angular displacement about β_s. Expressing the primary's moment of inertia as $I = k_{\rm p}^2 M_{\rm p} R_{\rm p}^2$, (6.10) for T and the synchronous condition (6.12) then give the oscillation period as

$$P_0 = 38.0 \frac{\left(\frac{k_{\rm p}}{0.42}\right)\left(\frac{M_{\rm p}}{0.6 M_\odot}\right)^{\frac{1}{2}}\left(\frac{R_{\rm p}}{8.67\times 10^6\,{\rm m}}\right)\tan^{\frac{1}{2}}(\beta_s - \bar{\delta})}{\left(\frac{q}{1.1}\right)^{\frac{1}{4}}\left(\frac{M_{\rm s}}{0.14\,M_\odot}\right)^{\frac{1}{6}}\left(\frac{M}{0.74 M_\odot}\right)^{\frac{1}{3}}\left(\frac{\dot{M}_{\rm p}}{10^{-10}\,M_\odot\,{\rm year}^{-1}}\right)^{\frac{1}{2}}}\ {\rm year}. \tag{6.18}$$

where $0.1 < k_{\rm p}^2 < 0.2$. Taking $k_{\rm p}^2 = 0.18$, corresponding to $M_{\rm p} = 0.6 M_\odot$, and the foregoing parameters, yields $P_0 = 46$ year.

Beuermann et al. (2014) used phase resolved optical light curves of DP Leo, and found that the data were consistent with the accreting poles oscillating about a synchronous state with a period of $\simeq 60$ year. The formula (6.18) can give this period for a range of possible parameters.

It is noted from (6.4) that for an asynchronous primary with $\beta = \omega t$ the average of $\mathbf{T}_{\rm m}$ over a synodic period is zero. Hence such a torque does not play a part in the approach to synchronism.

6.3 Accretion and Magnetism in Three Dimensions

6.3.1 Orientations with Zero Torque

The general case, in which the secondary's magnetic moment has an orientation (δ, γ), was considered by Campbell (1989) and is shown in Fig. 6.3. A spherical primary is considered, so synchronism at (α_s, β_s) requires zero torque, and such a state must be stable to all angular perturbations.

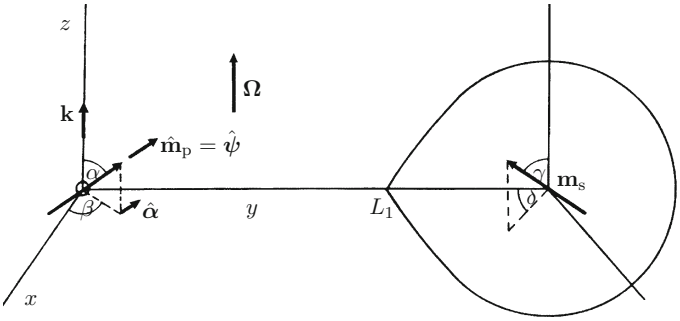

Fig. 6.3 The dipole orientations in three dimensions (from Campbell 1989)

The components of the secondary's magnetic field at the position of the primary are

$$(B_{\rm sp})_x = -\frac{\mu_0 m_{\rm s}}{4\pi D^3}\sin\gamma\sin\delta, \tag{6.19}$$

$$(B_{\rm sp})_y = -\frac{\mu_0 m_{\rm s}}{2\pi D^3}\sin\gamma\cos\delta, \tag{6.20}$$

$$(B_{\rm sp})_z = -\frac{\mu_0 m_{\rm s}}{4\pi D^3}\cos\gamma. \tag{6.21}$$

The magnetic torque on the primary is

$$\mathbf{T}_{\rm m} = \mathbf{m}_{\rm p} \times \mathbf{B}_{\rm sp}, \tag{6.22}$$

where the unit vector $\hat{\mathbf{m}}_{\rm p}$ is

$$\hat{\mathbf{m}}_{\rm p} = \sin\alpha\cos\beta\,\mathbf{i} + \sin\alpha\sin\beta\,\mathbf{j} + \cos\alpha\,\mathbf{k}. \tag{6.23}$$

Equations (6.19)–(6.23) give the components of the magnetic torque as

$$T_{{\rm m}x} = \frac{\mu_0 m_{\rm p} m_{\rm s}}{4\pi D^3}(2\sin\gamma\cos\delta\cos\alpha - \cos\gamma\sin\alpha\sin\beta), \tag{6.24}$$

$$T_{{\rm m}y} = \frac{\mu_0 m_{\rm p} m_{\rm s}}{4\pi D^3}(\cos\gamma\sin\alpha\cos\beta - \sin\gamma\sin\delta\cos\alpha), \tag{6.25}$$

$$T_{{\rm m}z} = \frac{\mu_0 m_{\rm p} m_{\rm s}}{4\pi D^3}(\sin\delta\sin\beta - 2\cos\delta\cos\beta)\sin\alpha\sin\gamma. \tag{6.26}$$

The components of the accretion torque, $\mathbf{T}_{\rm a}(\alpha,\beta)$ are given by (5.63)–(5.65). If matter becomes field-channelled at some distance from L_1 it was seen that $T_{{\rm a}z}$ becomes effectively independent of (α,β). The horizontal components then only vary by $\simeq 10\%$ as β is varied over an interval of $\pi/2$. The simplest form for the accretion torque containing these properties is then

$$T_{{\rm a}x} = A^2\Omega\dot{M}_{\rm p}N_x\cos\alpha, \tag{6.27}$$

$$T_{{\rm a}y} = A^2\Omega\dot{M}_{\rm p}N_y\cos\alpha, \tag{6.28}$$

$$T_{{\rm a}z} = A^2\Omega\dot{M}_{\rm p}, \tag{6.29}$$

where the constants N_x and N_y are negative for $0 < \beta < \pi$ and positive for $\pi < \beta < 2\pi$, and their magnitudes depend on the channelling radius.

The necessary condition for a synchronous state is that $\mathbf{T}_{\rm m}$ and $\mathbf{T}_{\rm a}$ cancel. The torque component equations (6.24)–(6.29), together with the components of $\hat{\mathbf{m}}$

from (6.23), then give the synchronous conditions

$$-\cos\gamma\,\hat{m}_{\mathrm{p}y}+(2\sin\gamma\cos\delta+QN_x)\hat{m}_{\mathrm{p}z}=0, \tag{6.30}$$

$$\cos\gamma\,\hat{m}_{\mathrm{p}x}+(QN_y-\sin\gamma\sin\delta)\hat{m}_{\mathrm{p}z}=0, \tag{6.31}$$

$$-2\sin\gamma\cos\delta\,\hat{m}_{\mathrm{p}x}+\sin\gamma\sin\delta\,\hat{m}_{\mathrm{p}y}=-Q, \tag{6.32}$$

where the characteristic ratio of the accretion and magnetic torques is

$$Q=\frac{4\pi D^3A^2\Omega\dot{M}_{\mathrm{p}}}{\mu_0 m_{\mathrm{p}}m_{\mathrm{s}}}. \tag{6.33}$$

Solving (6.30)–(6.32) yields the synchronous orientation of the primary in terms of the components of its dipole moment unit vector as

$$\hat{m}_{\mathrm{p}x}=\sin\alpha_s\cos\beta_s=\frac{QN_y-\sin\gamma\sin\delta}{\sin\gamma(N_x\sin\delta+2N_y\cos\delta)}, \tag{6.34}$$

$$\hat{m}_{\mathrm{p}y}=\sin\alpha_s\sin\beta_s=-\frac{QN_x+2\sin\gamma\cos\delta}{\sin\gamma(N_x\sin\delta+2N_y\cos\delta)}, \tag{6.35}$$

$$\hat{m}_{\mathrm{p}z}=\cos\alpha_s=-\frac{1}{\tan\gamma(N_x\sin\delta+2N_y\cos\delta)}. \tag{6.36}$$

However, since $\hat{\mathbf{m}}_{\mathrm{p}}$ is a unit vector, the condition $\hat{\mathbf{m}}_{\mathrm{p}}\cdot\hat{\mathbf{m}}_{\mathrm{p}}=1$ must be satisfied. Equations (6.34)–(6.36) then yield a quadratic equation for Q which has solutions

$$Q=\frac{-\sin\gamma(2N_x\cos\delta-N_y\sin\delta)\pm\sqrt{P}}{N_x^2+N_y^2}, \tag{6.37}$$

where

$$P=(N_x^2+N_y^2-1)\sin^2\gamma(N_x\sin\delta+2N_y\cos\delta)^2-(N_x^2+N_y^2)\cos^2\gamma. \tag{6.38}$$

It follows from (6.33) for Q, together with (6.37) and (6.38) that, for given orbital parameters, the orientation and surface polar strength of the secondary's magnetic field cannot be chosen independently if the primary is to experience zero torque. This restriction did not occur in the simple two-dimensional case.

The values of N_x and N_y depend on where material lost from the secondary becomes field-channelled. As seen in Sect. 5.4, N_x involves gravitational coupling to the orbit and is more sensitive to the extent of the field-channelling region than N_y, which is due to the more evenly distributed Coriolis torque. If field channelling is far from L_1 (i.e. $\gtrsim A/3$) then $N_x^2+N_y^2<1$ and it follows from (6.37) and (6.38) that

Q becomes complex. Hence, in such a situation, an orientation cannot be found at which the magnetic and accretion torques cancel. However, if $Q \ll 1$ the magnetic torque dominates and synchronous states are essentially possible.

6.3.2 *Stability of the Synchronous State*

Having found a synchronous state, its stability to small disturbances must be established. A general perturbation consists of a twist about an axis through the primary. Subsequently the star's rotational motion is defined by an instantaneous angular velocity $\boldsymbol{\omega}$ where, relative to the orbital frame,

$$\boldsymbol{\omega} = \dot{\alpha}\hat{\boldsymbol{\alpha}} + \dot{\beta}\mathbf{k} + \dot{\psi}\hat{\boldsymbol{\psi}}. \tag{6.39}$$

It follows from Fig. 6.3 that the components of $\boldsymbol{\omega}$ are

$$\omega_x = -\dot{\alpha}\sin\beta + \dot{\psi}\sin\alpha\cos\beta, \tag{6.40}$$

$$\omega_y = \dot{\alpha}\cos\beta + \dot{\psi}\sin\alpha\sin\beta, \tag{6.41}$$

$$\omega_z = \dot{\beta} + \dot{\psi}\cos\alpha. \tag{6.42}$$

Equations (6.24)–(6.29) give the components of the total torque acting on the white dwarf as

$$T_x = -C_\mathrm{m}\cos\gamma\sin\alpha\sin\beta + (C_\mathrm{a}N_x + 2C_\mathrm{m}\sin\gamma\cos\delta)\cos\alpha, \tag{6.43}$$

$$T_y = C_\mathrm{m}\cos\gamma\sin\alpha\cos\beta + (C_\mathrm{a}N_y - C_\mathrm{m}\sin\gamma\sin\delta)\cos\alpha, \tag{6.44}$$

$$T_z = C_\mathrm{m}\sin\gamma\sin\alpha(\sin\delta\sin\beta - 2\cos\delta\cos\beta) + C_\mathrm{a}, \tag{6.45}$$

where

$$C_\mathrm{m} = \frac{\mu_0 m_\mathrm{p} m_\mathrm{s}}{4\pi D^3}, \tag{6.46a}$$

$$C_\mathrm{a} = A^2\Omega\dot{M}_\mathrm{p}. \tag{6.46b}$$

The equation describing the evolution of a perturbation in $\boldsymbol{\omega}$, relative to the orbital frame, is

$$I(\dot{\boldsymbol{\omega}}' + \Omega\mathbf{k}\times\boldsymbol{\omega}') = \mathbf{T}', \tag{6.47}$$

where I is the moment of inertia of the primary. Expanding (6.40)–(6.45) for $\boldsymbol{\omega}$ and $\mathbf{T}$ to first order about the synchronous state gives the components of the equation of

motion (6.47) as

$$
\begin{aligned}
&-\sin\beta_s\ddot{\alpha}' - \Omega\cos\beta_s\dot{\alpha}' \\
&+[\bar{C}_{\rm m}(\cos\gamma\cos\alpha_s\sin\beta_s + 2\sin\gamma\cos\delta\sin\alpha_s) + \bar{C}_{\rm a}N_x\sin\alpha_s]\alpha' \\
&+\bar{C}_{\rm m}\cos\gamma\sin\alpha_s\cos\beta_s\beta' + \sin\alpha_s\cos\beta_s\ddot{\psi}' - \Omega\sin\alpha_s\sin\beta_s\dot{\psi}' = 0, \qquad (6.48)
\end{aligned}
$$

$$
\begin{aligned}
&\cos\beta_s\ddot{\alpha}' - \Omega\sin\beta_s\dot{\alpha}' \\
&-[\bar{C}_{\rm m}(\cos\gamma\cos\alpha_s\cos\beta_s + \sin\gamma\sin\delta\sin\alpha_s) - \bar{C}_{\rm a}N_y\sin\alpha_s]\alpha' \\
&+\bar{C}_{\rm m}\cos\gamma\sin\alpha_s\sin\beta_s\beta' + \sin\alpha_s\sin\beta_s\ddot{\psi}' + \Omega\sin\alpha_s\cos\beta_s\dot{\psi}' = 0, \qquad (6.49)
\end{aligned}
$$

$$
\begin{aligned}
&\bar{C}_{\rm m}\sin\gamma\cos\alpha_s(2\cos\delta\cos\beta_s - \sin\delta\sin\beta_s)\alpha' + \ddot{\beta}' \\
&-\bar{C}_{\rm m}\sin\gamma\sin\alpha_s(2\cos\delta\sin\beta_s + \sin\delta\cos\beta_s)\beta' + \cos\alpha_s\ddot{\psi}' = 0, \qquad (6.50)
\end{aligned}
$$

where $\bar{C}_{\rm m} = C_{\rm m}/I$, $\bar{C}_{\rm a} = C_{\rm a}/I$ and subscript s denotes the synchronous state.

The angular perturbations can be written as the product of an exponential time dependence and constant amplitudes, so

$$\alpha' = a_1\exp(i\sigma t), \quad \beta' = a_2\exp(i\sigma t), \quad \psi' = a_3\exp(i\sigma t). \qquad (6.51)$$

Substitution of these in (6.48)–(6.50) gives a system of equations for the amplitudes and the vanishing of the determinant of their coefficients, for consistency, yields the following characteristic equation for σ,

$$\sigma^6 + C_1\sigma^4 + C_2\sigma^2 + C_3\sigma = 0, \qquad (6.52)$$

where

$$
\begin{aligned}
C_1 =&\bar{C}_{\rm m}\sin\gamma\sin\alpha_s(2\cos\delta\sin\beta_s + \sin\delta\cos\beta_s) \\
&+\bar{C}_{\rm m}\frac{\cos\gamma}{\cos\alpha_s}(1+\cos^2\alpha_s) - \Omega^2, \qquad (6.53)
\end{aligned}
$$

$$
\begin{aligned}
C_2 =&\bar{C}_{\rm m}^2\frac{\sin\gamma\cos\gamma\sin\alpha_s}{\cos\alpha_s}(2\cos\delta\sin\beta_s + \sin\delta\cos\beta_s) + \bar{C}_{\rm m}^2\cos^2\gamma \\
&-\bar{C}_{\rm m}\Omega^2\sin\gamma\sin\alpha_s(2\cos\delta\sin\beta_s + \sin\delta\cos\beta_s), \qquad (6.54)
\end{aligned}
$$

$$C_3 = -i\Omega\bar{C}_{\rm m}^2 Q\cos\gamma\cos\alpha_s. \qquad (6.55)$$

Consider, first, the case with accretion absent, so that Q vanishes and hence $C_3 = 0$. Equation (6.52) then has the solution $\sigma^2 = 0$, which results from the fact that the torques are independent of the Euler angle ψ. The two finite frequencies are given by the roots of

$$\sigma^4 + C_1\sigma^2 + C_2 = 0. \tag{6.56}$$

Solving this equation for σ^2, using (6.23) for the components of $\hat{\mathbf{m}}$ and the synchronous state equations (6.30)–(6.32) with $Q = 0$, gives

$$\sigma^2 = -\bar{C}_{\rm m}\frac{\cos\gamma}{\cos\alpha_s} + \frac{\Omega^2}{2}\left[1 \pm \left(1 - 4\frac{\bar{C}_{\rm m}}{\Omega^2}\cos\gamma\cos\alpha_s\right)^{\frac{1}{2}}\right]. \tag{6.57}$$

If no rotation were present, in this case, (6.57) gives the single magnetic mode frequency $\sigma_{\rm m}$ from

$$\sigma_{\rm m}^2 = -\bar{C}_{\rm m}\frac{\cos\gamma}{\cos\alpha_s}. \tag{6.58}$$

From Eqs. (6.30)–(6.32), with $Q = 0$, it follows that two values of $\cos\gamma/\cos\alpha_s$ are possible, having the same magnitudes but different signs. The negative value corresponds to $\mathbf{m}_{\rm p}$ aligned with the secondary's field in the synchronous state, and all perturbations result in stable oscillations with frequency $\sigma_{\rm m}$.

Equations (6.39) and (6.51) give a general perturbation in the angular velocity as

$$\boldsymbol{\omega}' = i\sigma(a_1\hat{\boldsymbol{\alpha}}_s + a_2\mathbf{k} + a_3\hat{\boldsymbol{\psi}}_s)\exp(i\sigma t). \tag{6.59}$$

Equations (6.30)–(6.32), (6.50), (6.51) and (6.58) give

$$a_2\cos\alpha_s + a_3 = 0. \tag{6.60}$$

Using this to eliminate a_3 in (6.59) yields $\boldsymbol{\omega}'$ for the non-rotating magnetic modes as

$$\boldsymbol{\omega}' = i\sigma_{\rm m}[a_1\hat{\boldsymbol{\alpha}}_s + a_2\{\mathbf{k} - (\mathbf{k}\cdot\hat{\boldsymbol{\psi}}_s)\hat{\boldsymbol{\psi}}_s\}]\exp(i\sigma_{\rm m}t). \tag{6.61}$$

It follows that $\hat{\boldsymbol{\psi}}_s \cdot \boldsymbol{\omega}' = 0$ and hence the angular velocity of these modes is normal to the synchronous direction of $\mathbf{m}_{\rm p}$. Any displacement from equilibrium will result in such an oscillation and so the state is stable.

The presence of rotation results in two distinct types of mode, whose frequencies are given by (6.57). The dimensionless quantity $\bar{C}_{\rm m}/\Omega^2$ can be written as

$$\frac{\bar{C}_{\rm m}}{\Omega^2} = 4.6\times 10^{-11} q^3 \frac{\left(\frac{(B_{\rm p})_0}{20\,{\rm MG}}\right)\left(\frac{(B_{\rm s})_0}{10^2\,{\rm G}}\right)\left(\frac{R_{\rm p}}{8.67\times 10^6\,{\rm m}}\right)\left(\frac{M_{\rm s}}{0.2M_\odot}\right)^3}{\left(\frac{k_{\rm p}^2}{0.2}\right)\left(\frac{M_{\rm p}}{0.6M_\odot}\right)\left(\frac{M}{0.8M_\odot}\right)}. \tag{6.62}$$

Equation (6.58) gives $\sigma_{\rm m}^2 \sim \bar{C}_{\rm m}$ and hence it follows that $\sigma_{\rm m}/\Omega \sim 10^{-5}$, so the frequency of magnetic oscillations is much less than that of the orbital motion. Expansion of the square root term in (6.57) in the small ratio $\bar{C}_{\rm m}/\Omega^2$ then yields the two mode frequencies, to high accuracy, as

$$\sigma_+^2 = \Omega^2, \tag{6.63}$$

$$\sigma_-^2 = -\bar{C}_{\rm m}\frac{\cos\gamma}{\cos\alpha_s}\sin^2\alpha_s. \tag{6.64}$$

Substituting (6.63) for σ_+ in the equations of motion (6.48) and (6.49), using (6.58) for $\sigma_{\rm m}$ and dropping terms in $(\sigma_{\rm m}/\Omega)^2$, gives

$$a_1 = i\sin\alpha_s a_3. \tag{6.65}$$

The equation of motion (6.50) yields

$$a_2 = -\cos\alpha_s a_3. \tag{6.66}$$

Hence the angular velocity perturbation for the σ_+ mode is

$$\boldsymbol{\omega}' = i\Omega a_3[i\sin\alpha_s\hat{\boldsymbol{\alpha}}_s + \hat{\boldsymbol{\psi}}_s - (\hat{\boldsymbol{\Omega}}\cdot\hat{\boldsymbol{\psi}}_s)\hat{\boldsymbol{\Omega}}]\exp(i\Omega t). \tag{6.67}$$

It follows that $\boldsymbol{\omega}'\cdot\hat{\boldsymbol{\Omega}} = 0$ so $\boldsymbol{\omega}'$ lies in the $z=0$ plane and rotates with frequency Ω in the orbital frame. This is an inertial mode corresponding to perturbation twists normal to $\boldsymbol{\Omega}$. In this mode the magnetic torque is ineffective since it produces responses on a time-scale $2\pi/\sigma_{\rm m} \gg P$, where P is the orbital period.

The angular velocity perturbation for the σ_- mode is found by using (6.64) for σ_- in the equations of motion (6.48) and (6.49), remembering that $\sigma_{\rm m}/\Omega \ll 1$. This yields

$$a_1 = 0, \tag{6.68a}$$

$$a_3 = 0. \tag{6.68b}$$

The mode therefore has

$$\boldsymbol{\omega}' = i\sigma_- a_2 \exp(i\sigma_- t)\hat{\boldsymbol{\Omega}}. \tag{6.69}$$

This is the purely magnetic mode, given by (6.61), modified by rotation which changes its frequency to $\sigma_{\rm m} \sin\alpha_s$ and aligns it with the $\boldsymbol{\Omega}$ axis. The existence of this aligned magnetic mode can be seen directly from the equations of motion. Using (6.30)–(6.32) with $Q = 0$ and (6.58) for $\sigma_{\rm m}$, linear combinations of the equations of motion (6.48)–(6.50) give

$$\ddot{\alpha}' + \sigma_{\rm m}^2 \alpha' = -\Omega \sin\alpha_s \dot{\psi}', \tag{6.70}$$

$$\ddot{\beta}' + \sigma_{\rm m}^2 \sin^2\alpha_s \beta' = -\cos\alpha_s \ddot{\psi}', \tag{6.71}$$

$$-\sigma_{\rm m}^2 \sin\alpha_s \cos\alpha_s \beta' + \sin\alpha_s \ddot{\psi}' = \Omega\dot{\alpha}'. \tag{6.72}$$

If $\psi' \ll \beta'$ then (6.71) implies that β' varies harmonically with frequency $\sigma = \sigma_{\rm m} \sin\alpha_s$. With $\psi' \ll \beta'$, (6.72) yields $\alpha' \sim (\sigma_{\rm m}/\Omega)\beta'$ and hence (6.70) gives $\psi' \sim (\sigma_{\rm m}/\Omega)^2\beta' \ll \beta'$ consistently. Because $\sigma_{\rm m}/\Omega \sim 10^{-5}$, for realistic secondary star fields, it follows that the σ_- mode exists to high accuracy.

For the synchronous state to exist the magnetic torque must balance the accretion torque, or dominate it, since there is no three-dimensional orientation at which the latter vanishes. It follows that $Q = \bar{C}_{\rm a}/\bar{C}_{\rm m} \lesssim 1$ is necessary for synchronism and hence that $\bar{C}_{\rm a}/\Omega^2 \sim (\sigma_{\rm m}/\Omega)^2 \ll 1$. It is therefore clear that the additional terms due to accretion, occurring in the coefficients of α' in the equations of motion (6.48) and (6.49), do not affect the inertial mode given by (6.67). Similarly, the rotationally aligned mode still exists, except that accretion modifies its frequency. The frequency can be obtained directly from the equation of motion (6.50) which yields a harmonic equation for β' when α' and ψ' essentially vanish. Using the synchronous state solutions (6.34) and (6.35) then gives

$$\sigma^2 = \bar{C}_{\rm m}\left[\frac{\sin\gamma(\sin^2\delta + 4\cos^2\delta) + Q(2N_x\cos\delta - N_y\sin\delta)}{N_x\sin\delta + 2N_y\cos\delta}\right]. \tag{6.73}$$

A stable synchronous state requires $\sigma^2 > 0$.

6.3.3 Stable Synchronous Orientations

The values of N_x and N_y, which occur in the horizontal components of the accretion torque, depend on where matter becomes field-channelled. The values used here are $K_x = \pm 1.05$, $K_y = \pm 0.30$, where the negative and positive signs apply for $0 < \beta < \pi$ and $\pi < \beta < 2\pi$, respectively.

Table 6.1 Stable synchronous orientations for magneto-accretion balance. (from Campbell 1989)

γ	δ	Q	α_s	β_s
70	100	0.45	113.0	190.3
70	100	0.59	113.0	201.6
70	275	0.24	111.5	5.7
70	275	0.52	111.5	26.2
75	115	0.87	112.6	118.6
75	115	1.01	112.6	203.3
75	295	0.87	112.6	8.6
75	295	1.01	112.6	23.3
80	105	0.96	101.9	216.6
80	300	1.23	106.8	32.9
85	110	1.11	96.4	218.8
85	280	0.88	95.4	39.1
95	120	1.30	81.7	218.2
95	295	1.21	82.8	38.6
100	125	1.30	70.0	208.9
100	280	0.84	79.1	37.1
105	115	0.87	67.4	188.6
105	115	1.01	67.4	203.3
105	295	0.87	67.4	8.6
105	295	1.01	67.4	23.3
110	100	0.45	67.0	190.3
110	100	0.59	67.0	201.6
110	280	0.45	67.0	10.3
110	280	0.59	67.0	21.6

The simplest way of determining synchronous orientations is to choose (γ, δ) in (6.37) to calculate Q, and then find (α_s, β_s) from (6.34)–(6.36). The sign of σ^2 follows from (6.73). A sample of the results are shown in Table 6.1. The values of β_s illustrate that stable synchronous states, in which the magnetic and accretion torques balance, only occur with the accreting pole lagging the motion of the line of stellar centres.

Observations of AM Her systems suggest some tendency for the accreting pole to lead the line of stellar centres (Cropper 1988). The foregoing analysis shows that, for dipolar fields, a balance between magnetic and accretion torques cannot produce such observed orientations. The fact that only certain combinations of secondary field strength and orientation allow cancellation of the accretion torque reduces the likelihood of such a balance. Field-channelling far from L_1 makes a magneto-accretion balance in three-dimensions impossible since then $N_x^2 + N_y^2 < 1$ and real values of Q, given by (6.37), do not result. However, the above restrictions are essentially lifted if the magnetic torque dominates, which occurs for $Q \ll 1$.

Equation (6.33) can be expressed as

$$Q = 0.63 q^{\frac{1}{2}} \frac{\left(\frac{\dot{M}_{\rm p}}{10^{-10}\, M_\odot\, {\rm year}^{-1}}\right)\left(\frac{M}{0.8\, M_\odot}\right)^{\frac{5}{3}}}{\left(\frac{(B_{\rm p})_0}{20\,{\rm MG}}\right)\left(\frac{(B_{\rm s})_0}{10^2\,{\rm G}}\right)\left(\frac{R_{\rm p}}{8.67\times 10^6\,{\rm m}}\right)^3\left(\frac{M_{\rm s}}{0.2\, M_\odot}\right)^{\frac{2}{3}}}. \tag{6.74}$$

It follows that $Q \sim 10^{-2}$ for $(B_{\rm s})_0 = 6 \times 10^3$ G and then the magnetic torque alone could produce essentially stable synchronous states with, for appropriate (γ, δ), the accretion pole leading the line of stellar centres. Observations and theoretical models of lower main-sequence stars indicate that the secondary star could possess surface magnetic fields of several kG (see Chap. 12).

Dissipation has been ignored in the foregoing stability analysis. The typical growth time of an unstable magnetic mode is $\sim$ 10 year. Small perturbations about the synchronous state will be dissipated since they will induce currents in the secondary star. The resulting damping time will be approximately the same as the synchronization time for small ω/Ω, given by (4.93). This typically gives $\tau_{\rm syc} \sim 60$ year, suggesting that the dissipation may be too weak to quench an instability. However, these time-scales have a significant dependence on the system parameters, so quenching may be possible in some systems.

6.4 Quadrupolar Magnetic Fields

Observations suggest that the white dwarf in some systems may have a quadrupolar component in its magnetic field. The interaction of this with a dipolar secondary field would generate a torque which has a characteristic magnitude, relative to that of the dipole-dipole torque, of $(B_q/B_p)(R_{\rm p}/D)$, where B_q and B_p are the polar field strengths. Since $R_{\rm p}/D \ll 1$, the situation $B_q \sim B_p$ generally results in a relatively small quadrupole-dipole torque. However, for some orientations this torque would not be ignorable. Also the situation $B_q \gg B_p$ could make the torque significant, although there is no compelling evidence for dominant quadrupolar surface fields.

The role of a quadrupole field was considered by Wu and Wickramasinghe (1993). The secondary was taken to have a dipole moment $\mathbf{m}_{\rm s}$ perpendicular to the orbital plane, and the primary to have a dipole and quadrupole field with an angle θ between their symmetry axes. The primary's dipole moment was taken to be antiparallel to $\mathbf{m}_{\rm s}$ so the dipole-dipole torque vanished. The z-component of the quadrupole-dipole torque is

$$T_z = -\frac{m_{\rm s} B_q}{2}\left(\frac{R_{\rm p}}{D}\right)^4 \sin 2\theta \sin\phi, \tag{6.75}$$

where ϕ is the azimuth of the quadrupole symmetry axis, measured from the x-axis of Fig. 6.3. A small tilt of $\mathbf{m}_\mathrm{p}$ results in zero horizontal torque. It was shown that T_z has a magnitude sufficient to cancel the z-component of the accretion torque, though detailed orientations were not found. This calculation requires the horizontal components of the accretion torque to essentially vanish. As shown in Sect. 5.4, the x-component of the accretion torque is ignorable if matter becomes field-channelled far from L_1. However, the y-component is significant unless channelling only occurs very close to the white dwarf. Hence, this quadrupole analysis requires such channelling.

6.5 Gravity and Magnetism

6.5.1 The Synchronous State

It was pointed out by Joss et al. (1979) that a small distortion of the white dwarf would produce a significant gravitational torque due to interaction with the secondary. Katz (1989) showed that an internal toroidal magnetic field, with an associated poloidal current, can produce significant distortions of the white dwarf. The difference in the principal moments of inertia of a prolate body was found to be

$$I_3 - I_\perp = -\frac{2\pi}{3\mu_0}\frac{B_0^2 R_\mathrm{p}^6}{GM_\mathrm{p}}, \tag{6.76}$$

where I_3 is the moment about the symmetry axis. The resulting gravitational torque was estimated and can be at least comparable to the accretion torque for $B_0 \sim 10^7$ G. Internal fields of this magnitude, or even somewhat larger, are reasonable given that the observed surface fields are $10\,\mathrm{MG} \lesssim (B_\mathrm{p})_0 \lesssim 100\,\mathrm{MG}$.

The detailed consequences of a distorted white dwarf were considered in Campbell (1990). The primary is taken to have a magnetic moment $\mathbf{m}_\mathrm{p}$, as shown in Fig. 6.3, but to be a spheroidal body with its symmetry axis coincident with $\mathbf{m}_\mathrm{p}$. The moments of inertia about $\mathbf{m}_\mathrm{p}$ and orthogonal axes in the magnetic equatorial plane are denoted by I_3 and $I_\perp$, respectively. Treating the secondary as a spherical gravitational source, the torque it exerts on the primary is

$$\mathbf{T}_\mathrm{g} = \frac{3GM_\mathrm{s}(I_3 - I_\perp)}{D^3}\sin\alpha\sin\beta\mathbf{j}\times\hat{\mathbf{m}}_\mathrm{p}, \tag{6.77}$$

where $\hat{\mathbf{m}}_\mathrm{p}$ is given by (6.23). This expression follows from (A56) in the Appendix, since $\cos\theta = \sin\alpha\sin\beta$, $\hat{\mathbf{r}} = \mathbf{j}$ and $\mathbf{e}_3 = \hat{\mathbf{m}}_\mathrm{p}$.

If the secondary has a magnetic moment $\mathbf{m}_\mathrm{s}$, as shown in Fig. 6.3, the primary will experience a magnetic torque given by (6.22). It will also experience the accretion torque given by (5.63)–(5.65). Since the primary is non-spherical, its inertial angular velocity $\boldsymbol{\omega}$, with the subscript now dropped, and angular momentum

L will not in general be parallel. It is therefore convenient to work in the body frame coincident with the principal axes, thereby diagonalizing the inertia tensor. The principal unit vectors are chosen so $\mathbf{e}_3 = \hat{\mathbf{m}}_\mathrm{p}$ and hence $\mathbf{e}_1$ and $\mathbf{e}_2$ lie in the primary's magnetic equatorial plane. The Euler angles describing the orientation of the body frame $O\bar{x}\bar{y}\bar{z}$ relative to the orbital frame $Oxyz$ are (α, β, ψ). The transformation of the components of a vector **V** in the orbital frame to those in the body frame is

$$\bar{V}_i = R_{ij} V_j, \tag{6.78}$$

where from (2.454), with β replacing ϕ, the elements of the rotation matrix are

$$\begin{aligned}
R_{11} &= \cos\alpha \cos\beta \cos\psi - \sin\beta \sin\psi, \\
R_{12} &= \cos\alpha \sin\beta \cos\psi + \cos\beta \sin\psi, \\
R_{13} &= -\sin\alpha \cos\psi, \\
R_{21} &= -\cos\alpha \cos\beta \sin\psi - \sin\beta \cos\psi, \\
R_{22} &= -\cos\alpha \sin\beta \sin\psi + \cos\beta \cos\psi, \\
R_{23} &= \sin\alpha \sin\psi, \\
R_{31} &= \sin\alpha \cos\beta, \\
R_{32} &= \sin\alpha \sin\beta, \\
R_{33} &= \cos\alpha.
\end{aligned} \tag{6.79}$$

In the synchronous state the angular velocity of the primary is $\boldsymbol{\omega} = \boldsymbol{\Omega}$, a constant vector. In general, such a state cannot be one of zero torque since then **L** would be conserved and $\boldsymbol{\omega}$ would precess. Hence the synchronous orientation (α_s, β_s) must be such that a torque acts to cancel the precession of $\boldsymbol{\omega}$, so resulting in a precession of **L**.

Denoting the time derivative of a vector relative to inertial axes by d/dt, and that relative to the body axes by a dot, in the body frame **L** obeys the equation

$$\dot{\mathbf{L}} + \boldsymbol{\omega} \times \mathbf{L} = \mathbf{T}, \tag{6.80}$$

where **T** is the total torque acting on the primary. The angular momentum in this frame is

$$\mathbf{L} = I_\perp(\omega_1 \mathbf{e}_1 + \omega_2 \mathbf{e}_2) + I_3 \omega_3 \mathbf{e}_3. \tag{6.81}$$

In the synchronous state $\boldsymbol{\omega} = \boldsymbol{\Omega}$ and hence

$$\left(\frac{d\boldsymbol{\omega}}{dt}\right)_s = \dot{\boldsymbol{\omega}}_s = \mathbf{0}, \tag{6.82}$$

so it follows from (6.81) that $\dot{\mathbf{L}}_s = \mathbf{0}$. Equation (6.80) then gives

$$\mathbf{T}_s = \boldsymbol{\Omega} \times \mathbf{L}_s \tag{6.83}$$

for the synchronous torque. Equations (6.78), (6.81) and (6.83) yield the components of this torque along the body axes as

$$T_{s1} = \Omega^2 (I_3 - I_\perp) \sin\alpha_s \cos\alpha_s \sin\psi_s, \tag{6.84}$$

$$T_{s2} = \Omega^2 (I_3 - I_\perp) \sin\alpha_s \cos\alpha_s \cos\psi_s, \tag{6.85}$$

$$T_{s3} = 0. \tag{6.86}$$

In general $\mathbf{T}$ will be the sum of the magnetic, gravitational, accretion and dissipative torques. It follows from (6.22) and (6.77) that $\mathbf{T}_\mathrm{m}$ and $\mathbf{T}_\mathrm{g}$ satisfy (6.86), since $\hat{\mathbf{m}}_\mathrm{p} = \mathbf{e}_3$. However, the accretion torque has a finite component in the $\mathbf{e}_3$ direction and so must be dominated by $\mathbf{T}_\mathrm{m}$ and $\mathbf{T}_\mathrm{g}$ if such a distorted primary is to be synchronous. From the torque ratio (6.74), this requires a surface secondary field of $(B_\mathrm{s})_0 \gtrsim 10^3$ G. The accretion torque is, accordingly, excluded in the following analysis and the consistency of this assumption is subsequently checked. The effect of the dissipation torque is considered in Chap. 7.

The components of $\mathbf{T}_\mathrm{m}$ in the body frame are found from (6.24)–(6.26), together with the rotational transformations given by (6.78) and (6.79), yielding

$$\begin{aligned} T_{\mathrm{m}1} = {} & \frac{\mu_0 m_\mathrm{p} m_\mathrm{s}}{4\pi D^3} [\sin\gamma \cos\psi_s (2\cos\delta \cos\beta_s - \sin\delta \sin\beta_s) \\ & + \sin\psi_s \{\cos\gamma \sin\alpha_s - \sin\gamma \cos\alpha_s (\sin\delta \cos\beta_s + 2\cos\delta \sin\beta_s)\}], \end{aligned} \tag{6.87}$$

$$\begin{aligned} T_{\mathrm{m}2} = {} & -\frac{\mu_0 m_\mathrm{p} m_\mathrm{s}}{4\pi D^3} [\sin\gamma \sin\psi_s (2\cos\delta \cos\beta_s - \sin\delta \sin\beta_s) \\ & - \cos\psi_s \{\cos\gamma \sin\alpha_s - \sin\gamma \cos\alpha_s (\sin\delta \cos\beta_s + 2\cos\delta \sin\beta_s)\}], \end{aligned} \tag{6.88}$$

$$T_{\mathrm{m}3} = 0. \tag{6.89}$$

The components of $\mathbf{T}_\mathrm{g}$ are given by (6.23), and (6.77)–(6.79) as

$$T_{\mathrm{g}1} = \frac{3GM_\mathrm{s}(I_3 - I_\perp)}{D^3} \sin\alpha_s \sin\beta_s (\cos\beta_s \cos\psi_s - \cos\alpha_s \sin\beta_s \sin\psi_s), \tag{6.90}$$

$$T_{\mathrm{g}2} = -\frac{3GM_\mathrm{s}(I_3 - I_\perp)}{D^3} \sin\alpha_s \sin\beta_s (\cos\beta_s \sin\psi_s + \cos\alpha_s \sin\beta_s \cos\psi_s), \tag{6.91}$$

$$T_{\mathrm{g}3} = 0. \tag{6.92}$$

It follows from the synchronous torque conditions (6.84) and (6.85) that

$$T_{s1}\sin\psi_s + T_{s2}\cos\psi_s = \Omega^2(I_3 - I_\perp)\sin\alpha_s\cos\alpha_s, \tag{6.93}$$

$$T_{s1}\cos\psi_s - T_{s2}\sin\psi_s = 0. \tag{6.94}$$

The torque component equations (6.87), (6.88), (6.90) and (6.91) then give

$$\cos\beta_s = -\frac{\sin\gamma\sin\delta}{\left[\dfrac{\Omega^2}{\bar{C}_\mathrm{m}}\dfrac{(I_3 - I_\perp)}{I_\perp} - \dfrac{\cos\gamma}{\cos\alpha_s}\right]\sin\alpha_s}, \tag{6.95}$$

$$\frac{\bar{C}_\mathrm{g}}{\bar{C}_\mathrm{m}} = \frac{\sin\gamma(\sin\delta\sin\beta_s - 2\cos\delta\cos\beta_s)}{\sin\alpha_s\sin\beta_s\cos\beta_s}, \tag{6.96}$$

where

$$\bar{C}_\mathrm{m} = \frac{\mu_0 m_\mathrm{p} m_\mathrm{s}}{4\pi D^3 I_\perp}, \tag{6.97}$$

$$\bar{C}_\mathrm{g} = \frac{3GM_\mathrm{s}(I_3 - I_\perp)}{D^3 I_\perp}. \tag{6.98}$$

Synchronous states can be found by specifying Ω^2, $\bar{C}_\mathrm{m}$, $(I_3 - I_\perp)/I_\perp$ and the orientation (γ, δ) in (6.95), then choosing values of α_s to determine β_s. Equation (6.96) then determines $\bar{C}_\mathrm{g}/\bar{C}_\mathrm{m}$.

The quantities $\bar{C}_\mathrm{m}$ and $\bar{C}_\mathrm{g}$ can be written as

$$\bar{C}_\mathrm{m} = \frac{\pi}{10\mu_0}\frac{M_\mathrm{s}R_\mathrm{p}^3(B_\mathrm{p})_0(B_\mathrm{s})_0}{MI_\perp}, \tag{6.99}$$

$$\bar{C}_\mathrm{g} = \frac{3\Omega^2 M_\mathrm{s}}{M}\frac{(I_3 - I_\perp)}{I_\perp}, \tag{6.100}$$

where $M = M_\mathrm{s} + M_\mathrm{p}$. For a lobe-filling secondary, choosing Ω fixes M_s, then this and the chosen values of $\bar{C}_\mathrm{m}$ and $(I_3 - I_\perp)/I_\perp$, together with the determined ratio $\bar{C}_\mathrm{g}/\bar{C}_\mathrm{m}$, fixes $\bar{C}_\mathrm{g}$ and hence M via (6.100). The values of M_s and M then give M_p. For a given white dwarf polar field $(B_\mathrm{p})_0$, substitution in (6.99) yields the secondary's polar field $(B_\mathrm{s})_0$.

6.5.2 *Stability of the Synchronous State*

In order to test the linear stability of the synchronous state normal modes of oscillation are sought, though it is not clear *a priori* that such modes exist here, since the basic state is dynamical.

The equation describing the evolution of small perturbations in $\mathbf{L}$ about the synchronous state, expressed in the body frame, is

$$\dot{\mathbf{L}}' + \boldsymbol{\Omega} \times \mathbf{L}' = \mathbf{T}'_{\mathrm{m}} + \mathbf{T}'_{\mathrm{g}}, \tag{6.101}$$

where

$$\mathbf{L}' = I_{\perp}(\omega'_1 \mathbf{e}_1 + \omega'_2 \mathbf{e}_2) + I_3 \omega'_3 \mathbf{e}_3. \tag{6.102}$$

Perturbations must be calculated in an inertial frame $OXYZ$ and then expressed in the body frame. To linear order, only the synchronous body frame is required. In an inertial frame $\boldsymbol{\omega}$ has components

$$\omega_X = \dot{\psi} \sin\alpha \cos\phi - \dot{\alpha} \sin\phi, \tag{6.103}$$

$$\omega_Y = \dot{\psi} \sin\alpha \sin\phi + \dot{\alpha} \cos\phi, \tag{6.104}$$

$$\omega_Z = \dot{\phi} + \dot{\psi} \cos\alpha, \tag{6.105}$$

where $\phi = \beta + \Omega t$. Perturbation about the synchronous state $\dot{\alpha} = \dot{\psi} = 0$, $\dot{\phi} = \Omega$, and the use of the transformation (6.79) with ϕ replacing β, gives

$$\omega'_1 = \dot{\alpha}' \sin\psi_s - \dot{\beta}' \sin\alpha_s \cos\psi_s, \tag{6.106}$$

$$\omega'_2 = \dot{\alpha}' \cos\psi_s + \dot{\beta}' \sin\alpha_s \sin\psi_s, \tag{6.107}$$

$$\omega'_3 = \dot{\beta}' \cos\alpha_s + \dot{\psi}'. \tag{6.108}$$

From (6.22) and (6.77), the perturbations in $\mathbf{T}_{\mathrm{m}}$ and $\mathbf{T}_{\mathrm{g}}$ are

$$\mathbf{T}'_{\mathrm{m}} = m_{\mathrm{p}} \mathbf{e}'_3 \times \mathbf{B}_{\mathrm{sp}}, \tag{6.109}$$

$$\mathbf{T}'_{\mathrm{g}} = \frac{3GM_{\mathrm{s}}(I_3 - I_{\perp})}{D^3}(S'\mathbf{j} \times \mathbf{e}_{3s} + S_s \mathbf{j} \times \mathbf{e}'_3), \tag{6.110}$$

where $S = \sin\alpha \sin\beta$.

The components of the equation of motion (6.101) are found using (6.19)–(6.21), (6.23), (6.78), (6.79) and (6.102)–(6.110). Suitable linear combinations of the $\bar{x}$ and $\bar{y}$-components are taken, using multiples of $\sin\psi_s$ and $\cos\psi_s$, to generate equations independent of ψ_s. The resulting equations, together with the

$\bar{z}$-component, are

$$I_\perp \ddot{\alpha}' + (I_3 - I_\perp)\Omega \sin\alpha_s \cos\alpha_s \dot{\beta}' + I_3 \Omega \sin\alpha_s \dot{\psi}'$$
$$- C_\mathrm{m}[\sin\gamma \sin\alpha_s(\sin\delta\cos\beta_s + 2\cos\delta\sin\beta_s) + \cos\gamma\cos\alpha_s]\alpha'$$
$$+ C_\mathrm{g}[(\cos^2\alpha_s - \sin^2\alpha_s)\sin^2\beta_s\alpha' + \sin\alpha_s\cos\alpha_s\sin\beta_s\cos\beta_s\beta'] = 0, \tag{6.111}$$

$$I_\perp \Omega\cos\alpha_s\dot{\alpha}' + I_\perp \sin\alpha_s\ddot{\beta}'$$
$$- C_\mathrm{m}[\sin\gamma\sin^2\alpha_s(\sin\delta\cos\beta_s + 2\cos\delta\sin\beta_s) + \cos\gamma\sin\alpha_s\cos\alpha_s]\beta'$$
$$+ C_\mathrm{g}[\cos\alpha_s\sin\beta_s\cos\beta_s\alpha' + (\cos^2\beta_s - \sin^2\alpha_s\sin^2\beta_s)\sin\alpha_s\beta'] = 0, \tag{6.112}$$

$$- I_\perp\Omega\sin\alpha_s\dot{\alpha}' + I_3\cos\alpha_s\ddot{\beta}' + I_3\ddot{\psi}' - C_\mathrm{m}\sin\gamma(\sin\delta\sin\beta_s - 2\cos\delta\cos\beta_s)\alpha'$$
$$- C_\mathrm{m}[\sin\gamma\sin\alpha_s\cos\alpha_s(\sin\delta\cos\beta_s + 2\cos\delta\sin\beta_s) - \cos\gamma\sin^2\alpha_s]\beta'$$
$$+ C_\mathrm{g}[\sin\alpha_s\sin\beta_s\cos\beta_s\alpha' - \sin^2\alpha_s\cos\alpha_s\sin^2\beta_s\beta'] = 0, \tag{6.113}$$

where $C_\mathrm{m} = I_\perp\bar{C}_\mathrm{m}$ and $C_\mathrm{g} = I_\perp\bar{C}_\mathrm{g}$.

The angular perturbations can be written as the product of a constant amplitude and an exponential time dependence, so

$$\alpha' = a\exp(i\sigma t), \quad \beta' = b\exp(i\sigma t), \quad \psi' = c\exp(i\sigma t). \tag{6.114}$$

Substitution in the equations of motion (6.111)–(6.113) yields a linear set of equations for a, b and c. Vanishing of the determinant of their coefficients, for consistency, gives the following characteristic equation for σ,

$$\sigma^6 + C_1\sigma^4 + C_2\sigma^2 + C_3\sigma = 0, \tag{6.115}$$

where

$$C_1 = -\Omega^2 + 2\bar{C}_\mathrm{m}W - \bar{C}_\mathrm{g}[\cos^2\beta_s + \sin^2\beta_s(\cos^2\alpha_s - 2\sin^2\alpha_s)], \tag{6.116}$$

$$C_2 = -\Omega^2\bar{C}_\mathrm{m}\sin\alpha_s\sin\gamma(\sin\delta\cos\beta_s + 2\cos\delta\sin\beta_s)$$
$$- \Omega^2\bar{C}_\mathrm{g}\sin^2\alpha_s(\sin^2\beta_s - \cos^2\beta_s) + \bar{C}_\mathrm{m}^2W^2$$

$$- \bar{C}_{\rm g}^2 \sin^2\beta_s[\cos^2\alpha_s\cos^2\beta_s - (\cos^2\alpha_s - \sin^2\alpha_s)(\cos^2\beta_s - \sin^2\alpha_s\sin^2\beta_s)],$$

$$- \bar{C}_{\rm m}\bar{C}_{\rm g} W[\cos^2\beta_s - \sin^2\alpha_s\sin^2\beta_s + \sin^2\beta_s(\cos^2\alpha_s - \sin^2\alpha_s)], \tag{6.117}$$

$$C_3 = -i\frac{(I_3 - I_\perp)}{I_\perp}\Omega^2\bar{C}_{\rm g}\sin^2\alpha_s\cos^2\alpha_s\sin\beta_s\cos\beta_s, \tag{6.118}$$

with

$$W = \sin\gamma\sin\alpha_s(\sin\delta\cos\beta_s + 2\cos\delta\sin\beta_s) + \cos\gamma\cos\alpha_s. \tag{6.119}$$

It follows from the synchronous state condition (6.96) that $\bar{C}_{\rm m} \sim \bar{C}_{\rm g}$. The ratio $\bar{C}_{\rm m}/\Omega^2$ can be expressed, from (6.99) for $\bar{C}_{\rm m}$, as

$$\frac{\bar{C}_{\rm m}}{\Omega^2} = 4.6\times10^{-10}q^3\frac{\left(\frac{(B_{\rm p})_0}{20\,{\rm MG}}\right)\left(\frac{(B_{\rm s})_0}{10^3\,{\rm G}}\right)\left(\frac{R_{\rm p}}{8.67\times10^6\,{\rm m}}\right)\left(\frac{M_{\rm s}}{0.2M_\odot}\right)^3}{\left(\frac{I_\perp}{I}\right)\left(\frac{k_{\rm p}^2}{0.2}\right)\left(\frac{M_{\rm p}}{0.6M_\odot}\right)\left(\frac{M}{0.8\,M_\odot}\right)}. \tag{6.120}$$

The quantity $\bar{C}_{\rm m}$ is of order $\sigma_{\rm m}^2$, where $\tau_{\rm m} = 2\pi/\sigma_{\rm m}$ is the characteristic response time of the primary to the torque perturbations $\mathbf{T}'_{\rm m}$ and $\mathbf{T}'_{\rm g}$. Consequently

$$\bar{C}_{\rm m}/\Omega^2 \sim \bar{C}_{\rm g}/\Omega^2 \ll 1. \tag{6.121}$$

Limits can be placed on the range of the solutions for σ from (6.115) by noting that, if the inertial terms dominate the torque terms in the equations of motion, then $\sigma \sim \Omega$, otherwise $\sigma \sim \sigma_{\rm m}$. Equations (6.116)–(6.119) then show that the linear term in (6.115) is always negligible, due to the above small ratios, so the characteristic equation becomes

$$\sigma^4 + C_1\sigma^2 + C_2 = 0. \tag{6.122}$$

The $\sigma^2 = 0$ solution, which results from the ψ-independence of the torques, has been cancelled.

The solutions of (6.122) give the normal mode frequencies as

$$\sigma^2 = \frac{1}{2}(-C_1 \pm \Omega^2\sqrt{U}), \tag{6.123}$$

where

$$U = 1 - 4\frac{\bar{C}_{\rm m}}{\Omega^2}\cos\gamma\cos\alpha_s + 2\frac{\bar{C}_{\rm g}}{\Omega^2}(\cos^2\alpha_s - \sin^2\alpha_s\cos^2\beta_s) + \left(\frac{\bar{C}_{\rm g}}{\Omega^2}\right)^2(\cos^2\beta_s + \cos^2\alpha_s\sin^2\beta_s)^2. \tag{6.124}$$

Expansion to first order in $\bar{C}_{\rm m}/\Omega^2$ and $\bar{C}_{\rm g}/\Omega^2$ gives the solutions

$$\sigma_+^2 = \Omega^2, \tag{6.125}$$

$$\sigma_-^2 = -\bar{C}_{\rm m}\sin\gamma\sin\alpha_s(\sin\delta\cos\beta_s + 2\cos\delta\sin\beta_s) + \bar{C}_{\rm g}\sin^2\alpha_s(\cos^2\beta_s - \sin^2\beta_s). \tag{6.126}$$

The nature of the modes can now be investigated. For $\sigma_+ = \Omega$, the use of the angle perturbation (6.114) in the equations of motion (6.111)–(6.113) yields

$$-I_\perp a + i(I_3 - I_\perp)\sin\alpha_s\cos\alpha_s b + iI_3\sin\alpha_s c = 0, \tag{6.127}$$

and

$$[(I_\perp - I_3)\sin^2\alpha_s + I_3]b + I_3\cos\alpha_s c = 0, \tag{6.128}$$

where the torque terms have been dropped, since they are of relative order $\bar{C}_{\rm m}/\Omega^2$. Because $\bar{C}_{\rm m}/\Omega^2 \sim 10^{-9}$, it follows from (6.95) that $(I_3 - I_\perp)/I_\perp$ must be of this order to allow synchronous solutions. Hence the above equations give

$$a = i\frac{I_3}{I_\perp}\sin\alpha_s c, \tag{6.129}$$

$$b = -\cos\alpha_s c. \tag{6.130}$$

The angular velocity for the σ_+ mode is therefore

$$\boldsymbol{\omega}' = i\Omega c\left[i\frac{I_3}{I_\perp}\sin\alpha_s\hat{\boldsymbol{\alpha}}_s + \hat{\boldsymbol{\psi}}_s - (\hat{\boldsymbol{\psi}}_s\cdot\hat{\boldsymbol{\Omega}})\hat{\boldsymbol{\Omega}}\right]\exp(i\Omega t). \tag{6.131}$$

It follows that $\boldsymbol{\omega}'\cdot\hat{\boldsymbol{\Omega}} = 0$ and, relative to the orbital frame, $\boldsymbol{\omega}'$ rotates with angular frequency Ω. This is essentially the inertial mode corresponding to (6.67), since $I_3/I_\perp$ is close to 1. The Euler angle perturbations vary with a period $2\pi/\Omega$ which is much shorter than the primary's response time to the torque perturbations, so they are ineffective in this mode.

Equation (6.126) shows that the remaining mode frequency has the property $\sigma_-^2 \sim \bar{C}_\mathrm{m} \ll \Omega^2$. The equations of motion (6.111) and (6.112) then yield

$$a = 0, \tag{6.132a}$$

$$c = 0 \tag{6.132b}$$

to high accuracy. Hence this mode has an angular velocity perturbation

$$\boldsymbol{\omega}' = i\sigma_- b \exp(i\sigma_- t)\hat{\boldsymbol{\Omega}}, \tag{6.133}$$

and is therefore aligned with $\boldsymbol{\Omega}$. This is the same rotationally aligned magnetic mode as that given by (6.69). Its existence can be seen directly by combining the equations of motion (6.112) and (6.113) to eliminate the $\dot{\alpha}'$ terms. If α' and ψ' are small, this gives a harmonic equation for β' with frequency σ_-. Since any angular velocity perturbation can be expressed as a superposition of an inertial mode and the aligned mode, the sign of σ_-^2 determines the stability of the synchronous state.

6.5.3 *Distribution of Synchronous States*

To obtain an example of synchronous orientations, $\bar{C}_\mathrm{m}/\Omega^2 = 1.5 \times 10^{-9}$ is used. Specifying (γ, δ) and using a distortion of $(I_3 - I_\perp)/I_\perp = 10^{-9}$, orientations (α_s, β_s) can be found satisfying (6.95). Taking $P = 2.1\,\mathrm{h}$, $M_\mathrm{s} = 0.2M_\odot$ and $(B_\mathrm{p})_0 = 2 \times 10^3\,\mathrm{T}\,(2 \times 10^7\,\mathrm{G})$, (6.96) and (6.100) for $\bar{C}_\mathrm{g}/\bar{C}_\mathrm{m}$ and $\bar{C}_\mathrm{g}$ determine M_p and then (6.120) for $\bar{C}_\mathrm{m}/\Omega^2$ fixes $(B_\mathrm{s})_0$. Stability can be tested using (6.126) for σ_-^2. Table 6.2 shows a sample of stable synchronous orientations.

It is seen that the surface magnetic field on the secondary is $\sim 10^3$ G, so justifying neglect of the accretion torque. For given (γ, δ) synchronous states are possible for a wide range of M_p. States in which the accreting pole leads the motion of the line of stellar centres are possible, as well as those in which it lags. It is noted that, for all other parameters fixed, $(B_\mathrm{s})_0$ cannot be chosen independently of (γ, δ) if synchronous states are to result. Equation (6.95) is invariant to the transformation $\beta_s \to -\beta_s$. However, (6.96) for $\bar{C}_\mathrm{g}/\bar{C}_\mathrm{m}$ does not possess this invariance and hence different values of M_p and $(B_\mathrm{s})_0$ result. The synchronous state distribution generated in this way is similar to that shown in Table 6.2, but with the south magnetic pole accreting.

Table 6.3 shows synchronous orientations for $(I_3 - I_\perp)/I_\perp = -10^{-9}$. This case could correspond to the distortion caused by an internal toroidal field proposed by Katz (1989), where, from (6.76), $B_0 \sim 10^7$ G.

Table 6.2 Stable states for $(I_3 - I_\perp)/I_\perp = 10^{-9}$ (from Campbell 1990)

γ	δ	α_s	β_s	$M_p/M_\odot$	$(B_s)_0/10^3$ G
20	125	166.0	135.0	0.41	0.43
20	125	165.0	131.2	0.88	2.68
20	206	164.0	70.7	0.36	0.32
20	206	161.0	73.9	1.13	6.18
40	143	149.0	118.7	0.37	0.33
40	143	145.0	114.8	0.89	2.81
40	216	149.5	61.5	0.32	0.25
40	216	145.5	65.4	0.76	1.77
60	146	130.0	115.9	0.43	0.47
60	146	125.0	112.5	0.93	3.14
60	192	126.0	81.6	0.47	0.58
60	192	120.0	82.9	1.13	6.15
80	118	112.5	146.9	0.37	0.33
80	118	109.5	140.8	0.91	2.96
80	242	112.5	33.1	0.37	0.33
80	242	109.5	39.2	0.91	2.96
100	126	69.0	137.7	0.39	0.37
100	126	73.0	131.2	0.96	3.50
100	242	68.0	34.2	0.43	0.46
100	242	71.0	40.2	1.09	5.22
120	134	48.0	126.3	0.48	0.60
120	134	52.0	122.2	1.05	4.58
120	200	52.0	75.3	0.42	0.43
120	200	57.0	77.2	0.80	2.05
140	156	32.5	108.0	0.36	0.32
140	156	37.5	105.2	0.91	2.91
140	218	32.0	61.7	0.47	0.57
140	218	34.5	64.1	0.83	2.31
160	120	14.0	138.4	0.62	1.09
160	120	14.5	136.1	1.02	4.15
160	240	13.5	39.2	0.39	0.37
160	240	14.5	43.9	1.02	4.15

6.6 Orbital Torques

In the foregoing analysis the magnetic fields of the primary and secondary stars were taken as dipolar, with corresponding moments $\mathbf{m}_p$ and $\mathbf{m}_s$. King et al. (1990) pointed out that there is a non-central force between the dipoles, and calculated the resulting magnetic orbital torque.

Table 6.3 Stable states for $(I_3 - I_\perp)/I_\perp = -10^{-9}$ (from Campbell 1990)

γ	δ	α_s	β_s	$M_p/M_\odot$	$(B_s)_0/10^3$ G
20	125	121.5	106.0	0.42	0.45
20	125	126.5	112.5	0.85	2.47
20	206	117.0	83.1	0.37	0.34
20	206	123.0	80.3	1.09	5.32
40	143	108.0	103.0	0.37	0.35
40	143	110.5	105.8	0.86	2.54
40	216	107.5	77.8	0.33	0.26
40	216	110.0	75.2	0.75	1.72
60	146	100.0	102.9	0.36	0.33
60	146	101.5	105.6	1.07	4.97
60	192	99.5	85.6	0.43	0.47
60	192	100.5	84.9	0.97	3.58
80	118	94.0	118.6	0.33	0.26
80	118	94.5	124.4	0.76	1.80
80	242	94.0	61.4	0.33	0.26
80	242	94.5	55.6	0.76	1.80
100	126	86.0	116.0	0.54	0.79
100	242	86.0	61.4	0.33	0.26
100	242	85.5	55.6	0.76	1.80
120	134	79.0	109.0	0.41	0.43
120	134	77.5	112.9	1.13	6.09
120	200	80.5	82.7	0.38	0.35
120	200	79.5	81.7	0.80	2.08
140	156	73.0	98.1	0.37	0.33
140	156	70.5	99.8	0.92	3.01
140	218	71.0	75.6	0.50	0.64
140	218	69.5	73.8	0.83	2.26
160	120	54.5	112.6	0.62	1.06
160	120	51.0	117.6	1.03	4.37
160	240	58.0	71.5	0.39	0.38
160	240	51.0	62.4	1.03	4.37

The primary's magnetic field can be expressed as

$$\mathbf{B}_p = \nabla \times \left(\frac{\mu_0 \mathbf{m}_p \times \mathbf{r}}{4\pi r^3} \right) = \frac{\mu_0}{4\pi r^3} [3(\hat{\mathbf{r}} \cdot \mathbf{m}_p)\hat{\mathbf{r}} - \mathbf{m}_p]. \tag{6.134}$$

The torque on the secondary is then

$$\mathbf{T}_{ms} = \mathbf{m}_s \times \mathbf{B}_p(\mathbf{r}_s) = \frac{\mu_0}{4\pi D^3} [3(\mathbf{n} \cdot \mathbf{m}_p)\mathbf{m}_s \times \mathbf{n} - \mathbf{m}_s \times \mathbf{m}_p], \tag{6.135}$$

where $\mathbf{n}$ is a unit vector directed from the primary to the centre of the secondary. Similarly the torque on the primary due to interaction with the secondary's magnetic field is

$$\mathbf{T}_{\rm mp} = \frac{\mu_0}{4\pi D^3}[3(\mathbf{n}\cdot\mathbf{m}_{\rm s})\mathbf{m}_{\rm p}\times\mathbf{n} - \mathbf{m}_{\rm p}\times\mathbf{m}_{\rm s}]. \tag{6.136}$$

Equations (6.135) and (6.136) show that, in general, $\mathbf{T}_{\rm ms} + \mathbf{T}_{\rm mp} \neq \mathbf{0}$. This result is a consequence of a non-central force between the dipoles, arising from the spatial dependence of their fields. The force on $\mathbf{m}_{\rm s}$ due to the primary's field $\mathbf{B}_{\rm p}$, given by (6.134), is

$$\begin{aligned}\mathbf{F}_{\rm sp} &= [\nabla(\mathbf{m}_{\rm s}\cdot\mathbf{B}_{\rm p})]_{\mathbf{r}=D\mathbf{n}}\\ &= \frac{\mu_0}{4\pi D^4}\left[\{3(\mathbf{m}_{\rm p}\cdot\mathbf{m}_{\rm s}) - 15(\mathbf{n}\cdot\mathbf{m}_{\rm p})(\mathbf{n}\cdot\mathbf{m}_{\rm s})\}\mathbf{n}\right.\\ &\left.+3(\mathbf{n}\cdot\mathbf{m}_{\rm s})\mathbf{m}_{\rm p} + 3(\mathbf{n}\cdot\mathbf{m}_{\rm p})\mathbf{m}_{\rm s}\right].\end{aligned} \tag{6.137}$$

The force on the primary due to the secondary's field is $\mathbf{F}_{\rm ps} = -\mathbf{F}_{\rm sp}$. The non-central terms in (6.137) lead to a magnetic orbital torque

$$\mathbf{T}_{\rm mo} = D\mathbf{n}\times\mathbf{F}_{\rm sp} = \frac{3\mu_0}{4\pi D^3}[(\mathbf{n}\cdot\mathbf{m}_{\rm s})\mathbf{n}\times\mathbf{m}_{\rm p} + (\mathbf{n}\cdot\mathbf{m}_{\rm p})\mathbf{n}\times\mathbf{m}_{\rm s}]. \tag{6.138}$$

If follows from (6.135), (6.136) and (6.138) that

$$\mathbf{T}_{\rm ms} + \mathbf{T}_{\rm mp} + \mathbf{T}_{\rm mo} = \mathbf{0}. \tag{6.139}$$

Hence the total magnetic torque vanishes, corresponding to no magnetic coupling beyond the binary system due to these torques.

The angular momentum evolution equations for the primary, secondary and orbit are

$$\frac{d\mathbf{L}_{\rm p}}{dt} = \mathbf{T}_{\rm a} + \mathbf{T}_{\rm mp} + \mathbf{T}_{\rm dp} + \mathbf{T}_{\rm g}, \tag{6.140}$$

$$\frac{d\mathbf{L}_{\rm s}}{dt} = \mathbf{T}_{\rm br} + \mathbf{T}_{\rm ms} + \mathbf{T}_{\rm ds} + \mathbf{T}_{\rm tid}, \tag{6.141}$$

$$\frac{d\mathbf{L}_{\rm o}}{dt} = \mathbf{T}_{\rm gr} - \mathbf{T}_{\rm a} + \mathbf{T}_{\rm mo} + \mathbf{T}_{\rm do} - \mathbf{T}_{\rm g} - \mathbf{T}_{\rm tid}, \tag{6.142}$$

where the non-dissipative magnetic torques obey (6.139). These evolution equations apply to an asynchronous state, with all torques operable. The dissipative magnetic torques, arising from the inductive processes considered in Chap. 4, satisfy

$$\mathbf{T}_{\rm ds} + \mathbf{T}_{\rm dp} + \mathbf{T}_{\rm do} = \mathbf{0}, \tag{6.143}$$

where $\mathbf{T}_{\rm do}$ is an orbital torque due to a non-central force between the stars. The gravitational torque $\mathbf{T}_{\rm g}$ occurs if the primary is non-spherical, and the tidal torque $\mathbf{T}_{\rm tid}$ results if the secondary has asynchronous motions with dissipation. A magnetically influenced wind from the secondary generates the braking torque $\mathbf{T}_{\rm br}$, while $\mathbf{T}_{\rm gr}$ is the orbital torque due to gravitational radiation losses. Adding (6.140)–(6.142), then using the total torque conservation equations (6.139) and (6.143), gives

$$\frac{d\mathbf{L}_{\rm o}}{dt} + \frac{d\mathbf{L}_{\rm s}}{dt} + \frac{d\mathbf{L}_{\rm p}}{dt} = \mathbf{T}_{\rm br} + \mathbf{T}_{\rm gr}. \tag{6.144}$$

This shows that the total angular momentum of the system evolves under the influence of magnetic wind braking and gravitational waves, both of which remove angular momentum.

The tidal torque is believed to keep the secondary's spin near to corotation with the orbit, while the primary may be kept in synchronism by the foregoing locking mechanisms. The stellar spin angular momenta are then given by

$$|\mathbf{L}_{\rm s}| = k_{\rm s}^2 M_{\rm s} R_{\rm s}^2 \Omega \tag{6.145a}$$

and

$$|\mathbf{L}_{\rm p}| = k_{\rm p}^2 M_{\rm p} R_{\rm p}^2 \Omega, \tag{6.145b}$$

where typically $k_{\rm s}^2 \sim k_{\rm p}^2 \sim 0.2$. The orbital angular momentum can be expressed as

$$|\mathbf{L}_{\rm o}| = \frac{M_{\rm s} M_{\rm p}}{M} D^2 \Omega. \tag{6.146}$$

It follows that $|\mathbf{L}_{\rm o}| \gg |\mathbf{L}_{\rm s}| \gg |\mathbf{L}_{\rm p}|$, while, due to synchronous rotations, the angular momentum evolution time-scales are the same. Hence $|d\mathbf{L}_{\rm o}/dt| \gg |d\mathbf{L}_{\rm s}/dt| \gg |d\mathbf{L}_{\rm p}/dt|$ and (6.144) can be written

$$\frac{d\mathbf{L}_{\rm o}}{dt} = \mathbf{T}_{\rm br} + \mathbf{T}_{\rm gr}, \tag{6.147}$$

to a good approximation. This removal of orbital angular momentum drives mass transfer (see Sects. 2.4.3 and 13.3.1) and the binary evolves on the time-scale $\tau_M = M_{\rm s}/|\dot{M}_{\rm s}|$. Typically, for an AM Her system, $\tau_M \sim 10^9$ year. The characteristic adjustment time of perturbations from synchronism of the primary is given by (6.18), typically being $P_0 \sim 40$ year. Hence the corotating primary has ample time to adjust to the orbital evolution.

6.7 Summary and Discussion

The magneto-gravitational balance, unlike the magneto-accretion balance, can produce synchronous states in which the accreting pole leads the motion of the line of stellar centres, as well as other states. Both balances have the property that in 3D situations the secondary's surface magnetic field cannot be chosen independently of its orientation, if synchronous states of the primary are to exist. In both cases these restrictions are lifted if the magnetic torque dominates, so determining (α_s, β_s). This requires $(I_3 - I_\perp)/I_\perp < 10^{-9}$ and $(B_s)_0 \sim 10^3$ G, or larger distortions and $(B_s)_0 > 10^3$ G. Secondary surface fields of such values are expected to occur (see Chap. 12). Observations of DP Leo by Beuermann et al. (2014), over two extended periods, are consistent with the white dwarf oscillating about synchronism with a period of $\simeq 60$ year. The foregoing theory can account for such periods.

Cases in which the white dwarf has a quadrupolar component in its magnetic field, considered so far, require field-channelling to only be operable very close to the star. The accretion torque then only has a significant vertical component. However, observations and simulations suggest channelling often occurs well before material approaches the primary (e.g. Schwope et al. 1997).

References

Beuermann, K., Dreizler, S., Hessman, F.V., Schwope, A.D., 2014, A&A, 562, A63.
Campbell, C.G., 1985, MNRAS, 215, 509.
Campbell, C.G., 1989, MNRAS, 236, 475.
Campbell, C.G., 1990, MNRAS, 244, 367.
Cropper, M., 1988, MNRAS, 231, 597.
Joss, P.C., Katz, J.I., Rappaport, S.A., 1979, ApJ, 230, 176.
Katz, J.I., 1989, MNRAS, 239, 751.
King, A.R., Frank, J., Whitehurst, R., 1990, MNRAS, 244, 731.
Paczyński, B., 1967, AcA, 17, 287.
Schwope, A.D., Mantel, K., Horne, K., 1997, A&A, 319, 894.
Wu, K., Wickramasinghe, D.T., 1993, MNRAS, 260, 141.

Chapter 7
AM Her Stars: The Attainment of Synchronism

Abstract Even if a synchronous state exists, with a stable balance of torques, certain conditions must be met if such a state is to be attained. The synchronous state is a magnetic orientation corresponding to a minimum in a potential energy well. As corotation is approached from an over-synchronous state, the primary must be able to lose its remaining synodic rotational energy plus the energy gained via the accretion torque over a synodic period to prevent over-shooting of the synchronous state. Synodic energy is removed via dissipation of the magnetic field induced in the secondary star, and synchronism can only be attained if the stellar magnetic diffusivity is below a critical value η_0. For values of $\eta > \eta_0$, over-shooting of the synchronous state will keep occurring since the primary cannot lose sufficient rotational energy to become trapped in the energy well. A slightly asynchronous state then results, with a variation of the angular velocity due to the periodic imbalance of the torques. A stronger surface magnetic field on the primary favours the attainment of synchronism by raising the value of η_0. These restrictions do not occur for an under-synchronous primary.

7.1 The Combined Effect of Torques

Having calculated the torques acting on the primary, their combined effect must be considered. Even if a stable synchronous state exists, it is not clear a priori that this state can be reached in the presence of accretion. It will be seen that the situations of initially under and over-synchronous states are not symmetrical as far as attaining corotation is concerned.

In considering the approach to synchronism it is valid to use synodically averaged torques provided that the instantaneous synchronization time significantly exceeds the synodic period. Hence

$$\tau_{\rm syc} \gg \frac{2\pi}{|\omega|} \tag{7.1}$$

C. G. Campbell, *Magnetohydrodynamics in Binary Stars*, Astrophysics and Space Science Library 456, https://doi.org/10.1007/978-3-319-97646-4_7

is necessary. The synchronization torques were calculated in Chap. 4 for the vacuum surroundings, time-dependent case and for the steady aligned case with a magnetosphere. The torques are of similar magnitude and both have a maximum value attained at an intermediate value of ω/Ω_o. They can differ at higher values of asynchronism, but these differences do not affect the key results reached here and so the vacuum case can be used.

The averaged dissipation torque, given by (4.79), can be written as

$$\mathbf{T}_D = \mp \frac{5\pi (B_p)_0^2 R_s^3 R_p^6 \sin^2 \alpha}{\mu_0 D^6} f(|\omega|/\eta)\, \mathbf{k}, \tag{7.2}$$

where the negative and positive signs apply to over-synchronous and under-synchronous states, respectively. In the absence of other torques, this dissipation torque would synchronize the primary in a characteristic time

$$\tau_{syc} = \frac{k_p^2 M_p R_p^2 |\omega|}{|T_D|}, \tag{7.3}$$

where k_p^2 lies in the range $0.1 < k_p^2 < 0.2$. In general τ_{syc} is a function of the degree of asynchronism.

The synodic average of the accretion torque is given by (5.81) as

$$\mathbf{T}_a = A^2 \Omega \dot{M}_p \mathbf{k}. \tag{7.4}$$

If material becomes field-channelled far from L_1 some angular momentum is fed back into the orbit and the magnitude of $\mathbf{T}_a$ is reduced by $\simeq 6\%$. It was shown in Sect. 4.4 that asynchronous motions can lower or raise the value of $|\dot{M}_s|$, for over and under-synchronous states respectively. However, the frequency independent form will be used here to illustrate the essential features of the torque balances, and modifications to allow for the dependence on ω can be made when needed.

For simplicity, the case in which the dipole moment lies in the orbital plane was considered by Campbell (1986). The system DP Leo is believed to have its main accretion column close to the orbital plane (e.g. Biermann et al. 1985). However, the conclusions reached here regarding the attainment of synchronism should have general validity. When the primary's dipole moment lies in the orbital plane, it follows from (6.24)–(6.26) and (6.77), with $\alpha = \pi/2$ and $\beta = \omega t$, that the non-dissipative magnetic and gravitational torques have zero synodic averages. The spin evolution of the primary is therefore determined by the action of $\mathbf{T}_D$ and $\mathbf{T}_a$.

The magnitudes of T_D and T_a are plotted, on a logarithmic scale, in Fig. 7.1 as a function of the asynchronism ω/Ω_o. Equations (7.2) and (7.4) show that only in the over-synchronous case can the torques have the possibility of cancelling, since in the under-synchronous case T_D and T_a have the same sign. It is noted that T_D vanishes as ω tends to zero, while T_a remains finite. Hence in the absence of a locking mechanism the primary cannot attain exact synchronism. The function

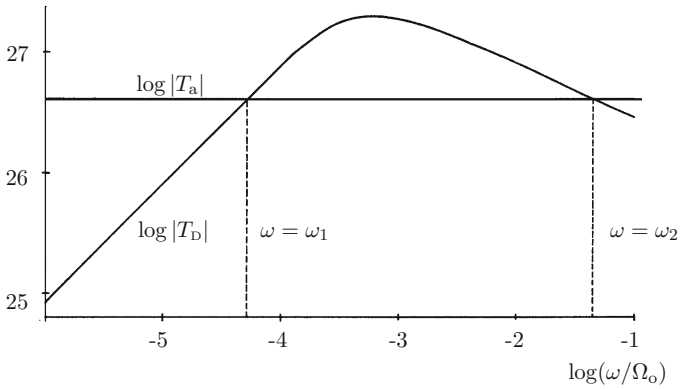

Fig. 7.1 The dissipation torque and accretion torque versus degree of asynchronism (from Campbell 1986)

$f(\omega/\eta)$, shown in Fig. 4.2, has a single maximum so, in general, there will be two finite values of ω at which $T_{\rm D} + T_{\rm a}$ vanishes.

The parameters used to plot Fig. 7.1 are $M_{\rm s} = 0.14 M_\odot$, $M_{\rm p} = 0.4 M_\odot$, $R_{\rm p} = 1.08 \times 10^7$ m, and $A = 0.6D$. These values are consistent with a lobe-filling secondary star, and employ (2.294) for A/D, the mass-radius relation (2.297) and the period-mass relation (2.298) with $q = 1.1$. The primary's polar magnetic field and the accretion rate are taken as $(B_{\rm p})_0 = 1.4 \times 10^3$ T and $\dot{M}_{\rm p} = 10^{-10}\, M_\odot {\rm year}^{-1}$. It is noted that the qualitative nature of the curves shown in Fig. 7.1 is independent of the precise parameters used.

Figure 7.1 illustrates that a critical accretion rate, $\dot{M}_c$, exists at which the accretion torque line is tangent to the dissipation torque curve. If $\dot{M}_{\rm p}$ exceeds $\dot{M}_c$ then $T_{\rm a}$ exceeds $|T_{\rm D}|$ whatever the degree of asynchronism and the primary is spun up. The frequency-dependent accretion torque, due to the dependence of $\dot{M}_{\rm s}$ on ω, derived in Sect. 4.4, has a minimum corresponding to the maximum in $f(\omega/\eta)$. This can be accounted for here by replacing $\dot{M}_{\rm p}$ in (7.4) by the reduced form $\bar{f}\dot{M}_{\rm p}$, with $\bar{f} < 1$. The critical accretion rate then arises when the minimum accretion torque equals the maximum magnetic torque. The function $f(|\omega|/\eta)$ is given by (4.56) and can be written as

$$f(\omega/\eta) = f_1(\omega/\eta) + \left(\frac{R_{\rm s}}{D}\right)^2 f_2(\omega/\eta), \tag{7.5}$$

where

$$f_1 = \frac{3}{4}\left(C_1^2 \delta_1'\right)_{\rm s} F_1 \quad \text{and} \quad f_2 = \left(C_2^2 \delta_2'\right)_{\rm s} F_2. \tag{7.6}$$

It follows from (4.56)–(4.65) that f_1 and f_2 are pure functions of ω/η. Their maximum values are found to be 8.6×10^{-2} and 0.242, respectively. The factor $(R_s/D)^2$ is weakly dependent on the stellar mass ratio, for a lobe-filling secondary, so the maximum value of f is essentially independent of the binary parameters. Equating the maximum value of $|T_D|$ to the minimum value of the accretion torque gives

$$\dot{M}_c = \frac{N_1 \left(\frac{(B_p)_0}{14\,\mathrm{MG}}\right)^2 \left(\frac{R_p}{1.08 \times 10^7\,\mathrm{m}}\right)^6}{\bar{f} q^{\frac{7}{2}} \left(\frac{M}{0.54\,M_\odot}\right)^{\frac{8}{3}} \left(\frac{M_s}{0.14\,M_\odot}\right)^{\frac{4}{3}}} M_\odot \mathrm{year}^{-1}, \tag{7.7}$$

where

$$N_1 = 8.18 \times 10^{-10} \left[0.86 + 2.42 \left(\frac{R_s}{D}\right)^2\right] \sin^2 \alpha. \tag{7.8}$$

It is noted that $\dot{M}_c$ does not depend on η, because f is a function of ω/η and changing η simply changes the value of ω at which the maximum in this function occurs.

It follows from Fig. 7.1 that, for $\dot{M}_p < \dot{M}_c$, two synodic frequencies exist at which T_D cancels T_a. This is still the case for the frequency-dependent form of accretion torque. It is clear that the frequency ω_2 is unstable, since a small change in ω about this state causes the primary to spin away from it. The smaller frequency ω_1 corresponds to a stable state. Hence, in the absence of a locking mechanism, if the initial asynchronism is $< \omega_2/\Omega_o$, the primary will spin down to the slightly asynchronous state with synodic period $P_1 = 2\pi/\omega_1$.

An expression can be derived for ω_2/Ω_o, the value of the initial asynchronism above which the primary will be spun away from corotation, since then T_a exceeds $|T_D|$. This is done by using the fact that, for $\dot{M}_p$ significantly less than $\dot{M}_c$, the spin rate ω_2 lies in the regime of low field penetration in which the dissipation torque is given by the asymptotic form (4.89). Equating this to (7.4) for T_a gives

$$\frac{\omega_2}{\Omega_o} = \frac{N_2 \left(\frac{(B_p)_0}{14\,\mathrm{MG}}\right)^4 \left(\frac{R_p}{1.08 \times 10^7\,\mathrm{m}}\right)^{12} \left(\frac{\eta}{5 \times 10^8\,\mathrm{m^2 s^{-1}}}\right)}{q^{\frac{15}{2}} \left(\frac{\dot{M}_p}{10^{-10}\,M_\odot\,\mathrm{year}^{-1}}\right)^2 \left(\frac{M}{0.54\,M_\odot}\right)^{\frac{16}{3}} \left(\frac{M_s}{0.14\,M_\odot}\right)^{\frac{11}{3}}} \tag{7.9}$$

where

$$N_2 = 7.00 \times 10^{-2} \left[1 + \frac{16}{3} \left(\frac{R_s}{D} \right)^2 \right]^2 \sin^4 \alpha. \tag{7.10}$$

In general, both the time-dependent induction effect and that due to motions induced in the secondary will operate. The magnetic torque curve would then have a reduced turn down at higher the values of ω/Ω_o, or saturate at a constant value depending on the relative strengths of the two effects. This would increase the value of ω_2 or, in the case of saturation, remove this restriction. Hence, for $|\dot{M}_s| < \dot{M}_c$, spin down will occur for $\omega/\Omega_o \lesssim 0.1$, with no restriction if the inductive magnetic torque saturates.

The synodic period P_1 of the slightly asynchronous state can be found by utilizing the fact that, for $\dot{M}_p$ significantly less than $\dot{M}_c$, the spin rate ω_1 corresponds to the regime of high field penetration in which the dissipation torque is given by (4.92). Equating this to T_a gives

$$P_1 = \frac{N_3 \left(\frac{(B_p)_0}{14\,\mathrm{MG}} \right)^2 \left(\frac{R_p}{1.08 \times 10^7\,\mathrm{m}} \right)^6 \left(\frac{M_s}{0.14\,M_\odot} \right)^{\frac{2}{3}}}{q^{\frac{3}{2}} \left(\frac{\dot{M}_p}{10^{-10}\,M_\odot\,\mathrm{year}^{-1}} \right) \left(\frac{M}{0.54\,M_\odot} \right)^{\frac{8}{3}} \left(\frac{\eta}{5 \times 10^8\,\mathrm{m^2 s^{-1}}} \right)} \mathrm{year}, \tag{7.11}$$

where

$$N_3 = 5.16 \left[1 + \frac{48}{35} \left(\frac{R_s}{D} \right)^2 \right] \sin^2 \alpha. \tag{7.12}$$

The synchronization time in the high field penetration regime is given by (4.93), and is independent of ω.

The inequality (7.1) gives the condition for the validity of the synodic time average. The synchronization time increases monotonically with ω, and only values of $\omega \gtrsim \omega_1$ are of interest here. Condition (7.1) is therefore equivalent to $\tau_{syc}/P_1 \gg 1$. Using the previously quoted orbital parameters, together with $\alpha = \pi/2$, (4.93) and (7.11) give $\tau_{syc}/P_1 = 22$, showing that the time averaging is just valid in this case. However, it is noted that τ_{syc}/P_1 is proportional to η^2 and the value of η is uncertain by at least an order of magnitude. It follows that, for fixed orbital parameters, there is a minimum value of η below which $\tau_{syc}/P_1 < 1$ so invalidating the synodic averaging process when ω is close to ω_1, although it will still be valid

for $\omega \gg \omega_1$. Equations (4.93) and (7.11) give this minimum diffusivity value as

$$\eta_0 = \frac{N_4 \left(\frac{(B_p)_0}{14\,\mathrm{MG}}\right)^2 \left(\frac{R_p}{1.08\times 10^7\,\mathrm{m}}\right)^5 \left(\frac{M_s}{0.14\,M_\odot}\right)^{\frac{5}{6}}}{q^{\frac{5}{4}} \left(\frac{k_p^2}{0.2}\right)^{\frac{1}{2}} \left(\frac{\dot{M}_p}{10^{-10}\,M_\odot\,\mathrm{year}^{-1}}\right)^{\frac{1}{2}} \left(\frac{M_p}{0.4\,M_\odot}\right)^{\frac{1}{2}} \left(\frac{M}{0.54\,M_\odot}\right)^{\frac{7}{3}}} \mathrm{m}^2\mathrm{s}^{-1} \tag{7.13}$$

where

$$N_4 = 1.40\times 10^8 \left[1 + \frac{48}{35}\left(\frac{R_s}{D}\right)^2\right] \sin^2\alpha. \tag{7.14}$$

In the absence of a locking mechanism, the spin rate of the primary will evolve towards ω_1 irrespective of whether η is below or above η_0, or whether its initial spin is under or over-synchronous. For $\eta \gg \eta_0$ the primary will settle at ω_1 in an essentially time-independent state. For $\eta < \eta_0$ the primary will reach a state in which its angular velocity varies about ω_1 since $T_D + T_a$ will vary about zero as the dissipation varies, and the star can respond to this. Without a stable locking mechanism the white dwarf can never reach synchronism in the presence of accretion.

7.2 The Effect of a Locking Mechanism

Mechanisms for locking the white dwarf in corotation were investigated in Chap. 6. Assuming that a stable synchronous state exists, there are necessary conditions for the primary to be able to reach this state while accretion is occurring. The locking mechanism of Sect. 6.2 will be considered here and the conditions derived under which the primary can attain corotation. These conditions have a general validity, independent of the precise locking mechanism considered.

The sum of the accretion and non-dissipative magnetic torques on the primary is given by (6.10) which, by using the synchronous condition $T = 0$, can be written as

$$\mathbf{T} = A^2\Omega\dot{M}_p\left[1 - \frac{\sin(\beta - \bar{\delta})}{\sin(\beta_s - \bar{\delta})}\right]\mathbf{k}, \tag{7.15}$$

where β_s is the stable synchronous orientation, and the angle $\bar{\delta}$ is shown in Fig. 6.1.

The work done in rotating the primary from some reference orientation β_0 to a general orientation β is

$$W(\beta) = -\int_{\beta_0}^{\beta} T(\beta)d\beta, \tag{7.16}$$

so (7.15) gives

$$W(\beta) = -A^2\Omega\dot{M}_{\rm p}\left[(\beta-\beta_0) + \frac{\cos(\beta-\bar{\delta}) - \cos(\beta_0-\bar{\delta})}{\sin(\beta_s-\bar{\delta})}\right]. \tag{7.17}$$

It is clear that the form of $W(\beta)$ is independent of the orbital parameters. The first term in the bracket arises from the work done against the accretion torque, while the second term derives from the work done against the magnetic torque. It is seen that for $\beta = \beta_0 \pm 2n\pi$, where n is an integer, the work done against the accretion torque is $\mp 2n\pi A^2\Omega\dot{M}_{\rm p}$, while no work is done against the magnetic torque for a complete number of rotations of the primary.

Figure 7.2 is a plot of $W(\beta)/A^2\Omega\dot{M}_{\rm p}$ for $\beta_s = 76°$, $\bar{\delta} = 50°$ and $\beta_0 = \beta_s - 2\pi$. The synchronous orientation occurs at local minima in $W(\beta)$ and adjacent minima differ in height by $2\pi A^2\Omega\dot{M}_{\rm p}$ due to the work done against $T_{\rm a}$. Similarly, adjacent maxima in $W(\beta)$ differ in height by $2\pi T_{\rm a} = 2\pi A^2\Omega\dot{M}_{\rm p}$ and as a consequence of this it is necessary to distinguish between the cases of an initially under-synchronous and over-synchronous primary.

An Initially Under-Synchronous Primary In this case $\omega = \dot{\beta}$ is negative and both the dissipation and accretion torques act to reduce $|\omega|$. Since $T_{\rm a}$ and $T_{\rm D}$ are both positive a state in which they cancel cannot occur as ω tends to zero. The synodic rotational energy of the primary will decrease until it is just sufficient to allow the star to pass through a maximum in $W(\beta)$, such as point B in Fig. 7.2. It is then clear that after passing through B the primary cannot gain sufficient rotational energy to allow it to reach the next maximum at A and hence β will oscillate in the well, eventually settling at β_s due to the action of the dissipation torque.

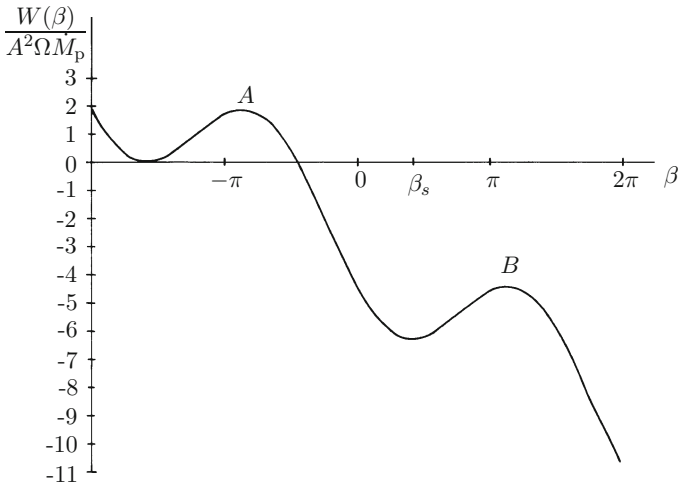

Fig. 7.2 The function $W(\beta)/A^2\Omega\dot{M}_{\rm p}$, showing the synchronous state β_s (from Campbell 1986)

An Initially Over-Synchronous Primary For an over-synchronous primary $\omega = \dot{\beta}$ is positive and $T_{\rm D}$ is negative. Figure 7.1 shows that for $\omega_1 < \omega < \omega_2$, $|T_{\rm D}|$ exceeds $T_{\rm a}$ and hence ω decreases. However, synchronism at β_s can only result if a value of ω exists such that when the primary has passed through a maximum in $W(\beta)$ (e.g. point A), at least its existing synodic rotational energy plus $2\pi T_{\rm a}$ is dissipated before it can reach the next maximum (i.e. point B). The dissipation torque will then vary significantly over a synodic rotation period, but the required synchronization condition is approximately given by

$$4\pi(|T_{\rm D}| - A^2\Omega\dot{M}_{\rm p}) \geq k_{\rm p}^2 M_{\rm p} R_{\rm p}^2 \omega^2. \tag{7.18}$$

The value of ω satisfying (7.18) will lie in the regime of high field penetration, in which $T_{\rm D}$ is given by (4.92). The equality in (7.18) then gives a quadratic equation for ω and, for given orbital parameters, the condition for its roots to be real places a maximum value on the magnetic diffusivity of the secondary. To within a factor of $\sqrt{2}$, the expression so obtained for this limiting value of η is the same as that for η_0 given by (7.13). This is a result of the fact that (7.18) is essentially equivalent to the condition $\tau_{\rm syc} \lesssim 2\pi/\omega_1$.

If $\eta \gg \eta_0$ synchronism cannot be attained in the presence of accretion since the primary will always have too much synodic rotational energy to be dissipated in one synodic cycle. Then, despite the fact that a stable synchronous state exists at β_s, the lowest value attained by ω will be ω_1, as in the case when no locking mechanism is present. If $\eta < \eta_0$ then the primary will ultimately become trapped in the energy well about β_s and settle to the locked state.

7.3 Summary and Discussion

The form of $W(\beta)$, and hence the above conclusions, will be unchanged for any torque $T_{\rm B}(\beta)$ balancing accretion which has a vanishing integral around one cycle. If the balancing torque has a finite cyclic integral then the height difference of adjacent maxima in $W(\beta)$ would differ from that shown in Fig. 7.2. In the special case of the cyclic integral of $T_{\rm B}$ exactly cancelling that of $T_{\rm a}$ there would be no height difference in adjacent maxima of W. Synchronism would then ultimately result whether the primary was initially under or over-synchronous, without a limit on the value of η. However, apart from such a special coincidence, there would be a limiting value of η necessary to ensure that the primary becomes trapped in the energy well about β_s.

It was shown in Sect. 6.3 that the characteristic ratio of the accretion torque to the magnetic torque, denoted by Q, is given by (6.74). For primary fields of $(B_{\rm p})_0 \gtrsim 7 \times 10^7$ G it follows that, for typical parameters, $Q \lesssim 10^{-2}$. In such cases, η_0, given by (7.13), becomes sufficiently large that the condition $\eta < \eta_0$ for the attainment of synchronism is likely to be satisfied. As pointed out by Campbell and Schwope (1999), it is conceivable that some AM Her systems may satisfy the conditions for attaining synchronism, whilst others may not. In the latter cases small degrees of

asynchronism would result. Observations indicate that most AM Her systems are close to corotation, but several systems have significant degrees of asynchronism (e.g. Pavlenko 2006; Lipkin & Liebowitz 2008).

Although the two-dimensional case, with accretion in the orbital plane, was considered here, the conditions for attaining synchronism should be similar in the general three-dimensional case. In particular, a limiting value of η will generally result.

References

Biermann, P., Schmidt, G.D., Liebert, J., Stockman, H.S., Tapia, S., Kuhr, H., Strittmatter, P.A., West, S., Lamb, D.Q., 1985, ApJ., 293, 303.
Campbell, C.G., 1986, MNRAS, 219, 589.
Campbell, C.G., Schwope, A.D., 1999, A&A, 343, 132.
Lipkin, Y.M., Liebowitz, E.M., 2008, MNRAS, 387, 289.
Pavlenko, E.P., 2006, Ap, 49, 105.

Chapter 8
Binaries with Partial Accretion Discs

Abstract The intermediate polars have white dwarf primary stars with magnetic moments strong enough to disrupt the inner region of their accretion discs. Matter is channelled from the inner edge of the disc on to the star via an accretion curtain flow. The vertical shear between the stellar magnetosphere and the disc leads to the creation of toroidal magnetic field from the poloidal component, and the resulting magnetic stresses cause angular momentum exchange to occur between the star and the disc. Angular momentum is also transferred through the curtain flow. If the magnetic field winding becomes sufficiently large, field lines can open and channel wind flows from the disc and star. A range of spin behaviour can result for the primary star. Some X-ray binary pulsars and the accreting millisecond pulsars have magnetic neutron star primaries which disrupt the inner region of their discs, and so these systems have similarities to the intermediate polars. The magnetic disruption of the disc and channelling of the curtain flow pose MHD problems. The basic properties of these systems are reviewed here

8.1 Introduction

The intermediate polars, some X-ray binary pulsars and the accreting millisecond pulsars are believed to contain magnetic primary stars accreting from partially disrupted discs. The primary magnetic moments are weaker than those occurring in AM Her stars, so partial accretion discs can form. The accreting star has a stronger magnetic interaction with the differentially rotating disc than with the synchronized secondary. As a consequence, the spin behaviour of primary stars in these partial disc systems is very different from that observed in the AM Her binaries, where the absence of a disc enables orbital synchronism to be approached.

C. G. Campbell, *Magnetohydrodynamics in Binary Stars*, Astrophysics and Space Science Library 456, https://doi.org/10.1007/978-3-319-97646-4_8

8.2 The Intermediate Polars

8.2.1 Discovery and Classification

Charles et al. (1979) identified TV Col as an X-ray source with a spectrum like AM Her, but lacking detectable polarization. There were several observed periodicities and some uncertainty in their origin. This was resolved by the X-ray observations of Schrijver et al. (1987) which showed the primary rotation period to be 31.8 min, and eclipse observations by Hellier et al. (1991) giving the orbital period as 5 h 29.2 min. Griffiths et al. (1980) discovered AO Psc. Photometry by Warner (1980) showed a modulation of its spectrum with the orbital period of 3.6 h.

TV Col and AO Psc were the first two members of a class of cataclysmic variables now designated the intermediate polars. Photometric and spectroscopic observations led to a model in which a magnetic white dwarf accretes matter transferred from the secondary star via a partially disrupted disc. An X-ray emitting region on the white dwarf is carried around by its rotation, causing periodic illumination of some region fixed in the binary frame (e.g. Hutchings et al. 1981; Warner et al. 1981; Hassall et al. 1981; Patterson and Price 1981). In contrast to the polars, TV Col and AO Psc showed no detectable polarization at optical wavelengths, indicating a weaker magnetic field. A weaker field and the presence of a partial accretion disc are consistent with the observed asynchronous rotation of the primary. Binaries currently classified as definite intermediate polars are hard X-ray emitters and multiperiodic. Table 8.1, shown in the Appendix below, lists the main systems in this class.

The DQ Herculis binaries are a subset of the intermediate polars. They have short primary rotation periods and lack hard X-ray emission. The main systems are listed in Table 8.2, shown in the Appendix below. These binaries played an important part in the early work on the nature of cataclysmic variables. AE Aqr was shown by Joy (1954) to be a spectroscopic binary. It was subsequently used by Crawford and Kraft (1956) towards deriving the basic model of a cataclysmic variable. DQ Her is the remnant of Nova Herculis 1934, and was identified by Walker (1954) as an eclipsing binary with an orbital period of 4 h 39 min.

8.2.2 Rotation Periods and Magnetic Fields

Tables 8.1 and 8.2 show the primary star rotation periods, $P_{\rm R}$, and their rates of change, expressed as $\dot{P}_{\rm R}/P_{\rm R}$. Examples of systems in which rotation period changes have been observed are GK Per (Patterson 1991), FO Aqr (e.g. Osborne and Mukai 1989; Kruszewski and Semeniuk 1993), AO Psc (Kaluzny and Semeniuk 1988), V1223 Sgr (van Amerongen et al. 1987), BG CMi (Patterson and Thomas 1993), V647 Aur (Kozhevnikov 2014) and EX Hya (Vogt et al. 1980; Bond and Freeth 1988). The magnitude of typical errors in the quoted values of $\dot{P}_{\rm R}/P_{\rm R}$ is $\sim 10\%$. The

DQ Her period change observations are: AE Aqr (de Jager et al. 1994), V533 Her (Lamb and Patterson 1983), and DQ Her (Balachandran et al. 1983). Negative and positive values of $\dot{P}_{\rm R}$ occur.

The white dwarf surface magnetic field values quoted in Table 8.1 are based on circular polarization measurements using broad band polarimetry (Cropper 1986; Stockman et al. 1992). The polarization of BG CMi can be modelled with an accretion arc covering a fractional area of $\sim$ 0.01 of the primary's surface and a polar field of $(B_{\rm p})_0 \sim 3$ MG (Wickramasinghe et al. 1991). Polarization measurements of PQ Gem (Rosen et al. 1993), and a similar accretion model, give $(B_{\rm p})_0 \sim 8$ MG. This suggests the intermediate polars have white dwarf surface fields typically an order of magnitude lower than those in the AM Her binaries.

8.3 The X-Ray Binary Pulsars

8.3.1 Discovery and Classification

X-ray pulsations from a binary system were first discovered by Giacconi et al. (1971) during observations of Centaurus X-3 with the Uhuru satellite. The binary nature of Cen X-3 was revealed in a further analysis of the Uhuru data by Schreier et al. (1972). This showed 2.1 d periodic variations of X-ray intensity with an eclipse, and a sinusoidal variation of the 4.8 s pulsation period, also with a period of 2.1 d. Soon after, Tananbaum et al. (1972) discovered another X-ray pulsar, Hercules X-1, which showed a periodic intensity variation with a 1.7 d binary period and an associated sinusoidal modulation of the 1.24 s pulse period.

The large luminosities observed can be understood as resulting from the gravitational energy released by matter transferred from a normal companion star on to a neutron star. The radius of a neutron star is typically a factor of $\sim 10^{-3}$ smaller than that of a white dwarf, so the potential well into which accreting material falls is far deeper in these systems than in the standard cataclysmic variables.

Orbital parameters have been determined for several systems from pulse timing analyses, using the Doppler effect due to the binary motion of the compact star. Optical observations of the companion star then lead to accurate values for the stellar parameters, confirming neutron star primaries. The pulse period histories reveal a general tendency for spin-up in the X-ray binary pulsars, contrary to the general spin-down of radio pulsars. This is consistent with X-ray systems accreting matter through the magnetosphere. However, more recent observations have shown a wide variety of pulse period changes in the X-ray pulsars.

X-ray pulsars can be classified into three catagories; (I) binaries with early-type massive companions, (II) binaries with Be star companions, and (III) low mass binaries. Class (I) can be divided into two subclasses; (Ia) short pulse-period systems with very large X-ray luminosity, and (Ib) long pulse-period systems with moderate X-ray luminosity (e.g. Corbet 1986). Some of the low mass binaries lack pulse periods.

8.3.2 Systems with Accretion Discs

The short pulse-period systems with early-type massive companions and the low mass binaries are thought to have accretion discs around their neutron stars. Observations of Her X-1 in the X-ray and optical bands give direct evidence for an accretion disc (e.g. Middleditch 1983). Observational evidence of the neutron star magnetic field was given by Trumper et al. (1978). They interpreted a prominant emission line feature at 58KeV in the energy spectrum of Her X-1 as cyclotron emission at the magnetic poles of the neutron star. The estimated surface field was 5×10^{12} G. White et al. (1983) used cyclotron absorption features of 4U0115+63 to obtain a surface magnetic field of 10^{12} G. Kii et al. (1986) proposed a magnetic field 8×10^{12} G for 4U1626−67 by simulating the observed energy dependence of the pulse profile with a calculation of anisotropic radiative transfer in a strong magnetic field. The nature of the pulse profiles indicates the presence of accretion columns on the neutron star. Like the intermediate polars, partial discs are believed to be present with material becoming field-channelled after disruption. Consequently, the neutron star cannot become synchronized with the orbital motion, since its magnetic interaction with the secondary star is much weaker than its coupling to the disc.

Table 8.3, shown in the Appendix below, gives a representative sample the X-ray binary pulsars believed to contain strongly magnetic neutron stars (i.e. $(B_{\rm p})_0 \sim 10^{12}$ G) accreting from partially disrupted discs. The systems listed are those most extensively observed. Typical rates of change of the neutron star's spin period are given, where available. The associated time-scales are generally shorter than those listed in Tables 8.1 and 8.2, since neutron stars have smaller moments of inertia than white dwarfs. The values shown are averages over various periods of observation and give an estimate of spin change time-scales. Many variations to these values, and their signs, are observed.

8.3.3 Neutron Star Spin Evolution

Pulse period monitoring of X-ray binary pulsars has been performed by various satellites, which reveal a wide variety of changes. Schreier and Fabbiano (1976) noted a secular trend of spin-up for Her X-1 and Cen X-3, from early observations. These systems were subsequently observed to exhibit wavy fluctuations in their spin rates, with time-scales of years. Also, short-term fluctuations of the pulse period on a time-scale of days to months, including evidence of spin-down episodes, were found in Her X-1 (Giacconi 1974) and Cen X-3 (Fabbiano and Schreier 1977) from Uhuru satellite observations. Between 1971 and 1980 a spin-up rate of $\dot{P}_{\rm R}/P_{\rm R} = -2.6 \times 10^{-2}\,{\rm year}^{-1}$ was observed for GX 1+4. A short time-scale spin-up episode in this system, superposed on the constant decrease in $P_{\rm R}$, was noted by Doty et al. (1981).

From 1979 to 1988 the systems SMC X-1 and 4U1626−67 exhibited secular spin-up at almost constant rates of $\dot{P}_{\rm R}/P_{\rm R} = -6.0 \times 10^{-4}\,{\rm year}^{-1}$ and $\dot{P}_{\rm R}/P_{\rm R} = -2.0\times10^{-4}\,{\rm year}^{-1}$, respectively. Subsequently, Makishima et al. (1988) used Ginga satellite observations to show that the spin-up rate of SMC X-1 was no longer constant, but decreasing. Makishima et al. (1988) found a spin-down in GX 1+4.

Bildsten et al. (1997) analysed the data obtained from 5 years of continuous monitoring of accretion powered pulsars. Because of the continuity and uniformity over such a long baseline, shorter time-scale variations in spin behaviour can be detected. This showed that Cen X-3 exhibits 10 to 100 day intervals at steady spin-up and spin-down at a higher rate than the previously observed values, in which the faster variations tended to cancel to give a smaller average. Rapid changes in spin behaviour were found to be common. The system 4U1626-67 underwent a torque reversal in 1991, changing from spin-up to spin-down (Chakrabarty et al. 1997), with the two rates being nearly equal. The system OAO1657-415 showed a spin behaviour similar to that of Cen X-3 (Chakrabarty et al. 1993). A possible explanation for these torque reversals is discussed in Chap. 10.

8.4 The Accreting Millisecond Pulsars

The accreting millisecond pulsars are short period binaries believed to contain a magnetic neutron star accreting from a disrupted disc. The surface magnetic field of the neutron star is estimated to be typically $\sim 10^9$ G. The first of these systems to be discovered was J1808, which exhibits outbursts lasting a few weeks during which coherent pulsations are observed (e.g. Wijnands and van der Klis 1998). Three of the known systems have ultra short orbital periods, implying very low mass secondary stars which may be brown dwarfs (see Poutanen 2006 for a review). Table 8.4, shown in the Appendix below, lists these systems with their orbital and spin periods.

The outbursts occur every few years. Ibragimov and Poutanen (2009) analysed data obtained during the 2002 outburst of J1808. This indicated that the area covered by the accretion hotspot on the neutron star surface changed during the outburst. This is consistent with the accretion curtain width changing due to a movement of the disruption radius in response to the varying accretion rate. Kajava et al. (2011) investigated data taken during the 2008 outburst of J1808. A major pulse profile change was accompanied by a large variation of the disc luminosity, and this may be related to changes in the accretion geometry.

8.5 MHD Problems

The nature of the interaction of the primary star's magnetic field and its associated magnetosphere with the accretion disc, together with the curtain flow, pose MHD problems. The stellar magnetic field is believed to penetrate the highly diffusive disc

and vertical shears generate toroidal magnetic field from the poloidal component. The resulting magnetic stresses modify the structure of the disc and the magnetosphere. In the outer parts of the disc, where the stellar field is weak, the magnetic force is small and the disc structure will be essentially unperturbed. Closer to the primary star the magnetic perturbation becomes significant and ultimately disrupts the disc. The physical mechanism causing disruption needs detailed investigation. After disruption material will be channelled by the magnetic field to form an accretion curtain through which mass and angular momentum are transferred to the star. Figure 8.1 is a simplified schematic picture of such a system. The observed systems have the primary star magnetic axis tilted to its spin axis.

Chapter 9 investigates the inner disruption of the disc, which requires consideration of a full MHD problem, including the thermal equations. The thin nature of the disc, and its high magnetic diffusivity can enable the equations to be simplified, aiding analytic progress. Numerical simulations have also increased our understanding of the star-disc interaction, allowing cases of lower disc magnetic diffusivity to be investigated. In these cases magnetic field line opening can occur, with stellar and disc winds developing. For sufficiently low η values, episodic behaviour results with an oscillating disruption radius. The disruption radius depends on the stellar spin rate, since this affects the radial distribution of vertical shear in the disc. Any disrupted disc solution must match to the inner curtain flow.

Chapter 10 considers the magnetic interaction of the primary star with the undisrupted part of the disc. Magnetic stresses enable the disc and star to exchange angular momentum, and disc solutions can be used to calculate the torque on the star. Angular momentum is also transferred due to the magnetic channelling of material accreting on to the star via the curtain flow. The combined effect of these processes can be compared to spin behaviour observed in the intermediate polars and the X-ray binary pulsars, previously outlined. In particular, a stable equilibrium state can be

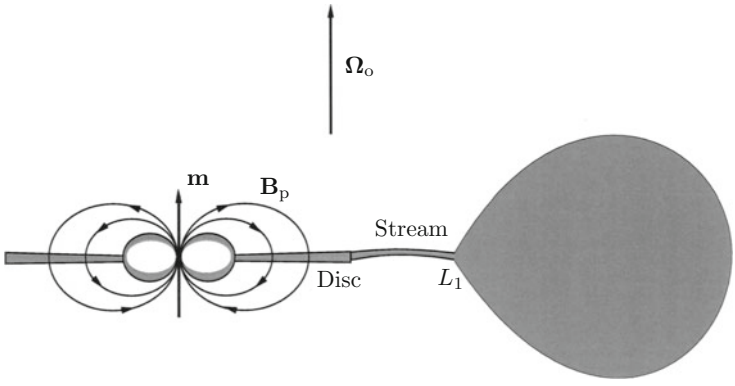

Fig. 8.1 Schematic model of a compact magnetic primary star accreting material via a curtain flow connected to a truncated disc. The disc is fed by a stream generated by Roche lobe overflow from the secondary star. The idealized case with $\mathbf{m}$ parallel to $\mathbf{\Omega}_o$ is shown. The closed field line configuration is valid for sufficiently large values of magnetic diffusivity in the disc

found in which the disc torque balances the accretion torque. Perturbations about this state can lead to spin-up and spin-down behaviour due to torque reversals. In the cases in which field channelled stellar winds occur significant braking of the star can result.

Appendix: Confirmed Systems

Table 8.1 Intermediate polars

Name	P (h)	$P_{\rm R}$ (min)	$\dot{P}_{\rm R}/P_{\rm R}$ (year^{-1})	$(B_{\rm p})_0$ (MG)	References
GK Per	47.92	5.86	-2.2×10^{-6}		58
V2731 Oph	15.42	2.13			18, 21
KO Vel	10.13	68.00			51
V1062 Tau	9.98	61.73			26, 35
NY Lup	9.86	11.55			16
V902 Mon	8.16	36.83			6
V2069 Cyg	7.48	12.38			38
J2133	7.19	9.52			5, 29
EI UMa	6.43	12.4			44, 46
J0457	6.19	20.38			7
XY Ari	6.06	3.43		32	1, 39,
J1509	5.89	13.50			12, 43
TX Col	5.72	8.72			37
V667 Pup	5.61	8.54			11
WX Pyx	5.54	26.00			53
TV Col	5.49	31.82			45
J1830	5.37	30.33			56
V709 Cas	5.33	5.20			14
PQ Gem	5.19	13.88		8	20, 25
FO Aqr	4.85	20.91	8.6×10^{-7}		59
MU Cam	4.72	19.79			34, 54
HY Leo	4.42	69.17			50
V1323 Her	4.40	25.34			4
V2306 Cyg	4.35	12.00			60
SL Peg	4.19	29.60		10	44, 48
V405 Aur	4.14	9.08			23, 42, 55
V1033 Cas	4.03	9.40			5, 8
J1719	4.01	18.99			22, 43
DO Dra	3.97	8.82			3, 24
J0153	3.94	32.90			40
J1654	3.72	9.15			36, 52
J1649	3.62	9.97			43

(continued)

Table 8.1 (continued)

Name	P (h)	P_R (min)	$\dot{P}_R/P_R$ (year^{-1})	$(B_p)_0$ (MG)	References
AO Psc	3.59	13.42	-2.6×10^{-6}		28
UU Col	3.46	14.38			10, 17
V2400 Oph	3.41	15.45			9, 47
V1223 Sgr	3.37	12.42	9.7×10^{-7}		57
BG CMi	3.23	14.12	2.0×10^{-6}	3	31, 41
V515 And	2.73	7.75			32
V647 Aur	2.73	15.53	2.8×10^{-4}		33
J1740	2.08	12.15			30
EX Hya	1.64	67.03	-3.0×10^{-7}		2
J1817	1.53	27.72			56
J1853	1.45	7.96			56
DW Cnc	1.44	38.60			13, 49
HT Cam	1.43	8.58			15, 19
V1025 Cen	1.41	35.78			27

Table 8.1 Reference Number Key: 1. Allan et al. 1996; 2. Andronov and Breus 2013; 3. Andronov et al. 2008; 4. Anzolin et al. 2008; 5. Anzolin et al. 2009; 6. Aungwerojwit et al. 2012; 7. Bernardini et al. 2015; 8. Bonnet-Bidaud et al. 2007; 9. Buckley et al. 1995; 10. Burwitz et al. 1996; 11. Butters et al. 2007; 12. Butters et al. 2009; 13. Crawford et al. 2008; 14. de Martino et al. 2001; 15. de Martino et al. 2005; 16. de Martino et al. 2006a; 17. de Martino et al. 2006b; 18. de Martino et al. 2008; 19. Evans and Hellier 2005; 20. Evans et al. 2006; 21. Gansicke et al. 2005; 22. Girish and Singh 2012; 23. Harlaftis and Horne 1999; 24. Haswell et al. 1997; 25. Hellier 1997; 26. Hellier et al. 2002a; 27. Hellier et al. 2002b; 28. Johnson et al. 2006; 29. Katajainen et al. 2007; 30. Kaur et al. 2010; 31. Kim et al. 2005; 32. Kozhevnikov 2012; 33. Kozhevnikov 2014; 34. Kozhevnikov et al. 2006; 35. Lipkin et al. 2004; 36. Lutovinov et al. 2010; 37. Mhlahlo et al. 2007; 38. Nasiroglu et al. 2012; 39. Norton and Mukai 2007; 40. Norton and Tanner 2006; 41. Norton et al. 1992; 42. Piirola et al. 2008; 43. Pretorius 2009; 44. Ramsay et al. 2008; 45. Rana et al. 2004; 46. Reimer et al. 2008; 47. Revnivtsev et al. 2004; 48. Rodriguez-Gil et al. 2001; 49. Rodriguez-Gil et al. 2004; 50. Rodriguez-Gil et al. 2005; 51. Sambruna et al. 1992; 52. Scaringi et al. 2011; 53. Schlegel 2005; 54. Staude et al. 2008; 55. Still et al. 1998; 56. Thorstensen and Halpern 2013; 57. van Amerongen et al. 1987; 58. Vrielmann et al. 2005; 59. Williams 2003; 60. Zharikov et al. 2002.

Table 8.2 DQ Herculis binaries

Name	P (h)	$P_{\rm R}$ (min)	$\dot{P}_{\rm R}/P_{\rm R}$ (year^{-1})	References
AE Aqr	9.88	0.55	5.4×10^{-8}	2, 3
V533 Her	5.04	1.06	1.5×10^{-7}	4, 6
DQ Her	4.65	1.18	-3.6×10^{-7}	1, 5

Table 8.2 Reference Number Key: 1. Bloemen et al. 2010; 2. Hill et al. 2014; 3. Mauche 2009; 4. Patterson 1979; 5. Saito and Baptista 2009; 6. Thorstensen and Taylor 2000.

Table 8.3 Disc accreting X-ray binary pulsars

System	P (days)	$P_{\rm R}$ (s)	$\dot{P}_{\rm R}/P_{\rm R}$ (year^{-1})	References
GX 1+4	304	114	-2.1×10^{-2}	4, 12
4U0115+63	24.31	3.61	-3.2×10^{-5}	1, 11
OAO 1657-415	10.44	38.0	-1.0×10^{-3}	6, 13
SMC X-1	3.892	0.72	-6.0×10^{-4}	5, 14
Cen X-3	2.087	4.84	-2.8×10^{-4}	10, 14
Her X-1	1.700	1.24	-2.9×10^{-6}	7, 15
LMC X-4	1.408	13.5		8, 9
GX 109.1−1.0	0.080	6.98		3
4U1626−67	0.023	7.68	-2.0×10^{-4}	2

Table 8.3 Reference Number Key: 1. Baushev 2009; 2. Bildsten et al. 1997; 3. Downes 1983; 4. Gonzalez-Galan et al. 2012; 5. Hickox and Vrtilek 2005; 6. Jenke et al. 2012; 7. Leahy and Igna 2013; 8. Molkov et al. 2017; 9. Naik and Paul 2003; 10. Naik et al. 2011; 11. Nakajima et al. 2006; 12. Paul et al. 2005; 13. Pradhan et al. 2014; 14. Raichur and Paul 2010; 15. Simon 2015.

Table 8.4 Accreting millisecond pulsars

System	P (h)	$P_{\rm R}$ (ms)	References
J1814	4.28	3.18	9
J00291	2.45	1.67	4, 10
J1808	2.02	2.49	1, 13
J1900	1.39	2.65	5, 11
J0929	0.73	5.41	3, 12
J1751	0.71	2.30	7, 8
J1807	0.67	5.24	2, 6

Table 8.4 Reference Number Key: 1. Chakrabarty and Morgan 1998; 2. Falanga et al. 2005; 3. Galloway et al. 2002; 4. Galloway et al. 2005; 5. Kaaret et al. 2005;

6. Kirsch et al. 2004; 7. Markwardt and Swank 2002; 8. Markwardt et al. 2002; 9. Markwardt et al. 2003; 10. Markwardt et al. 2004; 11. Morgan et al. 2005; 12. Remillard et al. 2002; 13. Wijnands and van der Klis 1998.

References

Allan, A., Hellier, C., Ramseyer, T.F., 1996, MNRAS, 282, 699.
Andronov, I.L., Breus, V.V., 2013, Ap, 56, 518.
Andronov, I.L., Chinarova, L., Han, W., Kim, J., Yoon, J.N., 2008, A&A, 486, 855.
Anzolin, G., de Martino, D., Bonnet-Bidaud, J.M., Mouchet, M., Gansicke, B.T., Matt, G., Makai, K., 2008, A&A, 489, 1243.
Anzolin, G., de Martino, D., Falango, M., Makai, K., Bonnet-Bidaud, J.M., Mouchet, M., Terada, Y. Ishida, M., 2009, A&A, 501, 1047.
Aungwerojwit, A., Gansicke, B.T., Wheatley, P.J., Pyrzas, S., Staels, B., Krajci, T., Rodriguez-Gil, P., 2012, ApJ, 758. 79.
Balachandran, S., Robinson, E.L., Kepler, S.O., 1983, PASP, 95, 653.
Baushev, A.N., 2009, ARep, 53, 67.
Bernardini, F., de Martino, D., Mukai, K., Israel, G., Falango, M., Ramsay, G., Masetti, N., 2015, MNRAS, 453, 3100.
Bildsten, L. et al., 1997, ApJ, 113, 367.
Bloemen, S., Marsh, T.R., Steeghs, D., Ostensen, R.H., 2010, MNRAS, 407, 1903.
Bond, I.A., Freeth, R.V., 1988, MNRAS, 232, 753.
Bonnet-Bidaud, J.M., de Martino, D., Falango, M., Mouchet, M., Masetti, N., 2007, A&A, 473, 185.
Buckley, D.A.H., Sekiguchi, K., Motch, C., O'Donoghue, D., Chen, A.L., Schwarzenberg- Czerny, A., Pietsch, W., Harrop-Allin, M.K., 1995, MNRAS, 275, 1028.
Burwitz, V., Reinsch, K., Beuermann, K., Thomas, H.C., 1996, A&A, 310, L25.
Butters, O.W., Barlow, E.J., Norton, A.J., Mukai, K., 2007, A&A, 475, L29.
Butters, O.W., Norton, A.J., Mukai, K., Barlow, E.J., 2009, A&A, 498, L17.
Chakrabarty, D., Morgan, E.H., 1998, Nature, 394, 346.
Chakrabarty, D., Grunsfeld, J.M., Prince, T.A., Bildsten, L., Finger, M.H., Wilson, R.W., Fisher, G.J., Meegan, C.A., 1993, ApJ, 403, L33.
Chakrabarty, D., Bildsten, L., Grunsfeld, J.M., Koh, D.T., Prince, T.A., Vaughan, B.A., Finger, M.H., Scott, D.M., Wilson, R.B., 1997, ApJ, 474, 414.
Charles, P.A., Thorstensen, J., Bowyer, S., Middleditch, J., 1979, ApJ, 231, L131.
Corbet, R.H.D., 1986, MNRAS, 220, 1047.
Crawford, J.A., Kraft, R.P., 1956, ApJ, 123, 44.
Crawford, T., Boyd, D., Gualdoni, C., Gomez, T., Mac Donald, W., Oksanen, A., 2008, JAVSO, 36, 60.
Cropper, M.S., 1986, MNRAS, 222, 225.
de Jager, O.C., Meintjes, P.J., O'Donoghue, D., Robinson, E.L., 1994, MNRAS, 267, 577.
de Martino, D., Matt, G., Mukai, K., Belloni, T., Bonnet-Bidaud, J.M., Chiappetti, L., Gansicke, B.T., Haberl, F., Mouchet, M., 2001, A&A, 377, 499.
de Martino, D., Matt, G., Mukai, K., Bonnet-Bidaud, J.M., Gansicke, B.T., Gonzalez Peres, J.M., Harberl, F., Mouchet, M., Solheim, J.E., 2005, A&A, 437, 935.
de Martino, D., Bonnet-Bidaud, J.M., Mouchet, M., Gansicke, B.T., Habel, R., Motch. C., 2006a, A&A, 449, 1151.
de Martino, D., Matt, G., Mukai, K., Bonnet-Bidaud, J.M., Burwitz, V., Gansicke, B.T., Haberl, F., Mouchet, M., 2006b, A&A, 454, 287.
de Martino, D., Matt, G., Mukai, K., Bonnet-Bidaud, J.M., Falango, M., Gansicke, B.T., Haberl, F., Marsh, T.R., Mouchet, M., Littlefair, S.P., Dhillon, V., 2008, A&A, 481, 149.

Doty, J.P., Hoffman, J.A., Lewin, W.H.G., 1981, ApJ, 243, 257.
Downes, A., 1983, MNRAS, 203, 695.
Evans, P.A., Hellier, C., 2005, MNRAS, 359, 1531.
Evans, P.A., Hellier, C., Ramsay, G., 2006, MNRAS, 369, 1229.
Fabbiano, G., Schreier, E.J., 1977, ApJ, 214, 235.
Falanga, M., Bonnet-Bidaud, J.M., Poutanen, J., Farinelli, R., Martocchia, A., Goldoni, P., Qu, J.L., Kuiper, L., Goldwurm, A., 2005, A&A, 436, 647.
Galloway, D.K., Chakrabarty, D., Morgan, E.H., Remillard, R.A., 2002, ApJ, 576, L137.
Galloway, D., Markwardt, C.B., Morgan, E.H., Chakrabarty, D., Strohmayer, T.E., 2005, ApJ, 622, L45.
Gansicke, B.T. et al, 2005, MNRAS, 361, 141.
Giacconi, R., 1974, asgr.proc, Editions de l'Université de Bruxelles, 27.
Giacconi, R., Gursky, H., Kellogg, E., Schreier, E., Tananbaum, H., 1971, ApJ, 167, L67.
Girish, V., Singh, K.P., 2012, MNRAS, 427, 458.
Gonzalez-Galan, A., Kuulkers, E., Kretschmar, P., Larsson, S., Postnov, K., Kochetkova, A., Finger, M.H., 2012, A&A, 537, A66.
Griffiths, R.E., Lamb, D.Q., Ward, M.J., Wilson, A.J., Charles, P.A., Thorstensen, J., McHardy, I.M., Lawrence, A., 1980, MNRAS, 193, 25P.
Harlaftis, E.T., Horne, K., 1999, MNRAS, 305, 437.
Hassall, B.J.M., Pringle, J.E., Ward, M.J., Whelan, J.A.J., Mayo, S.K., Echevarria, J., Jones, D.H.P., Wallis, R.E., Allen, D.A., Hyland, A.R., 1981, MNRAS, 197, 275.
Haswell, C.A., Patterson, J., Thorstensen, J.R., Hellier, C., Skillman, D.R., 1997, ApJ, 476, 847.
Hellier, C., 1997, MNRAS, 288, 817.
Hellier, C., Mason, K.O., Mittaz, J.P.D., 1991, MNRAS, 248, 5P.
Hellier, C., Wynn, G.A., Buckley, D.A.H., 2002a, MNRAS, 333, 84.
Hellier, C., Beardmore, A.P., Mukai, K., 2002b, A&A, 389, 904.
Hickox, R.C., Vrtilek, S.D., 2005, ApJ, 633, 1064.
Hill, C., Watson, C., Shahbaz, T., Steeghs, D., Dhillon, V.S., 2014, MNRAS, 444, 192.
Hutchings, J.B., Crampton, D., Cowley, A.P., Thorstensen, J.R., Charles, P.A., 1981, ApJ, 249, 680.
Ibragimov, A., Poutanen, J., 2009, MNRAS, 400, 492.
Jenke, P.A., Finger, M.H., Wilson-Hodge, C.A., Camero-Arranz, A., 2012, ApJ, 759, 124.
Johnson, E.M., Imamura, J.N., Steiman-Cameron, T.Y., 2006, PASP, 118, 797.
Joy, A.H., 1954, ApJ, 120, 377.
Kaaret, P. Morgan, E., Vanderspek, R., 2005, ATel, 538.
Kajava, J.J.E., Ibragimov, A., Annala, M., Patruno, A., Poutanen, J., 2011, MNRAS, 417, 1454.
Kaluzny, J., Semeniuk, I., 1988, IBVS, 3145, 1.
Katajainen, S., Butters, O.W., Norton, A.J., Lehto, H.J., Piirola, V., 2007, A&A, 475, 1011.
Kaur, R., Wijnands, R., Biswajit, P., Patruno, A., Degenaav, N., 2010, MNRAS, 402, 2388.
Kii, T., Hayakawa, S., Nagase, F., Ikegami, T., Kawai, N., 1986, PASJ, 38, 751.
Kim, Y.G., Andronov, I.C., Park, S.S., Jeon, Y.B., 2005, A&A, 441, 663.
Kirsch, M.G.F., Mukerjee, K., Breitfellner, M.G., Djavidnia, S., Freyberg, M.J., Kendziorra, E., Smith, M.J.S., 2004, A&A, 423, L9.
Kozhevnikov, V.P., 2012, MNRAS, 422, 1518.
Kozhevnikov, V.P., 2014, MNRAS, 443, 2444.
Kozhevnikov, V.P., Zakharova, P.E., Nikiforova, T.P., 2006, ARep, 50, 902.
Kruszewski, A., Semeniuk, I., 1993, AcA, 43, 127.
Lamb, D.Q., Patterson, J., 1983, ASSC, 101, 229.
Leahy, D.A., Igna, C.D., 2013, IAUS, 290, 125.
Lipkin, Y.M., Leibowitz, E.M., Orio, M., 2004, MNRAS, 349, 1323.
Lutovinov, A.A., Burenin, R.A., Revnivtnev, M.G., Suleimanov, V.F., Tkachenko, A., 2010, AstL, 36, 904.
Makishima, K., et al, 1988, Nature, 333, 746.
Mauche, C.W., 2009, ApJ, 706, 130.

Markwardt, C.B., Swank, J.H., 2002, IAUC, 7867, 1.
Markwardt, C.B., Swank, J.H., Strohmayer, T.E., Marshall, F.E., 2002, ApJ, 575, L21.
Markwardt, C.B., Swank, J.H., Strohmayer, T.E., 2003, ATel, 164.
Markwardt, C.B., Galloway, D.K., Chakrabarty, D., Morgan, E.H., Strohmayer, T.E., 2004, ATel, 360, 1.
Mhlahlo, N., Buckley, D.A.H., Dhillon, V.S., Potter, S.B., Warner, B., Woudt, P., Bolt, G., McCormick, J., Rea, R., Sullivan, J., Velhuis, F., 2007, MNRAS, 380, 133.
Middleditch, J., 1983, ApJ, 275, 278.
Molkov, S., Lutovinov, A., Falango, M., Tsygankov, S., Bozzo, E., 2017, MNRAS, 646, 2039.
Morgan, E., Kaaret, P., Vanderspek, R., 2005, ATel, 523.
Naik, S., Paul, B., 2003, A&A, 401, 265.
Naik, S., Paul, B., Ali, Z., 2011, ApJ, 737, 79.
Nakajima, M., Mihara, T., Makishima, K., Niko, H., 2006, ApJ, 646, 1125.
Nasiroglu, I., Slowikowska, A., Kanbach, G., Haberl, F., 2012, MNRAS, 420, 3350.
Norton, A.J., Mukai, K., 2007, A&A, 472, 225.
Norton, A.J., Tanner, J.D., 2006, A&A, 447, L17.
Norton, A.J., Mc Hardy, I.M., Lehto, H.J., Watson, M.G., 1992, MNRAS, 258, 697.
Osborne, J.P., Mukai, K., 1989, MNRAS, 238, 1233.
Patterson, J., 1979, ApJ, 233, L13.
Patterson, J., 1991, PASP, 103, 1149.
Patterson, J., Price, C.M., 1981, ApJ, 243, L83.
Patterson, J., Thomas, G., 1993, PASP, 105, 59.
Paul, B., Dotani, T., Nagase, F., Mukherjee, U., Naik, S., 2005, ApJ, 627, 915.
Piirola, V., Vornanen, T., Berdyugin, A., 2008, ApJ, 684, 558.
Poutanen, J., 2006, AdSpR, 38, 2697.
Pradhan, P., Maitra, C., Paul, B., Islam, M., Paul, B.C., 2014, MNRAS, 442, 2691.
Pretorius, M.L., 2009, MNRAS, 395, 386.
Raichur, H., Paul, B., 2010, MNRAS, 401, 1532.
Ramsay, G., Wheatley, P.J., Norton, A.J., Hakula, P., Baskill, D., 2008, MNRAS, 387, 1157.
Rana, V.R., Singh, K.P., Schlegel, E.M., Barrett, P., 2004, ApJ, 127, 489.
Reimer, T.W., Welsh, W.F., Mukai, K., Ringwald, F.A., 2008, ApJ, 678, 376.
Remillard, R.A., Swank, J.H., Strohmayer, T.E., 2002, IAUC 7893, 1.
Revnivtsev, M.G., Lutovinov, A.A., Suleimanov, B.F., Molkov, S.V., Sunyaev, R.A., 2004, AstL, 30. 772.
Rodriguez-Gil, P., Casares, J., Martinez-Pias, I.G., Hakula, P., Steeghs, D., 2001, ApJ, 548, 49.
Rodriguez-Gil, P., Gansicke, B.T., Araujo-Betancor, S., Casares, J., 2004, MNRAS, 349, 367.
Rodriguez-Gil, P., Gansicke, B.T., Hagen, H.J., Nogami, D., Tores, M.A.P., Lehto, H., Aungwerojwit, A., Littlefair, S., Araujo-Betancor, S., Engels, D., 2005, A&A, 440, 701.
Rosen, S.R., Mittaz, J.P.D., Hakala, P.J., 1993, MNRAS, 264, 171.
Saito, R.K., Baptista, R., 2009, ApJ, 693, L16.
Sambruna, R.M., Chiappetti, L., Treves, A., Bonnet-Bidaud, J.M., Bouchet, P., Maraschi, L., Motch, C., Mouchet, M., van Amerongen, S., 1992, ApJ, 391, 750.
Scaringi, S. et al., 2011, A&A, 530, A6.
Schlegel, E.M., 2005, A&A, 433, 635.
Schreier, E.J., Fabbiano, G., 1976, X-Ray Binaries, NASA SP-389 (National Technical Information Service, Springfield, Virginia).
Schreier, E., Levinson, R., Gursky, H., Kellogg, E., Tananbaum, H., Giacconi, R., 1972, ApJ Lett, 172, L79.
Schrijver, J., Brinkman, A.C., van de Woerd, H., 1987, Ap&SS, 130, 261.
Simon, V., 2015, AJ, 150, 3.
Staude, A., Schwope, A.D., Vogel, J., Krumpe, M., Nebot Gomez-Moran, A., 2008, A&A, 486, 899.
Still, M.D., Duck, S.R., Marsh, T.R., 1998, MNRAS, 299, 759.

Stockman, H.S., Schmidt, G.D., Berriman, G., Liebert, J., Moore, R.L., Wickramasinghe, D.T., 1992, ApJ, 401, 628.
Tananbaum, H., Gursky, H., Kellogg, E.M., Levinson, R., Schreier, E., Giacconi, R., 1972, ApJ, 174, L143.
Thorstensen, J.R., Halpern, J., 2013, AJ, 146, 107.
Thorstensen, J.R., Taylor, C.J., 2000, MNRAS, 312, 629.
Trumper, J., Pietsch, W., Reppin, C., Voges, W., Staubert, R., Kendziorra, E., 1978, ApJ, 219, L105.
van Amerongen, S., Augusteijn, T., van Paradijs, J., 1987, MNRAS, 228, 377.
Vogt, N., Krzeminski, W., Sterken, C., 1980, ApJ, 85, 106.
Vrielmann, S., Ness, J.U., Schmitt, J.H., 2005, A&A, 439, 287.
Walker, M.F., 1954, PASP, 66, 230.
Warner, B., 1980, MNRAS, 190, 69P.
Warner, B., O'Donoghue, D., Fairall, A.P., 1981, MNRAS, 196, 705.
White, N.E., Swank, J.H., Holt, S.S., 1983, ApJ, 270, 711.
Wickramasinghe, D.T., Wu, K., Ferrario, L., 1991, MNRAS, 249, 460.
Wijnands, R., van der Klis, M., 1998, Nature, 394, 344.
Williams, G., 2003, PASP, 115, 618.
Zharikov, S.V., Tovmassian, G.H., Echevarria, J., 2002, A&A, 390, L23.

Chapter 9
Disc Disruption and Accretion Curtains

Abstract The intermediate polars, some X-ray binary pulsars and the accreting millisecond pulsars have magnetic primary stars accreting from a partially disrupted disc via an inner magnetically channelled curtain flow. The stellar magnetic field and the associated magnetosphere interact with the disc in a way which is affected by the strength of its magnetic diffusivity. For sufficiently large η values, the stellar poloidal field lines remain closed and linked to the disc. For smaller values of η field line opening can occur and wind flows can result from the disc and the primary star. Angular momentum can be transported in a variety of ways.

Field lines inside the corotation radius tend to remain closed and the disc becomes disrupted as a result of vertical expansion due to magnetic heating. Expanding material can be accelerated through a sonic point and then flow through a magnetically channelled curtain region to accrete on to the star through a narrow shock region. A detailed study of disc disruption and the curtain flow is presented here.

9.1 Introduction

The discovery of X-ray pulsations from Cen X-3 (Giacconi et al. 1971) and Her X-1 (Tananbaum et al. 1972) led to theoretical work to investigate the nature of these systems. Pringle and Rees (1972) proposed a model for Cen X-3 in which a strongly magnetic neutron star, rotating with the observed pulsation period of 4.8 s and having a magnetic moment misaligned with its rotation axis, accretes matter from a differentially rotating disc. They suggested that the magnetic field causes disruption of the inner part of the disc and that accretion on to the star occurs via a magnetically controlled flow connecting the inner edge of the disc to radially localized columns surrounding the stellar magnetic poles. The hot compressed gas in these accretion columns would emit radiation with an intensity modulated by the stellar rotation, giving rise to the observed X-ray pulsations. A corotation radius was defined at which the Keplerian angular velocity of the disc equals the stellar angular velocity. They noted that, for accretion to take place, the inner radius of the disc should lie inside the corotation radius. A similar oblique magnetic rotator model

C. G. Campbell, *Magnetohydrodynamics in Binary Stars*, Astrophysics and Space Science Library 456, https://doi.org/10.1007/978-3-319-97646-4_9

was proposed for DQ Her by Bath et al. (1974), but with the accretor being a white dwarf rather than a neutron star. The inner radius of the disrupted disc was estimated to be where the magnetic torque on the disc, due to its interaction with the stellar field, becomes equal to the viscous torque.

The magnetic accretor model was developed further by Ghosh and Lamb (1979a,b). They argued that the stellar magnetic field is likely to penetrate the thin turbulent disc via instabilities and reconnection processes. An extended stellar magnetosphere was assumed to corotate with the star, so the vertical shear between the surrounding gas and the differentially rotating disc material leads to the generation of toroidal magnetic field from the poloidal component. A cylindrical coordinate system (ϖ, ϕ, z) can be used centred on the star. The disc surface magnetic stress $B_{\phi s} B_{zs}$ leads to torques which result in angular momentum exchange between the disc and the star. Outside the corotation radius ϖ_{co} the star adds angular momentum to the disc, while inside this radius angular momentum is extracted from the disc and transferred to the star. Hence inside ϖ_{co} magnetic torques contribute to driving the disc inflow. As in Bath et al. (1974), it was suggested that disc disruption occurs where the magnetic torque becomes equal to the viscous torque. The disc flow was taken to join the magnetically channelled flow through a narrow radial boundary layer.

Some models took the stellar magnetic field to be completely excluded from the disc and calculated the resulting external field structure (e.g. Aly 1980; Kundt and Robnik 1980). However, it is generally believed that such configurations, especially in the inner regions of the disc, are unlikely to be stable and numerical simulations support this view (e.g. Goodson et al. 1997; Zanni and Ferreira 2013). The simulations show that diffusion and reconnection cause penetration of the field into the disc, as suggested by Ghosh and Lamb (1979a).

Much work has focused on calculating the torque on the star (e.g. Ghosh and Lamb 1979b; Campbell 1987; Wang 1987; Campbell 1992; Armitage and Clarke 1996; Matt and Pudritz 2005), making various assumptions to determine the disruption radius. Other work has investigated the effect of the magnetic field on the disc structure and perturbations to the magnetosphere due to its interaction with the disc. The nature of the inner accretion flow has also been considered. The spin evolution of the star is investigated in Chap. 10, after the disc structure, magnetosphere and curtain flow have been considered here.

Beyond ϖ_{co} the magnetospheric field is significantly perturbed by its interaction with the disc, but most of this region has a weak effect on the disc. Closer to ϖ_{co}, and inside this radius, magnetic perturbation of the disc becomes significant.

Campbell (1992) investigated the effect of the ratio of magnetic to viscous torque on the disc structure. A solution can be found in which the magnetic torque is large compared to the viscous torque in the inner part of the disc if the magnetic diffusivity, η, is taken as a physically unspecified function of ϖ. However, if parametrized turbulent or buoyancy forms are taken, so η depends on ρ and T, the vertical equilibrium cannot be satisfied. More general solutions were found by Campbell and Heptinstall (1998a,b), using turbulent and buoyancy forms for η. If no inner boundary condition is imposed, viscous heating causes the disc to expand

vertically inside the corotation radius due to growing thermal and radiation pressures which cannot be balanced by the vertical component of the stellar gravity or the vertical magnetic force. The expansion occurs over a narrow region and this would allow material to enter a magnetically controlled accretion flow and pass through a sonic point. These investigations have the consequence that, for η dependent on ρ and T, the disc ends where the magnetic torque starts to exceed the viscous torque and they indicate that disc disruption may be thermally related.

Shu et al. (1994) proposed a model in which the main interaction of the stellar magnetic field with the disc occurs in a small region centred on the corotation radius. Disruption and subsequent field channelled flow on to the star were taken to occur just inside $\varpi_{\rm co}$, but just beyond $\varpi_{\rm co}$ the field lines become open and a significant fraction of the accretion flow is lost via a magnetically influenced wind. Such a large mass loss in the wind results in a much reduced accretion torque on the star. The model was developed for application to T Tauri systems, in which the accreting protostar has a relatively low spin rate, rather than for the compact white dwarfs and neutron stars occurring in binary systems. However, the idea of some wind flow occurring beyond $\varpi_{\rm co}$, but having lower mass loss rates, has been investigated in the context of magnetic accretors in binary stars.

Lovelace et al. (1995) suggested that if the field winding ratio $|B_{\phi {\rm s}}/B_{\rm ps}|$ at the disc surface exceeds a critical value then the poloidal magnetic field lines will inflate and become open. Bardou and Heyvaerts (1996) showed that, if the magnetosphere adopts a nearly force-free state, field winding can cause significant field inflation. This was further confirmed by Agapitou and Papaloizou (2000), who considered the effects of larger values of the winding ratio.

Matthews et al. (2005) applied the condition that the vertically integrated dynamical viscosity, and its radial derivative, vanish at the inner edge of the disc. This enables a disruption radius to be found which depends on the stellar rotation rate, and these conditions are consistent with magnetic stresses becoming dominant over a narrow radial region. An analytic model was developed by Campbell (2010) in which a modified form of the boundary conditions of Matthews et al. (2005) was used, to allow for a small viscosity at inner edge, and magnetic heating was included. Allowance was also made for electron scattering opacity and radiation pressure. The disc was found to end over a narrow radial region in which magnetic heating causes increases in the vertical pressure gradient which cannot be balanced by the vertical component of stellar gravity or the vertical magnetic force. This model allows self consistent fitting of the disc flow to a magnetically channelled accretion curtain flow.

Numerical simulations have been developed to an increasing extent. Goodson et al. (1997) and Goodson and Winglee (1999) showed how the magnetic diffusivity in the disc can affect its interaction with the magnetosphere. Their numerical simulations showed that, for values of η less than those characteristic of turbulence, time-dependent fast collimated outflows can develop near the central axis of the system. Numerical simulations by Romanova et al. (2002) and Romanova et al. (2003) found that funnel flows develop inside $\varpi_{\rm co}$ and that these flows are driven by vertical pressure gradients. Time-dependent, global numerical simulations performed by Zanni and Ferreira (2009, 2013) resulted in disc disruption and curtain

flow inside $\varpi_{\rm co}$ and a variety of outflows from the system which depend on the magnitude of η in the disc. These simulations were applied to T Tauri systems, but they should have relevance to the discs surrounding magnetic stars in binary systems.

Detailed aspects of the magnetosphere and disc structures are discussed below. Then the accretion curtain structure is considered, together with the consequences for angular momentum transfer to the star. The non-axisymmetric case, of a tilted magnetic axis, is reviewed. Finally, the propeller regime is discussed. This leads naturally to the consideration of the stellar spin evolution in Chap. 10. The theory described here has application to the disc accreting X-ray binary pulsars, the intermediate polars and the accreting millisecond pulsars. [Sections 9.8.8 and 9.8.9 are derived in part from Campbell (2014), copyright Taylor and Francis, available online at https://doi.org/10.1080/03091929.2013.830719].

9.2 The Magnetosphere

9.2.1 The Angular Velocity

The magnetosphere surrounding the disc consists of low density ionized material. Most calculations take the central star to have a centred magnetic dipole moment **m** aligned with its rotation axis, which is parallel to the orbital angular momentum vector. Hence the system is axisymmetric, and is often taken to be time-independent. The validity of the assumption of time-independence will be shown to be related to the nature of the magnetic diffusion processes operating in the disc.

A cylindrical coordinate system (ϖ, ϕ, z) can be used, centred on the star. Motions of material in the magnetosphere obey the induction equation

$$\nabla \times (\mathbf{v} \times \mathbf{B}) = \mathbf{0}. \tag{9.1}$$

The toroidal and poloidal components of this yield

$$\mathbf{v}_{\rm p} = \kappa \mathbf{B}_{\rm p}, \tag{9.2}$$

$$\Omega - \frac{\kappa B_\phi}{\varpi} = \alpha, \tag{9.3}$$

where κ is a function of position and α is a constant on a field-streamline, corresponding to its angular velocity. It follows that, for field lines frozen to the star, $\alpha = \Omega_*$ the stellar rotation rate and hence

$$\Omega = \Omega_* \left[1 + \frac{v_{\rm p}}{\varpi \Omega_*} \frac{B_\phi}{B_{\rm p}} \right], \tag{9.4}$$

with $B_{\rm p} > 0$ and $\Omega_* > 0$. A steady corotating magnetosphere therefore requires

$$\frac{|v_{\rm p}|}{\varpi \Omega_*} \frac{|B_\phi|}{B_{\rm p}} \ll 1. \tag{9.5}$$

9.2.2 Poloidal Field Bending

The components of the unperturbed dipole magnetic field can be written as

$$B_\varpi = \frac{3}{2} B_0 R^3 \frac{\varpi z}{(\varpi^2 + z^2)^{\frac{5}{2}}}, \tag{9.6}$$

$$B_z = -\frac{1}{2} B_0 R^3 \frac{(\varpi^2 - 2z^2)}{(\varpi^2 + z^2)^{\frac{5}{2}}}, \tag{9.7}$$

where B_0 and R are the primary star's polar surface magnetic field and radius. For convenience, the previously adopted subscript p used to denote primary star quantities is dropped here.

The stellar magnetic field is modified due to its interaction with the disc. The poloidal field is distorted by the inflow through the disc and via inflation due to twisting caused by the vertical shear. The inflow leads to poloidal field bending, with an associated current density given by

$$\mu_0 \eta \mathbf{J} = \mathbf{E} + \mathbf{v} \times \mathbf{B}. \tag{9.8}$$

For a steady, axisymmetric flow $E_\phi = 0$ and hence

$$\mu_0 \eta J_\phi = v_z B_\varpi - v_\varpi B_z. \tag{9.9}$$

This shows that the poloidal flow in the disc generates J_ϕ. This acts as a source of $\mathbf{B}_{\rm p}$ which modifies the current-free stellar dipole field. The toroidal current density can be written, to a good approximation, as

$$J_\phi = \frac{1}{\mu_0} \frac{\partial B'_\varpi}{\partial z}, \tag{9.10}$$

where B'_ϖ is the perturbation in B_ϖ. Since $|v_z B_\varpi| \ll |v_\varpi B_z|$, it follows that

$$\frac{\partial B'_\varpi}{\partial z} = \frac{|v_\varpi|}{\eta} B_z. \tag{9.11}$$

This represents a balance between the outward slippage of B_z due to diffusion and its inward advection due to the radial flow. Integrating from $z = 0$ to $z = h$, assuming

the inflow to be mainly viscously driven, then yields

$$\left|\frac{B'_{\varpi s}}{B_{zs}}\right| \simeq \frac{|v_\varpi|}{\eta} h \simeq \frac{\nu}{\eta}\frac{h}{\varpi}. \tag{9.12}$$

If the condition $\nu/\eta \lesssim 1$ is satisfied, then moderate values of $|B'_{\varpi s}/B_{zs}|$ result and poloidal field bending due to the inflow is small.

The conclusion of small field bending, derived from the above simple analysis, is consistent with the more detailed calculation of Lubow et al. (1994). They considered a disc threaded by an externally imposed vertical magnetic field, with an inflow driven by viscosity. The time-dependent induction equation was solved for the poloidal flux function by numerical methods. A steady state is reached in which the field bending is essentially determined by the ratio $(\nu/\eta)(h/\varpi)$. Hence for $\nu/\eta \lesssim 1$ field bending due to the inflow was found to be small, consistent with (9.12).

9.2.3 Poloidal Field Inflation

The other source of distortion of $\mathbf{B}_p$ is field line inflation. For a magnetically dominated magnetosphere,

$$\frac{2\mu_0 P}{B^2} \ll 1 \tag{9.13}$$

will apply and the field will then be essentially force-free, with

$$(\nabla \times \mathbf{B}) \times \mathbf{B} = \mathbf{0}. \tag{9.14}$$

This condition, together with significant values of $|B_\phi/B_z|$ at the disc surface, leads to a modification of $\mathbf{B}_p$ from its current-free state. The poloidal field can be expressed as

$$\mathbf{B}_p = \nabla \times \left(\frac{\psi_m}{\varpi}\hat{\boldsymbol{\phi}}\right), \tag{9.15}$$

where $\psi_m(\varpi, z)$ is a magnetic flux function, being proportional to the poloidal flux through a ring of radius ϖ at height z. The use of this expression for $\mathbf{B}_p$ in the force-free field condition (9.14) leads to the Grad-Shafranov equation

$$\varpi \frac{\partial}{\partial \varpi}\left(\frac{1}{\varpi}\frac{\partial \psi_m}{\partial \varpi}\right) + \frac{\partial^2 \psi_m}{\partial z^2} = -\frac{1}{2}\frac{d}{d\psi_m}\left(I^2\right), \tag{9.16}$$

where $I(\psi_{\rm m}) = \varpi B_\phi$. Solving this equation, subject to boundary conditions, gives the force-free field structure. The solution depends on the disc surface field winding ratio $|B_{\phi {\rm s}}/B_{z{\rm s}}|$. If this ratio is small then $\mathbf{B}_{\rm p}$ is nearly dipolar and B_ϕ is small. Hence the field structure of the magnetosphere will be related to the structure of $\mathbf{B}$ in the disc.

The significance of field inflation was investigated by Bardou and Heyvaerts (1996). In order to consider numerical as well as analytic solutions for $\psi_{\rm m}$, they employed spherical polar coordinates (r, θ, ϕ). Equation (9.16) then becomes

$$\frac{\partial}{\partial r}\left(\frac{1}{\sin\theta}\frac{\partial \psi_{\rm m}}{\partial r}\right) + \frac{\partial}{\partial \theta}\left(\frac{1}{r^2 \sin\theta}\frac{\partial \psi_{\rm m}}{\partial \theta}\right) = -\frac{1}{2\sin\theta}\frac{d}{d\psi_{\rm m}}\left(I^2\right) \tag{9.17}$$

and the poloidal field components are

$$B_r = \frac{1}{r^2 \sin\theta}\frac{\partial \psi_{\rm m}}{\partial \theta}, \tag{9.18a}$$

$$B_\theta = -\frac{1}{r \sin\theta}\frac{\partial \psi_{\rm m}}{\partial r}. \tag{9.18b}$$

Equation (9.17) was solved numerically, and analytically via a similarity solution. The flux function $\psi_{\rm m}$ was taken to vanish on the central axis $\theta = 0$ and as $r \to \infty$. The poloidal field was also constrained to be vertical at $\theta = \pi/2$.

The analytic solution gives good agreement with the numerical results for a range of values of $|B_{\phi {\rm s}}/B_{z{\rm s}}|$. A self-similar flux function can be written as

$$\psi_{\rm m}(r, \theta) = r^{-p} f(\mu), \tag{9.19}$$

where p is a constant and $\mu = \cos\theta$. Substitution of this in (9.17) gives the separated equations

$$(1 - \mu^2) f'' + p(p+1) f = -C f^{(p+2)/p}, \tag{9.20}$$

$$I I' = C \psi_{\rm m}^{(p+2)/p}, \tag{9.21}$$

where C is a constant. The function $f(\mu)$ obeys the boundary conditions

$$f(0) = 1, \tag{9.22a}$$

$$f(1) = 0, \tag{9.22b}$$

$$f'(0) = 0. \tag{9.22c}$$

The first of these conditions is a normalisation, while the second and third correspond to $\psi_{\rm m}(r, 0) = 0$ and $B_r(r, \pi/2) = 0$ respectively. Integration of (9.21)

yields

$$\varpi B_\phi = \left(\frac{Cp}{p+1}\right)^{\frac{1}{2}} \psi_{\rm m}^{(p+1)/p}. \tag{9.23}$$

For moderate values of p, Bardou and Heyvaerts showed that

$$p = \frac{1}{[1 + (B_{\phi {\rm s}}/B_{z{\rm s}})^2]^{\frac{1}{2}}}, \tag{9.24}$$

and hence $p < 1$ results. The poloidal field components are

$$B_r = \frac{1}{\sin\theta} r^{-(p+2)} f', \tag{9.25a}$$

$$B_\theta = \frac{p}{\sin\theta} r^{-(p+2)} f. \tag{9.25b}$$

An analytic solution was found for small values of p, corresponding to $|B_{\phi {\rm s}}/B_{z{\rm s}}| > 1$. When $(B_{\phi {\rm s}}/B_{z{\rm s}})^2 \ll 1$ the poloidal magnetic field is nearly current-free and inflation is small, with (9.24) yielding $p \simeq 1$. The term involving $I = \varpi B_\phi$ on the right hand side of (9.16) or (9.17) can then be ignored, corresponding to $|J_\phi| \ll |J_{\rm p}|$, and $C = 0$ can be applied to (9.20). The ignored J_ϕ component is the source of perturbations to $\mathbf{B}_{\rm p}$, and hence these are small for small winding ratios. However, a small but finite B_ϕ component exists so C cannot be ignored in (9.21). This corresponds to the nearly force-free condition $\mathbf{B}_{\rm p} \cdot \nabla(\varpi B_\phi) = 0$. For an exact dipole field $p = 1$ and $C = 0$, so it is seen from (9.24) that inflation causes $\mathbf{B}_{\rm p}$ to fall more slowly with increasing r than for a dipole field.

The poloidal field inflation effect was considered further by Agapitou and Papaloizou (2000). The Grad-Shafranov equation, expressed in polar coordinates, was transformed into a parabolic equation by including a term proportional to $\partial\psi_{\rm m}/\partial t$, which tends to zero as a steady state is reached. Larger values of $|B_{\phi {\rm s}}/B_{z{\rm s}}|$ can then be considered than previously. The computational domain had inner and outer radii of $r_{\rm in}$ and $r_{\rm out}$, and the boundary conditions $\psi_{\rm m}(r_{\rm in}, \theta) = 0$ and $\psi_{\rm m}(r, 0) = 0$ were employed. Two outer boundary conditions were also introduced; a Dirichlet condition $\psi_{\rm m}(r_{\rm out}, \theta) = 0$ and a Neumann condition $(\partial\psi_{\rm m}/\partial r)_{\rm out} = 0$.

The disruption radius was taken to be at the corotation radius, so cases with $r < r_{\rm co}$ were not considered. For moderate values of $|B_{\phi {\rm s}}/B_{z{\rm s}}| > 1$ field line inflation occurs similar to that found by Bardou and Heyvaerts (1996). For $|B_{\phi {\rm s}}/B_{z{\rm s}}| \gtrsim 30$ a deflation of field lines occurs, which is not sensitive to the location of the outer boundary. In these larger field winding cases, $\mathbf{B}_{\rm p}$ has a larger radial component near the disc surface than that of the unperturbed dipole field. This gives a reduction of the ratio $|B_\phi/B_{\rm p}|$, where $B_{\rm p} = (B_r^2 + B_\theta^2)^{1/2}$.

The Neumann boundary condition case requires $\mathbf{B}_{\rm p}$ to be radial at the outer boundary, as might occur if a wind existed there. In this case $|B_\phi/B_{\rm p}| < 1$ was

found near the disc surface, and this ratio was small beyond it. Generally, the force-free condition kept $|B_\phi/B_\mathrm{p}| \sim 1$, by an increase in B_r accompanying an increase in $|B_\phi/B_z|$.

The work of Bardou and Heyvaerts (1996) showed that field line inflation is usually small inside the corotation radius, and the field lines are closed there. Large values of field winding can result in significant magnetic compression of the disc. Large, oppositely directed values of B_ϕ above and below a thin turbulent disc are generally believed to be unstable, leading to reconnection and associated dissipation across the disc and hence to a reduction in the winding value. This can be considered to be effectively equivalent to an enhanced magnetic diffusivity in the disc, as described below. The results of the foregoing analytic and semi-analytic studies of field line inflation are consistent with the field inflation effects seen in numerical simulations of the interaction between the disc and the magnetosphere (e.g. Goodson et al. 1997; Goodson and Winglee 1999; Zanni and Ferreira 2009, 2013). These simulations are described later.

9.3 Magnetic Diffusion in the Disc

Several processes are believed to contribute to the diffusion of the stellar magnetic field in the disc. As in other astrophysical situations, turbulence can greatly enhance diffusion compared to Ohmic processes. Magnetic buoyancy and small-scale reconnection may also play a significant role. Because there is no rigorous formulation of these complex processes, simplified representations are usually employed to account for their effects. Due to the difference in the radial and vertical length-scales in thin discs, an anisotropic representation may be applicable. However, a simple scalar form is often used, consisting of the product of a mean transport speed, a mixing length and a dimensionless adjustable parameter. For turbulence, the form

$$\eta_\mathrm{T} = \epsilon_\mathrm{T} c_\mathrm{s} h \tag{9.26}$$

is used, with $\epsilon_\mathrm{T} < 1$. Magnetic buoyancy is represented by

$$\eta_\mathrm{B} = \epsilon_\mathrm{B} \frac{|B_{\phi\mathrm{s}}|}{(\mu_0 \rho_\mathrm{c})^{\frac{1}{2}}} h, \tag{9.27}$$

with $\epsilon_\mathrm{B} \lesssim 1$ (see Sect. 2.2.11). This approach is similar to that adopted for the kinematic turbulent viscosity coefficient.

Another possible contribution to the magnetic diffusivity of the disc arises here, due to the large values that may occur for the field winding ratio $|B_{\phi\mathrm{s}}/B_{z\mathrm{s}}|$ as the result of vertical shearing of $\mathbf{B}_\mathrm{p}$. If this ratio reaches a critical value then instabilities are likely to occur. These, together with the reconnection of oppositely directed B_ϕ

field across the disc, may effectively reduce the growth rate of $|B_{\phi s}/B_{zs}|$. This can be represented by an enhanced diffusion coefficient containing a dynamical mean speed characteristic of Keplerian values, these being considerably larger than the sound speed or the Alfvén speed used in the turbulent and buoyancy forms of η. The dynamical diffusivity can be expressed as

$$\eta_{\rm dyn} = \epsilon_{\rm m} v_{\rm dyn} h, \tag{9.28}$$

with $\epsilon_{\rm m} \sim 1$ and $v_{\rm dyn}$ typically taken as the Keplerian speed $v_{\rm K}$.

9.4 The Disc Equations

9.4.1 The Momentum Equation

The disc equations describe the dynamical, magnetic and thermal problems. The thin nature of the disc allows some simplifications to be made. Because the disc poloidal velocity is well subsonic, the poloidal inertial terms can be ignored in the momentum equation. In cylindrical coordinates (ϖ, ϕ, z), the three components of the momentum equation can then be written as

$$\frac{v_\phi^2}{\varpi} = \frac{\partial \psi}{\partial \varpi} + \frac{1}{\rho}\frac{\partial P}{\partial \varpi} + \frac{1}{\varpi^2 \rho}\frac{\partial}{\partial \varpi}\left(\frac{\varpi^2 B_\phi^2}{2\mu_0}\right) - \frac{B_z J_\phi}{\rho}, \tag{9.29}$$

$$v_\varpi \frac{\partial}{\partial \varpi}(\varpi^2 \Omega) + v_z \frac{\partial}{\partial z}(\varpi^2 \Omega) = \frac{1}{\varpi \rho}\frac{\partial}{\partial \varpi}\left(\rho \nu \varpi^3 \frac{\partial \Omega}{\partial \varpi}\right) + \frac{1}{\mu_0 \varpi \rho}\frac{\partial}{\partial \varpi}(\varpi^2 B_\varpi B_\phi) + \frac{1}{\mu_0 \varpi \rho}\frac{\partial}{\partial z}(\varpi^2 B_\phi B_z), \tag{9.30}$$

$$\frac{\partial \psi}{\partial z} + \frac{1}{\rho}\frac{\partial}{\partial z}\left(P + \frac{B_\phi^2}{2\mu_0}\right) + \frac{B_\varpi J_\phi}{\rho} = 0, \tag{9.31}$$

where $\Omega = v_\phi/\varpi$ and

$$J_\phi = \frac{1}{\mu_0}\left(\frac{\partial B_\varpi}{\partial z} - \frac{\partial B_z}{\partial \varpi}\right). \tag{9.32}$$

Since the disc mass is negligible compared to the stellar mass, M, the gravitational potential has the stellar monopole form

$$\psi = -\frac{GM}{(\varpi^2 + z^2)^{\frac{1}{2}}}. \tag{9.33}$$

The continuity equation is

$$\frac{1}{\varpi}\frac{\partial}{\partial \varpi}(\varpi \rho v_{\varpi}) + \frac{\partial}{\partial z}(\rho v_z) = 0. \tag{9.34}$$

Some simplifications can be made by using the fact that many of the intrinsic disc quantities have a radial length-scale much longer than their vertical length-scale. Consider first the ϖ-component of the momentum equation, given by (9.29). It will be shown that $B^2/2\mu_0 \lesssim P$ holds in the disc. As in the non-magnetic disc, the radial pressure gradient is $\sim c_s^2/\varpi$ and hence is ignorable relative to the gravity term v_K^2/ϖ. Since B_ϕ varies on a radial length-scale of $\sim \varpi$, and $B_\phi^2/2\mu_0 < P$, the first magnetic term in (9.29) is ignorable. It follows from (9.32) for J_ϕ that the second magnetic term in (9.29) is

$$\frac{B_z J_\phi}{\rho} \simeq \frac{B_z^2 |v_\varpi|}{\mu_0 \eta \rho} \simeq \frac{B_z^2}{\mu_0 \varpi \rho}\frac{\nu}{\eta} \tag{9.35}$$

and, for $\nu/\eta < 1$, this magnetic term is also ignorable relative to the gravitational term. Hence (9.29) reduces to

$$v_\phi = v_K = \left(\frac{GM}{\varpi}\right)^{\frac{1}{2}} = \varpi \Omega_K. \tag{9.36}$$

This holds in the bulk of the disc. Deviations of Ω from Ω_K occur as the disc surfaces are approached, since Ω tends to the magnetospheric value of Ω_*, and near the disruption radius at the inner edge where the disc joins the curtain flow. Since ρ falls most sharply near the disc surface, the magnetic terms in (9.29) will only be significant in a thin surface layer through which Ω tends to Ω_*. Except inside ϖ_m, the disc angular velocity and diffusivity can be expressed as

$$\Omega(\varpi, z) = \begin{cases} \Omega_K = (GM/\varpi^3)^{\frac{1}{2}}, & |z| < h - \Delta, \\ \to \Omega_*, & h - \Delta < |z| \le h, \end{cases} \tag{9.37}$$

$$\eta = \begin{cases} \eta(\varpi), & z < h - \Delta, \\ \to 0, & h - \Delta < |z| \le h, \end{cases} \tag{9.38}$$

where Δ is a boundary layer width over which Ω changes to Ω_* as η becomes small. This gives a vertical step function idealization for Ω, with the vertical shear concentrated near the disc surface. However, B_ϕ results throughout the disc since it is a solution of the induction equation involving an integral over the disc sources.

The ϕ-component of the momentum equation is given by (9.30). Multiplying this be $\varpi\rho$ and combining it with the continuity equation (9.34) yields

$$\frac{\partial}{\partial\varpi}(\varpi\rho v_\varpi\varpi^2\Omega)+\frac{\partial}{\partial z}(\varpi\rho v_z\varpi^2\Omega)=\frac{\partial}{\partial\varpi}\left(\rho\nu\varpi^3\frac{\partial\Omega}{\partial\varpi}\right)+\frac{1}{\mu_0}\frac{\partial}{\partial\varpi}(\varpi^2B_\varpi B_\phi)+\frac{1}{\mu_0}\frac{\partial}{\partial z}(\varpi^2B_\phi B_z). \tag{9.39}$$

This relates the divergence of the angular momentum flux to the viscous and magnetic torques. Since $|B_\varpi|\sim(h/\varpi)|B_z|$ and $|\partial B_\phi/\partial\varpi|\sim(h/\varpi)|\partial B_\phi/\partial z|$, the $B_\varpi B_\phi$ radial transport term is ignorable, leaving

$$\frac{\partial}{\partial\varpi}(\varpi\rho v_\varpi\varpi^2\Omega)+\frac{\partial}{\partial z}(\varpi\rho v_z\varpi^2\Omega)=\frac{\partial}{\partial\varpi}\left(\rho\nu\varpi^3\frac{\partial\Omega}{\partial\varpi}\right)+\frac{1}{\mu_0}\frac{\partial}{\partial z}(\varpi^2B_\phi B_z) \tag{9.40}$$

as the disc angular momentum equation.

This leaves the vertical component of the disc momentum equation, given by (9.31). The last magnetic term is

$$\frac{B_\varpi J_\phi}{\rho}=\left(\frac{B_\varpi}{B_z}\right)\frac{B_zJ_\phi}{\rho}\simeq\left|\frac{B_\varpi}{B_z}\right|\frac{h}{\varpi}\frac{\nu}{\eta}\frac{B_z^2}{\mu_0h\rho}\ll\frac{B_\phi^2}{\mu_0h\rho}, \tag{9.41}$$

using (9.35) for B_zJ_ϕ/ρ and $|B_\varpi/B_z|\sim h/\varpi$. Hence, employing (9.33) for ψ, the vertical equation becomes

$$\Omega_{\rm K}^2z\rho+\frac{\partial}{\partial z}\left(P+\frac{B_\phi^2}{2\mu_0}\right)=0, \tag{9.42}$$

giving equilibrium between the stellar gravity and a total pressure gradient. The vertical gradient of the magnetic pressure acts to compress the disc, since B_ϕ^2 increases with increasing $|z|$.

9.4.2 The Induction Equation

The poloidal and toroidal components of the steady induction equation are

$$v_\varpi B_z-v_zB_\varpi+\mu_0\eta J_\phi=0, \tag{9.43}$$

$$\frac{\eta}{\varpi}\left(\nabla^2B_\phi-\frac{B_\phi}{\varpi^2}\right)+\frac{1}{\varpi^2}\frac{d\eta}{d\varpi}\frac{\partial}{\partial\varpi}(\varpi B_\phi)=-\mathbf{B}_{\rm p}\cdot\nabla\Omega+\nabla\cdot\left(\frac{B_\phi}{\varpi}\mathbf{v}_{\rm p}\right). \tag{9.44}$$

The poloidal component relates J_ϕ to its source $(\mathbf{v} \times \mathbf{B})_\phi$, and this leads to modifications of $\mathbf{B}_\mathrm{p}$ from its current-free form. It was previously shown that such modification, due to the subsonic poloidal flow, is small. The toroidal equation (9.44) can be simplified. Since B_ϕ varies on a vertical length-scale of $\sim h$, its vertical derivatives dominate in the diffusion operator. The vertical derivative term in $\mathbf{B}_\mathrm{p} \cdot \nabla\Omega$ exceeds the radial derivative by a factor of $\sim (\varpi/h)^2$. Finally, the advection and compression term is

$$\nabla \cdot \left(\frac{B_\phi}{\varpi} \mathbf{v}_\mathrm{p} \right) \sim \frac{B_{\phi\mathrm{s}}}{\varpi} \frac{v_\varpi}{\varpi} \sim \frac{\eta}{\varpi} \frac{\nu}{\eta} \frac{B_{\phi\mathrm{s}}}{\varpi^2} \sim \frac{h^2}{\varpi^2} \frac{\nu}{\eta} \frac{\eta}{\varpi} \frac{B_{\phi\mathrm{s}}}{h^2} \ll \frac{\eta}{\varpi} \left| \frac{\partial^2 B_\phi}{\partial z^2} \right|. \tag{9.45}$$

Hence this term is ignorable and the toroidal induction equation becomes

$$\eta \frac{\partial^2 B_\phi}{\partial z^2} = -\varpi B_z \frac{\partial \Omega}{\partial z}, \tag{9.46}$$

representing a balance between the vertical diffusion of B_ϕ and its creation due to the vertical shearing of B_z.

9.4.3 The Thermal Equations

The thermal equilibrium equation relates the divergence of the heat flux to the energy generated per unit volume, since the heat advection term is ignorable, as in the standard viscous disc. This gives

$$\frac{\partial F_\mathrm{R}}{\partial z} = \rho\nu(\varpi\Omega')^2 + \mu_0 \eta J^2, \tag{9.47}$$

having viscous and magnetic contributions. The poloidal components of the current density are

$$J_\varpi = -\frac{1}{\mu_0} \frac{\partial B_\phi}{\partial z}, \tag{9.48a}$$

$$J_z = \frac{1}{\mu_0 \varpi} \frac{\partial}{\partial \varpi} (\varpi B_\phi). \tag{9.48b}$$

It follows that $|J_\varpi| \sim (\varpi/h)|J_z| \gg |J_z|$. Then using (9.10) and (9.11) for J_ϕ together with (9.48a) gives

$$\frac{|J_\phi|}{|J_\varpi|} \sim \frac{\nu}{\eta} \left| \frac{B_z}{B_\phi} \right| \frac{h}{\varpi} \ll 1. \tag{9.49}$$

Hence the radial component of **J** dominates and (9.47) becomes

$$\frac{\partial F_{\mathrm{R}}}{\partial z} = \frac{9}{4}\rho\nu\Omega_{\mathrm{K}}^2 + \frac{\eta}{\mu_0}\left(\frac{\partial B_\phi}{\partial z}\right)^2. \tag{9.50}$$

The main body of the disc is optically thick in the vertical direction and hence the radiative diffusion approximation holds to give the heat flux as

$$F_{\mathrm{R}} = -\frac{4\sigma_{\mathrm{B}}}{3\kappa\rho}\frac{\partial}{\partial z}(T^4), \tag{9.51}$$

where the Rosseland mean opacity is taken as

$$\kappa = K\rho T^{-\frac{7}{2}} + \kappa_{\mathrm{es}}, \tag{9.52}$$

with K a constant in the Kramers opacity, and the electron scattering opacity is

$$\kappa_{\mathrm{es}} = 2 \times 10^{-2}(1 + X)\,\mathrm{m}^2\,\mathrm{kg}^{-1}, \tag{9.53}$$

where X is the fraction by mass of hydrogen.

Allowing for radiation pressure, the equation of state is

$$P = \frac{\mathcal{R}}{\mu}\rho T + \frac{4\sigma_{\mathrm{B}}}{3c}T^4. \tag{9.54}$$

9.4.4 The Reduced Disc Equations

It is useful to gather the foregoing reduced dynamical, magnetic and thermal equations together as;

$$\Omega(\varpi, z) = \begin{cases} \Omega_{\mathrm{K}} = (GM/\varpi^3)^{\frac{1}{2}}, & |z| < h - \Delta, \\ \to \Omega_*, & h - \Delta < |z| \le h, \end{cases} \tag{9.55}$$

$$\frac{\partial}{\partial\varpi}(\varpi\rho v_\varpi \varpi^2\Omega) + \frac{\partial}{\partial z}(\varpi\rho v_z \varpi^2\Omega) = \frac{\partial}{\partial\varpi}\left(\rho\nu\varpi^3\frac{\partial\Omega}{\partial\varpi}\right) + \frac{1}{\mu_0}\frac{\partial}{\partial z}(\varpi^2 B_\phi B_z), \tag{9.56}$$

$$\Omega_{\mathrm{K}}^2 z\rho + \frac{\partial}{\partial z}\left(P + \frac{B^2}{2\mu_0}\right) = 0, \tag{9.57}$$

$$\frac{1}{\varpi}\frac{\partial}{\partial\varpi}(\varpi\rho v_\varpi) + \frac{\partial}{\partial z}(\rho v_z) = 0, \tag{9.58}$$

$$v_\varpi B_z - v_z B_\varpi + \mu_0 \eta J_\phi = 0, \tag{9.59}$$

$$\eta \frac{\partial^2 B_\phi}{\partial z^2} = -\varpi B_z \frac{\partial \Omega}{\partial z}, \tag{9.60}$$

$$\frac{\partial F}{\partial z} = \frac{9}{4}\rho \nu \Omega_{\text{K}}^2 + \frac{\eta}{\mu_0}\left(\frac{\partial B_\phi}{\partial z}\right)^2, \tag{9.61}$$

$$F_{\text{R}} = -\frac{4\sigma_{\text{B}}}{3\kappa\rho}\frac{\partial}{\partial z}(T^4), \tag{9.62}$$

$$\kappa = K\rho T^{-\frac{7}{2}} + \kappa_{\text{es}}, \tag{9.63}$$

$$P = \frac{\mathcal{R}}{\mu}\rho T + \frac{4\sigma_{\text{B}}}{3c}T^4. \tag{9.64}$$

Parametrized forms of ν and η are usually employed. These simplified equations enable analytic progress to be made.

9.5 The Toroidal Magnetic Field

The solution of the toroidal induction equation gives the field B_ϕ, and its form will depend on the nature of the magnetic diffusivity. Although the approximate equation (9.60) gives good accuracy, it is of interest to note that in special cases exact solutions of the full equation can be found which allow for the effects of the radial derivative terms. It was shown in Campbell (1987) that, for some cases of η, such solutions are possible. The last term in the full equation (9.44), representing advection and compression effects, makes the smallest contribution and so can be dropped.

For constant η the toroidal equation then becomes

$$\nabla^2 B_\phi - \frac{B_\phi}{\varpi^2} = -\frac{\varpi}{\eta}\mathbf{B}_{\text{p}} \cdot \nabla\Omega. \tag{9.65}$$

This equation can be transformed into a Poisson equation by multiplying by an integrating factor $\exp(i\phi)$, giving

$$\nabla^2 (B_\phi e^{i\phi}) = -\frac{\varpi}{\eta}\mathbf{B}_{\text{p}} \cdot \nabla\Omega e^{i\phi}. \tag{9.66}$$

The Poisson integral solution then leads to

$$B_\phi = \frac{1}{4\pi\eta}\int_{-h}^{h}\int_{\varpi_{\text{m}}}^{\varpi_{\text{D}}} \varpi_0^2 (\mathbf{B}_{\text{p}} \cdot \nabla\Omega)_0 G(\varpi, z, \varpi_0, z_0) d\varpi_0 dz_0, \tag{9.67}$$

with

$$G(\varpi, z, \varpi_0, z_0) = \frac{2}{b(a+b)^{\frac{1}{2}}}\left[2aF\left(\frac{\pi}{2}, k\right) - (a+b)E\left(\frac{\pi}{2}, k\right) - (a-b)\Pi\left(\frac{\pi}{2}, k^2, k\right)\right], \tag{9.68}$$

where

$$a = \varpi^2 + \varpi_0^2 + (z - z_0)^2, \tag{9.69a}$$

$$b = 2\varpi\varpi_0, \tag{9.69b}$$

and

$$k = \left[\frac{4\varpi\varpi_0}{(\varpi + \varpi_0)^2 + (z - z_0)^2}\right]^{\frac{1}{2}}, \tag{9.70}$$

with F, E and Π being elliptic integrals of the first, second and third kinds (see Appendix). The integral in (9.67) is over the disc, which is taken to be the major source of the electric currents.

Another exact solution is possible if a quadratic dependence is taken for η. The toroidal induction equation can then be expressed as

$$\nabla^2(\varpi B_\phi) = -\frac{\varpi^2}{\eta}\mathbf{B}_\mathrm{p} \cdot \nabla\Omega. \tag{9.71}$$

This has a Poisson integral solution which can be written

$$B_\phi = \frac{1}{4\pi\varpi}\int_{-h}^{h}\int_{\varpi_\mathrm{m}}^{\varpi_\mathrm{D}} \frac{\varpi_0^3}{\eta(\varpi_0)}(\mathbf{B}_\mathrm{p} \cdot \nabla\Omega)_0 W(\varpi, z, \varpi_0, z_0) d\varpi_0 dz_0, \tag{9.72}$$

where

$$W(\varpi, z, \varpi_0, z_0) = \frac{F(\pi/2, k)}{\left[(\varpi + \varpi_0)^2 + (z - z_0)^2\right]^{\frac{1}{2}}}, \tag{9.73}$$

where F is an elliptic integral of the first kind and k is defined by (9.70).

These exact solutions illustrate that, in general, the B_ϕ field has sources distributed through the disc, including a source due to the radial shearing of B_ϖ. It is noted that B_ϕ does not vanish at the corotation point in this solution, which accounts for the effects of the radial derivatives. The radial shearing term $B_\varpi d\Omega_\mathrm{K}/d\varpi$ leads to a small but finite value of B_ϕ at ϖ_co.

For thin discs, the approximate toroidal equation (9.60) can be used to good accuracy. For sustainable field winding, corresponding to a dynamical form of η, $|B_{\phi s}/B_{zs}| \lesssim 1$ applies and poloidal field line inflation will be small. This is particularly the case for $\varpi < \varpi_{co}$, which is the region of interest for disc disruption. The toroidal current density J_ϕ is then ignorable in the disc and, to lowest order in z/ϖ, the poloidal field components (9.6) and (9.7) become

$$B_\varpi = \frac{3}{2} B_0 \left(\frac{R}{\varpi}\right)^3 \frac{z}{\varpi}, \tag{9.74a}$$

$$B_z = -\frac{1}{2} B_0 \left(\frac{R}{\varpi}\right)^3. \tag{9.74b}$$

The toroidal induction equation (9.60) must be solved subject to suitable boundary conditions. For a force-free magnetosphere B_ϕ obeys the equation

$$\mathbf{B}_p \cdot \nabla(\varpi B_\phi) = 0 \tag{9.75}$$

and this becomes the surface condition at $z = h$. Since the vertical derivative dominates, the condition reduces to

$$\left(\frac{\partial B_\phi}{\partial z}\right)_{z=h} = 0, \tag{9.76}$$

Because B_ϕ is antisymmetric about $z = 0$, it follows that

$$B_\phi(\varpi, 0) = 0, \tag{9.77}$$

applies in the central plane.

Integration of the toroidal equation (9.60) from z up to h, using (9.55) for Ω, the z-independence of B_z and the surface condition (9.76), yields

$$\frac{\partial B_\phi}{\partial z} = \frac{\varpi B_z}{\eta}(\Omega_* - \Omega_K) H(z - h), \tag{9.78}$$

where the Heaviside step function is

$$H(z - h) = \begin{cases} 1, z < h, \\ 0, z \geq h. \end{cases} \tag{9.79}$$

Then integrating (9.78) from 0 to z, using the central plane condition (9.77), gives

$$B_\phi = \frac{\varpi B_z}{\eta}(\Omega_* - \Omega_K) z. \tag{9.80}$$

This solutions is valid down to the outer edge of the disruption region, through which Ω changes from $\Omega_{\rm K}$ to Ω_*. A parametrized form is usually chosen for η.

9.6 Disc and Magnetosphere Models

9.6.1 Analytic and Semi-Analytic Models

A range of models have been presented for the magnetically modified structure of the disc and of the magnetosphere. These investigations make, by necessity, various assumptions about the disc magnetic diffusivity, η, and specify an initial structure for the magnetosphere. It will be seen that η is of central importance to the outcomes of these studies.

The model of Ghosh and Lamb (1979a) gave a detailed consideration of the star-disc interaction. A dipolar stellar field was taken with its moment aligned with the rotation axis. It was argued that the stellar magnetic field will penetrate the disc via Kelvin-Helmholtz instabilities and turbulent diffusion, with magnetic reconnection occurring. The surrounding magnetosphere was taken to be magnetically dominated, without extensive poloidal flows, and corotating with the star. The vertical shear between the magnetosphere and the differentially rotating disc generates B_ϕ field from B_z, leading to a growth in the winding ratio $|B_{\phi {\rm s}}/B_{z{\rm s}}|$. This growth was limited by mixing, diffusion and reconnection processes operating across the disc.

The magnetic field lines were assumed to stay closed, and hence connect the disc to the star. The magnetic torque felt by the disc, which is related to the $B_{\phi {\rm s}} B_{z{\rm s}}$ stress, results in angular momentum exchange between the disc and the star. The disc was assumed to end in a radial boundary layer, over which its angular velocity changes to the stellar value Ω_*. The disc flow becomes vertically diverted through this layer into a magnetically influenced curtain flow, with accretion occurring in narrow circular regions near the magnetic poles. Angular momentum is transferred to the star via magnetic stresses operating along the curtain flow. The boundary layer was modelled by assuming a radial dependence for the vertical mass transfer rate, and that the magnetic diffusion can adjust in a suitable way.

Beyond the corotation radius the disc magnetic torque reverses sign and angular momentum is transferred from the star to the disc. However, provided that the viscous torque exceeds the magnetic torque, an inflow still results. For plausible parameters, the positive and negative torques on the star can balance and this defines an equilibrium period.

Wang (1987) reassessed the Ghosh and Lamb (1979a) model and found an inconsistency in their expression for the winding ratio $|B_{\phi {\rm s}}/B_{z{\rm s}}|$. This arose from their expression for the growth rate $\partial B_\phi/\partial t$, due to the vertical shear, being taken to be proportional to B_ϕ. However, the induction equation shows that this rate should be proportional to B_z due to winding of the poloidal field. Wang showed that the Ghosh and Lamb expression for $|B_{\phi {\rm s}}/B_{z{\rm s}}|$ leads to an increase in the ratio $B_\phi^2/2\mu_0 P$

with increasing distance beyond $\varpi_{\rm co}$, and that this is inconsistent with their picture of weak magnetic perturbation of the disc in this outer region. The stellar magnetic torque expression derived in Ghosh and Lamb (1979b) is also affected by this error. Nevertheless, the key features of the Ghosh and Lamb picture of a penetrated stellar magnetic field being perturbed by differential rotation between the disc and the magnetosphere, with disruption inside the corotation radius and angular momentum exchange via magnetic stresses, remain a valid possibility for the case of a disc with sufficiently high magnetic diffusivity.

In order to investigate the cause of magnetic disruption, Campbell (1992) considered whether an inner region of the disc could exist in which the magnetic torque dominated the viscous torque. With a dominant magnetic torque, and a turbulent magnetic Prandtl number of $\nu/\eta \sim 1$, the stellar gravity term makes a small contribution to the vertical equilibrium so the vertical gradients of P and $B_\phi^2/2\mu_0$ balance. If the disc magnetic diffusivity is taken as an unspecified function $\eta(\varpi)$, then a solution can be found for the radial structure of the inner magnetically dominated region. The central density $\rho_{\rm c}$ decreases inwards and, for a moderate dependence of η on ϖ, the inflow speed rapidly increases inwards compared to the unperturbed viscously driven form of v_ϖ.

Since η is expected to depend on disc quantities such as $\rho_{\rm c}$ and h, a buoyancy related magnetic diffusivity of the form (9.27) was then used in the ϕ-component of the induction equation. Because the vertical equilibrium yields $P_{\rm c} = B_{\phi{\rm s}}^2/2\mu_0$, this form of η has the same dependence on disc quantities as the turbulent form given by (9.26). Matching of the resulting solution for $B_{\phi{\rm s}}$ to that obtained from the magnetically dominated angular momentum equation gives a solution for $\rho_{\rm c}$ which decreases rapidly with decreasing ϖ. The vertical equilibrium and the gas equation of state then yield $P_{\rm c}$ and $T_{\rm c}$. The central temperature was found to increase rapidly inwards.

Thermal equilibrium, with magnetic dissipation and radiative transfer with a Kramers opacity, must then be satisfied with these forms for $P_{\rm c}$, $\rho_{\rm c}$ and $T_{\rm c}$. This leads to a disc height $h(\varpi)$ which diverges inwards and strongly violates the thin disc condition. Electron scattering opacity rapidly exceeds the Kramers contribution with decreasing ϖ. Employing a dominant $\kappa_{\rm es}$ still leads to a strong divergence of $h(\varpi)$ and the radiation pressure exceeds the gas pressure. The slow increase of $B_{\phi{\rm s}}^2/2\mu_0$ with decreasing ϖ cannot balance the rapid increase of $P_{\rm R}$ and vertical equilibrium is impossible.

This analysis indicated that the disc will become rapidly thermally disrupted inside $\varpi_{\rm co}$ where the magnetic torque starts to exceed the viscous torque. The vertical expansion would enable material to surmount the potential barrier imposed by the vertical component of the stellar gravity, and pass through a sonic point before being accelerated through the curtain flow and accreted.

The disc disruption mechanism was investigated further by Campbell and Heptinstall (1998a). The vertically integrated disc equations were considered, using a turbulent form for η, allowing for magnetic and viscous terms, electron scattering opacity and radiation pressure. The equations were numerically integrated inwards from a starting point $\varpi_{\rm D}$, satisfying $\varpi_{\rm D} \gg \varpi_{\rm co}$, where the disc has its

unperturbed standard viscous structure. Magnetic effects become significant as $\varpi_{\rm co}$ is approached.

Inside $\varpi_{\rm co}$ the magnetic torque grows and the dynamical viscosity $\nu\Sigma$ increases to give a viscous torque which allows steady angular momentum balance, with the sign of $d(\nu\Sigma)/d\varpi$ changing from that of its unperturbed form. Dissipation heats the disc and, as the radiation pressure starts to exceed the gas pressure, $h(\varpi)$ rapidly increases with decreasing ϖ. The magnetic torque approaches the viscous torque as the disc expands. It was shown that the increase in $\nu\Sigma$, due to the increase in the magnetic torque, results in the disc becoming viscously unstable to short wavelength perturbations.

Similar results were obtained by Campbell and Heptinstall (1998b), in which a buoyancy form was used for η. Brandenburg and Campbell (1998) considered a dynamical form for η, with $v_{\rm K}$ as the mean transport speed. This results in more moderate values of the winding ratio $|B_{\phi{\rm s}}/B_{z{\rm s}}|$ and of $\nu\Sigma$ inside $\varpi_{\rm co}$. Again, rapid vertical disruption occurs accompanied by viscous instability. Campbell (1998) derived an analytic solution for the inner part of the disc, including an expression for the disruption radius, using a dynamical form for η.

These investigations indicated that disc disruption is due to magnetic modification of the thermal balance in the disc. Without imposed inner boundary conditions $\nu\Sigma$ can grow inside $\varpi_{\rm co}$, leading to expansion and viscous instability. However, $\nu\Sigma$ must subsequently decrease inwards so the magnetic stresses can dominate the viscous stresses and a curtain flow can form.

Matthews et al. (2005) found a solution for the radial structure of the disc for various mononomial power law opacities, but not including radiation pressure, magnetic pressure or magnetic heating. A dynamical form was adopted for η. They determined the inner radius of the disc by imposing the boundary conditions

$$(\nu\Sigma)_{\varpi_{\rm m}} = 0, \tag{9.81a}$$

$$\left[\frac{d}{d\varpi}(\nu\Sigma)\right]_{\varpi_{\rm m}} = 0, \tag{9.81b}$$

on the integral for the total angular momentum flux. These conditions correspond to the viscous torque per unit radial length vanishing, so the magnetic torque accounts for all the local angular momentum transport at the inner edge of the disc. The disc remains thin as this inner radius is approached, so a disruption mechanism does not arise. However, the conditions (9.81a) and (9.81b) enable an expression to be derived for $\varpi_{\rm m}$ as a function of the stellar rotation rate.

Campbell (2010) found a solution for the radial structure of the disc which includes the effects of electron scattering opacity, magnetic heating, magnetic pressure and radiation pressure. A modified form of the inner boundary condition (9.81a) was used, allowing for a small but finite value of $\nu\Sigma$ at the inner edge of the disc. The disc expands due to magnetic heating and this allows material to make the transition from a disc flow to a magnetically channelled accretion curtain flow. In Campbell (2014) it was shown that matching the flows determines the width of the

radial transition region and the position of the slow magnetosonic point. The details of this are given in Sect. 9.8.

All the above studies assumed that the stellar poloidal magnetic field threading the disc remains closed. Lovelace et al. (1995) noted that for η values characteristic of turbulence, typically given by (9.26) with $\epsilon_{\rm T} \lesssim 0.1$, the winding ratio $|B_{\phi {\rm s}}/B_{z{\rm s}}|$ can become large if no other process limits its growth. They suggested that poloidal field lines will inflate and at a critical value of the winding ratio they will become open. This is most likely to occur in the outer regions of the disc, and wind outflows may result if the slow magnetosonic surface is not too far above the disc surface. It was also suggested that field lines originating near the stellar magnetic poles may also open. However, no disruption of the inner disc was considered. A similar disc and stellar wind model was proposed by Paatz and Camenzind (1996). Poloidal field line inflation was confirmed by the work of Bardou and Heyvaerts (1996), and with larger winding ratios by Agapitou and Papaloizou (2000), as previously described.

9.6.2 Numerical Simulations

Time-dependent numerical simulations of the star-disc interaction have allowed the possibility of wind flows to be investigated. They show that this is particularly related to the values of η in the disc. These simulations have been performed using T Tauri parameters, rather than for those of the magnetic white dwarfs and neutron stars occurring in binary systems. Nevertheless, the results should have relevance to the binary star cases.

Goodson et al. (1997) solved the time-dependent resistive MHD equations for the case of a rotationally aligned stellar dipolar magnetic field. The disc magnetic diffusivity was taken as a constant, with a value significantly smaller than those characteristic of turbulence. An initial structure was assumed for the magnetosphere, with a density $\rho(r) \propto 1/r^4$ and values giving an Alfvén speed of typically a few times free-fall values. An α disc model was used and an initial value was assumed for the disruption radius $\varpi_{\rm m}$. The B_ϕ field grows, due to vertical shearing and the growing magnetic pressure of $B_\phi^2/2\mu_0$ causes $\mathbf{B}_{\rm p}$ to become inflated. Magnetospheric material moves with the inflating field lines and hence an outflow results, separated from the ambient medium by a fast MHD shock. A strong vertical flow develops near the rotation axis, with the density increasing in this region and near the disc surfaces. Stellar field lines originating nearer the equator remain closed, while those nearer the poles open. Hence, as suggested by Lovelace et al. (1995) and by Paatz and Camenzind (1996), a configuration results with regions of open stellar and disc field lines separated nearer the star by closed lines connecting it to the inner part of the disc.

The inner part of the disc spirals in towards the star. Reconnection then results in the inner field lines reverting to a nearly dipolar configuration, and the disc unloads material on to the star via a curtain flow. Reconnection near the disc surface mixes plasma from the disc with the magnetosphere. A second phase of expansion

then occurs. A central highly collimated and hot jet, driven by material converging towards the axis, is established. A weakly collimated, but magnetically channelled and centrifugally launched, disc wind develops in the open field region of the disc. The central jet narrows and the wind region expands with time. The jet and wind regions are separated by denser regions of gas (plasmoids), formed during the rapid inflation process, which flow outwards. There is episodic behaviour, with multiple expansion phases. Each phase drives plasma into the jet and wind, with the jet becoming fed by disc material. The inner edge of the disc oscillates with these phases.

Goodson and Winglee (1999) proposed three types of disc-magnetosphere configurations, based on their numerical simulation results. It was suggested that for sufficiently large η, corresponding to the diffusion velocity exceeding the Keplerian velocity, a steady, closed field configuration with no outflow results. Figure 8.1 shows this configuration, which is often adopted and corresponds to the original configuration of the Ghosh and Lamb (1979a) model. For intermediate values of η the diffusion velocity is less than $v_{\rm K}$ but exceeds the inflow speed. This results in larger values of $|B_{\phi {\rm s}}/B_{z{\rm s}}|$ and a current sheet separates the stellar and disc regions of open field lines. This configuration is subject to tearing mode instabilities, leading to reconnection and some time-dependent behaviour. Figure 9.1 is a schematic representation of this case. Finally, for a diffusion speed less than the inflow speed, the periodic behaviour found in the simulations of Goodson et al. (1997) results. The stellar and disc outflows remove angular momentum from the system. The inner edge of the disc oscillates between maximum and minimum values, with accretion occurring on to the star via a curtain flow when reconnection occurs as $\varpi_{\rm m}$ reaches its minimum value. Figure 9.2 represents this case, with a typical configuration shown at some time in the cycle. The closed field lines tend to be inflated from

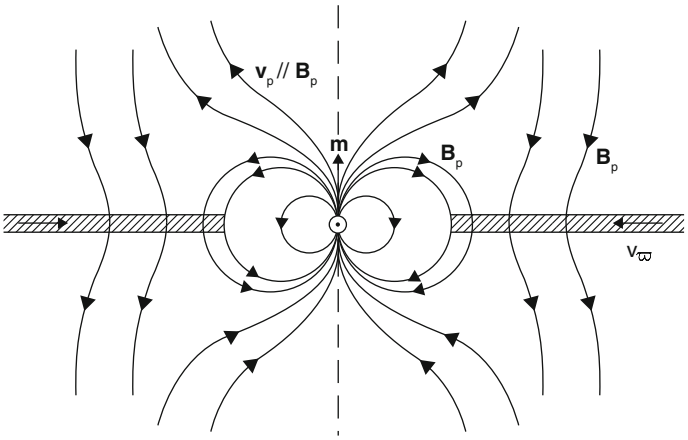

Fig. 9.1 Structure of the magnetospheric magnetic field for intermediate values of η. Wind flows occur along the open stellar poloidal field lines (not to scale)

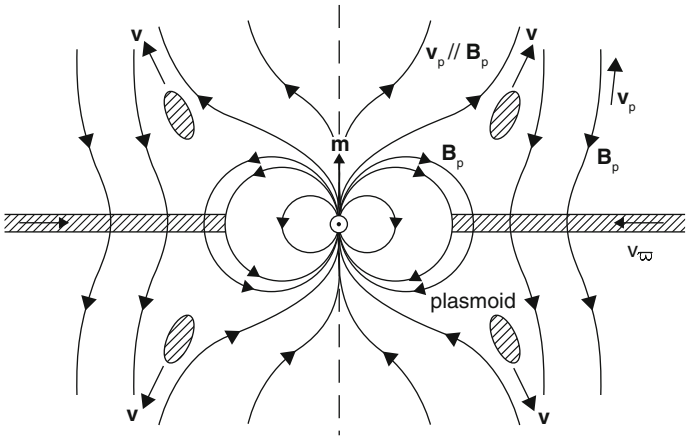

Fig. 9.2 Structure of the magnetospheric magnetic field for lower values of η. Stellar and disc wind flows occur along open poloidal field lines, and plasma ejections occur in the regions connecting oppositely directed open field lines (not to scale)

a dipole state, but return to the nearly dipolar form when $\varpi_{\rm m}$ reaches its minimum value.

Romanova et al. (2002) performed numerical simulations of the aligned dipole case. The time-dependent equations were solved, using an adiabatic equation to replace the thermal problem, and a standard parametrized form was used for the disc viscosity. Only numerical magnetic diffusivity was included. A large spherical region was adopted, to minimize the effects of external boundaries, but only the inner parts of this are relevant. The radial derivatives of P, ρ, T, $(\mathbf{v} - \mathbf{\Omega}_* \times \mathbf{r})$ and rB_ϕ were taken to vanish at the stellar surface. A low temperature disc was embedded in a high temperature corona, with an inner edge initially located where $P + \rho v_\phi^2 = B^2/2\mu_0$. To avoid rapid collapse of the disc, the corona was initially taken to rotate with the same angular velocity distribution as the disc, and with an angular velocity of Ω_* inside the inner radius. The condition $B_\phi(\mathbf{r}, 0) = 0$ was employed and $\mathbf{B}_{\rm p}(\mathbf{r}, 0)$ was taken as dipolar. The initial magnetospheric pressure was taken to have a baratropic distribution $P(\rho)$. Spherical polar coordinates were used.

Two sets of simulations were run; the first taking the initial inner disc radius $r_{\rm m}$ to lie inside $r_{\rm co}$, and the second set with $r_{\rm m} = r_{\rm co}$. In the first cases B_ϕ increases and $\mathbf{B}_{\rm p}$ inflates, with field lines in the outer parts of the disc becoming open. The inner field lines remained closed, and the magnetically affected part of the disc is thinner than the outer disc. Magnetic braking occurs inside $r_{\rm co}$, but the disc inflow speed becomes reduced when $B^2/2\mu_0 \simeq \rho v_\phi^2$ and vertical funnel flow occurs.

In the second case, the simulations were run for more than 80 rotation periods of the inner edge of the disc. The disc edge moved inwards, due to viscous transport of angular momentum, and when $B^2/2\mu_0 \simeq \rho v_\phi^2$ funnel flow developed, typically after 10 rotations. The disc angular velocity became sub-Keplerian inside $r_{\rm co}$.

The lines of $\mathbf{B}_\mathrm{p}$ were dragged in due to the low values of η adopted. Periodic opening and reconnection of field lines was observed, with an accompanying oscillation in r_m. Field loops were stretched and then released by reconnection allowing accretion to occur via funnel flow on to the star. This behaviour is similar to that found by Goodson et al. (1997), when lower values of η were used.

A high magnetospheric density was taken, with a slower fall off with increasing r than in the simulations of Goodson et al. (1997). Consequently, the magnetosphere never completely corotates with the star, and there is differential rotation near the stellar surface. Vertical thermal pressure gradients accelerate material into the funnel/curtain flow.

Zanni and Ferreira (2009) investigated the time-dependence of the aligned dipole case. They calculated the initial disc structure using a standard parametrization for the viscosity. A self-similar disc solution was found, using a polytropic equation, with a constant aspect ratio of $h/\varpi = 0.1$. A cooling term was included in the energy equation, which balanced the heating due to the viscous and magnetic dissipations. The initial magnetospheric structure was polytropic and spherically symmetric. The specific entropy of the disc was taken to exceed that of the magnetosphere, and the initial magnetospheric density was a factor 10^{-2} of the disc central density.

The $\mathbf{B}_\mathrm{p}$ field was assumed to be frozen to the star, so $\mathbf{B} \times (\mathbf{v} - \mathbf{\Omega}_* \times \mathbf{r}) = \mathbf{0}$, and the initial dipolar structure of $\mathbf{B}_\mathrm{p}$ was assumed to be maintained at the stellar surface. The value of the magnetic torque, consistent with corotation at $r = R_*$, was determined from the angular momentum equation which gives a value for $\partial B_\phi / \partial r$. The lines of $\mathbf{B}_\mathrm{p}$ linked to the disc were initially set into corotation with the $\Omega_\mathrm{K}(\varpi)$ distribution. The value of $\Omega(R_*, \theta)$ was taken to match this, but was reduced to Ω_* after two stellar rotation periods. Field lines which cross the central plane inside the disruption radius were taken to have $\Omega = \Omega_*$. An extended magnetosphere was used with $R_* < r < 30R_*$, with conditions set at the outer boundary so that no artificial torques were exerted on the star. The inner edge of the disc was set where $P = B^2/2\mu_0$. The viscosity and magnetic diffusivity parameters taken were equivalent to $\epsilon_\mathrm{v} = \nu/c_\mathrm{s}h = 1.0$ and $\epsilon_\mathrm{T} = \eta/c_\mathrm{s}h = 1.5$. These relatively large values were chosen so a quasi-steady state could be reached.

The winding ratio $|B_{\phi\mathrm{s}}/B_{z\mathrm{s}}|$ grows and reaches a maximum. Some field line inflation occurs, with lines nearer the magnetic poles opening and a stellar wind flow develops. The outer field lines threading the disc become open, but there is an extensive inner region of closed lines. Curtain flow occurs near the truncation radius, where Ω tends to Ω_*. There are similar time dependences in the accretion rate and stellar wind flow, with the wind being initiated by pressure gradients. The system reaches a steady state after about 15 stellar rotations. This case corresponds to the magnetospheric configuration shown in Fig. 9.1.

Zanni and Ferreira (2013) performed further numerical simulations using a smaller value of η, corresponding to $\epsilon_\mathrm{T} = 0.1$, and a range of viscosity parameters $\epsilon_\mathrm{v} = 0.07, 0.20, 0.67$. As before, open field lines occur near the magnetic poles, and well beyond ϖ_co in the disc. The disc truncates in an inner region of closed field lines and a curtain flow forms. However, the outer region of the disc now develops a wind

flow channelled along the open field lines. Also, episodic ejections of plasma occur in the region between the open field lines, with this material being supplied mainly by the disc, and being related to reconnection events. The enthalpy flux needed to supply the initial stellar wind is a small fraction of the accretion power. Centrifugal force subsequently drives the wind. A cyclic time dependence is observed, with a typical recurrence time of two stellar rotation periods. This is a similar evolution to that found by Goodson et al. (1997), for smaller values of η. This behaviour is represented by the magnetospheric configuration shown in Fig. 9.2.

9.7 The Disc Disruption Mechanism

9.7.1 The Magnetic Field

A model which explains disc disruption, and fits to a curtain flow region, was developed in Campbell (2010). A dynamical diffusivity is taken for the disc as

$$\eta = \epsilon_{\rm m} v_{\rm K}(\varpi_{\rm m}) \left(\frac{\varpi}{\varpi_{\rm m}}\right)^n h, \tag{9.82}$$

with the dimensionless parameter $\epsilon_{\rm m} \sim 1$, n is a constant and $\varpi_{\rm m}$ is the outer radius of the disruption region. Taking $n > 0$ ensures that the surface ratio $|B_{\phi{\rm s}}/B_{z{\rm s}}|$ remains moderate. Poloidal field line inflation is then small, especially for $\varpi < \varpi_{\rm co}$, and the components of $\mathbf{B}_{\rm p}$ are given by (9.74a) and (9.74b). Equation (9.80) gives the surface toroidal magnetic field as

$$B_{\phi{\rm s}} = \frac{\varpi B_z}{\eta} \gamma(\Omega_* - \Omega_{\rm K}) h, \tag{9.83}$$

where the dimensionless parameter $\gamma < 1$ has been introduced to allow for a vertical shear which is not entirely concentrated near the disc surface. The corotation radius is related to the stellar rotation period by

$$\varpi_{\rm co} = \left(\frac{GMP^2}{4\pi^2}\right)^{\frac{1}{3}}, \tag{9.84}$$

and a rotation fastness parameter ξ is defined by

$$\xi = \frac{\varpi_{\rm m}}{\varpi_{\rm co}} = \left(\frac{\Omega_*}{\Omega_{\rm Km}}\right)^{\frac{2}{3}}, \tag{9.85}$$

with $\Omega_{\rm Km} = \Omega_{\rm K}(\varpi_{\rm m})$. Since disruption occurs inside $\varpi_{\rm co}$, it follows that $\xi < 1$.

9.7.2 Angular Momentum Transport

The disc angular momentum equation is given by (9.56). Assuming that there is no significant mass loss from the surfaces for $\varpi > \varpi_{\rm m}$, vertical integration yields the angular momentum transport equation

$$\frac{d}{d\varpi}(\dot{M}\varpi^2\Omega + 2\pi\varpi^3\Omega'\nu\Sigma) + \frac{4\pi}{\mu_0}\varpi^2 B_{\phi{\rm s}}B_{z{\rm s}} = 0, \tag{9.86}$$

with the mass inflow rate given by

$$\dot{M} = -4\pi\int_0^h \varpi\rho v_\varpi dz \tag{9.87}$$

and

$$\Sigma = 2\int_0^h \rho dz. \tag{9.88}$$

The standard parametrization is employed for ν, so

$$\nu = \epsilon_{\rm v} c_{\rm s} h, \tag{9.89}$$

with $\epsilon_{\rm v} < 1$ and the isothermal sound speed

$$c_{\rm s} = \left(\frac{\mathcal{R}}{\mu}T_{\rm c}\right)^{\frac{1}{2}}. \tag{9.90}$$

The viscous torque per unit radial length is

$$T_{\rm v} = \frac{d}{d\varpi}\left(2\pi\varpi^3\Omega'\nu\Sigma\right), \tag{9.91}$$

contributing an outward radial transport of angular momentum through the disc. Using (9.55), (9.74b) and (9.82) for $\Omega_{\rm K}$, B_z and η, the magnetic torque per unit radial length becomes

$$T_{\rm m} = \frac{4\pi}{\mu_0}\varpi^2 B_{\phi{\rm s}}B_{z{\rm s}} = \frac{\pi}{\mu_0}\frac{\gamma}{\epsilon_{\rm m}}B_0^2 R^6 \frac{\varpi_{\rm m}^{n+\frac{1}{2}}}{\varpi^{n+\frac{9}{2}}}\left[\left(\frac{\varpi}{\varpi_{\rm co}}\right)^{3/2} - 1\right]. \tag{9.92}$$

For $\varpi < \varpi_{\rm co}$, this torque acts to remove angular momentum from the disc and transfer it to the star. For $\varpi > \varpi_{\rm co}$, angular momentum is transferred from the star to the disc. Well beyond $\varpi_{\rm co}$ magnetic perturbation of the disc becomes small and it has its unperturbed structure.

The angular momentum equation (9.86) can be integrated to obtain $\nu\Sigma$, subject to an inner boundary condition. It is anticipated that inside $\varpi_{\rm m}$ the disc flow will be diverted vertically into a magnetically channelled curtain flow, over a narrow radial region. As this region is entered the magnetic torque rapidly exceeds the viscous torque so an appropriate boundary condition on $\nu\Sigma$ is

$$(\nu\Sigma)_{\varpi_{\rm m}} = q\frac{\dot{M}}{3\pi}, \tag{9.93}$$

with the dimensionless factor $q \ll 1$. This small but finite value of q will allow for a finite density at $\varpi_{\rm m}$, consistent with mass loading on to the field lines just inside $\varpi_{\rm m}$. The factor q can be determined as a function of the stellar rotation parameter ξ, by consideration of the angular momentum balance across the boundary layer connecting the disc to the accretion curtain (see Sect. 9.8.5).

Integrating the disc angular momentum equation (9.86), using (9.92) for the magnetic torque and applying condition (9.93), yields

$$\nu\Sigma = \frac{\dot{M}}{3\pi} f(x), \tag{9.94}$$

with $x = \varpi/\varpi_{\rm m}$,

$$\begin{aligned} f(x) =& 1 - (1-q)x^{-\frac{1}{2}} \\ &+ Q\left[x^{-(n+4)} - \frac{(2n+7)}{2(n+2)}\xi^{3/2}x^{-(n+\frac{5}{2})} + \left\{\frac{(2n+7)}{2(n+2)}\xi^{\frac{3}{2}} - 1\right\}x^{-\frac{1}{2}}\right], \end{aligned} \tag{9.95}$$

where

$$Q = \frac{2}{(2n+7)}\frac{\gamma}{\epsilon_{\rm m}}\left(\frac{\varpi_{\rm A}}{\varpi_{\rm m}}\right)^{\frac{7}{2}} \tag{9.96}$$

and

$$\varpi_{\rm A} = \left[\frac{\pi B_0^2 R^6}{\mu_0 (GM)^{\frac{1}{2}}\dot{M}}\right]^{\frac{2}{7}}. \tag{9.97}$$

The radius $\varpi_{\rm A}$, which arises naturally from the angular momentum transport equation, is equivalent to an Alfvén radius. Its full significance will become apparent later.

9.7.3 Vertical Equilibrium and the Thermal Problem

The vertical equilibrium condition is given by (9.57). Integrating this from $z = 0$ to $z = h$, using (9.64) for P together with $P(\varpi, h) \ll P(\varpi, 0)$ and $B_{\phi s}(\varpi, 0) = 0$, yields

$$\Omega_{\rm K}^2 \int_0^h z\rho dz + \frac{B_{\phi s}^2}{2\mu_0} = \frac{\mathcal{R}}{\mu}\rho_{\rm c} T_{\rm c} + \frac{4\sigma_{\rm B}}{3c} T_{\rm c}^4, \tag{9.98}$$

where the subscript 'c' denotes central plane values.

Expressing the density as

$$\rho(\varpi, z) = \rho_{\rm c}(\varpi) f_\rho(\zeta), \tag{9.99}$$

where $\zeta = z/h$, it follows that

$$\Sigma = 2\int_0^h \rho dz = 2I_1 \rho_{\rm c} h \tag{9.100a}$$

with

$$I_1 = \int_0^1 f_\rho(\zeta) d\zeta \tag{9.100b}$$

and

$$\int_0^h z\rho dz = I_2 \rho_{\rm c} h^2 \tag{9.101a}$$

with

$$I_2 = \int_0^1 \zeta f_\rho(\zeta) d\zeta. \tag{9.101b}$$

Using (9.89) for ν, together with (9.100a) for Σ, gives

$$\nu\Sigma = 2I_1 \epsilon_{\rm v} c_{\rm s} \rho_{\rm c} h^2. \tag{9.102}$$

Employing this and the integral (9.101a) in the vertical equilibrium (9.98) yields the disc height as

$$h = \left[I_2 \frac{\mu}{\mathcal{R}} \frac{\Omega_{\rm K}^2}{T_{\rm c}} + I_1 \frac{\epsilon_{\rm v}}{\mu_0} \left(\frac{\mu}{\mathcal{R}}\right)^{1/2} \frac{B_{\phi s}^2}{\nu\Sigma} \frac{1}{T_{\rm c}^{\frac{1}{2}}} - \frac{8\sigma_{\rm B}}{3c} \left(\frac{\mu}{\mathcal{R}}\right)^{\frac{1}{2}} \frac{\epsilon_{\rm v} I_1}{\nu\Sigma} T_{\rm c}^{\frac{7}{2}} \right]^{-\frac{1}{2}}. \tag{9.103}$$

The last two terms in the square bracket give the effects due to magnetic force and radiation pressure. Since $B_{\phi s}$ is a known function of ϖ via (9.82) and (9.83), while $\nu\Sigma$ is given by (9.94) and (9.95), the expression (9.103) yields h as a function of ϖ and T_c.

Another expression relating T_c to h and ϖ and can be found from the thermal equations. Vertical integration of the thermal equilibrium equation (9.61) gives

$$F_s = \frac{1}{2}(\varpi\Omega_K')^2\nu\Sigma + \int_0^h \frac{\eta}{\mu_0}\left(\frac{\partial B_\phi}{\partial z}\right)^2 dz, \tag{9.104}$$

relating the surface heat flux $F_s = F_R(\varpi, h)$ to the sum of the viscous and magnetic dissipation rates per unit area. Using (9.55) for Ω_K and (9.80) for B_ϕ then yields

$$F_s = \frac{9}{8}\Omega_K^2\nu\Sigma + \frac{\eta}{\mu_0}\frac{B_{\phi s}^2}{h}. \tag{9.105}$$

Vertical integration of the radiative diffusion equation (9.62), employing the vertical average $\langle\kappa\rho F\rangle_z \simeq \kappa_c\rho_c F_s$, leads to

$$\frac{4}{3}\sigma_B T_c^4 = \frac{1}{2I_1}\kappa_c\Sigma F_s, \tag{9.106}$$

with the opacity taken as the sum of a Kramers form and that due to electron scattering, so

$$\kappa_c = K\rho_c T_c^{-\frac{7}{2}} + \kappa_{es}, \tag{9.107}$$

with κ_{es} given by (9.53). Using (9.105) to eliminate F_s in (9.106), together with (9.82) for η and (9.83) for $B_{\phi s}$, gives

$$\frac{8}{3}\sigma_B I_1 T_c^4 = \kappa_c\Sigma\left[\frac{9}{8}\Omega_K^2\nu\Sigma + \frac{\gamma^2}{\epsilon_m}v_{Km}\frac{B_z^2}{\mu_0}\left(\frac{\varpi_m}{\varpi}\right)^{n+1}\left\{1-\left(\frac{\varpi}{\varpi_{co}}\right)^{\frac{3}{2}}\right\}^2\right], \tag{9.108}$$

where $\kappa_c\Sigma$ can be expressed as

$$\kappa_c\Sigma = \frac{1}{2I_1}\frac{K}{\epsilon_v^2}\frac{\mu}{\mathcal{R}}\frac{(\nu\Sigma)^2}{h^3T_c^{\frac{9}{2}}} + \frac{\kappa_{es}}{\epsilon_v}\left(\frac{\mu}{\mathcal{R}}\right)^{\frac{1}{2}}\frac{\nu\Sigma}{hT_c^{\frac{1}{2}}}. \tag{9.109}$$

The disc height equation (9.103) can be used with (9.108) and (9.109) to solve for $T_c(\varpi)$.

9.7.4 Solution of the Equations and Disc Structure

Before solving the equations, it is convenient to express them in a dimensionless form. Dimensionless variables can be defined as

$$x = \frac{\varpi}{\varpi_{\rm m}}, \tag{9.110a}$$

$$\bar{T}_{\rm c} = \frac{T_{\rm c}}{T_0}, \tag{9.110b}$$

$$\bar{h} = \frac{h}{h_0}, \tag{9.110c}$$

where

$$T_0 = \left(\frac{K}{64\sqrt{2}\pi^3\sigma_{\rm B}}\right)^{\frac{1}{10}} \left(\frac{\mu G}{\mathcal{R}}\right)^{\frac{1}{4}} \frac{M^{\frac{1}{4}}\dot{M}^{\frac{3}{10}}}{\epsilon_{\rm v}^{\frac{1}{10}}\varpi_{\rm m}^{\frac{3}{4}}}, \tag{9.111}$$

and

$$h_0 = \left(\frac{\mathcal{R}}{\mu}\frac{\varpi_{\rm m}^3 T_0}{I_2 G M}\right)^{\frac{1}{2}} \tag{9.112}$$

are the values that $T_{\rm c}$ and h would have in the absence of the stellar magnetic field at the radius $\varpi = \varpi_{\rm m}$. Equations (9.108) and (9.103) then give

$$\bar{T}_{\rm c}^4 - \kappa_{\rm c}\Sigma\left[c_1\frac{f}{x^3} + \frac{c_2}{x^{n+7}}\left(1-\xi^{\frac{3}{2}}x^{\frac{3}{2}}\right)^2\right] = 0, \tag{9.113}$$

with

$$\kappa_{\rm c}\Sigma = c_3\frac{f^2}{\bar{h}^3\bar{T}_{\rm c}^{\frac{9}{2}}} + c_4\frac{f}{\bar{h}\bar{T}_{\rm c}^{\frac{1}{2}}}, \tag{9.114}$$

and

$$\bar{h} = \left[\frac{1}{x^3\bar{T}_{\rm c}} + c_5\frac{\left(1-\xi^{\frac{3}{2}}x^{\frac{3}{2}}\right)^2}{x^{2n+7}f\bar{T}_{\rm c}^{\frac{1}{2}}} - \frac{c_6}{f}\bar{T}_{\rm c}^{\frac{7}{2}}\right]^{-\frac{1}{2}}, \tag{9.115}$$

where $f(x)$ is given by (9.95) and the coefficients c_i are dimensionless constants depending on the system parameters.

Equations (9.113)–(9.115) can be combined to give an implicit equation connecting x and $\bar{T}_c$, which can be solved numerically for a suitable range of system parameters. The numerical results show that, for the cases of interest, the last two terms in the square bracket in (9.115) make a modest contribution relative to the first term in determining $\bar{h}$. The last two terms, which are related to magnetic compression and expansion due to radiation pressure, respectively, can then be ignored to a first approximation to give

$$\bar{h} \simeq x^{\frac{3}{2}} \bar{T}_c^{\frac{1}{2}}. \tag{9.116}$$

Using this to eliminate $\bar{h}$ in (9.114) and substituting the resulting expression for $\kappa_c \Sigma$ in (9.113) leads to

$$\bar{T}_c^{10} - c_4 \frac{fF}{x^{\frac{3}{2}}} \bar{T}_c^5 - c_3 \frac{f^2 F}{x^{\frac{9}{2}}} = 0, \tag{9.117}$$

where

$$F = c_1 \frac{f}{x^3} + \frac{c_2}{x^{n+7}} \left(1 - \xi^{\frac{3}{2}} x^{\frac{3}{2}}\right)^2. \tag{9.118}$$

Equation (9.117) is a quadratic in $\bar{T}_c^5$ for which the positive root yields

$$\bar{T}_c = \left[\frac{c_4}{2} \frac{fF}{x^{\frac{3}{2}}} + \frac{1}{2} \frac{f}{x^{\frac{3}{2}}} \left(c_4^2 F^2 + 4 c_3 \frac{F}{x^{\frac{3}{2}}} \right)^{\frac{1}{2}} \right]^{\frac{1}{5}}. \tag{9.119}$$

This expression for $\bar{T}_c$ can then be used in (9.115) to obtain a more accurate expression for $\bar{h}$. The dimensionless central density follows by eliminating $\nu \Sigma$ between (9.94) and (9.102) to give

$$\bar{\rho}_c = \frac{\rho_c}{\rho_0} = \frac{f}{\bar{h}^2 \bar{T}_c^{\frac{1}{2}}}, \tag{9.120}$$

where

$$\rho_0 = \frac{1}{6\pi} \left(\frac{\mu}{\mathcal{R}} \right)^{\frac{1}{2}} \frac{\dot{M}}{\epsilon_v I_1 h_0^2 T_0^{\frac{1}{2}}}. \tag{9.121}$$

A condition, related to the power n occurring in (9.82) for η, can be derived for disc disruption to occur at $\varpi = \varpi_m$. An inwardly expanding disc requires

$$\left(\frac{d\bar{h}}{dx} \right)_{x=1} < 0. \tag{9.122}$$

The second term in the expression (9.115) for $\bar{h}$ represents the effect of the vertical gradient in magnetic pressure, and this is always small. The last term contributes to expansion of the disc due to radiation pressure and hence inward expansion will occur if the first term decreases with decreasing x, giving the condition that $x^3\bar{T}_c$ increases inwards. Noting that the viscous dissipation and Kramers opacity make small contributions to the disc structure near $x = 1$, and so the corresponding terms involving the constants c_1 and c_3 can be dropped from (9.118) for F and (9.119) for $\bar{T}_c$, the condition of $d(x^3\bar{T}_c)/dx < 0$ at $x = 1$ then yields

$$n > \frac{13}{2} - \frac{3\xi^{\frac{3}{2}}}{(1-\xi^{\frac{3}{2}})}. \tag{9.123}$$

This is satisfied, for all relevant values of ξ, for $n > -6.8$. Since $n > 0$ is consistent with moderate field winding, the disruption condition is always satisfied.

The disruption radius of the disc is given in terms of the corotation radius via (9.85) as

$$\varpi_m = \xi\varpi_{co}. \tag{9.124}$$

An expression can be found for the rotation parameter ξ by considering boundary conditions at ϖ_m. The form (9.94) gives the condition (9.93) on $\nu\Sigma$ as

$$f(1) = q. \tag{9.125}$$

Following the arguments of Matthews et al. (2005), the gradient of $\nu\Sigma$ should essentially vanish at the inner edge of the disc where the viscous torque per unit radial length becomes small, so

$$\left[\frac{d}{d\varpi}(\nu\Sigma)\right]_{\varpi=\varpi_m} = 0 \tag{9.126}$$

should apply. They also took the condition $\nu\Sigma = 0$ at $\varpi = \varpi_m$, while here $\nu\Sigma$ is small but finite at ϖ_m. Since they did not include magnetic heating, their analysis gave a truncated disc due to the inner boundary conditions used, but did not lead to a disruption mechanism. Using (9.94) for $\nu\Sigma$, the condition (9.126) becomes

$$f'(1) = 0. \tag{9.127}$$

Applying this to (9.95) for $f(x)$ leads to

$$2\frac{\gamma}{\epsilon_m}\frac{(1-\xi^{\frac{3}{2}})}{\xi^{\frac{7}{2}}}\left(\frac{\varpi_A}{\varpi_{co}}\right)^{\frac{7}{2}} = 1 - q. \tag{9.128}$$

To a good approximation, this yields the solution

$$\xi = \left[\frac{\{C^2 + 4(1-q)C\}^{\frac{1}{2}} - C}{2(1-q)} \right]^{\frac{2}{5}}, \tag{9.129}$$

where

$$C = 2\frac{\gamma}{\epsilon_{\rm m}} \left(\frac{\varpi_{\rm A}}{\varpi_{\rm co}} \right)^{\frac{7}{2}}. \tag{9.130}$$

This relates ξ to the rotation period of the star. Eliminating $\varpi_{\rm co}$ between (9.124) and (9.128) gives

$$\varpi_{\rm m} = \left(\frac{2\gamma}{\epsilon_{\rm m}} \right)^{\frac{2}{7}} \left(1 - \xi^{\frac{3}{2}} \right)^{\frac{2}{7}} \varpi_{\rm A}. \tag{9.131}$$

The Alfvén radius can be expressed in the form

$$\varpi_{\rm A} = 2.61 \times 10^6 \frac{\left(\frac{B_0}{10^8\,{\rm T}} \right)^{\frac{4}{7}} \left(\frac{R}{10^4\,{\rm m}} \right)^{\frac{12}{7}}}{\left(\frac{M}{1.4\,M_\odot} \right)^{\frac{1}{7}} \left(\frac{\dot{M}}{10^{-9}\,M_\odot\,{\rm year}^{-1}} \right)^{\frac{2}{7}}} {\rm m}. \tag{9.132}$$

To illustrate the disc solution, the example of an accreting neutron star in an X-ray binary is considered, taking $M = 1.4\,M_\odot$, $R = 10^4\,{\rm m}$, $B_0 = 2 \times 10^8\,{\rm T}$, $\dot{M} = 4 \times 10^{-9}\,{\rm M}_\odot\,{\rm year}^{-1}$ and $P = 2\,{\rm s}$. The parameters and vertical integrals are taken as $\gamma = \epsilon = 0.5$, $\epsilon_V = 0.1$, $q = 0.1$, $n = 3$, $I_1 = 0.7$ and $I_2 = 0.4$. Figure 9.3 shows that the ratio of magnetic to viscous dissipation rapidly increases inside $\varpi_{\rm co}$, while Fig. 9.4 shows there is a corresponding increase in the temperature. The magnetic dissipation, given by $\eta B_{\phi{\rm s}}^2/\mu_0 h$, rapidly increases with decreasing ϖ mainly due to the increase in $|B_z|$ which acts as the source of B_ϕ. Figure 9.5 illustrates that the disc expands due to the increased heating which leads to increases in the vertical gradients of the gas and radiation pressures which cannot be balanced by the slower increases in the vertical gravity and magnetic pressure gradient. Figure 9.6 shows there is a sharp increase in the ratio of the magnetic to viscous torque, consistent with the magnetic force becoming dominant in controlling the accretion flow as the disc ends.

Figure 9.7 illustrates that the field winding ratio $|B_{\phi{\rm s}}/B_{z{\rm s}}|$ remains moderate everywhere, with $(B_{\phi{\rm s}}/B_{z{\rm s}})^2 \ll 1$, so justifying the assumption of small poloidal field inflation. For $\varpi > \varpi_{\rm co}$ perturbation of the disc is usually small, but a special case arises which will be discussed in Chap. 10.

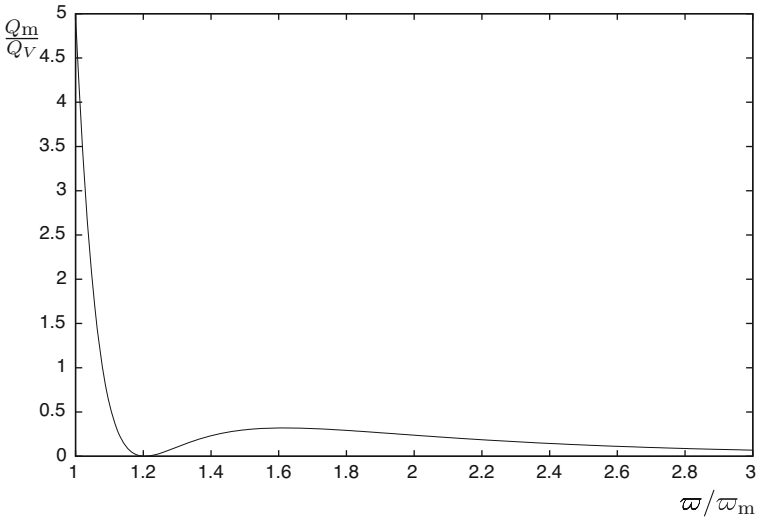

Fig. 9.3 The ratio of magnetic to viscous dissipation (from Campbell 2010)

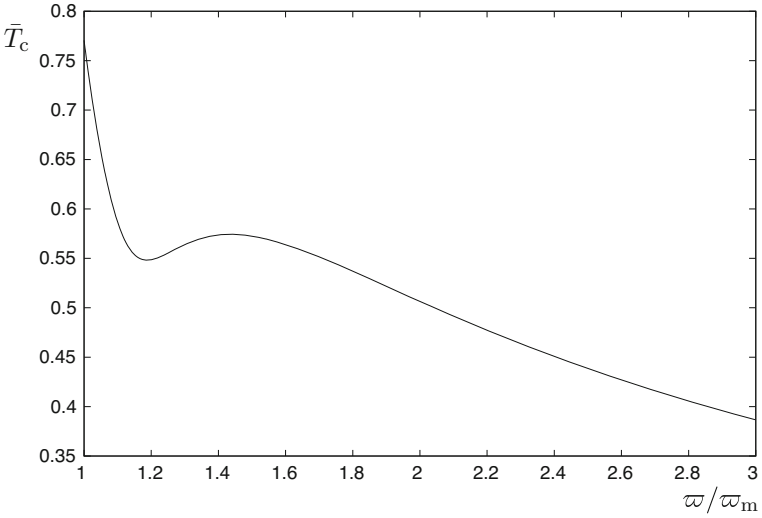

Fig. 9.4 The dimensionless central temperature (from Campbell 2010)

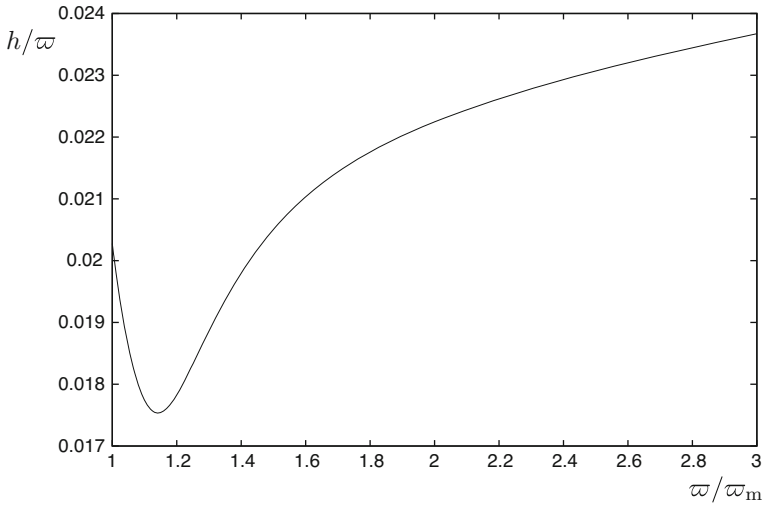

Fig. 9.5 The disc aspect ratio (from Campbell 2010)

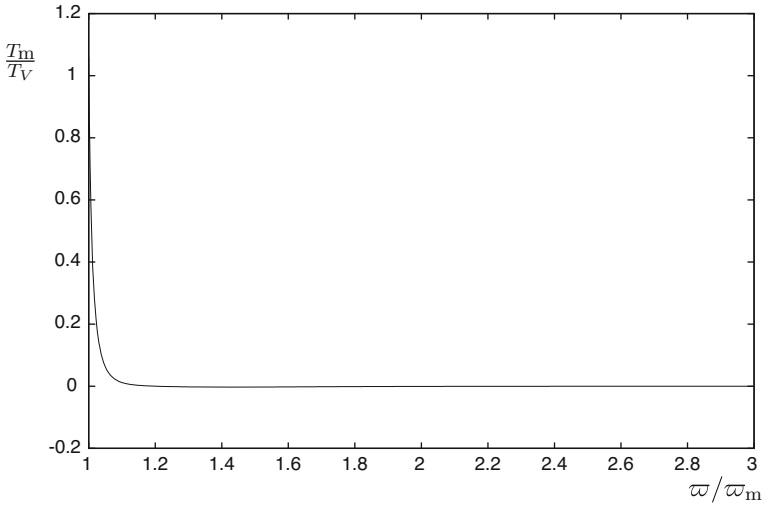

Fig. 9.6 The magnetic to viscous torque ratio (from Campbell 2010)

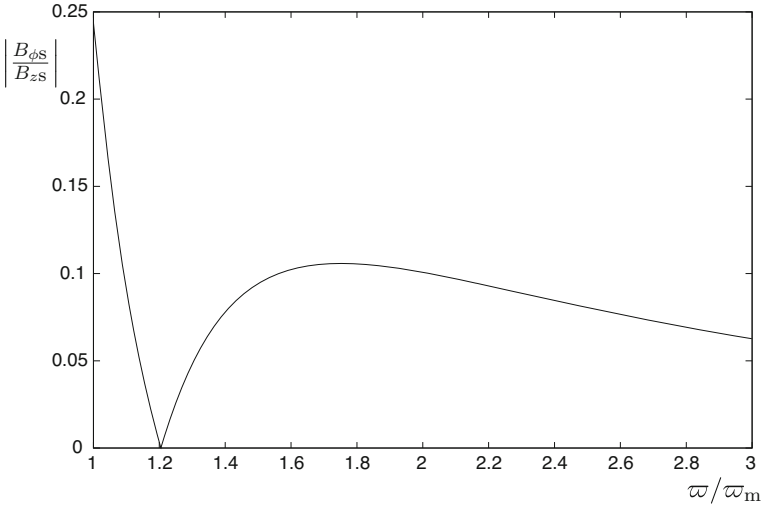

Fig. 9.7 The surface field winding ratio (from Campbell 2010)

9.8 The Accretion Curtain Flow

9.8.1 Background

Material at the inner edge of the disrupted disc still has significant angular momentum which must be lost if accretion on to the star is to occur. The accretion curtain flow allows angular momentum to be transferred to the star continuously via magnetic stresses. Thermal expansion at disruption allows matter to make the transition from the disc to the curtain flow and to pass through a sonic point. Inside this point the stellar gravitational force tangential to the constraining field lines accelerates the flow to nearly free-fall speeds. The highly supersonic flow must pass through a standing slow magnetosonic shock before settling on to the stellar surface. Strong compression and heating will occur.

A model for the structure of the curtain flow was presented by Koldoba et al. (2002). It was assumed that the curtain flow is well sub-Alfvénic everywhere, so the stellar magnetic field structure remains nearly dipolar. A polytropic equation $P = K\rho^{\gamma}$ was adopted, with $\gamma \neq 1$. The ideal MHD equations were solved and it was found that, for $\gamma < 7/5$, the Mach number $|v_p|/c_s$ increases monotonically as the cylindrical coordinate ϖ decreases. The density ρ decreases initially, reaching a minimum beyond the sonic point, and then increases monotonically. The angular velocity was sub-stellar and nearly constant throughout the curtain flow. The fastness parameter $\xi = \varpi_m/\varpi_{co}$ was found to have a minimum value $\xi_{min} = (2/3)^{1/3}$ at which the sonic point coincides with the disc surface at the curtain base. Hence ξ must lie in the range $\xi_{min} < \xi < 1$ for a trans-sonic curtain flow to occur inside ϖ_{co}.

The numerical simulations of Romanova et al. (2002) found that magnetically channelled funnel/curtain flows developed at disruption. These flows were initially driven by vertical pressure gradients, and matter passed through a sonic point. The flow reached speeds of $\simeq 70\%$ of the free-fall speed near the stellar surface. The flow speed was well sub-Alfvénic throughout the curtain region. The simulations of Zanni and Ferreira (2009) also found sub-Alfvénic curtain flows with a similar structure.

An analytic model is presented below which describes the fundamental features of the curtain flow, and allows the width of the disc transition region to be calculated and related to the position of the sonic point. A strong magnetic regime, related to the rotation period of the star, can be identified, in which matter can be transferred from the disc to the curtain flow at a steady rate.

9.8.2 The Governing Equations

The structure of the curtain flow and the resulting accretion torque were considered in Campbell (2012, 2014). Just inside $\varpi_{\rm m}$ the disc expands over a narrow radial region which acts as the base of the field controlled curtain flow. The magnetic diffusivity becomes small as the curtain flow is entered and the steady induction equation is then given by (9.1). This gives

$$\mathbf{v}_{\rm p} = \kappa \mathbf{B}_{\rm p}, \tag{9.133}$$

$$\Omega - \frac{\kappa B_\phi}{\varpi} = \Omega_*. \tag{9.134}$$

A slow magnetosonic shock front will exist just above the stellar surface, leading to $v_{\rm p}$, and hence κ, essentially vanishing as the flow ends. The poloidal field is assumed to be frozen to the stellar material, and hence the field lines rotate with angular velocity Ω_*. Conservation of mass and magnetic flux lead to the quantity

$$\epsilon = \rho\kappa = \frac{\rho v_{\rm p}}{B_{\rm p}}, \tag{9.135}$$

being conserved along poloidal field-streamlines. The steady, high magnetic Reynolds number equations describing the curtain flow are similar to those occurring in steady, axisymmetric wind theory (see Chap. 13). However, some important differences arise here since the curtain flow will be shown to be sub-Alfvénic as opposed to the trans-Alfvénic outflow of a magnetic wind. Since $\mathbf{v}_{\rm p}$ and $\mathbf{B}_{\rm p}$ are anti-parallel here for $z > 0$, κ and ϵ are negative.

The total rate of transport of angular momentum, carried jointly by the gas and magnetic stresses, is given by

$$\epsilon \varpi^2 \Omega - \frac{\varpi B_\phi}{\mu_0} = -\beta, \tag{9.136}$$

which is conserved along poloidal field-streamlines. Equations (9.134)–(9.136) give

$$\Omega = \frac{\Omega_* - \mu_0 |\epsilon| \beta / \varpi^2 \rho}{1 - \mu_0 \epsilon^2 / \rho}, \tag{9.137}$$

$$B_\phi = \frac{\mu_0 \beta / \varpi - \mu_0 |\epsilon| \Omega_* \varpi}{1 - \mu_0 \epsilon^2 / \rho}. \tag{9.138}$$

It follows from (9.135) for ϵ that

$$\frac{\mu_0 \epsilon^2}{\rho} = \frac{\rho v_{\rm p}^2}{B_{\rm p}^2 / \mu_0} = \frac{v_{\rm p}^2}{v_{\rm A}^2}, \tag{9.139}$$

where $v_{\rm A}$ is the poloidal field Alfvén speed. Hence $v_{\rm p}^2 / v_{\rm A}^2$ gives the ratio of the poloidal kinetic energy density to the poloidal magnetic energy density. This ratio will be shown to be of fundamental importance to the properties of the curtain flow.

The vertical optical depth of material sharply decreases from the disc to the curtain region, so it is reasonable to take the curtain flow as isothermal with sound speed a. Consideration of the rate of work done by the forces acting on the gas yields the energy integral

$$\frac{1}{2} v_{\rm p}^2 + \frac{1}{2} \varpi^2 \Omega^2 - \frac{GM}{(\varpi^2 + z^2)^{\frac{1}{2}}} + a^2 \ln \rho - \Omega_* \varpi^2 \Omega = E. \tag{9.140}$$

This is the sum of the kinetic energy, the gravitational energy and the work done by the pressure gradient and magnetic torque, per unit mass. The specific energy E is conserved along poloidal field streamlines on which $z = z(\varpi)$.

9.8.3 The Poloidal Flow Speed

Firstly, the poloidal flow speed of material in the accretion curtain can be investigated. Inside $\varpi_{\rm m}$ the disc inflow is vertically diverted, over a region of width δ, into the field channelled curtain flow. It enters at a subsonic speed and is accelerated by vertical pressure gradients until $v_{\rm p}$ reaches the sound speed at a point above the curtain base. The sonic point will be shown to be essentially the same as the slow magnetosonic point. Figure 9.8 shows a schematic picture of the system.

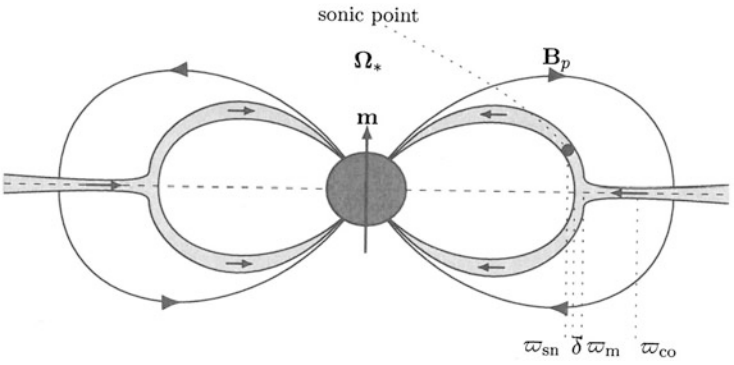

Fig. 9.8 A vertical cross-section of the curtain flow region connecting to the inner part of the disc. The corotation radius, ϖ_{co}, the outer edge of the transition region, ϖ_m, its width δ and the sonic point coordinate ϖ_{sn} are shown (from Campbell 2014)

At disruption the flow divides evenly between the upper and lower halves of the disc, so only $z > 0$ needs to be considered. Matter is fed into the upper curtain through its base at a rate

$$\frac{\dot{M}}{2} = 2\pi \varpi_m (\rho v_z)_0 \delta, \tag{9.141}$$

where the subscript zero refers to the base point (ϖ_0, h_0) at which the flow is essentially vertical. The disruption region is $\varpi_m - \delta \le \varpi \le \varpi_m$, with $\delta \sim h_0 \ll \varpi_m$.

The amount of poloidal field distortion caused by the curtain flow will depend on the ratio of the kinetic and magnetic energy densities, given by (9.139). Evaluating this ratio at the curtain base gives

$$\left(\frac{v_p^2}{v_A^2}\right)_0 = \left(\frac{\rho v_z^2}{B_z^2/\mu_0}\right)_0 = \left(\frac{\varpi_m}{\varpi_A}\right)^{\frac{7}{2}} \left(\frac{\varpi_0}{h_0}\frac{a}{v_{km}}\right) \frac{h_0}{\delta}\frac{v_{z0}}{a}, \tag{9.142}$$

where the last expression follows by using (9.74b) for B_z and eliminating $\dot{M}$ between (9.97) for ϖ_A and (9.141) in order to express $(\rho v_z)_0$ in terms of ϖ_A.

Equations (9.82) and (9.83) yield the field winding ratio at the curtain base as

$$\left(\frac{B_{\phi s}}{|B_z|}\right)_0 = \frac{\gamma}{\epsilon_m}\left(1 - \xi^{\frac{3}{2}}\right), \tag{9.143}$$

then substituting for $(1 - \xi^{3/2})$ from (9.131) for ϖ_m gives

$$\left(\frac{\varpi_m}{\varpi_A}\right)^{\frac{7}{2}} = 2\left(\frac{B_{\phi s}}{|B_{zs}|}\right)_0. \tag{9.144}$$

It follows from the previous definitions that

$$\frac{\gamma}{\epsilon_{\rm m}} < 1 \tag{9.145}$$

holds and it will be shown that a minimum value exists for ξ. This ensures that $(B_{\phi{\rm s}}/|B_{z{\rm s}}|)_0 \lesssim 0.2$ and hence (9.144) shows that

$$\frac{\varpi_{\rm m}}{\varpi_{\rm A}} < 1 \tag{9.146}$$

is satisfied. Then, since $(\varpi_0 a/h_0 v_{\rm K0})(h_0/\delta) \lesssim 1$ and $v_{z0}/a \ll 1$, (9.142) gives

$$\left(\frac{v_{\rm p}^2}{v_{\rm A}^2}\right)_0 \ll 1. \tag{9.147}$$

Hence the initial curtain flow is well sub-Alfvénic, so the poloidal magnetic field will only be slightly distorted from its current-free state and (9.6) and (9.7) can be used for the components of $\mathbf{B}_{\rm p}$.

The density decreases from the curtain base to the sonic point and hence it follows from (9.139) that the ratio $v_{\rm p}^2/v_{\rm A}^2$ increases. The conservation of $\rho v_{\rm p}/B_{\rm p}$ gives

$$\frac{v_{z0}}{a} = \frac{|B_z(\varpi_0)|}{B_{\rm p}(\varpi_{\rm sn})}\frac{\rho_{\rm sn}}{\rho_0}. \tag{9.148}$$

The equation describing poloidal field lines is

$$\frac{dz}{d\varpi} = \frac{B_z}{B_\varpi}, \tag{9.149}$$

then using (9.6) and (9.7) for B_ϖ and B_z, integration subject to $z(\varpi_0) = h_0$ gives the field line equation

$$z^2 = \varpi_0^{\frac{2}{3}}\left(1 + \frac{h_0^2}{\varpi_0^2}\right)\varpi^{\frac{4}{3}} - \varpi^2. \tag{9.150}$$

Evaluating the field strength $B_{\rm p} = (B_\varpi^2 + B_z^2)^{1/2}$ along a field line yields

$$B_{\rm p} = 2|B_{z0}|\frac{\varpi_0^2}{\varpi^2}\left[1 - \frac{3}{4}\left(\frac{\varpi}{\varpi_0}\right)^{\frac{2}{3}}\right]^{\frac{1}{2}}. \tag{9.151}$$

This shows that $B_{\rm p}$ increases monotonically as ϖ decreases from the curtain base to the stellar surface. Equation (9.139) gives the sonic point ratio

$$\left(\frac{v_{\rm p}^2}{v_{\rm A}^2}\right)_{\rm sn} = \frac{\rho_0}{\rho_{\rm sn}}\left(\frac{v_{\rm p}^2}{v_{\rm A}^2}\right)_0, \tag{9.152}$$

and then using (9.142) for $(v_{\rm p}^2/v_{\rm A}^2)_0$ together with (9.148) for v_{z0}/a yields

$$\left(\frac{v_{\rm p}^2}{v_{\rm A}^2}\right)_{\rm sn} = \left(\frac{\varpi_{\rm m}}{\varpi_{\rm A}}\right)^{\frac{7}{2}}\left(\frac{\varpi_0}{h_0}\frac{a}{v_{\rm K0}}\right)\frac{h_0}{\delta}\frac{|B_z(\varpi_0)|}{B_{\rm p}(\varpi_{\rm sn})}. \tag{9.153}$$

This is significantly less than unity and hence the curtain flow is well sub-Alfvénic between the curtain base and the sonic point, justifying using the current-free stellar field for $\mathbf{B}_{\rm p}$.

Using (9.151) to eliminate $B_{\rm p}$ in (9.135) for $\rho v_{\rm p}/B_{\rm p}$ gives $v_{\rm p}$ in terms of ϖ and ρ. Then employing this to eliminate $v_{\rm p}$, and (9.137) to eliminate Ω, in the energy integral (9.140) yields an equation implicitly relating ϖ and ρ. This can be solved numerically, for calculated values of the Lagrangian invariants ϵ and β, to obtain $\rho(\varpi)$ along poloidal field-streamlines in the accretion curtain. Initially $\rho(\varpi)$ decreases with decreasing ϖ, attains a minimum value inside the sonic point, and then increases monotonically down to the boundary layer edge just above the stellar surface. This is consistent with the density distribution found by Koldoba et al. (2002), in which a non-isothermal equation was used relating P and ρ. The poloidal flow speed is well sub-Alfvénic throughout the curtain region.

9.8.4 The Curtain Base Angular Velocity

The poloidal and toroidal equations (9.133) and (9.134) give the angular velocity in the curtain flow as

$$\Omega = \Omega_* - \frac{|v_z|}{\varpi}\frac{B_\phi}{|B_z|}. \tag{9.154}$$

At the curtain base $\Omega = \Omega_0$ with

$$\Omega_0 = \Omega(\varpi_0, h_0) = \Omega_* - \frac{v_{z0}}{\varpi_0}\left(\frac{B_{\phi \rm s}}{|B_z|}\right)_0. \tag{9.155}$$

Using (9.143) for the disc surface field winding ratio $|B_{\phi \rm s}/B_z|$ at the curtain base ensures that the fields are matched and gives

$$\Omega_0 = \Omega_*\left[1 - \frac{\gamma}{\epsilon_{\rm m}}\frac{v_{z0}}{v_{\rm Km}}\frac{\left(1-\xi^{\frac{3}{2}}\right)}{\xi^{\frac{3}{2}}}\right], \tag{9.156}$$

using $\Omega_* = \xi^{3/2}\Omega_{\rm Km}$. This shows that Ω_0 is slightly below Ω_*, It follows that matter entering the transition region must change its angular velocity from its value at $z = 0$ to the value Ω_0 at $z = h_0$. This will be shown to have consequences for the angular momentum transfer via the curtain flow. Sub-stellar values for Ω were observed in the curtain flows arising in the numerical simulations of Romanova et al. (2002) and of Zanni and Ferreira (2009).

9.8.5 *Angular Momentum Transfer*

The angular momentum transfer due to the curtain flow can now be considered. The total angular momentum flux per unit poloidal magnetic field is given by (9.136). Since this is conserved along field-streamlines, it can be evaluated at the curtain base to give

$$\beta = |\epsilon|\varpi_0^2\Omega_0 + \frac{\varpi_0}{\mu_0}B_{\phi{\rm s}}(\varpi_0). \tag{9.157}$$

Since $\epsilon = \rho v_z/B_z$, the ratio of the magnetic term to the material term at the curtain base can be expressed as

$$\begin{aligned}\frac{\varpi_0 B_{\phi{\rm s}}(\varpi_0)}{\mu_0|\epsilon|\varpi_0^2\Omega_0} &= \frac{1}{\xi^{\frac{3}{2}}}\left(\frac{v_{\rm A}^2}{v_{\rm p}^2}\frac{v_z}{v_{\rm K}}\frac{B_{\phi{\rm s}}}{|B_z|}\right)_0 = \frac{1}{\xi^{\frac{3}{2}}}\frac{\delta}{\varpi_0}\left(\frac{B_{\phi{\rm s}}}{|B_z|}\right)_0\left(\frac{\varpi_{\rm A}}{\varpi_{\rm m}}\right)^{\frac{7}{2}} \\ &= \frac{1}{2\xi^{\frac{3}{2}}}\frac{\delta}{\varpi_0} \ll 1,\end{aligned} \tag{9.158}$$

using (9.142) for $(v_{\rm p}^2/v_{\rm A}^2)_0$ and (9.144) for $\varpi_{\rm m}/\varpi_{\rm A}$. It follows that

$$\beta = |\epsilon|\varpi_0^2\Omega_0\left(1 + \frac{1}{2\xi^{\frac{3}{2}}}\frac{\delta}{\varpi_0}\right). \tag{9.159}$$

Using the mass conservation equation (9.141) to express $(\rho v_z)_0$ in terms of $\dot{M}$ gives

$$|\epsilon|\varpi_0^2\Omega_0 = \frac{\dot{M}\varpi_0^2\Omega_0}{4\pi\varpi_{\rm m}\delta|B_{z0}|}. \tag{9.160}$$

It is noted that β is positive.

It was seen that at $\varpi = \varpi_{\rm m}$ the angular velocity Ω must change from $\Omega_{\rm Km} = \Omega_{\rm K}(\varpi_{\rm m})$ at $z = 0$ to Ω_0 at the curtain base $z = h(\varpi_0)$. Since $\Omega_0 < \Omega_{\rm Km}$, the transition from $z = 0$ to $z = h_0$ involves a loss of angular momentum per unit mass of $\varpi_{\rm m}^2(\Omega_{\rm Km} - \Omega_0)$. To account for this, consider the disc angular momentum

equation

$$\frac{\partial}{\partial \varpi}(\varpi \rho v_\varpi \varpi^2 \Omega) + \frac{\partial}{\partial z}(\varpi \rho v_z \varpi^2 \Omega) = \frac{\partial}{\partial \varpi}\left(\rho \nu \varpi^3 \frac{\partial \Omega}{\partial \varpi}\right) + \frac{1}{\mu_0}\frac{\partial}{\partial z}(\varpi^2 B_\phi B_z). \tag{9.161}$$

Integrating this over $0 < z < h_0$, noting that B_ϕ and v_z vanish at $z = 0$, yields

$$\varpi_0 (\rho v_z)_0 \varpi^2 \Omega_0 - \frac{\varpi^2}{\mu_0} B_{\phi s} B_{zs} = \frac{d}{d\varpi}\left(\varpi^3 \int_0^{h_0} \rho \nu \frac{\partial \Omega}{\partial \varpi} dz - \varpi^3 \int_0^{h_0} \rho v_\varpi \Omega dz\right). \tag{9.162}$$

The transition region of the disc has a radial extent of $\varpi_m - \delta \le \varpi \le \varpi_m$. Since the flow is truncated and magnetically dominated at the inner edge, appropriate boundary conditions there are

$$\rho(\varpi_m - \delta, z) = 0 \tag{9.163a}$$

and

$$\left(\frac{\partial \Omega}{\partial \varpi}\right)_{\varpi_m - \delta} = 0. \tag{9.163b}$$

At the outer edge

$$\left(\frac{\partial \Omega}{\partial \varpi}\right)_{\varpi_m} = \Omega_\kappa'(\varpi_m) = -\frac{3}{2}\frac{\Omega_{\kappa m}}{\varpi_m}. \tag{9.164}$$

Integrating (9.162) over this region, applying these boundary conditions, gives

$$\left[\varpi_m (\rho v_z)_0 \varpi_m^2 \Omega_0 - \frac{\varpi_m^2}{\mu_0} B_{\phi s} B_{z0}\right] \delta = -\frac{3}{4}\varpi_m^2 \Omega_{\kappa m} (\nu \Sigma)_{\varpi_m} + \frac{\dot{M}}{4\pi}\varpi_m^2 \Omega_{\kappa m}, \tag{9.165}$$

where

$$\Sigma = 2\int_0^{h_0} \rho dz \tag{9.166a}$$

and

$$\dot{M} = -4\pi \int_0^{h_0} \varpi \rho v_\varpi dz. \tag{9.166b}$$

Mass is transferred at the rate $\dot{M}$ into the outer surface at $\varpi = \varpi_m$. Equation (9.93) gives the vertically integrated dynamical viscosity condition

$$(\nu \Sigma)_{\varpi_m} = q\frac{\dot{M}}{3\pi}, \tag{9.167}$$

with $q \ll 1$. Using this, together with (9.141) for $\dot{M}$ to eliminate $(\rho v_z)_0$, and the result (9.158) in (9.165) yields

$$\dot{M}\varpi_{\rm m}^2(\Omega_{\rm km} - \Omega_0) = q\dot{M}\varpi_{\rm m}^2\Omega_{\rm km}. \tag{9.168}$$

Then noting that $\Omega_0 = \Omega_*$ can be used to high accuracy, and $\Omega_* = \xi^{3/2}\Omega_{\rm km}$, (9.168) gives the angular momentum balance condition

$$q = 1 - \xi^{\frac{3}{2}}. \tag{9.169}$$

This shows that the angular momentum change as material flows from $z = 0$ to $z = h_0$ is accounted for by viscous transport, and relates the factor q to the stellar rotation parameter ξ. It will be shown that a minimum value of ξ is set by steady flow conditions and this is consistent with (9.169), giving small values of q for the valid range of ξ.

Having calculated the rate of angular momentum transfer through the curtain flow, the accretion torque can be evaluated.

9.8.6 The Accretion Torque

The accretion torque on the star can be evaluated from

$$T_{\rm a} = \int_S \beta \mathbf{B}_{\rm p} \cdot d\mathbf{S}, \tag{9.170}$$

where the area S consists of the regions where the upper and lower curtain flows meet the stellar surface as ring accretion columns, and β is the angular momentum flux per unit poloidal field. By symmetry, there will be equal contributions to the torque from the columns above and below the equatorial plane $z = 0$. The surface field ratio $B_{\theta {\rm s}}/B_{r{\rm s}}$, evaluated where the centre of the thin accretion column meets the stellar surface, is

$$\frac{B_{\theta {\rm s}}}{B_{r{\rm s}}} = \frac{1}{2}\tan\theta_{\rm a} = \frac{1}{2}\tan\left[\sin^{-1}\left(\frac{R}{\varpi_{\rm m}}\right)^{\frac{1}{2}}\right], \tag{9.171}$$

where $\theta_{\rm a}$ is the angle the unit vector $\hat{\mathbf{B}}_{\rm ps}$ makes to the vertical. For white dwarfs and neutron stars, $R/\varpi_{\rm m} \ll 1$ so $\theta_{\rm a}$ is small and $B_{r{\rm s}} \gg B_{\theta {\rm s}}$. Hence the accretion column is nearly normal to the stellar surface and $\hat{\mathbf{B}}_{\rm ps}$ is nearly parallel to $\hat{\mathbf{z}}$. The magnetic flux through the accretion column base is then

$$\psi_{\rm m} = 2\pi\varpi_*\delta_* B_{z*}, \tag{9.172}$$

where δ_* is the width of the circular band of cylindrical radius ϖ_*, forming the column base. Hence evaluation of the integral (9.170) gives

$$T_\mathrm{a} = 2\beta\psi_\mathrm{m} = 4\pi\varpi_*\delta_* B_{z*}\beta. \tag{9.173}$$

Conservation of magnetic flux through the accretion curtain gives $\varpi_*\delta_* B_{z*} = \varpi_\mathrm{m}\delta|B_{z0}|$ and so

$$T_\mathrm{a} = 4\pi\varpi_\mathrm{m}\delta|B_{z0}|\beta = \dot{M}\varpi_0^2\Omega_0, \tag{9.174}$$

using (9.159) and (9.160) for β, with the additional small term dropped since it would only generate a second order term in (9.174). Noting that (9.156) gives $\Omega_0 = \Omega_*$ to high accuracy, and using $\Omega_0 = \xi^{3/2}\Omega_{\mathrm{K}m}$, (9.174) yields

$$\mathbf{T}_\mathrm{a} = \xi^{\frac{3}{2}}\dot{M}\varpi_\mathrm{m}^2\Omega_\mathrm{K}(\varpi_\mathrm{m})\,\hat{\mathbf{z}}. \tag{9.175}$$

The reduction factor of $\xi^{3/2} < 1$ is due to the specific angular momentum $\varpi_\mathrm{m}^2(\Omega_{\mathrm{K}m} - \Omega_0)$ that is transferred back to the disc via the viscous stress as material flows from $z = 0$ to $z = h_0$ in the transition region over which Ω changes from $\Omega_\mathrm{K}(\varpi_\mathrm{m})$ to Ω_0.

9.8.7 The Slow Magnetosonic and Sonic Points

Material enters the accretion curtain with a subsonic poloidal speed. The gas is accelerated by pressure gradients along $\mathbf{B}_\mathrm{p}$ until it reaches the slow magnetosonic point. The poloidal speed is always significantly sub-Alfvénic and it will be shown that this results in the slow magnetosonic and the sonic points essentially merging. The energy integral, given by (9.140), is conserved along poloidal field-streamlines. The curtain flow will be shown to have a thin cross sectional area, so the central field line with equation $z = z(\varpi)$ can be considered. On this line (9.140) can be written as

$$H(\varpi, \rho) = E. \tag{9.176}$$

Since $dH = 0$, this gives

$$\frac{d\rho}{d\varpi} = -\frac{\partial H/\partial\varpi}{\partial H/\partial\rho}. \tag{9.177}$$

The condition $\partial H/\partial\rho = 0$ generally yields the slow and fast magnetosonic critical points for v_p. However, since $v_\mathrm{p} < v_\mathrm{A}$ holds in the curtain flow, only the slow speed $v_\mathrm{p} = v_\mathrm{sl}$ will result. Equation (9.177) shows that, to avoid a singularity at this critical point, $\partial H/\partial\varpi = 0$ is a necessary condition. This determines the sonic

point coordinates. The Bernoulli integral H can be expressed as

$$H(\varpi,\rho)=\frac{\epsilon^2 B_{\rm p}^2}{2\rho^2}+\frac{1}{2}\Omega_*^2\varpi^2\left(\frac{\Omega}{\Omega_*}\right)\left(\frac{\Omega}{\Omega_*}-2\right)-\frac{GM}{[\varpi^2+z(\varpi)^2]^{\frac{1}{2}}}+a^2\ln\rho. \tag{9.178}$$

Because $v_{\rm p}^2/v_{\rm A}^2\ll 1$, distortions of $\mathbf{B}_{\rm p}$ will be small and the unperturbed, current-free form can be used. It follows from (9.139) for ϵ and (9.159) for β, together with (9.137) for Ω, that the angular velocity can be expressed as

$$\Omega=\Omega_*\left[1-\left(1+\frac{1}{2\xi^{\frac{3}{2}}}\frac{\delta}{\varpi_0}\right)\left(\frac{v_{\rm p}^2}{v_{\rm A}^2}\right)\frac{\varpi_0^2}{\varpi^2}\right]\left[1-\left(\frac{v_{\rm p}^2}{v_{\rm A}^2}\right)\right]^{-1}. \tag{9.179}$$

The toroidal magnetic field is given by (9.138), (9.139) and (9.159) for B_ϕ, ϵ and β as

$$B_\phi=\mu_0|\epsilon|\varpi_0\Omega_*\left[\left(1+\frac{1}{2\xi^{\frac{3}{2}}}\frac{\delta}{\varpi_0}\right)\frac{\varpi_0}{\varpi}-\frac{\varpi}{\varpi_0}\right]\left[1-\left(\frac{v_{\rm p}^2}{v_{\rm A}^2}\right)\right]^{-1}. \tag{9.180}$$

The first square bracket term in this expression is always positive and hence, to avoid a singularity in B_ϕ, the denominator cannot vanish, so ensuring that $v_{\rm p}^2/v_{\rm A}^2<1$ and $B_\phi>0$.

Using (9.150) for $z(\varpi)$ and (9.179) for Ω in (9.178) for H leads to the derivatives

$$\begin{aligned}\frac{\partial H}{\partial\varpi}=&-v_{\rm p}^2\frac{|B_{\rm p}'|}{B_{\rm p}}+\frac{2}{3}\frac{v_{\kappa 0}^2}{\varpi_0}\left(\frac{\varpi_0}{\varpi}\right)^{\frac{5}{3}}\left(1+\frac{h_0^2}{\varpi_0^2}\right)^{-\frac{1}{2}}\\&-\Omega_*^2\varpi\left[1-2\left(\frac{v_{\rm p}^2}{v_{\rm A}^2}\right)+\left(\frac{v_{\rm p}^2}{v_{\rm A}^2}\right)^2\frac{\varpi_0^4}{\varpi^4}\right]\left[1-\left(\frac{v_{\rm p}^2}{v_{\rm A}^2}\right)\right]^{-2},\end{aligned} \tag{9.181}$$

$$\frac{\partial H}{\partial\rho}=\frac{a^2}{\rho}-\frac{v_{\rm p}^2}{\rho}-\frac{\Omega_*^2\varpi^2}{\rho}\left(\frac{v_{\rm p}^2}{v_{\rm A}^2}\right)^2\left[\left(1+\frac{1}{2\xi^{\frac{3}{2}}}\frac{\delta}{\varpi_0}\right)\frac{\varpi_0^2}{\varpi^2}-1\right]^2\left[1-\left(\frac{v_{\rm p}^2}{v_{\rm A}^2}\right)\right]^{-3}. \tag{9.182}$$

Using $v_{\rm p}^2/v_{\rm A}^2\ll 1$ and expanding (9.181) and (9.182) to second order in $v_{\rm p}^2/v_{\rm A}^2$ yields

$$\begin{aligned}\frac{\partial H}{\partial\varpi}=&-v_{\rm p}^2\frac{|B_{\rm p}'|}{B_{\rm p}}+\frac{2}{3}\frac{v_{\kappa 0}^2}{\varpi_0}\left(\frac{\varpi_0}{\varpi}\right)^{\frac{5}{3}}\left(1+\frac{h_0^2}{\varpi_0^2}\right)^{-\frac{1}{2}}\\&-\Omega_*^2\varpi\left[1+\left(\frac{v_{\rm p}^2}{v_{\rm A}^2}\right)^2\left(\frac{\varpi_0^4}{\varpi^4}-1\right)\right],\end{aligned} \tag{9.183}$$

$$\frac{\partial H}{\partial \rho} = \frac{a^2}{\rho} - \frac{v_{\rm p}^2}{\rho} - \frac{\Omega_*^2 \varpi^2}{\rho} \left(\frac{v_{\rm p}^2}{v_{\rm A}^2} \right)^2 \left(\frac{\varpi_0^2}{\varpi^2} - 1 \right)^2 . \tag{9.184}$$

The conditions $\partial H/\partial \rho = 0$ and $\partial H/\partial \varpi = 0$ apply at the slow magnetosonic point. Using $\partial H/\partial \rho = 0$ in (9.184) and solving for $v_{\rm sl}$ gives

$$v_{\rm sl} = a \left[1 - \frac{1}{2} \xi^{\frac{3}{2}} \frac{v_{\rm K0}^2}{(v_{\rm A}^2)_{\rm sl}} \frac{a^2}{(v_{\rm A}^2)_{\rm sl}} \frac{\varpi_{\rm sl}^2}{\varpi_0^2} \left(\frac{\varpi_0^2}{\varpi_{\rm sl}^2} - 1 \right)^2 \right] \tag{9.185}$$

This gives the slow magnetosonic speed and, since the last term is small, it follows that $v_{\rm sl} = a$ to high accuracy. Hence, because $v_{\rm p}$ is well sub-Alfvénic, the slow magnetosonic point and the sonic point essentially merge. The density reaches a minimum value shortly after the flow has become supersonic.

9.8.8 The Sonic Point Coordinates

The condition $\partial H/\partial \varpi = 0$ determines the curtain flow sonic point coordinate $\varpi_{\rm sn}$ from (9.183). This equation can be expressed as

$$\frac{\partial H}{\partial \varpi} = -v_{\rm p}^2 \frac{|B_{\rm p}'|}{B_{\rm p}} + \frac{d\psi}{d\varpi} - \Omega_*^2 \varpi \left(\frac{v_{\rm p}^2}{v_{\rm A}^2} \right)^2 \left(\frac{\varpi_0^4}{\varpi^4} - 1 \right), \tag{9.186}$$

where

$$\psi = -\frac{GM}{[\varpi^2 + z(\varpi)^2]^{\frac{1}{2}}} - \frac{1}{2} \Omega_*^2 \varpi^2 \tag{9.187}$$

is the effective potential along the field line $z = z(\varpi)$. The first and last terms in (9.186) are small compared to the middle term and hence the condition $\partial H/\partial \varpi = 0$ reduces to $d\psi/d\varpi = 0$ which is equivalent to

$$\mathbf{B}_{\rm p} \cdot \nabla \psi = 0. \tag{9.188}$$

This corresponds to the components of the gravitational force and the centrifugal force tangential to the poloidal field line cancelling at the sonic point.

Since the curtain flow cross section is thin, the flow close to a central poloidal field in a meridional plane can be considered. Most of the mass will flow close to this central line, with the density decreasing rapidly normal to the central line in this plane. The field line given by (9.150) passes through the curtain base point (ϖ_0, h_0). The condition for this line to pass through the central plane point $(\varpi_{\rm m} - \delta/2, 0)$ in

the middle of the radial boundary layer is

$$\varpi_0 = \left(\varpi_\mathrm{m} - \frac{\delta}{2}\right)\left(1 + \frac{h_0^2}{\varpi_0^2}\right)^{-\frac{3}{2}}. \tag{9.189}$$

First order expansion gives

$$\frac{\varpi_\mathrm{m}}{\varpi_0} = 1 + \frac{\delta}{2\varpi_\mathrm{m}}. \tag{9.190}$$

Using the field line equation (9.150) and $\Omega_* = \xi^{\frac{3}{2}}\Omega_\mathrm{KM}$ in (9.187) yields

$$\psi(\varpi, z(\varpi)) = -\frac{GM}{\varpi_0^{\frac{1}{3}}}\left(1 + \frac{h_0^2}{\varpi_0^2}\right)^{-\frac{1}{2}}\frac{1}{\varpi^{\frac{2}{3}}} - \frac{1}{2}\xi^3\Omega_\mathrm{KM}^2\varpi^2. \tag{9.191}$$

The condition $d\psi/d\varpi = 0$, together with (9.190), leads to the sonic point coordinates

$$\varpi_\mathrm{sn} = \left(\frac{2}{3}\right)^{\frac{3}{8}}\frac{1}{\xi^{\frac{9}{8}}}\left(1 + \frac{\delta}{2\varpi_\mathrm{m}}\right)^{\frac{9}{8}}\varpi_0, \tag{9.192}$$

$$z_\mathrm{sn} = \left(\frac{2}{3}\right)^{\frac{1}{4}}\frac{1}{\xi^{\frac{3}{4}}}\left(1 + \frac{\delta}{2\varpi_\mathrm{m}}\right)^{\frac{3}{4}}\left[1 + \frac{h_0^2}{\varpi_0^2} - \left(\frac{2}{3}\right)^{\frac{1}{4}}\frac{1}{\xi^{\frac{3}{4}}}\left(1 + \frac{\delta}{2\varpi_\mathrm{m}}\right)^{\frac{3}{4}}\right]^{\frac{1}{2}}\varpi_0. \tag{9.193}$$

The condition $\varpi_\mathrm{sn} < \varpi_0$ must be satisfied for the sonic point to lie above the disc. Equation (9.192) gives this condition as

$$\left(\frac{2}{3}\right)^{\frac{3}{8}}\frac{1}{\xi^{\frac{9}{8}}}\left(1 + \frac{\delta}{2\varpi_\mathrm{m}}\right)^{\frac{9}{8}} < 1. \tag{9.194}$$

The quantity δ/ϖ_m will depend on ξ and a function can be defined as

$$b(\xi) = \left(\frac{2}{3}\right)^{\frac{1}{3}}\left(1 + \frac{\delta}{2\varpi_\mathrm{m}}\right). \tag{9.195}$$

This leads to a critical value for ξ, given by (9.194) as $b(\xi_\mathrm{c}) = \xi_\mathrm{c}$, corresponding to $\varpi_\mathrm{sn} = \varpi_0$ and $z_\mathrm{sn} = h_0$. The sonic point coordinates can then be expressed as

$$\varpi_\mathrm{sn} = \left(\frac{b}{\xi}\right)^{\frac{9}{8}}\varpi_0, \tag{9.196}$$

$$z_{\rm sn} = \left(\frac{b}{\xi}\right)^{\frac{3}{4}} \left[1 + \frac{h_0^2}{\varpi_0^2} - \left(\frac{b}{\xi}\right)^{\frac{3}{4}}\right]^{\frac{1}{2}} \varpi_0. \tag{9.197}$$

The condition (9.194) then becomes

$$b(\xi) < \xi, \tag{9.198}$$

ensuring that the sonic point lies above the disc surface.

9.8.9 *Determination of the Curtain Base Width*

The transition region between the disc and the curtain flow has radial and vertical extents of $\varpi_{\rm m} - \delta \le \varpi \le \varpi_{\rm m}$ and $0 \le z \le h_0$. Material enters the outer vertical face of this region at $\varpi = \varpi_{\rm m}$ and leaves it at the upper surface at $z = h_0$. The density is maximum in the central plane of the disc, and most material entering the vertical face will have a nearly horizontal velocity. The mass flow rate into the transition region is therefore

$$\frac{\dot{M}}{2} = 2\pi \int_0^{h_{\rm m}} \varpi_{\rm m} (\rho |v_\varpi|)_{\varpi_{\rm m}} dz = 2\pi \varpi_{\rm m} I_1 (\rho_{\rm c} |v_{\varpi {\rm c}}|)_{\varpi_{\rm m}} h_{\rm m}, \tag{9.199}$$

where $h_{\rm m} = h(\varpi_{\rm m})$, the subscript 'c' denotes central plane values and I_1 is a dimensionless factor incorporating the vertical integral of the mass flux, with $I_1 < 1$. An equal mass flow rate occurs through the upper horizontal surface at $z = h_0$, given by

$$\frac{\dot{M}}{2} = 2\pi \int_{\varpi_{\rm m}-\delta}^{\varpi_{\rm m}} \varpi \rho_0 v_{z0} d\varpi = 2\pi \varpi_{\rm m} I_2 \rho_0(\varpi_{\rm m}) v_{z0} \delta, \tag{9.200}$$

where I_2 incorporates the horizontal integral, with $I_2 < 1$. Equating (9.199) to (9.200), using the fact that $(v_{\varpi {\rm c}})_{\varpi_{\rm m}}$ is mainly viscously driven, $\delta \simeq h$ and $I_1 \simeq I_2$, yields

$$\frac{v_{z0}}{a} = \frac{3}{2} \epsilon_V \frac{h_{\rm m}}{\varpi_{\rm m}} \left(\frac{c_{\rm s} \rho_{\rm c}}{a \rho_0}\right)_{\varpi_{\rm m}} \frac{h_{\rm m}}{\delta}. \tag{9.201}$$

It follows from this expression that the value of the curtain base flow speed v_{z0}, derived by mass conservation through the transition region, is well subsonic. This must match the value calculated by consideration of the curtain flow just above $z = h_0$.

The energy integral for a poloidal field line is, to a good approximation,

$$\frac{1}{2}v_{\rm p}^2 + \psi + a^2 \ln \rho = E, \tag{9.202}$$

with the potential given by (9.187). Evaluating this at the curtain base and at the sonic point, then equating these expressions leads to

$$\frac{\rho_{\rm sn}}{\rho_0} = \exp\left[-\left(\frac{1}{2} + \frac{1}{a^2}(\psi_{\rm sn} - \psi_0)\right)\right], \tag{9.203}$$

with

$$\psi_{\rm sn} - \psi_0 = v_{\kappa 0}^2 \left[1 - \frac{4}{3}\left(\frac{\xi}{b}\right)^{\frac{3}{4}} + \frac{1}{3}\left(\frac{\xi}{b}\right)^3\right]. \tag{9.204}$$

The conservation of mass and magnetic flux give

$$\frac{v_{z0}}{a} = \frac{|B_{z0}|}{(B_{\rm p})_{\rm sn}}\frac{\rho_{\rm sn}}{\rho_0}, \tag{9.205}$$

where

$$\frac{|B_{z0}|}{(B_{\rm p})_{\rm sn}} = \frac{1}{2}\left(\frac{b}{\xi}\right)^{\frac{9}{4}}\left[1 - \frac{3}{4}\left(\frac{b}{\xi}\right)^{\frac{3}{4}}\right]^{-\frac{1}{2}}. \tag{9.206}$$

Equations (9.201)–(9.206) then yield

$$\frac{v_{z0}}{a} = \frac{1}{2}\left(\frac{b}{\xi}\right)^{\frac{9}{4}}\left[1 - \frac{3}{4}\left(\frac{b}{\xi}\right)^{\frac{3}{4}}\right]^{-\frac{1}{2}} \exp\left[-\left(\frac{1}{2} + \frac{v_{\kappa 0}^2}{a^2}\tilde{f}(\xi)\right)\right] \tag{9.207}$$

with

$$\tilde{f}(\xi) = 1 - \frac{4}{3}\left(\frac{\xi}{b}\right)^{\frac{3}{4}} + \frac{1}{3}\left(\frac{\xi}{b}\right)^3. \tag{9.208}$$

Equating (9.201) to (9.207) gives the condition for the continuity of v_{z0} across the curtain base. Equation (9.201) can be written as

$$\frac{v_{z0}}{a} = \frac{3}{2}\epsilon_\nu \frac{h_{\rm m}}{\varpi_{\rm m}}\left(\frac{\rho_{\rm c} T_{\rm c}^{\frac{1}{2}}}{\rho_0 T_0^{\frac{1}{2}}}\right)_{\varpi_0}\frac{h_{\rm m}}{\delta}. \tag{9.209}$$

This typically gives $v_{z0}/a \sim 10^{-2}$ and hence (9.207) must match this value. The most sensitive dependence in (9.207) arises from the term $(v_{\kappa 0}^2/a^2)\tilde{f}(\xi)$ in the exponential. Since $v_{\kappa 0}^2/a^2 \sim \varpi_{\rm m}^2/h_{\rm m}^2 \gg 1$, values of $v_{z0}/a \sim 10^{-2}$ can only be obtained for $\tilde{f} \sim a^2/v_{\kappa 0}^2 \ll 1$. Then expression (9.208) for $\tilde{f}(\xi)$ shows that $b(\xi)$ must have a value close to ξ to ensure that $\tilde{f}$ is small. Writing

$$b(\xi) = \xi - \tilde{\epsilon}(\xi), \tag{9.210}$$

with $0 < \tilde{\epsilon}(\xi) \ll \xi$, satisfies this and $b < \xi$ holds. Using

$$\frac{b}{\xi} = 1 - \frac{\tilde{\epsilon}}{\xi} \tag{9.211}$$

in (9.207) and (9.208) and expanding in $\tilde{\epsilon}/\xi$ leads to

$$\frac{v_{z0}}{a} = \exp\left[-\left(\frac{1}{2} + \frac{9}{8}\frac{v_{\kappa 0}^2}{a^2}\frac{\tilde{\epsilon}^2}{\xi^2}\right)\right]. \tag{9.212}$$

Equating this to (9.209) and solving for $\tilde{\epsilon}$ gives

$$\tilde{\epsilon}(\xi) = \frac{2}{3}\frac{a}{v_{\kappa 0}}\left[2\ln\left\{\frac{2}{3}\frac{1}{\epsilon_V}\frac{\varpi_{\rm m}}{h_{\rm m}}\left(\frac{\rho_0 T_0^{\frac{1}{2}}}{\rho_{\rm c} T_{\rm c}^{\frac{1}{2}}}\right)_{\varpi_{\rm m}}\frac{\delta}{h_{\rm m}}\right\} - 1\right]^{\frac{1}{2}}\xi. \tag{9.213}$$

Eliminating b between (9.195) and (9.210) yields

$$\frac{\delta}{\varpi_{\rm m}} = 2\left[\left(\frac{3}{2}\right)^{\frac{1}{3}}[\xi - \tilde{\epsilon}(\xi)] - 1\right]. \tag{9.214}$$

The δ-dependence contained in the logarithmic function in (9.213) is weak, and since $\delta/h_{\rm m} \simeq 1$, it is a good approximation to use $\delta/h_{\rm m} = 1$ to give an explicit solution for δ from (9.213) and (9.214). Employing (9.131) for $\varpi_{\rm m}$ in (9.214) leads to the boundary layer expression

$$\delta(\xi) = 2\left(\frac{2\gamma}{\epsilon_{\rm m}}\right)^{\frac{2}{7}}\left[\left(\frac{3}{2}\right)^{\frac{1}{3}}[\xi - \tilde{\epsilon}(\xi)] - 1\right]\left(1 - \xi^{\frac{3}{2}}\right)^{\frac{2}{7}}\varpi_{\rm m}, \tag{9.215}$$

where $\tilde{\epsilon}(\xi)$ is given by (9.213) with $\delta/h_{\rm m} = 1$. Hence matching flows at the curtain base has determined the transition region width as a function of ξ.

Using (9.211) for b/ξ in (9.196) and (9.197) for the sonic point coordinates and expanding to first order gives

$$\varpi_{\rm sn} = \left(1 - \frac{9}{8}\frac{\tilde{\epsilon}}{\xi}\right)\varpi_0, \tag{9.216}$$

$$z_{\rm sn} = \left(1 + \frac{3}{4}\frac{\varpi_0^2}{h_0^2}\frac{\tilde{\epsilon}}{\xi}\right)^{\frac{1}{2}} h_0. \tag{9.217}$$

Since $\tilde{\epsilon}/\xi \sim a/v_{\rm K0} \sim h_0/\varpi_0$, (9.217) yields

$$z_{\rm sn} \simeq \frac{\sqrt{3}}{2}\left(\frac{\varpi_0}{h_0}\right)^{\frac{1}{2}} h_0. \tag{9.218}$$

This shows that the sonic point lies just inside ϖ_0, but is well above the disc surface.

It is noted that in the formal limit of $\delta \to 0$, the condition (9.194) gives a minimum value for ξ of

$$\xi_{\rm min} = \left(\frac{2}{3}\right)^{\frac{1}{3}}. \tag{9.219}$$

For $\xi \to \xi_{\rm min}$ the sonic point would approach the curtain base and there would be no potential barrier to the flow. The resulting high mass loss rate would not be consistent with the steady rate $\dot{M}$ supplied by the disc. Conversely, for $\delta \to 0$ and ξ well above $\xi_{\rm min}$, the mass loss rate would be insufficient to match $\dot{M}$. The foregoing analysis shows that the finite width δ, and the sonic point position, can adjust to accommodate the steady mass transfer rate imposed by the disc. The minimum value of ξ, given by (9.219), was also found by Koldoba et al. (2002) for sub-Alfvénic flow along dipolar field lines. They concluded that transonic flow required $\xi > \xi_{\rm min}$, so a sonic point exists above the disc surface.

9.8.10 The Strong Magnetic Regime

The condition (9.146) of $\varpi_{\rm m} < \varpi_{\rm A}$ was shown to be consistent with small values of $B_\phi/|B_{\rm p}|$, corresponding to strong magnetic channelling in the curtain flow. Since $\varpi_{\rm m} < \varpi_{\rm co}$ holds, then $\varpi_{\rm m} < \varpi_{\rm A}$ will be satisfied if $\varpi_{\rm A} > \varpi_{\rm co}$. Using (9.84) for $\varpi_{\rm co}$ and (9.97) for $\varpi_{\rm A}$, the condition $\varpi_{\rm A} = \varpi_{\rm co}$ then gives an upper limit to the stellar rotation period of

$$P_{\rm mag} = 6.4 \frac{\left(\dfrac{B_0}{4\times10^8\,{\rm T}}\right)^{\frac{6}{7}}\left(\dfrac{R}{10^4\,{\rm m}}\right)^{\frac{18}{7}}}{\left(\dfrac{M}{1.4\,M_\odot}\right)^{\frac{5}{7}}\left(\dfrac{\dot{M}}{10^{-9}\,M_\odot\,{\rm year}^{-1}}\right)^{\frac{3}{7}}}\,{\rm s}, \tag{9.220}$$

with the normalization corresponding to a typical X-ray binary pulsar. Then

$$P < P_{\rm mag} \tag{9.221}$$

defines a strong magnetic regime consistent with a thin, sub-Alfvénic curtain flow. Equation (9.219) gives the minimum value of ξ consistent with steady flow and the corresponding period can be expressed as

$$P_{\rm max} = \left(\frac{2\gamma}{\epsilon_{\rm m}}\right)^{\frac{3}{7}} \frac{(1-\xi_{\rm min}^{\frac{3}{2}})^{\frac{3}{7}}}{\xi_{\rm min}^{\frac{3}{2}}} P_{\rm mag}. \tag{9.222}$$

Since $\gamma/\epsilon_{\rm m} < 1$, it follows that $P_{\rm max} < P_{\rm mag}$, so steady mass transfer is consistent with the system lying in the strong magnetic regime having ξ in the range

$$\xi_{\rm min} < \xi < 1. \tag{9.223}$$

9.9 The Effects of Magnetic Tilt

9.9.1 The Tilted Dipole

Most investigations of the star-disc interaction have considered the case in which the stellar dipole moment and angular velocity are aligned with the orbital angular momentum vector. This idealization has enabled progress to be made in understanding the nature of the interaction, but the observed systems have $\mathbf{m}$ tilted to $\mathbf{\Omega}_*$.

For a tilted dipole, with $\mathbf{m}$ inclined at an angle α to $\mathbf{\Omega}_*$, the unperturbed poloidal magnetic field is given by

$$\mathbf{B}_{\rm p} = -\nabla \Psi_{\rm m} \tag{9.224}$$

where

$$\Psi_{\rm m} = \frac{\mu_0 m}{4\pi r^3} \mathbf{r} \cdot \hat{\mathbf{m}} \tag{9.225}$$

with

$$\hat{\mathbf{m}} = \sin\alpha \cos\Omega_* t\, \mathbf{i} + \sin\alpha \sin\Omega_* t\, \mathbf{j} + \cos\alpha\, \mathbf{k}. \tag{9.226}$$

It follows that $\Psi_{\rm m}$ can be expressed as

$$\Psi_{\rm m} = \Psi_{\rm m}^{\parallel} + \Psi_{\rm m}^{\perp}, \tag{9.227}$$

where

$$\Psi_{\rm m}^{\parallel} = \frac{\mu_0 m}{4\pi} \frac{z\cos\alpha}{(\varpi^2 + z^2)^{\frac{3}{2}}} \tag{9.228}$$

and

$$\Psi_{\rm m}^{\perp} = \frac{\mu_0 m}{4\pi} \frac{\varpi\sin\alpha}{(\varpi^2 + z^2)^{\frac{3}{2}}} \cos(\phi - \Omega_* t). \tag{9.229}$$

Hence $\mathbf{B}_{\rm p}$ splits into two parts, corresponding to the components of $\mathbf{m}$ parallel and perpendicular to $\mathbf{\Omega}_* = \Omega_* \mathbf{k}$.

In and near a thin disc, $|z|/\varpi \ll 1$ holds and first order expansion of $\Psi_{\rm m}$ leads to

$$B_{\varpi}^{\parallel} = \frac{3}{2} B_0 \cos\alpha \left(\frac{R}{\varpi}\right)^3 \frac{z}{\varpi}, \tag{9.230}$$

$$B_z^{\parallel} = -\frac{1}{2} B_0 \cos\alpha \left(\frac{R}{\varpi}\right)^3, \tag{9.231}$$

$$B_{\varpi}^{\perp} = B_0 \sin\alpha \left(\frac{R}{\varpi}\right)^3 \cos(\phi - \Omega_* t), \tag{9.232}$$

$$B_z^{\perp} = \frac{3}{2} B_0 \sin\alpha \left(\frac{R}{\varpi}\right)^3 \frac{z}{\varpi} \cos(\phi - \Omega_* t). \tag{9.233}$$

When these fields diffuse into the disc they are sheared to create B_ϕ at a rate

$$\varpi \mathbf{B}_{\rm p} \cdot \nabla\Omega = \varpi B_{\varpi} \frac{\partial\Omega}{\partial\varpi} + \varpi B_z \frac{\partial\Omega}{\partial z}. \tag{9.234}$$

Since $\partial\Omega/\partial z \sim (\varpi/h)\partial\Omega/\partial\varpi$, it follows from (9.230)–(9.234) that the dominant source of B_ϕ is $B_z^{\parallel}$. Hence the major contribution to B_ϕ is axisymmetric and time-independent, and only differs by a factor of $\cos\alpha$ from the B_ϕ field of the aligned case with $\alpha = 0$. In the extreme case of α close to 90°, the time-dependent part of $\mathbf{B}_{\rm p}$ can become a main source of B_ϕ in the disc. Apart from this case, the disc disruption mechanism should be essentially the same as that found for the aligned case.

9.9.2 The Non-axisymmetric Curtain Region Equations

For a tilted magnetic axis the time dependence can be removed by using a frame corotating with the star. The equations are then steady, but non-axisymmetric.

The momentum and continuity equations are

$$(\mathbf{v}\cdot\nabla)\mathbf{v} = -\frac{1}{\rho}\nabla P - \nabla\left(\psi - \frac{1}{2}\Omega_*^2\varpi^2\right) - 2\boldsymbol{\Omega}_*\times\mathbf{v} + \frac{1}{\mu_0\rho}(\nabla\times\mathbf{B})\times\mathbf{B}, \tag{9.235}$$

$$\nabla\cdot(\rho\mathbf{v}) = 0. \tag{9.236}$$

The steady induction equation in the curtain flow is

$$\nabla\times(\mathbf{v}\times\mathbf{B}) = \mathbf{0}, \tag{9.237}$$

and for an isothermal gas

$$P = a^2\rho. \tag{9.238}$$

Equation (9.237) is satisfied by

$$\mathbf{v} = \kappa(\mathbf{r})\mathbf{B} \tag{9.239}$$

and then the continuity equation (9.236), together with $\nabla\cdot\mathbf{B} = 0$, gives

$$\epsilon = \kappa\rho = \frac{\rho v}{B} \tag{9.240}$$

as a conserved quantity along field-streamlines.

The momentum equation (9.235) can be expressed as

$$(\nabla\times\mathbf{v})\times\mathbf{v} = -\nabla\left(\frac{1}{2}\mathbf{v}^2 + \psi - \frac{1}{2}\Omega_*^2\varpi^2 + a^2\ln\rho\right) - 2\boldsymbol{\Omega}_*\times\mathbf{v} + \frac{1}{\mu_0\rho}(\nabla\times\mathbf{B})\times\mathbf{B}. \tag{9.241}$$

Then taking the scalar product with $\mathbf{v}$ leads to the energy integral

$$\frac{1}{2}v^2 - \frac{GM}{(\varpi^2+z^2)^{\frac{1}{2}}} - \frac{1}{2}\Omega_*^2\varpi^2 + a^2\ln\rho = E \tag{9.242}$$

giving the energy per unit mass, which is conserved along field-streamlines. It is noted that the expressions (9.239) and (9.240) are similar to those occurring in the aligned, axisymmetric case, given by (9.133) and (9.135), but with the total fields $\mathbf{v}$ and $\mathbf{B}$ replacing the poloidal components $\mathbf{v}_\mathrm{p}$ and $\mathbf{B}_\mathrm{p}$.

The ϕ-component of the angular momentum equation can be written as

$$\mathbf{B}\cdot\nabla\left(\epsilon\varpi^2(\Omega-\Omega_*) - \frac{\varpi}{\mu_0}B_\phi\right) = \frac{\partial}{\partial\phi}\left(P + \frac{B_\phi^2}{2\mu_0}\right). \tag{9.243}$$

This shows that angular momentum is exchanged between field lines due to an azimuthal gradient of the sum of the gas and magnetic pressures.

9.9.3 Numerical Simulations for a Tilted Magnetic Axis

Romanova et al. (2003) considered the case of an inclined dipole field. The MHD equations were solved using similar numerical techniques to those described in Sect. 9.6.2 for the aligned case of Romanova et al. (2002). For an inclination $\alpha \lesssim 30°$ matter flows to the star from the inner disrupted region of the disc mainly in two streams, which follow paths to the closest magnetic pole. For $30° \lesssim \alpha \lesssim 60°$ several streams can develop. For $\alpha \gtrsim 60°$ two streams occur again, but flowing to the star near the equatorial plane. The inner parts of the disc often become warped. The vertical component of the accretion torque is weakly dependent on α, and is positive. The horizontal components of the torque can lead to a slow precession of the stellar symmetry axis.

Long et al. (2007) allowed for the star to have aligned dipole and quadrupole moments, but tilted at an angle α to the stellar angular momentum vector. The MHD equations were solved numerically for inclinations $\alpha = 0°, 30°, 60°$. The effect of a quadrupolar field is to cause some material to accrete via a magnetic equatorial belt, which is displaced into the southern hemisphere if a dipole component is present. The pure quadrupole case leads to a smaller accretion torque than in the pure dipole case, since the material can accrete directly through the quadrupolar magnetic belt. For large inclinations most material accretes on to the magnetic poles. The accretion torque is always positive.

Romanova et al. (2012) performed MHD simulations which allowed for turbulence to be generated in the disc via the magnetorotational instability. A tilted stellar dipole was considered. Interchange instabilities were observed, as well as spiral waves. The disc became truncated and a curtain flow developed, transferring matter to the magnetic poles. A positive accretion torque results.

9.10 The Propeller Regime

If the central star is rapidly rotating, with fastness parameter $\xi > 1$, then there is a strong centrifugal effect and matter will be ejected from the system. This was suggested as a spin down mechanism for neutron stars in X-ray binary pulsars (e.g Illarionov and Sunyaev 1975). Wynn et al. (1997) suggested that a propeller mechanism may be operating in the low accretion rate DQ Her binary AE Aqr. Bult and van der Klis (2014) discussed the possibility that the accreting millisecond pulsar J1808 may sometimes operate in the propeller regime during low accretion states. Various estimates of the effectiveness of the mechanism have been made

(e.g. Davies and Pringle 1981; Wang and Robertson 1985). More recently, numerical simulations have enabled more progress to be made.

Ustyugova et al. (2006) performed MHD simulations in this regime, allowing for parametrized turbulent viscosity and magnetic diffusivity in the disc. They considered strong and weak propeller regimes. In the strong regime, intense wide angle conical outflows develop from the disc in the vicinity of the neutral line of the poloidal magnetic field. Magnetic jets emanate from the star, and these become well collimated parallel to its spin axis. In the weak regime no disc outflows occur, but there are weak flows parallel to the vertical axis. In all cases there is non-stationary, quasi-periodic behaviour, and a spin-down torque is exerted on the star. This behaviour is similar to that described above for the cases with lower disc η values, but which have $\xi < 1$.

Larger values of $\mathbf{m}$, $\boldsymbol{\Omega}_*$ and ν lead to enhanced wind and jet mass flow rates, with reduced accretion rates. Expressions were derived for the mass flow rates as power laws in m, ν and η. There is an optimal value for η, which maximises the mass loss rates. Lower values of η lead to less mixing of the disc matter with the magnetospheric magnetic field, with a consequent reduction in angular momentum exchange between the disc and star. Higher values of η reduce the coupling between the disc and magnetosphere. Both these effects reduce the wind and jet mass loss rates.

Lii et al. (2014) performed numerical simulations for a disc having turbulence driven by the magnetorotational instability. Their results were consistent with those of Ustyugova et al. (2006).

9.11 Summary and Discussion

Investigations have made it clear that the nature of the magnetic diffusivity in the disc is of central importance to the star-disc interaction. Various forms of η have been considered, related to turbulence, magnetic buoyancy, reconnection and instabilities. Another major aspect is the structure of the magnetosphere, which is related to the coupling of the stellar magnetic field to the disc and hence to diffusion mechanisms. It is often assumed that the magnetosphere has low density material and is magnetically dominated and corotating with the star. Time-dependent simulations assume an initial structure for the magnetosphere and can follow how this evolves. Despite these uncertainties, analytic and semi-analytic models, together with numerical simulations, have led to an improved understanding of the types of interactions that may occur between the star and the disc.

The highest values of η correspond to the effects of dynamical instabilities and reconnection processes, represented by $\eta \simeq v_{\rm K} h$, and are considerably larger than standard turbulent values. These cases lead to a picture of closed field lines threading the disc being moderately wound by the vertical shear, and resulting in angular momentum exchange between the disc and star via magnetic stresses. The disc

becomes disrupted inside the corotation radius and a field channelled curtain flow transfers material to the star.

For moderate values of η, typically with $\eta \simeq c_s h$, which allow larger values of the winding ratio $|B_{\phi s}/B_{zs}|$ to be attained, inflation of the poloidal field can result in opening of field lines near the stellar magnetic poles and in the outer parts of the disc. A stellar wind flow can occur along the open field lines and the system may reach a quasi-steady state. Again, disruption occurs inside ϖ_{co} and a curtain flow results.

For smaller values of η, typically with $\eta < 0.1 c_s h$, inflation and field line opening occur but an outer disc wind flow now develops as well as a stellar wind. The system remains time-dependent, with oscillations of the disruption radius between minimum and maximum values. Reconnection occurs at the minimum values of ϖ_m, with transfer of material to the star via a curtain flow before the cycle repeats. Episodic ejections of plasma occur in the region between the stellar and disc open field lines.

In all the diffusivity cases, the inner region of the disc has closed field lines and, at least for some time intervals, curtain flows occur which transfer material from the disrupted area of the disc to the star. The numerical simulations have used a simple polytropic equation as an alternative to solving the thermal problem. These simulations tend to lead to compressional heating and increased vertical pressure gradients as the disc ends, allowing material to pass into the curtain flow. The analytic model presented here can account for radiative transfer and dissipation, and this also leads to vertical expansion caused by heating. This expansion takes place over a narrow radial region which results from the rapid increase in the strength the imposed magnetic field with decreasing distance from the star, and an associated increase of the magnetic dissipation.

The analytic and numerical investigations give a consistent picture for the structure of the curtain flow region. The work done by pressure gradients enables material to surmount the potential barrier associated with reaching the sonic point, which is essentially coincident with the slow magnetosonic critical point. Inside this radius, the gravitational force tangential to the poloidal magnetic field exceeds the tangential component of the centrifugal force and matter is accelerated up towards free-fall speeds as the star is approached. The flow is slowed to subsonic values by passing through a standing slow magnetosonic shock front close to the stellar surface.

The steady analytic model shows that the condition of continuity of the azimuthal magnetic field at the curtain base is consistent with a slightly sub-stellar angular velocity of material in this region, as is observed in the numerical simulations. This can result in some angular momentum being fed back into the disc via viscous stresses, and hence the accretion torque is reduced from its conservative form. Expressions can be found for the disruption radius and the width of the transition region as functions of the stellar rotation rate. The width of the transition region is connected to the position of the sonic point and this can adjust to allow the mass transfer rate into the curtain region to match that supplied by the disc, for a given stellar rotation rate. A minimum value results for the stellar angular velocity

consistent with the condition of steady flow. The model of a thermally disrupted disc feeding a narrow magnetically channelled accretion curtain is consistent provided that the stellar rotation period does not exceed a maximum value which is determined by the system parameters.

The effects of a tilted dipole, and an additional quadrupolar magnetic component, have been investigated. The mechanism of disc disruption is essentially the same as in the aligned dipole case, but accretion on to the equatorial regions can occur for larger tilt angles.

The propeller mechanism may operate in some systems that have a sufficiently rapidly spinning accretor. Matter ejected via wind and jet flows can lead to significant braking torques on the central star.

References

Agapitou, V., Papaloizou, J.C.B., 2000, MNRAS, 317, 273.
Aly, J.J., 1980, A&A, 86, 192.
Armitage, P.J., Clarke, C.J., 1996, MNRAS, 280, 458.
Bardou, A., Heyvaerts, J., 1996, A&A, 307, 1009.
Bath, G.T., Evans, W.D., Pringle, J.E., 1974, MNRAS, 166, 113.
Brandenburg, A., Campbell, C.G., 1998, MNRAS, 298, 223.
Bult, P., van der Klis, M., 2014, ApJ, 789, 99.
Campbell, C.G., 1987, MNRAS, 229, 405.
Campbell, C.G., 1992, GAFD, 63, 179.
Campbell, C.G., 1998, MNRAS, 301, 754.
Campbell, C.G., 2010, MNRAS, 403, 1339.
Campbell, C.G., 2012, MNRAS, 420, 1034.
Campbell, C.G., 2014, GAFD, 108, 333.
Campbell, C.G., Heptinstall, P., 1998a, MNRAS, 299, 31.
Campbell, C.G., Heptinstall, P., 1998b, MNRAS, 301, 558.
Davies, R.E., Pringle, J.E., 1981, MNRAS, 196, 209.
Ghosh, P., Lamb, F.K., 1979a, ApJ, 232, 259.
Ghosh, P., Lamb, F.K., 1979b, ApJ, 234, 296.
Giacconi, R., Gursky, H., Kellogg, E., Schreier, E., Tananbaum, H., 1971, ApJ, 167, L67.
Goodson, A.P., Winglee, R.M., 1999, ApJ, 524, 159.
Goodson, A.P., Winglee, R.M., Bohm, K.H., 1997, ApJ, 489, 199.
Illarionov, A.F., Sunyaev, R.A., 1975, A&A, 39. 105.
Koldoba, A.V., Lovelace, R.V.E., Ustyugova, G.V., Romanova, M.M., 2002, ApJ, 123, 2019.
Kundt, W., Robnik, M., 1980, A&A, 91, 305.
Lii, P.S., Romanova, M.M., Ustyugova, G.V., Koldoba, A.V., Lovelace, R.V.E., 2014, MNRAS, 441, 86.
Long, M., Romanova, M.M., Lovelace, R.V.E., 2007, MNRAS, 374, 436.
Lovelace, R.V.E., Romanova, M.M., Bisnovatyi-Kogan, G.S., 1995, MNRAS, 275, 244.
Lubow, S.H., Papaloizou, J.C.B., Pringle, J.E., 1994, MNRAS, 267, 235.
Matt, S., Pudritz, R.E., 2005, MNRAS, 356, 167.
Matthews, O.M., Speith, R., Truss, M.R., Wynn, G.A., 2005, MNRAS, 356, 66.
Paatz, G., Camenzind, M., 1996, A&A, 308, 77.
Pringle, J. E., Rees, M. J., 1972, A&A, 21, 1.
Romanova, M.M., Ustyugova, G.V., Koldoba, A.V., Lovelace, R.V.E., 2002, ApJ, 578, 420.

Romanova, M.M., Ustyugova, G.V., Koldoba, A.V., Wick, J.V., Lovelace, R.V.E., 2003, ApJ, 595, 1009.
Romanova, M.M., Ustyugova, G.V., Koldoba, A.V., Lovelace, R.V.E., 2012, MNRAS, 421, 63.
Shu, F., Najita, J., Ostriker, E., Wilkin, F., Ruden, S., Lizano, S., 1994, ApJ, 429, 781.
Tananbaum, H., Gursky, H., Kellogg, E.M., Levinson, R., Schreier, E., Giacconi, R., 1972, ApJ, 174, L143.
Ustyugova, G.V., Koldoba, A.V., Romanova, M.M., Locelace, R.V.E., 2006, ApJ, 646, 304.
Wang, Y.M., 1987, A&A, 183, 257.
Wang, Y.M., Robertson, J.A., 1985, A&A, 151, 361.
Wynn, G.A., King, A.R., Horne, K., 1997, MNRAS, 286, 436.
Zanni, C., Ferreira, J., 2009, A&A, 508, 1117.
Zanni, C., Ferreira, J., 2013, A&A, 550, A99.

Chapter 10
Disrupted Discs: Stellar Spin Evolution

Abstract The torques exerted on the magnetic primary star due to its interaction with the accretion disc and curtain flow are considered. For sufficiently large values of the disc magnetic diffusivity, η, the stellar field lines remain closed and connected to the disc. A spin-up torque is exerted through the accretion curtain flow and through magnetic stresses due to interaction with the region of the disc inside the corotation radius, $\varpi_{\rm co}$. The magnetic torque from the region of the disc outside $\varpi_{\rm co}$ spins the star down. In the cases of closed field lines, an equilibrium spin period can be found at which the torques on the primary cancel. The approach to this state is analysed and a mechanism is found that generates torque reversals, as are observed in the neutron star cases.

For smaller values of η, field line opening can occur and wind flows from the star and disc can lead to spin-down torques on the primary. However, even in these lower η cases, field lines tend to remain closed in the region of the disc inside $\varpi_{\rm co}$, but can become inflated.

10.1 Introduction

Torques are exerted on the magnetic star due to the interaction of its field and magnetosphere with the differentially rotating disc. As previously discussed, investigations indicate that there are three regimes arising for the star-disc system depending on the disc magnetic diffusivity, η. The relation of these regimes to the stellar torque is considered here.

If η is sufficiently high then the disc surface winding ratio $|B_{\phi {\rm s}}/B_{z{\rm s}}|$ only attains moderate values and the stellar field remains closed and connected to the disc. Magnetic disc torques of opposite sign arise from the regions inside and outside the corotation radius, $\varpi_{\rm co}$. The curtain flow results in a spin-up torque on the star transmitted via magnetic stresses operating through the flow. The total torque can be positive, negative or zero, depending on the spin rate of the star.

For intermediate values of η the winding ratio can become sufficiently large for the toroidal field magnetic pressure to cause poloidal field line inflation. Open stellar

C. G. Campbell, *Magnetohydrodynamics in Binary Stars*, Astrophysics and Space Science Library 456, https://doi.org/10.1007/978-3-319-97646-4_10

and disc field lines can result, with wind flows from the star contributing a negative torque. A quasi-steady state may be reached.

When η has lower values field line opening occurs, but with outer disc winds as well as stellar winds. In addition, plasma ejections result from the region connecting the stellar and disc open field lines. These ejections can transport significant amounts of angular momentum from the system and lead to a spin down torque on the star. Episodic time dependence results, with the disc disruption radius $\varpi_{\rm m}$ oscillating between minimum and maximum values. Accretion curtain flow occurs when $\varpi_{\rm m}$ reaches its minimum value. The cyclic time dependence remains in these cases.

Various models have been considered which calculate the stellar torques, with a range of assumptions about η. The numerical simulations have tended to focus on T Tauri systems, which contain magnetic protostars accreting from a disc. These systems have significant differences from the binary star cases of magnetic white dwarfs and neutron stars. The inner disc in T Tauri stars experiences a weaker gravitational field than that felt by the inner disc regions around compact accretors. The corotation radius in a T Tauri system is a much smaller multiple of the stellar radius than in the binary star discs. Also, protostellar discs are partially ionized and have ambipolar diffusion mechanisms. Nevertheless, the simulation results should have relevance to binary systems.

10.2 Stellar Torque Models

Most calculations of the stellar torque have been made with the assumption of closed field lines. Campbell (1987) used the solutions for B_ϕ given by (9.67) and (9.72) to calculate the stellar magnetic torque, including the use of a modified form of Ω which incorporates a turn-down towards Ω_* as $\varpi_{\rm m}$ is approached. The disruption radius was taken as $\varpi_{\rm m} = 0.5\varpi_{\rm A}$. Using an accretion torque of $\varpi_{\rm m}^2\Omega_*\dot{M}$, an equilibrium state can be found at which the torques balance. This has a significant dependence on the form adopted for the disc magnetic diffusivity η.

Wang (1987) used a magnetic buoyancy form for η and defined $\varpi_{\rm m}$ to be where the magnetic torque dominates the viscous torque. Campbell (1992) employed buoyancy and turbulent forms for η, and determined $\varpi_{\rm m}$ from the condition $T_{\rm m} = 2T_{\rm v}$. A dipole field was used in both investigations and equilibrium states result with a fastness parameter, defined by $\xi = \varpi_{\rm m}/\varpi_{\rm co}$, typically lying in the interval $0.8 < \xi_{\rm eq} < 1$. A balance cannot be attained at lower values of ξ since the negative contribution of the magnetic stellar torque is too weak to balance the positive magnetic torque plus the accretion torque. The negative magnetic torque derives from the disc region with $\varpi > \varpi_{\rm co}$ and, for lower values of ξ, the values of $\varpi^2 B_{\phi{\rm s}} B_{z{\rm s}}$ in this region are insufficient to supply the required negative torque.

Wang (1997) considered the case of a dipole field having its magnetic moment tilted to the stellar angular velocity vector. The stellar frame was used, so the time-independent equations apply. The ϕ-component of $\mathbf{B}$ is the sum of an azimuthal

component, due to the tilt of the magnetic axis, and a toroidal component generated by interaction with the disc. The induction equation yields the toroidal component. The angular momentum equation was azimuthally and vertically integrated through the disc, and the stellar torques were found. An equilibrium balance can be found provided that the tilt angle, α, does not exceed a maximum value of $\alpha_{\max} \simeq 67°$.

Torkelsson (1998) pointed out that a dynamo may be operating in the disc, and that this could significantly affect the stellar torque. The ratio B_ϕ/B_z was taken to be approximately constant for the stellar field interaction, and the ratio B_ϕ/B_ϖ was also assumed to be constant for the dynamo field. For a quadrupolar symmetry dynamo field, the $B_\varpi B_\phi$ stress contributes to driving the disc inflow. Assuming that this effect dominates the viscosity, gives $B_\phi \propto \varpi^{-5/4}$ for the dynamo field, which is a significantly slower decrease with distance than for the stellar source generated B_ϕ field.

This idea was developed further by Tessema and Torkelsson (2010). They showed that with such a dynamo operating the disc surface stress $B_\phi B_z$ is made up of several contributions, containing the two field source components. This stress can be significant at larger distances from $\varpi_{\rm co}$ than in the absence of the dynamo, and hence the spin-down contribution to the stellar magnetic torque may be larger. Power law solutions were found for the radial structure of the disc, with magnetic heating, radiation pressure and electron scattering opacity excluded. Inner boundary conditions were applied, corresponding to the viscous stress or the viscous torque per unit radial length vanishing at the outer edge of an inner boundary layer. It was pointed out that a time-dependent dynamo could lead to variations in the stellar torque, and that these might cause torque reversals on the star.

Agapitou and Papaloizou (2000) considered the effects of field line inflation on the stellar magnetic torque. It was found that larger values of $|B_{\phi {\rm s}}/B_{z{\rm s}}|$ greatly reduce the magnetic torque due to a reduction of $B_{z{\rm s}}$, caused by field line inflation, and the loss of flux connection to the disc where the field lines open. Matt and Pudritz (2005) also found significant torque reductions due to the loss of field linkage with the disc. Both these studies assumed that large amounts of field winding can be sustained.

The numerical simulations of Romanova et al. (2002) took small values of η, but had a higher density magnetosphere that did not corotate with the star. The vertical shears are then reduced and the resulting moderate values of $|B_{\phi {\rm s}}/B_{z{\rm s}}|$ allow the maintenance of field line connection to the inner parts of the disc where the magnetic torques largely determine the disc contribution to the stellar torque. An equilibrium spin state can be reached with $\xi_{\rm eq} \simeq 0.7$.

In the simulations of Zanni and Ferreira (2009) a quasi-steady state is reached after about 55 stellar rotation periods. There are inner closed field lines, but the stellar magnetic torque is only $\simeq 10\%$ of the accretion torque. The stellar wind can contribute $\simeq 20\%$ of $T_{\rm a}$. Some time dependence remains and a torque balance is never reached. In the lower η value case considered by Zanni and Ferreira (2013) periodic time dependence occurs. Plasma ejections in the volume between the stellar and disc open field line regions can advect a significant amount of angular momentum from the system. This process can extract angular momentum from the star, and the stellar wind can account for $\simeq 20 - 30\%$ of $T_{\rm a}$. The spin-down effects

of plasma ejections and the stellar wind can balance the accretion torque during the time intervals in which curtain flow occurs, when $\varpi_{\rm m}$ is minimum. Typically $\xi_{\rm eq} \simeq 0.6$ in these intervals.

In the cases with lower η values, that lead to field line opening and wind flows, a usable analytic theory has not yet been developed to calculate the torques and stellar spin evolution. For the cases of higher and intermediate values of η, a closed field line model gives a reasonable description of the stellar torque. Since the model considered in Sect. 9.8 describes the disc structure, determines $\varpi_{\rm m}$, fits to a curtain flow and determines the accretion torque, it will be used below to calculate the stellar torque. This is based on the analysis of Campbell (2011) and it leads to a mechanism which may explain the torque reversals observed in X-ray binary pulsars.

10.3 Stellar Torques and Spin Evolution

10.3.1 The Stellar Torque

The magnetic torque exerted on the star due to its interaction with the disc is

$$T_{\rm m*} = -\frac{4\pi}{\mu_0}\int_{\varpi_{\rm m}}^{\varpi_{\rm D}} \varpi^2 B_{\phi \rm s} B_{z\rm s} d\varpi, \tag{10.1}$$

where $\varpi_{\rm D}$ is the outer radius of the disc. Using (9.92) for $\varpi^2 B_{\phi \rm s} B_{z\rm s}$ in (10.1) and evaluating the integral, employing (9.97) to eliminate $B_0 R^3$ in terms of $\varpi_{\rm A}$, leads to

$$T_{\rm m*} = -\dot{M}\varpi_{\rm m}^2 \Omega_{\rm K}(\varpi_{\rm m}) \frac{\gamma}{\epsilon_{\rm m}} \left(\frac{\varpi_{\rm A}}{\varpi_{\rm co}}\right)^{\frac{7}{2}} \frac{1}{\xi^{\frac{7}{2}}} \left[\frac{\xi^{\frac{3}{2}}}{(n+2)} - \frac{2}{(2n+7)}\right]. \tag{10.2}$$

Adding this to the accretion torque, given by (9.175), and employing (9.131) for $\varpi_{\rm m}$, using $\varpi_{\rm m} = \xi \varpi_{\rm co}$ to eliminate $\varpi_{\rm A}/\varpi_{\rm co}$ in (10.2), gives the total stellar torque as

$$T_* = \dot{M}\varpi_{\rm m}^2 \Omega_{\rm K}(\varpi_{\rm m}) \left[\xi^{\frac{3}{2}} - \frac{1}{2(1-\xi^{\frac{3}{2}})} \left\{\frac{\xi^{\frac{3}{2}}}{(n+2)} - \frac{2}{(2n+7)}\right\}\right], \tag{10.3}$$

where

$$\varpi_{\rm m}^2 \Omega_{\rm K}(\varpi_{\rm m}) = \left(\frac{2\gamma}{\epsilon_{\rm m}}\right)^{\frac{1}{7}} (GM\varpi_{\rm A})^{\frac{1}{2}} \left(1-\xi^{\frac{3}{2}}\right)^{\frac{1}{7}}. \tag{10.4}$$

10.3.2 The Spin Evolution Rate

The angular velocity of the star obeys the spin evolution equation

$$I\dot{\Omega}_* = T_*, \tag{10.5}$$

where the moment of inertia can be expressed as $I = k^2R^2M$, with kR being the radius of gyration. The evolution equation for the period is then

$$\frac{\dot{P}}{P} = -\frac{\dot{\Omega}_*}{\Omega_*} = -\frac{T_*}{k^2R^2M\Omega_*}. \tag{10.6}$$

Using (9.84), (9.85) and (9.131) for $\varpi_{\rm co}$, ξ and $\varpi_{\rm m}$ to relate P, and hence Ω_*, to ξ yields

$$\Omega_* = \left(\frac{\epsilon_{\rm m}}{2\gamma}\right)^{\frac{3}{7}} \left(\frac{GM}{\varpi_{\rm A}^3}\right)^{\frac{1}{2}} \frac{\xi^{\frac{3}{2}}}{(1-\xi^{\frac{3}{2}})^{\frac{3}{7}}}. \tag{10.7}$$

Substituting this, together with (10.3) and (10.4) for T_*, in (10.6) gives

$$\frac{\dot{P}}{P} = -\frac{\left(\frac{\gamma}{\epsilon_{\rm m}}\right)^{\frac{4}{7}} \left(\frac{B_0}{2\times10^8\,{\rm T}}\right)^{\frac{8}{7}} \left(\frac{R}{10^4\,{\rm m}}\right)^{\frac{10}{7}} \left(\frac{\dot{M}}{4\times10^{-9}\,M_\odot\,{\rm year}^{-1}}\right)^{\frac{3}{7}}}{1.37\times10^3 \left(\frac{k^2}{0.4}\right) \left(\frac{M}{1.4\,M_\odot}\right)^{\frac{9}{7}}} F_P(\xi)\,{\rm year}^{-1}, \tag{10.8}$$

where

$$F_P(\xi) = \frac{(1-\xi^{\frac{3}{2}})^{\frac{4}{7}}}{\xi^{\frac{3}{2}}} \left[\xi^{\frac{3}{2}} - \frac{1}{2(1-\xi^{\frac{3}{2}})} \left\{\frac{\xi^{\frac{3}{2}}}{(n+2)} - \frac{2}{(2n+7)}\right\}\right], \tag{10.9}$$

with the normalization values being characteristic of a typical X-ray binary pulsar.

Equation (9.129) gives the spin parameter as $\xi = \xi(C)$, with

$$C(P,\dot{M}) = \frac{1}{\mu_0} \left(\frac{4\pi^2}{G}\right)^{\frac{5}{3}} \frac{\gamma}{\epsilon_{\rm m}} \frac{B_0^2R^6}{M^{\frac{5}{3}}\dot{M}P^{\frac{7}{3}}}. \tag{10.10}$$

The star will be spun up or spun down depending on the values of P and $\dot{M}$. The spin evolution time-scales are much longer than the adjustment time-scales in the disc, so its structure can evolve through quasi-steady states as the stellar spin period changes.

10.3.3 The Equilibrium State

The equilibrium period occurs when $\dot{P} = 0$, corresponding to $F_P(\xi) = 0$. Equation (10.9) then yields

$$\xi_{\rm eq} = \left[\frac{2n+3}{4n+8} + \left[\left(\frac{2n+3}{4n+8}\right)^2 + \frac{1}{2n+7}\right]^{\frac{1}{2}}\right]^{\frac{2}{3}}. \tag{10.11}$$

It is noted that $\xi_{\rm eq}$ depends purely on the parameter n, this being related to the length-scale ℓ of the magnetic diffusivity via $\ell = \eta/(d\eta/d\varpi) = \varpi/n$. This length-scale affects the distribution of the magnetic torque in the disc, and hence $\xi_{\rm eq}$. The equilibrium period follows from (10.7) for Ω_* as

$$P_{\rm eq} = 4.2\left(\frac{\gamma}{\epsilon_{\rm m}}\right)^{\frac{3}{7}} \frac{(1-\xi_{\rm eq}^{\frac{3}{2}})^{\frac{3}{7}}}{\xi_{\rm eq}^{\frac{3}{2}}} \frac{\left(\frac{B_0}{2\times 10^8\,{\rm T}}\right)^{\frac{6}{7}}\left(\frac{R}{10^4\,{\rm m}}\right)^{\frac{18}{7}}}{\left(\frac{M}{1.4\,M_\odot}\right)^{\frac{5}{7}}\left(\frac{\dot{M}}{4\times 10^{-9}\,M_\odot\,{\rm year}^{-1}}\right)^{\frac{3}{7}}}\,{\rm s}. \tag{10.12}$$

Perturbations about the equilibrium state obey the linearized equation

$$I\dot{\Omega}_{*1} = -\frac{3}{2}\frac{\dot{M}(\varpi_{\rm m}^2\Omega_{\rm K m})_{\rm eq}}{(1-\xi_{\rm eq}^{\frac{3}{2}})}\left[\xi_{\rm eq}^2 + \frac{1}{(2n+7)\xi_{\rm eq}}\right]\xi_1. \tag{10.13}$$

The perturbation ξ_1 can be related to Ω_{*1} by (10.7) which yields

$$\xi_1 = \frac{14}{3}\left(\frac{1-\xi_{\rm eq}^{\frac{3}{2}}}{7-4\xi_{\rm eq}^{\frac{3}{2}}}\right)\frac{\xi_{\rm eq}}{(\Omega_*)_{\rm eq}}\Omega_{*1}. \tag{10.14}$$

Equations (10.13) and (10.14) show that perturbations about the equilibrium state of Ω_* decay exponentially on the time-scale

$$\tau = \frac{k^2}{7}\left(\frac{\epsilon_{\rm m}}{2\gamma}\right)^{\frac{4}{7}}\frac{\xi_{\rm eq}^{\frac{1}{2}}(7-4\xi_{\rm eq}^{\frac{3}{2}})}{(1-\xi_{\rm eq}^{\frac{3}{2}})^{\frac{4}{7}}}\left[\xi_{\rm eq}^2 + \frac{1}{(2n+7)\xi_{\rm eq}}\right]^{-1}\left(\frac{R}{\varpi_{\rm A}}\right)^2\frac{M}{\dot{M}}, \tag{10.15}$$

and hence the state is stable.

10.3.4 The Approach to Equilibrium

As P evolves, $\xi(P, \dot{M})$ changes and the disc structure evolves through quasi-steady states. The disc temperature distribution is given by (9.119) and the height by (9.115). The magnetic dissipation rate, given by the second term in (9.118), vanishes at $\varpi_{\rm co}$, increases outwards to reach a maximum and then decreases to negligible values for $\varpi \gtrsim 5\varpi_{\rm co}$. The maximum occurs at

$$x_{\rm max} = \left(\frac{n+7}{n+4}\right)^{\frac{2}{3}} x_{\rm co}, \tag{10.16}$$

and the temperature reaches a maximum close to this radius. The temperature maximum increases as ξ approaches $\xi_{\rm eq}$ and this causes a local vertical expansion of the disc close to $x_{\rm max}$. Figure 10.1 shows the temperature distribution for values of ξ approaching $\xi_{\rm eq}$, while Fig. 10.2 shows the corresponding variations of the aspect ratio. The system parameters used are those shown in (10.12), for a typical X-ray binary system.

The temperature and aspect ratio are also calculated for a typical intermediate polar system, having $M = 0.6\,M_\odot$, $R = 7 \times 10^6\,$m, $B_0 = 4 \times 10^2\,$T and $\dot{M} = 10^{-10}\,M_\odot{\rm year}^{-1}$. The results are shown in Figs. 10.3 and 10.4 respectively. There is a significant increase in the temperature maximum as ξ approaches $\xi_{\rm eq}$, but no sharp increase in the aspect ratio. This difference arises because the value of $\varpi_{\rm co}$ in the neutron star case is typically a factor of $\lesssim 10^{-2}$ smaller than in the white dwarf case, with the neutron star magnetic field being a factor of $\gtrsim 5 \times 10^3$ larger

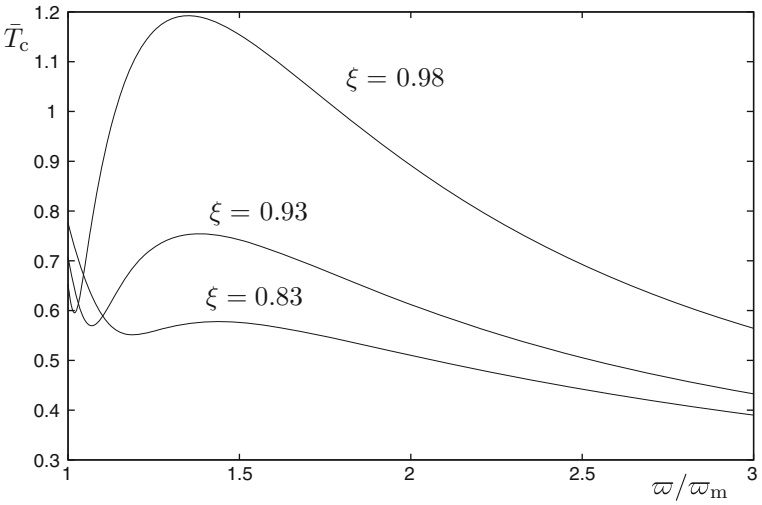

Fig. 10.1 The disc central temperature for a neutron star accretor (from Campbell 2011)

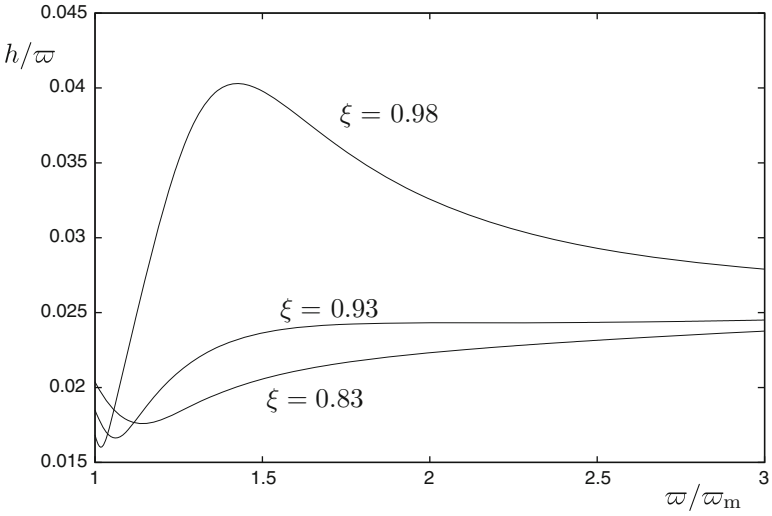

Fig. 10.2 The disc aspect ratio for a neutron star accretor (from Campbell 2011)

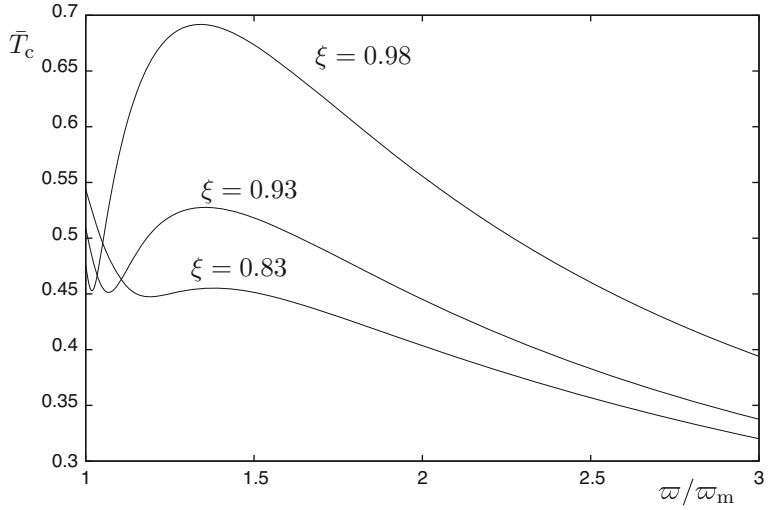

Fig. 10.3 The disc central temperature for a white dwarf star accretor (from Campbell 2011)

in the region of $\varpi_{\rm co}$. The density and temperature are larger in this region of the disc for the neutron star case, and the central plane gas and radiation pressures are larger. Although the vertical component of the stellar gravity is also larger, it is not sufficient to prevent local expansion of the disc. In the white case, the stellar gravity can prevent such expansion in this region.

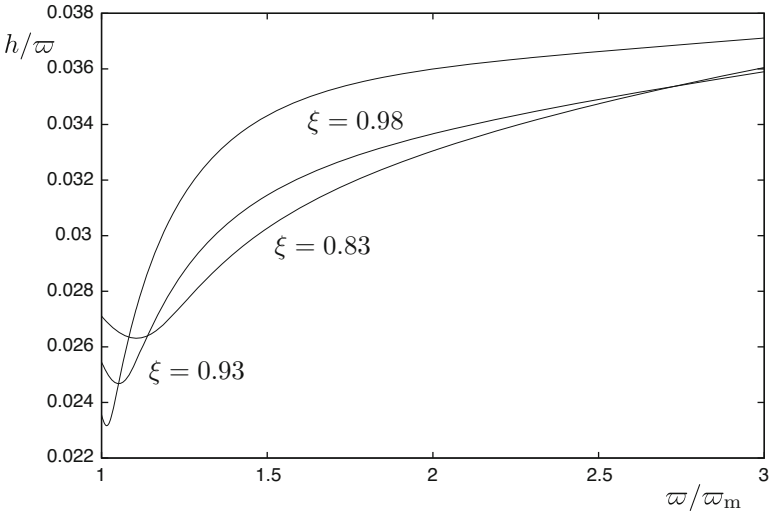

Fig. 10.4 The disc aspect ratio for a white dwarf star accretor (from Campbell 2011)

The local heating and expansion of the disc beyond $\varpi_{\rm co}$, occurring in the neutron star case, may result in some surface mass loss. The consequences of such an outflow, developing as ξ approaches $\xi_{\rm eq}$, can be investigated. The outflow will have an associated small mass loss rate $\delta\dot{M}$ occurring from a narrow region near $\varpi_{\rm max} = x_{\rm max}\varpi_{\rm m}$, with $x_{\rm max}$ given by (10.16). The sharp increase in h/ϖ as $\xi \to \xi_{\rm eq}$, shown in Fig. 10.2, indicates that $\delta\dot{M}$ would be generated on a time-scale significantly shorter than that for reaching equilibrium, given by (10.15). Hence the stellar spin period P would be essentially constant over the development time of $\delta\dot{M}$, but the disc would still have time to adjust its structure quasi-steadily over this time interval. A perturbation in $\xi(P, \dot{M})$ at essentially constant P is related to $\delta\dot{M}$ by

$$\delta\xi = \frac{\partial\xi}{\partial\dot{M}}\delta\dot{M}, \tag{10.17}$$

and (9.129) for ξ yields

$$\frac{\partial\xi}{\partial\dot{M}} = -\frac{2}{3}\frac{C(1-\xi^{\frac{3}{2}})}{\dot{M}(C^2+4C)^{\frac{1}{2}}}. \tag{10.18}$$

Hence $\partial\xi/\partial\dot{M} < 0$ and since $\delta\dot{M} < 0$ it follows from (10.17) that $\delta\xi > 0$.

It is noted that $\xi_{\rm eq}$, given by (10.11), is independent of $\dot{M}$. Before the mass loss occurs ξ will be slightly below $\xi_{\rm eq}$, with a deviation of

$$\xi_1 = \xi(P, \dot{M}) - \xi_{\rm eq} \tag{10.19}$$

and hence $\xi_1 < 0$. As ξ increases towards $\xi_{\rm eq}$ the perturbation $\delta\dot{M}$ will be generated over a time interval $\ll \tau$, where τ is the spin evolution time given by (10.15). The change in $\dot{M}$ causes a short time-scale change of $\delta\xi$ to occur and ξ_1 becomes

$$\xi_1 = \xi(P, \dot{M}) + \delta\xi - \xi_{\rm eq}. \tag{10.20}$$

Since $\delta\xi > 0$, then ξ_1 will become positive if

$$\delta\xi > \xi_{\rm eq} - \xi(P, \dot{M}). \tag{10.21}$$

The stellar torque, given by (10.3), will then become negative and the star will change from a spin-up state to a spin-down state. This is consistent with (10.12) for $P_{\rm eq}$, which shows that a reduction in $\dot{M}$ will cause an increase in the equilibrium period, so the star will then spin down to this new state of torque balance. The period difference δP corresponding to the difference $(\xi_{\rm eq} - \xi)$ is given by

$$\xi_{\rm eq} - \xi(P, \dot{M}) = \frac{\partial\xi}{\partial P}\delta P \tag{10.22}$$

and then (10.10), (10.17) and (10.21) lead to the torque reversal condition

$$\frac{|\delta\dot{M}|}{\dot{M}} > \frac{7}{3}\frac{|\delta P|}{P_{\rm eq}}. \tag{10.23}$$

For periods close to the equilibrium state, only a small reduction in $\dot{M}$ due to mass loss near $\varpi_{\rm max}$ in needed to cause a torque reversal.

10.4 Summary and Discussion

There are various possibilities for the torques that can be exerted on the magnetic star. If η is large enough for the stellar magnetic field lines to remain closed, interaction with the disc leads to positive and negative torques. The accretion curtain flow results in a positive torque. Equilibrium states of zero stellar torque tend to occur with the fastness parameter in the interval $0.8 < \xi_{\rm eq} < 1$, with $\varpi_{\rm m} = \xi\varpi_{\rm co}$. As ξ approaches $\xi_{\rm eq}$ a local expansion of the disc can occur beyond $\varpi_{\rm co}$, for the case of an accreting neutron star. A small mass loss rate from this region can lead to torque reversals. Chakrabarty et al. (1997) found that the X-ray binary pulsar 4U1626-67 showed an abrupt torque reversal in 1990, switching to steady spin-down after 13 years of spin-up. Bildsten et al. (1997), using frequently sampled data, found spin-up and spin-down behaviour over short time-scales in Cen X-3 and other systems. Since the time-scale for reaching the equilibrium state is much shorter than the mass transfer time, it is likely that many of the observed systems are

close to equilibrium. Hence the spin periods will lie in the strong magnetic regime, defined by (9.220) and (9.221).

If the winding ratio $|B_{\phi s}/B_{zs}|$ can become large, due to low η values, then field line opening can occur and reduce the flux linkage to the disc. However, stellar winds flowing along the open field lines can carry angular momentum away and lead to a significant braking torque on the star. Episodic mass ejections from the volume between the stellar and disc regions of open field lines can also result in an effective braking torque on the star. Simulations suggest that torques due to stellar winds and mass ejections may be able to balance the accretion torque. The time dependence of such disc-star states may be related to the observed torque reversals.

The minimum value derived for ξ, given by (9.219), indicates that slower rotation states will not be steady, even in the cases of higher η values, since the mass transfer rates in the disc and curtain flows cannot be balanced for $\xi < \xi_c$.

References

Agapitou, V., Papaloizou, J.C.B., 2000, MNRAS, 317, 273.
Bildsten et al., 1997, ApJS, 113, 367.
Campbell, C.G., 1987, MNRAS, 229, 405.
Campbell, C.G., 1992, GAFD, 66, 243.
Campbell, C.C., 2011, MNRAS, 414, 3071.
Chakrabarty, D., et al., 1997, ApJ, 474, 414.
Matt, S., Pudritz, R.E., 2005, MNRAS, 356, 167.
Romanova, M.M., Ustyugova, G.V., Koldoba, A.V., Lovelace, R.V.E., 2002, ApJ, 578, 420.
Tessema, S.B., Torkelsson, U., 2010, A&A, 509, A45.
Torkelsson, U., 1998, MNRAS, 298, L55.
Wang, Y.M., 1987, A&A, 183, 257.
Wang, Y.M., 1997, ApJ, 475, L135.
Zanni, C., Ferreira, J., 2009, A&A, 508, 1117.
Zanni, C., Ferreira, J., 2013, A&A, 550, A99.

Chapter 11
Intrinsic Magnetism in Accretion Discs

Abstract The generation of magnetic fields in accretion discs is addressed, together with the effects of large-scale magnetic fields on the disc structure. Standard mean-field dynamos are considered, which can generate large-scale magnetic fields in discs. Toroidal magnetic field is generated by the shearing of the radial field, while turbulence with Coriolis force and vertical stratification lead to the α-effect which converts toroidal field to poloidal field. The magnetorotational instability can act as a source of turbulence, since sub-thermal magnetic fields de-stabilize Keplerian disc flows, drawing energy from the differential rotation via the magnetic coupling of fluid elements. The validity of standard dynamo theory is discussed, in the context of this powerful instability. MHD dynamos are considered in connection with disc turbulence generated by the magnetorotational instability. An accretion disc model is then presented, with a large-scale, dynamo generated magnetic field of quadrupolar symmetry, including the determination of the radial and vertical disc structures. Turbulence plays a dual role of contributing to the α-effect in the dynamo and in partly driving the disc inflow via the outward viscous transport of angular momentum.

11.1 Introduction

In a standard cataclysmic binary an accretion disc forms around a non-magnetic white dwarf, and extends down to the stellar surface. The disc is fed by the stream originating from the L_1 region of the secondary star. In a steady state, matter will be transported through the disc at the rate it is supplied by the stream and angular momentum must be transferred outwards. Angular momentum transfer requires coupling between rings of material and, as shown in Sect. 2.4.3, ordinary molecular viscosity is far too weak to provide this. Hence some form of anomalous viscosity must be invoked to explain mass inflow through the disc. The standard accretion disc model of Shakura and Sunyaev (1973) employs a parametrized form of turbulent viscosity to supply the necessary coupling. However, no instability has been found which leads to turbulence in a non-magnetic Keplerian disc.

C. G. Campbell, *Magnetohydrodynamics in Binary Stars*, Astrophysics and Space Science Library 456, https://doi.org/10.1007/978-3-319-97646-4_11

The foregoing situation led to a search for an alternative coupling mechanism to generate the anomalous viscosity in accretion discs. Magnetic fields present the most plausible means of angular momentum transport, through the stresses they exert on material. The possibility of magnetic angular momentum transport was suggested early in the development of accretion disc theory (e.g. Lynden-Bell 1969; Shakura and Sunyaev 1973; Eardley and Lightman 1975; Ichimaru 1977; Coroniti 1981). These models are based on the notion that the disc contains small-scale magnetic cells which are sheared by the differential rotation, resulting in reconnection of oppositely directed fields and a magnetic torque. Such topological dissipation produced by reconnection was discussed by Parker (1972). The associated magnetic field has a turbulent configuration. However, Galeev et al. (1979) and Stella and Rosner (1984) showed that magnetic buoyancy effects should transport the strong toroidal magnetic field vertically through the disc in less than the radial inflow time of material. Hence a dynamo mechanism is required to regenerate the magnetic field. As seen in Sect. 2.3.1, differential rotation creates toroidal magnetic field from poloidal field (the Ω-effect), but an α-effect is required to generate the poloidal field from the toroidal component and give a self-sustaining dynamo. The α-effect might be generated from the magnetic turbulence, but at the time of these early models no mechanism had been found to create such turbulence. Hence such models were subject to the same fundamental dilemma that existed in the non-magnetic turbulent disc model.

Blandford and Payne (1982) developed a model of a hydromagnetic wind from an accretion disc, as a means of removing angular momentum and driving the inflow. This idea has been investigated by subsequent authors and is discussed in Chap. 14. However, the mechanism relies on a source of poloidal field and hence, for binary star discs, is likely to require a dynamo.

A major step towards explaining angular momentum transport in accretion discs was taken by Balbus and Hawley (1991). They showed that a local magnetorotational instability occurs in discs, which have an angular velocity decreasing outwards, in the presence of a sub-thermal magnetic field. The global form of this hydromagnetic instability was discovered by Velikhov (1959) in the context of Couette flow and generalized by Chandrasekhar (1960, 1961). The instability derives its energy from the strong radial shear in the disc. Balbus and Hawley (1991) suggested that this may be a major source of turbulence in accretion discs. Subsequent work confirmed such turbulent generation (e.g. Hawley and Balbus 1991, 1992; Brandenburg et al. 1995; Hawley et al. 1995; Fromang et al. 2007; Davis et al. 2010).

Most studies of the consequences of the magnetorotational instability in accretion discs employ a local box Cartesian model. While all these investigations confirm that turbulence results from the instability, a reliable set of mean field equations to describe the large-scale magnetic field and its sources has yet to be formulated. Tout and Pringle (1992) developed a simple local model of an accretion disc dynamo, incorporating the Balbus-Hawley instability, together with the Parker instability and reconnection. The model gives rise to finite, but non-stationary, magnetic field configurations.

Having established a large-scale, mean magnetic field in the disc by a dynamo mechanism, its effect on angular momentum transport and the large-scale structure of the disc must be investigated. Campbell (1992) constructed a dynamical model of a magnetic accretion disc, incorporating a turbulent $\alpha\Omega$ dynamo. For a buoyancy diffusivity, the magnetic stress dominates the viscous stress in the transport of angular momentum, and only weak turbulence is required for the necessary dynamo α-effect. More general solutions were found by Campbell and Caunt (1999), allowing for a sum of buoyancy and turbulent diffusivities, and a model including vertical structure was presented by Campbell (2003).

Section 11.2 reviews standard $\alpha\Omega$ dynamo theory in thin discs, as a source of large-scale magnetic fields. In Sect. 11.3 the magnetorotational instability is described, in relation to disc turbulence, and hydromagnetic dynamos are discussed. A magnetic disc model is presented in Sect. 11.4, with a field generated by an $\alpha\Omega$ dynamo, including the resulting radial and vertical disc structure.

11.2 Standard Mean-Field Dynamos in Discs

11.2.1 Turbulent αΩ Dynamos in Thin Discs

This section discusses the properties of thin disc, mean-field $\alpha\Omega$ dynamos. It is assumed that some form of turbulence generates the α-effect. It will be shown that the standard mean-field dynamo equations have some consistency issues, related to the nature of the magnetorotational instability. However, in the absence of an alternative set of mean-field equations, the standard equations are still used to derive possible large-scale magnetic fields in accretion discs. These dynamo models have the merit that they can produce magnetic fields with associated stresses which can lead to the angular momentum transport consistent with various disc models. It is possible to compare the simple α-effect with turbulence simulation data, allowing estimates of the associated parameters.

The toroidal and poloidal mean field equations appropriate to an $\alpha\Omega$ dynamo follow from (2.246) and (2.247) as

$$\frac{\partial B_\phi}{\partial t} = \varpi \mathbf{B}_\mathrm{p} \cdot \nabla\Omega + \eta\left(\nabla^2 B_\phi - \frac{B_\phi}{\varpi^2}\right) - \varpi\nabla\cdot\left(\frac{B_\phi}{\varpi}\mathbf{v}_\mathrm{p}\right), \tag{11.1}$$

$$\frac{\partial A}{\partial t} = \alpha B_\phi + \eta\left(\nabla^2 A - \frac{A}{\varpi^2}\right) - \frac{1}{\varpi}\mathbf{v}_\mathrm{p}\cdot\nabla(\varpi A), \tag{11.2}$$

where

$$\mathbf{B}_\mathrm{p} = \nabla\times(A\hat{\boldsymbol{\phi}}), \tag{11.3}$$

and the α terms have been dropped in (11.1) since they are negligible in this regime. In thin disc dynamo models the poloidal advection and compression terms are usually excluded, so the field equations to be solved in the disc are

$$\frac{\partial B_\phi}{\partial t} = \varpi \mathbf{B}_\mathrm{p} \cdot \nabla \Omega + \eta \left(\nabla^2 B_\phi - \frac{B_\phi}{\varpi^2} \right), \tag{11.4}$$

$$\frac{\partial A}{\partial t} = \alpha B_\phi + \eta \left(\nabla^2 A - \frac{A}{\varpi^2} \right). \tag{11.5}$$

It is often reasonable to treat the surrounding medium as a vacuum, giving

$$B_\phi = 0, \tag{11.6}$$

$$\nabla^2 A - \frac{A}{\varpi^2} = 0, \tag{11.7}$$

where (11.6) follows from axisymmetry. Equation (11.3) gives the poloidal field components in terms of the vector potential as

$$B_\varpi = -\frac{\partial A}{\partial z}, \tag{11.8a}$$

$$B_z = \frac{1}{\varpi} \frac{\partial}{\partial \varpi} (\varpi A). \tag{11.8b}$$

These are continuous across the disc surfaces $z = \pm h(\varpi)$, while the continuity of B_ϕ is satisfied by its vanishing on the boundaries.

The basic properties of dynamos in thin galactic discs, formulated by Parker (1971), are relevant to binary star accretion discs. The key idea is that in a thin disc, for which $h(\varpi)/\varpi \ll 1$, solutions of the toroidal and poloidal equations (11.4) and (11.5) should exist which have a radial length-scale long compared to the characteristic disc height. The vertical derivatives therefore dominate in the diffusion terms, and local magnetic Reynolds numbers can be defined as

$$R_\alpha = \frac{h\tilde{\alpha}}{\eta}, \tag{11.9a}$$

$$R_\Omega = \frac{h^2}{\eta} \varpi \frac{d\Omega}{d\varpi}, \tag{11.9b}$$

where Ω is taken as independent of z, and the α-effect is described by the separable form

$$\alpha = \tilde{\alpha}(\varpi) f(\zeta), \tag{11.10}$$

with

$$\zeta = \frac{z}{h}, \tag{11.11}$$

and $f(\zeta)$ antisymmetric. The local dynamo number is given by

$$D = R_\alpha R_\Omega, \tag{11.12}$$

which principally determines the field generation at a given radius.

Parker (1971) considered a thin disc of constant height h and sought local solutions with the separable forms

$$B_\phi = B_0 R_\Omega \bar{B}(\zeta) \exp[i(k\varpi - \omega t)], \tag{11.13}$$

$$A = B_0 h \bar{A}(\zeta) \exp[i(k\varpi - \omega t)], \tag{11.14}$$

where B_0 is a constant, and ζ is the scaled z-coordinate defined by (11.11). Substitution in (11.4) and (11.5) shows that the dimensionless functions $\bar{B}$ and $\bar{A}$ must satisfy the coupled vertical dependence equations

$$\bar{B}'' - (\bar{k}^2 - i\omega^*)\bar{B} = \bar{A}', \tag{11.15}$$

$$\bar{A}'' - (\bar{k}^2 - i\omega^*)\bar{A} = -Df\bar{B}, \tag{11.16}$$

where the primes denote differentiation, while the dimensionless wavenumber and frequency are

$$\bar{k} = hk, \tag{11.17a}$$

$$\omega^* = \tau_{\rm d}\omega, \tag{11.17b}$$

with the vertical diffusion time being

$$\tau_{\rm d} = \frac{h^2}{\eta}. \tag{11.18}$$

The function $f(\zeta)$ occurring in (11.16) is the vertical dependence of α, in accordance with (11.10). Matching the solutions (11.13) and (11.14) to an exterior vacuum field leads to the boundary conditions

$$\bar{B} = 0, \qquad \bar{A}' \pm |\bar{k}|\bar{A} = 0, \quad \text{on} \quad \zeta = \pm 1. \tag{11.19}$$

The foregoing derivations assume that the modes have radial wavelengths satisfying $h \ll \lambda < \varpi$. Such modes will therefore have $\bar{k} \ll 1$. The radial derivatives of R_Ω and k are dropped in obtaining (11.15) and (11.16), the radial diffusion being represented by the $\bar{k}^2$ terms.

Since $f(\zeta)$ is antisymmetric the modes are of two types. The quadrupole modes of even parity have

$$\bar{B}(-\zeta) = \bar{B}(\zeta), \quad \text{and} \quad \bar{A}(-\zeta) = -\bar{A}(\zeta), \tag{11.20}$$

which imply that

$$\bar{B}'(0) = 0 \quad \text{and} \quad \bar{A}(0) = 0. \tag{11.21}$$

The dipole modes of odd parity have

$$\bar{B}(-\zeta) = -\bar{B}(\zeta), \quad \text{and} \quad \bar{A}(-\zeta) = \bar{A}(\zeta), \tag{11.22}$$

giving

$$\bar{B}(0) = 0 \quad \text{and} \quad \bar{A}'(0) = 0. \tag{11.23}$$

The most readily excited modes of a given class are usually of long wavelength, satisfying $\bar{k} \ll 1$. For this reason, Moffatt (1978) proposed the approximation of setting $\bar{k} = 0$ in (11.15), (11.16) and (11.19). For steady modes, these equations then give

$$\bar{B}''' + Df\bar{B} = 0, \tag{11.24}$$

$$\bar{A} = K + \bar{B}', \tag{11.25}$$

where K is a constant. Since (11.24) is a third order equation, the possibility arises that the four boundary conditions on the original fourth order system may be inconsistent. The boundary conditions on the steady quadrupole modes reduce consistently to

$$\bar{B}'(0) = 0, \quad \bar{B}(1) = 0 \quad \text{and} \quad \bar{B}''(1) = 0, \tag{11.26}$$

with $K = 0$. An inconsistency arises for steady dipole modes because four independent boundary conditions emerge for $\bar{B}$. This is overcome by considering a small but finite $\bar{k}$ and using the expansions

$$\bar{A} = \bar{k}^{-1}\bar{A}_{-1} + \bar{A}_0 + O(\bar{k}), \tag{11.27}$$

and

$$\bar{B} = \bar{B}_0 + O(\bar{k}), \tag{11.28}$$

where $\bar{A}_{-1}$ is independent of ζ. At zeroth order $\bar{B}$ is again governed by (11.24). The symmetry conditions (11.23) on $\zeta = 0$ and the vanishing of $\bar{B}$ on $\zeta = 1$ imply that

$$\bar{B}(0) = 0, \quad \bar{B}''(0) = 0, \quad \text{and} \quad \bar{B}(1) = 0, \tag{11.29}$$

while the remaining boundary condition at $\zeta = 1$, given by the second condition in (11.19), yields

$$\bar{A}_{-1} = -\bar{B}_0''(1). \tag{11.30}$$

The dynamo numbers for steady modes with $\bar{k} \ll 1$ can be expanded in the form

$$D = D_0 + D_1\bar{k} + D_2\bar{k}^2 + O(\bar{k}^3), \tag{11.31}$$

where D_0, D_1 and D_2 all have the same sign. The quadrupole and dipole modes have eigenvalues of opposite signs, being negative and positive respectively. At lowest order (11.24) is solved subject to either (11.26), or (11.29), and the eigenvalue problem yields D_0. At first order the radial structure influences the solution via (11.19), which expresses the match of the poloidal disc field to an external potential field. At this order the external field links different parts of the disc. Radial diffusion only becomes effective at second order through the $\bar{k}^2$ terms in (11.15) and (11.16).

Account can be taken of a slowly varying disc height $h(\varpi)$ and WKBJ approximations have been used to allow for the effect of radial disc structure (see Soward 1992a, and references therein). For most dynamo modes in a thin disc the foregoing asymptotic analysis gives reasonable results. It should be noted that the most readily excited oscillatory dipole mode has a radial length-scale comparable to h, so $\bar{k}$ is of order unity for this mode and a different analysis is required (see Soward 1992b).

Simple forms for a turbulent η and the separable radial dependence of α, occurring in (11.10), can be defined as

$$\eta = \epsilon_{\mathrm{T}} c_{\mathrm{s}} h, \tag{11.32}$$

$$\tilde{\alpha} = \epsilon_{\mathrm{T}} c_{\mathrm{s}}, \tag{11.33}$$

with $\epsilon_{\mathrm{T}} = v_{\mathrm{T}}/c_{\mathrm{s}}$, where v_{T} is the rms turbulent speed, so $\epsilon_{\mathrm{T}} < 1$ for subsonic turbulence. For a Keplerian disc, with a vertical equilibrium weakly affected by

B, disc theory gives $c_s = h\Omega_K$ so substitution of (11.32) and (11.33) in (11.9a), (11.9b), and (11.12) yields

$$\left|\frac{R_\alpha}{R_\Omega}\right| = \frac{2}{3}\frac{\tilde{\alpha}}{h\Omega_K} = \frac{2}{3}\epsilon_T, \tag{11.34}$$

$$D = -\frac{3h^3\tilde{\alpha}\Omega_K}{2\eta^2} = -\frac{3}{2\epsilon_T}. \tag{11.35}$$

Taking the turbulent Mach number ϵ_T as independent of ϖ therefore gives a spatially uniform dynamo number in this case. If the turbulent viscosity is $\nu \simeq \eta$, then a viscously driven inflow has $|v_\varpi| \sim \eta/\varpi$. The poloidal advection terms in (11.1) and (11.2) are then of the same order as the radial diffusion terms, and hence are ignorable to a good approximation. This is a consequence of the vertical diffusion time being much shorter than the radial inflow time.

Pudritz (1981) considered dynamo action in a turbulent Keplerian disc. Forms for η and $\tilde{\alpha}$ similar to (11.32) and (11.33) were used, so yielding a uniform D. The total α function was taken as

$$\alpha = \tilde{\alpha}(\varpi)\frac{z}{h}, \tag{11.36}$$

with a constant height h. Separable, steady state solutions of the toroidal and poloidal equations (11.4) and (11.5) were found and matched to the solutions of the vacuum equations, using the properties $\epsilon_T < 1$ and $h/\varpi \ll 1$. The quadrupole solution, for $z > 0$, is

$$B_\varpi = \beta B(\kappa)\lambda^{(1-\kappa^2)/4}e^{-3\lambda/8}\sin\left(\frac{3\sqrt{3}}{8}(\lambda_0-\lambda)+\frac{2\pi}{3}\right)J_1(\kappa^{\frac{1}{2}}s), \tag{11.37}$$

$$B_\phi = B(\kappa)\lambda^{-(1+\kappa^2)/4}e^{-3\lambda/8}\sin\left(\frac{3\sqrt{3}}{8}(\lambda_0-\lambda)\right)J_1(\kappa^{\frac{1}{2}}s), \tag{11.38}$$

$$B_z = -\beta B(\kappa)\lambda^{-\kappa^2/4}e^{-3\lambda/8}\cos\left(\frac{3\sqrt{3}}{8}(\lambda_0-\lambda)-\frac{2\pi}{3}\right)J_0(\kappa^{\frac{1}{2}}s), \tag{11.39}$$

where

$$\beta = \left|\frac{R_\alpha}{R_\Omega}\right|^{\frac{1}{2}}, \tag{11.40a}$$

$$s = |D|^{\frac{1}{4}}\frac{\varpi}{h}, \tag{11.40b}$$

$$\lambda = |D|^{\frac{1}{3}}\left|\frac{z}{h}\right|^{\frac{4}{3}}, \tag{11.40c}$$

$\kappa^{1/2}$ is a dimensionless radial wavenumber, being equivalent to $\bar{k}$ defined by (11.17a), $B(\kappa)$ is the field amplitude and J_0 and J_1 are Bessel functions. These are the most readily excited modes, the critical dynamo number being $D_c = 13.8$. Consistency of the model requires $\kappa^{1/2} < \epsilon_{\mathrm{T}}$.

Stepinski and Levy (1990) considered a Keplerian disc in which

$$\alpha = \tilde{K}\Omega_{\mathrm{K}} z, \tag{11.41}$$

where $\tilde{K}$ is a constant. The magnetic diffusivity was taken as uniform, giving a local dynamo number

$$D = \tilde{D}\left(\frac{h}{\varpi}\right)^3, \tag{11.42}$$

with $\tilde{D}$ constant. The fields were expressed in the forms

$$B_\phi = e^{\gamma t}\sum_{k=1}^{\infty} B_k(z) J_1\left(\alpha_k \frac{\varpi}{R_{\mathrm{D}}}\right), \tag{11.43}$$

$$A = e^{\gamma t}\sum_{k=1}^{\infty} A_k(z) J_1\left(\alpha_k \frac{\varpi}{R_{\mathrm{D}}}\right), \tag{11.44}$$

where R_{D} is the disc radius, J_1 is a Bessel function and, in general, γ is complex. Solutions were sought for which $\Re(\gamma) = 0$, resulting in oscillatory or steady behaviour. Substitution of (11.41)–(11.44) in (11.4) and (11.5), radial integration over the disc using the orthogonality property of J_1 given by (A30), and truncation of the summations at N gives a set of 2N ordinary differential equations containing 2N z-dependent functions. The problem can then be expressed in matrix form with eigenvalues γ, and eigenvectors containing A_n and B_n. The critical values of the global dynamo number, corresponding to $\Re(\gamma) = 0$, yield quadrupole and dipole solutions when the appropriate boundary conditions are applied. Two types of disc surface boundary conditions were used, by considering the surrounding medium to have high or low conductivity.

In the very high conductivity case the field is unable to diffuse beyond the disc, so $\mathbf{B}$ is contained in $|z| < h$. This assumes that no wind flows occur from the disc surfaces, which could allow poloidal magnetic field to extend into the surrounding medium. The steady dipole modes are then the most easily excited. With a contained field, the dipole and quadrupole modes both have a strong component of $\mathbf{B}_{\mathrm{p}}$ across the Keplerian shear surfaces, leading to the generation of B_ϕ in (11.4). However, the dipole mode has its poloidal field lines crossing the central plane, while the quadrupole mode does not. Hence the vertical spatial scale of $\mathbf{B}_{\mathrm{p}}$ in the basic dipole mode is larger than the corresponding scale in the quadrupole mode. The dipole mode is therefore dissipated less rapidly and is the more easily generated mode

in this case. The fields are localized to the inner parts of the disc, this being a consequence of D, given by (11.42), having its largest values in this region. The lowest order mode consists of a single structure centred in the innermost part of the disc. The higher order modes have several structures with the field spreading out further radially.

In the case of a vacuum exterior the steady quadrupole modes are the most easily excited. The field structures are radially localized in a similar way to the dipole modes that were generated with highly conducting surroundings. The result that the quadrupole modes are the most easily excited when the exterior has low conductivity agrees with all the foregoing calculations, which made a variety of assumptions about the spatial variation of the dynamo number D. The reason for this is that with a vacuum exterior the poloidal field lines extend beyond the disc. In a dipole mode $\mathbf{B}_{\rm p}$ is therefore nearly vertical through the disc, and so nearly parallel to the surfaces of Keplerian shear. The shear term $\varpi B_{\varpi}\Omega_{\rm K}'$, which creates toroidal field in (11.4), is consequently small and a relatively high dynamo number is required to sustain the field. Conversely, in a quadrupole mode the lines of $\mathbf{B}_{\rm p}$ do not cross the central plane and hence there is a relatively large B_{ϖ} component crossing the Keplerian shear surfaces, leading to generation of B_{ϕ} via radial shear at lower dynamo numbers.

The magnetic fields generated in this model differ in radial structure to those found in Pudritz (1981), given by (11.37)–(11.39). The difference arises from assumptions made about the spatial variation of the local dynamo number $D(\varpi)$. Pudritz used forms for η and $\tilde{\alpha}$ similar to (11.32) and (11.33) and hence found a uniform D. Stepinski and Levy (1990) assumed the form (11.41) for α, together with constant η, so obtaining $D \propto \varpi^{-3}$. A uniform D produces a field of a global nature, extending radially through the disc. A form $D(\varpi)$ with maximum values produces a field with localized structures. Stepinski and Levy took the inner five percent by radius of their disc to have uniform rotation. $D(\varpi)$ therefore has one maximum near the disc centre, and most of the field is generated in this region.

Stepinski and Levy (1990) did not consider the effects of the disc inflow or the possibility of wind mass loss from the disc surfaces in their dynamo equations and boundary conditions. The inflow will affect the dipole modes and a wind flow is consistent with field lines extending into the surrounding region even when it has high conductivity relative to material in the disc. This changes the nature of the dipole mode field structure. Such a situation will be considered in Chap. 14.

Dynamo action in Keplerian viscous discs was also considered by Rudiger et al. (1995). They took a uniform D and solved the dynamo equations (11.4) and (11.5) numerically. For a vacuum exterior their results agree with those of Pudritz (1981), the steady quadrupole being the most easily excited mode with the field structure extending radially. The case in which the exterior has a magnetic diffusivity satisfying $0 < \eta^{\rm ext} < \eta^{\rm disc}$ was also considered. For $\eta^{\rm ext} = 0.01\eta^{\rm disc}$ the quadrupole modes are still the most readily generated, in fact occurring at lower dynamo numbers than in the vacuum case. The condition $\eta^{\rm ext} \ll 0.01\eta^{\rm disc}$ is required to produce the dipole modes found by Stepinski and Levy (1990) to be the most easily excited in the case $\eta^{\rm ext} \to 0$.

Rudiger et al. (1995) also solved the dynamo equations, for the case with a vacuum exterior, but using an α-quenching term

$$\alpha = \frac{\alpha_0}{1 + (B/B_{\rm eq})^2}, \tag{11.45}$$

where $B_{\rm eq} = (\mu_0 \rho v_{\rm T}^2)^{1/2}$ is an equilibrium magnetic field obtained by equating the turbulent kinetic energy density to the magnetic energy density. The field solution has approximately quadrupolar symmetry, but with a radial structure differing from that of the corresponding normal mode. The magnetic field strength has a radial profile similar to that of $B_{\rm eq}$, having a maximum in the innermost part of the disc. Typically $B \simeq 9 B_{\rm eq}$ through the disc.

After the discovery of the local magnetorotational instability in Keplerian discs, and investigations of its consequences, more recent work has focused on the nature of magnetohydrodynamic dynamos and the effects of large-scale magnetic fields on the disc structure.

11.3 Magnetohydrodynamic Dynamos

11.3.1 Weak Field Shearing Instabilities

Nearly two decades passed from the presentation of the classic disc model of Shakura and Sunyaev (1973) without a satisfactory explanation for the source of the turbulence required to give the enhanced viscosity employed in accretion discs. A mechanism for generating this turbulence was presented by Balbus and Hawley (1991) as the destabilization of the disc flow due to the presence of a subthermal magnetic field. For an angular velocity which decreases outwards, the slow magnetosonic mode becomes unstable, with free rotational energy being transferred to magnetic energy and to turbulence. The instability is local and evanescent. The global form of this magnetorotational instability was discovered by Velikhov (1959) for Couette flow in the presence of a vertical magnetic field and generalized by Chandrasekhar (1960, 1961). However, the relevance of a local form of the instability to turbulent generation in accretion discs was not realized until the work of Balbus and Hawley (1991) showed how it occurs in Keplerian discs and elucidated its basically simple origin.

The basic nature of the instability can be understood by considering a differentially rotating disc containing a vertical magnetic field. In a highly conducting disc a fluid element will be essentially tethered by the magnetic field. If the element is displaced radially outwards the magnetic field will try to keep it rotating with the angular velocity of its ring of origin. Consequently, in its new position the element will not be in centrifugal balance with the radial component of the accretor's gravity. For outwardly decreasing Ω the force imbalance will accelerate the element away from its equilibrium position. There is a restoring force due to the elastic nature of

the magnetic field, but at wavelengths longer than a critical value this is weak and destabilization wins.

Balbus and Hawley (1998) pointed out that the destabilization mechanism is most easily illustrated by considering two fluid elements orbiting in an axisymmetric disc which is threaded by a vertical weak magnetic field. Incompressible linear perturbations are taken having a spatial dependence of $\exp(ikz)$. The components of the displacement $\boldsymbol{\xi}$ then have the coupled equations of motion

$$\ddot{\xi}_\varpi - 2\Omega\dot{\xi}_\phi = -\left[\frac{d\Omega^2}{d\ln\varpi} + (\mathbf{k}\cdot\mathbf{v}_\mathrm{A})^2\right]\xi_\varpi, \tag{11.46}$$

$$\ddot{\xi}_\phi + 2\Omega\dot{\xi}_\varpi = -(\mathbf{k}\cdot\mathbf{v}_\mathrm{A})^2\xi_\phi, \tag{11.47}$$

where

$$\mathbf{v}_\mathrm{A} = \frac{B_0}{(\mu_0\rho)^{\frac{1}{2}}}\hat{\mathbf{z}}. \tag{11.48}$$

As well as being the leading order WKB equations for the local fluid displacement in a magnetic disc, these also describe two orbiting mass elements connected by a light spring with a stiffness constant of $(\mathbf{k}\cdot\mathbf{v}_\mathrm{A})^2$. The two particles are displaced to neighbouring orbits, one to an outer orbit and the other to an inner orbit. The consequent difference in angular velocities stretches the spring and a tension pulls backwards on the inner mass and forwards on the outer mass. Hence the inner mass loses angular momentum while the outer mass gains it. This causes the inner particle to drop to a lower orbit and the outer particle to move to a higher orbit. The widening separation leads to an increased tension and the process runs away. If the spring constant is sufficiently large that the natural oscillation frequency is well above Ω then stability will occur. A sufficiently strong spring constant suggests, from (11.46), the stability condition

$$(\mathbf{k}\cdot\mathbf{v}_\mathrm{A})^2 > -\frac{d\Omega^2}{d\ln\varpi}. \tag{11.49}$$

The equations of motion (11.46) and (11.47) lead to the dispersion relation

$$\omega^4 - [\kappa^2 + 2(\mathbf{k}\cdot\mathbf{v}_\mathrm{A})^2]\omega^2 + (\mathbf{k}\cdot\mathbf{v}_\mathrm{A})^2\left[(\mathbf{k}\cdot\mathbf{v}_\mathrm{A})^2 + \frac{d\Omega^2}{d\ln\varpi}\right] = 0, \tag{11.50}$$

where

$$\kappa^2 = \frac{1}{\varpi^3}\frac{d}{d\varpi}(\varpi^4\Omega^2). \tag{11.51}$$

The condition (11.49) arises formally from the dispersion relation (11.50) as a requirement for the two roots of the quadratic for ω^2 to satisfy $\omega^2 > 0$, so ω is real. For small enough k there will always be instability unless $d\Omega/d\varpi > 0$.

A more formal derivation of the instability was given by Balbus and Hawley (1991) The disc was taken to contain an initially weak poloidal magnetic field, so its dynamical effect on the unperturbed state is negligible. Axisymmetric, large wavenumber linear perturbations were considered which take the form $\exp[i(k_\varpi \varpi + k_z z - \omega t)]$, where the local spatial variations of the components of $\mathbf{k}$ can be ignored since the ϖ and z length-scales of the unperturbed disc structure are long relative to the wavelengths of the perturbations in these directions. Adiabatic perturbations were taken and the Boussinesq approximation was used, which consists of ignoring pressure perturbations in all equations except the momentum equation. The special case of vanishing radial field, B_ϖ, was addressed first.

The linearized equations of momentum, continuity, induction and heat lead to the dispersion relation

$$\frac{k^2}{k_z^2}\sigma^4 - \left[K^2 + \left(\frac{k_\varpi}{k_z}N_z - N_\varpi\right)^2\right]\sigma^2 - 4\Omega^2 k_z^2 v_{Az}^2 = 0, \tag{11.52}$$

where

$$\sigma^2 = \omega^2 - k_z^2 v_{Az}^2, \tag{11.53}$$

$$v_{Az}^2 = \frac{B_z^2}{\mu_0 \rho}, \tag{11.54}$$

$$K^2 = \frac{2\Omega}{\varpi}\frac{d}{d\varpi}(\varpi^2\Omega), \tag{11.55}$$

$$N_\varpi^2 + N_z^2 = -\frac{3}{5\rho}(\nabla P)\cdot[\nabla \ln(P\rho^{-\frac{5}{3}})], \tag{11.56}$$

with B_z, P and ρ denoting unperturbed disc quantities. In a Keplerian accretion disc,

$$\Omega = \Omega_K = \left(\frac{GM_p}{\varpi^3}\right)^{\frac{1}{2}}. \tag{11.57}$$

Then K, given by (11.55), is real. A non-magnetized disc is stable to inviscid adiabatic perturbations if N_ϖ and N_z, given by (11.56), are also real. By solving (11.52) for σ^2, it follows that σ^2 (and hence ω^2) is real. Disc stability can therefore be investigated by considering conditions in the neighbourhood of $\omega^2 = 0$, at which $\sigma^2 = -k_z^2 v_{Az}^2$. In this limit (11.52) becomes

$$(k_z^2 v_{Az}^2 + N_z^2)k_\varpi^2 - 2N_\varpi N_z k_z k_\varpi + k_z^2\left(\frac{d\Omega^2}{d\ln\varpi} + N_\varpi^2 + k_z^2 v_{Az}^2\right) = 0. \tag{11.58}$$

Regarded as a quadratic for k_ϖ, this equation does not allow real solutions, so assuring stability since ω^2 could then not pass through zero, provided the discriminant is negative. This stability condition can be expressed as

$$k_z^4 v_{Az}^4 + k_z^2 v_{Az}^2 \left(N^2 + \frac{d\Omega^2}{d \ln \varpi} \right) + N_z^2 \frac{d\Omega^2}{d \ln \varpi} \geq 0. \tag{11.59}$$

Since $N_z^2 > 0$, the inequality can only be satisfied for all non-vanishing k_z if

$$\frac{d\Omega^2}{d\varpi} \geq 0. \tag{11.60}$$

This is clearly violated in a Keplerian disc, so giving instability for values of k_z less than the critical value yielded from the equality in (11.59) as

$$(k_z)_{\text{crit}} = \frac{1}{v_{Az}} \left| \frac{d\Omega_K^2}{d \ln \varpi} \right|^{\frac{1}{2}} = \sqrt{3} \frac{\Omega_K}{v_{Az}}, \tag{11.61}$$

using $N_z^2 \gg N_\varpi^2$ for a thin disc. The inclusion of a radial field, B_ϖ, in the unperturbed disc does not affect the stability criterion, given by (11.60).

In a thin Keplerian disc $K^2 = \Omega_K^2$ and this term dominates in the coefficient of σ^2 in the dispersion relation (11.52). The unstable root of this equation, together with (11.53) for σ, leads to a time dependence $\exp(\gamma t)$ in which the growth rate is

$$\gamma = \left[-\frac{\Omega_K^2}{2} \frac{k_z^2}{k^2} - k_z^2 v_{Az}^2 + \frac{1}{2} \left(\Omega_K^4 \frac{k_z^4}{k^4} + 16 \Omega_K^2 \frac{k_z^4}{k^2} v_{Az}^2 \right)^{\frac{1}{2}} \right]^{\frac{1}{2}}. \tag{11.62}$$

For $k_z v_{Az} \ll \Omega_K$ first order expansion yields $\gamma \simeq \sqrt{3} k_z v_{Az}$. Differentiation of (11.62) with respect to k_z, using $k_z \gg k_\varpi$, gives a maximum growth rate

$$\gamma_{\max} \simeq \frac{\Omega_K}{\sqrt{2}} \quad \text{at} \quad k_z = \frac{\Omega_K}{v_{Az}}, \tag{11.63}$$

so $\gamma_{\max}$ is independent of the magnetic field. Balbus and Hawley (1998) showed that the magnetorotational instability corresponds to the slow magnetosonic mode becoming unstable. The instability is local and evanescent.

The foregoing analysis ignored dissipative effects. However, for sufficiently small $|B_z|$ the value of $(k_z)_{\text{crit}}$ given by (11.61) will become so large that there will be wavenumbers at which dissipation is important. This value of $|B_z|$ can be estimated for ordinary Ohmic dissipation, with the associated diffusivity

$$\eta_{\text{ohm}} = 5.2 \times 10^7 \ln \Lambda \, T^{-\frac{3}{2}} \, \text{m}^2 \text{s}^{-1}, \tag{11.64}$$

as discussed in Sect. 2.2.11. The dissipation and growth time-scales are

$$\tau_{\rm d} = \frac{4\pi^2}{\eta_{\rm ohm} k_z^2}, \qquad \tau_{\rm g} = \frac{2\pi}{\gamma}. \tag{11.65}$$

Using typical values of $\gamma \sim \Omega_{\rm K}$ and $k_z \sim \Omega_{\rm K}/v_{\rm Az}$, the condition $\tau_{\rm d} \gg \tau_{\rm g}$ for negligible dissipation becomes

$$v_{\rm Az}^2 \gg \eta_{\rm ohm} \frac{\Omega_{\rm K}}{2\pi}, \tag{11.66}$$

which can be expressed as

$$\frac{B_z^2}{2\mu_0 P} \gg \frac{\eta_{\rm ohm}\Omega_{\rm K}}{4\pi c_{\rm s}^2}, \tag{11.67}$$

where $c_{\rm s}^2 = (\mathcal{R}/\mu)T$. Taking $\ln\Lambda = 10$, (11.64) and (11.67) give

$$\frac{B_z^2}{2\mu_0 P} \gg 3.5\times 10^{-9} \left(\frac{M_{\rm p}}{M_\odot}\right)^{\frac{1}{2}} \left(\frac{T}{10^4\,{\rm K}}\right)^{-\frac{5}{2}} \left(\frac{\varpi}{10^8\,{\rm m}}\right)^{-\frac{3}{2}}, \tag{11.68}$$

where $M_{\rm p}$ is the mass of the accreting primary star. This indicates that quite weak initial fields can be considered for which the dissipation associated with the linear instability is ignorable. For $\rho \sim 10^{-6}\,{\rm kg\,m^{-3}}$, (11.68) yields $|B_z| \sim 10^{-6}\,{\rm T}$ for the field below which Ohmic dissipation becomes effective. Similar field values apply to the case of thermal conductivity.

The maximum value of k_z for instability is given by (11.61). A minimum value for k_z is set by the wavelength condition $\lambda_z \lesssim 2h$, where h is the disc scale height, so $(k_z)_{\rm min} \sim \pi/h$. The validity of the local analysis requires $\lambda_z \ll 2h$ and hence $k_z \gg \pi/h$. For a thin Keplerian disc with a weak magnetic field, $h \sim c_{\rm s}/\Omega_{\rm K}$, so the range of k_z for which the local instability is operable is

$$\pi\frac{\Omega_{\rm K}}{c_{\rm s}} \ll k_z < \sqrt{3}\frac{\Omega_{\rm K}}{v_{\rm Az}}. \tag{11.69}$$

This leads to $B_z^2/2\mu_0 P \ll 1$ which can be consistent with the negligible dissipation condition (11.66).

The foregoing derivation of the magnetic shear instability is a local analysis, and used the Boussinesq approximation. Papaloizou and Szuszkiewicz (1992) considered an axisymmetric, compressible, differentially rotating, non self-gravitating fluid containing a poloidal magnetic field. They performed a global stability analysis of axisymmetric, adiabatic modes by formulating a variational principle. The modes have a time dependence $\exp(\sigma t)$ and the self-adjoint nature of the operators leads

to real values for σ^2. Stability therefore requires $\sigma^2 < 0$ and, for a weak magnetic field, this gives the condition

$$\varpi(\mathbf{e}\cdot\nabla\varpi)(\mathbf{e}\cdot\nabla\Omega^2) - \left(\mathbf{e}\cdot\frac{\nabla P}{\rho}\right)\left[\mathbf{e}\cdot\left(\frac{\nabla P}{\Gamma_1 P} - \frac{\nabla\rho}{\rho}\right)\right] \geq 0, \tag{11.70}$$

where $\mathbf{e}$ is an arbitrary vector and the adiabatic exponent Γ_1 is defined by (2.128a). It follows that for $\mathbf{e}$ tangent to surfaces of constant pressure, or of constant entropy, stability requires

$$(\mathbf{e}\cdot\nabla\varpi)(\mathbf{e}\cdot\nabla\Omega^2) \geq 0. \tag{11.71}$$

For a thin disc this condition is essentially the same as (11.60), confirming the Balbus-Hawley result that a Keplerian disc is unstable. Gammie and Balbus (1994) showed that the field magnitude required for stabilization in a global problem may depend on the detailed boundary conditions.

Dubrulle and Knoblock (1993) considered incompressible motions in a thin disc, but allowed the basic state to have azimuthal as well as vertical magnetic field. With the unperturbed velocities $v_\varpi = v_z = 0$, together with $B_\varpi = 0$, the unperturbed Alfvén speeds $v_{A\phi}$ and v_{Az} are necessarily independent of z. Axisymmetric perturbations were considered with the separable form $f(\varpi)\exp[i(k_z z + \sigma t)]$, leading to a second order radial eigenvalue problem. When v_{Az} is constant the sufficient condition for stability becomes

$$\varpi^2\frac{d}{d\varpi}(\Omega^2) - \frac{1}{\varpi^2}\frac{d}{d\varpi}\left(\frac{\varpi^2 B_\phi^2}{\mu_0\rho}\right) \geq 0, \tag{11.72}$$

and this was found not to be sensitive to the boundary conditions imposed. In the weak field limit, this result reduces to (11.60).

11.3.2 Non-linear Development of the Shearing Instability

Balbus and Hawley (1991) pointed out that there are two possible outcomes of the magnetic shearing instability. Firstly, in the absence of sufficient dissipation, the magnetic field will grow to the point where the minimum critical wavelength exceeds the disc scale height. This occurs when the Alfvén and sound speeds are comparable, the magnetic field being left in a dynamically important state but no longer prone to shearing instability. The second, and more likely, possibility is that reconnection dissipates the growing field and a state is reached in which the growth rate of the instability is counterbalanced by dissipation at the smallest scales. Hence classical turbulence results.

Subsequent work strongly supported a turbulent outcome for the hydromagnetic instability. Hawley and Balbus (1991, 1992) performed non-linear simulations in both two and three dimensions. Their local analysis considered unstratified fluid in a box with periodic shearing boundary conditions. For initial conditions appropriate to axisymmetric modes, the three-dimensional case has a period of exponential growth after which the solutions break up into a turbulent state.

Hawley et al. (1995) showed that the magnetic shearing instability also operates in the presence of an irregular magnetic field. This field can sustain self-excited turbulence, even in the absence of vertical stratification. In the fully turbulent state, they found that the $B_\varpi B_\phi$ magnetic stress dominates the viscous stress so angular momentum transport is largely magnetic. Stone et al. (1996) included density stratification and found similar turbulence. They showed that the saturated state is essentially independent of the initial magnetic field geometry. Fromang et al. (2007) performed local box simulations with zero net magnetic flux. The net angular momentum transfer increases with magnetic Prandtl number, and the turbulence vanishes at a minimum value of ν/η.

Numerical simulations of the magnetorotational instability by Brandenburg et al. (1995) gave rise to turbulence with a finite mean helicity. A self-sustaining $\alpha\Omega$ dynamo generates mean magnetic fields, leading to radial angular momentum transport. The turbulence generated in simulations is highly anisotropic, and the microscopic magnetic Prandtl number affects the saturation level of $\mathbf{B}$. This and more recent dynamo simulations are discussed below.

11.3.3 Validity of Standard Mean-Field Dynamos

The discovery of the significance of the magnetorotational instability to accretion disc turbulence has brought into question the validity of the existing theory of mean-field electrodynamics for dynamos. This theory was outlined in Sect. 2.3. The mean field (with the subscript zero now dropped) obeys the equation

$$\frac{\partial \mathbf{B}}{\partial t} = \nabla \times (\mathbf{v} \times \mathbf{B}) + \nabla \times \boldsymbol{\mathcal{E}} - \nabla \times (\eta \nabla \times \mathbf{B}), \tag{11.73}$$

where the electric field

$$\boldsymbol{\mathcal{E}} = \langle \mathbf{v}_\mathrm{T} \times \mathbf{B}_\mathrm{T} \rangle. \tag{11.74}$$

A key assumption made in the standard theory is that the turbulent velocity field can be prescribed independently of the magnetic field, corresponding to a kinematic dynamo in which the magnetic field has a negligible effect on the turbulence. However, as pointed out by Balbus and Hawley (1998), in a fluid the pressure P is the only non-magnetic stress that sets a scale. In the weak field limit of $B^2/2\mu_0 \ll P$, the Alfvén and slow magnetosonic modes become degenerate, and have no

hydrodynamic analog (see Sect. 2.2.6). The dynamical effects of these purely magnetic modes can never be ignored. The weak magnetic field enters the dynamics only via the combination $\mathbf{k} \cdot \mathbf{v}_A$ and this defines a characteristic wavenumber scale of $k \sim \Omega / v_A$ at which magnetic effects become important. Provided that this scale is not small enough for micro resistivity to become dominant, the magnetic tension force is significant. The key assumption that $\mathbf{v}_T$ can be specified independently of $\mathbf{B}$ is then not satisfied.

Blackman (2010) noted that the effects of magnetic helicity should be incorporated in dynamo theory. Large-scale dynamos always involve some helical growth of the large-scale field which is coupled to the helical growth of small-scale fields of opposite sign and/or a compensating helical flux. The large and small-scale helicities obey the evolution equations

$$\frac{\partial}{\partial t}(\mathbf{A} \cdot \mathbf{B}) = 2\boldsymbol{\mathcal{E}} \cdot \mathbf{B} - 2\eta \mathbf{J} \cdot \mathbf{B} - \nabla \cdot \left(2\Psi \mathbf{B} + \mathbf{A} \times \frac{\partial \mathbf{A}}{\partial t} \right), \tag{11.75}$$

$$\frac{\partial}{\partial t}(\langle \mathbf{a} \cdot \mathbf{b} \rangle) = -2\boldsymbol{\mathcal{E}} \cdot \mathbf{B} - 2\eta \langle \mathbf{j} \cdot \mathbf{b} \rangle - \nabla \cdot \left(2\langle \psi \mathbf{b} \rangle + \left\langle \mathbf{a} \times \frac{\partial \mathbf{a}}{\partial t} \right\rangle \right), \tag{11.76}$$

where $\mathbf{a}$ and $\mathbf{A}$ are the small and large-scale vector potentials, while ψ and Ψ are the small and large-scale electric potentials. The growth of the large-scale field involves a finite $\boldsymbol{\mathcal{E}} \cdot \mathbf{B}$, which provides an equal and opposite source term for the large and small-scale magnetic helicities as shown by (11.75) and (11.76). Standard mean-field theory has focused on the large-scale equation (11.75), but does not use the coupled equation (11.76) for the small-scale helicity.

More recent dynamo theory takes an α-function as

$$\alpha = \alpha_{\mathrm{kin}} + \alpha_{\mathrm{mag}} = -\frac{1}{3}\tau [\langle \mathbf{v}_T \cdot \nabla \times \mathbf{v}_T \rangle - \langle \mathbf{b} \cdot \nabla \times \mathbf{b} \rangle], \tag{11.77}$$

where Alfvén unit scalings are used to make the equation dimensionless (see Blackman and Field 2004). The time evolution of α is directly coupled to the evolution of the magnetic helicity. If $\mathbf{A} \cdot \mathbf{B}$ grows initially from α_{kin} then $\langle \mathbf{a} \cdot \mathbf{b} \rangle$ grows with an opposite sign which quenches α.

The formulation of a set of mean-field equations which incorporate the magnetorotational instability is a formidable and, as yet, unsolved problem. Most information regarding the consequences of magnetically driven turbulence in accretion discs has been derived from local box simulations, using various boundary conditions. These can provide data which can be used to estimate α.

11.3.4 Magnetohydrodynamic Dynamos

Studies of magnetohydrodynamic dynamos in accretion discs, which incorporate the magnetorotational instability, have made been developed using semi-analytic and numerical methods.

Tout and Pringle (1992) developed a model for a magnetic accretion disc dynamo. The dynamo mechanism depends on the Balbus-Hawley instability, together with the Parker buoyancy instability and reconnection. The authors concentrate on a local description of the physical mechanisms involved, rather than on detailed spatial dependences. Their toroidal induction equation is

$$\frac{dB_\phi}{dt} = \frac{3}{2}\Omega_{\rm K} B_\varpi - \frac{B_\phi}{\tau_{\rm P}}. \tag{11.78}$$

This is the standard form for this equation, the toroidal field being created by the radial shearing of poloidal field and diffused, in this case by the Parker instability. The origin of this instability was discussed in Sect. 2.2.11, and the corresponding magnetic diffusivity is given by (2.242). The Parker diffusion time is therefore

$$\tau_{\rm P} = \frac{h}{\xi v_{{\rm A}\phi}}, \tag{11.79}$$

where h is the vertical scale height, $v_{{\rm A}\phi} = |B_\phi|/(\mu_0\rho)^{1/2}$, and $\xi < 1$.

The Balbus-Hawley instability creates radial field from vertical and Parker magnetic buoyancy diffuses the radial field. The radial equation, averaged over wavenumbers, was taken to be

$$\frac{dB_\varpi}{dt} = \bar{\gamma}_{\rm max}\Omega_{\rm K} B_z - B_\varpi/\tau_{\rm P}, \quad v_{{\rm A}z}/c_{\rm s} \le \sqrt{2}/\pi, \tag{11.80a}$$

$$\frac{dB_\varpi}{dt} = \bar{\gamma}_{\rm BH}\Omega_{\rm K} B_z - B_\varpi/\tau_{\rm P}, \quad \sqrt{2}/\pi < v_{{\rm A}z}/c_{\rm s} \le \sqrt{6}/\pi, \tag{11.80b}$$

$$\frac{dB_\varpi}{dt} = -B_\varpi/\tau_{\rm P}, \quad v_{{\rm A}z}/c_{\rm s} > \sqrt{6}/\pi, \tag{11.80c}$$

where

$$\bar{\gamma}_{\rm BH} = \bar{\gamma}_{\rm max}\left[1 - \frac{(1 - \pi v_{{\rm A}z}/\sqrt{2}c_{\rm s})^2}{(1-\sqrt{3})^2}\right]^{\frac{1}{2}}, \tag{11.81}$$

and $\bar{\gamma}_{\max} \sim 0.71$. Equation (11.80a) arises when the wavelength of the fastest growing mode of the Balbus-Hawley instability is $\lesssim 2h$. From (11.63) this mode has a vertical wavelength

$$\lambda_z^{\max} = \frac{2\pi v_{Az}}{\Omega_K}, \tag{11.82}$$

where $v_{Az} = |B_z|/(\mu_0\rho)^{1/2}$. It then follows from (11.61) that

$$\lambda_z^{\max} = \sqrt{3}\lambda_z^{\text{crit}}, \tag{11.83}$$

where the instability is cut off when $\lambda_z < \lambda_z^{\text{crit}}$. Hence in this first case the range of unstable wavelengths is $\lambda_z^{\max}/\sqrt{3} \leq \lambda_z \leq \lambda_z^{\max}$, with $\lambda_z^{\max} \lesssim 2h$. The unstable modes therefore all have growth rates near the maximum value of $\sim \bar{\gamma}_{\max}\Omega_K$, this being taken as the average value in equation (11.80a). The associated inequality $v_{Az}/c_s \lesssim \sqrt{2}/\pi$ arises from $\lambda_z^{\max} \lesssim 2h$, together with the assumption of an isothermal vertical structure which yields $h\Omega_K = \sqrt{2}c_s$. Equation (11.80b) gives the intermediate regime, while (11.80c) arises when $\lambda_z^{\text{crit}} \lesssim 2h$, so there are no unstable wavelengths in the disc and the generation of B_ϖ ceases. Equation (11.81) is an analytic fit to the results of Balbus and Hawley (1991).

The vertical equation was taken as

$$\frac{dB_z}{dt} = \frac{B_\phi}{\tau_P} - \frac{B_z}{\tau_{\text{rec}}}. \tag{11.84}$$

The Parker instability creates B_z from B_ϕ, while reconnection dissipates B_z. The reconnection time-scale is

$$\tau_{\text{rec}} = \frac{\lambda_{\text{rec}}}{\Gamma v_{Az}}, \tag{11.85}$$

where λ_{rec} is the mean distance between patches of B_z of opposite sign and $\Gamma^{-1} \sim \ln R_m$, with R_m the magnetic Reynolds number.

The authors first investigated the linear stability of the trivial solution $\mathbf{B} = \mathbf{0}$. They found this solution to be unstable with a growth time of order $(2/3)\Omega_K^{-1}$. An equilibrium solution with finite $\mathbf{B}$ was then sought. The growth terms for B_ϕ and B_ϖ involve the time-scale Ω_K^{-1}, whereas the loss terms involve the larger time-scales τ_P and τ_{rec}. Equilibrium can therefore only occur when the growth of B_ϖ via the Balbus-Hawley instability is inhibited by the presence of strong B_z. The equilibrium solution has $B_\phi^2/2\mu_0 \sim P$ and is shown to be overstable.

The non-linear evolution of the dynamo was investigated using numerical integration. In all cases the magnetic field remains finite, but oscillates about the equilibrium state. The cycle is largely controlled by how far B_z is from equilibrium. For weaker B_z the Balbus-Hawley instability leads to a rapid growth of B_ϖ, and a slower growth of B_ϕ. These lead to growth in B_z towards equilibrium and then B_ϖ

and B_ϕ decay, followed by B_z. Although B_ϖ and B_ϕ escape from the disc on the time-scale $\tau_{\rm P} \sim 4\Omega_{\rm K}^{-1}$, B_ϖ is converted to B_ϕ on the shear time-scale of $\sim 0.7\Omega_{\rm K}^{-1}$. Hence in equilibrium $B_\phi \sim 6B_\varpi$.

Brandenburg et al. (1995) used numerical methods to simulate the non-linear evolution of magnetized Keplerian shear flows in a local, three-dimensional model, including compressibility and stratification. The Balbus-Hawley instability was found to generate motions which regenerate a turbulent magnetic field which, in turn, reinforces the turbulence.

Local Cartesian coordinates (x, y, z) were used, with origin at a cylindrical radius ϖ_0 and unit vectors $\hat{\mathbf{x}} = \hat{\boldsymbol{\varpi}}$, $\hat{\mathbf{y}} = \hat{\boldsymbol{\phi}}$. The origin was taken to have the angular velocity $\Omega_0 = \Omega_{\rm K}(\varpi_0)$ so, to linear order, the Keplerian shear flow in this frame is

$$v_y^0(x) = -\frac{3}{2}\Omega_0 x. \tag{11.86}$$

The equations of momentum, induction, continuity and heat were solved in a local box to obtain the deviations, $\mathbf{v}$, from this flow. Equation (11.86) is consistent with no systematic variation of quantities with x, since only $dv_y^0(x)/dx$ occurs in the governing equations. A standard form was adopted for the viscous force, and the perfect gas equation was used. A simple form for the cooling rate was taken as

$$Q = -\Omega_0(E - E_0), \tag{11.87}$$

where

$$E = \frac{P}{(\gamma - 1)\rho} \tag{11.88}$$

is the thermal energy per unit mass, with E_0 its initial value. An initial isothermal stratification was assumed and the insulating boundary condition $\partial E/\partial z = 0$ at $z = \pm h$ was employed.

The velocity was taken to obey stress-free conditions at the upper and lower boundaries, so

$$\frac{\partial v_x}{\partial z} = \frac{\partial v_y}{\partial z} = v_z = 0 \quad \text{at} \quad z = \pm h. \tag{11.89}$$

The magnetic field was taken to be purely vertical at these boundaries. Using $\mathbf{B} = \nabla \times \mathbf{A}$, then gives the surface conditions $B_x = B_y = 0$ in terms of the vector potential as

$$\frac{\partial A_x}{\partial z} = \frac{\partial A_y}{\partial z} = 0 \quad \text{and} \quad A_z = 0 \quad \text{at} \quad z = \pm h. \tag{11.90}$$

Periodic boundary conditions were adopted in the y-direction. The quasi-periodic condition

$$F(\Delta x, y, z) = F(0, y + \frac{3}{2}\Omega_0 t \Delta x, z) \tag{11.91}$$

was used for any quantity on the radial boundaries, where Δx is the radial extent of the box. This sliding condition accounts for the effect of the Keplerian shear in the y-direction. The horizontal boundary conditions lead to vanishing vertical flux, since

$$\int\int B_z dx dy = \int_0^{\Delta y} \left[A_y\right]_0^{\Delta x} dy - \int_0^{\Delta x} \left[A_x\right]_0^{\Delta y} dx = 0. \tag{11.92}$$

This enables the field to decay to zero if the motions become too weak to sustain it.

The governing equations were solved using sixth-order compact derivatives, and a third-order Hyman scheme for the time-stepping (Nordlund and Stein 1990). Random velocity perturbations are taken, with an initial Mach number of $v_{\rm rms}/c_{\rm s} = 0.002$. The initial field was taken to be $\mathbf{B} = B_0 \sin(2\pi x/\Delta x)\hat{\mathbf{z}}$ with B_0 satisfying $2\mu_0 P/B_0^2 = 100$.

The Balbus-Hawley magnetic shear instability generates turbulence. Energy flows from the Keplerian motion into both magnetic and turbulent kinetic energies in the ratio of $\sim$ 6 to 1. However, the energy transfer rates (=energy flux/energy content) into these two reservoirs are approximately equal at $\sim$ $0.3\Omega_{\rm K}$. The Lorentz force pumps half this magnetic energy into turbulent kinetic energy. Hence three-quarters of the energy going from the Keplerian motion into turbulence first passes through a phase of magnetic energy. The magnetic and turbulent energies are subsequently dissipated and heat the disc. Poloidal magnetic field is regenerated at a rate of $\sim 0.6\Omega_0$, comparable to the growth rate of the magnetic shear instability.

The large-scale toroidal magnetic field is mainly of quadrupolar parity, and exhibits cyclic behaviour. The ratio of the mean magnetic energy density to the thermal energy density is $B^2/2\mu_0 P \lesssim 0.1$. The dynamo α-function was found to be negative for $0 < z < h$, contrary to standard theory which uses the Parker instability and Coriolis force to generate α. As discussed in Brandenburg and Donner (1997), the reason for this sign difference appears to be the strong effect of the magnetic shear instability. Oscillatory quadrupole modes are then favoured, but the average value of $B_\varpi B_\phi$ is still negative, as required for outward radial transport of angular momentum.

The standard inner boundary condition of vanishing torque, described in Sect. 2.4.4, leads to the stress equation

$$\left\langle \rho v'_\varpi v'_\phi - \frac{1}{\mu_0} B'_\varpi B'_\phi \right\rangle = -\rho \nu \varpi \frac{d\Omega_{\rm K}}{d\varpi}, \tag{11.93}$$

where primes denote turbulent components and the radial integration constant can be ignored for $\varpi \gg R_{\rm p}$, with $R_{\rm p}$ the radius of the accretor. In the Shakura-Sunyaev model the turbulent viscosity coefficient is expressed as

$$\nu = \epsilon_{\rm T} c_{\rm s} h, \tag{11.94}$$

with $\epsilon_{\rm T} < 1$. The value of $\epsilon_{\rm T}$ found here fluctuates in time, with a mean value of $\epsilon_{\rm T} \sim 10^{-2}$. Brandenburg et al. (1996) derived a parabolic fit for $\epsilon_{\rm T}$ of the form

$$\epsilon_{\rm T} \simeq \epsilon_0 + \epsilon_B \frac{B_\phi^2}{B_{\rm eq}^2}, \tag{11.95}$$

where $B_{\rm eq} = (\mu_0 \rho c_{\rm s}^2)^{1/2}$ is the equipartition field with respect to the thermal energy density and $\epsilon_B \simeq 0.5$.

The numerical simulations are consistent with a dynamo α-function above the central plane of

$$\alpha \simeq -5 \times 10^{-3} \Omega_{\rm K} h. \tag{11.96}$$

The turbulent magnetic diffusivity is

$$\eta_{\rm T} \simeq 8 \times 10^{-3} \Omega_{\rm K} h^2. \tag{11.97}$$

The ratio of field components is typically $|B_\varpi / B_\phi| \sim 10^{-2}$, characteristic of an $\alpha\Omega$-type dynamo.

Ogilvie (2003) constructed covariant evolution equations for the mean Reynolds and Maxwell tensors, including a linear interaction with the mean flow. Nonlinear and dissipation effects were modelled. The model explains the development of statistically steady anisotropic turbulent stresses, using a local representation of a differentially rotating disc. This agrees with the main results of local box simulations.

Gressel (2010) also considered a local box model with zero net flux, but with vertical stratification. A direct dynamo results from the magnetorotational instability, but an indirect dynamo effect also appears related to the Parker instability and buoyancy. The current helicity appears to play an important role in the dynamo process. Davis et al. (2010) showed that vertical stratification leads to the convergence of the turbulent energy density and stresses with increasing resolution. The horizontal magnetic field has cyclic behaviour, with a period of about 10 orbits. Including vertical stratification extends the range of the magnetic Prandtl number for which turbulent generation occurs.

Beckwith et al. (2011) performed global simulations for a thin disc, using an initially strong toroidal magnetic field. The fastest growing magnetorotational modes are well resolved and the system loses memory of the initial conditions. The

largest scales within the turbulence are controlled by the density and the effective turbulent viscosity parameter was found to be $\epsilon_{\mathrm{T}} \sim 2.5 \times 10^{-2}$.

Gressel and Pessah (2015) performed vertically stratified shearing box simulations and found a dynamo scaling separation of ~ 10. The α and η functions were found to scale linearly with the shear rate, and the model gives support to the $\alpha\Omega$ mechanism in discs.

Improved numerical techniques should allow further progress to be made in our understanding of the nature of magnetohydrodynamic dynamos operating in accretion discs. The development of global models is particularly important.

11.4 Disc Structure with Large-Scale Magnetic Fields

11.4.1 Background

Having established that magnetohydrodynamic dynamos can generate large-scale magnetic fields in discs, the effects of such fields needs to be investigated. Large-scale magnetic stresses can transport angular momentum in discs and hence provide a means of driving the inflow. Dipolar symmetry fields can only exert torques on disc rings if the $B_\phi B_z$ stress is finite at the disc surface. For an axisymmetric, steady disc surrounded by a vacuum B_ϕ vanishes at the surface and hence there will be zero net torque with a dipole symmetry field. However, if a wind emanates from the disc surface the conducting surroundings will give a finite $B_{\phi \mathrm{s}}$ and there will be a net torque with angular momentum carried away from the disc by the wind, so driving an inflow. This case is considered in detail in Chap. 14.

With a quadrupole magnetic field the $B_\varpi B_\phi$ stress can cause an outward radial transport of angular momentum, even for vacuum surroundings. Since a self-sustaining dynamo requires turbulence, there will also be a viscous torque on disc rings. The relative contributions of the magnetic and viscous torques is of central interest, as is the effect of the magnetic field on the disc structure. Because a mean field induction equation that self consistently incorporates the effects of the magnetorotational instability does not at present exist, the standard mean field dynamo equations are used to find field solutions. It will be seen that an $\alpha\Omega$ dynamo can generate large-scale magnetic fields leading to stresses which play a major part in driving the inflow. The Ω-effect, described by the $\mathbf{B}_{\mathrm{p}} \cdot \nabla\Omega$ term in the induction equation, has a rigorous basis but, as discussed previously, the α-effect due to turbulence has yet to have a completely consistent formulation. Nevertheless, parametrized forms for α allow solutions to the found for the magnetic field which can be used with the magnetohydrodynamic equations to find disc solutions corresponding to physically consistent structures. It will be shown that the magnetic fields generated by an $\alpha\Omega$ dynamo naturally lead to the required angular momentum transport and energy dissipation in the disc.

The α function is required to be antisymmetric about the disc mid-plane, but its sign above and below this plane is still not rigorously established. The case of $\alpha > 0$ for $z > 0$ will be considered here since this leads to steady quadrupolar symmetry magnetic field solutions. The case of $\alpha < 0$ for $z > 0$ tends to facilitate oscillatory quadrupolar and steady dipolar solutions. The period of oscillatory solutions is much shorter than the inflow time through the disc, so the inflow in this case will be essentially driven by the time average over an oscillation period of the $B_\varpi B_\phi$ stress. Hence, quadrupolar solutions are of relevance to both cases for the sign of α, but the simplest solutions result for the case of $\alpha > 0$ for $z > 0$ and these will be considered here.

Most studies of the effects of an intrinsic magnetic field on the disc have either taken vertical averages and focused on the radial structure (e.g. Campbell 1992; Rudiger et al. 1995; Campbell and Caunt 1999) or ignored the radial structure and calculated local vertical dependences (e.g. Rudiger and Shalybkov 2002). Parametric forms of turbulent and magnetic buoyancy diffusivities have been considered. In Campbell (2003) a solution was found for the radial and vertical structures of the disc, with a quadrupolar magnetic field generated by an $\alpha\Omega$ dynamo. The formulation below is based on this work.

11.4.2 Magnetic Disc Equations

A steady axisymmetric disc is considered around an accretor of mass M and radius R. For a thin disc self-gravity is ignorable, and the star is assumed to have a negligible magnetic field. The surroundings are taken to be a vacuum. Cylindrical coordinates (ϖ, ϕ, z) are used, centred on the star. For a thin disc the ratio h/ϖ is small and here the frequently occurring ratio of $(B_\varpi / B_\phi)^2$ is also small. These two small ratios can be used to simplify the equations.

Firstly, the ϖ-component of the momentum equation can be considered. As in the standard viscous disc, the subsonic poloidal velocity component terms are small relative to the stellar gravity term and the radial thermal pressure gradient is also ignorable. The radial magnetic force terms are small and hence the stellar gravity balances the centrifugal force to give a Keplerian angular velocity distribution of

$$\Omega = \Omega_{\rm K} = \left(\frac{GM}{\varpi^3} \right)^{\frac{1}{2}}, \tag{11.98}$$

where $\Omega = v_\phi / \varpi$. This is applicable down to the outer edge of a boundary layer at $\varpi = R + \delta$, of width $\delta \ll R$, through which Ω decreases to the stellar value of Ω_* so accretion can occur.

The continuity equation can be written as

$$\frac{\partial}{\partial \varpi}(\varpi \rho v_\varpi) + \frac{\partial}{\partial z}(\varpi \rho v_z) = 0. \tag{11.99}$$

Vertically integrating this equation between $-z$ and z, using the antisymmetry of v_z, gives

$$\frac{\partial}{\partial \varpi}\left(\varpi \int_{-z}^{z} \rho v_\varpi dz\right) = -2\varpi \rho v_z. \tag{11.100}$$

Since $v_z \ll |v_\varpi|$ and ρ decreases vertically, the vertical mass flux is ignorable relative to the radial mass flow. The radial derivative is then zero and a ϖ-independent mass flow rate is given by

$$\dot{M}(z) = -2\pi \int_{-z}^{z} \varpi \rho v_\varpi dz. \tag{11.101}$$

Combining the continuity equation, with the ρv_z term being ignorable, with the ϕ-component of the momentum equation yields the angular momentum equation

$$\frac{\partial}{\partial \varpi}\left(\varpi \rho v_\varpi \varpi^2 \Omega\right) = \frac{\partial}{\partial \varpi}\left(\rho \nu \varpi^3 \frac{\partial \Omega}{\partial \varpi}\right) + \frac{\partial}{\partial \varpi}\left(\frac{1}{\mu_0} \varpi^2 B_\varpi B_\phi\right), \tag{11.102}$$

relating the divergence of the radial angular momentum flux to the viscous and magnetic torques. The term involving $B_\phi B_z$ has been dropped, since it is small relative to the $B_\varpi B_\phi$ term for a quadrupolar field.

The poloidal velocity terms and the magnetic force term involving B_ϖ^2 are small in the vertical component of the momentum equation, which therefore reduces to

$$\Omega_\kappa^2 z \rho + \frac{\partial}{\partial z}\left(P + \frac{B_\phi^2}{2\mu_0}\right) = 0. \tag{11.103}$$

The magnetic pressure gradient reinforces the thermal pressure gradient, since B_ϕ^2 decreases with increasing $|z|$, giving forces that balance the vertical component of the stellar gravity.

The induction equation, with a standard α term, describes the generation of magnetic field in the disc. The toroidal and poloidal components of this equation are given by (11.1) and (11.2), together with (11.3) which relates $\mathbf{B}_\mathrm{p}$ to A. Noting that the poloidal advection terms and the radial derivatives in the diffusion terms are small, and that $\partial \Omega / \partial z = 0$, the poloidal and toroidal components reduce to

$$\eta \frac{\partial B_\varpi}{\partial z} = \alpha B_\phi, \tag{11.104}$$

and

$$\eta \frac{\partial^2 B_\phi}{\partial z^2} = -\varpi B_\varpi \Omega_\kappa', \tag{11.105}$$

noting that the vector potential A has been eliminated here in terms of B_ϖ. The poloidal equation (11.104) gives the balance between the creation of B_ϖ from B_ϕ via the α process, and its vertical diffusion. The toroidal equation (11.105) expresses the balance between the creation of B_ϕ by the winding of B_ϖ, due to radial shearing, and its vertical diffusion.

The advection of heat in the disc is small, so the steady thermal energy equation relates the divergence of the radiative flux to the energy generation rate per unit volume. The vertical derivative term dominates in the divergence, and the radial component of the current density gives the main contribution to the magnetic dissipation. Hence the thermal balance is

$$\frac{\partial F_{\mathrm{R}}}{\partial z} = \rho\nu\left(\varpi\Omega_{\mathrm{K}}'\right)^2 + \frac{\eta}{\mu_0}\left(\frac{\partial B_\phi}{\partial z}\right)^2. \tag{11.106}$$

For an optically thick disc the radiative heat flux is

$$F_{\mathrm{R}} = -\frac{4\sigma_{\mathrm{B}}}{3\kappa\rho}\frac{\partial}{\partial z}\left(T^4\right), \tag{11.107}$$

with the Rosseland mean opacity taken to have a Kramers form

$$\kappa = \bar{K}\rho T^{-\frac{7}{2}}, \tag{11.108}$$

where $\bar{K}$ is a constant.

Accretion discs are considered in which the radiation pressure is small and the gas equation of state is

$$P = \frac{\mathcal{R}}{\mu}\rho T, \tag{11.109}$$

with μ the mean molecular weight.

11.4.3 Magnetic Field Generation

Taking η to be independent of z and combining the induction equation components (11.104) and (11.105) to eliminate B_ϖ yields the dynamo equation

$$\frac{\partial^3 B_\phi}{\partial z^3} + \frac{\varpi\Omega_{\mathrm{K}}'\alpha}{\eta^2}B_\phi = 0. \tag{11.110}$$

The function $\alpha(\varpi, z)$ must be antisymmetric in z and local box simulations of magnetorotational instability induced turbulence suggest that $\alpha < 0$ for $z > 0$ may

apply (e.g. Brandenburg and Campbell 1997; Brandenburg and Donner 1997). This can lead to an oscillatory quadrupole magnetic field with a period of

$$P_{\rm m} \simeq \left(\frac{\Omega_{\rm K} h}{|\alpha|}\right)^{\frac{1}{2}} \frac{2\pi}{\Omega_{\rm K}}. \tag{11.111}$$

This typically gives

$$P_{\rm m} \simeq \frac{\varpi}{|v_\varpi|}\left(\frac{h}{\varpi}\right)^2 = \left(\frac{h}{\varpi}\right)^2 \tau_v, \tag{11.112}$$

where τ_v is the inflow time-scale. Hence $P_{\rm m} \ll \tau_{\rm v}$ so the magnetic field will oscillate many times as matter flows through the disc. It follows that it will be the average over a period $P_{\rm m}$ of the magnetic stress $B_\varpi B_\phi$ that effectively drives the inflow. For simplicity, $\alpha > 0$ for $z > 0$ is taken and steady quadrupolar fields result. This will represent the situation with $\alpha < 0$ for $z > 0$ with a time averaged magnetic stress for an oscillatory quadrupolar field.

The α function is taken to have the separable form

$$\alpha(\varpi, z) = \tilde{\alpha}(\varpi)\zeta = \epsilon c_{\rm s}\zeta, \tag{11.113}$$

where

$$\zeta = \frac{z}{h} \tag{11.114}$$

and $\epsilon < 1$ is a rms turbulent Mach number with

$$c_{\rm s} = \left(\frac{P_{\rm c}}{\rho_{\rm c}}\right)^{\frac{1}{2}} = \left(\frac{\mathcal{R}}{\mu} T_{\rm c}\right)^{\frac{1}{2}} \tag{11.115}$$

being the isothermal sound speed in the mid-plane.

A turbulent magnetic Reynolds number can be defined as

$$N_\alpha = \frac{\tilde{\alpha} h}{\eta} \tag{11.116}$$

and is taken as constant. This is consistent with defining a turbulent magnetic Prandtl number as

$$N_{\rm p} = \frac{\nu}{\eta} \tag{11.117}$$

where ν is the turbulent viscosity. It then follows that

$$\eta = \frac{\epsilon_{\rm T}}{N_\alpha} c_{\rm s} h \tag{11.118}$$

and

$$\nu = \frac{\epsilon_{\rm T} N_{\rm p}}{N_\alpha} c_{\rm s} h, \tag{11.119}$$

corresponding to the turbulent viscosity having a standard parametrized form for $N_{\rm p}$ constant.

The toroidal magnetic field can be expressed in the separated form

$$B_\phi(\varpi, z) = B_{\phi{\rm c}}(\varpi) f_\phi(\zeta), \tag{11.120}$$

with $B_{\phi{\rm c}}(\varpi) = B_\phi(\varpi, 0)$, $0 \le \zeta \le 1$ and

$$f_\phi(0) = 1. \tag{11.121}$$

Using (11.113), (11.114) and (11.120) for α, ζ and B_ϕ in the toroidal field equation (11.110) yields

$$f_\phi''' - |K|^3 \zeta f_\phi = 0 \tag{11.122}$$

with

$$K^3 = -\frac{3}{2} \frac{N_\alpha^2}{\epsilon} \frac{\Omega_{\rm K} h}{c_{\rm s}} \tag{11.123}$$

being the dynamo number. The dimensionless quantity $|K|$ can be written as $|K| = h/\ell_z$, where ℓ_z is the vertical length-scale of $\mathbf{B}$ in the disc. Self-consistent, steady disc solutions result for K constant, corresponding to $\Omega_{\rm K} h/c_{\rm s}$ being independent of ϖ as in the standard viscous disc. Equation (11.122) must be solved for $f_\phi(\zeta)$ subject to appropriate boundary conditions.

A quadrupolar symmetry field has $B_z(\varpi, 0) = 0$ and so $\nabla \cdot \mathbf{B} = 0$ yields

$$B_z(\varpi, z) = -\frac{1}{\varpi} \frac{\partial}{\partial \varpi} \left(\varpi \int_0^z B_\varpi \, dz \right). \tag{11.124}$$

Since the radial and vertical length-scales of B_ϖ are $\sim \varpi$ and $\sim h$, it follows that

$$B_z \lesssim \frac{z}{\varpi} B_{\varpi{\rm c}}. \tag{11.125}$$

Matching to a vacuum field at the surface, in which the potential function must have comparable length-scales in the ϖ and z directions in order to satisfy Laplace's equation, requires $B_{\varpi{\rm s}} \sim B_{z{\rm s}}$ and hence

$$B_{z{\rm s}} \sim B_{\varpi{\rm s}} \lesssim \frac{h}{\varpi} B_{\varpi{\rm c}}. \tag{11.126}$$

Hence, to leading order in h/ϖ, B_z is ignorable through the disc and B_ϖ becomes ignorable at the surface. The boundary conditions for a quadrupolar field in a thin disc surrounded by a vacuum are therefore

$$B_\phi(\varpi, h) = 0, \tag{11.127a}$$

$$\left(\frac{\partial B_\phi}{\partial z}\right)_{z=0} = 0, \tag{11.127b}$$

$$B_\varpi(\varpi, h) = 0. \tag{11.127c}$$

The first condition is necessary since a steady axisymmetric field in a vacuum has $B_\phi = 0$, while the second condition is a symmetry requirement and the last condition is the leading order result derived above.

Using (11.98), (11.118) and (11.120) for Ω, η and B_ϕ in the toroidal induction equation (11.105) yields

$$B_\varpi(\varpi, z) = \frac{N_\alpha}{|K|^3} B_{\phi \mathrm{c}}(\varpi) f_\phi''(\zeta), \tag{11.128}$$

which can be expressed as

$$B_\varpi(\varpi, z) = B_{\varpi \mathrm{c}}(\varpi) \frac{f_\phi''(\zeta)}{f_\phi''(0)} = B_{\varpi \mathrm{c}}(\varpi) f_\varpi(\zeta). \tag{11.129}$$

Using (11.120) for B_ϕ and (11.129) for B_ϖ in (11.127a), (11.127b), and (11.127c) gives the boundary conditions

$$f_\phi(1) = 0, \tag{11.130a}$$

$$f_\phi'(0) = 0, \tag{11.130b}$$

$$f_\phi''(1) = 0. \tag{11.130c}$$

The differential equation (11.122), together with the boundary conditions, constitutes a homogeneous boundary value problem with eigenfunctions $f_\phi(\zeta)$ and eigenvalues K^3.

Power series solutions can be found of the form

$$f_\phi(\zeta) = \sum_{k=0}^{\infty} a_k \zeta^k. \tag{11.131}$$

Only even solutions are relevant for a quadrupolar field, and the two even linearly independent solutions are

$$f_{\phi 1}(\zeta) = \sum_{k=0}^{\infty} \left(\frac{|K|^3}{64}\right)^k \frac{\zeta^{4k}}{\Gamma(k+1)\Gamma(k+\frac{3}{4})\Gamma(k+\frac{1}{2})}, \tag{11.132}$$

and

$$f_{\phi 2}(\zeta) = \sum_{k=0}^{\infty} \left(\frac{|K|^3}{64}\right)^k \frac{\zeta^{4k+2}}{\Gamma(k+\frac{3}{2})\Gamma(k+\frac{5}{4})\Gamma(k+1)}, \tag{11.133}$$

where Γ is the gamma function. The required solution is

$$f_\phi(\zeta) = c_1 f_{\phi 1}(\zeta) + c_2 f_{\phi 2}(\zeta), \tag{11.134}$$

where c_1 and c_2 are constants. Because the solutions are even, it follows that $f'_\phi(0) = 0$ is satisfied. The application of $f_\phi(0) = 1$ and $f_\phi(1) = 0$ determines c_1 and c_2, leading to

$$f_\phi(\zeta) = \pi^{\frac{1}{2}} \Gamma\left(\frac{3}{4}\right) \left[f_{\phi 1}(\zeta) - \frac{f_{\phi 1}(1)}{f_{\phi 2}(1)} f_{\phi 2}(\zeta) \right]. \tag{11.135}$$

Then applying $f''_\phi(1) = 0$ gives the condition

$$f''_{\phi 1}(1) f_{\phi 2}(1) - f_{\phi 1}(1) f''_{\phi 2}(1) = 0, \tag{11.136}$$

which determines K^3 as a set of eigenvalues for the quadrupole modes. Taking the first 40 terms in the power series solutions gives high accuracy. Using these in (11.136) and solving numerically gives the first eigenvalue, corresponding to $|K| = 2.324$, with $f_\varpi(\zeta)$ and $f_\phi(\zeta)$ monotonically decreasing between $\zeta = 0$ and $\zeta = 1$. These dynamo field solutions are shown in Figs. 11.1 and 11.2. The quadrupole magnetic field solution leads to consistent solutions for the disc structure.

11.4.4 Angular Momentum Transport

Integrating the angular momentum equation (11.102) from $-z$ to z yields

$$\frac{\partial}{\partial \varpi} \left(\frac{1}{2\pi} \dot{M}(z) \varpi^2 \Omega + \varpi^3 \Omega' \nu \Sigma + \frac{2}{\mu_0} \varpi^2 \int_0^z B_\varpi B_\phi dz \right) = 0, \tag{11.137}$$

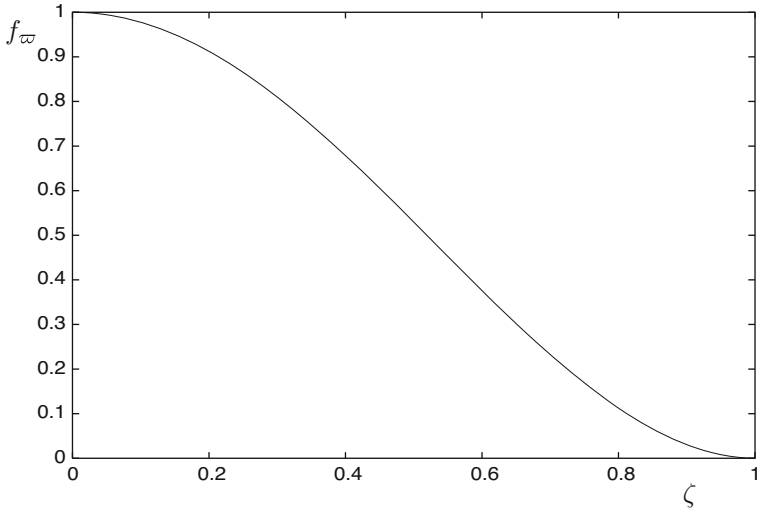

Fig. 11.1 Vertical variation of the radial magnetic field (from Campbell 2003)

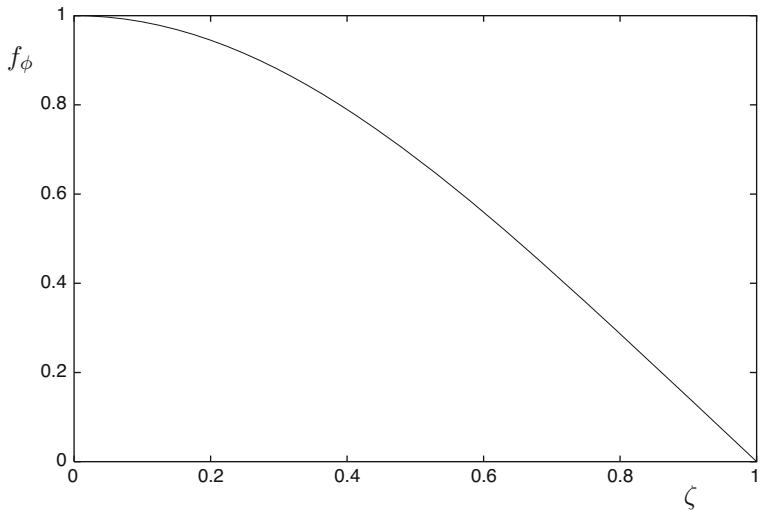

Fig. 11.2 Vertical variation of the toroidal magnetic field (from Campbell 2003)

where $\dot{M}(z)$ is given by (11.101) and

$$\Sigma(\varpi, z) = \int_{-z}^{z} \rho dz. \tag{11.138}$$

Equation (11.137) states that the term in brackets is independent of ϖ, and so is a pure function of z. This quantity represents the total rate of angular momentum

transport through an annular area of the disc between $-z$ and z. This rate is the sum of the rate of material angular momentum transport due to the inflow which is balanced by the outward radial transport of angular momentum carried by the viscous and magnetic stresses. The total $f(z)$ function is determined by applying boundary conditions at the outer edge of the boundary layer above the stellar surface. These conditions are taken as

$$\Omega' = 0 \quad \text{and} \quad B_\varpi B_\phi = 0 \quad \text{at} \quad \varpi = R + \delta, \tag{11.139}$$

with $\delta \ll R$. Integrating (11.137) and applying these conditions, taking a sharp turn-over so Ω is nearly Keplerian as $\varpi = R + \delta$ is approached, yields

$$\frac{\dot{M}(z)}{2\pi}\left[\varpi^2\Omega - (GMR)^{\frac{1}{2}}\right] + \varpi^3\Omega'\nu\Sigma + \frac{2}{\mu_0}\varpi^2\int_0^z B_\varpi B_\phi dz = 0. \tag{11.140}$$

The density and inflow speeds can be expressed in the separable forms

$$\rho(\varpi, z) = \rho_{\rm c}(\varpi) f_\rho(\zeta), \tag{11.141}$$

$$v_\varpi(\varpi, z) = v_{\varpi\rm c}(\varpi) f_v(\zeta), \tag{11.142}$$

where $\rho_{\rm c}(\varpi) = \rho(\varpi, 0)$ and $v_{\varpi\rm c}(\varpi) = v_\varpi(\varpi, 0)$. Both $f_\rho(\zeta)$ and $f_v(\zeta)$ have even symmetry so

$$f_\rho(0) = 1, \qquad f'_\rho(0) = 0, \tag{11.143}$$

$$f_v(0) = 1, \qquad f'_v(0) = 0. \tag{11.144}$$

Using these forms in (11.101) and (11.138) gives

$$\dot{M}(z) = \frac{\dot{M}}{I_1}\int_0^\zeta f_\rho f_v d\zeta, \tag{11.145}$$

and

$$\Sigma(\varpi, z) = \frac{\Sigma_{\rm s}(\varpi)}{I_2}\int_0^\zeta f_\rho d\zeta, \tag{11.146}$$

where

$$\dot{M} = \dot{M}(h) \quad \text{and} \quad \Sigma_{\rm s}(\varpi) = \Sigma(\varpi, h), \tag{11.147}$$

while

$$I_1 = \int_0^1 f_\rho f_v d\zeta \tag{11.148a}$$

and

$$I_2 = \int_0^1 f_\rho d\zeta. \tag{11.148b}$$

The toroidal induction equation gives

$$B_{\varpi} = \frac{2}{3}\frac{\eta}{\Omega_{\rm K} h^2} B_{\phi {\rm c}} f_\phi''(\zeta). \tag{11.149}$$

Using (11.120) and (11.149) to form $B_{\varpi} B_\phi$, together with (11.145) for $\dot{M}(z)$ and (11.146) for $\Sigma(\varpi, z)$ in the angular momentum equation (11.140) yields

$$\frac{3}{2I_2}\varpi^2 \Omega_{\rm K} \nu \Sigma_{\rm s} \int_0^\zeta f_\rho d\zeta = \frac{\dot{M}}{2\pi I_1}\left[\varpi^2 \Omega_{\rm K} - (GMR)^{\frac{1}{2}}\right] \int_0^\zeta f_\rho f_v d\zeta + \frac{4}{3}\frac{\varpi^2 \eta B_{\phi {\rm c}}^2}{\mu_0 \Omega_{\rm K} h} \int_0^\zeta f_\phi f_\phi'' d\zeta. \tag{11.150}$$

A separable solution arises by taking

$$\frac{4}{3}\frac{\varpi^2 \eta B_{\phi {\rm c}}^2}{\mu_0 \Omega_{\rm K} h} = C\frac{\dot{M}}{2\pi}\left[\varpi^2 \Omega_{\rm K} - (GMR)^{\frac{1}{2}}\right], \tag{11.151}$$

where C is a constant. This satisfies the second boundary condition (11.139) and leads to self consistent disc solutions. Using (11.151) in (11.150) gives the radial and vertical angular momentum equations as

$$\nu \Sigma_{\rm s} = k_1 \frac{\dot{M}}{3\pi}\left[1 - \left(\frac{R}{\varpi}\right)^{\frac{1}{2}}\right] \tag{11.152}$$

and

$$\frac{k_1}{I_2} f_\rho = \frac{1}{I_1} f_\rho f_v + C f_\phi f_\phi'', \tag{11.153}$$

where k_1 is a separation constant. It will be shown that $k_1 < 1$, so the radial equation gives the standard viscous form for $\nu \Sigma_{\rm s}$, but reduced by a factor k_1 due to the $B_{\varpi} B_\phi$ magnetic stress accounting for a fraction of the outward angular momentum transport, so less viscous transport is required.

11.4.5 Vertical Equilibrium

The thermal pressure and the temperature can be written as the separable forms

$$P(\varpi, z) = P_{\rm c}(\varpi) f_P(\zeta) \tag{11.154}$$

and

$$T(\varpi, z) = T_{\rm c}(\varpi) f_T(\zeta) \tag{11.155}$$

with

$$f_T(0) = 1, \quad f_T'(0) = 0. \tag{11.156}$$

The gas equation of state then yields

$$f_P = f_\rho f_T. \tag{11.157}$$

The vertical equilibrium equation (11.103) then becomes

$$\Omega_\kappa^2 h^2 \rho_{\rm c} \zeta f_\rho + P_{\rm c} \left(f_\rho f_T\right)' + \frac{B_{\phi{\rm c}}^2}{2\mu_0} \left(f_\phi^2\right)' = 0. \tag{11.158}$$

Separability requires

$$P_{\rm c} = A \frac{B_{\phi{\rm c}}^2}{2\mu_0}, \tag{11.159}$$

with A constant. The radial and vertical equations are then

$$\frac{B_{\phi{\rm c}}^2}{2\mu_0} = k_2 \Omega_\kappa^2 h^2 \rho_{\rm c} \tag{11.160}$$

and

$$A \left(f_\rho f_T\right)' + \left(f_\phi^2\right)' + \frac{1}{k_2} \zeta f_\rho = 0, \tag{11.161}$$

where k_2 is a separation constant. Integrating this from 0 to ζ leads to

$$f_T(\zeta) = \frac{1}{A k_2 f_\rho} \left[A k_2 + k_2 \left(1 - f_\phi^2\right) - \int_0^\zeta \zeta f_\rho d\zeta \right]. \tag{11.162}$$

The product Ak_2 can be expressed in terms of ϵ, N_α and $|K|$. Eliminating $B_{\phi c}^2$ between (11.159) and (11.160), noting that $P_c = c_s^2 \rho_c$, gives

$$Ak_2 = \frac{c_s^2}{\Omega_K^2 h^2}. \tag{11.163}$$

The use of (11.123) for $c_s/\Omega_K h$ then yields

$$Ak_2 = \frac{9}{4}\frac{N_\alpha^4}{\epsilon^2 K^6}. \tag{11.164}$$

11.4.6 Thermal Equilibrium and Radiative Transfer

It can now be shown that the thermal equations become separable. Integrating the thermal equilibrium equation (11.106) from 0 to z, using $F_R(\varpi, 0) = 0$, then integrating the magnetic dissipation term by parts and using the toroidal induction equation (11.105) to eliminate $\partial B_\phi/\partial z$, gives

$$F_R(\varpi, z) = \frac{\eta}{2\mu_0}\frac{\partial}{\partial z}\left(B_\phi^2\right) + \frac{\Omega_K'}{2\varpi}\left(\varpi^3 \Omega_K' \nu \Sigma + 2\frac{\varpi^2}{\mu_0}\int_0^z B_\varpi B_\phi dz\right). \tag{11.165}$$

Employing (11.120), (11.145) and (11.151) for B_ϕ, $\dot{M}(z)$ and $B_{\phi c}$ leads to the separable form

$$F_R(\varpi, z) = \frac{3\dot{M}}{8\pi}\Omega_K^2\left[1 - \left(\frac{R}{\varpi}\right)^{\frac{1}{2}}\right]\left[\frac{C}{2}\frac{d}{d\zeta}\left(f_\phi^2\right) + \frac{1}{I_1}\int_0^\zeta f_\rho f_v d\zeta\right]. \tag{11.166}$$

Another separable equation for F_R follows from the radiative transfer equation (11.107). Using (11.108) for the opacity, together with the separable forms for ρ and T, gives

$$F_R(\varpi, z) = -\frac{32}{45}\frac{\sigma_B}{\bar{K}}\frac{T_c^{\frac{15}{2}}}{\rho_c^2 h}\frac{1}{f_\rho^2}\frac{d}{d\zeta}\left(f_T^{\frac{15}{2}}\right). \tag{11.167}$$

Equating these two expressions for F_R, using (11.153) to eliminate $f_\rho f_v$, leads to the radial and vertical thermal equations

$$\frac{32}{45}\frac{\sigma_B}{\bar{K}}\frac{T_c^{\frac{15}{2}}}{\rho_c^2 h} = k_3\frac{3\dot{M}}{8\pi}\Omega_K^2\left[1 - \left(\frac{R}{\varpi}\right)^{\frac{1}{2}}\right], \tag{11.168}$$

and

$$-\frac{k_3}{f_\rho^2}\frac{d}{d\zeta}\left(f_T^{\frac{15}{2}}\right)=\frac{k_1}{I_2}\int_0^\zeta f_\rho d\zeta+C\int_0^\zeta {f'_\phi}^2 d\zeta. \tag{11.169}$$

11.4.7 Radial Structure

The radial structure of the disc can be found by solving the foregoing separated ϖ-dependent algebraic equations. Firstly, T_c can be found by deriving two equations for ρ_c in terms of c_s. Equations (11.119), (11.138) and (11.141) for ν, Σ and ρ yield

$$\nu\Sigma_\mathrm{s}=2I_2\frac{\epsilon N_\mathrm{p}}{N_\alpha}\rho_\mathrm{c}h^2c_\mathrm{s}. \tag{11.170}$$

Eliminating Ak_2 between (11.163) and (11.164) relates h to c_s by

$$h=\frac{2}{3}\frac{\epsilon|K|^3}{N_\alpha^2}\frac{c_\mathrm{s}}{\Omega_\mathrm{K}}. \tag{11.171}$$

Using this in (11.170) and equating the resulting expression for $\nu\Sigma_\mathrm{s}$ to the angular momentum relation expression (11.152) for $\nu\Sigma_\mathrm{s}$ gives

$$\rho_\mathrm{c}=\frac{3\dot{M}}{8\pi}\frac{k_1}{I_2}\frac{N_\alpha^5}{\epsilon^3N_\mathrm{p}K^6}\frac{\Omega_\mathrm{K}^2}{c_\mathrm{s}^3}f, \tag{11.172}$$

where

$$f=1-\left(\frac{R}{\varpi}\right)^{\frac{1}{2}}. \tag{11.173}$$

A second expression for ρ_c is found by using (11.115) for c_s and (11.171) to eliminate T_c and h in terms of c_s in the thermal equilibrium equation (11.168), leading to

$$\rho_\mathrm{c}=\left(\frac{16}{15}\frac{\sigma_\mathrm{B}}{\bar{K}}\right)^{\frac{1}{2}}\left(\frac{\mu}{\mathcal{R}}\right)^{\frac{15}{4}}\left(\frac{8\pi}{3\dot{M}}\right)^{\frac{1}{2}}\frac{1}{k_3^{\frac{1}{2}}}\frac{N_\alpha}{\epsilon^{\frac{1}{2}}|K|^{\frac{3}{2}}}\frac{c_\mathrm{s}^7}{\Omega_\mathrm{K}^{\frac{1}{2}}f^{\frac{1}{2}}}. \tag{11.174}$$

Equating this to (11.172), solving for c_s and using (11.115) fixes $T_\mathrm{c}(\varpi)$. Then h and ρ_c follow by using this expression for c_s in (11.171) and (11.172). Forming

$\rho_{\rm c}h^2$ in the vertical equilibrium equation (11.160) gives $B_{\phi{\rm c}}$, and $B_{\varpi{\rm c}}$ then follows from (11.149) for B_ϖ evaluated at $\zeta = 0$. Finally, the inflow speed in the mid-plane is found by using (11.101) for $\dot{M}(z)$ evaluated at $z = h$, which gives

$$v_{\varpi{\rm c}} = -\frac{\dot{M}}{4\pi I_1}\frac{1}{\varpi\rho_{\rm c}h} \tag{11.175}$$

with the solutions for $\rho_{\rm c}$ and h substituted in.

The foregoing solutions for the radial structure can be normalized using typical system parameters together with $\mu = 0.6$ and $\bar{K} = 10^{19}\,{\rm m}^2\,{\rm K}^{7/2}\,{\rm kg}^{-2}$. The results are

$$h = 8.4\times10^5\frac{\epsilon^{\frac{3}{4}}|K|^{\frac{51}{20}}}{N_\alpha^{\frac{8}{5}}N_{\rm p}^{\frac{1}{10}}}\frac{k_1^{\frac{1}{10}}k_3^{\frac{1}{20}}}{I_2^{\frac{1}{10}}}\frac{\dot{M}_{10}^{\frac{3}{20}}}{M_1^{\frac{3}{8}}}f^{\frac{3}{20}}x^{\frac{9}{8}}\,{\rm m}, \tag{11.176}$$

$$T_{\rm c} = 1.5\times10^4\frac{N_\alpha^{\frac{4}{5}}}{\epsilon^{\frac{1}{2}}N_{\rm p}^{\frac{1}{5}}}\frac{k_1^{\frac{1}{5}}k_3^{\frac{1}{10}}}{|K|^{\frac{9}{10}}I_2^{\frac{1}{5}}}M_1^{\frac{1}{4}}\dot{M}_{10}^{\frac{3}{10}}\frac{f^{\frac{3}{10}}}{x^{\frac{3}{4}}}\,{\rm K}, \tag{11.177}$$

$$\rho_{\rm c} = 3.3\times10^{-5}\frac{N_\alpha^{\frac{19}{5}}}{\epsilon^{\frac{9}{4}}N_{\rm p}^{\frac{7}{10}}}\frac{k_1^{\frac{7}{10}}}{k_3^{\frac{3}{20}}I_2^{\frac{7}{10}}}M_1^{\frac{5}{8}}\dot{M}_{10}^{\frac{11}{20}}\frac{f^{\frac{11}{20}}}{x^{\frac{15}{8}}}\,{\rm kg\,m^{-3}}, \tag{11.178}$$

$$v_{\varpi{\rm c}} = -1.8\times10^2\frac{\epsilon^{\frac{3}{2}}N_{\rm p}^{\frac{4}{5}}}{N_\alpha^{\frac{11}{5}}}\frac{I_2^{\frac{4}{5}}}{I_1}\frac{k_3^{\frac{1}{10}}}{k_1^{\frac{4}{5}}}|K|^{\frac{21}{10}}\frac{\dot{M}_{10}^{\frac{3}{10}}}{M_1^{\frac{1}{4}}}\frac{1}{f^{\frac{7}{10}}x^{\frac{1}{4}}}\,{\rm m\,s^{-1}}, \tag{11.179}$$

$$B_{\varpi{\rm c}} = 8.8\times10^{-2}\frac{N_\alpha^{\frac{3}{10}}}{\epsilon^{\frac{3}{8}}N_{\rm p}^{\frac{9}{20}}}\frac{k_1^{\frac{9}{20}}k_2^{\frac{1}{2}}}{k_3^{\frac{1}{40}}I_2^{\frac{9}{20}}}\frac{|f_\phi''(0)|}{|K|^{\frac{111}{40}}}M_1^{\frac{7}{16}}\dot{M}_{10}^{\frac{17}{40}}\frac{f^{\frac{17}{40}}}{x^{\frac{21}{16}}}\,{\rm T}, \tag{11.180}$$

$$B_{\phi{\rm c}} = -8.8\times10^{-2}\frac{N_\alpha^{\frac{3}{10}}}{\epsilon^{\frac{3}{8}}N_{\rm p}^{\frac{9}{20}}}\frac{k_1^{\frac{9}{20}}k_2^{\frac{1}{2}}}{k_3^{\frac{1}{40}}I_2^{\frac{9}{20}}}|K|^{\frac{9}{40}}M_1^{\frac{7}{16}}\dot{M}_{10}^{\frac{17}{40}}\frac{f^{\frac{17}{40}}}{x^{\frac{21}{16}}}\,{\rm T}, \tag{11.181}$$

where $M_1 = M/M_\odot$, $\dot{M}_{10} = \dot{M}/10^{-10}\,M_\odot\,{\rm year}^{-1}$ and $x = \varpi/10^8\,{\rm m}$. This radial structure solution has the same ϖ dependences as that for the standard viscous disc. However, a dynamo generated magnetic field is now incorporated so angular momentum is transported by magnetic stresses as well as by viscous stresses.

11.4.8 Vertical Structure

The vertical structure of the disc can now be calculated. An equation for $f_\rho(\zeta)$ can be found by using the vertical equilibrium equation (11.161), then employing the thermal equilibrium equation (11.169) to eliminate f'_ρ. This gives

$$f'_\rho = -\frac{1}{Ak_2 f_T}\left(2k_2 f_\phi f'_\phi + \zeta f_\rho\right) + \frac{2}{15}\frac{f_\rho^3}{k_3 f_T^{\frac{15}{2}}}\left(\frac{k_1}{I_2}\int_0^\zeta f_\rho d\zeta + C\int_0^\zeta {f'_\phi}^2 d\zeta\right), \tag{11.182}$$

with

$$f_T = \frac{1}{Ak_2 f_\rho}\left[Ak_2 + k_2\left(1 - f_\phi^2\right) - \int_0^\zeta \zeta f_\rho d\zeta\right]. \tag{11.183}$$

This yields a non-linear, integro-differential equation which can be solved numerically for $f_\rho(\zeta)$ once the constants k_1, k_2 and k_3 are determined.

The disc surface conditions on $f_\rho(\zeta)$ and $f_T(\zeta)$ must be formulated first. The disc surface $z = h$ is taken to be the photospheric base, where the density scale height equals the photon mean free path, so

$$-\left(\frac{\rho}{\partial\rho/\partial z}\right)_{\rm s} = \frac{1}{(\kappa\rho)_{\rm s}}. \tag{11.184}$$

It will be shown that this leads to ρ having a small but finite value at $z = h$, and falling rapidly beyond this. Hence all the significant electric currents are contained in the main body of the disc and the surrounding region is a vacuum. Substituting for κ, ρ and T in (11.184) gives

$$\frac{f'_\rho(1)}{f_\rho(1)} = -\frac{\bar{K}\rho_{\rm c}^2 h}{T_{\rm c}^{\frac{7}{2}}}\frac{f_\rho(1)^2}{f_T(1)^{\frac{7}{2}}}. \tag{11.185}$$

The flux expression (11.166) gives the surface value as

$$F_{\rm R}(\varpi, h) = \frac{3\dot{M}}{8\pi}\Omega_{\rm K}^2\left[1 - \left(\frac{R}{\varpi}\right)^{\frac{1}{2}}\right]. \tag{11.186}$$

Taking the surface temperature as the effective temperature gives

$$F_{\rm R}(\varpi, h) = \sigma_{\rm B} f_T(1) T_{\rm c}^4. \tag{11.187}$$

Using the thermal equation (11.168) in (11.186), equating the resulting expression for $F_{\mathrm{R}}(\varpi, h)$ to (11.187) and using this to simplify (11.185) yields

$$f'_{\rho}(1) = -\frac{32}{45}\frac{f_{\rho}(1)^3}{k_3 f_T(1)^{\frac{15}{2}}}. \tag{11.188}$$

Integrating the vertical angular momentum equation (11.153) from $\zeta = 0$ to $\zeta = 1$ gives

$$k_1 + CI = 1, \tag{11.189}$$

where

$$I = \int_0^1 f'^2_{\phi} d\zeta. \tag{11.190}$$

Then putting $\zeta = 1$ in (11.182) for $f'_{\rho}(\zeta)$ and using (11.189) yields

$$f'_{\rho}(1) = -\frac{1}{Ak_2}\frac{f_{\rho}(1)}{f_T(1)} + \frac{2}{15}\frac{f_{\rho}(1)^3}{k_3 f_T(1)^{\frac{15}{2}}}. \tag{11.191}$$

Equating this to (11.188) gives

$$f_{\rho}(1) = \left(\frac{45}{38}\frac{k_3}{Ak_2}\right)^{\frac{1}{2}} f_T(1)^{\frac{13}{4}}. \tag{11.192}$$

Evaluating the vertical equilibrium equation (11.183) at $\zeta = 1$ gives

$$f_T(1) = \frac{(Ak_2 + k_2 - I_3)}{Ak_2 f_{\rho}(1)}, \tag{11.193}$$

where

$$I_3 = \int_0^1 \zeta f_{\rho} d\zeta. \tag{11.194}$$

Finally, (11.192) and (11.193) lead to the surface equations

$$f_{\rho}(1) = \left(\frac{45}{32}k_3\right)^{\frac{2}{17}} \frac{(Ak_2 + k_2 - I_3)^{\frac{13}{17}}}{(Ak_2)^{\frac{15}{17}}}, \tag{11.195}$$

and

$$f_T(1) = \left(\frac{38}{45}\frac{1}{k_3}\right)^{\frac{2}{17}} \frac{(Ak_2 + k_2 - I_3)^{\frac{4}{17}}}{(Ak_2)^{\frac{2}{17}}}. \tag{11.196}$$

The separation constants can now be determined. Evaluating the angular momentum equation (11.153) at $\zeta = 0$ gives

$$k_1 = I_2 \left[\frac{1}{I_1} + C f''_\phi(0) \right]. \tag{11.197}$$

Using this with (11.189) to solve for k_1 and C yields

$$k_1 = \frac{I_2[I_1|f''_\phi(0)| - I]}{I_1[I_2|f''_\phi(0)| - I]}, \tag{11.198}$$

$$C = \frac{(I_2 - I_1)}{I_1[I_2|f''_\phi(0)| - I]}. \tag{11.199}$$

Equations (11.151) and (11.173) give

$$\frac{\eta B^2_{\phi c}}{\mu_0 h} = \frac{3\dot{M}}{8\pi} C \Omega^2_\kappa f. \tag{11.200}$$

Using $\rho_c h = \Sigma_s/2I_2$ in the radial part of the vertical equilibrium equation (11.160) leads to

$$\frac{\eta B^2_{\phi c}}{\mu_0 h} = \frac{k_2}{N_p I_2} \Omega^2_\kappa \nu \Sigma_s = \frac{k_1 k_2}{N_p I_2} \frac{\dot{M}}{3\pi} \Omega^2_\kappa f, \tag{11.201}$$

where the last expression follows from using (11.152) to eliminate $\nu\Sigma_s$. Equating (11.200) to (11.201), then using (11.198) and (11.199) for k_1 and C gives

$$k_2 = \frac{9}{8} \frac{N_p(I_2 - I_1)}{[I_1|f''_\phi(0)| - I]}. \tag{11.202}$$

The thermal separation constant k_3 can be found by eliminating $F_R(\varpi, h)$ between (11.186) and (11.187), then solving for T_c and equating this to the disc solution for T_c and using (11.196) for $f_T(1)$. This leads to

$$k_3 = \frac{k_1^{\frac{34}{3}} (k_2 A + k_2 - I_3)^{\frac{40}{3}}}{Q I^{\frac{34}{3}} (A k_2)^{\frac{20}{3}}}, \tag{11.203}$$

where

$$Q = 3.92 \times 10^{-21} \frac{\epsilon^{\frac{85}{3}} N_p^{\frac{34}{3}}}{N_\alpha^{\frac{136}{3}}} \frac{|K|^{51}}{\dot{M}_{10}^{\frac{17}{6}}}. \tag{11.204}$$

The integro-differential equation for $f_\rho(\zeta)$, given by (11.182) and (11.183) can be solved numerically by an improved Euler method. The solution is started at $\zeta = 0$ by using the Taylor expansions

$$f_\rho \sim 1 - \frac{1}{2}\left[\frac{1}{Ak_2}\left\{1 - 2|f_\phi''(0)|k_2\right\} - \frac{2}{15}\frac{k_1}{I_2 k_3}\right]\zeta^2, \tag{11.205}$$

$$f_T \sim 1 - \frac{1}{15}\frac{k_1}{I_2 k_3}\zeta^2. \tag{11.206}$$

The series solution (11.135) is used for $f_\phi(\zeta)$. The turbulence parameters ϵ, N_α and N_p are chosen and initial guesses made for the integrals I_1, I_2 and I_3. Assuming a Gaussian profile for $f_\rho(\zeta)$ and using $f_v = 1$ gives reasonable initial values for these integrals. The angular momentum equation (11.153), together with (11.198) for k_1 and (11.199) for C, gives

$$f_v(\zeta) = f_v(1) - \frac{[1 - f_v(1)]}{|f_\phi''(0)|}\frac{f_\phi f_\phi''}{f_\rho}, \tag{11.207}$$

with

$$f_v(1) = \frac{I_1|f_\phi''(0)| - I}{I_2|f_\phi''(0)| - I}. \tag{11.208}$$

This yields $f_v(\zeta)$ once $f_\rho(\zeta)$ is known, and the vertical equilibrium equation (11.183) gives $f_T(\zeta)$. The integrals are then evaluated numerically and compared with the initial values used. Improved values are then employed and the process is repeated until good agreement is found. Typically, only a few iterations are needed.

Figures 11.3, 11.4, and 11.5 show the results for the vertical structure functions f_ρ, f_T and f_v using $\epsilon = 10^{-2}$, $N_\mathrm{p} = 0.1$ and $N_\alpha = 0.15$. As expected, all these functions decrease monotonically with increasing ζ. It is noted that the surface value $f_\rho(1)$ is small, this being consistent with vacuum surroundings just beyond $z = h$.

11.4.9 The Nature of the Solutions

Table 11.1 shows the values of the main disc quantities, for the turbulent parameters used above, while Table 11.2 gives these quantities for $\epsilon = 0.1$, $N_\mathrm{p} = 0.32$ and $N_\alpha = 0.57$. A key quantity is the ratio of the magnetic to the viscous torque. Equation (11.137) shows that the total transport rate of angular momentum through a circular area of between $-z$ and z, is radially conserved. At each radius the rate of material transport of angular momentum due to the inflow is balanced by an outward

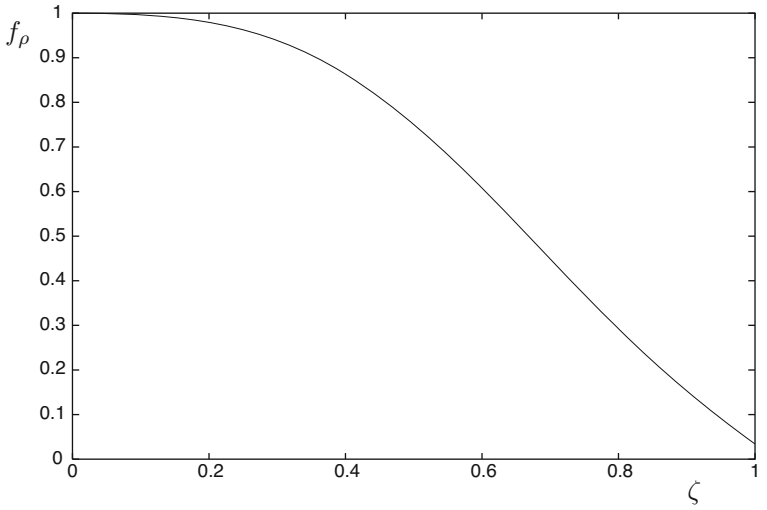

Fig. 11.3 Vertical variation of the density (from Campbell 2003)

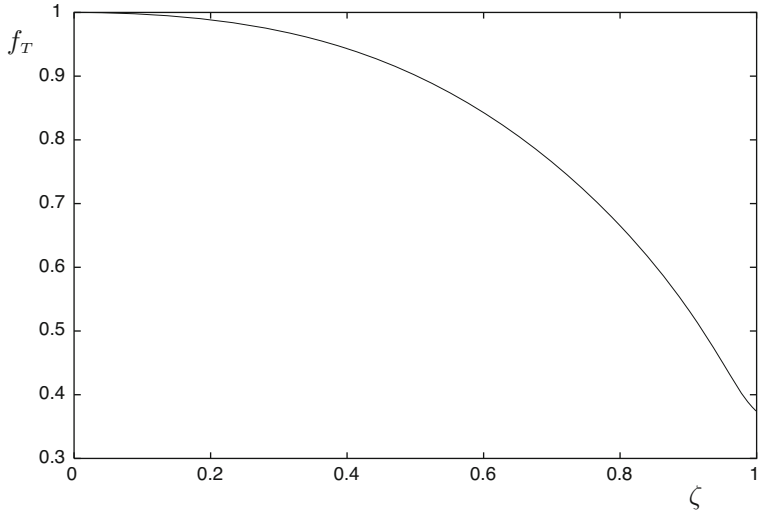

Fig. 11.4 Vertical variation of the temperature (from Campbell 2003)

transport rate carried by the viscous and magnetic stresses which have associated torques. Taking $z = h$ in (11.137), gives the viscous and magnetic torques over the whole circular area as

$$T_{\rm v} = \varpi^3 \Omega'_{\rm K} \nu \Sigma_{\rm s} \tag{11.209}$$

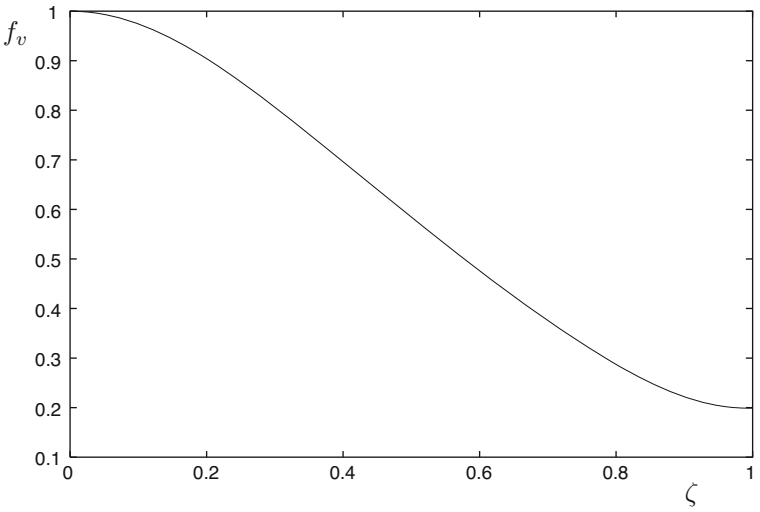

Fig. 11.5 Vertical variation of the inflow speed (from Campbell 2003)

Table 11.1 Disc quantities for $\epsilon = 0.01$, $N_\mathrm{p} = 0.1$, $N_\alpha = 0.15$ (from Campbell 2003)

$f_\rho(1)$	$f_T(1)$	$f_v(1)$	I_1	I_2	I_3	k_1	k_2
0.03	0.37	0.20	0.47	0.63	0.24	0.27	0.16
k_3	$T_\mathrm{m}/T_\mathrm{v}$	$B^2_{\phi\mathrm{c}}/2\mu_0 P_\mathrm{c}$	$\lvert B_{\varpi\mathrm{c}}/B_{\phi\mathrm{c}}\rvert$	τ_D	Ak_2	$(h/\varpi)_8$	
0.11	2.76	2.12	0.03	239	0.07	0.05	

Table 11.2 Disc quantities for $\epsilon = 0.1$, $N_\mathrm{p} = 0.32$, $N_\alpha = 0.57$ (from Campbell 2003)

$f_\rho(1)$	$f_T(1)$	$f_v(1)$	I_1	I_2	I_3	k_1	k_2
0.06	0.41	0.63	0.55	0.62	0.22	0.71	0.08
k_3	$T_\mathrm{m}/T_\mathrm{v}$	$B^2_{\phi\mathrm{c}}/2\mu_0 P_\mathrm{c}$	$\lvert B_{\varpi\mathrm{c}}/B_{\phi\mathrm{c}}\rvert$	τ_D	Ak_2	$(h/\varpi)_8$	
0.15	0.41	0.52	0.12	117	0.15	0.03	

and

$$T_\mathrm{m} = 2\frac{\varpi^2}{\mu_0}\int_0^h B_\varpi B_\phi dz. \tag{11.210}$$

The ratio of these torques can be expressed as

$$\frac{T_\mathrm{m}}{T_\mathrm{v}} = \frac{I}{I_2}\frac{[1-f_v(1)]}{|f''_\phi(0)|f_v(1)}. \tag{11.211}$$

The ratio of magnetic pressure to thermal pressure in the mid-plane can be written as

$$\frac{B^2_{\phi\mathrm{c}}}{2\mu_0 P_\mathrm{c}} = \frac{1}{2}\frac{\epsilon^2 N_\mathrm{p} K^6}{|f''_\phi(0)|N^4_\alpha}\frac{[1-f_v(1)]}{f_v(1)}. \tag{11.212}$$

The ratio of the magnetic field components, $|B_{\varpi}/B_{\phi}|$, has a maximum in the orbital plane given by

$$\left|\frac{B_{\varpi c}}{B_{\phi c}}\right| = \frac{N_{\alpha}}{|K|^3}|f_{\phi}''(0)|. \tag{11.213}$$

Tables 11.1 and 11.2 show that the magnetic and viscous torques are comparable in both cases, so the $B_{\varpi}B_{\phi}$ stress plays a major part in driving the inflow. The two key ratios of h/ϖ and $(B_{\varpi c}/B_{\phi c})^2$ are small, as required in the analysis. The optical depth through the disc is

$$\tau_{\rm D} = \int_0^h \kappa\rho dz, \tag{11.214}$$

and satisfies $\tau_{\rm D} \gg 1$, so justifying the use of the diffusive radiative transfer equation.

11.5 Summary and Discussion

The angular momentum transport needed to explain the mass transfer rates occurring in accretion discs requires a greatly enhanced form of viscosity, characteristic of the values expected to result from turbulence. A suitable instability to drive the turbulence has never been found in a non-magnetic disc. However, the presence of a sub-thermal magnetic field leads to a coupling between fluid elements which destabilises the slow magnetosonic mode, drawing energy from the Keplerian rotation. This strong local magnetorotational instability leads to turbulence.

Local box simulations have been used to investigate the effects of the turbulent motions. Initial conditions with and without a net magnetic field have been employed, and turbulence results in both cases. Vertical stratification appears to enhance the field creation process. Self-sustaining dynamos can occur, including oscillatory solutions. Large-scale fields with a quadrupolar symmetry can lead to outward radial angular momentum transport which can make a substantial contribution to driving the inflow, at least comparable to that supplied by viscous stresses. An effective viscous transport coefficient can be calculated and compared with the standard theory. More global calculations are needed to assess the nature of the transport coefficients.

A mean field dynamo theory which includes the effects of the magnetorotational instability has yet to be formulated.

References

Balbus, S.A., Hawley, J.F., 1991, ApJ, 376, 214.
Balbus, S.A., Hawley, J.F., 1998, RvMP, 70, 1.
Beckwith, K., Armitage, P.J., Simon, J.B., 2011, MNRAS, 416, 361.
Blackman, E.G., 2010, AN, 331, 101.
Blackman, E.G., Field, G.B., 2004, PhP1, 11, 3264.
Blandford, R.D., Payne, D.G., 1982, MNRAS, 199, 883.
Brandenburg, A., Campbell, C.G., 1997, in Accretion Disks-New Aspects, Springer.
Brandenburg, A., Donner, K.J., 1997, MNRAS, 288, L29.
Brandenburg, A., Nordlund, A., Stein, R.F., Torkelsson, U., 1995, ApJ, 446, 741.
Brandenburg, A., Nordlund, A., Stein, R.F., Torkelsson, U., 1996, ApJ, 458, L45.
Campbell, C.G., 1992, GAFD, 63, 197.
Campbell, C.G., 2003, MNRAS, 345, 1110.
Campbell, C.G., Caunt, S., 1999, MNRAS, 306, 122.
Chandrasekhar, S., 1960, PNAS.,46, 253.
Chandrasekhar, S., 1961, Hydrodynamic and Hydromagnetic Stability, Oxford University Press.
Coroniti, F.V., 1981, ApJ, 244, 587.
Davis, S.W., Stone, J.M., Pessah, M.E., 2010, ApJ, 713, 52.
Dubrulle, B., Knoblock, E., 1993, A&A, 274, 667.
Eardley, D.M., Lightman, A.P., 1975, ApJ, 200, 187.
Fromang, S., Papaloizou, J.C.B., Lesur, G., Heinemann, T., 2007, A&A, 476, 1123.
Galeev, A.A., Rosner, R., Vaiana, G.S., 1979, ApJ, 229, 318.
Gammie, C.F., Balbus, S.A., 1994, MNRAS, 270, 138.
Gressel, O, 2010, MNRAS, 405, 41.
Gressel, O., Pessah, M.E., 2015, ApJ, 810, 59.
Hawley, J.F., Balbus, S.A., 1991, ApJ, 376, 223.
Hawley, J.F., Balbus, S.A., 1992, ApJ, 400, 595.
Hawley, J.F., Gammie, C.F., Balbus, S.A., 1995, ApJ, 440, 742.
Ichimaru, S., 1977, ApJ, 214, 840.
Lynden-Bell, D., 1969, Nature, 223, 690.
Moffatt, H.K., 1978, Magnetic Field Generation in Electrically Conducting Fluids, Cambridge University Press.
Nordlund, A., Stein, R.F., 1990, CoPhC, 59, 119.
Ogilvie, G.I., 2003, MNRAS, 340, 969.
Papaloizou, J.C.B., Szuszkiewicz, E., 1992, GAFD, 66, 223.
Parker, E.N., 1971, ApJ, 163, 255.
Parker, E.N., 1972, ApJ, 174, 499.
Pudritz, R.E., 1981, MNRAS, 195, 897.
Rudiger, G., Shalybkov, D.A., 2002, A&A, 393, L81.
Rudiger, G., Elstner, D., Stepinski, T.F., 1995, A&A, 298, 934.
Shakura, N.I., Sunyaev, R.A., 1973, A&A, 24, 337.
Soward, A.M., 1992a, GAFD, 64, 163.
Soward, A.M., 1992b, GAFD, 64, 201.
Stella, L., Rosner, R., 1984, ApJ, 277, 312.
Stepinski, T.F., Levy, E.H., 1990, ApJ, 362, 318.
Stone, J.M., Hawley, J.F., Gammie, C.F., Balbus, S.A., 1996, ApJ, 463, 656.
Tout, C.A., Pringle, J.E., 1992, MNRAS, 259, 604.
Velikhov, E.P., 1959, Sov JETP, 36, 995.

Chapter 12
Stellar Magnetic Fields

Abstract The origins of the stellar magnetic fields in accreting binary systems are considered. Observations and theoretical models suggest that the M and K dwarf secondary stars should have dynamo generated magnetic fields, with surface values up to several kG, including large-scale structures. Significant magnetic fields can be generated in the fully convective secondaries, corresponding to the lower mass M dwarfs, even though these stars do not have a tachocline region. Rapid rotation of the tidally synchronized secondary together with strong convective motions leads to effective α^2 dynamo action. The higher mass M dwarfs and the K dwarfs have radiative cores and hence will possess an over-shoot tachocline region connecting the core to the convective envelope. This may affect the nature of the dynamo, particularly if some differential rotation remains across this transition layer.

The magnetic fields of the white dwarf and neutron star primaries are believed to be of fossil origin, but the binary formation process may have played a major role in their determination. Also, accretion of material can cause the degenerate primary to contract as it gains mass. This can lead to significant modification of the surface field due to advection, within the lifetime of the system, depending on the efficiency of magnetic buoyancy.

12.1 Introduction

Apart from accretion discs, the sources of magnetic fields in interacting binary systems are the secondary and primary stars. The majority of accreting binary stars are cataclysmic variables having orbital periods in the range $1.3\,\mathrm{h} < P < 8.0\,\mathrm{h}$, containing white dwarf primaries (e.g. Warner 1995). The lobe filling secondaries in these systems have masses in the range $0.13 \lesssim M_\mathrm{s}/M_\odot \lesssim 0.80$ and hence consist of M and K dwarfs. Accreting neutron stars occur in the X-ray binary pulsars and in the accreting millisecond pulsars, with some of the former systems having higher mass secondaries. The secondary stars in cataclysmic variables either have a significant convective envelope or are fully convective for $M_\mathrm{s} < 0.35\,M_\odot$. Tidal friction is believed to have synchronized the secondary so it is rapidly rotating (e.g. Zahn 1977; Campbell and Papaloizou 1983). Convection and rapid rotation are

C. G. Campbell, *Magnetohydrodynamics in Binary Stars*, Astrophysics and Space Science Library 456, https://doi.org/10.1007/978-3-319-97646-4_12

known to promote dynamo action and hence it is likely that the secondary stars have significant magnetic fields generated by some form of dynamo. There are expected to be similarities between the dynamos operating in single lower main sequence stars and those in binary systems. However, the binary candidates have particularly rapid rotation and may have little or no differential rotation, due to tidal effects.

In relation to AM Her systems, it was seen in Chap. 6 that surface magnetic fields on the secondary of $\gtrsim 10^2$ G can result in a significant torque on the magnetic white dwarf primary that can lead to synchronous states. A secondary magnetic field is also relevant to all cataclysmic variables above the period gap, which are believed to have mass transfer driven by a combination of magnetic wind braking of the secondary together with tidal coupling to the orbit. Suitable large-scale magnetic fields are required for this.

The intermediate polars and the AM Her binaries contain white dwarf primaries with polar surface magnetic fields of $(B_{\rm p})_0 > 10^6$ G. Their large magnetic moments result in fields which significantly modify the mass transfer process compared to that occurring in CVs containing essentially non-magnetic accreting white dwarfs. Magnetic modification either partially or totally disrupts the accretion disc and material is channelled on to the white dwarf surface via a curtain flow or a confined accretion stream.

The X-ray binary pulsars and the accreting millisecond pulsars contain magnetic neutron stars with surface magnetic fields in the range $10^9\,{\rm G} \lesssim (B_{\rm p})_0 \lesssim 10^{12}\,{\rm G}$. Magnetically disrupted discs with inner accretion curtains form in these systems and a range of spin behaviour of the neutron star is observed which is believed to be related to this accretion process.

The subjects of stellar dynamos, and of magnetic field sources in white dwarfs and neutron stars, cover a very extensive area of research. However, there are areas of specific relevance to accreting binary stars which can be outlined here. More recent studies have focused on magnetic field generation in fully convective M dwarfs by dynamo action, and direct magnetic field measurements have been made in a double M dwarf binary containing rapidly rotating fully convective stars. The effects of accretion on the magnetic fields of white dwarfs and neutron stars have been investigated for several decades. The accumulation of mass over periods less than the lifetime of the system can cause contraction of the degenerate primary star and significantly modify the structure of its surface magnetic field. The possible magnetic effects of common envelope evolution have recently been investigated. Dynamo action in a differentially rotating and convective envelope can generate magnetic fields which can diffuse into the degenerate core of the giant star. The resulting white dwarf can have its magnetic field enhanced by this process. These areas are discussed below.

12.2 The Secondary Star Magnetic Field

12.2.1 Observations and Background

Most secondary stars of interest here lie in the mass range $0.13 < M_s/M_\odot < 0.80$ and hence consist of M and K dwarf stars. Observations of the secondary star are difficult since its luminosity is greatly exceeded by that of the accretion disc and/or the accretion column (see Warner 1995, for a detailed account). Observations of single stars of the same spectral range give indications of the magnetic activity that is likely to occur in the binary cases. The observations of Hα equivalent widths and of X-ray emissions from M dwarfs are viewed as evidence of chromospheric magnetic fields. FeH molecular line ratios (e.g. Reiners and Basri 2007) and Zeeman Doppler imaging (e.g. Morin et al. 2008) are used to estimate magnetic field strengths and field topology in rapidly rotating M dwarfs. Magnetic activity is believed to be strongly correlated with rotation rate (e.g. Mohanty and Basri 2003; Browning et al. 2010).

Strong observational evidence related to magnetism in close binary secondary stars was given by Kochukhov and Lavail (2017). An analysis was made of the observations of the wide binary GJ65 AB which contains M dwarf components with the rapid rotation periods of $P_A = 5.84$ h and $P_B = 5.45$ h, corresponding to the A-component BL Cet and the B-component UV Cet. High spectral resolution circular polarization measurements were taken, and Zeeman Doppler imaging inversion techniques reveal the magnetic field topology. BL Cet has a large-scale surface magnetic field with a maximum value of 0.84 kG and a mean value of 0.34 kG, while UV Cet yields values of 2.34 kG and 1.34 kG for its maximum and mean fields. The field of BL Cet has a dipolar component containing $\simeq$ 70% of the magnetic energy, while the dipolar component of UV Cet contains $\simeq$ 92% of the field energy. However, $\simeq$ 95% of the magnetic energy is in small-scale fields, with the stars having similar total magnetic fluxes corresponding to average fields of 5.2 kG for BL Cet and 6.7 kG for UV Cet. Both stars are near spectral type M5, and hence are fully convective. This illustrates that fully convective, rapidly rotating M dwarf stars can have large-scale surface poloidal magnetic fields of kG strengths.

M dwarfs with masses of $M_s \leq 0.35\, M_\odot$ will be fully convective, while stars with $M_s > 0.35\, M_\odot$ will have a radiative core. A formula for the size of the radiative core is given by Hurley et al. (2002), covering the range from a fully convective star of mass $M_s = 0.35\, M_\odot$ to a fully radiative star of mass $M_s = 1.25\, M_\odot$. This can be combined with the approximate lower main sequence mass-radius relation (2.297) to give a formula to estimate the fractional depth of the convective envelope which spans the stellar mass range $0.35 \leq M_s/M_\odot \leq 0.80$. The result is

$$\frac{R_s - R_c}{R_s} = \frac{0.35}{(M_s/M_\odot)} \left[\frac{1.25 - (M_s/M_\odot)}{0.9} \right]^{\frac{1}{2}}, \tag{12.1}$$

where R_s and R_c are the radii of the secondary and its radiative core. For tidally distorted stars in binaries these become the mean radii. The upper end of the mass range corresponds to a K dwarf with $M_s = 0.8\,M_\odot$ for which (12.1) yields $(R_s - R_c)/R_s = 0.30$, so there is a large radiative core. For an M dwarf with $M_s = 0.4\,M_\odot$ the formula (12.1) gives $(R_s - R_c)/R_s = 0.85$ and hence there is a small radiative core. It follows that lower main sequence stars with and without radiative cores are relevant to the consideration of secondary stars in interacting binaries. It is usually assumed that tidal dissipation leads to the orbital synchronization of the secondary's spin well within the lifetime of the system, which is measured by the mass transfer time-scale $\tau_M = M_s/|\dot{M}_s|$.

Secondaries having a radiative core are expected to have a magnetic field, as in the solar case. The magnetic decay time of the longest lived mode in a spherical conductor, with constant magnetic diffusivity η, is given by (2.224) as

$$\tau_d = \frac{R_s^2}{\pi^2 \eta}. \tag{12.2}$$

Allowing for spatial variations of η gives similar results. This can be used to estimate the decay time of a magnetic field in a typical convective envelope, yielding $\tau_d \sim 30$ year. A radiative core of significant size has $\tau_d \sim 2 \times 10^7$ year. These times are much less than the binary lifetime and hence magnetic fields in the secondary must be generated and maintained by a dynamo process. Dynamo theory has been largely developed for single main sequence stars, for which the magnetic decay time is much shorter than the nuclear time. However, the main features of the single star cases should be of relevance to binary secondary stars, especially for the cases with high rotation rates.

12.2.2 Stars with Radiative Cores

The solar dynamo gives the classic case of a star with a radiative core and a significant convective envelope, and has been extensively studied (see Ossendrijver 2003, for a review). In the standard model of the solar dynamo the over-shoot region connecting the convective envelope to the radiative core is believed to be of fundamental importance. This narrow region, of width $\delta \simeq 0.04\,R_\odot$, and having large radial shears, is referred to as the tachocline (Spiegel and Zahn 1992). The shearing of poloidal magnetic field, described by the $\mathbf{B}_p \cdot \nabla\Omega$ term in the induction equation, generates B_ϕ field in the tachocline. This field accumulates until buoyancy forces cause it to rise into the main convective envelope. The α-effect, described in Sect. 2.3.1, converts B_ϕ to $\mathbf{B}_p$ and hence an $\alpha\Omega$ dynamo is operating. Rotation and convection are fundamental to the α-effect, and hence to magnetic activity. The Rossby number is defined as

$$R_T = \frac{v_T}{\ell\Omega_0} \sim \frac{|(\mathbf{v}_T \cdot \nabla)\mathbf{v}_T|}{|2\boldsymbol{\Omega}_0 \times \mathbf{v}_T|} \sim \frac{P_0}{\tau_T}, \tag{12.3}$$

where the turbulent velocity $\mathbf{v}_{\mathrm{T}}$ is measured in a frame rotating with the stellar angular velocity $\boldsymbol{\Omega}_0$, ℓ and τ_{T} are characteristic length and time-scales and $P_0 = 2\pi/\Omega_0$. This number measures the importance of the Coriolis force to the dynamics of the turbulent motions and is of fundamental relevance to all stellar dynamo models.

Rudiger and Brandenburg (1995) noted that the basic model of the solar dynamo has a magnetic diffusion time in the tachocline which is too short to allow for the storage of B_ϕ for periods as long as the 22 year solar cycle. However, the inclusion of poloidal flows connecting the tachocline to the main convective envelope can alleviate this problem, with the dynamo cycle periods being determined by the flow time-scale (e.g. Rempel 2006). Browning et al. (2006) modelled an $\alpha\Omega$ dynamo with simulations which included penetration by turbulent convection into the stable core, with an imposed tachocline shear. This gives a large-scale B_ϕ consistent with the parity observations of sunspots.

Secondary stars in interacting binaries that have a radiative core, and hence an over-shoot region, may be expected to have dynamo action with similarities to the solar case. However, the action of tides in the binary case may largely or completely remove differential rotation. This can occur if a standard stress tensor is used in the calculation of the turbulent viscous force, with orbital synchronization being achieved well within the binary lifetime. However, if the radiative core retained some asynchronism there would still be some shear in the tachocline region connecting it to the synchronous convective envelope. This would depend on the effectiveness of the coupling between the core and the envelope. Also, non-standard forms of the stress tensor can lead to states of differential rotation (see Campbell and Papaloizou 1983, and references therein). Even in the absence of shears, an α^2 dynamo may operate to generate significant magnetic fields.

12.2.3 Fully Convective Stars

Secondary stars with masses $M_{\mathrm{s}} \leq 0.35\, M_\odot$ will be fully convective and hence lack a tachocline region. Again, single star dynamo models are available and these can have relevance to the binary cases. Chabrier and Kuker (2006) considered a rotating, fully convective star with no differential rotation. They employed 3D numerical methods to solve the induction equation, retaining the α terms appropriate to an α^2 dynamo. An α-quenching form given by

$$\alpha = \frac{\alpha_0}{\left[1 + (B/B_{\mathrm{eq}})^2\right]^{\frac{1}{2}}} \tag{12.4}$$

was used, where $B_{\rm eq}$ is the equipartition field defined by

$$\frac{B_{\rm eq}^2}{2\mu_0} = \frac{1}{2}\rho v_{\rm T}^2. \tag{12.5}$$

Vacuum surface conditions were employed. A local mixing length approximation was adopted to allow for stratification in the computations of α and η. For rapid rotation α becomes independent of the Rossby number, but η retains a dependence. The computations were begun with a small-scale magnetic field of mixed parity, containing non-axisymmetric parts.

The α^2 dynamo generates a large-scale, non-axisymmetric $\mathbf{B}$ field which is symmetric in z (i.e. quadrupolar). Dynamo action occurs for a Rossby number of $R_{\rm T} < 25$. Field growth is limited by α-quenching to give $B \simeq B_{\rm eq}$ with values of a few kG, consistent with surface fields observed in M dwarfs (e.g. Kochukhov and Lavail 2017). Higher order multipoles can occur. The rotation rates used were considerably slower than those occurring in interacting binary stars, and hence fields of at least kG magnitudes may be expected for secondary stars.

Browning (2008) considered a 0.3 $M_\odot$ fully convective star, rotating at the solar rate. The 3D MHD equations were solved numerically using an anelastic spherical harmonic code. The anelastic approximation filters out sound waves and fast magnetosonic modes. Vacuum conditions were used at the stellar surface. Firstly, the hydrodynamic equations were solved, with an initially uniform Ω. Convection develops and differential rotation becomes established. The convective motions consist of small-scale intermittent motions near the surface and weaker large-scale flows in the interior.

A seed magnetic field was then introduced and the established flows act as a dynamo, sustaining $\mathbf{B}$ against decay. The resulting $\mathbf{B}$ field has structures on a range of spatial scales. Typically the magnetic field has larger length-scales in the deep interior and smaller scales near the surface. The mean field has a strong axisymmetric component and $B_\phi^2 \simeq 0.2B^2$, so most energy is in the poloidal component. The field polarity is stable on time-scales of $\gtrsim 20$ year and strengths of up to 10 kG can be attained. When equipartition is approached, the $\mathbf{J} \times \mathbf{B}$ forces can reduce $|\nabla\Omega|$ to small values. The mean field is still sustained as $|\nabla\Omega| \to 0$, so an α^2 dynamo is operating. Lowering the Rossby number gives higher values of $B^2/\mu_0\rho v^2$ and a $\mathbf{B}$ field with larger length-scales.

These studies indicate that dynamo action in fully convective secondary stars should still be possible even if tides have removed differential rotation. The fast rotation rates are particularly favourable for the α-effect and large-scale magnetic fields could be generated in the secondary having at least kG values. The presence of large-scale poloidal magnetic fields, which extend into the surrounding region, is of particular relevance to binary systems. Reviews of stellar dynamo theory are given in Mestel (2012) and Priest (2014).

12.3 White Dwarf Magnetic Fields

12.3.1 Observations and Background

The magnetic cataclysmic variables consist of the intermediate polars and the AM Hercules binaries. These are believed to account for $\simeq$ 25% of all CVs. The white dwarf primary stars in these systems have surface magnetic fields with polar strengths of $(B_{\rm p})_0 \gtrsim 10^6$ G, which places them in the strong magnetic field class. White dwarfs in other CVs are likely to have magnetic fields, but they must be significantly weaker since only the AM Her stars and the intermediate polars exhibit detectable magnetic effects. The white dwarf fields in the AM Her systems are measured via cyclotron harmonic observations or via photospheric Zeeman splitting. These methods give information on the strength and the structure of the field (e.g. Harrison and Campbell 2015). Because the intermediate polar white dwarfs have weaker magnetic fields than those in the AM Her systems, estimates of the field have only been made in a few cases, using circular polarization measurements. The resulting fields are typically an order of magnitude lower than those observed in the AM Her stars (see Warner 1995, for a review of observational techniques). Indirect estimates of the magnetic field can be made in intermediate polars by comparing theoretical predictions of the spin behaviour of the white dwarf due to its interaction with the accretion disc with spin period observations.

The main body of a white dwarf consists of non-degenerate ions and degenerate electrons. A temperature can be associated with the ions, with typical values of $\simeq 10^7$ K, while the electrons can be considered to be effectively at zero degrees Kelvin. There is a thin, non-degenerate surface layer at a much lower temperature than that of the ions in the core. The degenerate core has a high electrical conductivity due to the long mean free paths of the electrons. The decay time of a magnetic field in the core is typically $\tau_{\rm d} \gtrsim 10^{10}$ year (e.g. Wendell et al. 1987). Hence a fossil field origin is generally believed to account for the strong fields observed in white dwarfs, without the need for dynamo action. However, evolutionary processes associated with the formation of interacting binaries may play a part in determining the magnetic field.

Tout et al. (2004) considered the standard assumption that magnetic Ap and Bp stars are the progenitors of strongly magnetic white dwarfs. The assumption of a magnetic flux, estimated by

$$\psi_{\rm m} = 4\pi R^2 B, \tag{12.6}$$

being conserved during evolutionary contraction to the white dwarf state, with an initial field in the range 10^2 G $\lesssim B \lesssim 10^4$ G, leads to fields in the observed strong class range. Wickramasinghe and Ferrario (2005) pointed out that the magnetic field decay time in a white dwarf exceeds the cooling time, which is consistent with a fossil origin for **B**. Some contribution to **B** might be made by a dynamo operating

during post main sequence evolution, before flux freezing occurs. They suggested that white dwarf progenitors may not just be Ap and Bp stars, but also stars of mass $\gtrsim 4.5\, M_\odot$ containing magnetic fields not yet observed.

12.3.2 Field Enhancement Due to Common Envelope Evolution

Wickramasinghe et al. (2008) considered data obtained from the Sloan Digital Sky Survey. This consists of spectral observations of 1253 detached binaries, mainly containing a white dwarf and an M dwarf star, identified and catalogued by Silvestri et al. (2007). No magnetic white dwarf fields significantly above 10^6 G were detected in this large number survey of non-interacting binary systems. From this, the authors suggest that the origin of the strong magnetic field white dwarfs is linked to the formation processes of interacting binary systems.

It is argued that the white dwarfs in cataclysmic variables must have been the cores of giant star components. The orbital separation would decrease from a value of $\sim 100 R_\odot$, which accommodated the giant star, to $\sim R_\odot$, for the M dwarf to fill its Roche lobe. Such evolution is believed to be facilitated by the interaction of the stars with a common envelope (Paczynski 1976). The giant star fills its Roche lobe and unstable mass transfer occurs on a dynamical time-scale. Accretion on to the companion cannot occur on such a short time-scale, and instead transferred material forms a common envelope surrounding the two dense cores. Angular momentum and energy are transferred from the orbit to the common envelope, which is gradually ejected. As the cores approach each other the orbital period decreases and differential rotation is generated in the envelope. The envelope is expected to be convective, since it consists of material from the giant star, and this together with the differential rotation could lead to dynamo action. The resulting magnetic interaction may enhance the processes that cause the ejection of the envelope. The result of such evolution would be a strong $\mathbf{B}$ field surrounding the hot degenerate core. Penetrated field would become frozen as the core cools and contracts. Closer stellar cores could result in higher $\mathbf{B}$ fields, while wider separations may result in much lower field white dwarfs.

These ideas for the enhancement of white dwarf magnetic fields were investigated further by Potter and Tout (2010). They pointed out that fossil fields originating in Ap and Bp stars may not survive the convective phases of evolution. Developing further the model of Wickramasinghe et al. (2008), the degenerate core of the giant star was taken to be embedded in a simple, time-dependent common envelope field, assumed to be of dynamo origin, having the form

$$\mathbf{B} = B_z(t)\hat{\mathbf{z}}, \tag{12.7}$$

with $\hat{\mathbf{z}}$ parallel to the orbital angular momentum vector. This induces a field inside a spherical degenerate core of radius r_c, having a magnetic diffusivity $\eta(r, t)$ which was taken to be separable. The diffusive induction equation was solved inside the core, with the poloidal magnetic field scalar expanded in basis functions of the form $S_l(r, t) P_l(\cos\theta)$, where P_l are Legendre polynomials. A degenerate core conductivity due to Wendell et al. (1987) was adopted. The continuity of $\mathbf{B}$ at $r = r_c$ couples the core field to the inducing $B_z(t)$ field. Values of $r_c = 0.01 R_\odot$ and $M_c = 0.06 M_\odot$ were taken, with an $n = 1.5$ polytropic model.

The extent to which the magnetic field is able to penetrate the degenerate core depends on the lifetime of the common envelope. As the density increases towards the centre of the core the conductivity rises rapidly, inhibiting further penetration of the field. Typically, the field is confined to the outer 10% of the core by radius. An envelope magnetic field maintained in a single direction produces a much stronger white dwarf field than one that has rapid variations in its orientation. A constant field $\mathbf{B}_0$ was applied for a range of time intervals. There is an initial growth phase, then when the external field is removed the core field peaks and decays. The strength of $\mathbf{B}$ that remains is proportional to the application time of the envelope field. Cooling causes η to significantly decrease and this lengthens the field decay time, effectively freezing $\mathbf{B}$. An oscillatory $B_z(t)$ gives smaller field penetration and a less effective transfer of $\mathbf{B}$ from the envelope to the core compared to the constant applied field cases. For energy transferred via orbital decay, over a time interval of 3.6×10^4 year with a constant applied $\mathbf{B}$, white dwarf surface fields of $\simeq 10^7$ G can result.

12.3.3 Field Modification Due to Accretion

A typical decay time for a dipole mode magnetic field in a white dwarf is $\tau_d \sim 10^{10}$ year. With a stellar mass of $M_p = 0.5 M_\odot$ and an accretion rate of $\dot{M}_p = 10^{-10} M_\odot$ year^{-1}, the total mass transfer time is $\tau_M = M_p/\dot{M}_p = 5 \times 10^9$ year. Hence τ_d and τ_M are comparable. This has led to investigations of the effects of accretion on the evolution of the white dwarf magnetic field. Assuming that accreted matter is not lost, and that material is incorporated into the degenerate core, the star will contract as its mass increases. Hence a slow radial inflow will occur, and this may affect the magnetic field if its diffusion time-scale is not significantly shorter than the inflow time-scale.

Cumming (2002) constructed a model for the global evolution of an axisymmetric poloidal magnetic field, assuming spherical accretion of matter having the same composition as the core. Magnetically confined accretion columns will be much more localized, but it is assumed that accumulated material can gradually flow around the surface. The induction equation was solved, incorporating a radial velocity which was calculated from a series of stellar models with increasing masses to simulate the contraction due to accretion. Two different surface conditions were tested, one with an exterior vacuum and the other assuming that screening currents effectively reduce the surface field to zero. The interior field solution is shown not

to be sensitive to the choice of surface condition, so a vacuum surface condition can be used.

The evolution of the magnetic field was followed during the accretion of $0.1M_\odot$ of material on to a $0.6M_\odot$ white dwarf at a range of rates. For accretion rates above a critical value of $\dot{M}_c \simeq 3 \times 10^{-10} M_\odot \,\mathrm{year}^{-1}$, the surface field values are reduced as the field is advected into the interior. Reductions by factors of $\simeq 0.1$ are possible for higher accretion rates. It was noted that a typical accretion rate in an AM Her binary is $\dot{M}_p \simeq 5 \times 10^{-11} M_\odot \,\mathrm{year}^{-1} < \dot{M}_c$, while a typical rate in an intermediate polar is $\dot{M}_p \simeq 10^{-9} M_\odot \,\mathrm{year}^{-1} > \dot{M}_c$, and the intermediate polars have surface fields smaller than those of AM Her primaries by a factor of $\lesssim 0.1$. Hence it was suggested that intermediate polars may have white dwarfs with surface magnetic fields that have been reduced by their higher accretion rates. There are, however, significant uncertainties in such calculations due to the complex nature of the problem. In particular, magnetic buoyancy can play a significant role in the field evolution process.

12.4 Neutron Star Magnetic Fields

12.4.1 Background

The X-ray binary pulsars and the accreting millisecond pulsars have neutron star primaries with surface magnetic field strengths believed to be in the range $10^9 \mathrm{G} \lesssim (B_p)_0 \lesssim 10^{12} \mathrm{G}$. Neutron stars are believed to have an outer solid crust, with metallic transport properties, and an inner fluid core. The core has a complex multi-fluid structure, involving protons, neutrons and electrons. It is not known how the electric current sources of the magnetic field are distributed in the star, but the decay times of the regions are long so a fossil field origin for **B** is most likely. Like the cases of binary white dwarfs, the possible effects of accretion on the topology and evolution of neutron star magnetic fields have been investigated.

12.4.2 The Crustal Region

Konar and Bhattacharya (1997) explored the effects of accretion on magnetic field decay in neutron stars. They assumed that the current sources of **B** are initially confined to the outer crust. The crustal magnetic field undergoes Ohmic diffusion due to the electrical conductivity of the lattice, with a long decay time in the absence of accretion. When accretion is turned on, heating of the crust reduces σ by several orders of magnitude and hence τ_d is reduced. However, as its mass increases the neutron star contracts and newly accreted material adds to the crust while original crustal material becomes assimilated into the superconducting core. The original

current carrying layers are pushed into denser regions, with higher σ. This effect slows down the magnetic field decay rate.

The evolution of the crustal field due to Ohmic diffusion and material motions was investigated by solving the induction equation, incorporating an inward radial velocity of

$$v_r(r) = -\frac{\dot{M}_{\rm p}}{4\pi r^2 \rho(r)}. \tag{12.8}$$

The conductivity σ is a steeply increasing function of ρ, with a large increase occurring in ρ inwards through the crust. The mass of the crust is determined by the total mass of the star, and remains effectively constant for accreted masses of $\Delta M \simeq 0.1 M_\odot$. Hence accretion causes the continuous assimilation of material from the base of the crust into the core. The contraction of material shortens the length-scales in the crust. A surface boundary condition matched the internal magnetic field to an external dipole configuration, while a lower crustal boundary condition ensured that the field which becomes frozen here moves inside the core. The temperature of the crust was assumed to be uniform and constant during the accretion phase. The induction equation was solved numerically, for a range of accretion rates.

The magnetic field undergoes a phase of decay, first as a power law and then exponentially, subsequently becoming stabilized as its current distribution becomes assimilated into the highly conducting core. The duration of the exponential phase of decay, and hence the value of B at which freezing occurs, are strongly dependent on $\dot{M}_{\rm p}$. The higher the value of $\dot{M}_{\rm p}$ the sooner freezing sets in, giving a higher residual field. The decay proceeds faster at higher crustal temperatures. Higher accretion rates ensure quicker material transport to higher densities, causing B to level off at a higher value. Reductions in surface magnetic field strength by factors of ~ 0.1–0.01 can occur due to the effects of accretion.

Cumming et al. (2001) found that magnetic buoyancy instabilities can prevent the burial of the surface magnetic field by accretion. Payne and Melatos (2007) showed that accretion columns that are strongly magnetically confined on the surface of a neutron star can be stable at least for accreted masses of $\Delta M \simeq 10^{-3} M_\odot$. This may affect the results of models that make the assumption of spherical accretion.

12.4.3 The Core Region

Passamonti et al. (2007) considered aspects of magnetic field evolution in the superconducting core of neutron stars. The authors noted that it is usually assumed that the core structure evolves through quasi-static states, with the magnetic field evolving through Hall drift and Ohmic dissipation. However, they pointed out that only a restricted range of magnetic field configurations are consistent with this assumption and hence dynamical flows, having time-scales much shorter than the

field decay time, are more likely to occur. A complex, multiple fluid problem arises with associated equations describing the motions of the proton, electron and neutron components. For core temperatures of $\lesssim 10^{10}$K the proton fluid adopts a type II superconducting state, and the magnetic field then penetrates the core as a dense array of thin flux tubes. Advection effects are likely to have a significant influence on the evolution time-scales of core magnetic fields.

A recent review of magnetic field evolution in neutron stars, with a particular emphasis on accreting binary systems, is given by Konar (2017).

12.5 Summary and Discussion

Although direct measurements of magnetic fields on the secondary stars of interacting binaries have not been possible so far, observations of similar single stars and of the wide double M dwarf binary GJ65 AB strongly suggest that significant magnetic fields will exist on secondary stars. The fields measured on the rapidly rotating, fully convective components in GJ65 AB imply that secondary surface fields could have values $\gtrsim$ several kG. The dynamo models support this conclusion and illustrate that fully convective stars can have significant magnetic fields, even though a tachocline region is absent. Dynamos of an α^2 nature can be just as effective as $\alpha\Omega$ dynamos in rapidly rotating lower main sequence stars.

The large-scale poloidal magnetic fields found in investigations of stars with significant convective regions are of the type suitable for producing locked synchronous states in AM Her binaries, and for channelling magnetic winds which can cause braking in cataclysmic variables above the period gap.

The strong white dwarf fields occurring in magnetic CVs are likely to be of fossil origin, but the evolutionary stage at which flux freezing occurs is uncertain. The absence of strongly magnetic white dwarfs in the large number of non-interacting binaries in the Sloan Digital Sky Survey, containing white dwarf and M dwarf components, may suggest a connection between the formation of interacting binaries and strongly magnetic white dwarfs. The penetration of a strong magnetic field, generated by a dynamo in the common envelope, into the degenerate core of the giant star can result in a strongly magnetic white dwarf.

The higher accretion rates occurring in the intermediate polars may lead to some reduction of the white dwarf surface magnetic field strength. Accreted material increases the mass of the star and, provided that it becomes incorporated into the degenerate core, contraction will occur. The radial motions can affect the magnetic field structure and lead to a reduction in its surface values. Some models of this effect can lead to a reduction by a factor of $\simeq 0.1$. The models usually assume spherical accretion, while the magnetic field channels material to localized regions on the stellar surface. However, material may spread horizontally when a sufficient amount has accreted on to the star.

The magnetic fields of neutron stars are believed to be of fossil origin, since they have very long decay times. As with the case of binary white dwarfs, accretion may

significantly affect the field topology and surface strength over the lifetime of the binary. The core structure is complex and shorter time-scale motions could affect the field.

References

Browning, M.K., 2008, ApJ, 676, 1262.
Browning, M.K., Miesch, M.S., Brun, A.S., Toomre, J., 2006, ApJ, 648, L157.
Browning, M.K., Basri, G., Marcy, G.W., West, A.A., Zhang, J., 2010, ApJ, 139, 504.
Campbell, C.G., Papaloizou, J.C.B., 1983, MNRAS, 204, 433.
Chabrier, G., Kuker, M., 2006, A&A, 446, 1027.
Cumming, A., 2002, MNRAS, 333, 589.
Cumming, A., Zweibel, E., Bildsten, L., 2001, ApJ, 557, 958.
Harrison, T.E., Campbell, R.K., 2015, ApJS, 219, 32.
Hurley, J.R., Tout, C.A., Pols, O.R., 2002, MNRAS, 329, 897.
Kochukhov, O., Lavail, A., 2017, ApJ, 835, L4.
Konar, S., 2017, JApA, 38, 47.
Konar, S., Bhattacharya, D., 1997, MNRAS, 284, 311.
Mestel, L., 2012, Stellar Magnetism, Second Edition, Oxford University Press.
Mohanty, S., Basri, G., 2003, CSSS, 12, 683.
Morin, J., et al., 2008, MNRAS, 390, 567.
Ossendrijver, M., 2003, ASPC, 286, 97.
Paczynski, B., 1976, IAUS, 73, 75.
Passamonti, A., Akgun, T., Pons, J.A., Miralles, J.A., 2017, MNRAS, 469, 4979.
Payne, D.J.B., Melatos, A., 2007, MNRAS, 376, 609.
Potter, A.T., Tout, C.A., 2010, MNRAS, 402, 1072.
Priest, E., 2014, Magnetohydrodynamics in the Sun, Cambridge University Press.
Reiners, A., Basri, G., 2007, ApJ, 656, 1121.
Rempel, M., 2006, ApJ, 637, 1135.
Rudiger, G., Brandenburg, A., 1995, A&A, 296, 557.
Silvestri, N.M., et al., 2007, AJ, 134, 741.
Spiegel, E.A., Zahn, J.P., 1992, A&A, 265, 106.
Tout, C.A., Wickramasinghe, D.T., Ferrario, L., 2004, MNRAS, 355, L13.
Warner, B., 1995, Cataclysmic Variable Stars, CUP, Cambridge.
Wendell, C.E., van Horn, H.M., Sargent, D., 1987, ApJ, 313, 284.
Wickramasinghe, D.T., Ferrario, L., 2005, MNRAS, 356, 1576.
Wickramasinghe, D.T., Liebert, J., Ferrario, L., Pringle, J.E., 2008, MNRAS, 387, 897.
Zahn, J.P., 1977, A&A, 57, 383.

Chapter 13
Stellar Magnetic Winds

Abstract The tidally influenced secondary stars in interacting binaries are rapidly rotating and possess convective envelopes or are fully convective. This makes the generation of large-scale magnetic fields in such stars very likely, and magnetically influenced wind flows from the stellar surface would then lead to magnetic braking. The secondary would be spun down to an under-synchronous state and tides would then operate to spin the star up at the expense of the orbital angular momentum. This mechanism can account for the higher mass transfer rates occurring in binaries above the period gap, and hence the theory of magnetic braking has important application to interacting binaries.

The essentials of stellar magnetic braking theory are presented here, with particular emphasis on the fast rotator regime. This is applied to derive mass transfer rates in binaries with periods $\gtrsim 3.0\,\mathrm{h}$, for a range of laws relating the secondary's surface magnetic field to its rotation rate. Explanations for the period gap, and why AM Herculis binaries appear not to be affected by the gap, are discussed.

13.1 Introduction

The lobe-filling secondary stars in binaries with orbital periods $\lesssim 10\,\mathrm{h}$ have masses $\lesssim 1 M_\odot$ and so will possess significant convective envelopes, becoming fully convective for $M_\mathrm{s} \leq 0.35\,M_\odot$. Tidal synchronization means that these stars will be rapidly rotating. As seen in Sect. 2.3, turbulence and rapid rotation favour dynamo action, so such secondaries are likely to have a magnetic field. The observations and theory related to magnetic fields in secondary stars were discussed in Chap. 12.

A hot expanding corona will lead to some mass loss, driven by thermal pressure gradients and centrifugal acceleration. A small coronal mass flux, and a moderate magnetic field, result in highly conducting material being channelled along field lines which are only slightly distorted by the flow. Field distortion becomes large when the kinetic energy density of the outflowing material becomes comparable to the poloidal magnetic energy density, equality occurring at the Alfvén speed given

C. G. Campbell, *Magnetohydrodynamics in Binary Stars*, Astrophysics and Space Science Library 456, https://doi.org/10.1007/978-3-319-97646-4_13

by

$$v_{\rm A} = \left(\frac{B_{\rm p}^2}{\mu_0 \rho} \right)^{\frac{1}{2}} . \tag{13.1}$$

If this speed is reached before a magnetic coronal loop starts to close, then the field is dragged out with the flow. The Alfvénic points, defined by (13.1), constitute the Alfvén surface $S_{\rm A}$.

Within $S_{\rm A}$ the stellar magnetic field tries to bring the gas into corotation with the star. The magnetic torque imparts angular momentum to the flowing material, at the expense of the stellar angular momentum, causing a braking torque on the star. The open field lines constitute the wind zone, which accounts for the loss of stellar angular momentum. Magnetic wind braking of a lobe-filling secondary star in a binary system drives the star towards an under-synchronous state and the resulting tidal torque then leads to a loss of orbital angular momentum. This process is invoked to explain mass transfer in systems with orbital periods $\gtrsim$ 3 h, since gravitational radiation losses are not sufficient to account for the larger accretion rates believed to occur at these periods.

In Sect. 13.2 stellar magnetic wind theory is formulated. A simple field model is presented and results are derived for the fast rotator regime. Section 13.3 applies this wind theory to secondary stars as a means of driving mass transfer, and a range of dynamo laws are considered, relating the stellar rotation rate to the surface magnetic field. The origin of the period gap, and winds from AM Herculis stars are then addressed.

13.2 Stellar Magnetic Wind Theory

13.2.1 Background

The basic wind theory for a rotating, magnetic star is formulated here. Parker (1963) showed that a hot stellar corona cannot be contained by the pressure of the surrounding interstellar medium, and so expands to generate a wind. Schatzman (1962) pointed out that if a strong stellar magnetic field keeps the wind corotating with the star by magnetic torques out to large distances, then far more angular momentum per unit mass will be carried off than in a non-magnetic wind, in which the gas conserves its angular momentum. The theory of a steady, axisymmetric magnetic wind was formulated by Mestel (1967, 1968) and Weber and Davis (1967). Further work was done by many authors, including Pneuman and Kopp (1971), Okamoto (1974) and Sakurai (1985). The braking of late-type stars was considered by Mestel and Spruit (1987), including the fast rotator regime which is of particular relevance to corotating secondary stars in binaries. While fundamental results are common to these papers, specific models vary. The formulation presented here is based on that of Mestel (1968) and Mestel and Spruit (1987).

13.2.2 Angular Momentum Transport

Consider a star rotating with angular velocity Ω_s about the z-axis in a cylindrical coordinate system (ϖ, ϕ, z), with its origin at the stellar centre. The unperturbed magnetic field is taken to be dipolar with its moment along the z-axis, so the poloidal field $\mathbf{B}_p$ is axisymmetric. The dead zone will consist of field lines emanating from the stellar surface nearer to the equator than to the poles. The associated flux tubes form closed loops trapping hot gas within them. These loops close sufficiently near to the star so the magnetic pressure exceeds the gas pressure. The wind zone consists of field lines emerging nearer the poles which extend further and are unable to trap the hot gas. These flux tubes are pulled open by the flowing gas before it reaches the Alfvén surface S_A, so the outer poloidal field adopts a more radial structure. Angular momentum transport occurs in the wind zone. The star is taken to be a spherically symmetric gravity source, so in the absence of magnetic torques the wind material would conserve its specific angular momentum $\varpi^2\Omega$.

The steady state momentum, induction and continuity equations are

$$(\mathbf{v}\cdot\nabla)\mathbf{v} = -\frac{1}{\rho}\nabla P - \nabla\psi + \frac{1}{\mu_0\rho}(\nabla\times\mathbf{B})\times\mathbf{B}, \tag{13.2}$$

$$\nabla\times(\mathbf{v}\times\mathbf{B}) = \mathbf{0}, \tag{13.3}$$

$$\nabla\cdot(\rho\mathbf{v}) = 0, \tag{13.4}$$

where perfect conductivity is assumed, and ψ is the stellar gravitational potential given by

$$\psi = -\frac{GM_s}{r}. \tag{13.5}$$

The poloidal and toroidal components of the induction equation (13.3) yield

$$\mathbf{v}_p = \kappa\mathbf{B}_p, \tag{13.6}$$

$$\Omega - \frac{\kappa B_\phi}{\varpi} = \alpha, \tag{13.7}$$

where κ is a scalar function of position and α is a constant on each field-streamline, corresponding to the angular velocity of the field line. These equations combine to give

$$\mathbf{v} = \kappa\mathbf{B} + \varpi\alpha\hat{\boldsymbol{\phi}}. \tag{13.8}$$

Since $\nabla\cdot\mathbf{B}_p = 0$, (13.4) and (13.6) lead to

$$\mathbf{B}_p\cdot\nabla(\rho\kappa) = 0, \tag{13.9}$$

so

$$\rho\kappa = \frac{\rho v_{\rm p}}{B_{\rm p}} = \epsilon, \tag{13.10}$$

where ϵ is constant on a field line, being the mass flow rate per unit poloidal flux.

The wind angular momentum transport equation can be found by considering the azimuthal component of the momentum equation (13.2), together with the continuity equation (13.4), which yields

$$\nabla \cdot (\varpi^2 \Omega \rho \mathbf{v}_{\rm p}) = \frac{\varpi}{\mu_0} [(\nabla \times \mathbf{B}) \times \mathbf{B}]_\phi = \frac{1}{\mu_0} \mathbf{B}_{\rm p} \cdot \nabla(\varpi B_\phi), \tag{13.11}$$

relating the divergence of angular momentum flux to the magnetic torque. The use of (13.6) for $\mathbf{v}_{\rm p}$ and (13.10) for ϵ in (13.11) gives

$$\epsilon \varpi^2 \Omega - \frac{\varpi B_\phi}{\mu_0} = -\beta, \tag{13.12}$$

where β is constant on a field line. This represents the total rate of transport of angular momentum per unit poloidal flux tube, carried jointly by the gas and magnetic stresses.

Equations (13.7), (13.10) and (13.12) combine to yield

$$B_\phi = \frac{\mu_0 \beta/\varpi + \mu_0 \epsilon \alpha \varpi}{1 - \mu_0 \epsilon^2/\rho}, \tag{13.13}$$

and

$$\Omega = \frac{\alpha + \mu_0 \epsilon \beta / \varpi^2 \rho}{1 - \mu_0 \epsilon^2/\rho}. \tag{13.14}$$

It follows from (13.10) that

$$\frac{\mu_0 \epsilon^2}{\rho} = \frac{\mu_0 \rho v_{\rm p}^2}{B_{\rm p}^2} = \frac{v_{\rm p}^2}{v_{\rm A}^2}, \tag{13.15}$$

where $v_{\rm A}$ is the Alfvén speed. For the expected wind mass loss rates and surface magnetic fields, $v_{\rm p} \ll v_{\rm A}$ holds near the star. The density decreases outwards so $\mu_0 \epsilon^2/\rho$ increases until it reaches unity at the Alfvén point $P_{\rm A}$ where

$$v_{\rm p} = v_{\rm A} = \frac{B_{\rm p}}{(\mu_0 \rho)^{\frac{1}{2}}}, \tag{13.16}$$

and

$$\rho = \rho_{\rm A} = \mu_0 \epsilon^2. \tag{13.17}$$

Equations (13.13) and (13.14) then show that B_ϕ and Ω will only be non-singular at $P_{\rm A}$ if

$$-\beta = \frac{\alpha \varpi_{\rm A}^2 \rho_{\rm A}}{\mu_0 \epsilon} = \epsilon \alpha \varpi_{\rm A}^2 = \left(\frac{\rho v_{\rm p}}{B_{\rm p}}\right) \alpha \varpi_{\rm A}^2. \tag{13.18}$$

This shows that the angular momentum transport per unit flux tube, carried jointly by the gas and field, is equivalent to that which would be carried by the gas if it were kept corotating with angular velocity α out to the Alfvén point $P_{\rm A}$.

The use of (13.17) for ϵ and (13.18) for β in (13.13) and (13.14) gives

$$B_\phi = -\mu_0 \epsilon \varpi_{\rm A}^2 \alpha \frac{(1 - \varpi^2/\varpi_{\rm A}^2)}{\varpi (1 - \rho_{\rm A}/\rho)}, \tag{13.19}$$

and

$$\Omega = \frac{(1 - \varpi_{\rm A}^2 \rho_{\rm A}/\varpi^2 \rho)}{(1 - \rho_{\rm A}/\rho)} \alpha = \frac{[1 - (\varpi_{\rm A}^2 B_{\rm A}/\varpi^2 B_{\rm p})(v_{\rm p}/v_{\rm A})]}{(1 - \rho_{\rm A}/\rho)} \alpha, \tag{13.20}$$

where $B_{\rm A}$ is the value of $B_{\rm p}$ at $\varpi_{\rm A}$. For any realistic poloidal field, the quantity $\varpi^2 B_{\rm p}$ is slowly varying along a field-streamline, while $v_{\rm p}/v_{\rm A}$ and $\rho_{\rm A}/\rho$ decrease rapidly towards the coronal base. It therefore follows from (13.20) that well inside the Alfvénic point the rotational shear is small, since $\Omega \simeq \alpha$. At the cornal base, $r = r_0$, and $\Omega = \Omega_{\rm s}$ so

$$\alpha = \frac{(1 - \rho_{\rm A}/\rho_0)}{[1 - (\varpi_{\rm A}^2 B_{\rm A}/\varpi_0^2 B_0)(v_0/v_{\rm A})]} \Omega_{\rm s}, \tag{13.21}$$

showing that the constant α is very close to $\Omega_{\rm s}$. Hence, near to the star, $\Omega \simeq \Omega_{\rm s}$ and then (13.18) for β and (13.19) for B_ϕ show that the magnetic term in the angular momentum transport equation (13.12) dominates the material term by a factor $(\varpi_{\rm A}/\varpi)^2$. A nearly force-free field occurs in this region, with ϖB_ϕ approximately conserved along poloidal field lines. Well beyond $P_{\rm A}$, where $\rho_{\rm A}/\rho \gg 1$ and $v_{\rm p}/v_{\rm A} \gg 1$, (13.20) gives $\varpi^2 \Omega \simeq \varpi_{\rm A}^2 \Omega_{\rm s}$, and material angular momentum transport dominates, corresponding to the approximate conservation of material angular momentum.

Outward angular momentum transport requires $-\beta B_{\rm p} > 0$ so, from (13.18),

$$\rho v_{\rm p} \alpha \varpi_{\rm A}^2 > 0 \tag{13.22}$$

must hold. For outflows this implies $\alpha > 0$ and hence $\Omega_s > 0$. Equations (13.20) and (13.21) show that beyond the coronal base Ω lags Ω_s. The consequent shear generates B_ϕ and the resulting $B_p B_\phi$ stress gives a torque which acts to increase Ω. The reaction to this torque causes a decrease in the angular velocity of the star. The star spins down on the braking time-scale which far exceeds the wind flow time-scale of $\sim \varpi / v_p$. The flow can therefore be treated as evolving on the braking time-scale through quasi-steady states, in which the magnetic torque acting on the matter in a volume element at a fixed point is balanced by a divergence of the angular momentum flux, as described by (13.11).

13.2.3 The Wind Flow

The wind speed is analysed by considering the component of the equation of motion along the flow. The wind zone is taken to be isothermal with sound speed a_w, so

$$P = a_w^2 \rho. \tag{13.23}$$

Using this and the vector identity (A2), the momentum equation (13.2) can be written as

$$(\nabla \times \mathbf{v}) \times \mathbf{v} = -\nabla \left(\frac{1}{2} v^2 + a_w^2 \ln \rho - \frac{GM_s}{r} \right) + \frac{1}{\mu_0 \rho} (\nabla \times \mathbf{B}) \times \mathbf{B}. \tag{13.24}$$

Taking the scalar product of this with $\mathbf{v}$ gives

$$\mathbf{v} \cdot \nabla \left(\frac{1}{2} v^2 + a_w^2 \ln \rho - \frac{GM_s}{r} \right) = \frac{1}{\mu_0 \rho} \mathbf{v} \cdot [(\nabla \times \mathbf{B}) \times \mathbf{B}]. \tag{13.25}$$

The use of (13.8) for $\mathbf{v}$ then yields

$$\frac{1}{\mu_0 \rho} \mathbf{v} \cdot [(\nabla \times \mathbf{B}) \times \mathbf{B})] = \frac{\alpha \varpi}{\mu_0 \rho} [(\nabla \times \mathbf{B}) \times \mathbf{B})]_\phi = \alpha \mathbf{v} \cdot \nabla (\varpi^2 \Omega), \tag{13.26}$$

which is the rate of work done by the magnetic torque, with the last equality following from the angular momentum equation (13.11). Equations (13.25) and (13.26) show that

$$\frac{1}{2} v_p^2 + \frac{1}{2} \varpi^2 \Omega^2 + a_w^2 \ln \rho - \frac{GM_s}{r} - \alpha \varpi^2 \Omega = E \tag{13.27}$$

is constant on a field-streamline, where E is the total energy per unit mass. This is a generalized Bernoulli integral for an isothermal flow. The continuity equation

enables (13.27) to be written as

$$\nabla \cdot \left[\rho \mathbf{v} \left(\frac{1}{2} v_{\rm p}^2 + \frac{1}{2} \varpi^2 \Omega^2 + a_{\rm w}^2 \ln \rho - \frac{G M_{\rm s}}{r} - \alpha \varpi^2 \Omega \right) \right] = 0, \tag{13.28}$$

where the quantity in square brackets is the total energy flux. Equation (13.11), together with $\mathbf{v}_{\rm p} \cdot \nabla \alpha = 0$ and $\mathbf{B}_{\rm p} \cdot \nabla \alpha = 0$, gives the last term as

$$\begin{aligned} -\nabla \cdot (\rho \mathbf{v}_{\rm p} \alpha \varpi^2 \Omega) &= -\nabla \cdot \left(\frac{\alpha}{\mu_0} \varpi B_\phi \mathbf{B}_{\rm p} \right) \\ &= -\nabla \cdot \left(\frac{1}{\mu_0} (\mathbf{v} \times \mathbf{B}) \times \mathbf{B} \right) = \nabla \cdot (\mathbf{E} \times \mathbf{H}), \end{aligned} \tag{13.29}$$

where $\mathbf{H} = \mathbf{B}/\mu_0$ and the second and last equalities follow from (13.8) for $\mathbf{v}$ and Ohm's law with perfect conductivity, respectively. Hence (13.28) becomes

$$\nabla \cdot \left[\rho \mathbf{v} \left(\frac{1}{2} v_{\rm p}^2 + \frac{1}{2} \varpi^2 \Omega^2 + a_{\rm w}^2 \ln \rho - \frac{G M_{\rm s}}{r} \right) + \mathbf{E} \times \mathbf{H} \right] = 0, \tag{13.30}$$

where $\mathbf{E} \times \mathbf{H}$ is the Poynting flux of electromagnetic energy.

If the structure of $\mathbf{B}_{\rm p}$ is supposed known, the use of (13.10) and (13.20) to eliminate $v_{\rm p}$ and Ω in (13.27) gives a relation of the form

$$H(\varpi, \rho) = E \tag{13.31}$$

between ρ and ϖ on a field-streamline. The condition (13.18) on β ensures that B_ϕ and Ω are non-singular, and it then follows that all non-singular solutions for ρ pass through the Alfvénic point $P_{\rm A}$. The function $H(\varpi, \rho_{\rm A})$ is only finite at $\varpi = \varpi_{\rm A}$. Equation (13.31) yields

$$\frac{d\rho}{d\varpi} = -\frac{\partial H/\partial \varpi}{\partial H/\partial \rho}. \tag{13.32}$$

The use of (13.7) and (13.10) to eliminate Ω and $v_{\rm p}$ in the Bernoulli integral (13.27) gives

$$H = \frac{\epsilon^2 B_{\rm p}^2}{2\rho^2} + a_{\rm w}^2 \ln \rho - \frac{G M_{\rm s}}{r} + \frac{1}{2} \left(\alpha \varpi + \frac{\epsilon B_\phi}{\rho} \right)^2 - \alpha \varpi \left(\alpha \varpi + \frac{\epsilon B_\phi}{\rho} \right). \tag{13.33}$$

Taking $\partial H/\partial \rho$, and employing (13.19) for B_ϕ/ρ, yields

$$\rho \frac{\partial H}{\partial \rho} = -v_{\rm p}^2 + a_{\rm w}^2 - \frac{\epsilon^2 B_\phi^2}{\rho^2 (1 - \rho/\rho_{\rm A})}. \tag{13.34}$$

Then noting, from (13.17), that

$$\frac{\rho_{\rm A}}{\rho} = \frac{\mu_0 \epsilon^2}{\rho} = \frac{\mu_0 \rho v_{\rm p}^2}{B_{\rm p}^2} = \left(\frac{v_{\rm p}}{v_{\rm A}}\right)^2, \tag{13.35}$$

gives

$$\rho \frac{\partial H}{\partial \rho} = \frac{v_{\rm p}^4 - (a_{\rm w}^2 + v_{\rm Ap}^2 + v_{{\rm A}\phi}^2) v_{\rm p}^2 + a_{\rm w}^2 v_{\rm Ap}^2}{(v_{\rm Ap}^2 - v_{\rm p}^2)}, \tag{13.36}$$

where $v_{{\rm A}\phi} = B_\phi/(\mu_0\rho)^{1/2}$. The condition $\partial H/\partial\rho = 0$ gives $v_{\rm p}$ equal to $v_{\rm sl}$ or $v_{\rm f}$, the slow and fast magnetosonic wave speeds (see Sect. 2.2.6). At these values of $v_{\rm p}$ it follows from (13.32) that $\partial H/\partial\varpi = 0$ is necessary for smoothly varying ρ, defining the slow and fast critical points $\varpi_{\rm sl}$ and $\varpi_{\rm f}$. Then (13.31) gives

$$H(\varpi_{\rm sl}, \rho_{\rm sl}) = H(\varpi_{\rm f}, \rho_{\rm f}) = E. \tag{13.37}$$

These conditions suffice to fix the solution along each field-streamline in terms of a non-dimensionalized coronal temperature, stellar rotation rate and magnetic flux. These are, respectively,

$$\ell_{\rm w} = \frac{GM_{\rm s}}{r_0 a_{\rm w}^2}, \tag{13.38a}$$

$$\nu = \frac{\alpha^2 r_0^3}{GM_{\rm s}}, \tag{13.38b}$$

$$\zeta_{\rm w} = \frac{B_0^2}{2\mu_0 (\rho_0)_{\rm w} a_{\rm w}^2}, \tag{13.38c}$$

evaluated at the coronal base $r = r_0$. Usually, the wind speed at the slow point is close to the sound speed. The fast speed is approximately the local Alfvén speed determined by the total magnetic field.

13.2.4 The Braking Torque

A magnetic braking torque is exerted on the star due to the outward transport of angular momentum resulting from the wind flow. The total rate of angular momentum transport is found by integrating $-\beta B_{\rm p}$ over the coronal base surface $r = r_0$, from the poles to the limiting field lines that define the extent of the wind region. Near the stellar surface $\mathbf{B}_{\rm p}$ will be close to its unperturbed dipole structure,

having the components

$$B_r = B_0 \left(\frac{r_0}{r}\right)^3 \cos\theta, \tag{13.39a}$$

$$B_\theta = \frac{B_0}{2} \left(\frac{r_0}{r}\right)^3 \sin\theta, \tag{13.39b}$$

with the poles at $\theta = 0$ and $\theta = \pi$. The poloidal field strength is therefore

$$B_\mathrm{p} = B_0 \left(\frac{r_0}{r}\right)^3 \left(1 - \frac{3}{4}\sin^2\theta\right)^{\frac{1}{2}}. \tag{13.40}$$

The rate of angular momentum transport is

$$-\dot{J} = -\int_{S_0} \beta \mathbf{B}_\mathrm{p} \cdot \hat{\mathbf{r}} dS_0, \tag{13.41}$$

where $\dot{J}$ is the stellar torque, and S_0 is the coronal base surface. Hence

$$-\dot{J} = -4\pi \int_0^{\bar{\theta}_0} \left(\frac{B_r}{B_\mathrm{p}}\right)_0 \beta B_\mathrm{p}(r_0, \theta_0) r_0^2 \sin\theta_0 d\theta_0, \tag{13.42}$$

where the limiting field line cuts the stellar surface at $(r_0, \bar{\theta}_0)$, and the symmetry of $-\beta B_\mathrm{p}$ about the equatorial plane has been used. Equations (13.10) for ϵ and (13.18) for β give

$$-\beta = \epsilon\alpha\varpi_\mathrm{A}^2 = \frac{\rho_0 v_0 \alpha \varpi_\mathrm{A}^2}{B_\mathrm{p}(r_0, \theta_0)}, \tag{13.43}$$

where $v_0 = v_p(r_0, \theta_0)$, so (13.39a)–(13.41) yield

$$-\dot{J} = 4\pi\Omega_\mathrm{s} r_0^4 \int_0^{\bar{\theta}_0} \rho_0 v_0 \left(\frac{\alpha}{\Omega_\mathrm{s}}\right) \left(\frac{\varpi_\mathrm{A}}{r_0}\right)^2 \frac{\sin\theta_0 \cos\theta_0 d\theta_0}{(1 - \frac{3}{4}\sin^2\theta_0)^{\frac{1}{2}}}. \tag{13.44}$$

The factor $(\varpi_\mathrm{A}/r_0)^2$, which increases with field strength B_0, represents the enhanced braking due to the magnetic torque. The magnetic field also plays a part in determining the upper limit $\bar{\theta}_0$ which reflects the extent of the dead zone.

The associated mass loss rate from the stellar surface is given by

$$\dot{M}_\mathrm{w} = -4\pi r_0^2 \int_0^{\bar{\theta}_0} \rho_0 v_0 \left(\frac{B_r}{B_\mathrm{p}}\right)_0 \sin\theta_0 d\theta_0, \tag{13.45}$$

and hence

$$\dot{M}_{\rm w} = -4\pi r_0^2 \int_0^{\bar{\theta}_0} \rho_0 v_0 \frac{\sin\theta_0 \cos\theta_0 d\theta_0}{\left(1 - \frac{3}{4}\sin^2\theta_0\right)^{\frac{1}{2}}}. \tag{13.46}$$

It follows from (13.44) for $\dot{J}$ and (13.46) for $\dot{M}_{\rm w}$ that

$$\frac{\dot{J}}{r_0^2 \Omega_{\rm s} \dot{M}_{\rm w}} = \frac{I}{K} = \Gamma, \tag{13.47}$$

where

$$I = \int_0^{\bar{s}} \rho_0 v_0 \left(\frac{\varpi_{\rm A}}{r_0}\right)^2 \left(1 - \frac{3}{4}s\right)^{-\frac{1}{2}} ds, \tag{13.48}$$

and

$$K = \int_0^{\bar{s}} \rho_0 v_0 \left(1 - \frac{3}{4}s\right)^{-\frac{1}{2}} ds, \tag{13.49}$$

with $s = \sin^2\theta_0$, and $\alpha = \Omega_{\rm s}$ has been used. The quantity Γ measures the effect of the magnetic field in increasing the angular momentum loss rate for a given mass loss rate. For an unconstrained spherically symmetric wind, $\Gamma = 2/3$. Magnetic channelling can increase Γ by factors of up to $\sim 10^3$.

13.2.5 A Simple Field Model

Well within the Alfvénic surface $S_{\rm A}$ the magnetic energy density dominates the kinetic energy density of the wind. The poloidal field $\mathbf{B}_{\rm p}$ will therefore remain close to its unperturbed structure, and channel the wind flow. Well beyond $S_{\rm A}$ the kinetic energy density of the flow dominates the energy density of the magnetic field. In this region the field will be passive, being pulled out to follow the nearly radial wind.

The detailed construction of $\mathbf{B}_{\rm p}$ requires solution of the poloidal trans-$\mathbf{B}_{\rm p}$ component of the equation of motion. This poses a formidable problem (e.g. Sakurai 1990; Mestel 2012). A simple field model was used by Mestel and Spruit (1987) in considering the braking of late-type stars. The field structure, shown in Fig. 13.1, represents the basic properties of the distortion in the flow regions. The poloidal field is taken to be dipolar, with components given by (13.39a) and (13.39b), out to a radius $\bar{r}$ which corresponds to the equatorial boundary of the dead zone. Beyond

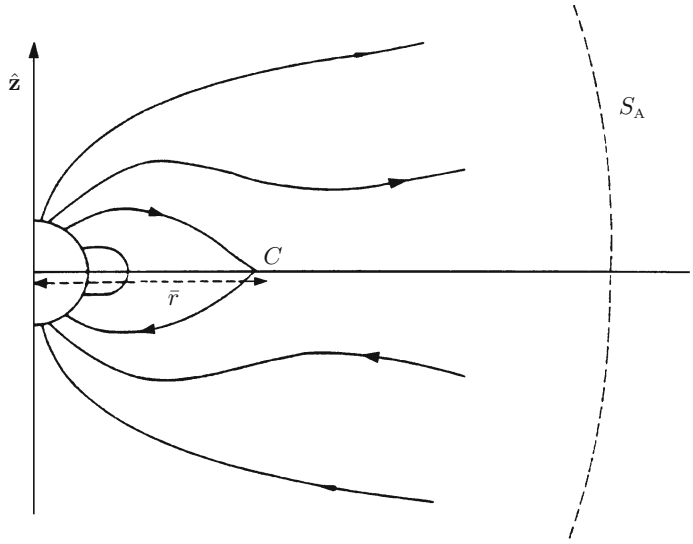

Fig. 13.1 The simplified wind magnetic field (from Mestel and Spruit 1987)

$\bar{r}$, $\mathbf{B}_p$ is taken as radial, so

$$\mathbf{B}_p = \bar{B}\left(\frac{\bar{r}}{r}\right)^2 \hat{\mathbf{r}}. \tag{13.50}$$

The field has a cusp on the equator at $\bar{r}$ and $B_p(r, \pi/2) = 0$ for $r > \bar{r}$. Close to $\theta = \pi/2$, B_r varies rapidly with θ and changes sign across the equator. Away from the equator B_r is expected to vary slowly with θ.

Material in the dead zone is in hydrostatic balance and is taken to be isothermal, with sound speed a_d. Hence

$$P = a_d^2 \rho, \tag{13.51}$$

and the force balance is

$$\nabla\left(\frac{GM_s}{r} + \frac{1}{2}\alpha^2 r^2 \sin^2\theta - a_d^2 \ln\rho\right) + \frac{1}{\mu_0 \rho}(\nabla \times \mathbf{B}) \times \mathbf{B} = \mathbf{0}. \tag{13.52}$$

Taking the scalar product with $\mathbf{B}$ then gives

$$\frac{GM_s}{r} + \frac{1}{2}\alpha^2 r^2 \sin^2\theta - a_d^2 \ln\rho = U, \tag{13.53}$$

where U is a constant along the field. It follows that the density along a field line is

$$\rho = (\rho_0)_{\rm d} \exp\left[-\frac{GM_{\rm s}}{R_{\rm s}a_{\rm d}^2}\left(1-\frac{R_{\rm s}}{r}\right)+\frac{\alpha^2 R_{\rm s}^2}{2a_{\rm d}^2}\left(\frac{r^2\sin^2\theta}{R_{\rm s}^2}-\sin^2\theta_0\right)\right], \tag{13.54}$$

with the coronal base $r_0 = R_{\rm s}$, being the stellar surface. Since the wind is an energy sink, a latitude-independent heat input at the coronal base should give a significantly lower temperature for the wind zone than for the dead zone. When the cusp C is well within $S_{\rm A}$, then $|B_\phi| \ll |B_{\rm p}|$, so the vertical continuity of the total pressure at C is

$$\left(\frac{B_{\rm p}^2}{2\mu_0}\right)_{\rm w} = P_{\rm d}, \tag{13.55}$$

using $P_{\rm d} \gg P_{\rm w}$. Taking $\bar{B} = (B_0/2)(R_{\rm s}/\bar{r})^3$, except at the equator $\theta = \pi/2$ where $\bar{B} = 0$, (13.50) becomes

$$\mathbf{B}_{\rm p} = \begin{cases} \pm\frac{B_0}{2}\left(\frac{R_{\rm s}}{\bar{r}}\right)^3\left(\frac{\bar{r}}{r}\right)^2\hat{\mathbf{r}}, & \theta \neq \pi/2, \\ 0, & \theta = \pi/2, \end{cases} \tag{13.56}$$

with the positive sign applying above the equatorial plane. Using (13.51), (13.54) and (13.56) for P, ρ and $B_{\rm p}$ in the cusp condition (13.55) gives

$$\left(\frac{\bar{r}}{R_{\rm s}}\right)^6 = \frac{B_0^2}{8\mu_0(\rho_0)_{\rm d}a_{\rm d}^2}\exp\left[\frac{GM_{\rm s}}{R_{\rm s}a_{\rm d}^2}\left(1-\frac{R_{\rm s}}{\bar{r}}\right)\right]\exp\left[-\frac{\alpha^2R_{\rm s}^2}{2a_{\rm d}^2}\left(\frac{\bar{r}^2}{R_{\rm s}^2}-\frac{R_{\rm s}}{\bar{r}}\right)\right], \tag{13.57}$$

which determines $\bar{r}$, the extent of the dead zone region.

As previously seen, the wind solution is fixed by applying energy conservation at the slow and fast magnetosonic points on a given field-streamline, as described by (13.37). The fast magnetosonic point is beyond $S_{\rm A}$ and so lies in the radial field domain, with r^2B_r = constant on a given field-streamline. The Bernoulli integral (13.27) can then be written as

$$H(r,\rho) = \frac{\epsilon^2 B_{\rm A}^2 r_{\rm A}^4}{2\rho^2 r^4} + \frac{1}{2}\alpha^2 r^2\sin^2\theta\left[\frac{\Omega}{\alpha}\left(\frac{\Omega}{\alpha}-2\right)\right] - \frac{GM_{\rm s}}{r} + a_{\rm w}^2\ln\frac{\rho}{\rho_{\rm A}}, \tag{13.58}$$

and (13.20) gives

$$\frac{\Omega}{\alpha} = \frac{1-\rho_{\rm A}r_{\rm A}^2/\rho r^2}{1-\rho_{\rm A}/\rho}. \tag{13.59}$$

The critical point conditions $\partial H/\partial r = 0$, $\partial H/\partial \rho = 0$ at $(r_\mathrm{f}, \rho_\mathrm{f})$ yield

$$2V^2 = -\gamma X^2 \frac{(V^2 - 2VX^2 + 1)}{(VX^2 - 1)^2}, \tag{13.60}$$

and

$$V^2 - \delta = \gamma V^2 X^2 \frac{(X^2 - 1)^2}{(VX^2 - 1)^3}, \tag{13.61}$$

with dimensionless quantities,

$$X = \frac{r_\mathrm{f}}{r_\mathrm{A}}, \tag{13.62a}$$

$$V = \frac{\rho_\mathrm{A}}{\rho_\mathrm{f}} \frac{1}{X^2} = \frac{v_\mathrm{f}}{v_\mathrm{A}}, \tag{13.62b}$$

$$\gamma = \frac{\alpha^2 r_\mathrm{A}^2}{v_\mathrm{A}^2} \sin^2 \theta, \tag{13.62c}$$

$$\delta = \frac{a_\mathrm{w}^2}{v_\mathrm{A}^2}. \tag{13.62d}$$

The gravitational term has been dropped in (13.60) since it is small compared with v_f^2 term.

In the case of rapid rotation, which is appropriate to the secondary stars in close binaries, centrifugal driving forces v_A to well above a_w, so that $\delta \ll 1$. Dividing (13.60) by (13.61) gives a quadratic equation for X^2 containing the small quantity δ in its coefficients. To leading order, this yields the finite root

$$X \simeq \left[\frac{1}{2\delta} V(V-1)(3-V)\right]^{\frac{1}{2}}, \tag{13.63}$$

which substituted in (13.60) gives $V \simeq \gamma^{\frac{1}{3}}$ and hence, from (13.62b),

$$v_\mathrm{f}^3 \simeq \alpha^2 \varpi_\mathrm{A}^2 v_\mathrm{A}. \tag{13.64}$$

Equation (13.63) shows that $V = v_\mathrm{f}/v_\mathrm{A}$ lies between 1 and 3 and, since $\delta \ll 1$, then $X \gg 1$. It therefore follows from (13.62b) that

$$\frac{\rho_\mathrm{A}}{\rho_\mathrm{f}} = VX^2 \gg 1. \tag{13.65}$$

Along a radial field-streamline the continuity equation gives

$$\frac{v_{\rm A}}{v_{\rm f}} = \frac{\rho_{\rm f}}{\rho_{\rm A}} \left(\frac{\varpi_{\rm f}}{\varpi_{\rm A}} \right)^2 . \tag{13.66}$$

The use of these results in (13.19) and (13.20) yields

$$\varpi_{\rm f} (B_\phi)_{\rm f} \simeq -4\pi \epsilon \alpha \varpi_{\rm A}^2 \left(\frac{v_{\rm A}}{v_{\rm f}} \right), \tag{13.67}$$

$$\varpi_{\rm f}^2 \Omega_{\rm f} \simeq \alpha \varpi_{\rm A}^2 \left(1 - \frac{v_{\rm A}}{v_{\rm f}} \right). \tag{13.68}$$

In the rapid rotation regime, the gravitational and thermal terms can be dropped in the Bernoulli integral (13.27). Noting that $\varpi_{\rm A}/\varpi_{\rm f} \ll 1$, (13.27), (13.64) and (13.68) give

$$H(\varpi_{\rm f}, \rho_{\rm f}) = v_{\rm A}^2 \left[\frac{3}{2} \left(\frac{v_{\rm f}}{v_{\rm A}} \right)^2 - \left(\frac{v_{\rm f}}{v_{\rm A}} \right)^3 \right]. \tag{13.69}$$

To determine the solution for rapid rotators, the flow must be made to pass through the slow magnetosonic point. Except for very rapid rotators, the Ω-terms can be dropped in (13.27) in the region closer to the axis in which the slow point $\varpi_{\rm sl}$ will occur. Hence

$$H = \frac{\epsilon^2 B_p^2}{2\rho^2} + a_{\rm w}^2 \ln \rho - \frac{G M_{\rm s}}{r}. \tag{13.70}$$

In this region $\mathbf{B}_{\rm p}$ is the dipole field (13.39a) and (13.39b), and on a field-streamline

$$\sin^2 \theta = \frac{r}{R_{\rm s}} \sin^2 \theta_0. \tag{13.71}$$

The conditions $\partial H/\partial \rho = 0$, $\partial H/\partial r = 0$ then yield

$$v_{\rm p} = a_{\rm w}, \tag{13.72a}$$

$$r_{\rm sl} = \frac{G M_{\rm s}}{3 a_{\rm w}^2}, \tag{13.72b}$$

and so from (13.70)

$$H(\varpi_{\rm sl}, \rho_{\rm sl}) = a_{\rm w}^2 \left[-\frac{5}{2} + \ln \left(\frac{\rho_{\rm sl}}{\rho_{\rm A}} \right) \right]. \tag{13.73}$$

Equation (13.72a) shows that the slow magnetosonic point coincides with the sonic point, within the accuracy of the approximations made.

Finally, the condition

$$H(\varpi_{\rm f}, \rho_{\rm f}) = H(\varpi_{\rm sl}, \rho_{\rm sl}) \tag{13.74}$$

must be applied. Since $a_{\rm w}^2 = \delta v_{\rm A}^2$, (13.69) and (13.73) yield

$$\frac{3}{2}\left(\frac{v_{\rm f}}{v_{\rm A}}\right)^2 - \left(\frac{v_{\rm f}}{v_{\rm A}}\right)^3 = \delta\left[-\frac{5}{2} + \ln\left(\frac{\rho_{\rm sl}}{\rho_{\rm A}}\right)\right]. \tag{13.75}$$

Noting that $V = v_{\rm f}/v_{\rm A}$, for $\delta \ll 1$ it follows that $V = 3/2$ which, together with (13.63) for $X = r_{\rm f}/r_{\rm A}$, gives

$$\frac{v_{\rm f}}{v_{\rm A}} = \frac{3}{2}, \tag{13.76a}$$

$$\frac{r_{\rm f}}{r_{\rm A}} = \frac{3}{4}\frac{v_{\rm A}}{a_{\rm w}}. \tag{13.76b}$$

Then (13.64) and (13.68) give

$$v_{\rm A} = 0.54\alpha\varpi_{\rm A}, \tag{13.77a}$$

$$\Omega_{\rm f} = \frac{\alpha}{3}\left(\frac{\varpi_{\rm A}}{\varpi_{\rm f}}\right)^2. \tag{13.77b}$$

Hence, for a fast rotator, centrifugal force drives the wind speed at the Alfvénic point up to about one half of the corotation speed.

This leaves the rate of braking to be found. The Alfvén speed is given to a reasonable approximation, applicable to slow and fast rotators, by

$$\frac{v_{\rm A}}{a_{\rm w}} = \left[\left(\frac{v_{\rm th}}{a_{\rm w}}\frac{r_{\rm A}}{R_{\rm s}}\right)^2 + \frac{\alpha^2 r_{\rm A}^2}{3a_{\rm w}^2}\sin^2\theta\right]^{\frac{1}{2}}, \tag{13.78}$$

where $v_{\rm th}$ is Parker's thermally driven wind. Then noting from (13.10), (13.17) and (13.56) for ϵ, $\rho_{\rm A}$ and $B_{\rm p}$ that

$$\mu_0\epsilon = \mu_0\frac{\rho_0 v_0}{(B_{\rm p})_0} = \frac{B_{\rm A}}{v_{\rm A}} = \frac{B_0}{2v_{\rm A}}\frac{R_{\rm s}}{\bar{r}}\left(\frac{R_{\rm s}}{r_{\rm A}}\right)^2, \tag{13.79}$$

(13.78) gives the Alfvén radius expression

$$\left(\frac{r_{\rm A}}{R_{\rm s}}\right)^3 = \frac{\zeta_{\rm w}}{(v_0/a_{\rm w})}\left(\frac{R_{\rm s}}{\bar{r}}\right)\left[\left(\frac{v_{\rm th}}{a_{\rm w}}\right)^2 + \frac{\alpha^2 R_{\rm s}^2}{3a_{\rm w}^2}\sin^2\theta\right]^{-\frac{1}{2}}, \tag{13.80}$$

where typically $v_0/a_{\rm w} \sim 0.15$, and $\zeta_{\rm w}$ is the wind zone parameter defined by (13.38c).

From (13.18) for β, the flux of angular momentum along a field-streamline can be expressed as

$$-\beta B_{\rm p} = \rho v_{\rm p}\alpha\varpi_{\rm A}^2. \tag{13.81}$$

The cylindrical Alfvén coordinate $\varpi_{\rm A} = r_{\rm A}\sin\theta$ will vary between field lines. However, a lower limit to the braking torque can be found by taking the flow beyond $\bar{r}$ to be spherically symmetric, with $v_{\rm p}(r)$ having its equatorial variation. The Alfvén surface $S_{\rm A}$ is therefore approximated as a sphere of radius $r_{\rm A} = \varpi_{\rm A}$ at $\theta = \pi/2$. Equation (13.80) shows that $r_{\rm A}$ varies slowly with θ, its most rapid variation being near $\theta = 0$ where the contribution to angular momentum transport is least. The integral of (13.81) over $S_{\rm A}$ is then

$$-\dot{J} = 4\pi\alpha\int_0^{\frac{\pi}{2}} \rho_{\rm A} v_{\rm A} r_{\rm A}^2 \sin^2\theta r_{\rm A}^2 \sin\theta d\theta, \tag{13.82}$$

giving

$$-\dot{J} = \frac{8\pi}{3}(\rho_{\rm A} v_{\rm A} r_{\rm A}^2)\alpha r_{\rm A}^2. \tag{13.83}$$

Since $\rho_{\rm A} v_{\rm A} = B_{\rm A}^2/\mu_0 v_{\rm A}$, then $-\dot{J}$ can also be written as

$$-\dot{J} = \frac{\Phi^2\alpha}{6\pi\mu_0 v_{\rm A}}, \tag{13.84}$$

where $\Phi = 4\pi r_{\rm A}^2 B_{\rm A}$ is the magnitude of the flux of open magnetic field lines that form the wind zone.

It follows from (13.21) that α is very close to the stellar rotation rate $\Omega_{\rm s}$ and so, for most purposes, $\alpha = \Omega_{\rm s}$ can be used. Mestel and Spruit considered rotation rates $\Omega_{\rm s} = k\Omega_\odot$ with $1 \le k \le 80$, where $\Omega_\odot = 2.5 \times 10^{-6}\,{\rm s}^{-1}$ corresponds to a period of $P_\odot = 29$ days. The magnetic field is assumed to be dynamo generated, with pole strength B_0 related to $\Omega_{\rm s}$ by the rotation law

$$B_0 = (B_0)_\odot\left(\frac{\Omega_{\rm s}}{\Omega_\odot}\right)^n. \tag{13.85}$$

The simplest model has $(\rho_0)_\mathrm{d}$ and a_d both independent of Ω_s. However, the authors point out that it is difficult to see how this could be consistent with X-ray observations of late-type stars, which show a luminosity $L_\mathrm{x} \propto \Omega_\mathrm{s}^2$ (e.g. Pallavicini et al. 1981). The variation of coronal emission is determined mostly by the variation in density, with $L_\mathrm{x} \propto \rho_0^2$ so $\rho_0 \propto \Omega_\mathrm{s}$. The X-ray luminosity is expected to depend on B_0, since this is a measure of the degree of activity of the star. The consistency of using (13.85) with $L_\mathrm{x} \propto \Omega_\mathrm{s}^2$ requires $L_\mathrm{x} \propto B_0^{2/n}$. The choice $n = 1$ is made, leading to

$$\zeta_\mathrm{d} = (\zeta_\mathrm{d})_\odot \frac{[B_0/(B_0)_\odot]^2}{(\rho_0)_\mathrm{d}/(\rho_0)_{\mathrm{d}\odot}} = (\zeta_\mathrm{d})_\odot \left(\frac{\Omega_\mathrm{s}}{\Omega_\odot}\right), \tag{13.86}$$

where

$$\zeta_\mathrm{d} = \frac{B_0^2}{2\mu_0(\rho_0)_\mathrm{d} a_\mathrm{d}^2} \tag{13.87}$$

occurs in (13.57), which determines the dead zone radius $\bar{r}$.

The cases $\zeta_\mathrm{d} \propto \Omega_\mathrm{s}$ and $\zeta_\mathrm{d} \propto \Omega_\mathrm{s}^2$ are considered, corresponding to $(\rho_0)_\mathrm{d} \propto B_0$, and $(\rho_0)_\mathrm{d}$ independent of B_0, respectively. The rotation rate Ω_s is varied from the solar value ($P = 29$ day) to a value of $80\Omega_\odot$ ($P = 9$ h), for the cases $(\zeta_\mathrm{d})_\odot = 4, 60$, taking stars of solar mass. The results are summarized in Table 13.1. In all cases the value $\Omega_\mathrm{s} \simeq 15\Omega_\odot$ marks a turn-over in the behaviour of $\bar{r}/R_\mathrm{s}$. For $\Omega_\mathrm{s} < 15\Omega_\odot$ the centrifugal effect on the pressure in the dead zone, described by (13.51) and (13.54), is weak, so $\bar{r}$ increases with Ω_s because the stronger field traps more gas. This effect occurs in (13.57) for $\bar{r}$ through the $B_0^2/(\rho_0)_\mathrm{d}$ term, which increases with Ω_s. For $\Omega_\mathrm{s} > 15\Omega_\odot$ the centrifugal effect, described by the second exponential in (13.57), dominates and $\bar{r}$ begins to shrink.

Table 13.1 The dead zone extent (from Mestel and Spruit 1987)

	$(\xi_\mathrm{d})_\odot = 4$		$(\xi_\mathrm{d})_\odot = 60$	
$\Omega_\mathrm{s}/\Omega_\odot$	$\bar{r}/R_\mathrm{s}$ ($\xi_\mathrm{d} \propto \Omega_\mathrm{s}$)	$\bar{r}/R_\mathrm{s}$ ($\xi_\mathrm{d} \propto \Omega_\mathrm{s}^2$)	$\bar{r}/R_\mathrm{s}$ ($\xi_\mathrm{d} \propto \Omega_\mathrm{s}$)	$\bar{r}/R_\mathrm{s}$ ($\xi_\mathrm{d} \propto \Omega_\mathrm{s}^2$)
1	2.5	2.5	5.0	5.0
2	3.1	3.5	5.8	6.6
3	3.4	4.1	6.2	7.8
5	3.9	5.5	6.8	9.2
7	4.1	6.2	7.2	10.0
10	4.4	6.9	7.4	10.7
20	4.6	7.2	6.9	9.6
30	4.4	6.5	6.1	8.2
60	3.4	4.7	4.3	5.4
80	3.0	3.9	3.6	4.5

Table 13.2 Equatorial values of the ratio r_A/R_s, with $(\xi_d)_\odot = 60$, $(\xi_w)_\odot = 120$ (from Mestel and Spruit 1987)

$\Omega_s/\Omega_\odot$	$(r_A/R_s)_{eq}$ $(\xi_w \propto \Omega_s)$	$(r_A/R_s)_{eq}$ $(\xi_w \propto \Omega_s^2)$
1	12	12
2	15	19
5	20	36
10	25	52
20	29	72
30	31	88
60	35	127
80	37	149

The Alfvén radius r_A is found from (13.80), using $v_0 \simeq 0.15 a_w$ and the previously determined value of $\bar{r}/R_s$, for each Ω_s. The wind zone parameter ζ_w is defined by (13.38c), where $B_0^2/(\rho_0)_w$ is taken to have the same Ω_s dependences as $B_0^2/(\rho_0)_d$ occurring in the dead zone parameter ζ_d. Since the wind zone has a lower density and temperature that the dead zone, $\zeta_w > \zeta_d$ is expected. The authors take $\zeta_w = 120$ for the sun so that (13.80) yields $r_A \simeq 12 R_s$, in agreement with observation (Pizzo et al. 1983). The wind zone temperature is taken to be one half that of the dead zone. The results are shown in Table 13.2.

The angular momentum loss rate is given by (13.83). The continuity equation for radial flow gives $\rho_A v_A r_A^2 = \bar{\rho}\bar{v}\bar{r}^2$, while the constancy of $\rho v_p/B_p$ along a field-streamline yields

$$\frac{\bar{\rho}\bar{v}}{(\rho_0)_w v_0} = \frac{\bar{B}}{B_0} = \frac{1}{2}\left(\frac{R_s}{\bar{r}}\right)^3, \tag{13.88}$$

where the last equality follows from (13.56) for $\mathbf{B}_p$. The use of these results allows $-\dot{J}$ to be expressed as

$$-\dot{J} = \frac{4\pi}{3}\left[(\rho_0)_\odot v_0 R_s^2\right]\Omega_\odot R_s^2 K(\Omega_s/\Omega_\odot), \tag{13.89}$$

where

$$K(\Omega_s/\Omega_\odot) = \left(\frac{R_s}{\bar{r}}\right)\left(\frac{r_A}{R_s}\right)^2\left(\frac{\Omega_s}{\Omega_\odot}\right)^q, \tag{13.90}$$

with $q = 1$ or 2. The case $q = 2$ corresponds to $(\rho_0)_w \propto \Omega_s \propto B_0$, while $q = 1$ occurs for $(\rho_0)_w$ independent of Ω_s. Table 13.3 shows values of $K(\Omega_s/\Omega_\odot)$. Braking is more efficient when $(\rho_0)_w \propto B_0$, primarily due to the increase in mass loss which more than compensates for the reduction in the Alfvén radius. The smaller extent of the dead zone in this case, illustrated in Table 13.1, also enhances the braking.

Table 13.3 The function $K(\Omega_s/\Omega_\odot)$ (from Mestel and Spruit 1987)

	$q = 2,\ (\rho_0)_w \propto B_0$	$q = 1,\ (\rho_0)_w$ independent of B_0
$\Omega_s/\Omega_\odot$	$K(\Omega_s/\Omega_\odot)$	$K(\Omega_s/\Omega_\odot)$
1	30.5	30.5
2	1.6×10^2	1.1×10^2
5	1.5×10^3	7.0×10^2
10	8.4×10^3	2.5×10^3
20	4.8×10^4	1.1×10^4
30	1.4×10^5	2.8×10^4
60	1.0×10^6	1.8×10^5
80	2.4×10^6	4.0×10^5

The braking laws predicted by (13.89) will be discussed in the next section, in the context of the secondary stars in binaries. The fast rotator theory will be relevant here, since for orbital periods of $P \lesssim 9$h synchronized secondaries have $\Omega_s \gtrsim 80\Omega_\odot$.

13.3 Stellar Magnetic Winds in Close Binaries

13.3.1 Orbital Angular Momentum Loss and Mass Transfer

A lobe-filling secondary star in a close binary system is expected to be kept near to orbital corotation, by the tidal field of the primary star. Asynchronous motions result in internal dissipations which cause the tidal bulge to lag the motion of the line of stellar centres. The resulting gravitational torque spins the star towards synchronism (see Sect. 2.4.2 for an outline of tidal theory). It follows from the period-mass relation (2.298) that for orbital periods of $P \leq 8$ h a main sequence secondary will have a mass $M_s \leq 0.80 M_\odot$, and hence possess a deep convective envelope. The star is fully convective for $M_s \leq 0.35 M_\odot$, corresponding to $P \leq 3.5$ h.

A rapidly rotating star with a convective envelope is likely to have a dynamo-generated magnetic field. As seen in Sect. 2.3, an $\alpha\Omega$-dynamo requires differential rotation, as well as turbulence, to operate. The secondary may retain some rotational shearing motions if a small radiative core is not completely synchronized, while the convective envelope is. Some differential rotation may remain in the convective region if the turbulent stress tensor has a non-standard form, allowing turbulent motions to generate non-uniform rotation (Campbell and Papaloizou 1983). Alternatively, an α^2-dynamo may operate. The generation of magnetic fields in secondary stars was considered in Chap. 12, where it was shown that observations and simulations indicate that rapidly rotating, lower main sequence stars are expected to have large-scale magnetic fields generated by dynamo action.

A magnetic secondary with a wind, generated by an expanding corona, would be subject to the braking effect formulated in the previous section. There will, of course, be some differences from the case of a single star. The presence of the primary means that, even if the secondary had a magnetic field symmetric about its rotation axis, the wind would not be axisymmetric due to the ϕ-dependence of the total gravitational field. Most of the tidal and rotational perturbation to the spherical structure occurs in the outer layers of the star where only a small fraction of the mass is contained. Hence, deviations of the external gravity field from spherical symmetry due to tidal distortion of the secondary will be small, but the gravity field of the primary could still be significant. The presence of a strongly magnetic primary can introduce a further complication, this being discussed in the Sect. 13.3.7.

The fundamental effect of a magnetically influenced wind from the secondary in a binary system will be the same as it is for a single star, namely the removal of stellar angular momentum. However, the spin evolution of the secondary star is affected by its tidal interaction with the primary. The synchronization process involves the exchange of angular momentum between the secondary and the orbital motion, via the tidal torque. The wind causes a spin down of the secondary, so driving Ω_s towards an under-synchronous state. However, tidal torques then become operable and act to increase Ω_s back to the orbital rate. The net effect is the continuous removal of orbital angular momentum from the binary system.

The orbital angular momentum can be expressed as

$$L_o = M_s M_p \left(\frac{GD}{M}\right)^{\frac{1}{2}}, \tag{13.91}$$

where $M = M_s + M_p$ and D is the stellar separation. For a mass ratio range of $0.1 \leq M_s/M_p \leq 0.8$, the mean radius of the secondary's Roche lobe obeys

$$\frac{M}{M_s}\left(\frac{R_L}{D}\right)^3 \simeq 0.1, \tag{13.92}$$

(Paczynski 1967). Taking M as constant, (13.91) and (13.92) give an evolution equation for R_L as

$$\frac{\dot{R}_L}{R_L} = 2\frac{\dot{L}_o}{L_o} - 2\frac{\dot{M}_s}{M_s}\left(\frac{5}{6} - \frac{M_s}{M_p}\right), \tag{13.93}$$

where $\dot{M}_s$ is the mass loss rate from the secondary due to Roche lobe overflow. The orbital evolution time-scale is $L_o/\dot{L}_o$, which is comparable to the mass transfer time-scale

$$\tau_M = \frac{M_s}{|\dot{M}_s|}. \tag{13.94}$$

Validity of the condition of constant M over the binary lifetime therefore requires

$$|\dot{M}_{\rm w}| \ll |\dot{M}_{\rm s}|, \tag{13.95}$$

where $\dot{M}_{\rm w}$ is the wind mass loss rate.

A lower main sequence secondary star, in thermal equilibrium, has a mean radius given approximately by

$$\frac{R_{\rm s}}{R_\odot} = q\left(\frac{M_{\rm s}}{M_\odot}\right), \tag{13.96}$$

with $q \simeq 1.1$ (Kippenhahn and Weigert 1990). For the secondary to continuously transfer mass to the primary, $R_{\rm L}$ must shrink at least as fast as $R_{\rm s}$ to keep matter in contact with the L_1 region. Equation (13.93) shows that for $M_{\rm p} > (6/5)M_{\rm s}$ a continuous decrease in $R_{\rm L}$ requires $\dot{L}_{\rm o} < 0$, since the last term is positive. Also, $|\dot{L}_{\rm o}|/L_{\rm o}$ must be sufficiently large to yield $\dot{R}_{\rm L} < 0$ and $|\dot{R}_{\rm L}| \geq |\dot{R}_{\rm s}|$. The secondary will remain in thermal equilibrium provided that $\tau_M \gg \tau_{\rm th}$, where $\tau_{\rm th}$ is the time-scale for thermal adjustment.

A loss of orbital angular momentum is caused by magnetic braking in conjunction with strong tidal coupling, as outlined above, and by gravitational radiation losses. Gravitational radiation orbital torques lead to the mass transfer rate

$$\dot{M}_{\rm s} = -1.9 \times 10^{-10} \frac{(1-\mu)^2}{(4-7\mu)\mu^{\frac{2}{3}}} M_\odot \,{\rm year}^{-1}, \tag{13.97}$$

where $\mu = M_{\rm s}/M$ and $R_{\rm s} = R_{\rm L}$ is taken (see Sect. 2.4.3). Over the range of mass ratios of interest (13.97) gives $|\dot{M}_{\rm s}| \sim 10^{-10} M_\odot {\rm year}^{-1}$. Observations of optical and X-ray luminosities imply mass transfer rates of this magnitude for systems with periods $P \lesssim 3\,{\rm h}$. However, longer period close binaries are believed to have $|\dot{M}_{\rm s}| \sim 10^{-9} M_\odot {\rm year}^{-1}$ which cannot be explained by gravitational radiation losses. The foregoing magnetic braking mechanism can provide a way of removing orbital angular momentum fast enough to explain the higher values of $|\dot{M}_{\rm s}|$. Verbunt and Zwaan (1981) estimated the magnetic braking torque by using the Skumanich (1972) spin-down law for single stars, assumed to be due to magnetic braking. By taking this law to apply to a binary secondary star, they derived the expression (2.337) for $\dot{M}_{\rm s}$. This yields sufficiently high values of $|\dot{M}_{\rm s}|$ for $P > 3\,{\rm h}$ but, since its derivation makes no direct use of braking theory, the expression cannot be related to the field structure of the secondary or to the details of the wind flow.

Campbell (1997) applied magnetic braking theory to find expressions for $\dot{M}_{\rm s}$. The foregoing fast rotator theory is relevant here, since for $P \lesssim 7\,{\rm h}$ it follows that $\Omega_{\rm s} \gtrsim 100\Omega_\odot$. Firstly, the effect of orbital evolution on the magnetic braking rate must be considered. If the secondary is kept close to orbital corotation by tidal forces then $\dot{L}_{\rm o} = \dot{J}$ can be used, where $\dot{J}$ is the loss rate of stellar angular momentum via magnetic braking. The tidal torque is dissipative and so will only be finite when there

is some asynchronism. For a turbulent viscosity the tidal torque can be comparable to the braking torque at small degrees of asynchronism, so Ω_s can be taken to be essentially the same as the orbital angular velocity Ω_o. Hence

$$\Omega_s^2 = \Omega_o^2 = \frac{GM}{D^3}. \tag{13.98}$$

The stellar angular momentum loss rate is given by (13.84) as

$$\dot{J} = -\frac{\Phi^2 \Omega_s}{6\pi \mu_0 v_A}, \tag{13.99}$$

where

$$\Phi = 4\pi \bar{r}^2 \bar{B} = 2\pi R_s^2 \left(\frac{R_s}{\bar{r}}\right) B_0, \tag{13.100}$$

with the last equality following from (13.56) for $\mathbf{B}_p$. Since the Alfvénic points occur in the radial field region, the magnitude of the wind mass loss rate can be written as $|\dot{M}_w| = 4\pi r_A^2 \rho_A v_A$. The use of this in (13.83) yields

$$\dot{J} = -\frac{2}{3}|\dot{M}_w| r_A^2 \Omega_s. \tag{13.101}$$

Equating this to (13.99) gives

$$r_A^2 = \frac{\Phi^2}{4\pi \mu_0 |\dot{M}_w| v_A}. \tag{13.102}$$

The fast rotator theory result (13.77a) gives $v_A \simeq 0.5 r_A \Omega_s$, so (13.101) and (13.102) lead to

$$\dot{J} = -\frac{2}{3(2\pi\mu_0)^{\frac{2}{3}}} |\dot{M}_w|^{\frac{1}{3}} \Phi^{\frac{4}{3}} \Omega_s^{\frac{1}{3}}. \tag{13.103}$$

Using (13.100) to substitute for Φ in (13.103) then yields

$$\dot{L}_o = \dot{J} = -\frac{2}{3}\left(\frac{2\pi}{\mu_0}\right)^{\frac{2}{3}} B_\odot^{\frac{4}{3}} \dot{M}_\odot^{\frac{1}{3}} \left(\frac{R_s}{\bar{r}}\right)^{\frac{4}{3}} \left(\frac{B_0}{B_\odot}\right)^{\frac{4}{3}} \left(\frac{\dot{M}_w}{\dot{M}_\odot}\right)^{\frac{1}{3}} R_s^{\frac{8}{3}} \Omega_s^{\frac{1}{3}}, \tag{13.104}$$

where $B_\odot$ is the coronal base polar value of the sun's magnetic field, and $\dot{M}_\odot$ is the solar wind mass loss rate. For a more complicated field than dipolar, $B_\odot$ and B_0 would be essentially the mean surface values. As the orbit evolves, with a nearly synchronous secondary having $\Omega_s = \Omega_o$, the stellar quantities R_s, B_0, $\dot{M}_w$ and $\bar{r}$ will

change as M_s and Ω_s evolve. The total mass M can be taken as constant provided that $|\dot{M}_w| \ll |\dot{M}_s|$.

The dead zone extent ratio $\bar{r}/R_s$ is determined by the solution of (13.57). This equation can be written in the implicit form

$$\frac{\bar{r}}{R_s} = \left(\frac{\zeta_d}{4}\right)^{\frac{1}{6}} \exp\left[\frac{GM_s}{6R_s a_d^2}\left(1 - \frac{R_s}{\bar{r}}\right)\right] \exp\left[-\frac{R_s^2\Omega_s^2}{12a_d^2}\left(\frac{\bar{r}^2}{R_s^2} - \frac{R_s}{\bar{r}}\right)\right], \tag{13.105}$$

where

$$\zeta_d = \frac{B_0^2}{2\mu_0(\rho_0)_d a_d^2}. \tag{13.106}$$

Eliminating D between the lobe-filling condition (13.92), with $R_L = R_s$, and the orbital equation (13.98) gives

$$R_s^2\Omega_s^2 = 0.1G\left(\frac{M_s}{R_s}\right). \tag{13.107}$$

The mass-radius relation (13.96) shows that M_s/R_s is constant and hence $R_s\Omega_s$ is also constant as the orbit evolves. The virial theorem gives approximate scalings for characteristic temperatures and densities in a star as $T \propto M_s/R_s$ and $\rho \propto M_s/R_s^3$. Taking the corona to follow these scalings yields

$$a_d^2 \propto \frac{M_s}{R_s}, \tag{13.108a}$$

$$(\rho_0)_d \propto \frac{M_s}{R_s^3}. \tag{13.108b}$$

For T_0 independent of Ω_s, (13.96) and (13.108a) lead to a_d being constant during evolution. The exponentiated coefficients $GM_s/R_s a_d^2$ and $(R_s\Omega_s)^2/a_d^2$ in (13.105) for $\bar{r}/R_s$ are therefore also constant. This leaves the factor $\zeta_d^{1/6}$ to be considered in the determination of $\bar{r}/R_s$. Using the dynamo law (13.85), with $1 \le n < 2$, together with $(\rho_0)_d \propto \Omega_s$ and $\propto M_s/R_s^3$, (13.106) and (13.108a) give

$$\zeta_d^{\frac{1}{6}} \propto \left[\frac{(R_s\Omega_s)^2\Omega_s^{2n-3}}{(M_s/R_s)^2}\right]^{\frac{1}{6}} \propto \Omega_s^{(2n-3)/6}, \tag{13.109}$$

where the last proportionality follows from the constancy of $R_s\Omega_s$ and M_s/R_s. For the above range of n, $\zeta_d^{1/6}$ is therefore weakly dependent on Ω_s. Since this factor occurs outside the exponentials in (13.105), and the exponentiated coefficients are constant, the solution $\bar{r}/R_s$ will be very slowly varying as mass transfer occurs and can therefore be taken as constant in (13.104) for $\dot{L}_o$.

Consider, now, the variation of the wind mass loss rate. Since the radial field region begins at $r = \bar{r}$, this can be written as

$$\dot{M}_{\rm w} = -4\pi \bar{r}^2 \bar{\rho} \bar{v}. \tag{13.110}$$

The conservation of mass and flux along a poloidal flux tube yield

$$\bar{\rho}\bar{v} = \rho_0 v_0 \left(\frac{\bar{B}}{B_0}\right) = \frac{1}{2}\rho_0 v_0 \left(\frac{R_{\rm s}}{\bar{r}}\right)^3, \tag{13.111}$$

and hence

$$\dot{M}_{\rm w} = -2\pi \left(\frac{R_{\rm s}}{\bar{r}}\right) R_{\rm s}^2 \rho_0 v_0. \tag{13.112}$$

The coronal base flow speed in the wind zone can be taken as

$$v_0 = 0.15 a_{\rm w}. \tag{13.113}$$

Then, since $R_{\rm s}/\bar{r}$ is constant,

$$|\dot{M}_{\rm w}| \propto R_{\rm s}^2 \left(\frac{M_{\rm s}}{R_{\rm s}^3}\right) \Omega_{\rm s} \left(\frac{M_{\rm s}}{R_{\rm s}}\right)^{\frac{1}{2}} \propto \left(\frac{M_{\rm s}}{R_{\rm s}}\right)^{\frac{3}{2}} \Omega_{\rm s}, \tag{13.114}$$

using the foregoing scalings. Because $M_{\rm s}/R_{\rm s}$ is constant, $\dot{M}_{\rm w}$ evolves with the orbit as

$$\frac{\dot{M}_{\rm w}}{\dot{M}_\odot} = \frac{\Omega_{\rm s}}{\Omega_\odot}. \tag{13.115}$$

The wind zone equivalent of $\zeta_{\rm d}$ is

$$\zeta_{\rm w} = \frac{B_0^2}{2\mu_0 (\rho_0)_{\rm w} a_{\rm w}^2}, \tag{13.116}$$

giving the ratio of the magnetic energy density to the thermal pressure at the coronal base. The use of (13.113) and (13.116) to eliminate $\rho_0 v_0$ in (13.112) gives the solar mass loss rate

$$\dot{M}_\odot = -\frac{0.15\pi}{\mu_0} \frac{R_\odot^2 B_\odot^2}{a_{\rm w} (\zeta_{\rm w})_\odot} \left(\frac{R_{\rm s}}{\bar{r}}\right). \tag{13.117}$$

Using the lobe-filling condition (13.92), with $R_{\rm L} = R_{\rm s}$, together with (13.96) for $R_{\rm s}$, enables the expression (13.91) for the orbital angular momentum to be written as

$$L_{\rm o} = 10^{\frac{1}{6}} q^{\frac{1}{2}} \left(\frac{G R_\odot}{M_\odot}\right)^{\frac{1}{2}} \frac{M_{\rm p} M_{\rm s}^{\frac{4}{3}}}{M^{\frac{1}{3}}}. \tag{13.118}$$

Using $R_{\rm L} = R_{\rm s}$ and (13.96) in the Roche lobe evolution equation (13.93), leads to the orbital evolution equation

$$\frac{\dot{L}_{\rm o}}{L_{\rm o}} = \left(\frac{4}{3} - \frac{M_{\rm s}}{M_{\rm p}}\right) \frac{\dot{M}_{\rm s}}{M_{\rm s}}. \tag{13.119}$$

Equation (13.104) for $\dot{L}_{\rm o}$, together with (13.118) and (13.119), enables expressions to be derived for $\dot{M}_{\rm s}$, for various dynamo laws. Consistency requires $|\dot{M}_{\rm w}| \ll |\dot{M}_{\rm s}|$ and thermal equilibrium holds for $\tau_{\rm th} \ll M_{\rm s}/|\dot{M}_{\rm s}|$. Hence it is necessary to derive expressions for $\dot{M}_{\rm w}$ and $\tau_{\rm th}$.

13.3.2 The Wind Mass Loss Rate and the Thermal Time-Scale

The wind mass loss rate follows from using (13.96), (13.107) and (13.117) for $R_{\rm s}$, $\Omega_{\rm s}$ and $\dot{M}_\odot$ in (13.115) as

$$\dot{M}_{\rm w} = -\frac{1.9 \times 10^{-11}}{q^{\frac{3}{2}} (\zeta_{\rm w})_\odot} \left(\frac{B_\odot}{1\,{\rm G}}\right)^2 \left(\frac{R_{\rm s}}{\bar{r}}\right) \left(\frac{M_\odot}{M}\right) \frac{1}{\mu} M_\odot\,{\rm year}^{-1}, \tag{13.120}$$

where $\mu = M_{\rm s}/M$. There is some suggestion that stellar dynamos may saturate above a critical rotation rate Ω_c. Assuming ρ_0, and hence $\dot{M}_{\rm w}$, also saturates at Ω_c, gives

$$\dot{M}_{\rm w} = -\frac{2.4 \times 10^{-13}}{(\zeta_{\rm w})_\odot} \left(\frac{B_\odot}{1\,{\rm G}}\right)^2 \left(\frac{R_{\rm s}}{\bar{r}}\right) \left(\frac{\Omega_c}{\Omega_\odot}\right) M_\odot\,{\rm year}^{-1}, \tag{13.121}$$

applicable for $\Omega_{\rm s} > \Omega_c$.

The Kelvin time-scale for thermal adjustment of the secondary is given by $\tau_{\rm th} \sim E_{\rm th}/L_{\rm s}$, where $E_{\rm th}$ and $L_{\rm s}$ are the star's thermal energy and surface luminosity. The virial theorem can be used to find $E_{\rm th}$, where, since the contributions of rotational and magnetic energies are negligible,

$$E_{\rm th} = -\frac{1}{2} E_{\rm G} \simeq \frac{3}{4} \frac{G M_{\rm s}^2}{R_{\rm s}}. \tag{13.122}$$

Taking the approximate main sequence mass-luminosity relation

$$\frac{L_{\rm s}}{L_\odot} = \left(\frac{M_{\rm s}}{M_\odot}\right)^5, \tag{13.123}$$

together with (13.96) for $R_{\rm s}$, yields the thermal time-scale

$$\tau_{\rm th} = \frac{2.3\times 10^7}{q}\left(\frac{M_\odot}{M}\right)^4 \frac{1}{\mu^4}\,\text{year}. \tag{13.124}$$

The self-consistency condition $|\dot{M}_{\rm w}| \ll |\dot{M}_{\rm s}|$, and the thermal equilibrium condition $\tau_{\rm th} \ll \tau_{\rm M}$, can be investigated for each dynamo law.

13.3.3 A Linear Dynamo Law

In the case of a linear dynamo rotation law $B_0(\Omega_{\rm s})$ is given by

$$\frac{B_0}{B_\odot} = \frac{\Omega_{\rm s}}{\Omega_\odot}. \tag{13.125}$$

Using (13.115) to eliminate $\dot{M}_{\rm w}/\dot{M}_\odot$ in (13.104) leads to

$$\dot{L}_{\rm o} = -\frac{2}{3}\left(\frac{2\pi}{\mu_0}\right)^{\frac{2}{3}} \frac{B_\odot^{\frac{4}{3}}\dot{M}_\odot^{\frac{1}{3}}}{\Omega_\odot^{\frac{5}{3}}}\left(\frac{R_{\rm s}}{\bar{r}}\right)^{\frac{4}{3}} R_{\rm s}^{\frac{8}{3}}\Omega_{\rm s}^2. \tag{13.126}$$

The mass transfer rate follows from using (13.96), (13.107), (13.117), (13.118) and (13.126) to eliminate $\dot{L}_{\rm o}/\dot{L}_{\rm o}$ in (13.119), giving

$$\dot{M}_{\rm s} = -\frac{7.7\times 10^{-10}}{q^{\frac{5}{6}}(\zeta_{\rm w})_\odot^{\frac{1}{3}}}\left(\frac{B_\odot}{1\,\text{G}}\right)^2\left(\frac{R_{\rm s}}{\bar{r}}\right)^{\frac{5}{3}}\left(\frac{M_\odot}{M}\right)^{\frac{1}{3}}\frac{\mu^{\frac{1}{3}}}{(4-7\mu)}\,M_\odot\text{year}^{-1}, \tag{13.127}$$

where $\mu = M_{\rm s}/M$, and the values $\Omega_\odot = 2.5\times 10^{-6}\,\text{s}^{-1}$ and $a_{\rm w} = 1.2\times 10^5\,\text{m s}^{-1}$ are used. Since the gas can expand freely in the wind zone, its temperature should be lower than that of gas in the dead zone. Taking $a_{\rm d}^2 = 2a_{\rm w}^2$, (13.106) and (13.116) give

$$\zeta_{\rm w} = 2\zeta_{\rm d}, \tag{13.128}$$

for uniform ρ_0. For $(\zeta_{\rm d})_\odot = 8$, the solution of (13.105) is $\bar{r}/R_{\rm s} = 1.5$. Then, using $q = 1.1$, $B_\odot = 10^{-4}\,\text{T}$, $M_{\rm p} = 1M_\odot$ and $M_{\rm s} = 0.4M_\odot$, (13.127) and (13.128) yield

$|\dot{M}_s| = 4.2 \times 10^{-11} M_\odot \text{year}^{-1}$. Using the same masses in (13.97) gives $|\dot{M}_s|_{gr} = 1.1 \times 10^{-10} M_\odot \text{year}^{-1}$, so the effect of gravitational radiation is stronger than that of magnetic braking in this case. Field saturation reduces $|\dot{M}_s|$.

Equations (13.120) and (13.127) give

$$\frac{|\dot{M}_w|}{|\dot{M}_s|} = \frac{2.5 \times 10^{-2}}{q^{\frac{2}{3}} (\zeta_w)_\odot^{\frac{2}{3}}} \left(\frac{\bar{r}}{R_s}\right)^{\frac{2}{3}} \left(\frac{M_\odot}{M}\right)^{\frac{2}{3}} \frac{(4 - 7\mu)}{\mu^{\frac{4}{3}}}. \tag{13.129}$$

Above the period gap, the range $3\,\text{h} \lesssim P \lesssim 6\,\text{h}$ is of interest for close binaries and the period-mass relation (2.298) yields the corresponding secondary mass range $0.3\,M_\odot \lesssim M_s \lesssim 0.6\,M_\odot$. Over this range of M_s, with $M = 1.4 M_\odot$, (13.129) gives $9 \times 10^{-3} < |\dot{M}_w|/|\dot{M}_s| < 8 \times 10^{-2}$, so justifying treating M as constant.

The ratio of the mass transfer time-scale to the thermal time-scale follows from (13.94), (13.124) and (13.127) for τ_M, τ_{th} and $\dot{M}_s$ as

$$\frac{\tau_M}{\tau_{th}} = 55 q^{\frac{11}{6}} (\zeta_w)_\odot^{\frac{1}{3}} \left(\frac{B_\odot}{1\,\text{G}}\right)^{-2} \left(\frac{\bar{r}}{R_s}\right)^{\frac{5}{3}} \left(\frac{M}{M_\odot}\right)^{\frac{16}{3}} (4 - 7\mu)\mu^{\frac{14}{3}}. \tag{13.130}$$

For $(\zeta_w)_\odot = 16$ and the above mass range, this gives $4 \lesssim \tau_M/\tau_{th} \lesssim 38$, with $\tau_M \sim 3\tau_{th}$ corresponding to $M_s \sim 0.3 M_\odot$. Hence, for a linear dynamo law, the secondary is in marginal thermal equilibrium close to the top of the period gap. However, explanations of the gap require the secondary to be out of thermal equilibrium at $M_s \sim 0.4 M_\odot$, while (13.130) yields $\tau_M \sim \tau_{th}$ at this mass. Also, (13.127) gives values of $|\dot{M}_s|$ that are at most comparable to $|\dot{M}_s|_{gr}$, and hence cannot explain the higher mass transfer rates believed to occur above the period gap. It is noted that $|\dot{M}_s|$ scales with $B_\odot^2$ and $B_\odot = 1\,\text{G}$ $(= 10^{-4}\text{T})$ has been used. There is some uncertainty in $B_\odot$, but values significantly higher than 2 G are unlikely. A value of $\bar{r}/R_s = 1.5$ has been taken here. An essentially synchronized secondary in a close binary has $\Omega_s \gtrsim 100\Omega_\odot$, and observations of rapidly rotating stars indicate that matter can escape from the dead zone (Collier Cameron and Robinson 1989). Presumably the high centrifugal force allows matter near $\bar{r}$ to escape from the magnetic constraint. This suggests that for the secondary star values of $\bar{r}/R_s$ nearer to 1 than to 10 are likely, supporting the value of 1.5 used here. With the presently available braking theory, it is therefore necessary to consider stronger dependences of B_0 on Ω_s than linear if magnetic winds are to explain mass transfer rates above the period gap.

13.3.4 An Inverse Rossby Number Dynamo Law

As the secondary star transfers mass to the primary its spectral type will change as M_s decreases. The depth of the convective envelope will increase as M_s decreases

towards 0.35 $M_\odot$, the mass at which the star becomes fully convective. This change may affect the value of B_0, in addition to the effect of a change in Ω_s. There is some observational evidence to suggest that B_0 scales as the inverse turbulent Rossby number $R_T^{-1} \propto \tau_T \Omega_s$, where τ_T is the convective turnover time-scale (Saar 1991).

The rms convective speed in a region with no energy sources is given by simple mixing length theory as

$$v_T = \left(\frac{|g| \lambda_T L_s}{2\pi r^2 \rho c_P T} \right)^{\frac{1}{3}}, \tag{13.131}$$

where λ_T is the mixing length, and L_s is the surface luminosity. Taking λ_T as a pressure scale height gives

$$\lambda_T = \lambda_P = \frac{c_s^2}{\gamma |g|}, \tag{13.132}$$

where c_s is the adiabatic sound speed. Using $P = (\mathcal{R}/\mu)\rho T$, with μ the mean molecular weight and $\tau_T \sim \lambda_T / v_T$, (13.131) and (13.132) yield the time-scale

$$\tau_T \propto \frac{r^2 T}{M(r)} \left(\frac{r^2 \rho}{L_s} \right)^{\frac{1}{3}}, \tag{13.133}$$

where $M(r)$ is the mass within a radius r (noting tidal distortion will be small deep in the convective envelope). Expression (13.133) gives the radial variation of τ_T so, to compare characteristic values between stars of different masses, the simple homologous scalings $r^2/M(r) \propto R_s^2/M_s$, $T \propto M_s/R_s$ and $\rho \propto M_s/R_s^3$ can be used at a given point. This gives

$$\tau_T \propto \left(\frac{R_s^2 M_s}{L_s} \right)^{\frac{1}{3}}. \tag{13.134}$$

Using the mass-luminosity relation (13.123) then leads to

$$\frac{B_0}{B_\odot} = \frac{\tau_T \Omega_s}{(\tau_T)_\odot \Omega_\odot} = \left(\frac{M_\odot^4}{R_\odot^2} \right)^{\frac{1}{3}} \left(\frac{R_s^2}{M_s^4} \right)^{\frac{1}{3}} \frac{\Omega_s}{\Omega_\odot}. \tag{13.135}$$

The rate of loss of orbital angular momentum follows from using (13.115) for $\dot{M}_w/\dot{M}_\odot$ and (13.135) for $B_0/B_\odot$ in (13.104), as

$$\dot{L}_o = -\frac{2}{3} \left(\frac{2\pi}{\mu_0} \right)^{\frac{2}{3}} q^{\frac{16}{9}} \frac{\dot{M}_\odot^{\frac{1}{3}} B_\odot^{\frac{4}{3}} R_\odot^{\frac{8}{9}}}{\Omega_\odot^{\frac{5}{3}}} \left(\frac{R_s}{\bar{r}} \right)^{\frac{4}{3}} R_s^{\frac{16}{9}} \Omega_s^2. \tag{13.136}$$

The resulting mass transfer rate is

$$\dot{M}_{\rm s} = -7.7 \times 10^{-10} \frac{q^{\frac{1}{18}}}{(\zeta_{\rm w})_{\odot}^{\frac{1}{3}}} \left(\frac{B_{\odot}}{1\,{\rm G}}\right)^2 \left(\frac{R_{\rm s}}{\bar{r}}\right)^{\frac{5}{3}} \left(\frac{M_{\odot}}{M}\right)^{\frac{11}{9}} \frac{1}{(4-7\mu)\mu^{\frac{5}{9}}} M_{\odot}{\rm year}^{-1}. \tag{13.137}$$

The foregoing parameters give $|\dot{M}_{\rm s}| = 10^{-10} M_{\odot}{\rm year}^{-1}$ for this case, which is comparable to $|\dot{M}_{\rm s}|_{\rm gr}$, at an orbital period of 4 h. Field saturation reduces $|\dot{M}_{\rm s}|$. Hence the inverse Rossby number scaling produces higher mass transfer rates then a simple linear scaling of B_0 with $\Omega_{\rm s}$, but still not high enough to explain values of $|\dot{M}_{\rm s}| \sim 10^{-9} M_{\odot}{\rm year}^{-1}$.

Equations (13.120) and (13.137) give

$$\frac{|\dot{M}_{\rm w}|}{|\dot{M}_{\rm s}|} = \frac{2.5 \times 10^{-2}}{q^{\frac{14}{9}} (\zeta_{\rm w})_{\odot}^{\frac{2}{3}}} \left(\frac{\bar{r}}{R_{\rm s}}\right)^{\frac{2}{3}} \left(\frac{M}{M_{\odot}}\right)^{\frac{2}{9}} \frac{(4-7\mu)}{\mu^{\frac{4}{9}}}. \tag{13.138}$$

For $M = 1.4 M_{\odot}$ and $0.3 M_{\odot} \leq M_{\rm s} \leq 0.6 M_{\odot}$, together with $(\zeta_{\rm w})_{\odot} = 16$, (13.138) yields $6.6 \times 10^{-3} < |\dot{M}_{\rm w}|/|\dot{M}_{\rm s}| < 2.2 \times 10^{-2}$, so justifying the constancy of M.

The time-scale ratio follows from (13.124) and (13.137) as

$$\frac{\tau_M}{\tau_{\rm th}} = 55 q^{\frac{17}{18}} (\zeta_{\rm w})_{\odot}^{\frac{1}{3}} \left(\frac{B_{\odot}}{1\,{\rm G}}\right)^{-2} \left(\frac{\bar{r}}{R_{\rm s}}\right)^{\frac{5}{3}} \left(\frac{M}{M_{\odot}}\right)^{\frac{56}{9}} (4-7\mu)\mu^{\frac{50}{9}}. \tag{13.139}$$

The above mass range gives $1 < \tau_M/\tau_{\rm th} < 22$, so at $M_{\rm s} = 0.3 M_{\odot}$ the secondary is marginally in thermal equilibrium. For $B_{\odot} = 2\,{\rm G}$ this case is close to having the required properties, but only without field saturation.

13.3.5 A Non-linear Dynamo Law

Consider the dynamo rotation law

$$\frac{B_0}{B_{\odot}} = \left(\frac{\Omega_{\rm s}}{\Omega_{\odot}}\right)^{\frac{7}{4}}. \tag{13.140}$$

Equation (13.104) then gives

$$\dot{L}_{\rm o} = \dot{J} = -\frac{2}{3} \left(\frac{2\pi}{\mu_0}\right)^{\frac{2}{3}} \frac{\dot{M}_{\odot}^{\frac{1}{3}} B_{\odot}^{\frac{4}{3}}}{\Omega_{\odot}^{\frac{8}{3}}} \left(\frac{R_{\rm s}}{\bar{r}}\right)^{\frac{4}{3}} R_{\rm s}^{\frac{8}{3}} \Omega_{\rm s}^3. \tag{13.141}$$

For a single star, of essentially constant mass, this corresponds to the braking equation

$$I\dot{\Omega}_{\rm s} = -K\Omega_{\rm s}^3, \tag{13.142}$$

where I is the moment of inertia and K is a positive constant. The solution is

$$\Omega_{\rm s} = \left(\frac{1}{\Omega_0^2} + \frac{2K}{I}t\right)^{-\frac{1}{2}}, \tag{13.143}$$

and for $\Omega_{\rm s} \ll \Omega_0$,

$$\Omega_{\rm s} = \left(\frac{I}{2K}\right)^{\frac{1}{2}} \frac{1}{t^{\frac{1}{2}}}, \tag{13.144}$$

which is the Skumanich (1972) law. This case can therefore be compared with the work of Verbunt and Zwaan (1981), which employed such a braking law and gave the mass transfer rate (2.337).

Eliminating $\dot{L}_{\rm o}$ between (13.119) and (13.141) leads to the mass transfer rate

$$\dot{M}_{\rm s} = -\frac{6.2\times10^{-8}}{q^{\frac{7}{3}}(\zeta_{\rm w})_\odot^{\frac{1}{3}}}\left(\frac{B_\odot}{1\,{\rm G}}\right)^2\left(\frac{R_{\rm s}}{\bar{r}}\right)^{\frac{5}{3}}\left(\frac{M_\odot}{M}\right)^{\frac{4}{3}}\frac{1}{(4-7\mu)\mu^{\frac{2}{3}}}\,M_\odot\,{\rm year}^{-1}. \tag{13.145}$$

At a period of 4 h, corresponding to $M_{\rm s} = 0.4M_\odot$, this gives $|\dot{M}_{\rm s}| = 7.5\times10^{-9}M_\odot{\rm year}^{-1}$. This is an order of magnitude higher than that derived from the Verbunt and Zwaan formula (2.337). The dependences on μ differ in these expressions, since (2.337) was derived using the observational fit (2.335) for $R_{\rm s}\Omega_{\rm s}$, which is independent of stellar parameters.

The forms for $|\dot{M}_{\rm w}|/|\dot{M}_{\rm s}|$ and $\tau_M/\tau_{\rm th}$ corresponding to the mass transfer rate (13.145) are

$$\frac{|\dot{M}_{\rm w}|}{|\dot{M}_{\rm s}|} = 3\times10^{-4}\frac{q^{\frac{5}{6}}}{(\zeta_{\rm w})_\odot^{\frac{2}{3}}}\left(\frac{\bar{r}}{R_{\rm s}}\right)^{\frac{2}{3}}\left(\frac{M}{M_\odot}\right)^{\frac{1}{3}}\frac{(4-7\mu)}{\mu^{\frac{1}{3}}}, \tag{13.146}$$

and

$$\frac{\tau_M}{\tau_{\rm th}} = 0.7q^{\frac{10}{3}}(\zeta_{\rm w})_\odot^{\frac{1}{3}}\left(\frac{B_\odot}{1\,{\rm G}}\right)^{-2}\left(\frac{\bar{r}}{R_{\rm s}}\right)^{\frac{5}{3}}\left(\frac{M}{M_\odot}\right)^{\frac{19}{3}}(4-7\mu)\mu^{\frac{17}{3}}. \tag{13.147}$$

For the mass range $0.3\,M_\odot \le M_{\rm s} \le 0.6\,M_\odot$ these expressions yield the ratios $1.1\times10^{-4} < |\dot{M}_{\rm w}|/|\dot{M}_{\rm s}| < 3.5\times10^{-4}$ and $1.6\times10^{-2} < \tau_M/\tau_{\rm th} < 0.4$, so M

Table 13.4 The ratio $\tau_M/\tau_{\rm th}$

$M_{\rm s}/M_\odot$	$\tau_M/\tau_{\rm th}$	$\lvert\dot{M}_{\rm s}\rvert/M_\odot\,{\rm year}^{-1}$
0.3	0.27	4.2×10^{-10}
0.4	0.51	9.5×10^{-10}
0.5	0.74	2.0×10^{-9}
0.6	0.86	4.2×10^{-9}

is conserved to high accuracy, and the secondary is well out of thermal equilibrium over the lower part of this mass range.

The values of $|\dot{M}_{\rm s}|$ given by (13.145) are rather large, so the case of field saturation at Ω_c can be considered. The resulting mass transfer rate is

$$\dot{M}_{\rm s}=-\frac{5.3}{10^{13}}\frac{q^{\frac{5}{3}}}{(\zeta_{\rm w})_\odot^{\frac{1}{3}}}\left(\frac{B_\odot}{1\,{\rm G}}\right)^2\left(\frac{R_{\rm s}}{\bar{r}}\right)^{\frac{5}{3}}\left(\frac{\Omega_c}{\Omega_\odot}\right)^{\frac{8}{3}}\left(\frac{M}{M_\odot}\right)^{\frac{4}{3}}\frac{\mu^2}{(4-7\mu)}\,M_\odot{\rm year}^{-1}. \tag{13.148}$$

This, together with (13.121) for $\dot{M}_{\rm w}$, gives

$$\frac{|\dot{M}_{\rm w}|}{|\dot{M}_{\rm s}|}=\frac{0.46}{q^{\frac{5}{3}}(\zeta_{\rm w})_\odot^{\frac{2}{3}}}\left(\frac{\bar{r}}{R_{\rm s}}\right)^{\frac{2}{3}}\left(\frac{M_\odot}{M}\right)^{\frac{4}{3}}\left(\frac{\Omega_\odot}{\Omega_c}\right)^{\frac{5}{3}}\frac{(4-7\mu)}{\mu^2}, \tag{13.149}$$

which yields $5\times10^{-4}<|\dot{M}_{\rm w}|/|\dot{M}_{\rm s}|<3.6\times10^{-3}$. The time-scale ratio is

$$\frac{\tau_M}{\tau_{\rm th}}=8\times10^4\frac{(\zeta_{\rm w})_\odot^{\frac{1}{3}}}{q^{\frac{2}{3}}}\left(\frac{B_\odot}{1\,{\rm G}}\right)^{-2}\left(\frac{\bar{r}}{R_{\rm s}}\right)^{\frac{5}{3}}\left(\frac{M}{M_\odot}\right)^{\frac{11}{3}}\left(\frac{\Omega_\odot}{\Omega_c}\right)^{\frac{8}{3}}(4-7\mu)\mu^3. \tag{13.150}$$

Table 13.4 shows values of $|\dot{M}_{\rm s}|/M_\odot{\rm year}^{-1}$ and $\tau_M/\tau_{\rm th}$ above the period gap, using the foregoing parameters and $\Omega_c=80\Omega_\odot$ in (13.148) and (13.150). The mass transfer rates are in good agreement with those implied by observations of systems with $P\gtrsim3\,{\rm h}$. The values of $\tau_M/\tau_{\rm th}$ show that at $M_{\rm s}=0.6M_\odot$ the secondary is marginally in thermal equilibrium. As $M_{\rm s}=0.3M_\odot$ is approached the star starts to be driven out of thermal equilibrium, since it cannot fully adjust thermally as it losses mass. This case therefore has the required properties for explanation of the period gap.

13.3.6 The Period Gap

The cataclysmic variables are binaries containing a white dwarf primary and a lobe-filling main sequence secondary. The majority of these systems have orbital periods lying in the range $1.3\,{\rm h}\lesssim P\lesssim8.0\,{\rm h}$ and their mass transfer rates span

$5 \times 10^{-11} \lesssim |\dot{M}_s|/M_\odot \text{year}^{-1} \lesssim 3 \times 10^{-9}$ (e.g. Warner 1995). There is an almost complete absence of accreting systems with periods in the range 2 to 3 h. However, the AM Herculis binaries appear to be the exception to this, and are discussed below. As seen in the foregoing discussion, gravitational radiation losses can account for the lower mass transfer rates occurring at periods $\lesssim$ 3 h, and hence for systems below the period gap. The foregoing analysis showed that magnetic braking can explain the larger values of $|\dot{M}_s|$ observed at $P > 3$ h, provided that the dynamo law relating B_0 to Ω_s is nearer to quadratic than linear. The gap is believed to contain systems in which the secondary star is detached from its Roche lobe, so mass transfer, which is the main source of luminosity via accretion on to the primary, is absent. This poses the problem of why the secondary becomes detached.

The current explanation for the origin of the period gap involves magnetic braking. It was seen in Sect. 13.3.5 that for $0.3 \lesssim M_s/M_\odot \lesssim 0.7$ the mass transfer time-scale $M_s/|\dot{M}_s|$ can become $\lesssim 10^9$ year and hence be comparable to the thermal time-scale τ_{th}. The secondary will then not have time to fully adjust thermally as it loses mass. This results in an over-luminous and over-sized star for its mass. If, at around a period of 3 h, something happens to sharply reduce magnetic braking, then the orbital angular momentum loss will become controlled by gravitational radiation. The time-scale for Roche lobe shrinkage due to this weaker process is $\gg \tau_{th}$, so the star contracts back to its thermal equilibrium radius faster than its lobe shrinks and therefore becomes detached. The resulting low luminosity system subsequently evolves through the period gap, driven by gravitational radiation braking, until the secondary fills its lobe and resumes mass transfer at a period of $\sim$ 2 h.

Various mechanisms have been proposed to account for a sudden decrease in the strength of magnetic braking at a period of $\sim$ 3 h. This period corresponds to a secondary mass of $\sim 0.3 M_\odot$, which is close to the mass at which a main sequence star is expected to become fully convective. It has been suggested that when this state is reached the stellar dynamo begins to operate in a different way, causing a reduction in field strength and/or a change in field configuration, which results in a lower magnetic torque (e.g. Spruit and Ritter 1983; Rappaport et al. 1983). If the dynamo mainly operates at the interface between the radiative core and the convective envelope (referred to as the tachocline), existing when $M_s > 0.35 M_\odot$, then the disappearance of this interface at $M_s \sim 0.3 M_\odot$ would cause a reduction in field strength. However, there is no compelling theoretical reason that this should be the case. Observational evidence in support of this hypothesis would require magnetic activity to decline abruptly in stars later than spectral type M5. The most favourable evidence for this is that X-ray emission from stars later than M5 has maximum luminosities that are at least an order of magnitude less than those of M stars of earlier spectral type (Golub 1983). However, present data are not extensive enough to prove that a sharp decrease in magnetic activity occurs close to M5. The observations and theory related to lower main sequence star magnetic fields were discussed in Chap. 12. Both fully convective and partially convective stars can have a large-scale magnetic field generated by a dynamo.

It should be noted that a reduction by a factor of 10 in the angular momentum loss rate is sufficient to produce a period gap of the observed width (e.g. Spruit and Ritter 1983). Equation (13.104) has $|\dot{J}| \propto B_0^{4/3}|\dot{M}_w|^{1/3}$ so, with a coronal base density $(\rho_0)_w \propto B_0$ and ignoring the small change in $\bar{r}/R_s$ generated in (13.104), it follows that $|\dot{J}| \propto B_0^{5/3}$. This theory therefore only requires a decrease in B_0 by a factor of 4 to cause $|\dot{J}|$ to drop by the required factor of 10.

Taam and Spruit (1989) argued that a sudden decline in magnetic braking when the secondary becomes fully convective is more likely to be due to a change in field configuration, rather than a sudden decrease in field strength. They pointed out that the spectroscopic data, taken as a whole, indicate a steady decline in magnetic activity through the M5 spectral type, rather than an abrupt decrease. They noted that at high rotation rates the irregular variability that is observed may be evidence for the dynamo operating in higher modes, generating fields with a smaller scale structure than those occurring in more slowly rotating stars.

The authors hypothesise that when the secondary becomes fully convective its dynamo process changes to produce fields of higher multipole structure. The foregoing braking theory of Mestel and Spruit (1987) was employed, except with the field inside $\bar{r}$ having a radial dependence of r^{-m}. Equation (13.89) is used to calculate the angular momentum loss rate, for several values of m corresponding to different multipoles. The function $K(\Omega_s/\Omega_\odot)$ is shown in Fig. 13.2. The angular momentum loss rate declines by a factor of 2000 between a dipole field and an asymptotically high order field at an orbital period of 3 h. This effect is mainly due to a decrease in the fraction of the magnetic surface flux that extends out to the

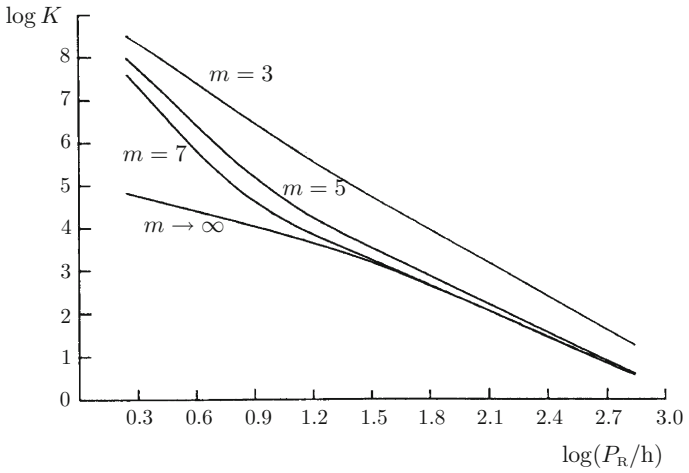

Fig. 13.2 The dimensionless angular momentum loss rate, $K(\Omega_s/\Omega_\odot)$, as a function of stellar rotation period for different multipole orders (reproduced from Taam and Spruit 1989, DOI: 10.1086/167966, with the permission of R.E. Taam and the AAS)

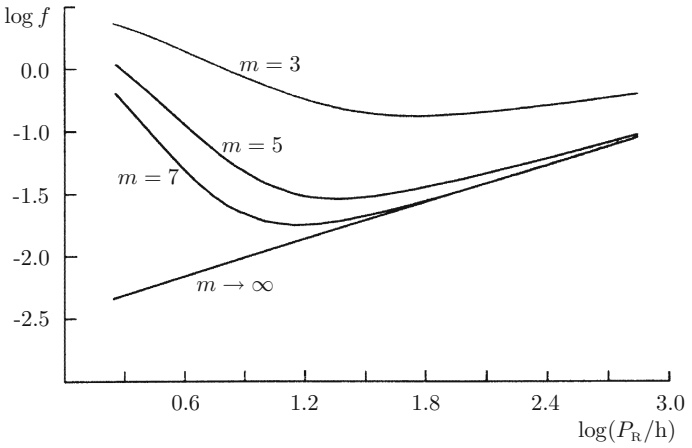

Fig. 13.3 The fraction of open field lines, f, as a function of stellar rotation period for different multipole orders (reproduced from Taam and Spruit 1989, DOI: 10.1086/167966, with the permission of R.E. Taam and the AAS)

Alfvén radius. This fraction of open field lines is

$$f = \left(\frac{\bar{r}}{R_\mathrm{s}}\right)^2 \frac{B(\bar{r})}{B(R_\mathrm{s})}. \tag{13.151}$$

The variation of f with period is shown in Fig. 13.3. With increasing multipole order, $\bar{r}$ moves closer to the stellar surface because the field strength decreases more rapidly with distance. At high rotation rates, the pressure and the density in the dead zone are strongly influenced by the centrifugal acceleration, which increases rapidly with distance from the star. For higher order multipoles, the effect of the centrifugal acceleration on f is therefore smaller than at low order, and fewer field lines are open. It should be noted, however that at high rotation rates the point where gravity and centrifugal force cancel is inside the dead zone. Hence the density of gas in hydrostatic equilibrium increases outwards in the outer part of this zone. Instabilities could then lead to the gas escaping from the field in the outer regions, so contributing to the wind and increasing $|\dot{J}|$ to some extent.

It should be noted that the mass transfer rates $\dot{M}_\mathrm{s}$ discussed in this section are average rates. Short-time scale variations in $\dot{M}_\mathrm{s}$ can occur; for example AM Her binaries have low states, lasting typically 2 to 3 months, during which $|\dot{M}_\mathrm{s}|$ is well below its average value.

13.3.7 AM Herculis Systems

The tables of confirmed AM Her binaries shown in Chap. 3 suggest that the period gap is not as significant for these systems as it is for binaries with essentially non-magnetic accretors. These tables show that $\simeq 23\%$ of the presently known AM Her systems have periods in the 2–3 hr gap. Li et al. (1994) proposed an explanation for this when, although fewer systems were known then, a significant fraction appeared in the gap. They noted that at a distance of 2–3 stellar radii from the secondary the primary's magnetic field is likely to significantly affect the wind dynamics, assuming typical binary parameters and a secondary polar surface field of 140 G. Both stars were taken to have dipolar fields with moments perpendicular to the orbital plane. For stellar masses of $M_\mathrm{p} = 0.7M_\odot$ and $M_\mathrm{s} = 0.4M_\odot$, the wind and dead zones were found using the criteria of Sect. 13.2.5, so a dead zone occurs when $B_\mathrm{p}^2/2\mu_0 > P$ and a wind zone of open fields lines when $P > B_\mathrm{p}^2/2\mu_0$. Figure 13.4 shows the wind and dead zones in the plane containing the dipole moments. This illustrates that the wind zones of the secondary are greatly reduced by the presence of the primary's magnetic field.

By considering a simple ring model, in which the surface segment between θ_{01} and θ_{02} is extended around the stellar surface, an estimate can be made for the magnetic braking. The foregoing braking theory was applied, using a linear dynamo law and a range of primary fields, to find $-\dot{J}$. The results are shown in Table 13.5, where $(B_\mathrm{p})_0$ is the primary star's surface polar field and κ is an estimate of the ratio of the total open flux of the secondary to the flux of a ring of angular width $\Delta\theta = \theta_{02} - \theta_{01}$. It is noted that even for $(B_\mathrm{p})_0 = 0$ the effect of magnetic braking is weaker

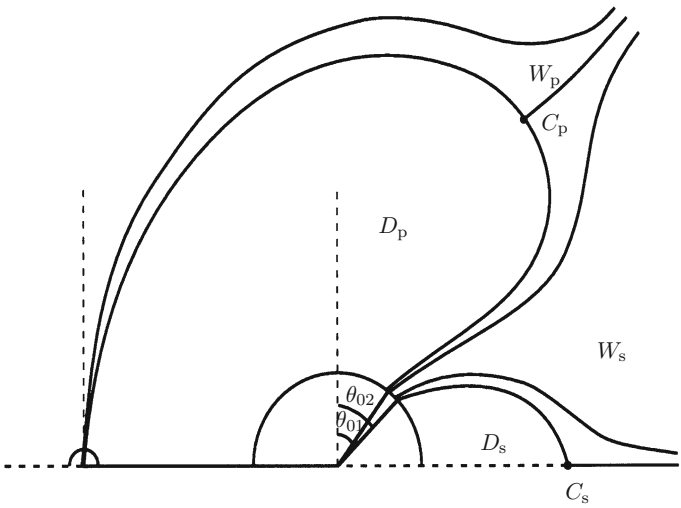

Fig. 13.4 The wind and dead zones in the plane of the dipole moments. Large dead zones, D_p and D_s, occur (based on Li et al. 1994)

Table 13.5 Reduction in magnetic braking (from Li et al. 1994)

$(B_p)_0$ (MG)	κ	$\lvert\dot{J}_{mb}\rvert/\lvert\dot{J}_{gr}\rvert$
0	1.0	8.2×10^{-2}
10	0.1	6.1×10^{-3}
30	3.2×10^{-2}	6.7×10^{-4}
50	1.0×10^{-2}	4.5×10^{-6}
70	2.4×10^{-4}	2.1×10^{-10}

than that of gravitational radiation, as shown in Sect. 13.3.3 for a linear dynamo law. However, the reduction in $|\dot{J}_{mb}|$ for $(B_p)_0 > 30$ MG, illustrated in Table 13.5, is sufficiently large that magnetic braking would still become negligible in this model even for the stronger dynamo laws considered in Sect. 13.3. It follows that magnetic braking would not be sufficient to drive the secondary out of thermal equilibrium in the AM Her systems, which would therefore evolve via gravitational radiation through the period gap with mass transfer continuing. This analysis assumes that the dead zones remain effective at high rotation rates.

13.4 Summary and Discussion

Magnetic braking due to a wind from the secondary star, together with tidal coupling to the orbit, provides a mechanism to explain the higher mass transfer rates believed to occur in binaries above the period gap. If the nature of the dynamo generating the secondary star magnetic field changes as a transition is made from partially convective to fully convective stars, then a suitable change in magnetic braking may be able to explain the existence of the period gap.

A better understanding of the nature of dynamos operating in lower main sequence stars is needed, in order to relate the magnetic field to the rotation rate and hence improve the calculation of the mass transfer rate due to magnetic braking.

The AM Her systems are particularly noteworthily, since they appear not to be affected by the period gap. The effect of their strong magnetic fields on the wind structure of the secondary star is a possible explanation for this, and further investigation is needed.

References

Campbell, C.G., 1997, MNRAS, 291, 250.
Campbell, C.G., Papaloizou, J.C.B., 1983, MNRAS, 204, 433.
Collier Cameron, A., Robinson, R.D., 1989, MNRAS, 238, 657.
Golub, L., 1983, In IAU Colloquium 71., Activity in Red Stars, eds., Byrne, P.B. and Rodono, M., Reidel, 102, 83.
Kippenhahn, R., Weigert, A., 1990, Stellar Structure and Evolution, Springer.
Li, J., Wu, K., Wickramasinghe, D.T., 1994, MNRAS, 268, 61.

Mestel, L., 1967, in Plasma Astrophysics, ed. Sturrock, P.A., Academic Press, London.
Mestel, L., 1968, MNRAS, 138, 359.
Mestel, L., 2012, Stellar Magnetism, Second Edition, Oxford University Press.
Mestel, L., Spruit, H.C., 1987, MNRAS, 226, 57.
Okamoto, I., 1974, MNRAS, 166, 683.
Paczynski, B., 1967, AcA, 17, 287.
Pallavicini, R., Golub, L., Rosner, R., Vaiana, G.S., Ayres, T., Linsky, J.L., 1981, ApJ, 248, 279.
Parker, E.N., 1963, Interplanetary Dynamical Processes, Interscience, New York.
Pizzo, V., Schwenn, R., Marsch, E., Rosenbrauer, H., Muehlhaeuser, K.H., Neubrauer, F.M., 1983, ApJ, 271, 335.
Pneuman, G.W., Kopp, R.A., 1971, SoPh, 18, 258.
Rappaport, S., Verbunt, F., Joss. P.C., 1983, ApJ, 275, 713.
Saar, S.H., 1991, in The Sun and Cool Stars: Activity, Magnetism, Dynamos., eds Tuominen, I., Moss, D., Rudiger, G., Springer, Berlin, 380, 389.
Sakurai, T., 1985, A&A, 152, 121.
Sakurai, T., 1990, CoPhR, 12, 247.
Schatzman, E., 1962, AnAp, 25, 18.
Skumanich, A., 1972, ApJ, 171, 565.
Spruit, H.C., Ritter, H., 1983, A&A, 124, 267.
Taam, R.E., Spruit. H.C., 1989, ApJ, 345, 972.
Verbunt, F., Zwaan, C., 1981, A&A, 100, L7.
Warner, B., 1995, Cataclysmic Variable Stars, Cambridge University Press.
Weber, E.J., Davis, L., 1967, ApJ, 148, 217.

Chapter 14
Accretion Disc Magnetic Winds

Abstract There is observational evidence that accretion discs in interacting binaries have wind flows emanating from their surfaces, and that the flow tends to become collimated parallel to the disc rotation axis. It is known that a differentially rotating, turbulent disc can have a large-scale magnetic field generated by dynamo action. Magnetically channelled winds are effective at removing angular momentum from accretion discs, provided that the initial flow is well sub-Alfvenic and the poloidal magnetic field has a suitable geometry with a sufficient inclination to the vertical at the disc surface.

Firstly, the wind launching and field source problems are considered, and wind structure calculations are reviewed. A detailed analysis of the disc-wind system is then presented, incorporating a dynamo generated magnetic field, with solutions for the radial and vertical structures of the disc and for the sub-Alfvénic wind region. The removal of angular momentum by the wind outflow can make a major contribution to driving the disc inflow, together with viscosity. A significant amount of mass can be lost from the inner region of the disc, due to enhanced wind mass fluxes. Disc models having inflows driven purely by magnetic winds tend to be subject to a field bending instability, but this can be quenched by allowing for a temperature dependent turbulent viscosity.

14.1 Introduction

Wind outflows and collimated jets are associated with systems that accrete matter via a disc. Winds were discovered in high state cataclysmic variables from the presence of blueshifted absorption troughs and P Cygni profiles in the ultraviolet resonance lines (Heap et al. 1978; Cordova and Mason 1982). Typical terminal velocities in the wind lines are near the escape velocity of the primary. In eclipsing systems the resonance lines that are seen in emission are only partially eclipsed, or completely unocculted, indicating that the winds are vertically extended (Mauche et al. 1994). Studies to interpret UV line profiles in high-state disc-dominated cataclysmic variables indicate that the mass loss rates in the winds can be a

C. G. Campbell, *Magnetohydrodynamics in Binary Stars*, Astrophysics and Space Science Library 456, https://doi.org/10.1007/978-3-319-97646-4_14

significant fraction ($\gtrsim$ 10%) of the accretion rate, and that the winds are strongly affected by the stellar rotation rate.

It has been suggested that a powerful disc wind may be responsible for the observed behaviour of SW Sex stars (Honeycutt et al. 1986; Dhillon and Rutten 1995) and that the single-peaked emission line profiles seen in these systems, and in other nova-like variables, are due to wind-induced velocity gradients in the line emitting material (Murray and Chiang 1996). Knigge et al. (1997) suggested that virtually all the lines in the UV spectrum of the typical high-state cataclysmic variable Z Cam are formed either in the supersonic region of the wind or in the lower velocity region near the wind interface with the disc photosphere. The extreme UV spectrum of the dwarf nova U Gem in outburst appears to be dominated by strong wind features (Long et al. 1996). Long and Knigge (2002) developed a method to model observed UV wind features and hence relate these to the wind geometries and mass loss rates. Froning et al. (2003) made a detailed analysis of the observed wind features of the nova-like cataclysmic variable UX UMa.

Outflow features are also associated with accreting neutron stars in X-ray binaries. Steady compact jets have been observed to emanate from the cores of these systems, even at low accretion rates (Fender et al. 2003; Migliari and Fender 2006).

Given the foregoing observations of wind features in binary systems, together with the association of winds and jets with young stellar objects (T Tauri stars) and active galactic nuclei (AGN), extensive theoretical studies have been made of disc associated winds. The high degree of collimation often observed in the outer wind regions led to the suggestion that large-scale magnetic fields may be of fundamental importance in the wind flow structure.

The pioneering model of Blandford and Payne (1982) showed that a magnetic field of suitable geometry that threads the disc can play a vital role in the wind launching process, and in determining the structure and properties of the wind. Highly conducting plasma leaving the disc surface will be channelled by the magnetic field, provided that its initial speed is well below the Alfvén speed. Gas pressure gradients along the poloidal magnetic field will accelerate matter so that the flow can reach the sound speed. The position of the sonic point affects the mass flux flowing into the wind region, as does the temperature of matter at the wind base. As will be shown below, the poloidal magnetic field inclination at the wind base affects the position of the sonic point. Beyond this point material is accelerated up to the Alfvén speed and then to the fast magnetosonic speed. Near and beyond the Alfvén surface the field distortion due to the flow is increased, and magnetic stresses can act to vertically collimate the wind. Hence such magnetically influenced winds can explain the collimation frequently observed in disc outflows. The wind can remove a significant amount of angular momentum per unit mass from the disc and so make a major contribution to driving the inflow.

The theory of magnetic disc winds is considered in detail in this chapter, including the launching process, the magnetic field source, the wind and disc structures and the stability of the system. Accretion discs occurring in interacting binary stars are of relevance here, rather than those occurring in T Tauri stars, which are also believed to have wind flows. T Tauri discs are expected to have differences

in their structure compared to those in binary systems, since they accrete on to protostars having much larger radii than those of the compact white dwarfs and neutron stars occurring in binaries. There are also expected to be differences in magnetic diffusion mechanisms in the two types of discs. However, despite these differences, many of the fundamental processes described here for binary star discs should have relevance to magnetic winds in other disc systems. [Section 14.6.2 is derived in part from Campbell (2014), copyright Taylor and Francis, available online at https://doi.org/10.1080/03091929.2013.870167].

14.2 Magnetic Wind Launching

14.2.1 The Critical Launching Angle

The model of Blandford and Payne (1982) treated the disc as an infinitely thin boundary. The initial wind flow from the disc is channelled by the poloidal magnetic field, having an inclination angle of i to the horizontal. The initial flow is subsonic and well sub-Alfvénic. Fluid elements can be considered to be threaded on the magnetic field lines and are subject to the stellar gravitational force and centrifugal force. A cylindrical coordinate system (ϖ, ϕ, z) can be used, centred on the accretor. The footpoint of a poloidal magnetic field line is at $\varpi = \varpi_0$, $z = 0$ and rotates with the local Keplerian angular velocity of $\Omega_0 = \Omega_\mathrm{K}$. Blandford and Payne showed numerically that there is a critical value of i, given by $i_\mathrm{c} = 60°$, such that for $i < i_\mathrm{c}$ the centrifugal force exceeds the gravitational force along $\mathbf{B}_\mathrm{p}$ at the wind base. Then fluid elements can freely leave the disc and be centrifugally accelerated to form the wind flow. This simplified picture is shown in Fig. 14.1.

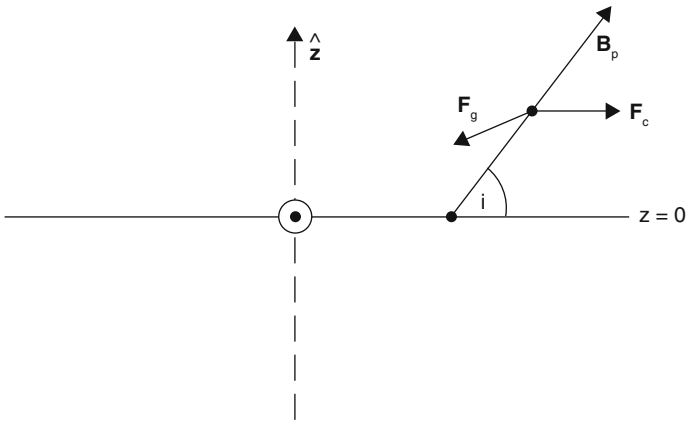

Fig. 14.1 Idealized picture of poloidal field inclination, showing the gravitational and centrifugal forces acting on a fluid element

The critical launching angle can be derived analytically. The axisymmetric wind equations are the same as those considered in Chap. 13, but with the disc as the wind base. Using $\alpha = \Omega_0$ in the energy integral (13.27), together with (13.10) for $\rho v_\mathrm{p}/B_\mathrm{p}$ to eliminate v_p in terms of B_p/ρ, gives the Bernoulli integral

$$H(\varpi, \rho) = \frac{\epsilon^2 B_\mathrm{p}^2}{2\rho^2} + \frac{1}{2}\varpi^2\Omega_0^2\left(\frac{\Omega}{\Omega_0}\right)\left(\frac{\Omega}{\Omega_0} - 2\right) - \frac{GM}{\left[\varpi^2 + z(\varpi)^2\right]^{\frac{1}{2}}} + a^2 \ln \rho, \tag{14.1}$$

for an isothermal wind with sound speed a, along a field line with equation $z = z(\varpi)$. For a well sub-Alfvénic flow Ω is close to Ω_0 and (14.1) can be written as

$$H(\varpi, \rho) = \frac{\epsilon^2 B_\mathrm{p}^2}{2\rho^2} + \psi + a^2 \ln \rho, \tag{14.2}$$

where

$$\psi(\varpi) = \psi(\varpi, z(\varpi)) = -\frac{GM}{[\varpi^2 + z(\varpi)^2]^{\frac{1}{2}}} - \frac{1}{2}\Omega_0^2\varpi^2, \tag{14.3}$$

is the effective potential along a field streamline and $B_\mathrm{p} = B_\mathrm{p}(\varpi)$. The slow and fast magnetosonic critical points are given by the conditions $\partial H/\partial\varpi = 0$ and $\partial H/\partial\rho = 0$ and, for $v_\mathrm{p} \ll v_\mathrm{A}$, the slow point merges with the sonic point to high accuracy. Equation (14.2) and $\epsilon = \rho v_\mathrm{p}/B_\mathrm{p}$ yield

$$\frac{\partial H}{\partial \varpi} = v_\mathrm{p}^2 \frac{B_\mathrm{p}'}{B_\mathrm{p}} + \frac{d\psi}{d\varpi}. \tag{14.4}$$

Noting that $v_\mathrm{p}^2|B_\mathrm{p}'|/B_\mathrm{p} \sim v_\mathrm{p}^2/\varpi \lesssim a^2/\varpi$ in the subsonic region, this term is small compared to either term in $d\psi/d\varpi$ and hence the sonic point condition becomes

$$\frac{d\psi}{ds} = \hat{\mathbf{B}}_\mathrm{p} \cdot \nabla\psi = 0, \tag{14.5}$$

where s is the distance along a poloidal field line from its base.

The effective potential along a field line can be expressed as

$$\psi(s) = -\frac{GM}{\varpi_0}\left[\frac{\varpi_0}{(\varpi^2 + z^2)^{\frac{1}{2}}} + \frac{1}{2}\left(\frac{\varpi}{\varpi_0}\right)^2\right], \tag{14.6}$$

with

$$\varpi = \varpi_0 + (1 + \tan^2 i)^{-\frac{1}{2}} s, \tag{14.7}$$

$$z = \tan i\,(1 + \tan^2 i)^{-\frac{1}{2}} s. \tag{14.8}$$

The sonic point condition (14.5), and expansion to second order in s/ϖ_0, then yields

$$\frac{s}{\varpi_0}\left[\frac{3}{2}q(1+3q^2)\frac{s}{\varpi_0}+4q^2-1\right]=0, \tag{14.9}$$

where $q=(1+\tan^2 i)^{-1/2}$. This gives two roots for s/ϖ_0, and so for z/ϖ_0, as

$$\frac{z}{\varpi_0}=0 \tag{14.10a}$$

and

$$\frac{z}{\varpi_0}=\frac{2}{3}\frac{\tan i(\tan^2 i-3)}{(\tan^2 i+4)}. \tag{14.10b}$$

Hence there are two points at which the gravitational force and the centrifugal force along $\mathbf{B}_\mathrm{p}$ cancel. The second solution is only valid for $\tan i > \sqrt{3}$ and so for $i > i_\mathrm{c}$ with $i_\mathrm{c}=60°$. This is the sonic point, which will be shown to be an unstable equilibrium point. The solution $z=0$ expresses the fact that the gravitational and centrifugal forces balance in the disc, independently of i. For $i \to i_\mathrm{c}$ the sonic point merges with the $z=0$ solution.

The stability of the balance points is determined by the sign of $d^2\psi/ds^2$. Equations (14.6)–(14.8) give

$$\frac{d^2\psi}{ds^2}=-\frac{GM}{\varpi_0^3}\left[3\left(q+\frac{s}{\varpi_0}\right)^2 Q^{-\frac{5}{2}}-Q^{-\frac{3}{2}}+q^2\right], \tag{14.11}$$

where

$$Q=1+2q\frac{s}{\varpi_0}+\frac{s^2}{\varpi_0^2}. \tag{14.12}$$

This gives

$$\left(\frac{d^2\psi}{ds^2}\right)_{s=0}=\frac{GM}{\varpi_0^3}\frac{(\tan^2 i-3)}{(\tan^2 i+1)}. \tag{14.13}$$

It follows that for $i > i_\mathrm{c}$ the mid-plane balance point is a minimum, since $d^2\psi/ds^2 > 0$, and hence is stable. For $i < i_\mathrm{c}$ this point becomes a maximum, since then $d^2\psi/ds^2 < 0$, and hence is unstable. Using (14.8) and (14.10b) to obtain s/ϖ_0 at the sonic point in (14.11), and expanding to leading order in s/ϖ_0, yields

$$\left(\frac{d^2\psi}{ds^2}\right)_\mathrm{sn}=-\frac{GM}{\varpi_0^3}\frac{(5\tan^2 i-8)(\tan^2 i-3)}{(\tan^2 i+1)(\tan^2 i+4)}. \tag{14.14}$$

For $i > i_\mathrm{c}$ the sonic point lies above the disc and is unstable, being a maximum in ψ.

The foregoing results show that for $i > i_c$ there is a potential barrier that matter must surmount in passing from the minimum in ψ at $z = 0$ to the maximum at $z = z_{sn}$. Gas pressure gradients can do the work necessary to allow matter to reach the sonic point, and beyond this the centrifugal force accelerates it outwards. For $i \to i_c$ the sonic point merges with the mid-plane equilibrium point, so there is no potential barrier to the flow. For $i < i_c$ there is only one balance point, at $z = 0$, and this is unstable. In this case the magnetically channelled wind can flow from the disc surface with minimal thermal assistance.

It will be shown later that allowing for the finite thickness of the disc leads to two sonic points above the disc, one for $i > i_c$ and the other for $i < i_c$. These correspond to two branches with different dependences on i and asymptotic behaviour as $i \to i_c$.

14.2.2 Magnetic Sources and Poloidal Field Bending

The generation of a magnetically channelled wind, that can effectively remove angular momentum from the disc, requires the presence of a large-scale poloidal magnetic field of suitable geometry. Such a field must be maintained against dissipative processes in the disc, and this requires an effective source. There are two main sources that can be considered for such a field.

Firstly, for a binary star disc, the accretion stream that feeds the disc may be able to supply magnetic field, advected from the secondary star. It was seen in Chap. 12 that it is very likely that the secondary star has a large-scale magnetic field, generated by a dynamo, with surface values of several kG. Poloidal magnetic field, with a significant vertical component, might be advected by the accretion stream from the L_1 region to the outer edge of the disc. If this occurred, then a suitable field source would exist where the stream meets the disc. The question then arises as to whether this field can be advected inwards through the disc without significant decay due to dissipative processes.

For an axisymmetric situation, the source of the poloidal magnetic field in the disc would be an azimuthal current density, J_ϕ. This current source would dissipate, due to the conductivity of the disc, at a rate per unit volume of $\mu_0 \eta J_\phi^2$. For a disc of height h, and for significant field bending, the poloidal magnetic field varies with a vertical length-scale of $\sim h$ and hence it follows that $J_\phi \sim B_p/\mu_0 h$. The energy density of the field, given by $B_p^2/2\mu_0$, decreases with a decay time-scale of $\tau_d \sim h^2/\eta$. This must be compared with the poloidal field advection time-scale needed for the inflow to carry the field a distance $\ell = \varpi_D - \varpi$ into the disc, where ϖ_D is the cylindrical coordinate of its outer edge. This time-scale is $\tau_v \sim \ell/|v_\varpi|$. If the magnetic field is to reach the internal radius ϖ without significant decay, then the condition $\tau_d \gg \tau_v$ must be satisfied. Using the above expressions for τ_d and τ_v, shows that this condition requires a typical disc inflow speed to satisfy $|v_\varpi| > (\varpi/h)(\eta/\nu)\epsilon_T c_s$ for the advected magnetic field to reach a point having $\varpi \ll \varpi_D$.

This condition on $|v_\varpi|$ employs a parametrized turbulent viscosity of $\nu = \epsilon_\mathrm{T} c_\mathrm{s} h$, with $\epsilon_\mathrm{T} < 1$ and c_s the isothermal sound speed. A typical disc, with $\varpi/h = 50$, $\eta/\nu \gtrsim 1$ and $\epsilon_\mathrm{T} = 5 \times 10^{-2}$, gives the requirement that $|v_\varpi| \gtrsim c_\mathrm{s}$. It will be shown that the extraction of angular momentum by a disc wind can lead to values of $|v_\varpi|$ significantly larger than those occurring in the viscously driven case of $|v_\varpi| \simeq \nu/\varpi$, but still well subsonic. Also, the consistency of thin accretion disc theory requires subsonic inflows.

This estimate indicates that, even if a suitable poloidal magnetic field could be supplied via the accretion stream, it would not survive dissipative processes in its passage through the disc, since its inward advection would not be fast enough. However, it was suggested by Rothstein and Lovelace (2008) that effective advection of poloidal magnetic field may be possible due to the action of the outer layers of the disc. It was argued that in the outer lower pressure region of the disc $B^2/2\mu_0 P > 1$ could hold, so the magnetorotational instability would not operate and hence this region would not be turbulent. The much lower values of η would result in much longer magnetic decay times than those in the main body of the disc. Assuming that most of the J_ϕ source of $\mathbf{B}_\mathrm{p}$ is located in the non-turbulent outer layers, then $\mathbf{B}_\mathrm{p}$ could be effectively advected inwards before significant decay occurred.

Although a magnetized accretion stream, together with effective field advection through the disc, cannot be excluded as a possible field source, dynamo action in discs is very likely to occur. It was seen in Chap. 11 that $\alpha\Omega$-type dynamos can operate in accretion discs to produce large-scale magnetic fields. The radial shear, turbulence and vertical stratification favour dynamo action. With the antisymmetric α function negative above the midplane, steady dipole symmetry magnetic fields can be produced which have the geometry required for an effective magnetic wind. Campbell (1999), Rekowski et al. (2000) and Reyes-Ruiz (2000) showed that an $\alpha\Omega$ dynamo can produce steady dipole symmetry magnetic fields in accretion discs. If a suitable poloidal magnetic field has been generated then it must be sufficiently inclined to the vertical at the disc surface, directed away from the rotation axis, for a significant wind mass flux to be produced. It was shown that inclination angles not far from the critical value of $i_\mathrm{c} = 60^\circ$ are required.

If the disc is threaded by a nearly vertical magnetic field, then the inflow causes this to bend outwards. The bending angle achieved depends on the balance between inward field advection and outward slippage due to diffusion. Poloidal field bending by the inflow was considered in Sect. 9.2.2., in the context of a poloidal magnetic field originating from the accretor threading the disc. The ratio $|v_\varpi| h/\eta$ determines the field bending and, for a typical viscously-driven disc, this is small. However, Campbell et al. (1998) showed that, for the case of a disc magnetic field generated by an $\alpha\Omega$ dynamo, poloidal field bending can be enhanced. The bending ratio then becomes $(|v_\varpi| h/\eta) g(K)$, where K^3 is the dynamo number. If K^3 is close to its critical value, then the factor $g(K)$ can significantly enhance poloidal field bending. It will be shown below that, even if K^3 is not close to its critical value, the enhancement of $|v_\varpi|$ due to wind magnetic braking of the disc can lead to values

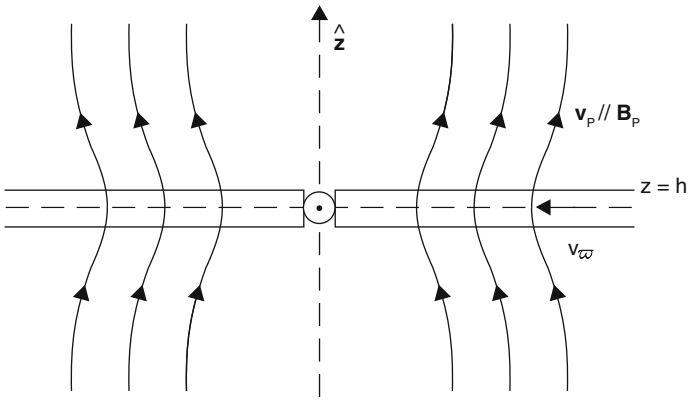

Fig. 14.2 A dipole symmetry magnetic field, bent by the inflow through the disc (not to scale)

of $|v_\varpi|$ significantly above those generated by viscosity. Figure 14.2 shows the required geometry for the poloidal magnetic field to accommodate wind launching.

14.3 The Wind Structure

In the model of Blandford and Payne (1982) the disc was treated as a boundary of ignorable thickness which is differentially rotating with a Keplerian angular velocity distribution. Self-similar solutions were found for the wind structure, assuming a polytropic relation between the pressure and density. The flow passes through a sonic point and then through an Alfvén point. A similar approach was used by Ferreira (1997), but with some consideration of the effect of the vertical equilibrium in the disc in relation to mass loading into the wind.

Heyvaerts and Norman (1989) considered steady, axisymmetric winds from accretion discs, with a poloidal field threading the disc of unspecified origin but of the required geometry. They made a detailed study of the transfield equation, which involves directions normal to the lines of $\mathbf{B}_\mathrm{p}$ in meridional planes. They concluded that axisymmetric MHD winds, with no closed field line topologies, tend to collimate along the disc rotation axis. Non-singular solutions with a finite poloidal current density lead to cylindrically collimated flows due to horizontal gradients of B_ϕ^2.

Pelletier and Pudritz (1992) analysed the wind structure for a disc containing a poloidal magnetic field with a power law flux function $\psi_\mathrm{m} \propto \varpi^n$. The disc viscosity and magnetic diffusivity were not included. Magnetic pinch forces tended to collimate the wind flow parallel to the rotation axis.

Stone and Norman (1994) performed numerical simulations of wind flows from a disc with $\nu = 0$ and $\eta = 0$ threaded by a vertical magnetic field, with an adiabatic equation of state. Firstly, the case of an initially sub-Keplerian disc with

$B^2/2\mu_0 P \gtrsim 1$ was considered. A strong B_ϕ field is generated and magnetic pressure gradients result in highly collimated, jet-like outflows. The disc initially collapses, due to magnetic braking, but this is halted due to the centrifugal barrier that develops. With a Keplerian rotation profile and $B^2/2\mu_0 P \gtrsim 1$, rapid collapse of the inner disc again occurs due to magnetic braking. This effect can be reduced if a larger difference is adopted between the disc density and that of its surroundings. Finally, simulations were performed with $\Omega = \Omega_\kappa$ and $B^2/2\mu_0 P \lesssim 1$. The disc is then subject to the magnetorotational instability. Radially channelled streams result in the surface regions of the disc, with high angular momentum material moving outwards and material of lower angular momentum moving inwards.

A self-similar solution for the disc and wind structure was found by Li (1995). A poloidal magnetic field was assumed to be advected inwards through a diffusive disc. Zero disc viscosity was assumed, so magnetic stresses drive the inflow. A polytropic equation of state was employed. Wind solutions result which pass through the critical points and become collimated. The magnetic field strength is a free parameter and a sufficiently strong field must be assumed for the initial flow to be sub-Alfvénic. In order to bend such a field, and launch the wind, the required inflow speed becomes supersonic. It will be shown below that such problems can be overcome by the consideration of a dynamo-generated magnetic field.

Ogilvie (1997) considered a thin differentially rotating disc threaded by a poloidal magnetic field of unspecified source. The idealized case of no magnetic diffusivity or viscosity was analysed. A polytropic relation was taken connecting the pressure and density. The poloidal velocity was initially ignored and isorotation was assumed, so no B_ϕ field is produced. Because the source of $\mathbf{B}_\mathrm{p}$ was not specified, fields of different strengths can be considered. An asymptotic analysis was performed, using the thin disc aspect ratio as a small parameter.

Firstly, the case of a weakly magnetized disc was considered, defined by $B^2/2\mu_0 P \lesssim 1$. The angular velocity is then Keplerain to leading order, but is altered to first order by the radial magnetic force. The magnetic field bends vertically through the disc and joins to an external field which is straight for $|z|/\varpi \ll 1$. For a field inclination to the horizontal of $i < 60°$, the sum of the gravitational and centrifugal potentials reaches a maximum above the disc along a field line. This maximum represents the slow magnetosonic point for the wind flow.

For strongly magnetized discs, having $B^2/2\mu_0 P \gg 1$, the disc angular velocity differs from a Keplerian form at leading order in h/ϖ. The disc is strongly compressed by the vertical magnetic force, which dominates the vertical component of gravity, so the vertical equilibrium becomes a balance between the vertical pressure gradient and the vertical magnetic force. A slow magnetosonic point may exist in the wind region, but only at a height $z \gg h$. Hence significant wind mass fluxes are unlikely to occur in this strong magnetic regime.

The case of weak magnetization can be adapted to allow for viscosity, magnetic diffusivity and an inflow, but only with the transport coefficients being a factor of h/ϖ smaller than those used in standard accretion disc theory. The main problem that arises for such a model is that nearly all the accretion energy released is carried away by the wind. The rate of dissipation in the disc is too small by a factor of

$\sim h/\varpi$ to release the accretion energy, since ν and η are smaller by this factor. Hence a disc with essentially no radiative emission results. However, such idealized models can illustrate some of the essentials of the required poloidal field geometry which are related to wind launching.

Ouyed and Pudritz (1997a,b, 1999) performed numerical simulations of magnetic disc winds, allowing for different initial conditions and following the time development of the flow. The wind becomes super-Alfvénic and reaches terminal velocities of the order of the Keplerian velocity at the disc base. Most of the energy in the outflow is shared between the poloidal kinetic energy and the toroidal magnetic energy. Initially, torsional Alfvén waves build up a radial gradient of toroidal magnetic pressure that adjusts the structure of the coronal magnetic field to give favourable launching angles. The flow is centrifugally ejected beyond the sonic point. Beyond the Alfvén surface the poloidal magnetic field becomes collimated parallel to the vertical axis due to the generation of a strong B_ϕ component. Some time-dependence remains, with episodic jets and knot structures being generated.

Ogilvie and Livio (2001) presented a solution for the vertical structure of the disc, incorporating the thermal problem with radiative transfer. This enables the wind loading process to be considered in more detail. As in all the foregoing studies, an unspecified source of poloidal magnetic field was assumed. A power law opacity was taken and the local disc solution was matched to a simple atmospheric model. Since the strength of the magnetic field is undetermined, strong and weak cases can be considered. Sub-thermal magnetic fields are consistent with the generation of turbulence via magnetorotational instabilities and wind launching is possible for moderate values of $B^2/2\mu_0 P < 1$. The mass loss rate increases with the poloidal field inclination, but the solution branch terminates before excessive mass loss results. For a well sub-Alfvénic initial flow, the poloidal field is locally straight in the subsonic wind region, consistent with a nearly force-free structure.

Fendt and Cemeljic (2002) considered time-dependent winds, but allowing for some magnetic diffusivity in the wind region. This has the effect of reducing the degree of collimation and increasing the wind terminal velocities. Tzeferacos et al. (2009) construct self-similar solutions for varying degrees of disc magnetisation, measured by $B^2/2\mu_0 P$. Steady collimated flow resulted for $B^2/2\mu_0 P < 1$.

Casse and Keppers (2002) solved the magnetic wind equations numerically, without the assumption of self-similarity. They incorporated some disc structure features, including a vertically varying form for η. The wind flow passes through the critical points and becomes magnetically collimated. The numerical study of Sheikhnezami et al. (2012) also considered a vertically varying η, but allowed for different poloidal and toroidal diffusivities. Lower values of diffusivity resulted in higher mass loading into the wind.

Zanni et al. (2007) considered a disc with zero viscosity but with a magnetic diffusivity of the form $\eta = \alpha_{\rm m}(v_{\rm A})_{z=0} h \exp(-2z^2/h^2)$. A cooling term was included in the heat equation and a polytropic equation of state was adopted. Self-similar solutions were considered, with a slightly sub-Keplerian rotation profile. The magnetic diffusivity was incorporated into the poloidal component of the induction equation, and a poloidal field was taken to thread the disc with $B_{\rm p}^2/2\mu_0 \simeq P$ in

the mid-plane. The surrounding atmosphere was taken to have an initial polytropic, spherically symmetric structure. The computational domain was defined by $0 < r < 40r_0$ and $0 < z < 120r_0$, with r_0 being the stellar radius. Zero gradients were taken for P, ρ and v_p ar $r = 40r_0$. The simulations were run for a time of $\simeq 63\, P_\kappa(r_0)$. The outer parts of the disc did not attain equilibrium, but the relevant region was well inside this.

Firstly, simulations for the case of $\alpha_\mathrm{m} = 1$ were run. A quasi-steady wind flow developed with a well ordered poloidal magnetic field. The wind flow passed through well separated critical points. Simulations were then run for $\alpha_\mathrm{m} = 0.1$. A highly unsteady wind flow resulted, with a poloidal magnetic field having a wavy structure. This behaviour was related to the lower values of η resulting in disc inflow advection effects having a stronger influence than diffusion. The incorporation of an anisotropic magnetic diffusivity resulted in less erratic behaviour.

Stepanovs and Fendt (2014) investigated the outflows generated from an inviscid disc which has separate magnetic diffusivities for the poloidal and toroidal field components. Numerical simulations were performed using spherical coordinates. An input magnetic field was imposed, so the magnetization ratio $B^2/2\mu_0 P$ could be varied. If this ratio was taken to be uniform, then a self-similar structure resulted. The disc structure was resolved, and the wind flow became centrifugally launched beyond the sonic point. The disc angular velocity maintained a Keplerian profile. Wind flows became collimated parallel to the spin axis. Some poloidal field bending instability was observed, but this became stabilized for higher η values. Such instabilities will be discussed later.

A review of the numerical simulation techniques used in magnetic disc wind calculations is included in the review of Pudritz et al. (2007).

All the above studies assumed that the required magnetic field is advected inwards from a source at the outer edge of the disc. However, as seen in Chap. 11, accretion discs are believed to possess some form of dynamo process which generates and maintains large-scale magnetic fields. Dynamo models can generate a magnetic field of dipolar symmetry, which is suitable for wind launching and angular momentum transport. Such a model was employed by von Rekowski et al. (2003) to study wind outflows. An $\alpha^2\Omega$ dynamo model was used in the disc, with a quenching term in α and a turbulent form for η. The α function was taken to be negative above the disc mid-plane, so a dipole symmetry $\mathbf{B}$ field results. A polytropic equation of state was used in the disc and wind regions, with a specific entropy that is smaller in the disc. The equations were solved numerically, and the outer boundaries did not have a significant effect on the computational domain. When the dynamo generated magnetic field in the disc was sufficiently strong, a fast magneto-centrifugal driven outflow developed in the inner parts of the disc, and a slow pressure-driven outflow occurred in the outer parts.

A solution was found by Campbell (2003, 2005) for the radial and vertical structures of the disc and the sub-Alfvénic region of the wind, incorporating a dynamo to generate the magnetic field. The essential properties of the outer wind are also considered. The possible development of inner jet solutions and the stability of the disc-wind system can then be investigated. The analysis below is based on this work.

14.4 The Disc-Wind System

14.4.1 The Disc Magnetic Field

A dipole-symmetry magnetic field facilitates wind flows from the disc, with an associated transport of angular momentum. An $\alpha\Omega$ dynamo, with the anti-symmetric α function negative for $z > 0$, leads to steady magnetic field solutions that have dipole-symmetry. A simple step function form can be used for α, given by

$$\alpha(\varpi, z) = \begin{cases} -\tilde{\alpha}(\varpi), & 0 < z < h, \\ 0, & z = 0, \\ \tilde{\alpha}(\varpi), & -h < z < 0, \end{cases} \tag{14.15}$$

with $\tilde{\alpha} > 0$ and parametrized by

$$\tilde{\alpha} = \epsilon c_{\rm s}, \tag{14.16a}$$

$$c_{\rm s} = \left(\frac{\mathcal{R}}{\mu} T_{\rm c}\right)^{\frac{1}{2}}, \tag{14.16b}$$

where ϵ is an rms turbulent Mach number having $\epsilon < 1$. A turbulent magnetic Reynolds number can be defined as

$$N_\alpha = \frac{\tilde{\alpha} h}{\eta} \tag{14.17}$$

and hence the magnetic diffusivity can be expressed as

$$\eta = \frac{\epsilon}{N_\alpha} c_{\rm s} h. \tag{14.18}$$

The radial derivative diffusion terms and most of the advection terms can be ignored in the mean-field induction equation, giving the poloidal and toroidal components as

$$v_\varpi B_z + \eta \frac{\partial B_\varpi}{\partial z} - \alpha B_\phi = 0, \tag{14.19}$$

$$\eta \frac{\partial^2 B_\phi}{\partial z^2} = -\varpi \Omega_{\rm K}' B_\varpi . \tag{14.20}$$

The poloidal component (14.19) represents a balance between field advection due to the inflow, turbulent diffusion and the creation of poloidal field from toroidal field due to the α-effect. The toroidal component (14.20) describes a balance between

the vertical diffusion of B_ϕ and its creation due to the radial shearing of B_ϖ. The magnetic terms in the ϖ-component of the momentum equation are small relative to the radial gravity term so, apart from in a boundary layer close to the stellar surface, the disc angular velocity has the Keplerian form

$$\Omega = \Omega_{\rm K}(\varpi) = \left(\frac{GM}{\varpi^3}\right)^{\frac{1}{2}}. \tag{14.21}$$

The elimination of B_ϖ between (14.19) and (14.20) yields

$$\frac{\partial^3 B_\phi}{\partial z^3} + \frac{\varpi \Omega_{\rm K}' \alpha}{\eta^2} B_\phi = \frac{\varpi \Omega_{\rm K}'}{\eta^2} v_\varpi B_z. \tag{14.22}$$

To leading order in h/ϖ_0, B_z is independent of z in the disc, so $B_z = B_{z\rm s}(\varpi_0)$ with a field line meeting the disc mid-plane at $(\varpi_0, 0)$. The forms of α and η, together with the very slow variation of h/ϖ_0, facilitate the separable solutions

$$B_\phi(\varpi, z) = B_{\phi\rm s}(\varpi_0) f_\phi(\zeta) \tag{14.23}$$

and

$$v_\varpi(\varpi, z) = v_{\varpi\rm c}(\varpi_0) f_v(\zeta), \tag{14.24}$$

where the subscript c refers to the central plane $z = 0$ and $\zeta = z/h$. It follows that

$$f_\phi(1) = 1. \tag{14.25a}$$

$$f_v(0) = 1. \tag{14.25b}$$

The substitution of the separable forms (14.23) and (14.24) in the toroidal field equation (14.22) leads to

$$f_\phi''' + D f_\phi = -DF f_v, \tag{14.26}$$

where the dynamo number

$$D = \frac{3\Omega_{\rm K}\tilde{\alpha}h^3}{2\eta^2} \tag{14.27}$$

and

$$F = \frac{v_{\varpi\rm c} B_{z\rm s}}{\tilde{\alpha} B_{\phi\rm s}}. \tag{14.28}$$

Self consistent solutions can be found for D and F independent of ϖ. Suitable boundary conditions for $f_\phi(\zeta)$ are

$$f_\phi(0) = 0, \quad f_\phi''(0) = 0, \tag{14.29a}$$

$$f_\phi'(1) = 0. \tag{14.29b}$$

The first two conditions give the vertical anti-symmetry of B_ϕ and B_ϖ, while the last condition arises from the matching of the disc field to the nearly force-free field of the initial wind region. An axisymmetric force-free field satisfies

$$\mathbf{B}_\mathrm{p} \cdot \nabla(\varpi B_\phi) = 0 \tag{14.30}$$

and, since the vertical derivative term dominates, this gives

$$\left(\frac{\partial B_\phi}{\partial z}\right)_{z=h} = 0 \tag{14.31}$$

so the use of (14.23) for B_ϕ yields $f_\phi'(1) = 0$.

Equation (14.26) relates f_v to f_ϕ. These functions will also be related by the angular momentum equation. It will be shown that most of the variation of $f_v(\zeta)$ occurs near the disc surface. The approximation $f_v(\zeta) \simeq 1$ can therefore be used in (14.26) when solving for $f_\phi(\zeta)$ and the solution can be employed in the relevant equations to solve for $f_v(\zeta)$. The slow variation of $f_v(\zeta)$, apart from near $\zeta = 1$, can then be confirmed. Accurate solutions for f_ϕ and f_v result. With $f_v(\zeta) \simeq 1$, the solution of (14.26) can be written as

$$f_\phi = y - F, \tag{14.32}$$

where y satisfies the homogeneous equation

$$y''' + K^3 y = 0, \tag{14.33}$$

with boundary conditions

$$y(0) = F, \quad y''(0) = 0, \tag{14.34a}$$

$$y'(1) = 0 \tag{14.34b}$$

and

$$K = D^{\frac{1}{3}} = \frac{h}{\ell_z}, \tag{14.35}$$

where ℓ_z is the vertical length-scale of B_ϕ in the disc. The solution of (14.33), satisfying the boundary conditions, is

$$y(\zeta) = \frac{2}{\sqrt{3}}\frac{F}{Q}e^{K/2}\left[e^{-K(\zeta-1)}\cos\left(\frac{\sqrt{3}}{2}K+\frac{\pi}{6}\right)\right.$$
$$\left.+e^{K(\zeta-1)/2}\left\{\cos\left(\frac{\sqrt{3}}{2}K\zeta-\frac{\pi}{6}\right)+e^{3K/2}\cos\left(\frac{\sqrt{3}}{2}K(\zeta-1)+\frac{\pi}{6}\right)\right\}\right] \tag{14.36}$$

with

$$Q = 1+2e^{3K/2}\cos\left(\frac{\sqrt{3}}{2}K\right). \tag{14.37}$$

The constant F is determined by the boundary condition $f_\phi(1) = 1$ as

$$F(K) = \frac{1+2e^{3K/2}\cos(\sqrt{3}K/2)}{2e^K[\sinh K - 2\sinh(K/2)\cos(\sqrt{3}K/2)]}. \tag{14.38}$$

Figure 14.3 shows the function $f_\phi(\zeta)$. Using (14.16a) for $\tilde{\alpha}$ and (14.18) for η in (14.27) for $D = K^3$ gives

$$\frac{\Omega_K h}{c_s} = \frac{2}{3}\frac{\epsilon K^3}{N_\alpha^2}. \tag{14.39}$$

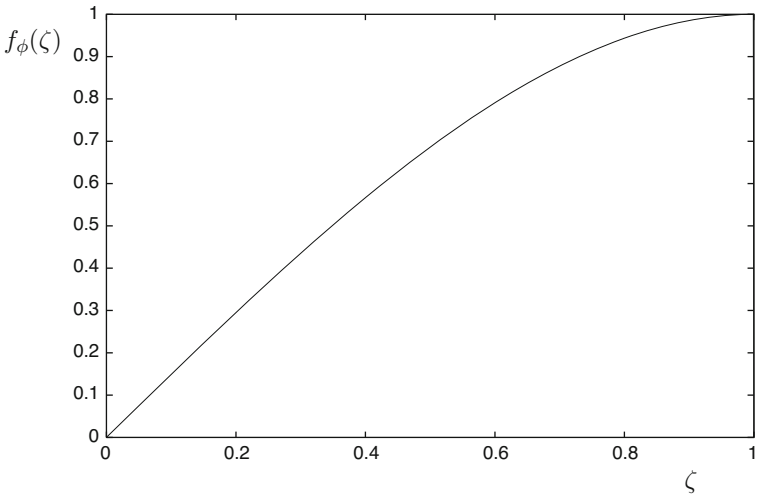

Fig. 14.3 The vertical variation of the disc azimuthal magnetic field (from Campbell 2003)

This, together with (14.18) for η, and (14.20) with (14.23) connecting B_ϕ to B_ϖ, yields

$$B_\varpi = \frac{N_\alpha}{K^3} B_{\phi \mathrm{s}} f_\phi'' = B_{\varpi \mathrm{s}}(\varpi_0) \frac{f_\phi''(\zeta)}{f_\phi''(1)}. \tag{14.40}$$

The poloidal field inclination at the disc surface is defined by

$$\tan i_\mathrm{s} = \frac{B_{z\mathrm{s}}}{B_{\varpi \mathrm{s}}}. \tag{14.41}$$

The amount of poloidal field bending is determined by a balance between the advective effect of the inflow and vertical diffusion. The field equations (14.19), (14.23), (14.26) and (14.28) lead to

$$\frac{\partial B_\varpi}{\partial z} = \frac{v_{\varpi \mathrm{c}} B_{z\mathrm{s}}}{\eta K^3 F} f_\phi'''. \tag{14.42}$$

Integrating this over $0 \le z \le h$, using the boundary condition $f_\phi''(0) = 0$, then yields

$$\frac{B_{z\mathrm{s}}}{B_{\varpi \mathrm{s}}} = \frac{1}{I} \frac{\eta}{|v_{\varpi \mathrm{c}}| h}, \tag{14.43}$$

where the dynamo number function $I(K)$ is given by

$$I(K) = \frac{|f_\phi''(1)|}{K^3 F} = \frac{e^{K/2}[e^{3K/2} - 2\cos(\sqrt{3}K/2 + \pi/3]}{K[1 + 2e^{3K/2}\cos(\sqrt{3}K/2)]}. \tag{14.44}$$

Equations (14.40) and (14.41) give

$$\frac{B_{\phi \mathrm{s}}}{B_{z\mathrm{s}}} = \frac{K^3}{N_\alpha f_\phi''(1) \tan i_\mathrm{s}}, \tag{14.45}$$

while it follows from (14.18) for η, together with (14.41) and (14.43) for the field component ratio, that the central plane inflow speed can be expressed as

$$v_{\varpi \mathrm{c}} = -\frac{\epsilon c_\mathrm{s}}{N_\alpha I \tan i_\mathrm{s}}. \tag{14.46}$$

It will be shown that the inflow speed is always subsonic, but is a larger fraction of c_s than in the standard viscously driven disc.

14.4.2 The Sub-Alfvénic Wind Region Magnetic Field

The foregoing solution for the disc magnetic field must match to a field solution for the initial part of the wind flow at the disc surface. For the magnetic torque to be significant, the Alfvén surface must lie well beyond the disc surface, such that $\varpi_{\rm A}^2/\varpi_{\rm s}^2 \gg 1$, so magnetic stresses dominate. The magnetic field in the initial part of the wind will then be nearly force-free, particularly in the region between the disc surface and the sonic surface. The magnetic field then satisfies the equation

$$(\nabla \times \mathbf{B}) \times \mathbf{B} = \mathbf{0}. \tag{14.47}$$

The poloidal field can be expressed in terms of a flux function $\psi_{\rm m}$ by

$$\mathbf{B}_{\rm p} = \nabla \times \left(\frac{\psi_{\rm m}}{\varpi} \hat{\boldsymbol{\phi}} \right) = \frac{1}{\varpi} (\nabla \psi_{\rm m}) \times \hat{\boldsymbol{\phi}}, \tag{14.48}$$

so ensuring that, for an axisymmetric field, $\nabla \cdot \mathbf{B} = 0$. The field components are

$$B_\varpi = -\frac{1}{\varpi} \frac{\partial \psi_{\rm m}}{\partial z}, \tag{14.49a}$$

$$B_z = \frac{1}{\varpi} \frac{\partial \psi_{\rm m}}{\partial \varpi} \tag{14.49b}$$

and it follows that

$$\mathbf{B}_{\rm p} \cdot \nabla \psi_{\rm m} = 0. \tag{14.50}$$

Substituting the components (14.49a) and (14.49b) in the force-free field condition (14.47) leads to the equation

$$\varpi \frac{\partial}{\partial \varpi} \left(\frac{1}{\varpi} \frac{\partial \psi_{\rm m}}{\partial \varpi} \right) + \frac{\partial^2 \psi_{\rm m}}{\partial z^2} = -\frac{1}{2} \frac{d}{d \psi_{\rm m}} (W^2), \tag{14.51}$$

where

$$W(\psi_{\rm m}) = \varpi B_\phi. \tag{14.52}$$

Then (14.50) and (14.52) give the force-free condition (14.30), used to determine the disc surface condition $f_\phi'(1) = 0$.

The wind field must match the dynamo generated disc field at $z = h$ for all ϖ. This can be achieved by taking a flux function of the form

$$\psi_{\rm m} = C \varpi^{\frac{3}{4}} f(\zeta), \tag{14.53}$$

where C is a constant. It will be shown that, to a very good approximation, $h = \bar{K}\varpi$ can be used here where $\bar{K}$ is a constant. The poloidal field components follow from (14.49a) and (14.49b) as

$$B_\varpi = -\frac{\varpi}{h} C \varpi^{-\frac{5}{4}} f', \tag{14.54a}$$

$$B_z = C\varpi^{-\frac{5}{4}} \left(\frac{3}{4} f - \zeta f' \right), \tag{14.54b}$$

where $f' = df/d\zeta$, and hence

$$\frac{B_z}{B_\varpi} = -\frac{3}{4}\frac{h}{\varpi}\frac{f}{f'} + \frac{h}{\varpi}\zeta. \tag{14.55}$$

Since $B_z/B_\varpi \sim 1$ and $(h/\varpi)\zeta \ll 1$ in the region of relevance, the last term in (14.55) is ignorable. Hence (14.54a) and (14.54b) give

$$B_\varpi = -\frac{\varpi}{h} C \varpi^{-\frac{5}{4}} f', \tag{14.56a}$$

$$B_z = \frac{3}{4} C \varpi^{-\frac{5}{4}} f, \tag{14.56b}$$

and

$$\frac{B_z}{B_\varpi} = -\frac{3}{4}\frac{h}{\varpi}\frac{f}{f'}. \tag{14.57}$$

Substituting the form (14.53) for ψ_m in the field equation (14.51) leads to the separated equations

$$f'' - \frac{15}{16}\frac{h^2}{\varpi^2} f = \bar{D} f^{-\frac{5}{3}} \tag{14.58}$$

and

$$\frac{d}{d\psi_\mathrm{m}} \left(W^2 \right) = -2 \frac{C^{\frac{8}{3}} \bar{D}}{\bar{K}^2} \psi_\mathrm{m}^{-\frac{5}{3}}, \tag{14.59}$$

where $\bar{D}$ is a constant. Integrating (14.59) and using (14.53) for ψ_m yields

$$B_\phi = -\left(\frac{3\bar{D}}{\bar{K}^2} \right)^{\frac{1}{2}} \frac{C}{\varpi^{\frac{5}{4}} f^{\frac{1}{3}}}. \tag{14.60}$$

Matching the wind field to the disc field determines C and $\bar{D}$.

Using the scaling

$$f(1) = 1 \tag{14.61}$$

and equating B_z from (14.56b) to the dynamo surface field B_{zs} gives

$$C = \frac{4}{3}\varpi_s^{\frac{5}{4}} B_{zs}. \tag{14.62}$$

Equating (14.40) for B_ϖ in the disc to the wind component given by (14.56a) at $z = h$, then using (14.60) to eliminate $B_{\phi s}$, yields

$$f'(1) = -\frac{N_\alpha}{K^3}|f''_\phi(1)|(3\bar{D})^{\frac{1}{2}}. \tag{14.63}$$

Another expression for $f'(1)$ follows from the surface value of the poloidal field component ratio (14.57) as

$$f'(1) = -\frac{3}{4}\frac{1}{\tan i_s}\frac{h}{\varpi}. \tag{14.64}$$

Equating these expressions for $f'(1)$ and using (14.45) for $B_{\phi s}/B_{zs}$ gives

$$\bar{D} = \frac{3}{16}\left(\frac{B_{\phi s}}{B_{zs}}\right)^2 \frac{h^2}{\varpi^2} \tag{14.65}$$

and hence (14.58) becomes

$$f'' - \frac{15}{16}\frac{h^2}{\varpi^2} f = \frac{3}{16}\left(\frac{B_{\phi s}}{B_{zs}}\right)^2 \frac{h^2}{\varpi^2} f^{-\frac{5}{3}}. \tag{14.66}$$

Using (14.62) for C and (14.65) for $\bar{D}$ in (14.56a), (14.56b) and (14.60), gives the wind field components as

$$B_\varpi = B_{\varpi s}\left(\frac{\varpi_s}{\varpi}\right)^{\frac{5}{4}} \frac{f'(\zeta)}{f'(1)}, \tag{14.67}$$

$$B_\phi = B_{\phi s}\left(\frac{\varpi_s}{\varpi}\right)^{\frac{5}{4}} \frac{1}{f(\zeta)^{\frac{1}{3}}}, \tag{14.68}$$

$$B_z = B_{zs}\left(\frac{\varpi_s}{\varpi}\right)^{\frac{5}{4}} f(\zeta). \tag{14.69}$$

The surface components can be found from the disc equations.

This leaves $f(\zeta)$ to be determined by solving (14.66) subject to the boundary conditions (14.61) and (14.64) for $f(1)$ and $f'(1)$. The dynamo solutions will have

a field winding ratio $|B_{\phi s}/B_{zs}| < 1$ and the wind region has $f \sim 1$. Hence the last term in (14.66) is ignorable to a good approximation and the solution is

$$f(\zeta) = \cosh[k(\zeta - 1)] - \frac{3}{\sqrt{15}} \frac{1}{\tan i_s} \sinh[k(\zeta - 1)], \tag{14.70}$$

where

$$k = \frac{\sqrt{15}}{4} \frac{h}{\varpi}. \tag{14.71}$$

The smallness of $\bar{D}$ corresponds to J_ϕ being small compared to J_p, so $\mathbf{B}_p$ is approximately current-free, but B_ϕ is finite and satisfies the force-free condition $\mathbf{B}_p \cdot \nabla(\varpi B_\phi) = 0$.

The field line equations can be derived from

$$\frac{dz}{d\varpi} = h \frac{d\zeta}{\varpi} + \frac{h}{\varpi}\zeta = \frac{B_z}{B_\varpi} \tag{14.72}$$

and (14.55) for B_z/B_ϖ then gives

$$\frac{df}{f} = -\frac{3}{4} \frac{d\varpi}{\varpi}. \tag{14.73}$$

Using $f(1) = 1$, this integrates to yield the field line equation

$$f(\zeta) = \left(\frac{\varpi_s}{\varpi}\right)^{\frac{3}{4}}, \tag{14.74}$$

with $f(\zeta)$ given by (14.70). Equation (14.71) shows that $k \ll 1$ and using the second order Taylor expansion of the solution (14.70) in (14.74) gives

$$\frac{\varpi}{\varpi_s} = 1 + \frac{1}{\tan i_s} \frac{h}{\varpi}(\zeta - 1) - \frac{5}{8}\left(1 - \frac{7}{5\tan^2 i_s}\right) \frac{h^2}{\varpi^2}(\zeta - 1)^2, \tag{14.75}$$

valid for $\zeta \ll \varpi/h$. To first order in h/ϖ, the field lines are straight in this region and have the equation

$$\frac{\varpi}{\varpi_s} = 1 - \frac{1}{\tan i_s} \frac{h}{\varpi_s} + \frac{1}{\tan i_s} \frac{z}{\varpi_s}. \tag{14.76}$$

The field line curvature is a second order effect and it can be shown that it changes sign from the disc to the wind region. The vertical length-scale of B_ϖ changes from $\sim h$ in the disc to $\sim \varpi$ in the wind and the field line inflects so that it starts to bend towards the vertical axis in the wind region. Numerical simulations of the wind flow also show this inflection in the poloidal magnetic field.

14.4.3 Angular Momentum Transport and Mass Conservation

Combining the ϕ-component of the momentum equation with the continuity equation gives

$$\frac{\partial}{\partial \varpi_0}\left(\varpi_0 \rho v_\varpi \varpi_0^2 \Omega\right) + \frac{\partial}{\partial z}\left(\varpi_0 \rho v_z \varpi_0^2 \Omega\right) = \frac{\partial}{\partial \varpi_0}\left(\rho \nu \varpi_0^3 \Omega'\right) + \frac{1}{\mu_0}\frac{\partial}{\partial z}\left(\varpi_0^2 B_\phi B_z\right). \tag{14.77}$$

This relates the divergence of the angular momentum flux to the viscous and magnetic torques. For a dipole symmetry magnetic field, the radial magnetic transport term involving the $B_\varpi B_\phi$ stress makes a small contribution compared to the $B_\phi B_z$ stress term, so it has not been included in (14.77). A turbulent magnetic Prandtl number is defined as

$$N_\mathrm{p} = \frac{\nu}{\eta} \tag{14.78}$$

and then using (14.18) for η gives the turbulent viscosity as

$$\nu = \frac{\epsilon N_\mathrm{p}}{N_\alpha} c_\mathrm{s} h. \tag{14.79}$$

The condition for a small mass loss rate from the disc surfaces is

$$\frac{4\pi \varpi_0^2 \dot{m}}{\dot{M}} \ll 1, \tag{14.80}$$

where $\dot{m}$ is the wind mass flux through the sonic point and

$$\dot{M} = -4\pi \int_0^h \varpi_0 \rho v_\varpi dz \tag{14.81}$$

is the total mass flow rate through the disc. To leading order in h/ϖ, (14.67), (14.69), (14.70) and (14.75) for B_ϖ, B_z, $f(\zeta)$ and the field line relation for ϖ/ϖ_s show that $B_\mathrm{p} = (B_\varpi^2 + B_z^2)^{1/2}$ is conserved along $\mathbf{B}_\mathrm{p}$ and, since $\rho v_\mathrm{p}/B_\mathrm{p}$ is conserved, it follows that ρv_p is conserved. Hence the mass flux through the sonic point can be expressed as

$$\dot{m} = (\rho v_\mathrm{p})_\mathrm{sn} = (\rho v_\mathrm{p})_\mathrm{s} = \frac{(1+\tan^2 i_\mathrm{s})^{\frac{1}{2}}}{\tan i_\mathrm{s}} (\rho v_z)_\mathrm{s}. \tag{14.82}$$

If the small mass loss condition (14.80) is satisfied then the ρv_z angular momentum flux term is ignorable relative to the ρv_ϖ term in (14.77). Also, mass conservation

in the disc gives

$$\dot{M}(z) = -2\pi \int_{-z}^{z} \varpi_0 \rho v_\varpi \, dz, \tag{14.83}$$

with the total mass transfer rate being $\dot{M} = \dot{M}(h)$. The vertical integration of the angular momentum equation (14.77) then gives

$$\frac{\partial}{\partial \varpi_0}\left[\frac{1}{2\pi}\dot{M}(z)\varpi_0^2\Omega + \varpi_0^3\Omega'\nu\Sigma\right] + \frac{2}{\mu_0}\varpi_0^2 B_\phi B_z = 0, \tag{14.84}$$

where the antisymmetry of $B_\phi B_z$ has been used and

$$\Sigma(\varpi_0, z) = \int_{-z}^{z} \rho \, dz. \tag{14.85}$$

The viscous torque leads to an outward radial transport of angular momentum in the disc, in the usual way. The magnetic torque, involving the $B_\phi B_z$ stress, facilitates the vertical transport of disc angular momentum into the wind flow. The wind flow angular momentum transport conservation equation at the disc surface is

$$\frac{\rho v_z}{B_z}\varpi_{\rm s}^2\Omega_{\rm K}(\varpi_{\rm s}) - \frac{\varpi_{\rm s}}{\mu_0}B_{\phi{\rm s}} = \frac{\rho v_z}{B_z}\varpi_{\rm A}^2\Omega_{\rm K}(\varpi_{\rm s}), \tag{14.86}$$

this being consistent with a trans-Alfvénic flow (see Sect. 13.2.2). For effective angular momentum transport from the disc via the wind, the condition $\varpi_{\rm A}^2/\varpi_{\rm s}^2 \gg 1$ is required and hence the magnetic transport term dominates in (14.86) to give

$$\frac{\varpi_0}{\mu_0}B_{\phi{\rm s}}B_{z{\rm s}} = -\frac{\tan i_{\rm s}}{(1+\tan^2 i_{\rm s})^{\frac{1}{2}}}\dot{m}\varpi_{\rm A}^2\Omega_{\rm K}(\varpi_0), \tag{14.87}$$

where (14.82) has been used for $(\rho v_z)_{\rm s}$ and the central plane coordinate ϖ_0 can replace the disc surface coordinate $\varpi_{\rm s}$ to leading order. Using (14.87) to eliminate $B_{\phi{\rm s}}$ in (14.23) for B_ϕ, and noting that B_z is independent of z to leading order in the disc, gives the disc magnetic torque per unit radial length as

$$\frac{2}{\mu_0}\varpi_0^2 B_\phi B_z = -\frac{2\tan i_{\rm s}}{(1+\tan^2 i_{\rm s})^{\frac{1}{2}}}\dot{m}\varpi_{\rm A}^2\varpi_0\Omega_{\rm K}(\varpi_0) f_\phi(\zeta). \tag{14.88}$$

It will be shown that $i_{\rm s}$ and $\dot{m}\varpi_{\rm A}^2$ are very weakly dependent on ϖ_0, except close to the stellar surface, and hence (14.88) can be incorporated into the disc angular momentum equation (14.84) to give

$$\frac{\partial}{\partial \varpi_0}\left[\frac{1}{2\pi}\dot{M}(z)\varpi_0^2\Omega_{\rm K} + \varpi_0^3\Omega'\nu\Sigma - \frac{4\tan i_{\rm s}}{(1+\tan^2 i_{\rm s})^{\frac{1}{2}}}\dot{m}\varpi_{\rm A}^2\varpi_0^2\Omega_{\rm K} f_\phi(\zeta)\right] = 0. \tag{14.89}$$

The standard condition at the outer edge of the boundary layer above the stellar surface is

$$\left(\Omega' \nu \Sigma\right)_{\varpi = R+\delta} = 0, \tag{14.90}$$

for a boundary layer width of $\delta \ll R$. Integrating (14.89) and applying this condition leads to

$$\nu\Sigma = \left[\frac{\dot{M}(z)}{3\pi} - \frac{8\tan i_{\rm s}}{3(1+\tan^2 i_{\rm s})^{\frac{1}{2}}}\dot{m}\varpi_{\rm A}^2 f_\phi(\zeta)\right]\left[1 - \left(\frac{R}{\varpi_0}\right)^{\frac{1}{2}}\right]. \tag{14.91}$$

The density can be expressed in the separable form

$$\rho(\varpi_0, z) = \rho_{\rm c}(\varpi_0) f_\rho(\zeta), \tag{14.92}$$

with the central plane conditions

$$f_\rho(0) = 1, \quad f'_\rho(0) = 0. \tag{14.93}$$

Equations (14.24) for v_ϖ and (14.92) for ρ enable (14.83) to be written as

$$\dot{M}(z) = \frac{\dot{M}}{I_1}\int_0^\zeta f_\rho f_v d\zeta, \tag{14.94}$$

with

$$\dot{M} = -4\pi I_1 \varpi_0 \rho_{\rm c} v_{\varpi {\rm c}} h \tag{14.95}$$

and

$$I_1 = \int_0^1 f_\rho f_v d\zeta. \tag{14.96}$$

Equation (14.85) becomes

$$\Sigma(\varpi_0, z) = \frac{\Sigma_{\rm s}(\varpi_0)}{I_2}\int_0^\zeta f_\rho d\zeta \tag{14.97}$$

with

$$\Sigma_{\rm s} = 2 I_2 \rho_{\rm c} h \tag{14.98}$$

and

$$I_2 = \int_0^1 f_\rho d\zeta. \tag{14.99}$$

Using (14.97) for Σ/Σ_s in (14.91) for $\nu\Sigma$ leads to the vertically dependent disc angular momentum equation

$$\frac{1}{I_1}\frac{\dot{M}}{3\pi} f_\rho f_v - \frac{8\tan i_s}{3(1+\tan^2 i_s)^{\frac{1}{2}}}\dot{m}\varpi_A^2 f_\phi' = \frac{1}{I_2}\left[\frac{\dot{M}}{3\pi} - \frac{8\tan i_s}{3(1+\tan^2 i_s)^{\frac{1}{2}}}\dot{m}\varpi_A^2\right] f_\rho. \tag{14.100}$$

Applying this at $\zeta = 0$ gives

$$I_1\left[1 - \frac{8\pi\tan i_s}{(1+\tan^2 i_s)^{\frac{1}{2}}}\frac{\dot{m}\varpi_A^2}{\dot{M}}\right] = I_2\left[1 - \frac{8\pi\tan i_s}{(1+\tan^2 i_s)^{\frac{1}{2}}}\frac{\dot{m}\varpi_A^2}{\dot{M}} I_1 f_\phi'(0)\right]. \tag{14.101}$$

Employing this in (14.100) yields the vertical dependence of v_ϖ as

$$f_v(\zeta) = 1 - \frac{8\pi I_1\tan i_s}{(1+\tan^2 i_s)^{\frac{1}{2}}}\frac{\dot{m}\varpi_A^2}{\dot{M}}\left[f_\phi'(0) - \frac{f_\phi'(\zeta)}{f_\rho(\zeta)}\right], \tag{14.102}$$

with (14.32) and (14.36) for $f_\phi(\zeta)$ giving

$$f_\phi'(0) = \frac{KF}{Q}\left[1 - 2e^{3K/2}\cos\left(\frac{\sqrt{3}}{2}K + \frac{\pi}{3}\right)\right]. \tag{14.103}$$

Equation (14.102) gives the surface value of $f_v(\zeta)$ as

$$f_v(1) = 1 - \frac{8\pi I_1\tan i_s}{(1+\tan^2 i_s)^{\frac{1}{2}}}\frac{\dot{m}\varpi_A^2}{\dot{M}} f_\phi'(0), \tag{14.104}$$

since the force-free surface boundary condition gives $f_\phi'(1) = 0$.

For dynamo numbers having $K < \pi/\sqrt{3}$ the horizontal components B_ϖ and B_ϕ have magnitudes that increase monotonically from $z = 0$ to $z = h$. The poloidal components B_ϖ and B_z are positive at the disc surface, consistent with conditions for wind launching. This corresponds to the dynamo operating below its critical state and then $f_\phi'(0) > 0$ so (14.104) gives $f_v(1) < 1$. It will be found that $f_v(1)$ is well below unity, consistent with $f_v(\zeta)$ vanishing over a narrow region connecting the disc inflow to the wind outflow. It is noted from (14.102) that in the absence of magnetic wind angular momentum transport, and with ν independent of z,

$f_v(\zeta) = 1$, corresponding to $\partial v_\varpi/\partial z = 0$. Hence magnetic stresses lead to a decrease in $|v_\varpi|$ with increasing $|z|$, consistent with $|v_\varpi| \to 0$ just beyond $z = \pm h$ where the wind outflow begins.

14.4.4 The Disc Vertical Equilibrium

The vertical equilibrium in the disc is given by

$$\Omega_\kappa^2 z\rho + \frac{\partial}{\partial z}\left(P + \frac{B_\varpi^2 + B_\phi^2}{2\mu_0}\right) = 0, \tag{14.105}$$

which expresses the balance of the compressive force of stellar gravity and the magnetic pressure gradient against the expansion force due to the gas pressure gradient. The thermal pressure can be expressed as

$$P(\varpi_0, z) = P_c(\varpi_0) f_P(\zeta), \tag{14.106}$$

with the central plane conditions

$$f_P(0) = 1, \quad f_P'(0) = 0. \tag{14.107}$$

Integrating (14.105) from 0 to z and using (14.23), (14.40), (14.92) and (14.106) for B_ϕ, B_ϖ, ρ and P gives

$$P_c(f_P - 1) + \frac{B_{\phi s}^2}{2\mu_0}\left(\frac{N_\alpha^2}{K^6} f_\phi''^2 + f_\phi^2\right) + \Omega_\kappa^2 h^2 \rho_c \int_0^\zeta \zeta f_\rho d\zeta = 0. \tag{14.108}$$

This equation is separable if

$$P_c = A\frac{B_{\phi s}^2}{2\mu_0}, \tag{14.109}$$

where A is a constant. It then follows that

$$\frac{B_{\phi s}^2}{2\mu_0} = k_1 \Omega_\kappa^2 h^2 \rho_c, \tag{14.110}$$

and

$$A(f_P - 1) + \frac{N_\alpha^2}{K^6} f_\phi''^2 + f_\phi^2 = -\frac{1}{k_1}\int_0^\zeta \zeta f_\rho d\zeta, \tag{14.111}$$

where k_1 is a separation constant.

The gas equation of state is

$$P = \frac{\mathcal{R}}{\mu}\rho T \tag{14.112}$$

and T can be expressed as

$$T(\varpi_0, z) = T_{\rm c}(\varpi_0) f_T(\zeta), \tag{14.113}$$

with the central plane conditions

$$f_T(0) = 1, \quad f_T'(0) = 0. \tag{14.114}$$

It follows from (14.112) that

$$f_P = f_\rho f_T. \tag{14.115}$$

Using this in (14.111) and solving for f_T gives

$$f_T = \frac{1}{k_1 A f_\rho}\left[k_1 A - k_1\left(\frac{N_\alpha^2}{K^6} f_\phi''^2 + f_\phi^2\right) - \int_0^\zeta \zeta f_\rho d\zeta\right]. \tag{14.116}$$

The product $k_1 A$ can be found by noting that $P_{\rm c} = c_{\rm s}^2 \rho_{\rm c}$, so (14.109) and (14.110) yield

$$k_1 A = \frac{c_{\rm s}^2}{\Omega_{\rm K}^2 h^2} = \frac{9}{4}\frac{N_\alpha^4}{\epsilon^2 K^6}, \tag{14.117}$$

where the last result follows from the dynamo relation (14.39).

14.4.5 The Disc Thermal Equations

Since thermal advection due to the disc inflow is small, thermal equilibrium gives the divergence of the radiative flux as the sum of the viscous and magnetic dissipations, so

$$\frac{\partial F_{\rm R}}{\partial z} = \rho\nu(\varpi_0\Omega_{\rm K}')^2 + \frac{\eta}{\mu_0}\left(\frac{\partial B_\phi}{\partial z}\right)^2, \tag{14.118}$$

noting that the vertical derivative term dominates in $\nabla \cdot \mathbf{F}_{\rm R}$ and J_{ϖ}^2 makes the main contribution in the magnetic dissipation. Vertical integration from 0 to z leads to

$$F_{\rm R}(\varpi_0, z) = \frac{9}{8}\Omega_{\rm K}^2 \nu \Sigma + \frac{\eta B_{\phi \rm s}^2}{\mu_0 h} I_{\rm m}(\zeta), \tag{14.119}$$

where

$$I_{\rm m}(\zeta) = \int_0^{\zeta} y'^2 d\zeta, \tag{14.120}$$

with $y(\zeta)$ given by (14.36).

For an optically thick disc, the radiative transfer equation is

$$F_{\rm R} = -\frac{4\sigma_{\rm B}}{3\kappa\rho}\frac{\partial}{\partial z}\left(T^4\right). \tag{14.121}$$

Using (14.98) for $\Sigma_{\rm s}$ to eliminate $\rho_{\rm c} h$ in (14.110) for $B_{\phi \rm s}$, together with $\eta = \nu / N_{\rm p}$, gives

$$\frac{\eta B_{\phi \rm s}^2}{\mu_0 h} = \frac{k_1}{N_{\rm p} I_2}\Omega_{\rm K}^2 \nu \Sigma_{\rm s}. \tag{14.122}$$

Substituting this in (14.119), and using the integral expressions for Σ and $I_{\rm m}(\zeta)$, yields

$$F_{\rm R}(\varpi_0, z) = \frac{1}{I_2}\Omega_{\rm K}^2 \nu \Sigma \left[\frac{9}{8}\int_0^{\zeta} f_\rho d\zeta + \frac{k_1}{N_{\rm p}} I_{\rm m}(\zeta)\right]. \tag{14.123}$$

The opacity is taken to have a Kramers form

$$\kappa = \tilde{K}\rho T^{-\frac{7}{2}}, \tag{14.124}$$

where $\tilde{K}$ is a constant, so (14.121) becomes

$$F_{\rm R}(\varpi_0, z) = -\frac{32}{45}\frac{\sigma_{\rm B}}{\tilde{K}}\frac{T_{\rm c}^{\frac{15}{2}}}{\rho_{\rm c}^2 h}\frac{1}{f_\rho^2}\frac{d}{d\zeta}\left(f_T^{\frac{15}{2}}\right). \tag{14.125}$$

Equating this to the separable form (14.123) gives the radial and vertical thermal equations as

$$\frac{32}{45}\frac{\sigma_{\rm B}}{\tilde{K}}\frac{T_{\rm c}^{\frac{15}{2}}}{\rho_{\rm c}^2 h} = k_2 \Omega_{\rm K}^2 \nu \Sigma_{\rm s} \tag{14.126}$$

and

$$-\frac{k_2}{f_\rho^2}\frac{d}{d\zeta}\left(f_T^{\frac{15}{2}}\right)=\frac{9}{8}\int_0^\zeta f_\rho d\zeta+\frac{k_1}{N_\mathrm{p}}I_\mathrm{m}(\zeta), \tag{14.127}$$

where k_2 is a separation constant.

14.4.6 The Disc Radial Structure

The separated radial equations can be solved algebraically to obtain the radial structure of the disc. Firstly, the temperature $T_\mathrm{c}(\varpi_0)$ can be found by deriving two expressions for $\nu\Sigma_\mathrm{s}$ as functions of T_c. Using (14.79) for ν and (14.98) for Σ_s gives

$$\rho_\mathrm{c}h=\frac{N_\alpha}{\epsilon N_\mathrm{p}}\frac{\nu\Sigma_\mathrm{s}}{2I_2c_\mathrm{s}h}. \tag{14.128}$$

Substituting for this and using (14.16b) for c_s in the energy equation (14.126) yields

$$\nu\Sigma_\mathrm{s}=\frac{4}{3}I_2\left(\frac{6\sigma_\mathrm{B}}{5\tilde{K}}\frac{\mathcal{R}}{\mu}\right)^{\frac{1}{3}}\frac{\epsilon^{\frac{2}{3}}N_\mathrm{p}^{\frac{2}{3}}}{N_\alpha^{\frac{2}{3}}k_2^{\frac{1}{3}}}\frac{T_\mathrm{c}^{\frac{17}{6}}h}{\Omega_\mathrm{K}^{\frac{2}{3}}}. \tag{14.129}$$

Another expression for $\nu\Sigma_\mathrm{s}$ can be found by using (14.98) for Σ_s to eliminate $\rho_\mathrm{c}h$ in (14.95) for $\dot{M}$. Then employing (14.46) for $v_{\varpi\mathrm{c}}$ and (14.79) for ν leads to

$$\nu\Sigma_\mathrm{s}=\frac{N_\mathrm{p}}{2\pi}\frac{I_2}{I_1}\dot{M}I\tan i_\mathrm{s}\frac{h}{\varpi_0}. \tag{14.130}$$

Equating this to (14.129) then gives $T_\mathrm{c}(\varpi_0)$.

The disc height follows from (14.117) as

$$h=\frac{2}{3}\frac{\epsilon K^3}{N_\alpha^2}\left(\frac{\mathcal{R}}{\mu}\right)^{\frac{1}{2}}\frac{T_\mathrm{c}^{\frac{1}{2}}}{\Omega_\mathrm{K}}. \tag{14.131}$$

The density ρ can be found by using (14.130) to eliminate $\nu\Sigma_\mathrm{s}$ in (14.128) to give

$$\rho_\mathrm{c}=\frac{1}{4\pi}\left(\frac{\mu}{\mathcal{R}}\right)^{\frac{1}{2}}\frac{N_\alpha}{\epsilon}\frac{I}{I_1}\frac{\dot{M}\tan i_\mathrm{s}}{\varpi_0 T_\mathrm{c}^{\frac{1}{2}}h}. \tag{14.132}$$

The central inflow speed is given by (14.46) as

$$v_{\varpi\mathrm{c}}=-\left(\frac{\mathcal{R}}{\mu}\right)^{\frac{1}{2}}\frac{\epsilon}{N_\alpha}\frac{T_\mathrm{c}^{\frac{1}{2}}}{I\tan i_\mathrm{s}}. \tag{14.133}$$

This leaves the radial dependences of the magnetic field components to be found. Using (14.128) to eliminate $\rho_{\rm c}h$ in (14.110) for $B^2_{\phi{\rm s}}$, and then (14.79) for ν gives

$$B^2_{\phi{\rm s}} = \mu_0 \frac{k_1}{I_2}\frac{N_\alpha}{\epsilon N_{\rm p}}\frac{\Omega_{\rm K} h}{c_{\rm s}}\frac{\nu\Sigma_{\rm s}}{h}\Omega_{\rm K}. \tag{14.134}$$

The use of (14.39) for $\Omega_{\rm K}h/c_{\rm s}$ and (14.130) for $\nu\Sigma_{\rm s}/h$ then yields $B_{\phi{\rm s}}(\varpi_0)$. Equation (14.40) for B_ϖ, evaluated at $\zeta = 1$, gives

$$B_{\varpi{\rm s}}(\varpi_0) = \frac{N_\alpha}{K^3} f''_\phi(1) B_{\phi{\rm s}}(\varpi_0) \tag{14.135}$$

and (14.41) for $\tan i_{\rm s}$ gives

$$B_{z{\rm s}}(\varpi_0) = \tan i_{\rm s} B_{\varpi{\rm s}}(\varpi_0). \tag{14.136}$$

Normalizing the above disc solutions, using parameters typical for a white dwarf accretor, yields

$$T_{\rm c} = 7.2\times 10^3 \frac{N_\alpha^{\frac{4}{17}} N_{\rm p}^{\frac{2}{17}}}{\epsilon^{\frac{4}{17}}}\left(\frac{I}{I_1}\right)^{\frac{6}{17}} k_2^{\frac{2}{17}} M_1^{\frac{2}{17}} \dot{M}_{10}^{\frac{6}{17}} \frac{(\tan i_{\rm s})^{\frac{6}{17}}}{x^{\frac{12}{17}}}\,{\rm K}, \tag{14.137}$$

$$h = 5.8\times 10^5 \frac{\epsilon^{\frac{15}{17}} N_{\rm p}^{\frac{1}{17}}}{N_\alpha^{\frac{32}{17}}}\left(\frac{I}{I_1}\right)^{\frac{3}{17}} K^3 k_2^{\frac{1}{17}} \frac{\dot{M}_{10}^{\frac{3}{17}}}{M_1^{\frac{15}{34}}} (\tan i_{\rm s})^{\frac{3}{17}} x^{\frac{39}{34}}\,{\rm m}, \tag{14.138}$$

$$\rho_{\rm c} = 8.8\times 10^{-6} \frac{N_\alpha^{\frac{47}{17}}}{\epsilon^{\frac{30}{17}} N_{\rm p}^{\frac{2}{17}}}\left(\frac{I}{I_1}\right)^{\frac{11}{17}} \frac{M_1^{\frac{13}{34}} \dot{M}_{10}^{\frac{11}{17}}}{K^3 k_2^{\frac{2}{17}}} \frac{(\tan i_{\rm s})^{\frac{11}{17}}}{x^{\frac{61}{34}}}\,{\rm kg\,m^{-3}}, \tag{14.139}$$

$$v_{\varpi{\rm c}} = -10^4 \frac{\epsilon^{\frac{15}{17}} N_{\rm p}^{\frac{1}{17}}}{N_\alpha^{\frac{15}{17}}} \frac{k_2^{\frac{1}{17}}}{I^{\frac{14}{17}} I_1^{\frac{3}{17}}} \frac{M_1^{\frac{1}{17}} \dot{M}_{10}^{\frac{3}{17}}}{(\tan i_{\rm s})^{\frac{14}{17}}} \frac{1}{x^{\frac{6}{17}}}\,{\rm m\,s^{-1}}, \tag{14.140}$$

$$B_{\varpi{\rm s}} = 3.1\times 10^{-2} N_\alpha^{\frac{1}{2}}\left(\frac{I}{I_1}\right)^{\frac{1}{2}} \frac{k_1^{\frac{1}{2}}}{K^{\frac{3}{2}}} |f''_\phi(1)| M_1^{\frac{1}{4}} \dot{M}_{10}^{\frac{1}{2}} \frac{(\tan i_{\rm s})^{\frac{1}{2}}}{x^{\frac{5}{4}}}\,{\rm T}, \tag{14.141}$$

$$B_{\phi{\rm s}} = -3.1\times 10^{-2}\left(\frac{I}{I_1}\right)^{\frac{1}{2}} \frac{k_1^{\frac{1}{2}}}{N_\alpha^{\frac{1}{2}}} K^{\frac{3}{2}} M_1^{\frac{1}{4}} \dot{M}_{10}^{\frac{1}{2}} \frac{(\tan i_{\rm s})^{\frac{1}{2}}}{x^{\frac{5}{4}}}\,{\rm T}, \tag{14.142}$$

$$B_{z{\rm s}} = 3.1\times 10^{-2} N_\alpha^{\frac{1}{2}}\left(\frac{I}{I_1}\right)^{\frac{1}{2}} \frac{k_1^{\frac{1}{2}}}{K^{\frac{3}{2}}} |f''_\phi(1)| M_1^{\frac{1}{4}} \dot{M}_{10}^{\frac{1}{2}} \frac{(\tan i_{\rm s})^{\frac{3}{2}}}{x^{\frac{5}{4}}}\,{\rm T}, \tag{14.143}$$

where $M_1 = M/M_\odot$, $\dot{M}_{10} = \dot{M}/10^{-10}\,M_\odot{\rm year}^{-1}$ and $x = \varpi_0/10^8{\rm m}$.

An expression can be derived for $\tan i_{\rm s}$. Using (14.45) for $B_{\phi {\rm s}}/B_{z{\rm s}}$ and (14.143) for $B_{z{\rm s}}$ to eliminate $B_{\phi {\rm s}}B_{z{\rm s}}$ in the wind angular momentum equation (14.87) gives

$$\dot{m}\varpi_{\rm A}^2 = \frac{\dot{M}}{3\pi}\frac{I}{I_1}k_1|f_\phi''(1)|(1+\tan^2 i_{\rm s})^{\frac{1}{2}}\tan i_{\rm s}. \tag{14.144}$$

Using this to eliminate $\dot{m}\varpi_{\rm A}^2/\dot{M}$ in the vertical part of the disc angular momentum equation given by (14.101), leads to

$$\tan^2 i_{\rm s} = \frac{3}{8}\frac{1}{k_1|f_\phi''(1)|}\frac{(I_2-I_1)}{I[I_2 f_\phi'(0)-1]}. \tag{14.145}$$

14.4.7 The Disc Vertical Structure

The vertical structure of the disc can now be found. Equations can be derived for the vertical dependences of the density and temperature, given by $f_\rho(\zeta)$ and $f_T(\zeta)$. Differentiating the vertical equilibrium equation (14.116), using the toroidal dynamo equation (14.26) with $f_v(\zeta) \simeq 1$ to eliminate f_ϕ''', and the thermal equation (14.127) to eliminate f_T', gives

$$f_\rho' = -\frac{1}{k_1 A f_T}\left[2k_1\left\{f_\phi f_\phi' - \frac{N_\alpha^2}{K^3}(F+f_\phi)f_\phi''\right\} + \zeta f_\rho\right] + \frac{3}{20}\frac{1}{k_2}\frac{f_\rho^3}{f_T^{\frac{15}{2}}}\left[\int_0^\zeta f_\rho d\zeta + \frac{9}{8}\frac{k_1}{N_{\rm p}}I_{\rm m}(\zeta)\right], \tag{14.146}$$

with f_T given by (14.116) as

$$f_T = \frac{1}{k_1 A f_\rho}\left[k_1 A - k_1\left(\frac{N_\alpha^2}{K^6}f_\phi''^2 + f_\phi^2\right) - \int_0^\zeta \zeta f_\rho d\zeta\right]. \tag{14.147}$$

Equations (14.146) and (14.147) constitute a non-linear integro-differential equation for $f_\rho(\zeta)$. The solution can be used in (14.147) to determine $f_T(\zeta)$. Surface conditions must now be formulated and expressions found for the separation constants k_1 and k_2.

The disc surface is taken to be the photospheric base, consistent with connection to an optically thin isothermal wind along poloidal field-streamlines. Equating the density scale height to the photon mean free path at $z = h$ gives

$$-\frac{\rho_{\rm s}}{(\partial\rho/\partial z)_{\rm s}} = \frac{1}{(\kappa\rho)_{\rm s}}. \tag{14.148}$$

Using the Kramers opacity and the separable forms for ρ and T then yields

$$-\frac{f_\rho'(1)}{f_\rho(1)} = \frac{\bar{K}\rho_c^2 h}{T_c^{\frac{7}{2}}}\frac{f_\rho(1)^2}{f_T(1)^{\frac{7}{2}}}. \tag{14.149}$$

Taking the surface temperature as the effective temperature and then using (14.123) for the radiative flux at $z = h$, gives

$$\sigma_B T_c^4 f_T(1)^4 = \frac{9}{8}\Omega_K^2 \nu \Sigma_s \left[1 + \frac{8}{9}\frac{k_1 I_m(1)}{N_p I_2}\right]. \tag{14.150}$$

Using the thermal equation (14.126) to eliminate $\Omega_K^2 \nu \Sigma_s$ and employing the result in (14.149) gives

$$f_\rho'(1) = -\frac{4}{5}\frac{I_2}{k_2}\left[1 + \frac{8}{9}\frac{k_1 I_m(1)}{N_p I_2}\right]\frac{f_\rho(1)^3}{f_T(1)^{\frac{15}{2}}}. \tag{14.151}$$

Another expression for $f_\rho'(1)$ follows from (14.146) evaluated at $\zeta = 1$ as

$$\begin{aligned} f_\rho'(1) = &-\frac{1}{k_1 A f_T(1)}\left[2k_1 N_\alpha^2 I F(F+1) + f_\rho(1)\right] \\ &+ \frac{3}{20}\frac{I_2}{k_2}\left[1 + \frac{8}{9}\frac{k_1 I_m(1)}{N_p I_2}\right]\frac{f_\rho(1)^3}{f_T(1)^{\frac{15}{2}}}, \end{aligned} \tag{14.152}$$

where $f_\phi''(1) = -IK^3 F$ has been used from the dynamo equation (14.44). All the relevant solutions have $2k_1 N_\alpha^2 I F(F+1) \ll f_\rho(1)$ and hence this term can be dropped. Then equating (14.152) to (14.151) to eliminate $f_\rho'(1)$ gives

$$\frac{f_T(1)^{\frac{13}{2}}}{f_\rho(1)^2} = \frac{19}{20}\frac{I_2}{k_2}k_1 A\left[1 + \frac{8}{9}\frac{k_1 I_m(1)}{N_p I_2}\right]. \tag{14.153}$$

The vertical equilibrium equation (14.147) evaluated at $\zeta = 1$ gives

$$f_T(1) = \frac{1}{k_1 A f_\rho(1)}\left[k_1 A - k_1(N_\alpha^2 I^2 F^2 + 1) - I_3\right], \tag{14.154}$$

where

$$I_3 = \int_0^1 \zeta f_\rho d\zeta. \tag{14.155}$$

Equations (14.153) and (14.154) then yield the surface values

$$f_\rho(1) = \left(\frac{20k_2}{19I_2}\right)^{\frac{2}{17}} \frac{[k_1 A - k_1(N_\alpha^2 I^2 F^2 + 1) - I_3]^{\frac{13}{17}}}{(k_1 A)^{\frac{15}{17}}} \left[1 + \frac{8}{9}\frac{k_1 I_{\rm m}(1)}{N_{\rm p} I_2}\right]^{-\frac{2}{17}}, \tag{14.156}$$

$$f_T(1) = \left(\frac{19I_2}{20k_2}\right)^{\frac{2}{17}} \frac{[k_1 A - k_1(N_\alpha^2 I^2 F^2 + 1) - I_3]^{\frac{4}{17}}}{(k_1 A)^{\frac{2}{17}}} \left[1 + \frac{8}{9}\frac{k_1 I_{\rm m}(1)}{N_{\rm p} I_2}\right]^{\frac{2}{17}}. \tag{14.157}$$

This leaves the separation constants k_1 and k_2 to be determined. A first expression relating these constants can be found by using the solution for h in (14.130) for $\nu\Sigma_{\rm s}$ and then equating the resulting expression to (14.91) for $\nu\Sigma$ evaluated at $\zeta = 1$. Then using (14.144) and (14.145) to eliminate $\dot{m}\varpi_{\rm A}^2$ and $\tan i_{\rm s}$ leads to

$$k_1 = \frac{3}{8}\frac{Q_1^{\frac{17}{10}}}{|f_\phi''(1)|}\frac{(I_2 - I_1)}{I I_1^{\frac{3}{10}}}\frac{[I_2 f_\phi'(0) - 1]^{\frac{7}{10}}}{[I_1 f_\phi'(0) - 1]^{\frac{17}{10}}} k_2^{\frac{1}{10}}, \tag{14.158}$$

where

$$Q_1 = \left(\frac{3}{8\pi}\right)^{\frac{3}{17}} \left(\frac{5\bar{K}}{6\sigma_{\rm B}}\right)^{\frac{1}{17}} \left(\frac{\mathcal{R}}{\mu G}\right)^{\frac{15}{34}} \frac{\epsilon^{\frac{15}{17}} N_{\rm p}^{\frac{18}{17}}}{N_\alpha^{\frac{32}{17}}} I^{\frac{20}{17}} K^3 R^{\frac{5}{34}} \frac{\dot{M}^{\frac{3}{17}}}{M^{\frac{15}{34}}} \frac{(\varpi_0/R)^{\frac{5}{34}}}{[1 - (R/\varpi_0)^{\frac{1}{2}}]}. \tag{14.159}$$

The quantity Q_1 is weakly dependent on ϖ_0, except close to the stellar surface.

A second expression relating k_1 to k_2 is obtained by considering two expressions for $f_T(1)$ and equating them. Using the solution for h in (14.130) and substituting the resulting expression for $\nu\Sigma_{\rm s}$ in the surface flux expression (14.150), then solving for $T_{\rm c}$ and equating this to the disc solution for $T_{\rm c}$ yields

$$f_T(1) = Q_2 \frac{I_1^{\frac{1}{17}} I_2^{\frac{1}{4}}}{(\tan i_{\rm s})^{\frac{1}{17}}} \left[1 + \frac{8}{9}\frac{k_1 I_{\rm m}(1)}{N_{\rm p} I_2}\right]^{\frac{1}{4}} \frac{1}{k_2^{\frac{7}{68}}}, \tag{14.160}$$

where

$$Q_2 = \left(\frac{8\pi}{3}\right)^{\frac{1}{17}} \left(\frac{6}{5}\right)^{\frac{7}{68}} \frac{G^{\frac{3}{136}}}{\sigma_{\rm B}^{\frac{5}{34}} \bar{K}^{\frac{7}{68}}} \left(\frac{\mathcal{R}}{\mu}\right)^{\frac{31}{136}} \frac{\epsilon^{\frac{31}{68}} N_{\rm p}^{\frac{5}{34}}}{N_\alpha^{\frac{12}{17}}} \frac{K^{\frac{3}{4}}}{I^{\frac{1}{17}}} \frac{M^{\frac{3}{136}}}{\dot{M}^{\frac{1}{17}} R^{\frac{1}{136}}}. \tag{14.161}$$

Using (14.158) to eliminate k_1 in (14.145), employing the resulting expression for $\tan i_{\rm s}$ in (14.160) and equating the result for $f_T(1)$ to (14.157) leads to an

expression for k_2. This can be simplified by noting that all the relevant solutions have $k_1(N_\alpha^2 I^2 F^2 + 1) \ll k_1 A - I_3$ and $k_1 I_{\rm m}(1)/N_{\rm p} I_2 \ll 1$, corresponding to magnetic compression making a small contribution in the disc vertical equilibrium and magnetic dissipation being small relative to viscous dissipation. The reduced expression for k_2 and (14.158) for k_1 give the results

$$k_1 = 0.36 \frac{Q_1^{\frac{17}{12}}}{Q_2^{\frac{17}{3}}} \frac{(I_2 - I_1)}{I|f_\phi''(1)|} \frac{(k_1 A - I_3)^{\frac{4}{3}}}{(k_1 A)^{\frac{2}{3}} I_1^{\frac{7}{12}} I_2^{\frac{3}{4}}} \frac{[I_2 f_\phi'(0) - 1]^{\frac{5}{12}}}{[I_1 f_\phi'(0) - 1]^{\frac{17}{12}}}, \tag{14.162}$$

$$k_2 = 0.71 \frac{(k_1 A - I_3)^{\frac{40}{3}}}{Q_1^{\frac{17}{6}} Q_2^{\frac{170}{3}} (k_1 A)^{\frac{20}{3}} I_1^{\frac{17}{6}} I_2^{\frac{15}{2}}} \left[\frac{I_1 f_\phi'(0) - 1}{I_2 f_\phi'(0) - 1} \right]^{\frac{17}{6}}. \tag{14.163}$$

The vertical structure solutions can now be found. Equations (14.146) and (14.147) form a non-linear integro-differential equation for $f_\rho(\zeta)$, with the constants depending on the integrals I_1, I_2 and I_3. Initial guesses are made for the values of these integrals and an improved Euler method is used to solve for $f_\rho(\zeta)$. Taylor expansions near $\zeta = 0$ yield

$$f_\rho \sim 1 - \frac{1}{2} \left[\frac{1}{k_1 A} - \frac{3}{20} \frac{1}{k_2} + 2 k_1 f_\phi'(0)^2 \left(\frac{1}{k_1 A} + \frac{N_\alpha^2 F^2}{k_1 A f_\phi'(0)^2} - \frac{1}{15 k_2 N_{\rm p}} \right) \right] \zeta^2, \tag{14.164}$$

$$f_T \sim 1 - \frac{1}{5 k_2} \left[\frac{3}{8} + \frac{1}{3} \frac{k_1^2}{N_{\rm p}} f_\phi'(0)^2 \right] \zeta^2. \tag{14.165}$$

The solution for $f_\rho(\zeta)$ is used in (14.147) to obtain $f_T(\zeta)$.

The vertical dependence of the inflow speed can be determined by eliminating $\dot{m} \varpi_{\rm A}^2 / \dot{M}$ by using (14.144) in (14.102), yielding

$$f_v(\zeta) = 1 - \frac{8}{3} I |f_\phi''(1)| k_1 \tan^2 i_{\rm s} \left[f_\phi'(0) - \frac{f_\phi'(\zeta)}{f_\rho(\zeta)} \right] \tag{14.166}$$

with $\tan i_{\rm s}$ given by (14.145). The functions $f_\rho(\zeta)$ and $f_v(\zeta)$ are then used to evaluate I_1, I_2 and I_3 numerically and the results are compared with the values previously used. Suitable adjustments are made to the values of the integrals to be used and the procedure is repeated until good agreement is found. The solutions shown here are for the typical turbulent parameters $\epsilon = 0.1$, $N_\alpha = 0.22$ and $N_{\rm p} = 9$. Figures 14.4, 14.5, and 14.6 show the vertical structure functions f_ρ, f_T and f_v. The function $f_v(\zeta)$ is not far below unity for $\zeta < 0.8$, so justifying using $f_v \simeq 1$ in the induction equation. There is a rapid decrease in f_v near $\zeta = 1$, consistent with v_ϖ passing through zero just beyond $z = h$ where the wind outflow begins.

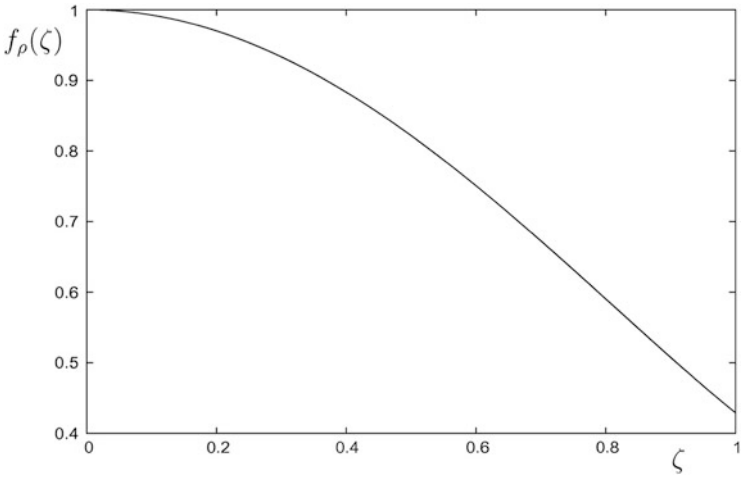

Fig. 14.4 The vertical variation of the disc density (from Campbell 2005)

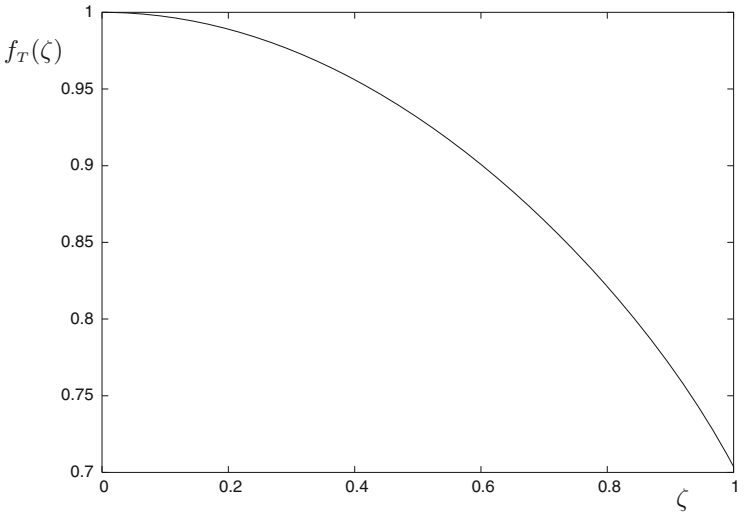

Fig. 14.5 The vertical variation of the disc temperature (from Campbell 2005)

Using a range of the turbulence parameters ϵ and N_α gives solutions of the same qualitative nature for the vertical dependence of the disc magnetic field, the disc structure and the inflow speed. Table 14.1 shows the essential results for the above case of turbulence parameters. The magnetic wind makes a major contribution to driving the inflow, with the Alfvén surface lying well above the disc. This results from only a small wind mass loss from the main body of the disc. The optical depth through the disc is large, so justifying the use of the radiative diffusion equation.

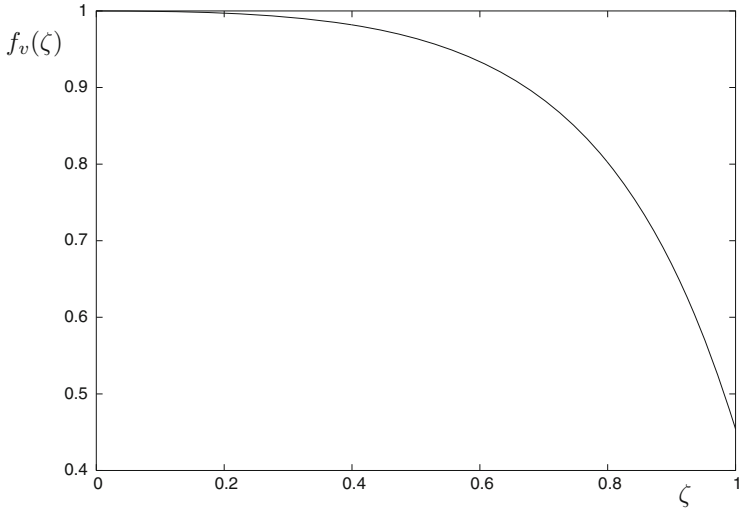

Fig. 14.6 The vertical variation of the disc inflow speed (from Campbell 2005)

Table 14.1 Disc and wind quantities for $\epsilon = 0.1$, $N_\alpha = 0.22$ and $N_p = 9$ (from Campbell 2005)

$f_\rho(1)$	$f_T(1)$	$f_v(1)$	i_s	$T_\mathrm{m}/T_\mathrm{v}$	$\varpi_\mathrm{A}/\varpi_0$	$4\pi\varpi_0^2\dot{m}/\dot{M}$	$\lvert B_{\phi\mathrm{s}}/B_{z\mathrm{s}}\rvert$
0.43	0.70	0.45	58.0°	1.04	3.09	3.14×10^{-2}	0.91
$B_{\phi\mathrm{s}}^2/2\mu_0 P_\mathrm{c}$	τ_D	I_1	I_2	I_3	k_1	k_2	$\lvert v_{\varpi\mathrm{c}}\rvert/c_\mathrm{s}$
3.43×10^{-2}	10.39	0.73	0.79	0.38	1.81×10^{-2}	0.27	0.53

The central inflow speed is significantly above purely viscously driven values, but still well subsonic. This gives sufficient poloidal field bending for wind launching.

14.4.8 Disc-Wind Coupling

The sonic point in the wind flow is determined by the condition $\mathbf{B}_\mathrm{p} \cdot \nabla\psi = 0$, with ψ given by (14.6) and the field line equation by (14.76). Two solutions result as

$$z_\mathrm{sn} = \frac{3}{(3 - \tan^2 i_\mathrm{s})} h \tag{14.167a}$$

and

$$z_\mathrm{sn} = \frac{2}{3} \frac{\tan i_\mathrm{s}(\tan^2 i_\mathrm{s} - 3)}{(\tan^2 i_\mathrm{s} + 4)} \varpi_\mathrm{s}. \tag{14.167b}$$

The first solution replaces the $z = 0$ solution, given by (14.10a), when a non-vanishing value of h is allowed for. The second solution is the same as (14.10b), but with ϖ_s replacing ϖ_0. The solution (14.167a) is valid for $i_s < 60°$, while the solution (14.167b) applies when $i_s > 60°$. Cases are considered here for which the first branch solution is valid, since this leads to disc winds with suitable mass fluxes.

The conservation of energy integral gives

$$H(\varpi, \rho) = \frac{1}{2}v_p^2 + \psi + a^2 \ln \rho. \tag{14.168}$$

Using $H(\varpi_s, \rho_s) = H(\varpi_{sn}, \rho_{sn})$ then gives the density at the sonic point in terms of its value at the disc surface as

$$\rho_{sn} = \rho_s \exp\left[-\left\{\frac{(\psi_{sn} - \psi_s)}{a^2} + \frac{1}{2}\right\}\right]. \tag{14.169}$$

Expansion of $(\psi_{sn} - \psi_s)$, to leading order, along a field-streamline gives

$$\rho_{sn} = \rho_s \exp\left[-\left\{\frac{\Omega_{Ks}^2 h^2}{2a^2}\frac{\tan^2 i_s}{(3 - \tan^2 i_s)} + \frac{1}{2}\right\}\right]. \tag{14.170}$$

The mass flux through the sonic point is

$$\dot{m} = \rho_{sn} a. \tag{14.171}$$

The Alfvén point cylindrical coordinate ϖ_A can be found from the wind angular momentum equation (14.144) as

$$\varpi_A^2 = \frac{I k_1}{3\pi I_1}|f_\phi''(1)|\frac{\dot{M}}{\dot{m}}(1 + \tan^2 i_s)^{\frac{1}{2}} \tan i_s. \tag{14.172}$$

These connections indicate that, for a magnetic field generated in the disc by a dynamo, the wind structure adjusts to the conditions set by the disc in terms of $\dot{m}$ and the surface magnetic field. This property was also shown in the simulations of disc magnetic winds, with a dynamo generated field, performed by von Rekowski et al. (2003).

14.5 Enhanced Mass Loss Near the Star

Through most of the disc the mass loss via the wind is small, so the mass transfer rate can be taken to be conserved at the source value $\dot{M}$ fed by the accretion stream at the outer edge of the disc. The field inclination i_s, which affects the position of the sonic point and hence $\dot{m}$, is constant to high accuracy through most of the disc. However,

it was shown in Campbell (2010) that the boundary condition near the stellar surface $\varpi_0 = R$ has an influence on i_s in a small inner region of the disc. For accretion to occur, the star must be rotating at a sub-Keplerian rate at $\varpi_0 = R$ and hence the disc angular velocity must decrease through a boundary layer of width $\delta \ll R$ to the stellar value Ω_*. An ansatz form representing this behaviour is given by

$$\Omega(\varpi_0) = \Omega_\kappa(R)\left[\left(\frac{R}{\varpi_0}\right)^{\frac{3}{2}} - (1-\xi)\left(\frac{R}{\varpi_0}\right)^{\frac{3}{2(1-\xi)}}\right], \tag{14.173}$$

where

$$\xi = \frac{\Omega_*}{\Omega_\kappa(R)}. \tag{14.174}$$

This form satisfies the conditions

$$\Omega(R) = \Omega_* \quad \text{and} \quad \Omega'(R) = 0, \tag{14.175}$$

and has boundary layer behaviour for $0.6 \lesssim \xi < 1$. Using this in the vertically integrated disc angular momentum equation leads to a modified form of $\nu\Sigma_s$ given by

$$\begin{aligned}\nu\Sigma_s = \frac{\dot{M}}{3\pi}\Bigg\{&\frac{1}{F_2}\left[1 - \frac{8}{3}\frac{(1-\xi)}{(1-4\xi)}\frac{I|f_\phi''(1)|}{I_1 F_1}k_1\tan^2 i_s\right]\left[F_1 - \xi\left(\frac{R}{\varpi_0}\right)^{\frac{1}{2}}\right]\\ &+\frac{8\xi}{(1-4\xi)}\frac{I|f_\phi''(1)|}{I_1 F_1 F_2}k_1\tan^2 i_s\left[1-\left(\frac{R}{\varpi_0}\right)^{\frac{1}{2}}\right]\Bigg\},\end{aligned} \tag{14.176}$$

where

$$F_1 = 1 - (1-\xi)\left(\frac{R}{\varpi_0}\right)^{\frac{3\xi}{2(1-\xi)}} \tag{14.177a}$$

and

$$F_2 = 1 - \left(\frac{R}{\varpi_0}\right)^{\frac{3\xi}{2(1-\xi)}}. \tag{14.177b}$$

Equating (14.176) to (14.130) for $\nu\Sigma_s$ yields

$$\tan^2 i_s + \frac{9}{16}\frac{(1-4\xi)}{(1-\xi)}\frac{N_p I_2}{k_1|f_\phi''(1)|}\frac{h}{\varpi_0}\frac{F_1 F_2}{F_3}\tan i_s$$

$$-\frac{3}{8}\frac{(1-4\xi)}{(1-\xi)}\frac{I_1}{k_1 I|f_\phi''(1)|}\frac{F_1}{F_3}\left[F_1 - \xi\left(\frac{R}{\varpi_0}\right)^{\frac{1}{2}}\right] = 0, \tag{14.178}$$

where

$$F_3 = F_1 - \xi\left(\frac{R}{\varpi_0}\right)^{\frac{1}{2}} - \frac{3\xi}{(1-\xi)}\left[1 - \left(\frac{R}{\varpi_0}\right)^{\frac{1}{2}}\right]. \tag{14.179}$$

The modified form of gravitational-centrifugal effective potential in the wind region, corresponding to Ω being given by (14.173), is

$$\psi = -\frac{GM}{\varpi_s}\left[\left(\frac{\varpi^2}{\varpi_s^2} + \frac{z}{\varpi_s^2}\right)^{-\frac{1}{2}} + \frac{1}{2}(1-\beta)^2\frac{\varpi^2}{\varpi_s^2}\right], \tag{14.180}$$

with

$$\beta = (1-\xi)\left(\frac{R}{\varpi_s}\right)^{\frac{3\xi}{2(1-\xi)}}. \tag{14.181}$$

Application of the sonic point condition $\mathbf{B}_p \cdot \nabla\psi = 0$, using (14.76) for the field line equation, yields the sonic point coordinates as

$$\varpi_{sn} = \left[1 + \frac{2\beta}{(3-\tan^2 i_s)}\right]\varpi_s + \frac{\tan i_s}{(3-\tan^2 i_s)}h, \tag{14.182}$$

$$z_{sn} = \frac{2\beta\tan i_s}{(3-\tan^2 i_s)}\varpi_s + \frac{3}{(3-\tan^2 i_s)}h. \tag{14.183}$$

It is noted that, since the star will have been spun up by accretion, relevant values of ξ will be nearer to 1 than to 0 and then the deviation of Ω from Ω_K is only significant in a region close to the stellar surface (i.e. $\varpi_0 \lesssim 3R$). Hence the modified equations for $\tan i_s$ and the sonic point coordinates are only applicable in this inner region of the disc. The remainder of the disc has its previously derived structure, with constant i_s and a small wind mass loss. This main region of the disc is essentially decoupled from the conditions at the stellar surface, and hence from the stellar rotation rate.

The quadratic equation (14.178) can be solved for $\tan i_s$ and the resulting variation with ϖ_0 is shown in Fig. 14.7, for $\xi = 0.95$. A sharp decrease in $\tan i_s$ occurs near $\varpi_0 = R$. Figure 14.8 illustrates that $\nu\Sigma_s$, and hence $\eta\Sigma_s$, decreases as the stellar surface is approached. This results in increased poloidal field bending, which lowers the sonic point. Conversely, the reduction in Ω to below Ω_K values

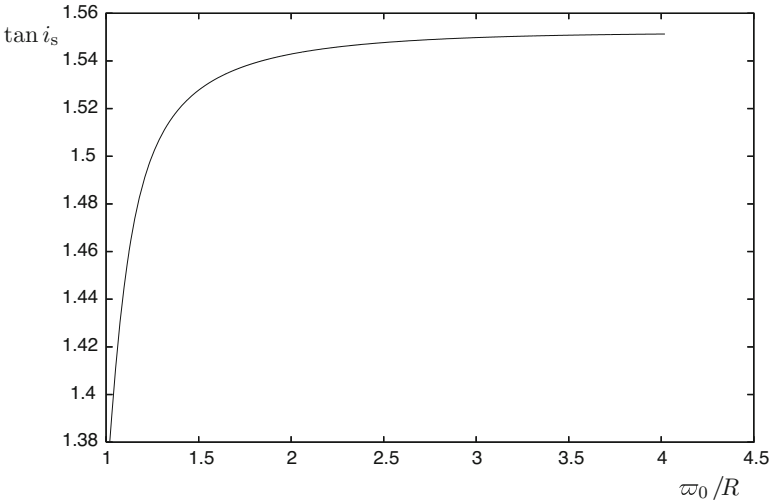

Fig. 14.7 The variation of magnetic poloidal field bending for modified Ω (from Campbell (2010))

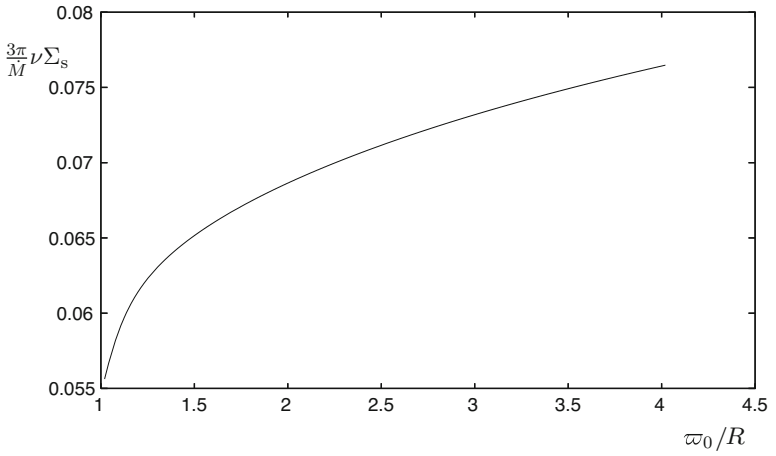

Fig. 14.8 The variation of $(3\pi/\dot{M})\nu\Sigma_s$ for modified Ω (from Campbell 2010)

reduces the centrifugal force felt along the field lines which raises the sonic point via the β terms in (14.182) and (14.183). These competing effects result in a lowering of the sonic point, and a consequent increase in $\dot{m}$, over a narrow region which is typically inside $\varpi = 3R$. In this region conservation of mass gives

$$\frac{d\dot{M}}{d\varpi_0} = 4\pi\varpi_0\rho_s v_{zs} = 4\pi\varpi_0\dot{m}\sin i_s. \tag{14.184}$$

The ratio of the wind mass loss rate $\dot{M}_{\rm w}$ to the source accretion rate $\dot{M} = \dot{M}(\varpi_{\rm D})$, where $\varpi_{\rm D}$ is the disc radius, is

$$\frac{\dot{M}_{\rm w}}{\dot{M}} = \frac{\dot{M} - \dot{M}(\varpi_0)}{\dot{M}} = \frac{4\pi}{\dot{M}} \int_{\varpi_0}^{\varpi_{\rm D}} \varpi_0 \rho_{\rm sn} a \sin i_{\rm s} d\varpi_0. \tag{14.185}$$

Calculating $\rho_{\rm sn}$ from (14.170), using the modified forms of ψ and the sonic point coordinates, leads to

$$\frac{\dot{M}_{\rm w}}{\dot{M}} = \frac{I N_{\rm p}}{\epsilon \bar{C} I_1} f_T(1)^{\frac{1}{2}} f_\rho(1) \times \int_x^{x_{\rm D}} \frac{1}{x^{\frac{39}{34}}} \frac{\tan^2 i_{\rm s}}{(1+\tan^2 i_{\rm s})^{\frac{1}{2}}} \exp\left\{ -\left[\frac{\Omega_\kappa^2 h^2}{2c_{\rm s}^2} \frac{F_4^2}{f_T(1)} \frac{\tan^2 i_{\rm s}}{(3-\tan^2 i_{\rm s})} + \frac{1}{2} \right] \right\} dx, \tag{14.186}$$

with

$$F_4 = 1 + \frac{2(1-\xi)}{\tan i_{\rm s}} \frac{\varpi_0}{h} \left(\frac{R}{\varpi_0} \right)^{\frac{3\xi}{2(1-\xi)}}, \tag{14.187}$$

and the integral is evaluated numerically. Figure 14.9 shows the variation of the integrand in (14.186), illustrating that the enhanced wind mass loss rate occurs over

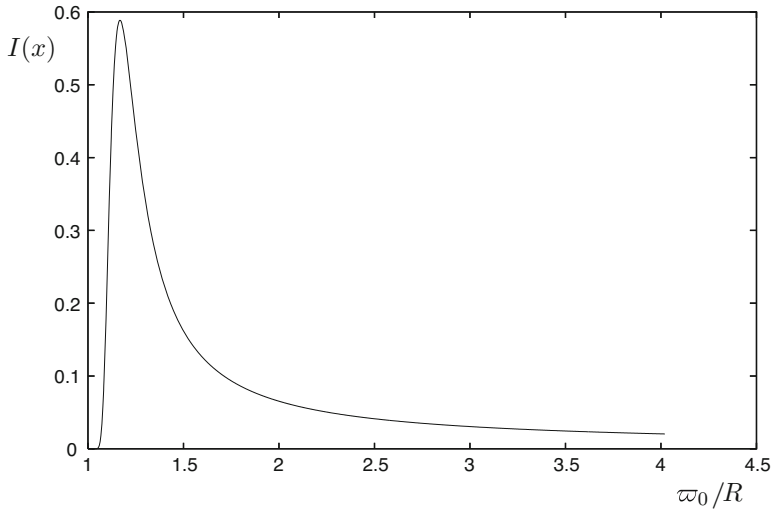

Fig. 14.9 The variation of the integrand in the $\dot{M}_{\rm w}/\dot{M}$ integral for modified Ω (from Campbell (2010))

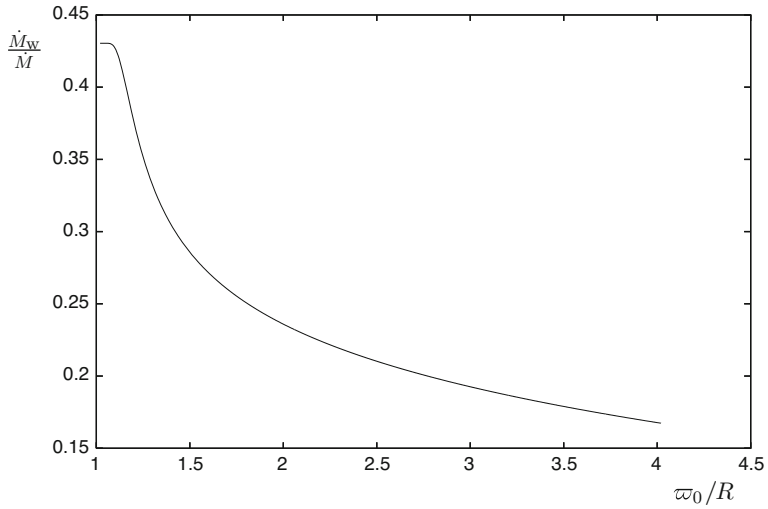

Fig. 14.10 The variation of the wind mass loss rate to the accretion rate for modified Ω (from Campbell (2010))

a narrow region in the inner part of the disc that is influenced by the stellar rotation rate. Figure 14.10 shows the ratio $\dot{M}_w/\dot{M}$, illustrating that a significant amount of mass can be lost in this narrow region of enhanced wind flow.

14.6 Wind Flow Stability

14.6.1 Poloidal Field Bending Effects

Having established that steady solutions can be found for magnetically channelled wind flows from accretion discs, the issue of stability must be investigated. A simple analysis of the purely magnetic case, ignoring viscosity, was made by Lubow et al. (1994). The disc structure was not calculated, but the basic conservation equations were employed. The vertically integrated disc angular momentum equation and a simplified wind angular momentum equation, assuming corotation out to the Alfvén point, were combined. A power law, self-similar form was used relating the poloidal magnetic field at the Alfvén point to that at the wind base by

$$B_{pA} = B_z(\varpi_0)\left(\frac{\varpi_0}{\varpi_A}\right)^n, \tag{14.188}$$

with $n > 1$, together with $v_{\rm A} \simeq \varpi_{\rm A}\Omega_{\rm K}(\varpi_0)$. Then combining the angular momentum equations and using the conservation of $\rho v_{\rm p}/B_{\rm p}$ along $\mathbf{B}_{\rm p}$ yields

$$\dot{m} = \rho_{\rm c} c_{\rm s} \frac{h}{\varpi_0} \left(\frac{c_{\rm s}}{v_{z\rm A}}\right)^{\frac{4}{n-1}} \left(\frac{|v_{\varpi \rm c}|}{c_{\rm s}}\right)^{\frac{n+1}{n-1}} . \tag{14.189}$$

This represents the wind mass flux causing the disc inflow via angular momentum extraction.

Assuming an isothermal vertical structure and a parabolic field line leads to

$$\dot{m} = \rho_{\rm c} c_{\rm s} e^{-\frac{1}{6}\tan^2 i_{\rm s}} . \tag{14.190}$$

This is the wind mass loss rate due to the flow of photospheric material along sufficiently inclined poloidal magnetic field lines which have been bent by the advective effect of the inflow. The authors analyse the stability by considering plots of the two forms of $\dot{m}/\rho_{\rm c} c_{\rm s}$, with the intersection of the curves giving solutions. They note that a small increase in $|v_{\varpi \rm c}|$ leads to a higher value of $\dot{m}$, via the curve of (14.190), than is required to maintain the increase in $|v_{\varpi \rm c}|$, via the curve of (14.189). The increase in $\dot{m}$ causes an increase in the extraction of disc angular momentum by the wind, leading to a further increase in $|v_{\varpi \rm c}|$. Hence instability results.

The field bending instability can also be demonstrated by relating the perturbations in $i_{\rm s}$ and $\dot{m}$ to the perturbation in $|v_{\varpi \rm c}|$. Equating (14.189) to (14.190) and taking perturbations gives

$$\delta i_{\rm s} = -\frac{6\cos^2(i_{\rm s})_{\rm sd}}{(n-1)\tan(i_{\rm s})_{\rm sd}} \frac{\delta|v_{\varpi \rm c}|}{|v_{\varpi \rm c}|_{\rm sd}} \tag{14.191}$$

and

$$\delta\dot{m} = \frac{2\dot{m}_{\rm sd}}{(n-1)} \frac{\delta|v_{\varpi \rm c}|}{|v_{\varpi \rm c}|_{\rm sd}}, \tag{14.192}$$

where the subscript sd refers to steady state quantities. It follows that $\delta|v_{\varpi \rm c}| > 0$ gives $\delta i_{\rm s} < 0$ and $\delta\dot{m} > 0$. So a small increase in $|v_{\varpi \rm c}|$ causes an increase in poloidal field bending and an increase in the wind mass flux, corresponding to instability.

The model is greatly simplified. It assumes an isothermal vertical structure and does not allow for a perturbation in η or in $v_{z\rm A}$, which would result from changes in the disc structure. Also, realistic discs will have a finite viscosity. Nevertheless, the model illustrates that an increase in $|v_{\varpi \rm c}|$ can have a de-stabilizing effect and this will be shown to have relevance to a more detailed analysis which allows for perturbation of the disc structure and coupling to the wind.

Cao and Spruit (2002) considered an inviscid disc threaded by a poloidal magnetic field. The B_z component was arbitrary, and the ratio $B_{\phi \rm s}/B_{z\rm s}$ was related to the radial momentum balance. The wind magnetic torque was incorporated, and the magnetic diffusivity was included in the poloidal component of the induction

equation. A short wavelength WKB perturbation analysis was performed. The cases of large magnetic torque exhibited the poloidal field bending instability, but this could be quenched for the weaker torque cases.

14.6.2 Perturbation of Magneto-Viscous Discs

The disc-wind solution of Sect. 14.4 allows a detailed investigation of stability using perturbation theory. This analysis is based on the work of Campbell (2001, 2005 and 2014).

Vertical integration of the time-dependent continuity equation gives

$$\frac{\partial \Sigma_{\rm s}}{\partial t} = -\frac{I_1}{I_2}\frac{1}{\varpi_0}\frac{\partial}{\partial \varpi_0}\left(\varpi_0 \Sigma_{\rm s} v_{\varpi {\rm c}}\right), \tag{14.193}$$

where the vertical integrals I_1 and I_2 are given by (14.96) and (14.99). The dynamical, thermal and magnetic time-scales are all much shorter than the disc angular momentum adjustment time-scale $\tau_{\rm am}$. Hence quantities such as $B_{\phi {\rm s}} B_{z {\rm s}}$ will evolve quasi-steadily on the time-scale $\tau_{\rm am}$, so explicit time derivatives can be ignored in all the time-dependent equations except the continuity equation. Vertical integration of the disc angular momentum equation yields

$$v_{\varpi {\rm c}}(\varpi_0, t) = -\frac{3I_2}{I_1 \varpi_0^2 \Omega_{\rm K} \Sigma_{\rm s}}\frac{\partial}{\partial \varpi_0}(\varpi_0^2 \Omega_{\rm K} \mu_{\rm s}) + \frac{4I_2}{\mu_0 I_1}\frac{B_{\phi {\rm s}} B_{z {\rm s}}}{\Omega_{\rm K} \Sigma_{\rm s}}, \tag{14.194}$$

where

$$\mu_{\rm s} = \nu \Sigma_{\rm s}. \tag{14.195}$$

The magnetic stress term can be expressed in terms of $\mu_{\rm s}$ and $v_{\varpi {\rm c}}$. Equation (14.45) gives

$$B_{\phi {\rm s}} B_{z {\rm s}} = \frac{N_\alpha}{K^3} f_\phi''(1) \tan i_{\rm s} B_{\phi {\rm s}}^2. \tag{14.196}$$

Using (14.41), (14.43), (14.98) and (14.110) to eliminate $\tan i_{\rm s}$ and $B_{\phi {\rm s}}^2$ yields

$$\frac{1}{\mu_0} B_{\phi {\rm s}} B_{z {\rm s}} = \frac{N_\alpha}{N_{\rm p}} \frac{|f_\phi''(1)|}{K^3 I}\frac{k_1}{I_2}\Omega_{\rm K}^2 \frac{\mu_{\rm s}}{v_{\varpi {\rm c}}}. \tag{14.197}$$

Substituting this in (14.194) gives

$$v_{\varpi {\rm c}} = -\frac{3I_2}{I_1 \varpi_0^2 \Omega_{\rm K} \Sigma_{\rm s}}\frac{\partial}{\partial \varpi_0}(\varpi_0^2 \Omega_{\rm K} \mu_{\rm s}) + S\frac{k_1 \Omega_{\rm K} \mu_{\rm s}}{v_{\varpi {\rm c}} \Sigma_{\rm s}}, \tag{14.198}$$

where

$$S = 4\frac{4N_\alpha}{I_1 N_\mathrm{p}}\frac{|f_\phi''(1)|}{K^3 I}. \tag{14.199}$$

Equations (14.193) and (14.198) give the mass conservation equation, incorporating the inflow speed driven by viscous and magnetic angular momentum transfer.

Using (14.79) for ν and (14.117) for $c_\mathrm{s}/\Omega_\mathrm{K} h$ to express h and T_c in terms of μ_s, then using this in the thermal equation (14.126) leads to

$$\mu_\mathrm{s} = \bar{C}\varpi^{\frac{15}{14}} k_2^{\frac{1}{7}} \Sigma_\mathrm{s}^{\frac{10}{7}}, \tag{14.200}$$

where $\bar{C}$ is a constant. The separation constants k_1 and k_2, given by (14.162) and (14.163), depend on $\dot{M}$ via Q_1 and Q_2. Using the result

$$\dot{M} = 2\pi\frac{I_1}{I_2}\varpi_0 |v_{\varpi\mathrm{c}}|\Sigma_\mathrm{s} \tag{14.201}$$

in these expressions gives

$$k_1 = C_1 \varpi_0^{\frac{7}{12}} |v_{\varpi\mathrm{c}}|^{\frac{7}{12}} \Sigma_\mathrm{s}^{\frac{7}{12}}, \tag{14.202}$$

$$k_2 = C_2 \varpi_0^{\frac{17}{6}} |v_{\varpi\mathrm{c}}|^{\frac{17}{6}} \Sigma_\mathrm{s}^{\frac{17}{6}}, \tag{14.203}$$

where C_1 and C_2 are constants. Employing these expressions to eliminate k_1 in (14.198) and k_2 in (14.200) gives

$$|v_{\varpi\mathrm{c}}| = \frac{3I_2}{I_1 \varpi_0^2 \Omega_\mathrm{K}\Sigma_\mathrm{s}}\frac{\partial}{\partial\varpi_0}\left(\varpi_0^2\Omega_\mathrm{K}\mu_\mathrm{s}\right) + \tilde{S}\frac{\varpi_0^{\frac{7}{12}}\Omega_\mathrm{K}\mu_\mathrm{s}}{|v_{\varpi\mathrm{c}}|^{\frac{5}{12}}\Sigma_\mathrm{s}^{\frac{5}{12}}}, \tag{14.204}$$

with

$$\mu_\mathrm{s} = \tilde{C}\varpi_0^{\frac{31}{21}} |v_{\varpi\mathrm{c}}|^{\frac{17}{42}} \Sigma_\mathrm{s}^{\frac{11}{6}}, \tag{14.205}$$

where $\tilde{S}$ and $\tilde{C}$ are constants. The incorporation of k_1 and k_2 allows for the effects of perturbations to the coupling between the radial and vertical structures of the disc to be accounted for.

Taking Eulerian perturbations of the continuity equation (14.193) gives

$$\frac{\partial}{\partial t}\left(\delta\Sigma_\mathrm{s}\right) = \frac{I_1}{I_2}\frac{1}{\varpi_0}\frac{\partial}{\partial\varpi_0}\left(\varpi_0\left[\left((\Sigma_\mathrm{s})_\mathrm{sd}\,\delta|v_{\varpi\mathrm{c}}| + |v_{\varpi\mathrm{c}}|_\mathrm{sd}\delta\Sigma_\mathrm{s}\right]\right). \tag{14.206}$$

Taking perturbation of (14.204) and (14.205) leads to

$$\delta|v_{\varpi c}| = -\frac{7}{10}\left(1-\frac{29}{12}U\right)\left(1+\frac{7}{10}U\right)^{-1}\frac{|v_{\varpi c}|_{sd}}{(\mu_s)_{sd}}\delta\mu_s + \frac{77}{20}\left(1+\frac{7}{10}U\right)^{-1}\frac{I_2}{I_1\varpi_0^2\Omega_K(\Sigma_s)_{sd}}\frac{\partial}{\partial\varpi_0}\left(\varpi_0^2\Omega_K\delta\mu_s\right), \tag{14.207}$$

and

$$\delta\Sigma_s = \frac{7}{10}\left(1+\frac{1}{84}U\right)\left(1+\frac{7}{10}U\right)^{-1}\frac{(\Sigma_s)_{sd}}{(\mu_s)_{sd}}\delta\mu_s - \frac{17}{20}\left(1+\frac{7}{10}U\right)^{-1}\frac{I_2}{I_1\varpi_0^2\Omega_K|v_{\varpi c}|_{sd}}\frac{\partial}{\partial\varpi_0}\left(\varpi_0^2\Omega_K\delta\mu_s\right), \tag{14.208}$$

where

$$U = \frac{\tilde{S}\varpi_0^{\frac{7}{12}}\Omega_K(\mu_s)_{sd}}{|v_{\varpi c}|_{sd}^{\frac{17}{12}}(\Sigma_s)_{sd}^{\frac{5}{12}}}. \tag{14.209}$$

It can be shown that

$$U = \frac{(T_m/T_v)_{sd}}{1+(T_m/T_v)_{sd}}, \tag{14.210}$$

where T_m and T_v are the magnetic and viscous torques per unit radial length. The ratio $(T_m/T_v)_{sd}$ is constant through the main body of the disc, so U is constant and it has the range $0 < U < 1$.

Using (14.207) and (14.208) to eliminate $\delta|v_{\varpi c}|$ and $\delta\Sigma_s$ in (14.206) leads to

$$\frac{7}{10}\frac{\partial}{\partial t}(\delta\mu_s) - \frac{17}{40}\frac{I_2}{I_1}\frac{\nu_{sd}}{\varpi_0|v_{\varpi c}|_{sd}}\frac{\partial}{\partial t}(\delta\mu_s) - \frac{17}{20}\frac{I_2}{I_1}\frac{\nu_{sd}}{\varpi_0|v_{\varpi c}|_{sd}}\varpi_0\frac{\partial}{\partial\varpi_0}\left(\frac{\partial}{\partial t}(\delta\mu_s)\right) = \frac{\nu_{sd}}{\varpi_0}\frac{\partial}{\partial\varpi_0}\left(\frac{17}{10}\frac{I_1}{I_2}\frac{\varpi_0|v_{\varpi c}|_{sd}}{\nu_{sd}}U\delta\mu_s + \frac{3}{\varpi_0\Omega_K}\frac{\partial}{\partial\varpi_0}\left(\varpi_0^2\Omega_K\delta\mu_s\right)\right). \tag{14.211}$$

Noting that (14.95), (14.98) and (14.130) for $\dot{M}$, Σ_s and $\nu\Sigma_s$ give

$$\frac{\nu_{sd}}{\varpi_0|v_{\varpi c}|_{sd}} = IN_p\tan(i_s)_{sd}\frac{h}{\varpi_0} \ll 1, \tag{14.212}$$

it follows that the second term in (14.211) is small relative to the first, so the equation reduces to

$$\frac{\partial}{\partial t}(\delta\mu_{\rm s}) - \frac{17}{14}\frac{I_2}{I_1}\frac{\nu_{\rm sd}}{\varpi_0|v_{\varpi{\rm c}}|_{\rm sd}}\varpi_0\frac{\partial}{\partial\varpi_0}\left(\frac{\partial}{\partial t}(\delta\mu_{\rm s})\right)$$
$$= \frac{45}{7}\frac{\nu_{\rm sd}}{\varpi_0}\left[\left(1+\frac{17}{45}\frac{I_1}{I_2}\tilde{U}\right)\frac{\partial}{\partial\varpi_0}(\delta\mu_{\rm s}) + \frac{2}{3}\varpi_0\frac{\partial^2}{\partial\varpi_0^2}(\delta\mu_{\rm s})\right], \tag{14.213}$$

where

$$\tilde{U} = \frac{\varpi_0|v_{\varpi{\rm c}}|_{\rm sd}}{\nu_{\rm sd}}U. \tag{14.214}$$

This equation describes the evolution of $\delta\mu_{\rm s}$ and it incorporates perturbations to the viscous and magnetic torques, including the effects of poloidal magnetic field bending due to changes in $|v_{\varpi{\rm c}}|$ and η. Perturbations in the thermal balance are accounted for, including viscous and magnetic dissipations and coupling of the radial and vertical structures.

The field bending instability of Lubow et al. (1994), discussed in Sect. 14.6.1, resulted because a positive perturbation in $|v_{\varpi{\rm c}}|$ caused an increase in the bending of the poloidal magnetic field, via the advection term in the induction equation. This lowers the sonic point which leads to an increase in the wind mass flux and hence an increase in the angular momentum loss rate. Consequently $|v_{\varpi{\rm c}}|$ is further increased and so instability results. However this analysis neglects perturbations to the thermal balance and the dependence of η on $T_{\rm c}$ and h. The foregoing analysis allows for these effects.

Firstly, the global stability is considered, with $\delta\mu_{\rm s}$ varying on a length-scale of $\sim\varpi_0$. The second term in (14.213) is then small relative to the first and hence the equation reduces to

$$\frac{\partial}{\partial t}(\delta\mu_{\rm s}) = \frac{45}{7}\frac{\nu_{\rm sd}}{\varpi_0}\left[\left(1+\frac{77}{45}\frac{I_1}{I_2}\tilde{U}\right)\frac{\partial}{\partial\varpi_0}(\delta\mu_{\rm s}) + \frac{2}{3}\varpi_0\frac{\partial^2}{\partial\varpi_0^2}(\delta\mu_{\rm s})\right]. \tag{14.215}$$

The unperturbed viscous coefficient can be expressed as

$$\nu_{\rm sd} = \frac{3}{2}N_{\rm p}\frac{N_\alpha}{K^3}\left(\frac{h}{\varpi_0}\right)^2_{\rm sd}\varpi_0^2\Omega_{\rm K}. \tag{14.216}$$

The perturbation $\delta\mu_{\rm s}$ can be written as

$$\delta\mu_{\rm s} = q(\varpi_0)e^{\sigma t}, \tag{14.217}$$

where σ is a constant, which in general is complex. Using this and (14.216) in (14.215) yields

$$x\frac{d^2q}{dx^2} + a\frac{dq}{dx} - b\sigma x^{\frac{1}{2}}q = 0, \tag{14.218}$$

with $x = \varpi_0/R$,

$$a = \frac{3}{2}\left(1 + \frac{17}{45}\frac{I_1}{I_2}\tilde{U}\right) \tag{14.219a}$$

and

$$b = \frac{7}{45}\frac{1}{N_\mathrm{p}}\frac{K^3}{N_\alpha}\left(\frac{\varpi_0}{h}\right)^2_{\mathrm{sd}}\left(\frac{R^3}{GM}\right)^{\frac{1}{2}}. \tag{14.219b}$$

Equation (14.218) can be written as

$$\frac{d}{dx}\left(x^a\frac{dq}{dx}\right) - b\sigma x^{a-\frac{1}{2}}q = 0. \tag{14.220}$$

The inner and outer disc edges are at $x = 1$ and $x = x_\mathrm{D}$, with $x_\mathrm{D} \gg 1$. For homogeneous boundary conditions σ is real and perturbations will be stable for $\sigma < 0$. Multiplying (14.220) by q and integrating through the disc gives

$$b\sigma\int_1^{x_\mathrm{D}} x^{a-\frac{1}{2}}q^2dx = \left[x^a q\frac{dq}{dx}\right]_1^{x_\mathrm{D}} - \int_1^{x_\mathrm{D}} x^a\left(\frac{dq}{dx}\right)^2 dx. \tag{14.221}$$

The maintenance during perturbation of the standard conditions of $\mu_\mathrm{s} \to 0$ as $\varpi_0 \to R$ and $\mu_\mathrm{s} \to$ constant for $\varpi_0 \gg R$ gives $q(1) = 0$ and $q'(x_\mathrm{D}) = 0$, so

$$\sigma = -\frac{1}{b}\left[\int_1^{x_\mathrm{D}} x^a\left(\frac{dq}{dx}\right)^2 dx\right]\left[\int_1^{x_\mathrm{D}} x^{a-\frac{1}{2}}q^2dx\right]^{-1}. \tag{14.222}$$

This gives $\sigma < 0$, and hence stability.

The differential equation (14.218) for the radial dependence of the perturbation $\delta\mu_\mathrm{s}$ can be solved analytically. Making the transformation

$$q(x) = x^\beta f(u) \quad \text{with} \quad u = cx^\gamma, \tag{14.223}$$

in (14.218), where β, γ and c are constants, leads to the equation

$$\frac{d^2f}{du^2} + \frac{1}{\gamma}(\gamma + 2\beta + a - 1)\frac{1}{u}\frac{df}{du} + \left[\frac{b|\sigma|u^{\frac{3}{2\gamma}-2}}{\gamma^2 c^{\frac{3}{2\gamma}}} + \frac{\beta(\beta + a - 1)}{\gamma^2u^2}\right]f = 0. \tag{14.224}$$

The choices

$$\gamma = \frac{3}{4}, \quad \beta = \frac{1}{2}(1-a) \quad \text{and} \quad c = \frac{4}{3}(b|\sigma|)^{\frac{1}{2}} \tag{14.225}$$

simplify (14.224) to

$$\frac{d^2 f}{du^2} + \frac{1}{u}\frac{df}{du} + \left(1 - \frac{w^2}{u^2}\right) f = 0, \tag{14.226}$$

where

$$w = \frac{2}{3}(a-1) \quad \text{and} \quad u = \frac{4}{3}(b|\sigma|)^{\frac{1}{2}} x^{\frac{3}{4}}. \tag{14.227}$$

This is Bessel's equation of order w, and hence it follows that the general solution is

$$q(x) = x^{-\frac{3}{4}w}[c_1 J_w(u) + c_2 Y_w(u)], \tag{14.228}$$

where J_w and Y_w are Bessel functions of the first and second kinds, while c_1 and c_2 are constants. It is noted that the solution applies in the disc region $1 < x < x_{\rm D}$, so the singularity in Y_w at $x = 0$ is excluded. When homogeneous boundary conditions are imposed at $x = 1$ and $x = x_{\rm D}$, a discrete set of eigenfunctions $q_n(x)$, with eigenvalues σ_n, result for the decay modes. The principal mode has a decay time of the order of the inflow time-scale through the disc, this being much longer than the dynamical and thermal time-scales.

The stability of short wavelength local perturbations can be investigated by expressing $\delta\mu_{\rm s}$ as

$$\delta\mu_{\rm s} = A e^{ik\varpi_0} e^{st}, \tag{14.229}$$

where A, k and s are constants, with $k\varpi_0 \gg 1$. The second term in (14.213) must now be retained, since it has a radial length-scale $\ll \varpi_0$. Substitution of (14.229) for $\delta\mu_{\rm s}$ in (14.213) yields $\sigma = \Re(s)$ as

$$\sigma = -\frac{30}{7}\frac{\nu_{\rm sd}}{\varpi_0^2}k^2\varpi_0^2\left[1 + \frac{51}{28}\left(\frac{I_2}{I_1} + \frac{17}{45}\tilde{U}\right)\frac{U}{\tilde{U}}\right]\left[1 + \left(\frac{17}{14}\frac{I_2}{I_1}\frac{U}{\tilde{U}}\right)^2 k^2\varpi_0^2\right]^{-1}, \tag{14.230}$$

showing that local perturbations are stable.

This quenching of the poloidal field bending instability can be understood by considering the connections between the perturbations. Equations (14.39), (14.43) and (14.46) for $\Omega_{\rm K}h/c_{\rm s}$, $B_{z{\rm s}}/B_{\varpi{\rm s}}$ and $v_{\varpi{\rm c}}$ enable the magnetic diffusivity to be

expressed as

$$\eta = \frac{2}{3}\frac{I^2K^3}{N_\alpha \Omega_\kappa} v_{\varpi c}^2 \tan^2 i_s, \tag{14.231}$$

and it follows that

$$\delta\eta = 2\frac{\eta_{sd}}{|v_{\varpi c}|_{sd}}\delta|v_{\varpi c}| + \frac{4\eta_{sd}}{\sin 2(i_s)_{sd}}\delta i_s. \tag{14.232}$$

Also, using (14.18) for η and (14.39) for $\Omega_\kappa h/c_s$ together with (14.231) to eliminate h and η yields

$$T_c = \frac{\mu}{\mathcal{R}}\frac{N_\alpha^2}{\epsilon^2} I^2 v_{\varpi c}^2 \tan^2 i_s \tag{14.233}$$

and hence

$$\delta T_c = 2\frac{(T_c)_{sd}}{|v_{\varpi c}|_{sd}}\delta|v_{\varpi c}| + 4\frac{(T_c)_{sd}}{\sin 2(i_s)_{sd}}\delta i_s. \tag{14.234}$$

For $\delta|v_{\varpi c}| > 0$ and $\delta i_s > 0$ (14.232) and (14.234) yield $\delta\eta > 0$ and $\delta T_c > 0$. This is consistent with a reduction in poloidal field bending due to an increase in η. Hence the field bending instability is quenched. The wind structure can adjust on a dynamical time-scale, with the Alfvén point position changing in response to a perturbation in the wind mass flux $\dot{m}$. The wind can adjust through quasi-steady states on the longer angular momentum adjustment time-scale.

The perturbation in η, which relieves poloidal field bending, results from the increases in temperature and disc height caused by the increased dissipation. Since the viscous dissipation is significantly larger than the magnetic dissipation, it is the presence of viscosity which mainly causes the increase in η due to the increase in T_c, and this quenches the field bending instability.

The foregoing analysis can be used to consider the purely magnetic case, for which the turbulent magnetic Prandtl number $N_p = 0$. Using (14.202) to eliminate the vertical equilibrium separation constant k_1 in the expression (14.145) for $\tan i_s$ and taking perturbations gives

$$\delta i_s = -\frac{7}{48}\sin 2(i_s)_{sd}\left(\frac{\delta|v_{\varpi c}|}{|v_{\varpi c}|_{sd}} + \frac{\delta\Sigma_s}{(\Sigma_s)_{sd}}\right). \tag{14.235}$$

Now $U = 1$, and $\nu = 0$, so the viscous terms vanish, and μ_s becomes $\mu_s = \eta\Sigma_s$. Then eliminating $\delta\mu_s$ between (14.207) and (14.208) yields

$$\frac{\delta\Sigma_s}{(\Sigma_s)_{sd}} = \frac{12}{17}\frac{\delta|v_{\varpi c}|}{|v_{\varpi c}|_{sd}}. \tag{14.236}$$

Using this to eliminate $\delta\Sigma_s$ in (14.235) leads to

$$\delta i_s = -\frac{1}{4}\sin 2(i_s)_{sd}\frac{\delta|v_{\varpi c}|}{|v_{\varpi c}|_{sd}}. \tag{14.237}$$

Hence $\delta|v_{\varpi c}| > 0$ gives $\delta i_s < 0$, corresponding to an increase in poloidal field bending. Equations (14.234) then yields $\delta T_c > 0$. Equation (14.170) for ρ_{sn} and (14.171) for $\dot{m}$ give

$$\dot{m} \propto \Sigma_s \exp\left[-\left(\frac{\Omega_K^2 h^2}{2a^2}\frac{\tan^2 i_s}{(3-\tan^2 i_s)}+\frac{1}{2}\right)\right]. \tag{14.238}$$

Then since $\delta\Sigma_s > 0$ and $\delta i_s < 0$, this gives $\delta\dot{m} > 0$ corresponding to instability. This result is in agreement with that of Lubow et al. (1994), despite their simplifying assumptions. However, since discs are turbulent, ν will not be ignorable and stability can result due to the effects of viscosity reducing the field bending effect.

14.7 Summary and Discussion

Observations strongly indicate that accretion discs have winds emanating from their surfaces, with enhanced mass loss from the inner region and collimation of the outer wind parallel to the spin axis of the disc. The foregoing analytic and numerical investigations show that, with a suitable magnetic field, centrifugally driven wind flows are possible. The flow passes through a slow magnetosonic point, then through an Alfvén point and a fast magnetosonic point. Provided that the Alfvén point is well beyond the slow point, disc angular momentum is effectively removed and this makes a significant contribution to driving the disc inflow. The slow magnetosonic point and the sonic point are then essentially coincident. Beyond the Alfvén surface the wind becomes collimated parallel to the disc spin axis, consistent with the observations.

The MHD equations, describing the disc and wind structures, can naturally incorporate an $\alpha\Omega$-type disc dynamo to generate a suitable magnetic field. The combined magnetic and viscous torques lead to inflow speeds that are sufficient to give the required poloidal field bending for effective wind launching, but still remain subsonic.

The matching of the disc angular velocity with the stellar rotation rate at the stellar surface leads to a local modification of the disc-wind structure. Poloidal magnetic field bending increases as the star is approached and an enhanced wind mass loss rate occurs over a narrow region in the inner part of the disc. This could explain the increased mass loss rates observed from the inner regions of discs.

Viscosity plays important roles in partly driving the inflow and in quenching the field bending disc-wind instability which occurs in disc models having the inflow driven purely by magnetic wind torques.

References

Blandford, R. D., Payne, D. G., 1982, MNRAS, 199, 883.
Campbell, C.G., 1999, MNRAS, 310, 1175.
Campbell, C. G., 2001, MNRAS, 323, 211.
Campbell, C. G., 2003, MNRAS, 345, 123.
Campbell, C. G., 2005, MNRAS, 361, 396.
Campbell, C. G., 2010, MNRAS, 401, 177.
Campbell, C. G., 2014, GAFD, 108, 350.
Campbell, C.G., Papaloizou, J.C.B., Agapitou, V., 1998, MNRAS, 300, 315.
Cao, X., Spruit, H.C., 2002, A&A, 385, 289.
Casse, F., Keppers, R., 2002, ApJ, 581, 988.
Cordova, F. A., Mason, K. O., 1982, ApJ, 260, 716.
Dhillon, V. S., Rutten, R. G. M., 1995, MNRAS, 277, 777.
Ferreira, J., 1997, A&A, 319, 340.
Fender, R. P., Gallo, E., Jonker, P., 2003, MNRAS, 343, L99.
Fendt, C., Cemeljic, M., 2002, A&A, 395, 1045.
Froning, C. S., Long, K. S., Knigge, C., 2003, ApJ, 584, 433.
Heap, S. R., et al., 1978, Nature, 275, 385.
Heyvaerts, J., Norman, C., 1989, ApJ, 347, 1055.
Honeycutt, R. K., Schlegal, E. M., Kaitchuck, R. H., 1986, ApJ, 302, 388.
Knigge, K., Long, K. S., Blair, W. P., Wade, R. A., 1997, ApJ, 476, 291.
Li, Z., 1995, ApJ, 444, 848.
Long, K. S., Knigge, C., 2002, ApJ, 579, 725.
Long, K. S., Mauche, C. W., Raymond, J. C., Szkody, P., Mattei, J. A., 1996, ApJ, 469, 841.
Lubow, S., Papaloizou, J.C.B., Pringle, J.E., 1994, MNRAS, 268, 1010.
Mauche, C. W., et al., 1994, ApJ, 424, 347.
Migliari, S., Fender, R. P., 2006, MNRAS, 366, 79.
Murray, N., Chiang, J., 1996, Nature, 382, 789.
Ogilvie, G.I., 1997, MNRAS, 288, 63.
Ogilvie, G. I., Livio, M., 2001, ApJ, 553, 158.
Ouyed, R., Pudritz, R. E., 1997a, ApJ, 482, 712.
Ouyed, R., Pudritz, R. E., 1997b, ApJ, 484, 794.
Ouyed, R., Pudritz, R. E., 1999, MNRAS, 309, 233.
Pelletier, G., Pudritz, R.E., 1992, ApJ, 394, 117.
Pudritz, R.E., Ouyed, R., Fendt, C., Brandenburg, A., 2007, in Protostars and Planets, Tucson, p277.
Rekowski, M.V., Rudiger, G., Elstner, D., 2000, A&A, 358, 813.
Reyes-Ruiz, M., 2000, MNRAS, 319, 1039.
Rothstein, D.M., Lovelace, R.V.E., 2008, ApJ, 677, 1221.
Sheikhnezami, S., Fendt, C., Porth, O., Vaidya, B., Ghanbari, J., 2012, ApJ, 757, 65.
Stepanovs, D., Fendt, C., 2014, ApJ, 793, 31.
Stone, J.M., Norman, M.L., 1994, ApJ, 433, 746.
Tzeferacos, P., Ferrari, A., Mignone, A., Zanni, C., Bodo, G., Massaglia, S., 2009, MNRAS, 400, 820.
von Rekowski, B., Brandenburg, A., Dobler, W., Shukurov, A., 2003, A&A, 398, 825.
Zanni, C., Ferrari, A., Rosner, R., Bodo, G., Massaglia, S., 2007, A&A, 469, 811.

Appendix A

A.1 Physical Constants and Solar Parameters

Speed of light $c = 2.998 \times 10^8\,\mathrm{m\,s^{-1}}$
Electron charge $e = 1.602 \times 10^{-19}\,\mathrm{C}$
Electron mass $m_\mathrm{e} = 9.109 \times 10^{-31}\,\mathrm{kg}$
Proton mass $m_\mathrm{p} = 1.673 \times 10^{-27}\,\mathrm{kg}$
Boltzmann constant $k = 1.381 \times 10^{-23}\,\mathrm{J\,K^{-1}}$
Gas constant $\Re = 8.314 \times 10^3\,\mathrm{m^2\,s^{-2}\,K^{-1}}$
Stefan-Boltzmann constant $\sigma_\mathrm{B} = 5.669 \times 10^{-8}\,\mathrm{J\,K^{-4}\,m^{-2}\,s^{-1}}$
Gravitational constant $G = 6.67 \times 10^{-11}\,\mathrm{N\,m^2\,kg^{-2}}$
Permittivity of free space $\epsilon_0 = 8.854 \times 10^{-12}$ farad $\mathrm{m^{-1}}$
Permeability of free space $\mu_0 = 4\pi \times 10^{-7}$ henry $\mathrm{m^{-1}}$
Solar mass $M_\odot = 1.989 \times 10^{30}\,\mathrm{kg}$
Solar radius $R_\odot = 6.960 \times 10^8\,\mathrm{m}$
Solar luminosity $L_\odot = 3.90 \times 10^{26}\,\mathrm{J\,s^{-1}}$

A.2 Vector Identities

$$\mathbf{E} \times (\mathbf{F} \times \mathbf{G}) = (\mathbf{E} \cdot \mathbf{G})\mathbf{F} - (\mathbf{E} \cdot \mathbf{F})\mathbf{G}. \tag{A1}$$

$$\nabla(\mathbf{F} \cdot \mathbf{G}) = (\mathbf{F} \cdot \nabla)\mathbf{G} + (\mathbf{G} \cdot \nabla)\mathbf{F} + \mathbf{F} \times (\nabla \times \mathbf{G}) + \mathbf{G} \times (\nabla \times \mathbf{F}). \tag{A2}$$

$$\nabla \cdot (\Psi\mathbf{F}) = \Psi\nabla \cdot \mathbf{F} + \mathbf{F} \cdot \nabla\Psi. \tag{A3}$$

$$\nabla \cdot (\mathbf{F} \times \mathbf{G}) = \mathbf{G} \cdot (\nabla \times \mathbf{F}) - \mathbf{F} \cdot (\nabla \times \mathbf{G}). \tag{A4}$$

C. G. Campbell, *Magnetohydrodynamics in Binary Stars*, Astrophysics and Space Science Library 456, https://doi.org/10.1007/978-3-319-97646-4

$$\nabla \times (\Psi \mathbf{F}) = \Psi \nabla \times \mathbf{F} + (\nabla \Psi) \times \mathbf{F}. \tag{A5}$$

$$\nabla \times (\mathbf{F} \times \mathbf{G}) = (\mathbf{G} \cdot \nabla)\mathbf{F} - (\mathbf{F} \cdot \nabla)\mathbf{G} + \mathbf{F}\nabla \cdot \mathbf{G} - \mathbf{G}\nabla \cdot \mathbf{F}. \tag{A6}$$

$$\nabla \times (\nabla \times \mathbf{F}) = \nabla(\nabla \cdot \mathbf{F}) - \nabla^2 \mathbf{F}. \tag{A7}$$

A.3 Operators in Orthogonal Coordinates

A.3.1 Spherical Polar Coordinates

$$\mathbf{B} = B_r \hat{\mathbf{r}} + B_\theta \hat{\boldsymbol{\theta}} + B_\phi \hat{\boldsymbol{\phi}}. \tag{A8}$$

$$\nabla \Psi = \frac{\partial \Psi}{\partial r}\hat{\mathbf{r}} + \frac{1}{r}\frac{\partial \Psi}{\partial \theta}\hat{\boldsymbol{\theta}} + \frac{1}{r \sin\theta}\frac{\partial \Psi}{\partial \phi}\hat{\boldsymbol{\phi}}. \tag{A9}$$

$$\nabla \cdot \mathbf{B} = \frac{1}{r^2}\frac{\partial}{\partial r}\left(r^2 B_r\right) + \frac{1}{r \sin\theta}\frac{\partial}{\partial \theta}(\sin\theta B_\theta) + \frac{1}{r \sin\theta}\frac{\partial B_\phi}{\partial \phi}. \tag{A10}$$

$$(\nabla \times \mathbf{B})_r = \frac{1}{r \sin\theta}\left[\frac{\partial}{\partial \theta}(\sin\theta B_\phi) - \frac{\partial B_\theta}{\partial \phi}\right], \tag{A11}$$

$$(\nabla \times \mathbf{B})_\theta = \frac{1}{r \sin\theta}\frac{\partial B_r}{\partial \phi} - \frac{1}{r}\frac{\partial}{\partial r}(r B_\phi), \tag{A12}$$

$$(\nabla \times \mathbf{B})_\phi = \frac{1}{r}\frac{\partial}{\partial r}(r B_\theta) - \frac{1}{r}\frac{\partial B_r}{\partial \theta}. \tag{A13}$$

A.3.2 Cylindrical Coordinates

$$\mathbf{B} = B_\varpi \hat{\boldsymbol{\varpi}} + B_\phi \hat{\boldsymbol{\phi}} + B_z \hat{\mathbf{z}}. \tag{A14}$$

$$\nabla \Psi = \frac{\partial \Psi}{\partial \varpi}\hat{\boldsymbol{\varpi}} + \frac{1}{\varpi}\frac{\partial \Psi}{\partial \phi}\hat{\boldsymbol{\phi}} + \frac{\partial \Psi}{\partial z}\hat{\mathbf{z}}. \tag{A15}$$

$$\nabla \cdot \mathbf{B} = \frac{1}{\varpi}\frac{\partial}{\partial \varpi}(\varpi B_\varpi) + \frac{1}{\varpi}\frac{\partial B_\phi}{\partial \phi} + \frac{\partial B_z}{\partial z}. \tag{A16}$$

$$(\nabla \times \mathbf{B})_{\varpi} = \frac{1}{\varpi}\frac{\partial B_z}{\partial \phi} - \frac{\partial B_\phi}{\partial z}, \tag{A17}$$

$$(\nabla \times \mathbf{B})_{\phi} = \frac{\partial B_{\varpi}}{\partial z} - \frac{\partial B_z}{\partial \varpi}, \tag{A18}$$

$$(\nabla \times \mathbf{B})_{z} = \frac{1}{\varpi}\left[\frac{\partial}{\partial \varpi}(\varpi B_\phi) - \frac{\partial B_{\varpi}}{\partial \phi}\right]. \tag{A19}$$

A.4 Viscosity Expressions

A.4.1 Viscous Force in Vector Operator Form

Equation (2.121) for the viscous force density $\mathbf{F}_{\rm v}$ follows from the tensor expressions (2.117)–(2.119). These give

$$F_{{\rm v}i} = \frac{\partial}{\partial x_j}\left(\rho\nu\frac{\partial v_i}{\partial x_j}\right) + \frac{\partial}{\partial x_j}\left(\rho\nu\frac{\partial v_j}{\partial x_i}\right) - \frac{2}{3}\frac{\partial}{\partial x_i}(\rho\nu\nabla\cdot\mathbf{v}). \tag{A20}$$

The first term is

$$\frac{\partial}{\partial x_j}\left(\rho\nu\frac{\partial v_i}{\partial x_j}\right) = \frac{\partial}{\partial x_j}(\rho\nu)\frac{\partial v_i}{\partial x_j} + \rho\nu\frac{\partial^2 v_i}{\partial x_j \partial x_j} = (\nabla(\rho\nu)\cdot\nabla)\mathbf{v} + \rho\nu\nabla^2\mathbf{v}. \tag{A21}$$

The second term is

$$\begin{aligned}\frac{\partial}{\partial x_j}\left(\rho\nu\frac{\partial v_j}{\partial x_i}\right) =& \frac{\partial}{\partial x_j}\left(\frac{\partial}{\partial x_i}(\rho\nu v_j) - v_j\frac{\partial}{\partial x_i}(\rho\nu)\right)\\ =& \frac{\partial}{\partial x_i}\left(\frac{\partial}{\partial x_j}(\rho\nu v_j)\right) - \frac{\partial v_j}{\partial x_j}\frac{\partial}{\partial x_i}(\rho\nu) - v_j\frac{\partial}{\partial x_j}\left(\frac{\partial}{\partial x_i}(\rho\nu)\right)\\ =& \nabla[\nabla\cdot(\rho\nu\mathbf{v})] - (\nabla\cdot\mathbf{v})\nabla(\rho\nu) - (\mathbf{v}\cdot\nabla)\nabla(\rho\nu).\end{aligned} \tag{A22}$$

The last term in (A20) is a gradient, so its addition to the first two terms gives

$$\begin{aligned}\mathbf{F}_{\rm v} =& \rho\nu\nabla^2\mathbf{v} + \nabla\left(\nabla\cdot(\rho\nu\mathbf{v}) - \frac{2}{3}\rho\nu\nabla\cdot\mathbf{v}\right)\\ &+ (\nabla(\rho\nu)\cdot\nabla)\mathbf{v} - (\mathbf{v}\cdot\nabla)\nabla(\rho\nu) - (\nabla\cdot\mathbf{v})\nabla(\rho\nu).\end{aligned} \tag{A23}$$

Use of the vector (A6) then yields

$$\begin{aligned}\mathbf{F}_{\rm v} =& \rho\nu\nabla^2\mathbf{v} + \nabla\left(\nabla\cdot(\rho\nu\mathbf{v}) - \frac{2}{3}\rho\nu\nabla\cdot\mathbf{v}\right)\\ &+ \nabla\times[\mathbf{v}\times\nabla(\rho\nu)] - [\nabla^2(\rho\nu)]\mathbf{v}.\end{aligned} \tag{A24}$$

A.4.2 Rate of Strain Tensor in Cylindrical Coordinates

$$e_{\varpi\varpi} = \frac{1}{\varpi}\frac{\partial}{\partial\varpi}(\varpi v_\varpi), \quad e_{\varpi\phi} = \frac{1}{2}\left(\varpi\frac{\partial}{\partial\varpi}\left(\frac{v_\phi}{\varpi}\right) + \frac{1}{\varpi}\frac{\partial v_\varpi}{\partial\phi}\right),$$
$$e_{\varpi z} = \frac{1}{2}\left(\frac{\partial v_\varpi}{\partial z} + \frac{\partial v_z}{\partial\varpi}\right), \quad e_{\phi\phi} = \frac{1}{\varpi}\frac{\partial v_\phi}{\partial\phi},$$
$$e_{\phi z} = \frac{1}{2}\left(\frac{1}{\varpi}\frac{\partial v_z}{\partial\phi} + \frac{\partial v_\phi}{\partial z}\right), \quad e_{zz} = \frac{\partial v_z}{\partial z}. \tag{A25}$$

A.5 Orthogonal Functions

A.5.1 Bessel Functions

Bessel's equation is

$$\frac{d^2y}{dx^2} + \frac{1}{x}\frac{dy}{dx} + \left(1 - \frac{\nu^2}{x^2}\right)y = 0. \tag{A26}$$

For ν a non-integer the general solution is

$$y = AJ_\nu(x) + BJ_{-\nu}(x), \tag{A27}$$

where A and B are constants and $J_\nu(x)$ is a Bessel function of the first kind of order ν. For $\nu = n$, an integer, $J_n(x)$ and $J_{-n}(x)$ are linearly dependent. The general solution of (A26) in this case is

$$y = AJ_n(x) + BY_n(x), \tag{A28}$$

where $Y_n(x)$ is a Bessel function of the second kind, which is singular at $x = 0$.

The functions $J_n(x)$ are given by

$$J_n(x) = \sum_{m=0}^{\infty}\frac{(-1)^m}{m!(m+n)!}\left(\frac{x}{2}\right)^{n+2m}. \tag{A29}$$

This set of functions has the orthogonality relation

$$\int_0^a J_n\left(\frac{\alpha_m}{a}r\right)J_n\left(\frac{\alpha_l}{a}r\right)rdr = -\frac{a^2}{2}J_{n+1}(\alpha_m)J_{n-1}(\alpha_l)\delta_{ml}, \tag{A30}$$

where α_m and α_l are zeros of J_n.

Bessel functions of order $n+\frac{1}{2}$, where n is an integer, are expressible as

$$J_{n+\frac{1}{2}}(x) = (-1)^n \left(\frac{2}{\pi}\right)^{\frac{1}{2}} x^{n+\frac{1}{2}} \frac{d^n}{(xdx)^n}\left(\frac{\sin x}{x}\right). \tag{A31}$$

A.5.2 Associated Legendre Functions

The associated Legendre equation is

$$\frac{d^2y}{dx^2} - \frac{2x}{(1-x^2)}\frac{dy}{dx} + \left[\frac{l(l+1)}{(1-x^2)} - \frac{m^2}{(1-x^2)^2}\right] y = 0. \tag{A32}$$

Solutions, $P_l^m(x)$, finite at $x = \pm 1$ only occur for l and m as integers. The general solution is

$$y = AP_l^m(x) + BQ_l^m(x), \tag{A33}$$

where the second solution $Q_l^m(x)$ is singular at $x = \pm 1$.

Due to the form $l(l+1)$ in (A32), negative values of l lead to the same set of functions as positive values, so $l > 0$ is used. The functions P_l^{-m} and P_l^m are linearly dependent and the choice $P_l^{-m} = P_l^m$ can be made. Legendre functions, free of singularity, are given by

$$P_l^{|m|}(x) = \frac{(1-x^2)^{\frac{|m|}{2}}}{2^l l!}\left(\frac{d}{dx}\right)^{|m|+l}(x^2-1)^l, \tag{A34}$$

where $|m| \leq l$. Their orthogonality relation is

$$\int_{-1}^{1} P_l^{|m|}(x) P_n^{|m|}(x) dx = \frac{2}{(2l+1)}\frac{(l+|m|)!}{(l-|m|)!}\delta_{ln}. \tag{A35}$$

Spherical harmonics are defined as

$$Y_l^m(\theta,\phi) = P_l^{|m|}(\cos\theta)e^{im\phi}. \tag{A36}$$

Noting that $x = \cos\theta$ and using the operator L^2 defined by (2.203), gives

$$\begin{aligned} L^2 Y_l^m &= -\left[\frac{1}{\sin\theta}\frac{d}{d\theta}\left(\sin\theta\frac{dP_l^{|m|}}{d\theta}\right) - \frac{m^2}{\sin^2\theta}P_l^{|m|}\right]e^{im\phi} \\ &= -\left[(1-x^2)\frac{d^2P_l^{|m|}}{dx^2} - 2x\frac{dP_l^{|m|}}{dx} - \frac{m^2}{(1-x^2)}P_l^{|m|}\right]e^{im\phi} \\ &= l(l+1)P_l^{|m|}e^{im\phi}, \end{aligned} \tag{A37}$$

where the last equality follows from (A32). Hence Y_l^m obey the eigenvalue equation

$$L^2 Y_l^m = l(l+1)Y_l^m. \tag{A38}$$

It follows from (A35) and (A36) that spherical harmonics have the orthogonality relation on the unit sphere of

$$\int_{4\pi} Y_l^m Y_n^{-r} d\Omega = \frac{4\pi}{(2l+1)} \frac{(l+|m|)!}{(l-|m|)!} \delta_{ln}\delta_{mr}, \tag{A39}$$

where the differential solid angle $d\Omega = \sin\theta d\theta d\phi$.

A.6 Elliptic Integrals

Elliptic integrals of the first, second and third kinds are;

$$F(\phi, k) = \int_0^\phi \frac{d\alpha}{(1-k^2\sin^2\alpha)^{\frac{1}{2}}}, \tag{A40}$$

$$E(\phi, k) = \int_0^\phi (1-k^2\sin^2\alpha)^{\frac{1}{2}} d\alpha, \tag{A41}$$

$$\Pi(\phi, p, k) = \int_0^\phi \frac{d\alpha}{(1+p\sin^2\alpha)(1-k^2\sin^2\alpha)^{\frac{1}{2}}}. \tag{A42}$$

Complete elliptic integrals have $\phi = \pi/2$.

A.7 Gravitational Torque on a Spheroid

If the primary star is non-spherical, due to non-radial internal forces, then it will experience a torque resulting from interaction with the secondary's gravitational field. The simplest way of finding this torque is to calculate the torque a distorted primary exerts on the centre of mass of the secondary, and then use the fact that the gravitational torque on the primary is equal and opposite to this.

The case of distortion symmetric about an axis is considered. This principal axis is taken to be along the $\mathbf{e}_3$ direction. Figure A.1 shows a mass element in the primary at position $\mathbf{r}'$ relative to its centre of mass O. The centre of mass of the secondary is at P. The gravitational potential at P is

$$U = -\int_{M_p} \frac{Gdm}{(r^2+r'^2-2rr'\cos\theta')^{\frac{1}{2}}}. \tag{A43}$$

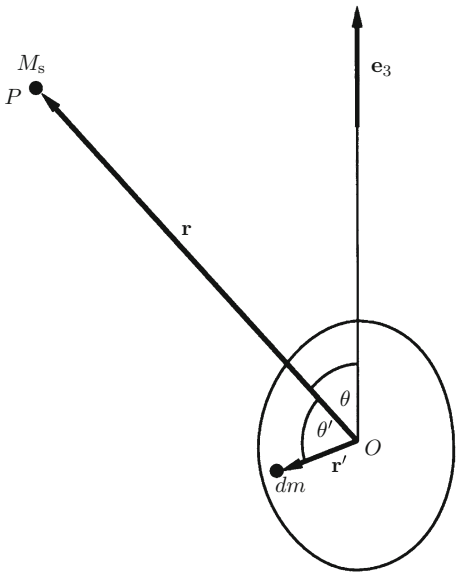

Fig. A.1 Coordinates for calculating the gravitational torque on the primary

This can be written as

$$U = -\frac{G}{r}\int_{M_p} \frac{dm}{[1 - 2(r'/r)\cos\theta' + (r'/r)^2]^{\frac{1}{2}}}. \tag{A44}$$

Since the orbital separation significantly exceeds the mean radius of the primary, it follows that $r'/r \ll 1$ in the above integrand over the range of integration. Binomial expansion of the integrand to second order in r'/r, noting that O is the primary's centre of mass, then enables the potential to be expressed as

$$U = -\frac{GM_p}{r} - \frac{G}{r^3}\left(I_O - \frac{3}{2}I\right), \tag{A45}$$

where

$$I_O = \int_{M_p} r'^2 dm, \qquad I = \int_{M_p} r'^2 \sin^2\theta' dm. \tag{A46}$$

I_O is the moment of inertia of the primary about O, while I is the moment of inertia about OP. It is simple to show that I_O is related to the principal moments of inertia by

$$I_O = \frac{1}{2}(I_1 + I_2 + I_3). \tag{A47}$$

For a symmetric body $I_1 = I_2 = I_\perp$, the moment of inertia about any axis in the equatorial plane. Hence

$$I_O = I_\perp + \frac{1}{2} I_3. \tag{A48}$$

The moment of inertia about OP can be written as

$$I = \lambda^2 I_1 + \mu^2 I_2 + \nu^2 I_3, \tag{A49}$$

where λ, μ and ν are the direction cosines of OP along the principal axes, given by

$$\lambda = \frac{x}{r}, \quad \mu = \frac{y}{r}, \quad \nu = \frac{z}{r}, \tag{A50}$$

taking the positive z-direction along $\mathbf{e}_3$. It follows that

$$I = I_\perp + (I_3 - I_\perp)\frac{z^2}{r^2}. \tag{A51}$$

Equations (A45), (A48) and (A51) give the potential as

$$U = -\frac{GM_\mathrm{p}}{r} - \frac{G(I_3 - I_\perp)}{2r^3} + \frac{3G(I_3 - I_\perp)}{2r^5} z^2. \tag{A52}$$

Since the gravitational force on M_s at P is $-\nabla U$, the torque exerted on the primary is

$$\mathbf{T}_\mathrm{g} = M_\mathrm{s} \mathbf{r} \times (\nabla U)_P. \tag{A53}$$

Noting that $z = r\cos\theta$, where θ is the angle between OP and $\mathbf{e}_3$, gives

$$\mathbf{T}_\mathrm{g} = M_\mathrm{s} \left(\frac{\partial U}{\partial \theta} \right)_P \hat{\mathbf{r}} \times \hat{\boldsymbol{\theta}}. \tag{A54}$$

The unit vector $\hat{\boldsymbol{\theta}}$ is related to $\mathbf{e}_3$ by

$$\sin\theta\, \hat{\boldsymbol{\theta}} = \cos\theta\, \hat{\mathbf{r}} - \mathbf{e}_3. \tag{A55}$$

The use of this and (A52) in (A54) yields

$$\mathbf{T}_\mathrm{g} = \frac{3GM_\mathrm{s}(I_3 - I_\perp)}{D^3} \cos\theta\, \hat{\mathbf{r}} \times \mathbf{e}_3, \tag{A56}$$

where D is the orbital separation.

Index

C. G. Campbell, *Magnetohydrodynamics in Binary Stars*, Astrophysics and Space Science Library 456, https://doi.org/10.1007/978-3-319-97646-4